Terms and Conditions of Use of Digitised Theses from Trinity College Library Dublin

Copyright statement

All material supplied by Trinity College Library is protected by copyright (under the Copyright and Related Rights Act, 2000 as amended) and other relevant Intellectual Property Rights. By accessing and using a Digitised Thesis from Trinity College Library you acknowledge that all Intellectual Property Rights in any Works supplied are the sole and exclusive property of the copyright and/or other IPR holder. Specific copyright holders may not be explicitly identified. Use of materials from other sources within a thesis should not be construed as a claim over them.

A non-exclusive, non-transferable licence is hereby granted to those using or reproducing, in whole or in part, the material for valid purposes, providing the copyright owners are acknowledged using the normal conventions. Where specific permission to use material is required, this is identified and such permission must be sought from the copyright holder or agency cited.

Liability statement

By using a Digitised Thesis, I accept that Trinity College Dublin bears no legal responsibility for the accuracy, legality or comprehensiveness of materials contained within the thesis, and that Trinity College Dublin accepts no liability for indirect, consequential, or incidental, damages or losses arising from use of the thesis for whatever reason. Information located in a thesis may be subject to specific use constraints, details of which may not be explicitly described. It is the responsibility of potential and actual users to be aware of such constraints and to abide by them. By making use of material from a digitised thesis, you accept these copyright and disclaimer provisions. Where it is brought to the attention of Trinity College Library that there may be a breach of copyright or other restraint, it is the policy to withdraw or take down access to a thesis while the issue is being resolved.

Access Agreement

By using a Digitised Thesis from Trinity College Library you are bound by the following Terms & Conditions. Please read them carefully.

I have read and I understand the following statement: All material supplied via a Digitised Thesis from Trinity College Library is protected by copyright and other intellectual property rights, and duplication or sale of all or part of any of a thesis is not permitted, except that material may be duplicated by you for your research use or for educational purposes in electronic or print form providing the copyright owners are acknowledged using the normal conventions. You must obtain permission for any other use. Electronic or print copies may not be offered, whether for sale or otherwise to anyone. This copy has been supplied on the understanding that it is copyright material and that no quotation from the thesis may be published without proper acknowledgement.

The stability of fully and partially embedded beam-columns in elastic Winkler foundations

by

Michael E. Heelis

B.A.

Thesis submitted to the University of Dublin, Trinity College,

for the Degree of Doctor of Philosophy.

July 1996

DECLARATION

The author hereby declares that this thesis, in whole or in part, has not been submitted to any other university as an exercise for a degree. Except where reference has been given in the text, it is entirely the author's own work.

The author confirms that the Library may lend or copy this thesis upon request, for academic purposes.

Michael E. Heelis

July 1996

ABSTRACT

The stability, in terms of the buckling load, of fully and partially embedded piles that are supported laterally along their embedded length by an elastic Winkler foundation is investigated. Exact solutions are presently available only for a few specific cases. This work describes the exact closed-form solution to the governing equations which is derived using four defining non-dimensional parameters. These parameters specify the homogenous nature of the soil (in terms of both soil stiffness and shaft friction), the degree by which the frictional force along the pile shaft reduces the load supported at the pile foot and the proportion of the pile which is unembedded in the supporting medium. With the algorithm developed it is possible to produce the exact solution for any combination of soil conditions, end boundary conditions, embedment ratio and degree of shaft friction supporting the applied load. In this manner, trends in buckling load and mode shape for each of these parametric variations are studied.

Solutions are then compared with the results found in the literature review. The published theoretical work comprises exact solutions and approximations. The published experimental work consists of scale model and full scale buckling load tests. It is found that the work in this thesis provides results which are identical to the exact solutions and can be used to test the approximate theoretical methods. Finally, the results from the proposed algorithm are shown to compare favourably with the experimental work.

ACKNOWLEDGEMENTS

This thesis is not exceptional, in one respect at least, in that there are a large number of people without whom either it would not have been possible, or it would not have been such an enjoyable task.

My heartfelt thanks go to Dr. Roger West, who initially introduced me to the concept of the buckling of piles and has provided injections of much needed enthusiasm whenever required. His experience in the field of modelling the dynamic behaviour of piles has been invaluable. The patience he has shown in the proof-reading the various drafts of this thesis has appeared limitless.

My parents, Philip and Mary, and my brother, Richard, have been supportive throughout, for which I would like to thank them. The friendly inquisition on the finer points of my project, whenever I returned home, kept me on my toes and their help has even extended to proof-reading my English grammar in parts of the final thesis. I would also like to thank my uncle, Howard Heelis, whom among others has helped in the translation of foreign literature.

I would like to express my thanks to all the members of the Department of Civil, Structural and Environmental Engineering for their friendly help, especially Prof. Simon Perry and Chris O'Donovan.

I would like to mention Dr. Damien Keogh, Andrew Morris, Anthony Dempsey, Tracey Kearney and Susanne O'Brien, who are all or were post-graduates in the Civil Department. I wish them well in their chosen careers, and have great expectations that they all will excel in their respective fields.

Lastly, as a visitor to Ireland, I would like to thank the College Manor posse, especially Tricia, Ruth, Brendan and Mary-Teresa, as well as the members, past and present, of the Trinity Hockey club, for their fine introduction to Irish life. In this respect, I would also like to express my thanks to Arthur G. for helping me get through the hard times, well the sober ones at least.

Table of Contents

List of Figures

List of Tables

Principal Notation

A_i	constants of integration, $0 \leq i \leq 3$ unembedded beam $4 \leq i \leq 7$ embedded beam
$\underline{\mathbf{A}}$	vector of constants of integration
EI	beam/pile flexural rigidity/stiffness
E_s	Young's modulus of elasticity of soil
F	non-dimensional soil stiffness homogeneity factor
f_1 and f_2	non-dimensional shaft friction homogeneity factor at depth l_1 and l_2 respectively
k and k(x)	modulus of subgrade reaction; Winkler spring stiffness
k_1 and k_2	Winkler spring stiffness at depth l_1 and l_2 respectively
l	length of pile/beam
l_1 and l_2	unembedded and embedded length of pile/beam
M	bending moment
M	matrix of transcendental coefficients
n_h	rate of change of subgrade reaction with depth
P	applied axial force
p(x)	force per unit area
P_{cr}	critical buckling load
P_E	critical Euler buckling load, $\pi^2 EI/l^2$
Q	shear force
Q_b and Q_s	base and shaft bearing capacity
$S(\beta, \lambda)$	sign count

$w(x)$	deflection
x	Cartesian co-ordinate; origin at interface between regions
x'	Cartesian co-ordinate; origin at pile head
y	Cartesian co-ordinate of lateral movement
Y_i	function of the solution to the defining differential equation
β	non-dimensional axial load
δ	embeddment ratio, l_2/l
γ	non-dimensional soil stiffness factor
ζ	non-dimensional co-ordinate of x'
θ	non-dimensional buckling load P_{cr}/P_E
λ	non-dimensional soil stiffness $\left(k_2 l^4 / EI\right)^{1/2}$
$\lambda_{average}$	non-dimensional factor of average soil stiffness $\left(\left(k_1 + k_2\right) l^4 / 2EI\right)^{1/2}$
μ	non-dimensional end-bearing factor $P(x' = 0)/P(x' = 1)$
ξ	non-dimensional co-ordinate of x
τ_s	shaft friction per unit area

Note

The correct term for the member embedded in the supporting media is a 'beam-column' as both lateral and axial forces are present. However, in most previous work the term 'beam' has been used and it is this term which will be used throughout this work.

Chapter 1

Introduction

The concept of the use of piles in supporting structures is a very simple one. If the overlying soil stratum onto which a structure is to be built is weak, then some form of load transfer to a stronger medium below is required. The simplest solution is some form of column transferring loads to the underlying material. This is, in essence, a pile.

Timber piles have been used since before the Romans occupied Britain. In the Bronze Age artificial islands, or crannógs, were built with the use of wooden piles embedded in the lake bottom. The use of wooden piles extends to the mediaeval times when the cathedrals in East Anglia were built. The carrying capacity of timber piles is limited by the width of the trees from which they originate and the strength of a natural material to withstand the forces applied to it.

In recent times, as fabrication techniques have improved and the supported loads increased, the use of concrete and steel piles has become widespread. Due to the compressive nature of the loads applied to a pile, concrete is an ideal medium to use, especially as it is now possible to cast such piles in-situ by drilling. Such construction techniques are very suitable where noise and vibration have to be avoided as is often the case in congested urban development. Steel piles can withstand better the forces produced by hammering and so make good general purpose piles. They can also be fabricated in a large variety of sizes. Increasingly micropiles are being used in the preservation of historic structures where the original foundation requires strengthening.

The problem this thesis will address is the calculation of the buckling capacity of piles. Presently the only exact solutions available are those proposed by Heténvi (1946) who solved for the problem of piles which are axially loaded at their extremities and are fully embedded in a Winkler foundation with constant soil stiffness with depth. Unfortunately, piles are equally likely to be embedded in a non-homogeneous medium, and there has been a large amount of research into the shaft friction produced in a pile when a load is applied. This friction means that it is unreasonable to assume all the applied load is transferred to the pile toe. It will be shown that shaft friction affects the buckling load of a pile considerably and that there is no simple rule of thumb available which allows for a pile which is only partially embedded into a supporting medium.

Initially, a literature review of related works in the field will be presented. It will be shown that a pile in a soil may be modelled as an Euler beam resting in a Winkler foundation, and that the

use of more complicated soil models are not applicable to the problem under investigation. The use of such models require more than one parameter in order to define the response of the soil in the model and the realistic evaluation of such soil parameters from measurements on real soils is extremely difficult. It will be shown that even for the most basic of parameters, the soil stiffness, there are many different suggested methods of calculation. Hence, the model chosen for this thesis is that of a Euler beam in an elastic Winkler foundation.

The formal analysis of the model chosen will be outlined in the following chapter, Chapter 3. A differential equation is derived which, in general, describes the buckling behaviour of a pile fully or partially embedded in an homogeneous or non-homogeneous elastic Winkler foundation with any combination of support from pure (uniform or linearly varying) friction to entirely end-bearing. The exact solution to this will allow for any pile extremity fixity conditions. The solution to this fourth order differential equation is in the form of an infinite power series solution which is defined by a recurrence relation. The recurrence relation will be formed for two cases. The first is the problem of a pile where the axial forces are applied at the upper and lower extremes. The second case is when the load applied at the top may be supported not only by a force at the bottom of the pile but also by an axial friction along the pile shaft. The problem can then be described by an 8x8 matrix (or in the case of fully embedded piles, a 4x4 matrix) for which the eigenvalues and eigenvectors must be calculated.

A parametric analysis of fully embedded beams is presented in Chapter 4. Initially the results for end-bearing piles in homogeneous soils are compared to the trigonometric/hyperbolic solution suggested by Hetényi (1946). A method of predicting where consecutive buckling modes approach each other is discussed. Unfortunately, the method cannot be applied to the subsequent problems. The lateral soil stiffness is allowed to vary with depth as is the case for some real soils (especially sands). The problem of a pile supported solely by shaft friction is then presented followed by a discussion on how the solution varies between these two extreme cases.

Chapter 5 concentrates on the variation of buckling load and mode shape as the proportion of the pile embedded in the supporting medium is varied. This variation is bounded by the Euler buckling problem, for an unsupported beam and the solution for fully embedded beams in the previous chapter.

A comparison with previous published work, discussed in Chapter 2, can be divided into several distinct sections. The first section comprises other 'exact' solutions. Some of these are solutions to part of the overall problem, for instance, Euler buckling and the solutions presented by Hetényi and Davisson. The results presented in this thesis are shown to be identical to these solutions. Several authors have solved the problems presented later in this thesis by making simplifying assumptions. The accuracy and validity of such assumptions will be discussed. Finally, the solution outlined in this thesis will be compared to the buckling loads of real piles presented by other authors. It will be shown that the technique of calculating the buckling load by neglecting the shaft friction and assuming a pinned end condition at the base of the pile, as outlined in some papers, is suspect and more accurate solutions can be produced using the previously outlined technique.

The final conclusions and suggestions for further work will be presented in Chapter 7.

Chapter 2

Literature Review

2.1. Introduction

The problem of beams and plates supported along their length on a deformable medium constitutes a major section in the field of structural mechanics especially when both static and dynamic solutions are taken into consideration. The design of railroad tracks, the modelling of the settlement of building foundations, earthquake response, impact response of jetties and wharves and the design of oil platforms are all relevant applications. An early discussion of such applications was presented by Hetényi (1966).

One of the more obvious structural applications is that of piles. Studies have taken one of two approaches, those of the geotechnical and those of the structural engineer. The geotechnical approach accepts that the imprecision of the properties of soils constrains the accuracy of any solution and so uses a more qualitative approach to the overall problem. The structural approach uses the idealised elements available to the mathematician in order to produce a complex solution to the problem, by which means the effects of changing specific conditions or parameters can be quantified. The structural engineer often introduces parameters which may make his mathematical model easier to describe and quantify, but which may have little relevance to that of the real problem. As will be shown later, the use of a two-parameter soil model may help to describe global soil reactions to deformations, however, the definition of even one parameter for soils is qualitative in nature and trying to relate more parameters to real soils is extremely difficult.

In this chapter the basic foundation models are presented first, followed by a study of the methods used by geotechnical engineers to determine soil parameters and to calculate the strength of pile foundations. The published works on the foundation models and their application in modelling soil-structure interaction effectively is then reviewed. This is followed by a discussion of the results of experiments that have been compared to theoretical buckling load capacities. The final conclusion outlines the model that will be used in this thesis. The relative merits and anticipated problems with the model will be presented.

2.2. Soil structure interaction models

The buckling behaviour of beams partially embedded in soils is the subject of this thesis. The nature of the mechanical interaction between the soil and the structure is of considerable importance. However, it should be noticed that, over the centuries, that there have been many models suggested for this interaction. They fall broadly into two categories:-

1. Mechanical models which consist of a variety of connected components such as springs, dashpots and beams.
2. Continuum models which consist of a three dimensional elastic medium with assumed-strain characteristics in order to simplify the problem.

2.2.1 Mechanical models

The simplest approach is to assume that the soil can be modelled by a series of discrete independent springs which deform in a Hookean manner, that is, that the deflection is proportional to the force applied.

That is, $$p(x) = k \cdot w(x) \qquad [2.2.1]$$

where p is the force applied per unit area (in N/m^2), w is the deflection (in m) and k is the modulus of subgrade reaction (in N/m^3).

This model was proposed in the early nineteenth century and discussed by Winkler (1867). It is based on an infinite Euler-Bernouilli beam (which is a beam which has no shear deformation and in which plane sections remain plane) resting on a series of springs. It is by far the simplest model possible and so produces straight forward solutions that have been used in theoretical work and engineering practice ever since.

The principal anomaly in the Winkler model arises due to the discrete nature of the springs. Outside the loaded area there is no deformation (figure 2.2.1). The lack of continuity in the soil at the end of the beam will be discussed later. It will be argued that the absence of such a force does not necessarily affect the validity in using the Winkler soil model for this particular application.

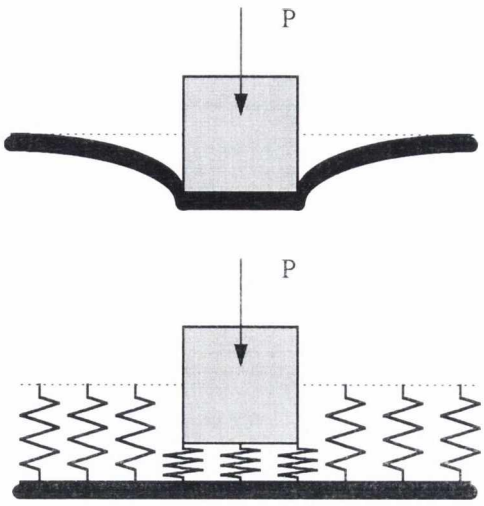

Figure 2.2.1. Real Soil and Winkler model under an applied load.

The first attempt to produce a model which could eliminate the anomalies in the Winkler model was made by Filonenko-Borodich (1940), who assumed that an elastic membrane was stretched across each spring of the Winkler model. This membrane was capable of resisting tensile stresses only, as shown in figure 2.2.2.

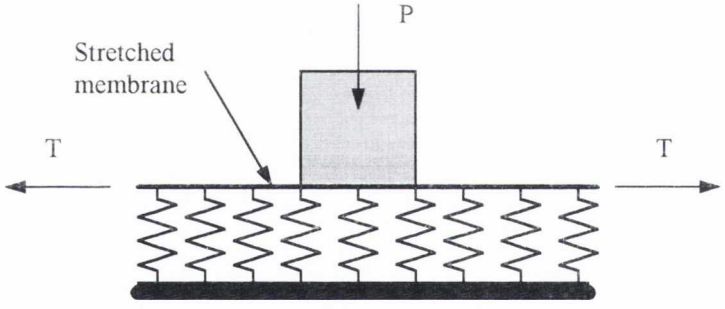

Figure 2.2.2. Filonenko-Borodich soil model.

The equation which describes this in a homogeneous and isotropic soil is,

$$p = k \cdot w - T\frac{d^2 w}{dx^2} \qquad [2.2.2]$$

where T is the tension, per unit width of the membrane (in N/m).

Hetényi (1946) proposed that the layer to produce the interaction between the springs should be achieved by the addition of an elastic plate with bending resistance only in the three dimensional case and an elastic beam in the two-dimensional case (figure 2.2.3). The equation governing this model is,

$$p = k \cdot w + D\frac{d^4 w}{dx^4} \qquad [2.2.3]$$

where $D = Eh^3 / 12(1-\nu^2)$ (in Nm), the flexural rigidity of the plate (E is the Youngs modulus of the plate, h, is the thickness of the plate and ν, is the Poisson's ratio of the plate).

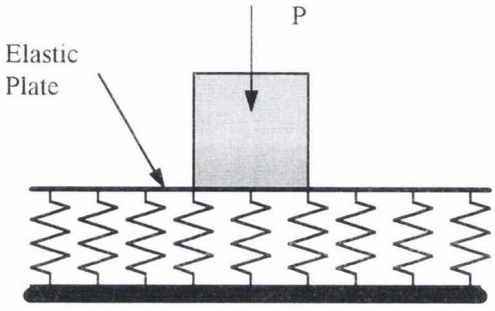

Figure 2.2.3. Hetényi soil model.

A similar model proposed by Pasternak (1954) replaced the plate with a beam which was vertically incompressible but showed a transverse shear stiffness (figure 2.2.4).

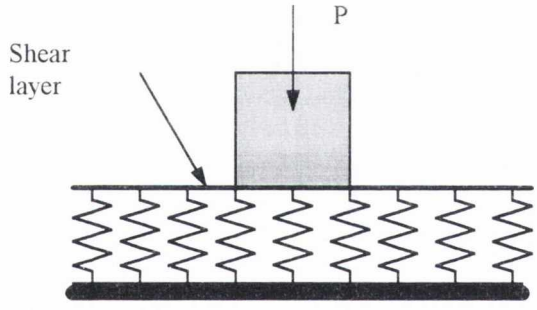

Figure 2.2.4. Pasternak soil model.

This led to the following equation relating deflection and applied load,

$$p(x,y) = k \cdot w(x,y) + G\nabla^2 w(x,y) \qquad [2.2.4]$$

where G is the shear modulus of the layer (in N/m).

Kerr (1961) extended the Pasternak model by the addition of an extra layer of springs between the shear layer and the structure. The response of this model (figure 2.2.5) is governed by

$$\left(1 + k/c\right)p - G/c\frac{d^2 p}{dx^2} = k \cdot w - G\frac{d^2 w}{dx^2} \qquad [2.2.5]$$

The extra spring elements eliminate undesirable edge effects in the Pasternak model.

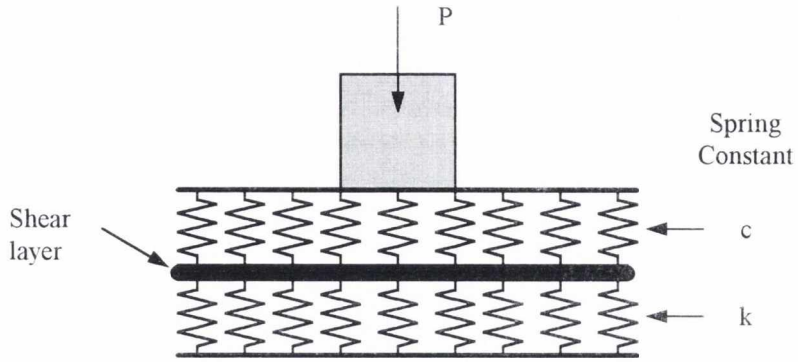

Figure 2.2.5. Kerr soil model.

Additional models have been put forward which incorporate dashpots to give a time dependence to the soil model. Examples of such models are the Viscous Pasternak (figure 2.2.6) and the Voigt-Pasternak (figure 2.2.7) models as described by Kerr (1964) and Selvadurai (1979). It should be noted that the application of such models is more relevant to the vibration of structures in a medium rather than the buckling problem, as there is no time dependence in the latter problem. The use of such models in the buckling problem would increase the complexity of any solution without adding additional information and, hence, is inappropiate.

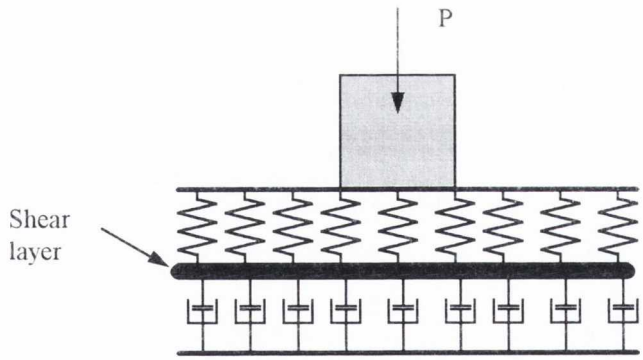

Figure 2.2.6. Viscous Pasternak soil model.

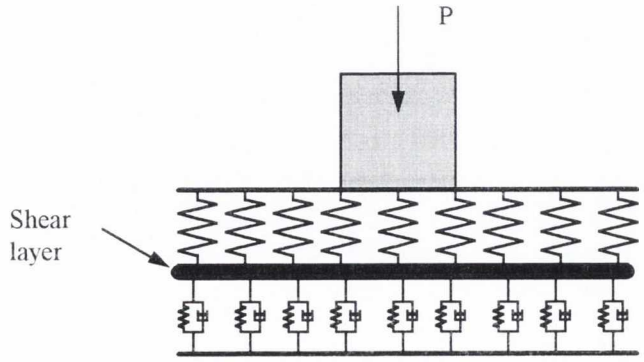

Figure 2.2.7. Voigt-Pasternak model.

2.2.2 Continuum models

The deflections which occur in the simple Winkler model are limited solely to the loaded area. Soils which are remotely cohesive and transmit shear forces clearly do not exhibit this behaviour. In order to produce a model which does exhibit this continuous behaviour, soil has been idealised as a three dimensional continuous elastic solid or elastic continuum.

Continuum models can be divided into two groups based on the assumptions which are applied to the nature of the stress-strain relationship of the medium. The groups are

1. isotropic materials
2. anisotropic materials

An isotropic material is one where the response is independent of the direction of the applied force. Only two properties are required to define its structural characteristics. They are the Young's modulus, E, and the Poisson ratio, ν.

Anisotropic materials have properties which are dependent on the direction of the applied load. In order to define its structural characteristics a total of 21 properties have to be defined (Selvadurai, 1979).

In soil mechanics, symmetry about the vertical axis is often assumed, as this reflects a homogeneous soil being deposited in layers. Five constants are required if this cross-anistropic criterion is met. Strictly, this is rarely the case because of the variations in soil properties with depth, but this simplification tends not to add significant computational error (Bowles, 1988).

The majority of the work in this area has been undertaken by considering isotropic materials, as the underlying mathematics is significantly simpler than other cases. Boussinesq (1885) found a solution for a concentrated load on the surface of an elastic half-space and from this it is possible to produce solutions for simple plates resting on elastic continua. However, the relevant work on the analysis of a two-dimensional beam makes use of the Flamant solution for a line load acting on a surface of a half plane (Timonshenko and Goodier, 1970). It is possible to solve for a distributed load on the half space but it produces a solution which does not give zero displacement at an infinite distance from the load and additional assumptions have to be made (Selvadurai, 1979).

Selvadurai details work on the use of anisotropic and orthotropic materials which is beyond the scope of this thesis. The simple case using an isotropic material produces a mathematical problem which is too complex to be of general use. Isotropic models all assume that the medium is homogeneous, that is, that the physical properties do not change according to their location in the medium. Soils tend to exhibit variations due to such considerations as overburden pressure and are, thus, termed heterogeneous or non-homogeneous. In order to analyse a continuum which can exhibit both anisotropy and heterogeneity it is necessary that some assumptions be made in order to simplify the mathematics concerned. Gibson (1967) used the assumption of incompressibility and a shear modulus which varied linearly with depth in order to produce a solution for a uniform surface load. In particular, when $\nu = 0.5$, he found that the response at the surface produced results which were identical to the behaviour shown by the Winkler model.

One of the earliest models was the Vlaslov (Vlaslov and Leontiev, 1956) foundation model, which assumed the existence of shear stresses in the continuum. The depth, H, in figure 2.2.8 is assumed to be large enough to approach semi-infinite conditions. The variation of deformation in the vertical direction is assumed a priori in order to produce a solution.

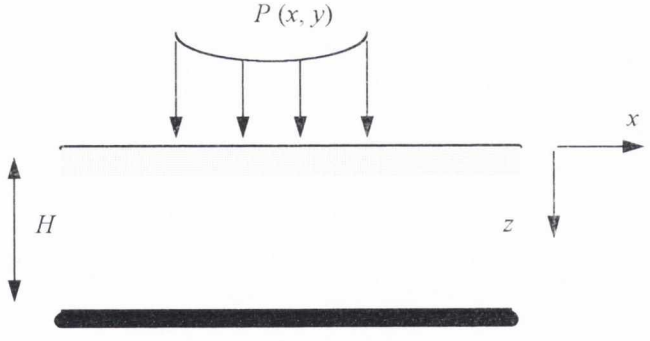

Figure 2.2.8. Vlaslov soil model.

In the simplest form the problem reduces to (Selvadurai, 1979),

$$p = k \cdot w - 2t\frac{d^2w}{dx^2} \qquad [2.2.6]$$

where $$k = \frac{E_0}{\left(1-\nu_0{}^2\right)}\int_0^H \left(\frac{dh}{dz}\right)^2 dz \text{ and } t = \frac{E_0}{4\left(1+\nu_0\right)}\int_0^H (h)^2\, dz \qquad [2.2.7], [2.2.8]$$

where $h(z)$ describes the variation of displacement in the y direction and E_0 and ν_0 are the Youngs modulus and Poisson ratio of the medium. The simplest suggested equation for h(z) is,

$$h(z) = \left(1 - \frac{z}{H}\right) \qquad [2.2.9]$$

which when substituted into equation [2.2.6] can be seen to provide similar displacements to Kerr's mechanical model. This work also establishes a relationship between k and the shape and rigidity of the beam. It was observed by Vlaslov and Leontiev (1966) that, as the ratio of the thickness of the elastic layer to the width of the loaded region decreases, the surface deflection profile closely resembles that obtained for the Winkler model.

Reissner (1936) assumed that in-plane stresses were negligible in the Reissner model which considerably simplified the mathematics involved. However it gives physically non-realistic results within the foundation. The results for surface response was,

$$p = C_1 w - C_2 \frac{d^2 w}{dx^2} + C_2 \Big/ 4C_1 \frac{d^2 P}{dx^2} \qquad [2.2.10]$$

It is clear that, for a constant or linear varying pressure, p, the Reissner model can be reduced to the Pasternak model.

Horvath (1983) modified the Reissner model by assuming that all non-vertical stresses were zero and using linear or square-root variations in soil modulus giving the Reissner Simplified Continuum Model. He suggested that this meant that the model could be simplified to a Winkler model with an equivalent Winkler Spring, the Winkler Type Simplified Continuum (WTSC) model. The WTSC model was rejected by Kerr (1985) on the basis that it does not reflect the actual problem as the WTSC represented a series of independent columns which no longer had any shear interaction between them.

However, perhaps the most important point arising from the discussion of all the continuum models is that they can all be realistically simplified to the Winkler model or the more physically realistic but more complex Kerr model. The Kerr model also incorporates the Pasternak model.

Kneifati (1985) compared the Winkler, Pasternak, Kerr and Elastic continuum models, the latter being solved by the use of finite elements (figure 2.2.9). The conclusion reached was that the Kerr model most closely approximated the continuum model, but that for deflections and pressure curves, Winkler and Pasternak were good approximations.

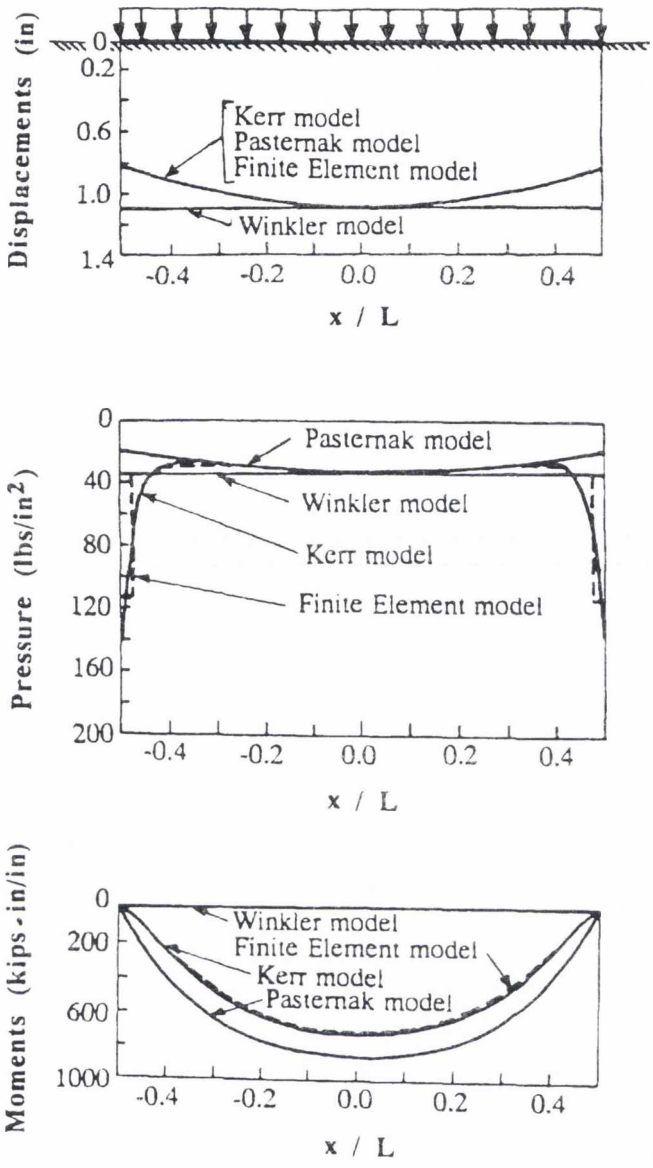

x/L is a non-dimensional length parameter

Figure 2.2.9. Deflection, moment and pressure plots for various soil models under a uniform load. (Kneifati, 1985).

2.2.3 Model variations

The simple Winkler model assumes identical response to both compressive and tensile forces. Clearly there are many applications where this does not apply, perhaps the most obvious being a beam resting on soil where the model does not allow for the separation of the beam and soil. The addition of such a condition is termed by Pavlović and Tsikkos (1981) as a quasi-Winkler foundation (figure

2.2.10) they conclude that the use of a Winkler model produces only moderate inaccuracies when the load is applied to a portion of the beam which deflects towards the foundation.

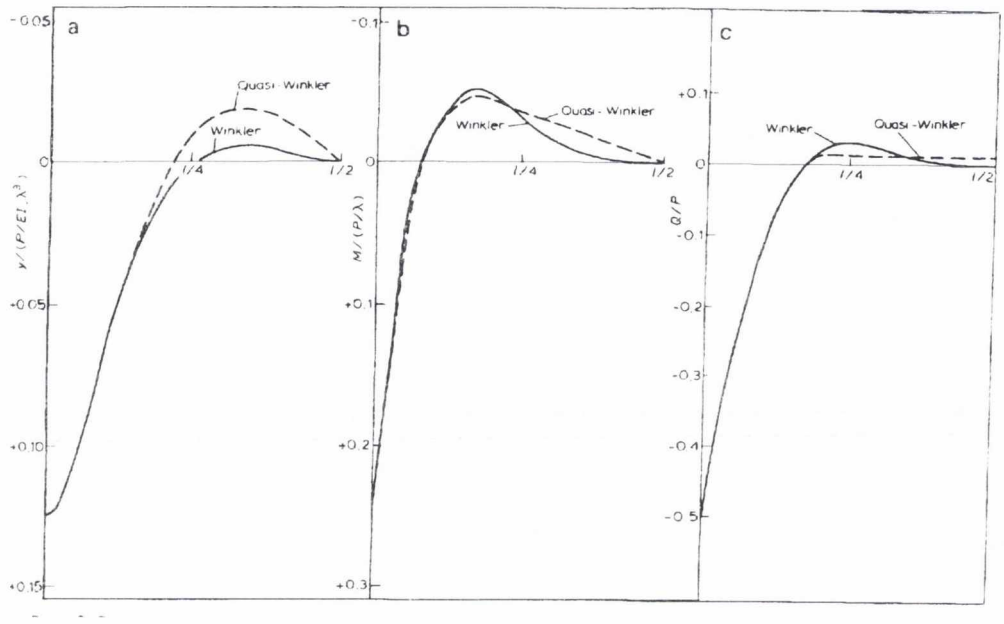

Figure 2.2.10. Results for a pinned-pinned beam with a central load (Pavlović and Tsikkos, 1982).

Beaufait and Hoadley (1980) suggest that the hyperbolic stress-strain relationship of a cohesive soil should be represented by a bi-linear curve and they produce a solution for a couple of particular examples. Since buckling loads are independant to the amplitude of the mode shape such a model will have limited relevance to the buckling problem in hand.

Yankelevsky and Eisenberger (1986) produced the formulation for an exact finite-element method by which means a variable piece-wise linear Winkler foundation can be modelled. This means that nodes are required only at the discontinuity in stiffness, loading or supports. However, this model does not appear to have been used in the buckling problem and like above is unlikely to be significant.

2.2.4 Conclusion

In the previous section the various soil models have been presented. They vary from the simple Winkler model to the elastic continuum model. It is now necessary to consider which soil model is the most relevant in the buckling problem to be considered. The elastic continuum model is the most complex and so it would be thought the more accurate. It is important not to confuse complexity with accuracy. The continuum model is based on a series of equations which structural engineers have suggested. In many cases these equations can be shown to model medium with a great

deal of accuracy, especially in the case of pure completely homogeneous solids such as steel. Its application to a medium, such as soil, which is full of voids, is suspect even before the effect of ground water is introduced to the model. Kerr (1985) describes the problems in relating the model parameters to the values produced by in-situ tests.

Two parameter models, as will be seen later, have problems in that the constants required to define such models are not always directly related to physical soil properties which can be measured in-situ or in the laboratory. The variations on the models have very limited applicability to the buckling problem as buckling loads are independent to the amplitudes of the mode shape and, hence, magnitude of soil displacements.

This leaves the simplest model of them all, the Winkler model. There are again problems in measuring a value for its sole parameter, k. However these problems are well known and have been discussed at length in journals since the first conception of the model. A review of these publications will be presented in the next section. The other main problem of the Winkler model is the lack of continuity at the boundaries of the loaded area. In the problem to be discussed this is not necessarily as large a problem as it first appears. At the top of a pile there is indeed a lack of continuity. The top normally coincides with the ground level above which there is only a gas, which will not provide a reaction to an applied displacement. Hence, the lack of continuity in lateral support is, in fact, required at this point.

The problem with continuity in lateral support at the bottom of the pile is more complicated and will be discussed in chapter 6 when the theoretical results are compared with real piles.

2.3. Soil Parameters

Fleming et al (1992) state that for most applications a simple linear analysis of horizontal reaction will be accurate. This can be achieved by the use of the Winkler model. However, a difficulty arises in the calculation of an appropriate k value for a particular soil. Comparisons between mechanical models and rigorous elastic analysis shows that k depends not only on soil properties but also on pile stiffness and the eccentricity of applied loads. The problems in relating results from geotechnical tests to the parameters for geotechnical models are discussed in West (1991) and are summarised here. In addition, the problem of relating the action of pile groups with the action of each individual pile in the group has to be achieved by empirical methods when using simple linear analysis.

Kerr (1985) proposed that all methods of establishing any soil parameter tend to fall into one of four general categories.

1. The analytical results for the structure, like deflection or bending moments, based on the adopted simple foundation model are compared with corresponding test data.
2. The analytical results based on the adopted foundation model are compared with the corresponding analytical results for which the base model is the elastic continuum model.
3. Using in-situ plate tests is another option. The results have to take into account scaling factors when the test represents larger footings or mat foundations. These factors can also be affected by the relative size and properties of the soil layers on which they are performed.
4. The foundation response expressions and the parameters, are derived directly from the equation of a continuum, by introducing simplifying assumptions. Kerr (1985) proposed that these assumptions tend to invalidate the results obtained because the results are dependent on the assumptions used rather than the reaction of the elastic continuum.

There has been considerable work on all these methods. The first can only be used in one-off situations and so does not lead to any general results from which trends of behaviour can be expressed. The second and fourth methods are of little practical use as they compare one model with another. It has already been seen that the use of the elastic continuum model is suspect in the field of

geotechnics. This leaves the third method as the only practical method of relating real geotechnical tests and data to a proposed model.

2.3.1 The coefficient of horizontal subgrade reaction, k

The Winkler model in particular and, subsequently, all other mechanical models, require the evaluation of k_s, the coefficient of horizontal subgrade reaction. Terzaghi (1955) defined this as the ratio between p, the pressure per unit area at the surface contact between a loaded beam and the subgrade onto which it transfers load and the settlement, y, produced by the load applied at that point:

$$k_s = \frac{p}{y} \qquad [2.3.1]$$

Despite using the Winkler model as the subject of his book, Hetenyi does not mention any factors which determine the numerical value of the coefficient by which the model is defined. Terzaghi recognised that the fundamental assumptions behind the above equation were invalid. First the value of k_s tends to increase as the pressure applied increases. This means that there is a non-linear response between the structure and the soil. Up to approximately 50% of the ultimate bearing pressure of the subgrade, however, the value of k is approximately constant. Garassino et al (1976) instrumented test piles and derived fifth and sixth order polynomials for the slope and moment in the piles. This led to the curves in figure 2.3.1 which describe the soil modulus of elasticity, E_s, with respect to p and x. The lines plotted can be defined by $E_s = ax^n$, $1 < n < 1.2$, where a is a constant.

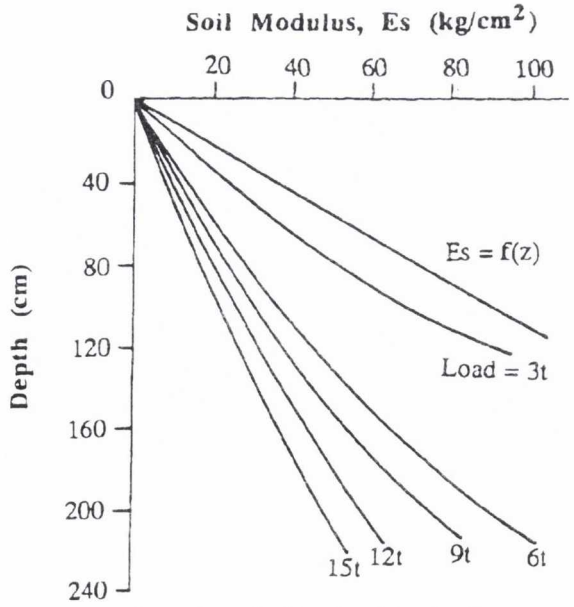

Figure 2.3.1. Variation of E_s with applied load and depth. (Garassino et al, 1976)

Terzaghi also related the value of k under a particular pressure to the size of the loaded area. Numerous authors have suggested that k varies with the width of the structure. Essenger (1893) and Terzaghi and Peck (1948) worked with rectangular areas, whereas Yoshida and Yoshinaka (1972) used the following plate shape function for arbitrary shaped plates (figure 2.3.2).

$$k = k_0 \left(\frac{B}{B_0} \right)^{-l} \qquad [2.3.2]$$

where B (in cm) is the diameter of the loading plate and k_0 is the subgrade reaction for a plate of standard diameter, B_0 (= 30 cm). The results from these plate tests are suspect especially when extrapolated to full-scale structures (Sutherland, 1974).

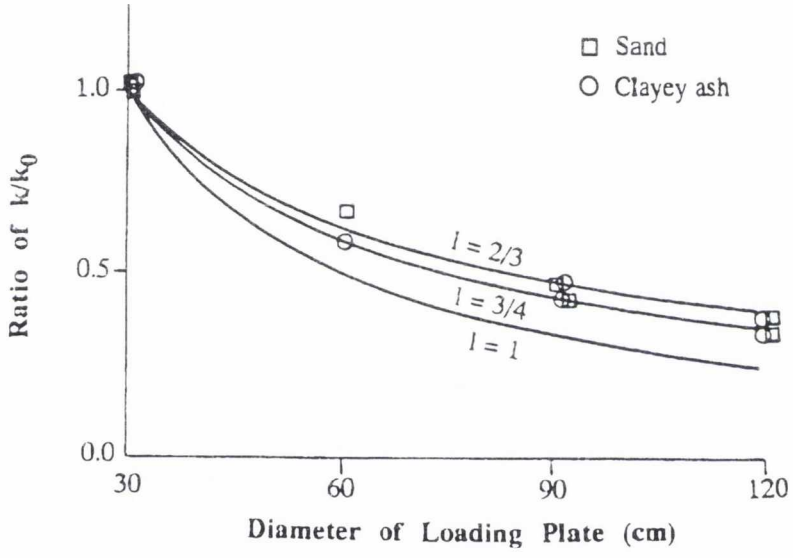

Figure 2.3.2. Effect of plate diameter on modulus ratio k/k_0 (Yoshida and Yoshinaka, 1972)

The value of k also varies across the contact surface. Terzaghi argued that k depended on the nature of the soil relative to that of the beam. The pressure at the edge of a beam resting on a medium is either greater or smaller than at the centre, as shown in figure 2.3.3. It has been shown already that the coefficient of subgrade reaction tends to depend on the pressure applied to the soil.

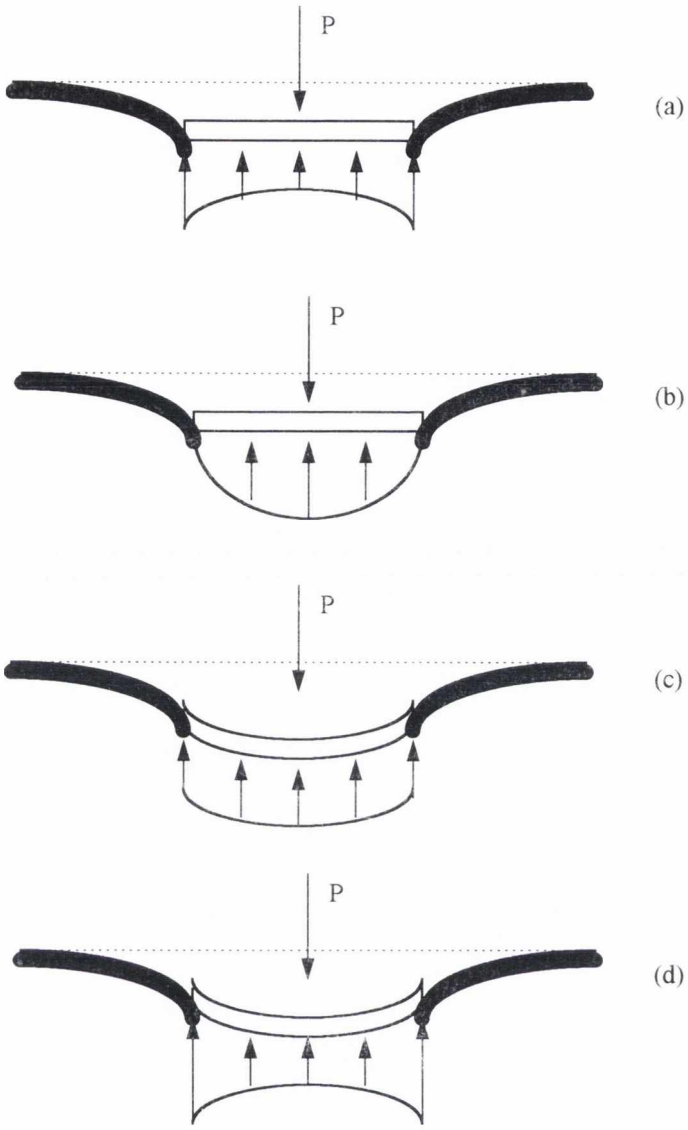

Figure 2.3.3. Real distribution of soil subgrade reaction under (a) rigid beam in clay, (b) rigid beam in sand, (c) flexible beam in clay and (d) flexible beam in sand (West (1991) based on Terzaghi (1955)).

A further complication arises from the assumption of homogeneity in the soil medium. Terzaghi argued that whilst clay based soils tend to exhibit homogeneous properties, sandy soils tend to be non-homogeneous with an approximately linear variation with depth in the value of k (figure 2.3.4).

The Winkler model can be modified to model this with the equation,

$$p = (n_h x)y \qquad [2.3.3]$$

where n_h depends on the relative density of the sand.

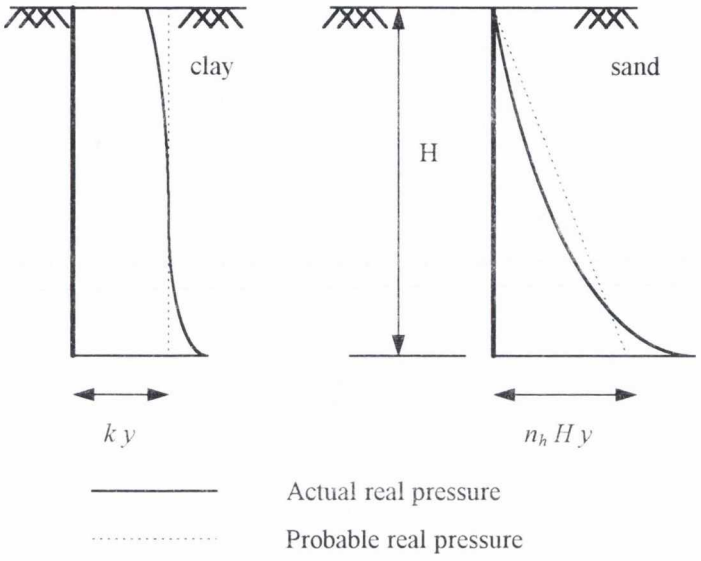

Figure 2.3.4. Distribution of assumed and probable real pressure distribution over the face of a rigid vertical plate in sand and clay. (Terzaghi, 1955)

In the particular case of piles, Terzaghi suggested that for clay and sandy soils respectively,

$$p = \left(\frac{k_s}{1.5B}\right) y \qquad [2.3.4]$$

and,

$$p = \left(\frac{n_h x}{B}\right) y \qquad [2.3.5]$$

where B is the diameter of the loading plate and typical values for k_s and n_h are given in tables 2.3.1 and 2.3.2.

	Stiff	Very Stiff	Hard
Precompressed Clay	75	150	300

Table 2.3.1. Values of k_s in tons/ft^3 for 1 ft square plates.

	Loose	Medium	Dense
Dry Sand	7	21	56
Submerged Sand	4	14	34

Table 2.3.2. Values of n_h in tons/ft^3 for 1 ft wide pile.

Reese et al (1974) used back-analysis of field test data for piles in sandy conditions which gave values as much as five times larger than those given by Terzaghi, as shown in figure 2.3.5. Reese gave an upper limit on n_h as 0.19 $D_r^{1.16}$, where D_r is the relative density of the sand.

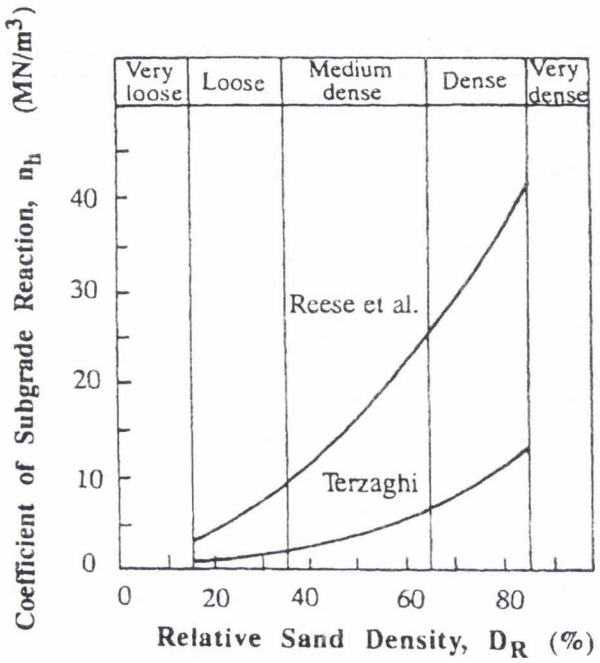

Figure 2.3.5. Values of n_h for varying sand density D_r. (Reese et al, 1974)

Having accepted that the subgrade modulus depends on depth, subsequent authors tried to model this variation with an arbitrary power of x, the depth below the surface of the soil. Hence,

$$k(x) = kx^m \qquad [2.3.6]$$

where k is a constant and m is the power term for x. Along with this variation authors have also suggested that there is not a directly linear relationship between the pressure applied to the beam and the deflection of the beam. Some form of power term has been suggested, hence

$$p = k(x)^m y^n \qquad [2.3.7]$$

Yoshida and Yoshinaka (1972) have listed various authors on this subject with suggestions that $0 < n < 1$, and that m is more arbitrary, but likely to again lie in the range $0 < m < 1$.

A text by Burland et al (1977) brings together all the arguments on the topic of non-homogeneity in soils.

2.3.2 The soil modulus, E_s

The elastic modulus or soil modulus, E_s, is a fundamental parameter of any soil. It is normally obtained from the slope (tangent or secant) of stress-strain curves from triaxial tests. Most of the above discussion with respect to k also applies to E_s. E_s varies with respect to the amount of deflection, depth below the surface, the loaded area/shape, beam stiffness and soil type. Atkinson (1973) also produces evidence that the elastic modulus in otherwise uniform soil deposits increases with depth as a result of overburden pressures and of natural deposition and consolidation processes.

The stress pattern along the pile may be broken into three regions; plastic soil near the surface where the soil flows, inelastic in the next lower region but non-flowing and elastic response with small strains in the lower regions furthest from the surface. McClelland and Focht (1956) suggested that the ratio of the pile stiffness to the soil stiffness below the first point of zero deflection has a limited effect on the behaviour at the surface. Bowles (1988) states that the use of E_s is for computational convenience which generally works until the soil stress reaches the ultimate value.

Vesic (1963) performed more detailed work on Biot's work on infinite flexible beams on an elastic subgrade, and showed that k and E_s are related by,

$$kB = 0.65 \sqrt[12]{\frac{E_s B^4}{EI} \frac{E_s}{1-\upsilon_s^2}} \qquad [2.3.8]$$

where it can be seen that the dependence on EI, the stiffness of the beam, is small. The above equation also applies to finite beams of length, L, with good accuracy provided $\lambda L > 2.25$, where the damping factor λ is defined by,

$$\lambda = \sqrt[4]{\frac{kB}{4EI}} \qquad [2.3.9]$$

2.3.3 Experimental determination of k

There are many experimental methods for establishing a value for the subgrade reaction, k, but the results are inconsistent due to the many factors given above. Casagrande (1948) classified soils and gave the value ranges for k (table 2.3.3).

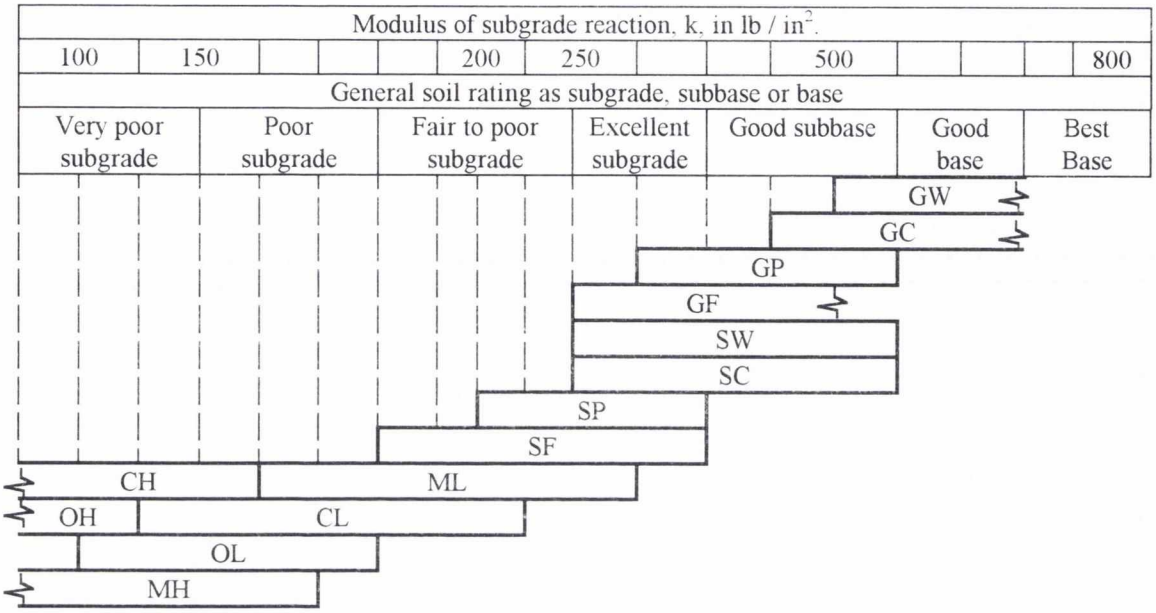

G - Gravel	F - Fines, material < 0.1 mm	L - Low to Med compressibility
S - Sand	O - Organic	H - High compressibility
M - 'Mo', very fine sand, silt	W - Well Graded	
C - Clay	P - Poorly Graded	

Table 2.3.3. Typical k values. (Casagrande, 1948)

The modulus of subgrade reaction can be obtained from the Plate Bearing test directly by $k = 1 / \Delta$, where Δ is the deflection of the plate. Previously it had been shown that such isolated values of k are practically useless, Kerr (1985).

There are many works trying to correlate E, the Young's modulus of soil and k, the modulus of subgrade reaction. A summary of such methods is listed in West (1991) and are discussed in most geotechnical books, for instance Bowles (1988). From the approaches used, it can be seen that there is no universal and accepted method.

2.3.4 Conclusion

The ability of the geotechnical engineer to relate the properties of real soils to the parameters required for a mechanical model have been discussed in the previous section. It can be seen that for

the simplest of such parameters, k, the modulus of subgrade reaction, there is no generally accepted method by which the real and theoretical properties can be related. It is, however, possible to produce order of magnitude estimates for this parameter.

The other parameters required for various mechanical models, such as a shear modulus in the Pasternak model and Poisson's ratio for the continuum model, are more difficult to quantify by the use of laboratory tests.

If it is accepted that the only meaningful parameter that can be used in the model is the modulus of subgrade reaction, then the model that has to be used is that of Winkler. In the original model suggested by Winkler, it was assumed that k is constant with depth, that is, that the soil is homogeneous. It is now recognised that this assumption is not valid in many cases, especially in sands, where, as discussed Terzaghi suggested a linear variation with depth. The model that will be used in this thesis will enable both homogeneous and non-homogeneous soils to be analysed. This will be done by enabling the soil stiffness at the head and foot of the pile to be defined. A linear variation in soil stiffness will be assumed between these extremes.

2.4. Load transfer between piles and soils

Piles subjected to axial forces have the ability to carry the load in two distinct manners. Firstly by shear forces generated by friction along the length of the pile and, secondly, by forces generated at the base of the pile (figure 2.4.1).

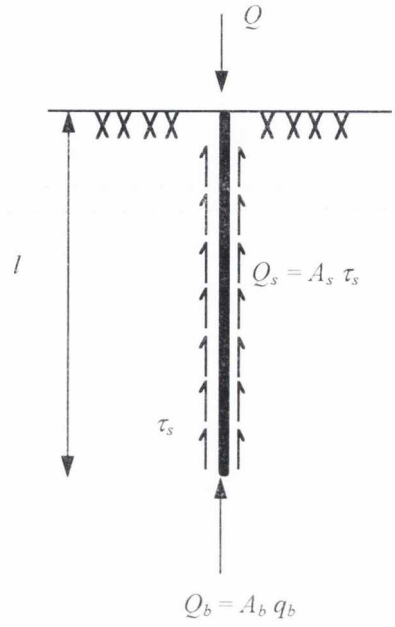

Figure 2.4.1. Axially loaded pile.

The ultimate bearing capacity of the pile, Q, is defined by the following equation (Bowles, 1988),

$$Q = Q_b + Q_s = A_b q_b + A_s \tau_s \qquad [2.4.1]$$

where Q_b and Q_s are the base and the shaft capacity respectively, A_b is the area of the pile base, Q_b is the end-bearing pressure, A_s is the area of the pile shaft and τ_s is the average shear stress down the pile shaft. End-bearing piles have little or no shear stress between the pile shaft and the supporting medium and, hence, Q_s is small compared to Q_b. Such piles generally penetrate a soft layer of soil and rest on a lower, firmer medium, sometimes of relatively stiffer soil, but more normally rock. If there is no firmer medium on which to rest, then the piles are held up by friction along the shaft length, and are termed friction or floating piles. Such piles have a Q_s relatively large compared to Q_b. Depending

on the length of the pile, the maximum shear stress along the pile and the load applied, these piles can also have significant end support. It is common-place to assume no friction for end bearing piles and no end-bearing for friction piles in calculating ultimate pile capacity as ignoring the relative effect allows for a margin of safety. The proportion of the load which is carried by the pile toe also depends on the ratio of pile length/diameter as shown in figure 2.4.2. from Bond (1989).

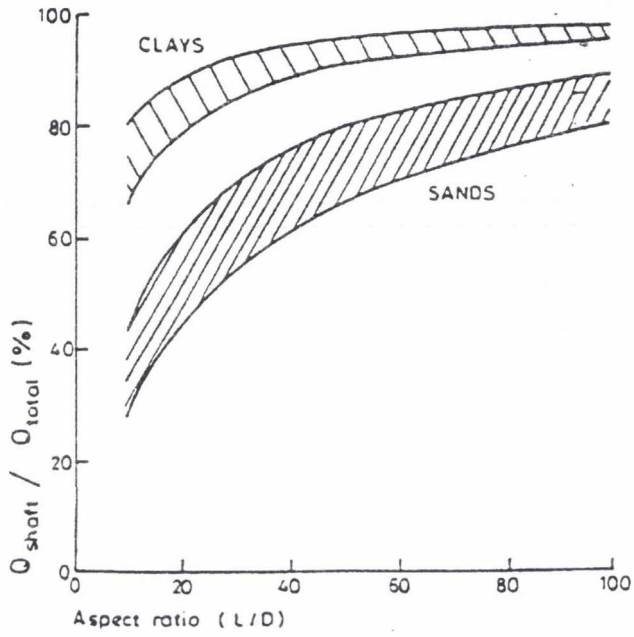

Figure 2.4.2. Ratio of point capacity to shaft capacity (Bond, 1989).

2.4.1 End-bearing point capacity

In cohesionless soils it is suggested by Tomlinson (1995) that the base resistance may be defined by,

$$Q_b = q_b A_b = N_q \sigma'_{vo} A_b \qquad [2.4.2]$$

where N_q is the bearing capacity factor and σ'_{vo} is the effective overburden pressure at the pile base level. N_q depends on many factors, primarily the ratio of the depth of penetration of the pile to its diameter and the angle of shearing resistance of the soil. Nordlund (1965), Vesic (1977) and Berezantsev (1961) have all made studies on the variation of N_q. A full discussion of factors effecting the parameters in this equation can be found in Tomlinson (1987, 1995).

In cohesive soils the equation used to model the base resistance is

$$Q_b = q_b A_b = N_c c_b A_b \qquad [2.4.3]$$

where N_c is the bearing capacity factor, c_b is the undisturbed undrained cohesion at the pile toe. Meyerhof (1951) showed theoretically that the bearing capacity N_c is approximately equal to 9 provided that the pile has been taken to a depth of at least five diameters into the bearing stratum.

A method of calculating the end-bearing point capacity force, P_{pu}, of foundations resting on a rock layer is based on a wedge failure. It is commonly used and is described in various texts, for example Bowles (1988) and Tomlinson (1995). The problem may be expressed by,

$$P_{pu} = A_p\left(cN'_c + \bar{q}N'_q + \frac{1}{2}\gamma B N'_\gamma s_\gamma\right) \qquad [2.4.4]$$

where the three bearing capacity factors, N'_c, N'_q and N'_γ are defined using a variety of methods, according to the individual author. N'_c is the bearing capacity for cohesion between the pile and soil adjusted for shape and depth. N'_q is the bearing capacity factor for the overburden effect at the pile tip and includes depth and shape effects. N'_γ is the bearing capacity factor for the base width since it is not affected by depth effects. The other terms in equation [2.4.4] are A_p, which is the area of the pile foot, c is the cohesion (or undrained shear strength s_u), B is the area of the base of the pile (usually used only when the pile tip is enlarged), q is the overburden pressure, γ is the density of the soil and s_γ is a shape factor. These bearing capacity factors are based on the initial in situ-soil parameters. In design, the ultimate point capacity is divided by a suitable safety factor of 1.5 to 3.

According to Vesic (1975) the bearing capacity factor N'_q can be computed as follows:

$$N'_q = \frac{3}{3-\sin\phi}\left\{\exp\left[\left(\frac{\pi}{2}-\phi\right)\tan\phi\right]\tan^2\left(\frac{\pi}{4}+\frac{\phi}{2}\right)I_{rr}^{(4\sin\phi)/[3(1+\sin\phi)]}\right\} \qquad [2.4.5]$$

where ϕ is the angle of internal friction in the soil. The reduced rigidity index I_{rr} in this equation is computed using the volumetric strain ε_v as,

$$I_{rr} = \frac{I_r}{1+\varepsilon_v I_r} \qquad [2.4.6]$$

The rigidity index I_r is computed using the shear modulus G' and shear strength s of the soil by,

$$I_r = \frac{G'}{c+q\tan\phi} = \frac{G'}{s} \qquad [2.4.7]$$

When undrained soil conditions exist or the soil is in a dense state, the ε_v term may be taken as zero and $I_{rr} = I_r$. Estimates for I_r may be made as follows (D_R is the relative density of the sample):

Soil	I_r
Sand (D_r = 0.5 to 0.8)	75-100
Silt	50-75
Clay	120-250

Table 2.4.1. Estimates for I_r (Bowles, 1988).

Baldi et al (1981) suggested the following equation for I_r.

For Dutch Cone Tip,

$$I_r = \frac{300}{f_R} \qquad [2.4.8]$$

For Electric Cone,

$$I_r = \frac{170}{f_R} \qquad [2.4.9]$$

where f_R is the friction ratio in percent.

Janbu (1976) computes N'_q by

$$N'_q = \left(\tan\phi + \sqrt{1+\tan^2\phi}\right)^2 \exp(2\psi\tan\phi) \qquad [2.4.10]$$

where ψ (in radians) is determined by the nature of the soil and varies from 60° in soft compressible to 105° in dense soils and is a measure of the extent of the pressure bulb at the pile base.

Vesic (1975) suggested that the bearing coefficient, N'_c can be calculated by,

$$N'_c = \frac{4}{3}(\ln I_{rr} + 1) + \frac{\pi}{2} + 1 \qquad [2.4.11]$$

whereas Meyerhof (1976) appears to use,

$$N'_c = \frac{4}{3}(\ln I_{rr} + 1) + 1 \qquad [2.4.12]$$

In Bowles (1988) N'_c and N'_γ are presented for Janbu and Vesic. The values calculated for particular values of ϕ often differ by 100% between the two methods. This casts doubt on the accuracy

of such methods to predict the end-bearing capacity of piles. The only reliable method of determination of the end-bearing capacity of piles is by instumented load tests of real piles.

2.4.2 Skin resistance capacity

There are three widely used methods, the α, γ and β methods, for calculating the skin resistance capacity in cohesive soils. The β method is also used for cohesionless soils. In all three cases, the skin resistance capacity is computed as,

$$P_s = \sum A_s \tau_s \qquad [2.4.13]$$

where A_s is the pile surface area, that is the perimeter multiplied by the embedded length and τ_s is the skin friction computed by one of the following methods.

Tomlinson (1971) defined the α method such that,

$$\tau_s = \alpha c + \bar{q} K \tan\delta \qquad [2.4.14]$$

where α is a dimensionless parameter calculated graphically (see Tomlinson, 1971, API, 1984), c is the average cohesion (or s_u) for the soil layer, $\bar{q}$ is the effective vertical stress, K is the coefficient of lateral earth pressure dependent on volume displaced, initial soil density, etc. and δ is the effective friction angle. The correlation for this method was $\pm$25 %.

Vijayvergiya and Focht (1972) presented the γ method for obtaining the skin resistance, τ_s, of a pile in clay with

$$\tau_s = \lambda\left(\bar{q} + 2s_u\right) \qquad [2.4.15]$$

where $\bar{q}$ and s_u are as defined before and λ is determined graphically. Reported correlation for this method was $\pm$10 %.

The starting point of the β method, suggested by Burland (1973), for calculating skin friction τ_s, for piles in non-cohesive soils is the equation

$$\tau_s = \sigma'_n \tan\delta = K\sigma'_v \tan\delta \qquad [2.4.16]$$

where σ'_n is the normal effective stress acting on the pile shaft after installation and δ is the angle of friction between pile and soil. The normal stress may be taken as some ratio K of the vertical stress

σ'_v. There have been many discussions of the value of K and the application of limiting values (see Bowles (1988) for a summary of most of the discussions).

Other authors have also suggested methods for obtaining τ_s. Meyerhof (1956) and Thorburn and Macvicar (1971) suggested,

$$\tau_s = 0.005 q_c \qquad [2.4.17]$$

where q_c is the cone-penetration resistance, in kPa. When a cone penetrometer is used and side friction q_{cs} is measured,

$$\tau_s = q_{cs} \text{ (small volume displacement piles)}$$

$$\tau_s = 1.5 \text{ to } 2.0\ q_{cs} \text{ (large volume piles)}$$

Meyerhof (1956, 1976) suggest that for SPT data,

$$\tau_s = \chi_m N \qquad [2.4.18]$$

where χ_m is 2.0 for large volume displacement and 1.0 for small volume piles. N is the statistical average blow count in the stratum. Vesic (1970) used the relative density D_r of the soil in order to calculate the shear resistance by,

$$\tau_s = \chi_v (10)^{1.54 D_r^4} \qquad [2.4.19]$$

where χ_v is equal to 8 for large volume piles and 2.5 for bored, open-end pipe piles, H piles.

Briaud and Tucker (1988) examined 13 methods which can be used to predict the ultimate resistance of piles. The methods included the α, λ and β methods among others. None of the methods made accurate predictions and for certain pile and site conditions the estimated skin friction could differ by a factor of 2 depending on the method employed.

2.4.3 Load transfer curves

In order to investigate the variation of friction along the pile shaft and the relative magnitudes of Q_s and Q_b it is necessary to look at how the ultimate bearing capacity is commonly calculated and to discuss the various methods. Fleming et al (1993) state that the shaft capacity of a pile is mobilised at much smaller vertical displacements of the pile, typically 0.5 to 2 % of the pile diameter, than the base capacity, which would require displacements as large as 5 to 10 % of the pile

base diameter. In granular soils it may be larger than the above estimates. Whitaker and Cooke (1966), Coyle and Reese (1966) and AISI (1975) state that a slip of 5 to 10 mm is required to develop maximum skin resistance and that it is relatively independent of shaft diameter and embedment length, and may also depend on soil parameters.

Fleming et al use results from tests carried out by Whitaker and Cooke (1966) on an instrumented bored pile of 0.6 m diameter and 10 m long installed in stiff clay to show how the ultimate capacity of a pile may have 40% of the capacity supplied by the base. However, at the working load of, for example, 400 kN, this may be reduced to as little as 6% depending on the choice of factor of safety, figure 2.4.3.

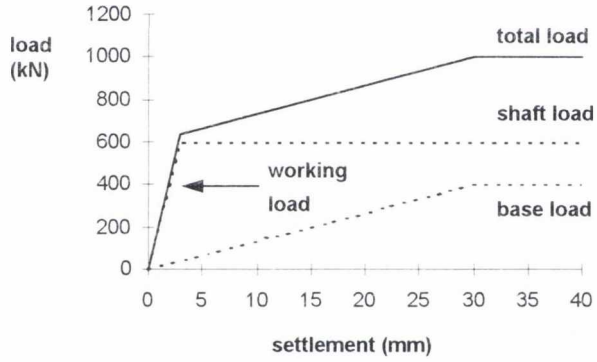

Figure 2.4.3. Idealised load settlement response (Fleming et al, 1992).

A major consideration in this choice is the required stiffness of the pile-soil system. It is possible for the pile base not to have been displaced by a load (that is for the pile to fail) yet the displacement at the head of the pile to be sufficiently large so as to cause structural damage. Before the ultimate shaft capacity has been reached, the pile stiffness, axial displacement at the pile head per axial load applied, is sufficiently larger than before it has been exceeded. This is a factor in deciding on the working load of a pile.

Bowles (1988) studied the large number of load transfer curves reported in the literature and concluded that the load transfer between the pile and soil is approximately parabolic and decreasing with depth for cohesive soils, figure 2.4.4 and 2.4.5. For cohesionless soils, however, the load transfer is more linear and somewhat dependent on embedment depth in all materials. He also speculated that a more linear load-transfer curve tends to be exhibited by a short pile compared to a long pile. The

reason for this non-linear behaviour is due to the overburden pressure increasing the soil stiffness with depth. There is also a complicated time dependence of load transfer, Tomlinson (1986).

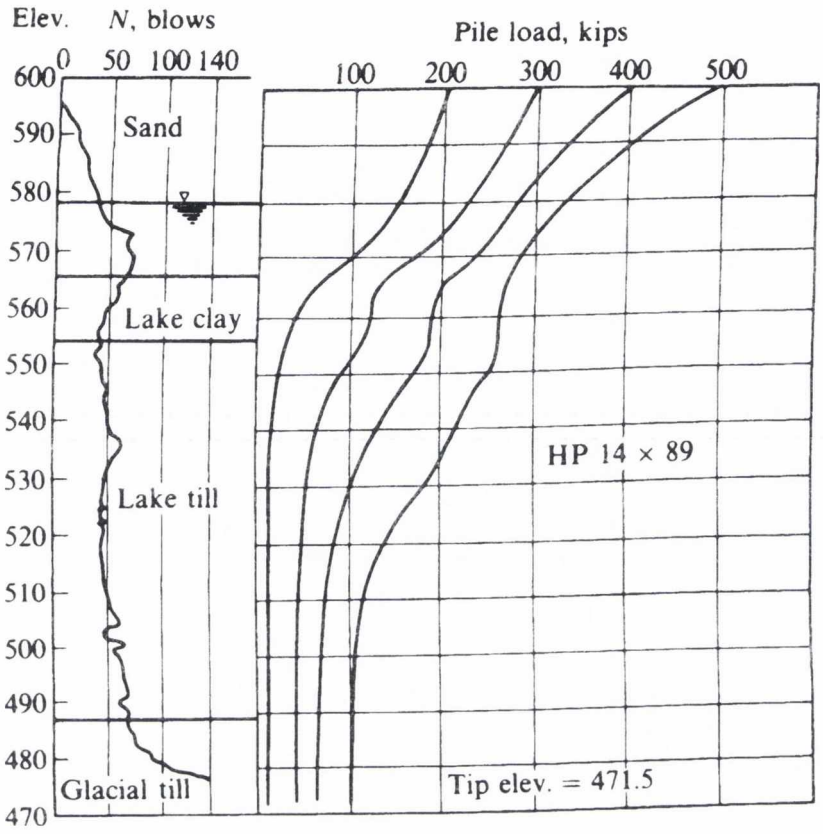

Figure 2.4.4. Load transfer curves for an H pile in cohesive soil (D'Appolonia and Romualdi, 1963).

Francis et al (1962) extensively instrumented a pile close to Melbourne. Even though it was driven into the underlying rock strata there appears to be very little end-bearing taken up at the pile foot (figure 2.4.6).

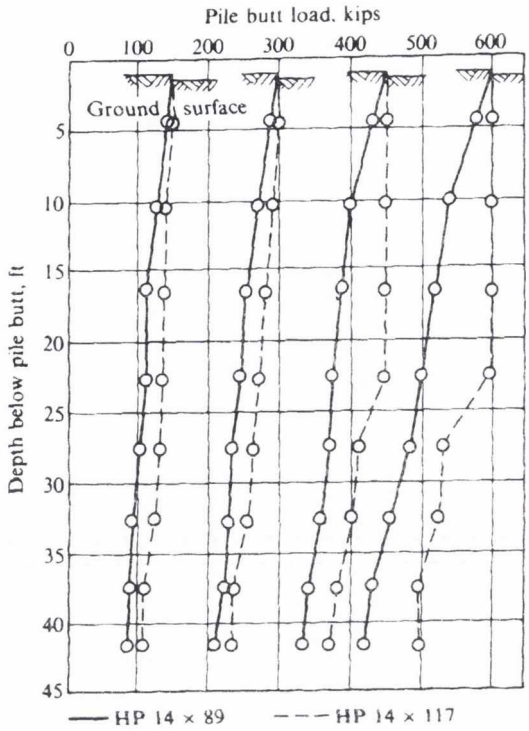

Figure 2.4.5. Load transfer for long H piles in sand. Note that the behaviour of the HP 14 x 117 is considerably different than the HP 14 x 89 at higher loads. (D'Appolonia, 1968)

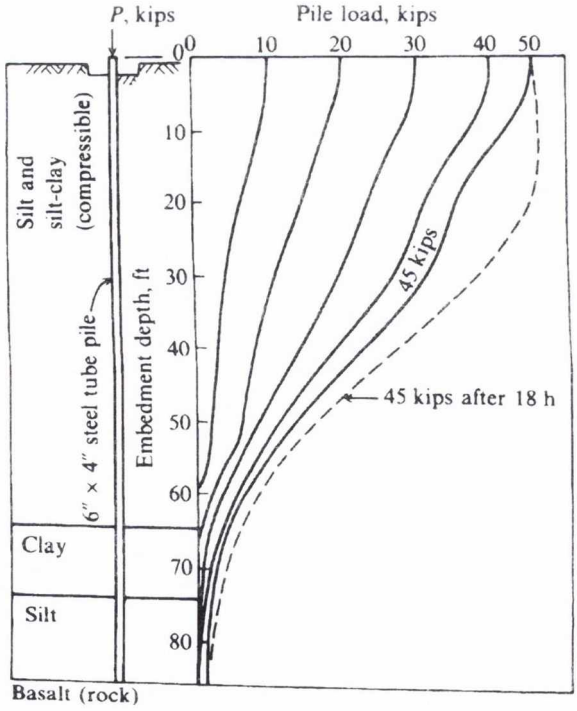

Figure 2.4.6. Load transfer curve for pile in compressible soil showing transfer to be time dependent (Francis et al, 1961).

Fleming et al (1993) suggested that the end-bearing pressure beneath a pile in a uniform, non-cohesive soil should be directly proportional to the local vertical effective stress and thus would increase approximately proportionally with depth. However Vesic (1977) showed that the end-bearing pressure appeared to have a limit after which there appears to be no further increase.

Poulos (1989) states that the load transfer is influenced by the distribution of the soil's Young's modulus along the pile shaft. Figure 2.4.7 shows how, in a homogeneous soil, the shear stress is relatively uniform with depth whereas with a Gibson soil, in which the soil modulus is linear with depth, the shear stress is approximately linear with depth.

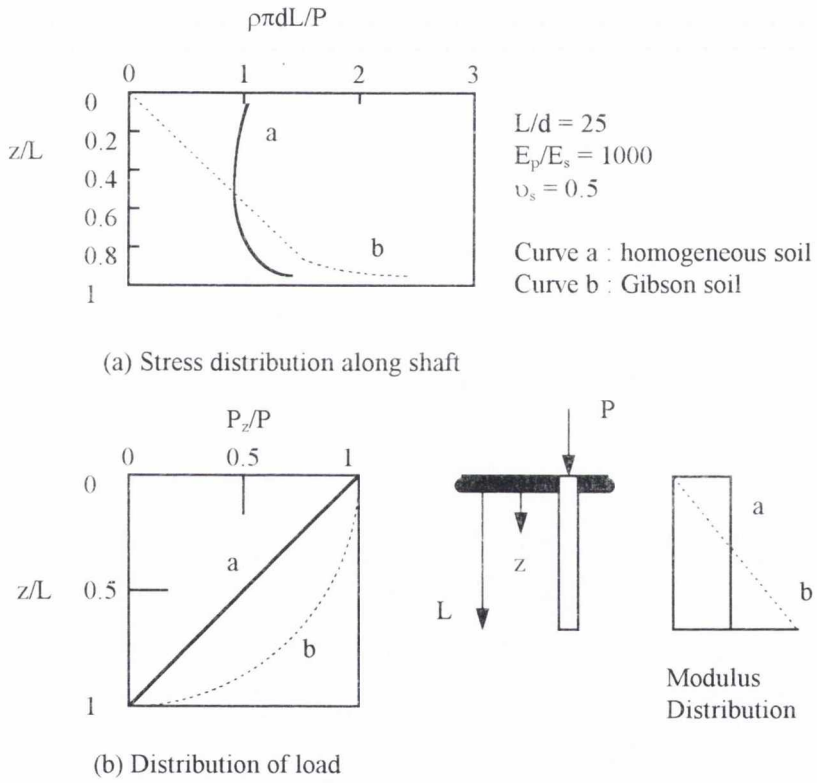

Figure 2.4.7. Influence of distribution of the Young's modulus of soil on load transfer. (Poulos, 1989)

Poulos and Mattes (1969) analysed a single axially loaded pile in an ideal elastic soil to give load distributions within the pile. They compared the results produced by the theoretical model with field tests carried out by Mansur and Kaufman (1956), D'Appolonia and Romualdi (1963) and Mohan, Jain and Kumar (1963). The results are shown in figure 2.4.8 The principal conclusions from the load distributions curves are, firstly, that in general the distributions are linear in nature indicating

a constant shaft friction. Secondly, the proportion of load transmitted to the bearing stratum can vary between 0-80 %

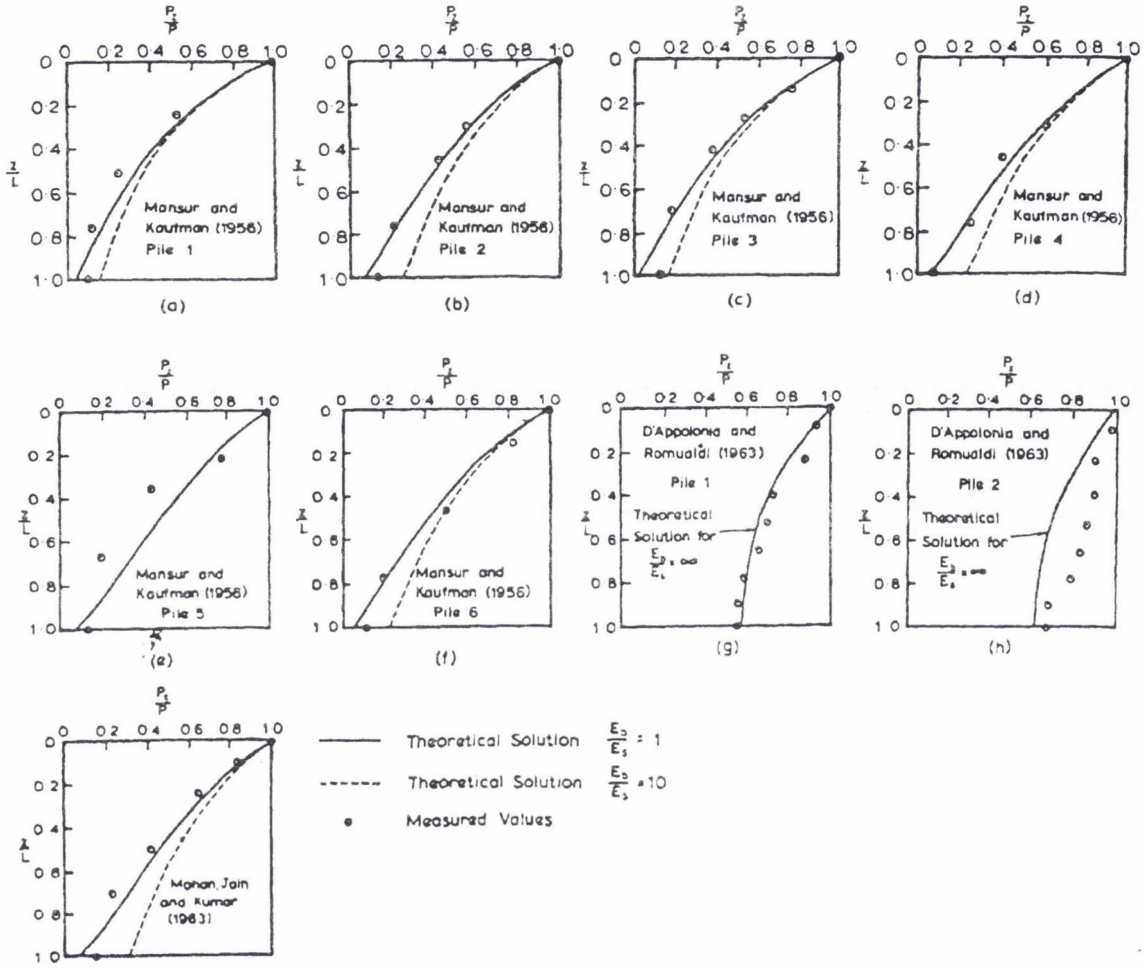

Figure 2.4.8. Comparison between theoretical and measured load distributions. (Poulos and Mattes, 1969)

Poulos and Mattes also plotted how the proportion of the applied load is transmitted to the base for the two different cases of uniform and triangular distribution of shear stress, τ, as in figure 2.4.9. Poulos and Mattes note that while the observed values are generally bounded by the two theoretical curves, they do in fact tend to be slightly closer to the curve for triangular τ distribution than to the curve for uniform τ.

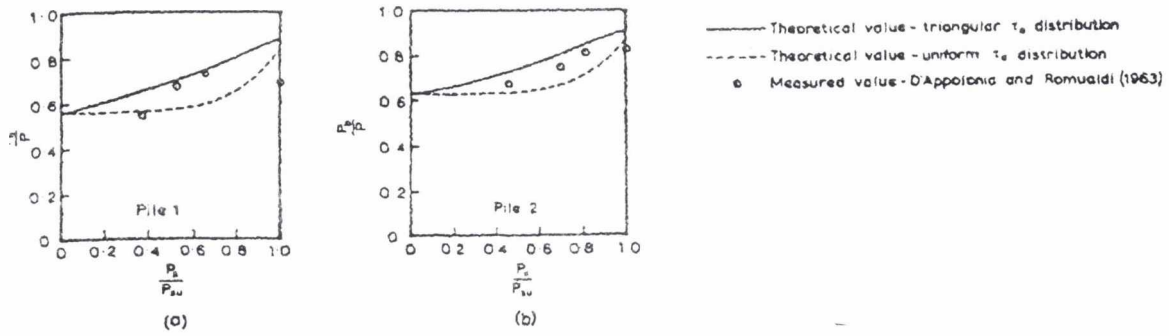

Figure 2.4.9. Comparison between theoretical and measured base load (Poulos and Mattes, 1969).

Tomlinson (1995) points out that the shear stress on a unloaded pile will eventually tend to zero as the soil relaxes. However, the shear stress on a loaded pile depends on relative movement between the pile and soil. This movement will obviously be maximum close to the applied load and, hence, it could be argued that the shear stress distribution will tend to decrease approximately linearly with depth. However, the shear strength of the soil close to the surface is less than further down the pile and this is the maximum value of shear stress that can occur at a particular depth. It is accepted that the shear strength increases linearly with depth (Poulos, 1989). Figure 2.4.10 shows a load transfer curve and the approximate shear stress distribution that would produce such a curve. As can be seen the shear stress increases linearly from zero to a maximum value near the top of the pile (as the shear stress is determined by the shear strength of the soil) and then decreases linearly again (as the relative movement between pile and soil decreases). However, in the previous load transfer plots compiled by Bowles (1988) and Poulos and Mattes (1969) this does not appear to occur in practice. This effect can only be seen in the plot by Francis et al (1961).

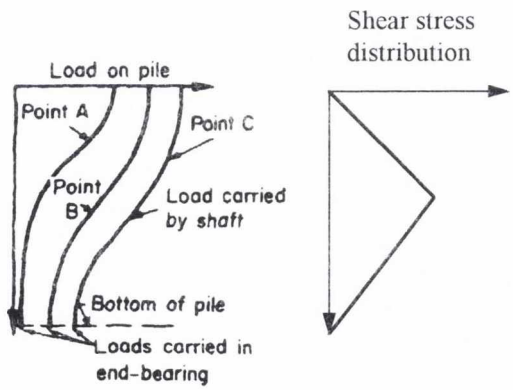

Figure 2.4.10. Effect of loading a pile, (a) strain gauge readings on pile shaft, (b) approximate shear stress distribution (Tomlinson, 1995).

2.4.4 Negative skin friction

Piles are frequently required for supporting structures that are sited in areas with a surface layer of poor quality fill. The piles carry the load through the fill to an underlying stiffer soil layer. No support can be assumed over the length of the pile shaft in the poor quality layer. There is also downward movement of the fill as it compresses over time or under the weight of further soil or structures, see figure 2.4.11. The downward movement causes drag-down forces, generally known as negative skin friction, on the pile shaft.

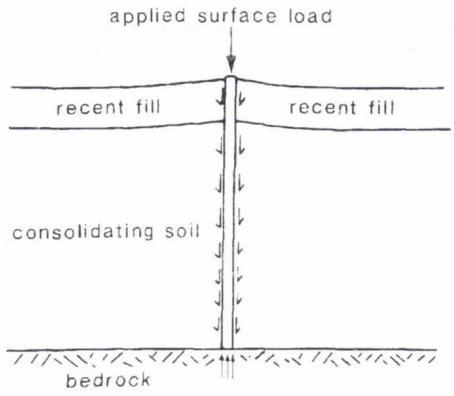

Figure 2.4.11. Piles in a consolidating soil subject to negative skin friction.

Tomlinson (1987) suggests the magnitude of the negative skin friction depends on the following factors:

1. The relative movement between the fill and the pile shaft.
2. The relative movement between any underlying soil and the pile shaft.
3. The elastic compression of the pile under the working load.
4. The rate of consolidation of the compressible layers.

It should be noted that the amount of negative skin friction tends to be an order of magnitude less than the applied load. It is in a downward direction and so would enhance the liklihood of buckling. However, the increased load in the pile is present over an effectively shorter pile, thus, reducing the liklihood of buckling.

2.4.5 Conclusion

In this section of the chapter the methods by which geotechnical engineers attempt to predict end bearing capacity and shaft friction for piles have been discussed. There are numerous techniques for both problems and the applicability of the solution depends on the type of soil and the relative strength of the medium and pile. There is still much disagreement on values that will be produced by the solutions and this thesis is not especially concerned with which method is the most accurate. However, it is possible to draw some general trends from such methods. These deal with the variation of skin friction along a pile and the ratio of the load that is carried at the pile toe to that carried by shaft friction.

The papers on load transfer curves, on the other hand, show some general trends for piles. For friction piles the maximum shear strength along the pile is either constant or increases linearly with depth for cohesive and cohesionless soils respectively. The other side of the argument, that the actual shear stress is dependent on the amount of slip between pile and soil, is also true, however this produces negative skin friction which tends to be an order of magnitude less than the applied load. This would mean that the shear stress distribution would decrease approximately linearly with depth. The real distribution is beyond the scope of this thesis and, hence, the decision has been made to model friction piles primarily with constant or linearly increasing friction along their length. There will also be comparisons with a shear stress distribution which decreases with depth in order to see if this trend produces significantly different results. It is possible having solved the linear increasing and linearly decreasing problems to combine them in order to produce solutions for the distribution which first increases and then decreases.

The theoretical base load has been shown to vary from anywhere between 20% and 100% of the applied load depending on whether the limit on skin friction is being approached along the pile shaft.

2.5. Buckling of beams on elastic foundations

2.5.1 The simple Winkler model

Early solutions for the elastic buckling loads of embedded piles were based on a subgrade modulus for the soil which was assumed to be constant over the length of the pile. Hetényi (1946) presented a comprehensive account based on the governing equation using a Winkler model of,

$$EI\frac{d^4y}{dx^4} + P\frac{d^2y}{dx^2} + ky = 0 \qquad [2.5.1]$$

where EI is the flexural stiffness of the pile, P, the axial load and k, the subgrade modulus, all of which were assumed to be constant with depth in the analysis. The solutions of the above equation were obtained in a non-dimensional form, letting

$$R = \sqrt[4]{\frac{EI}{k}} \text{ and } Z = \frac{x}{R} \qquad [2.5.2], [2.5.3]$$

Then

$$Z_{\max} = \frac{L}{R} \qquad [2.5.4]$$

where L is the embedded length of the pile, R, the relative stiffness factor and Z is the non-dimensional length coefficient. By substituting these definitions into the above equation and rearranging,

$$\frac{d^4y}{dz^4} + U\frac{d^2y}{dz^2} + y = 0 \qquad [2.5.5]$$

where, $U = PR^2/EI$. The critical values of the axial load coefficient, U_{cr}, are obtained by solving the above equation for U with the appropriate pile boundary conditions and pile length, Z_{max}. The technique and a computer program have been presented by Davisson and Gill (1963).

Case 1: k = constant.

This problem was initially solved using hyperbolic and trigonometric functions by Hetényi (1946). Hetényi's, method, however could only effectively be used to produce solutions when the

boundary conditions are symmetric, or for infinite or semi-infinite beams. His solutions were presented in terms of x and y where

$$x = \frac{N_{cr} l^2}{\pi^2 EI} = \frac{N_{cr}}{N_e} \text{ and } y = \sqrt{\frac{kl^4}{EI}} \qquad [2.5.6], [2.5.7]$$

where N_e denotes the Euler load for a pinned-pinned bar of length l and flexural rigidity EI. The buckling condition can then be defined for finite beams by the use of the following equations for the respective end conditions. Once the stiffness parameter, y, has been decided upon then the equation can be solved iteratively for x, the buckling load parameter.

Bar with free ends.

$$\frac{\sin \frac{1}{2}\sqrt{2y + \pi^2 x}}{\sinh \frac{1}{2}\sqrt{2y - \pi^2 x}} = \mp \frac{\left(y - \pi^2 x\right)\sqrt{2y + \pi^2 x}}{\left(y + \pi^2 x\right)\sqrt{2y - \pi^2 x}} \qquad [2.5.8]$$

Bar with hinged ends.

$$n^4 - n^2 x + \frac{1}{\pi^4} y^2 = 0 \qquad [2.5.9]$$

where n is any integer.

Bar with fixed ends.

$$\frac{\sin \frac{1}{2}\sqrt{\pi^2 x + 2y}}{\sin \frac{1}{2}\sqrt{\pi^2 x - 2y}} = \mp \frac{\sqrt{\pi^2 x + 2y}}{\sqrt{\pi^2 x - 2y}} \qquad [2.5.10]$$

Depending on the value of y, the soil stiffness parameter, the different signs or the different values of n will produce the lowest value of x, the non-dimensional buckling force. Figures 2.5.1 to 2.5.3 reproduce the results in Hetényi. The diagrams show the lowest buckling load and the mode shapes associated with the buckling load for the various sections of the load line. This effect will be discussed in more detail in chapter 4.

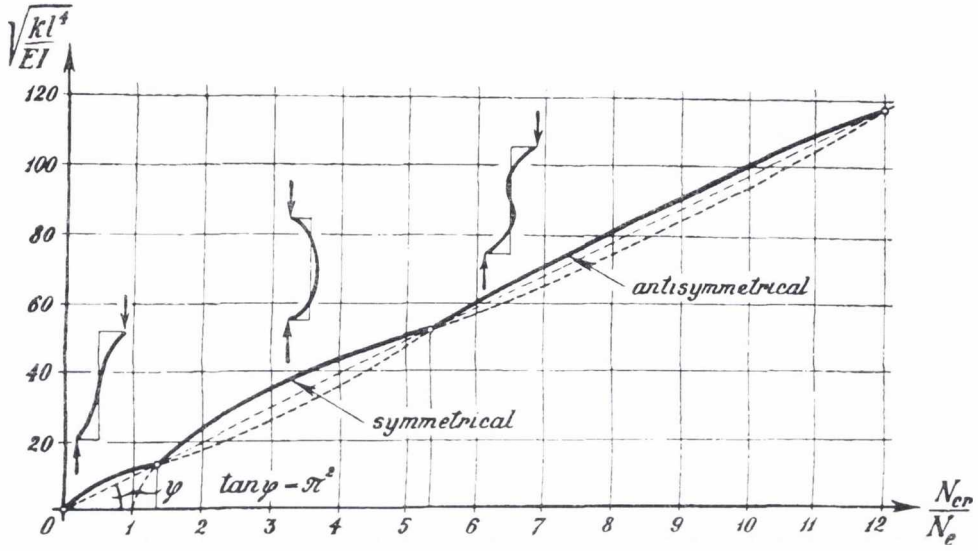

Figure 2.5.1. The buckling load of bars with free ends fully embedded in a homogeneous soil (Heténvi, 1946).

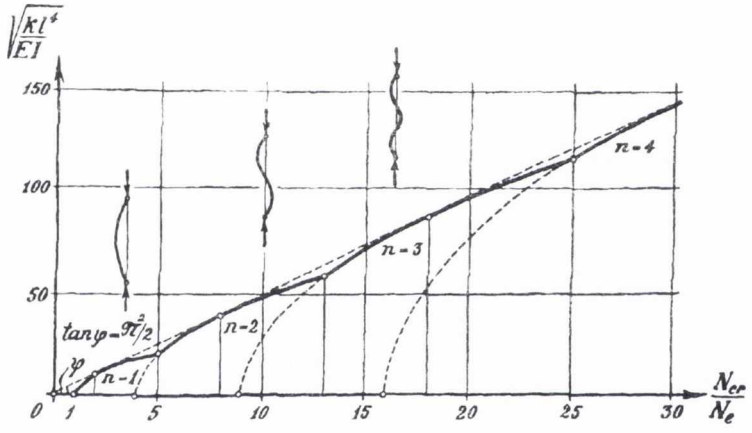

Figure 2.5.2. The buckling load of bars with hinged ends fully embedded in a homogeneous soil (Heténvi, 1946).

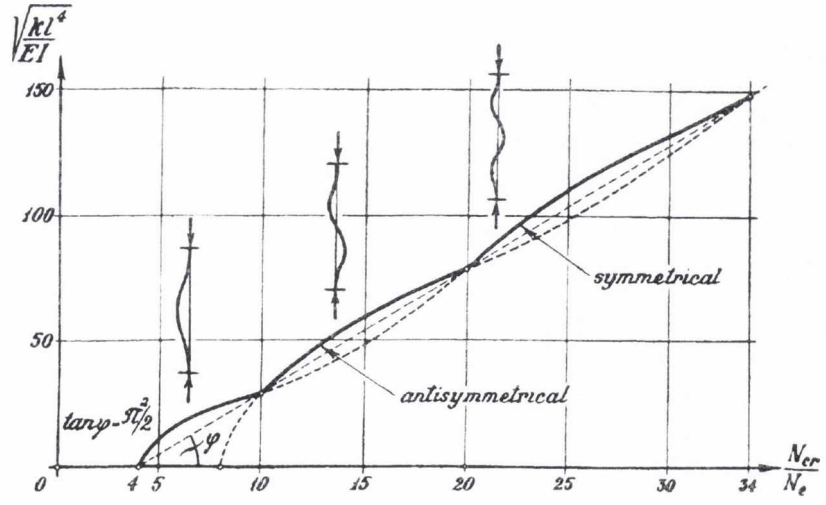

Figure 2.5.3. The buckling load of bars with fixed ends fully embedded in a homogeneous soil (Heténvi, 1946).

An alternative solution was presented by Davisson (1963) for several boundary conditions as shown in figure 2.5.4. Figure 2.5.4 shows that the boundary conditions exert a controlling influence on U_{cr}. Prakash and Sharma (1989) concluded that buckling appears to be controlled by the boundary condition offering the least restraint. It is suggested that a head fixed against rotation, but not translation, may represent a pile in a group.

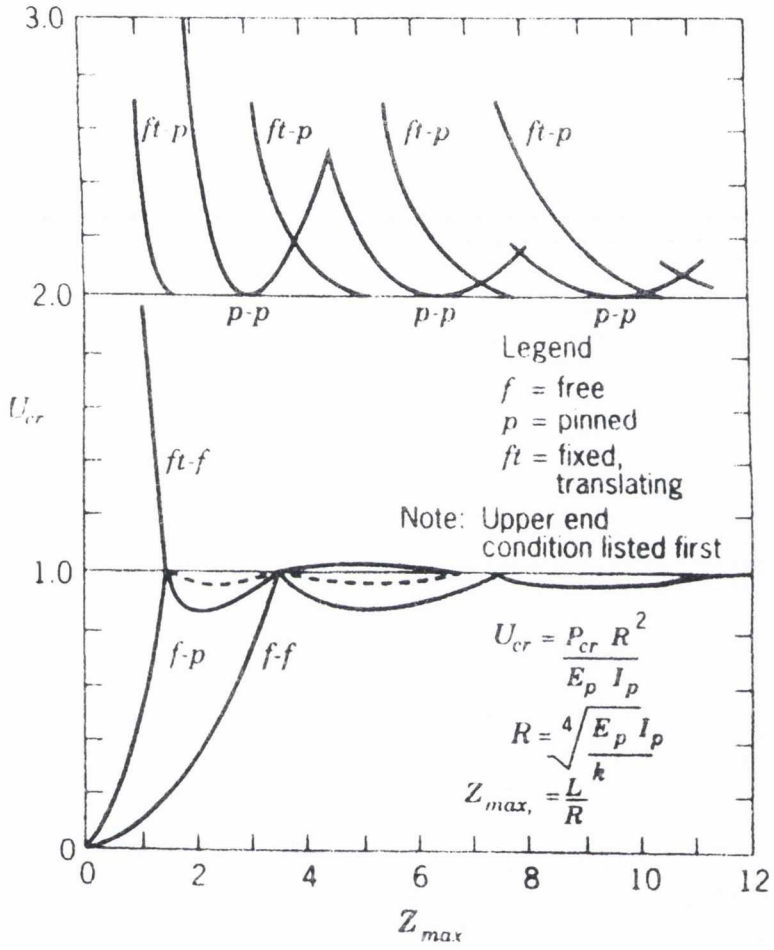

Figure 2.5.4. Buckling load vs length for k_h = constant. (Davisson, 1963)

Case 2: $k = n_h . x$.

When a soil profile is considered for which $k = n_h . x$, the boundary condition at the pile head becomes the dominant factor, because the pile tends to buckle in the region where the subgrade modulus is the lowest. Instability will tend to occur immediately adjacent to the pile head. The governing equation thus becomes,

$$EI\frac{d^4y}{dx^4} + P\frac{d^2y}{dx^2} + n_h xy = 0 \qquad [2.5.11]$$

Let

$$T = \sqrt[5]{\frac{EI}{n_h}} \text{ and } Z = \frac{x}{T} \qquad [2.5.12], [2.5.13]$$

where T is the relative stiffness factor and Z is the non-dimensional depth coefficient. By substitution, the above equation becomes,

$$\frac{d^4y}{dz^4} + V\frac{d^2y}{dz^2} + Zy = 0 \qquad [2.5.14]$$

where $V = PT^2/EI$. The solutions are given in Davisson (1963) and reproduced in figure 2.5.5 The solutions are exact, but, as will be shown in chapter 6, incomplete. They are discussed in Prakash and Sharma (1989), who say that, because most real piles are initially deformed and because the theoretical elastic buckling load is an unconservative upper bound to the actual failure load, the

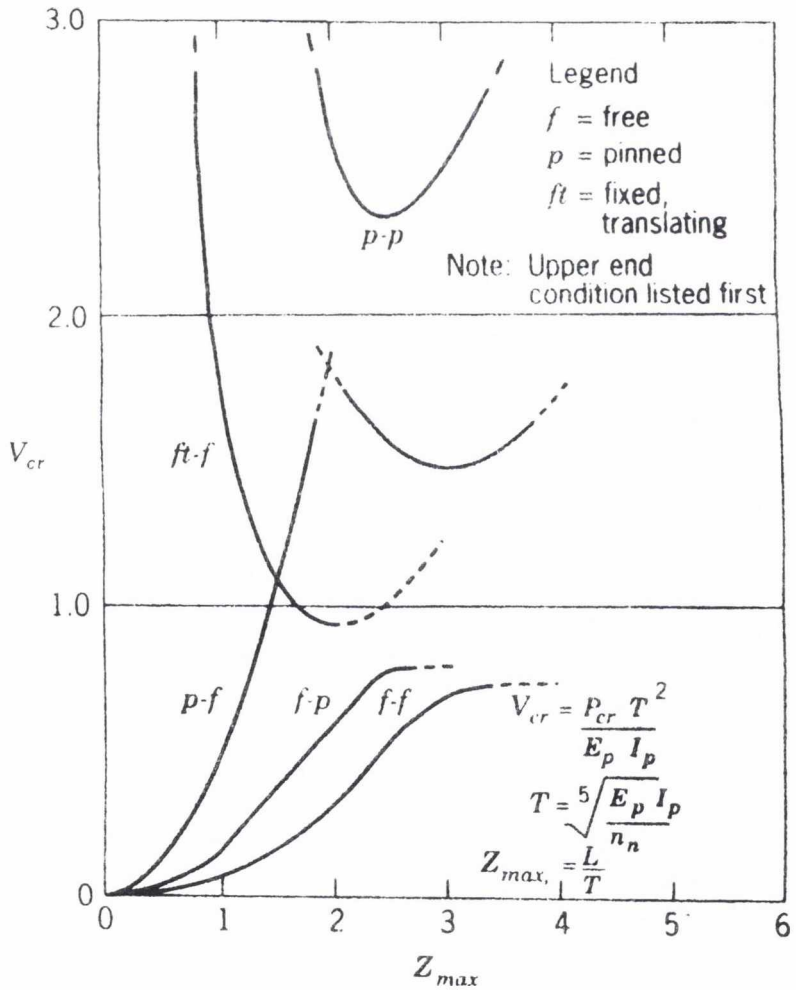

Figure 2.5.5. Buckling load vs length for $k_h = n_h x$. (Davisson, 1963)

computed buckling loads are often only an aid to the judgement of the engineer faced with the task of predicting the buckling load of a pile, The use of load tests is also unconservative. Most load tests are performed in a relatively short period of time during which a large part of the axial load in the pile is dissipated by skin friction. Under service conditions, the skin friction may be much less than that in the short term tests and the tendency to buckle would be greater (Davisson, 1963).

Prakash (1987) obtained solutions for buckling loads using closed-form energy methods for fully embedded vertical piles for boundary conditions with initial value $k_0 > 0$. The effects of pile length, soil stiffness and boundary conditions on buckling and mode of buckling have been studied for pile length up to 24 m with EI of 477 tm^2, k_0 from 0 to 2000 t/m^2 and n_h from 0 to 2000 t/m^3 (t = tonne).

The critical load was determined by calculating the smallest eigenvalue of the leading principal submatrix. Results are produced in figure 2.5.6 and figure 2.5.7 where buckling loads are plotted against length of pile. Prakash calculated the buckling loads by calculating the number of equal half-sine waves in the buckling mode which would give the least buckling load. This method

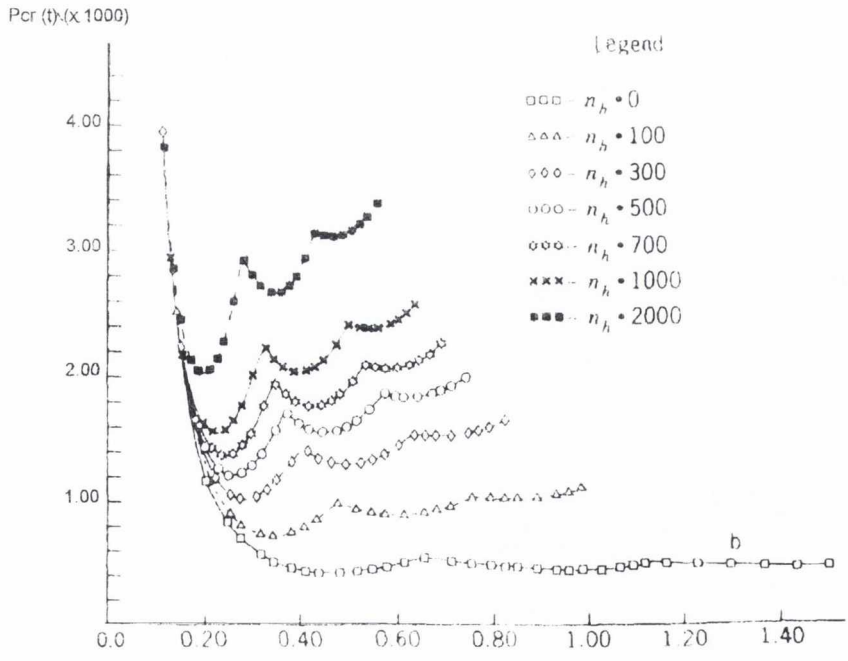

Figure 2.5.6.Critical load for a pinned-pinned pile with $k = k_0 + n_h$, $k_0 = 100$ t/m^2. (Prakash, 1987)

produces an upper estimate of buckling load and it also cannot predict the actual buckling load as will be discussed chapter 6.

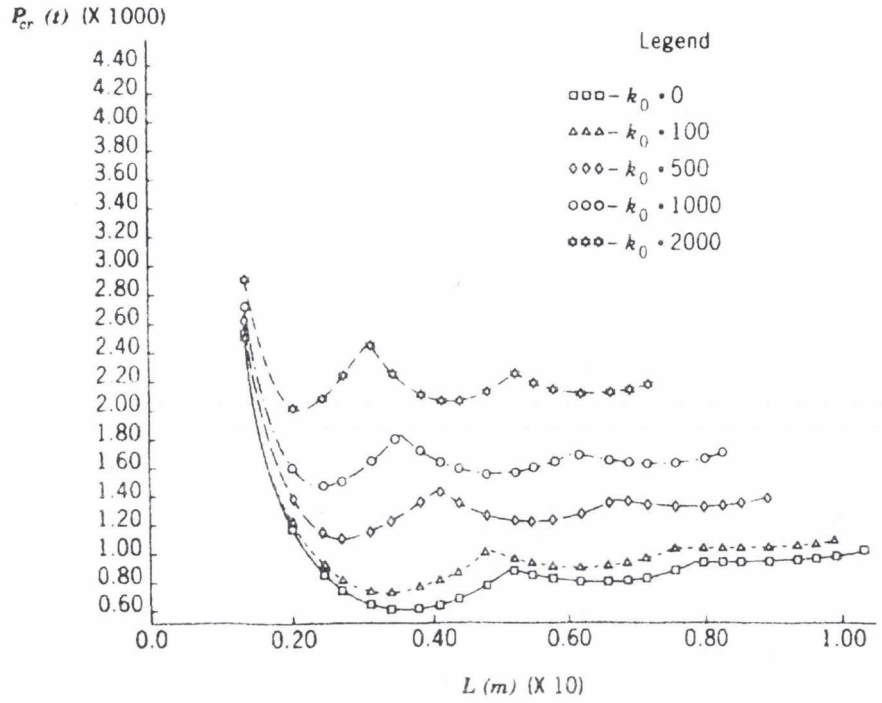

Figure 2.5.7. Critical load for a pinned-pinned pile with $k = k_0 + n_h$, n_h = 100 t/m^3. (Prakash, 1987)

2.5.2 Effect of axial load transfer

The above solutions assumed that the axial load applied at the head of the pile was transferred totally to the toe of the pile, that is, that the friction along the sides of the pile was negligible. In floating piles and compressible end-bearing piles this is clearly not the case and load transfer occurs along the shaft. The effect of this on the buckling load of fully and partially embedded piles has been investigated by Reddy and Valsangkar (1970), using a Rayleigh-Ritz energy method and beam vibration functions. The results for various conditions are presented in the figure 2.5.8. They concluded that there was a considerable increase in buckling loads even when only 50% of the load is supported by skin friction. They also noted that skin friction effects were most obvious for fixed-free without sway conditions and least obvious for free-free end-conditions. They finally concluded that if the ratio of unsupported length to the length of the pile is greater than 0.4 then the effects of skin friction were practically negligible. In chapter 6 this conclusion will be discussed.

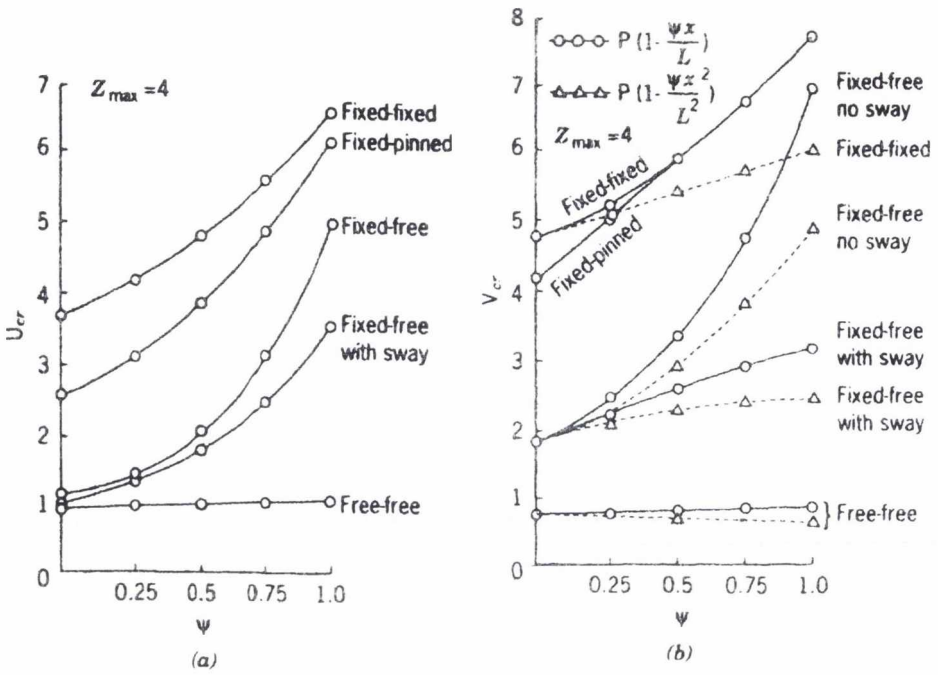

Figure 2.5.8. Effect of skin friction on buckling loads of fully embedded piles for (a) Constant soil modulus, (b) Linear soil modulus. (Reddy and Valsangkar, 1970)

2.5.3 Other foundation models

The buckling of beams on two parameter foundations can, generally, be reduced to the problem of a generalised foundation (Eisenberger and Clastornik, 1987) whose behaviour is defined by the following equation.

$$EI\frac{d^4y}{dx^4} - k_1\frac{d^2y}{dx^2} + k \cdot y = p(x) \qquad [2.5.15]$$

where k_1 is the shear parameter in the Pasternak model and the tension in the Filonenko-Borodich model.

Eisenberger and Clastornik (1987) presented two methods for a beam on a variable two-parameter elastic foundation. The number of segments required to converge on a single solution is plotted in figure 2.5.9. The first ① was based on the exact shape function for the beam. The second ② used cubic shape functions of a regular beam element and added the contribution of the foundation as elemental foundation stiffness matrices. These were compared to two other methods, ③ divided the beam into segments with a constant Pasternak foundation and ④ the division of the beam into

segments with concentrated springs at the joints. They produced the first buckling mode for the problem presented in figure 2.5.10

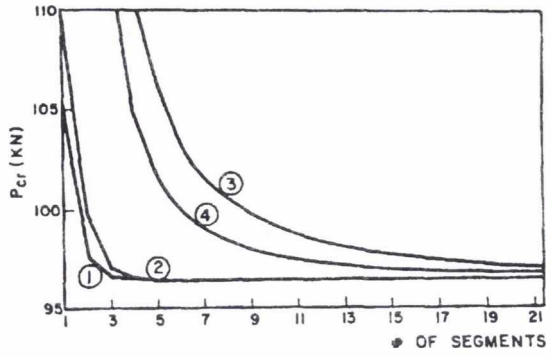

Figure 2.5.9. Buckling load for beam, four methods (Eisenberger and Clastornik, 1988).

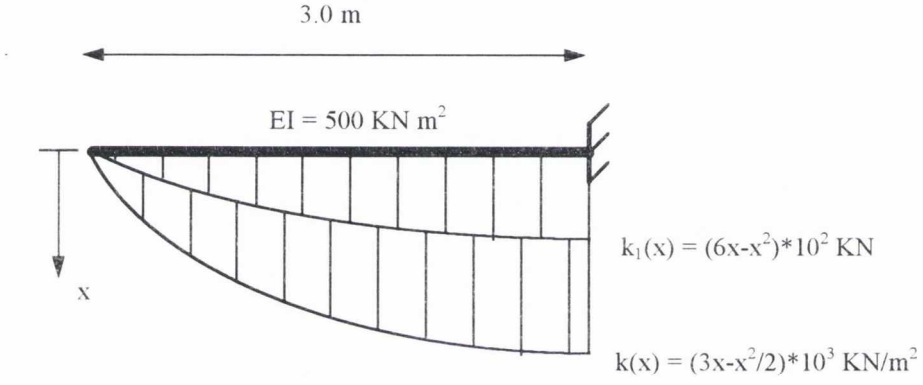

Figure 2.5.10. Beam on a two parameter foundation (Eisenberger and Clastornik, 1987).

2.5.4 Partially embedded piles

Davisson and Robinson (1965) presented solutions for the buckling loads of partially embedded piles in homogeneous media. In the analysis it is assumed that the embedded portion of the pile can be represented by a fixed base at a depth below the ground (figure 2.5.11).

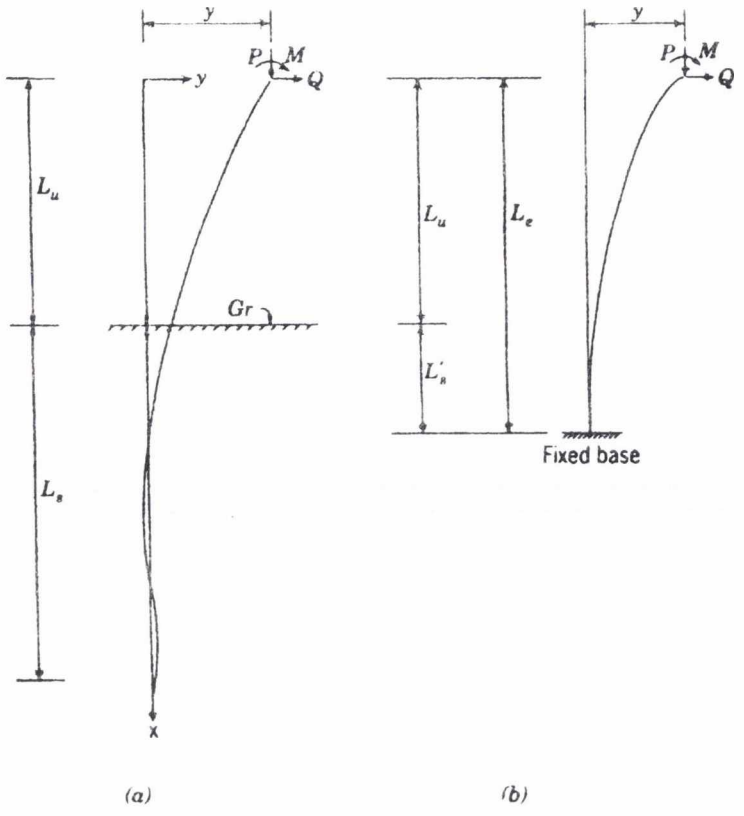

Figure 2.5.11. Partially embedded pile (a) Actual Pile, (b) Equivalent system (Davisson and Robinson, 1965).

The solution has been developed in non-dimensional form by the use of,

$$S_R = \frac{L_s'}{R} \text{ and } J_R = \frac{L_u}{R} \qquad [2.5.16], [2.5.17]$$

where L_s' is the equivalent length of the embedded portion of the pile, L_u is the unsupported length of the pile and R was defined in equation [2.5.2]. It was found that in the buckling problem S_R had a narrow range of approximately 1.33 to 1.6 and, therefore, for practical reasons S_R = 1.33 has been recommended. This recommendation will be discussed in chapter 6. For the two boundary conditions in figure 2.5.12 the buckling load P_{cr} may then be computed from the following equation,

$$P_{cr} = \frac{\pi^2 E_P I_P}{4\left(S_R + J_R\right)^2 R^2} \qquad [2.5.18]$$

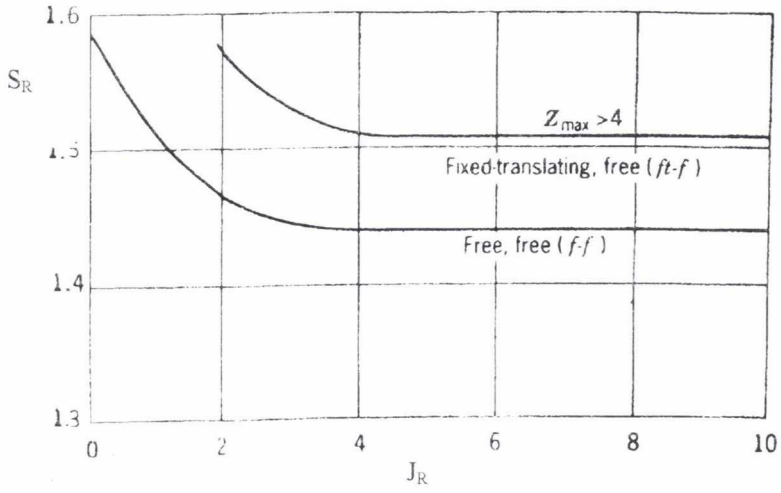

Figure 2.5.12. Dimensionless depth of fixity for buckling k = constant (Davisson and Robinson, 1965).

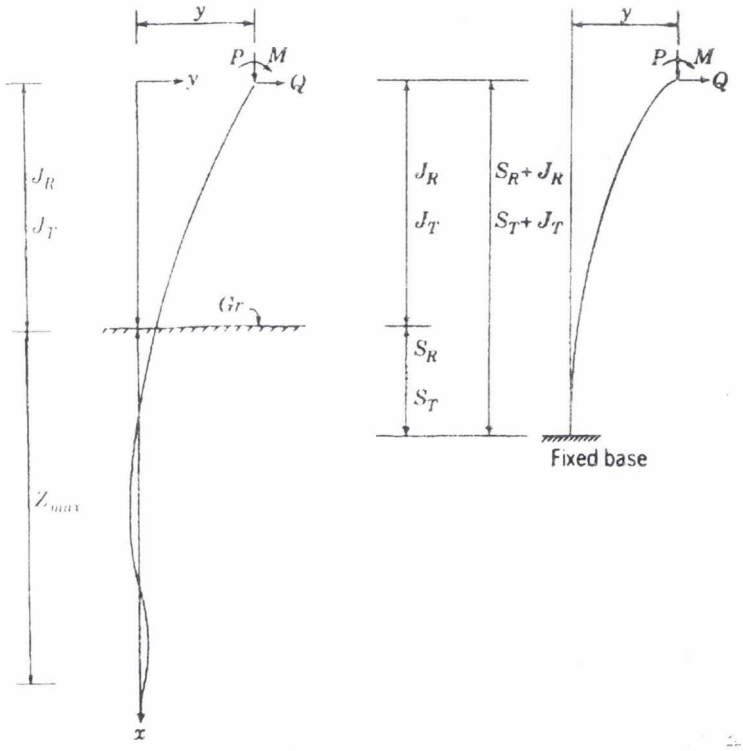

Figure 2.5.13. Non-dimensional representation of partially embedded pile (a) Actual Pile, (b) Equivalent pile (Davisson and Robinson, 1965).

Similarly (figure 2.5.13) for the case $k = n_h.x$ solutions are possible with the introduction of the following non-dimensional lengths,

$$S_T = \frac{L'_S}{T} \text{ and } J_T = \frac{L_U}{T} \qquad [2.5.19], [2.5.20]$$

where T is defined in equation [2.5.12]. The buckling load is,

$$P_{cr} = \frac{\pi^2 E_P I_P}{4\left(S_T + J_T\right)^2 T^2} \qquad [2.5.21]$$

where S_T is derived from figure 2.5.14. A value of S_T = 1.80 was recommended by Davisson and Robinson (1965).

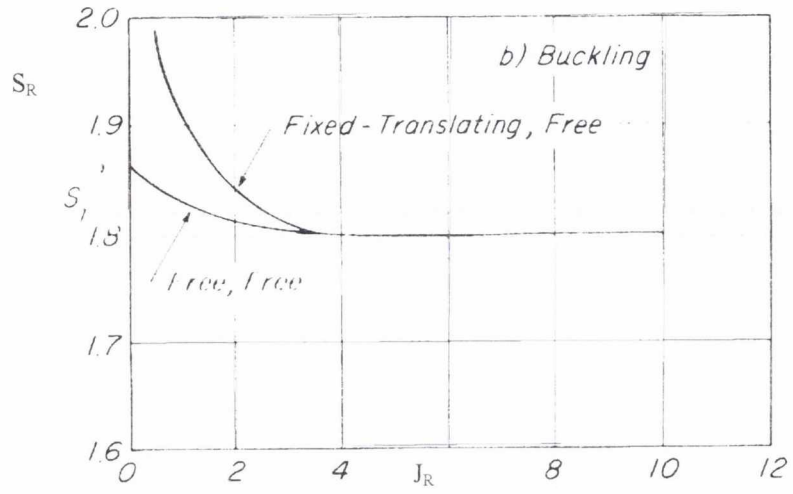

Figure 2.5.14. Dimensionless depth of fixity for buckling $k = n_h.x$ (Davisson and Robinson, 1965).

Fleming et al (1993) suggested a method based on the same concept. They suggest that the equivalent embedded length should be half the critical length of the embedded pile. The critical length is defined as the length beyond which the pile acts as if it was infinitely long. For piles in a homogeneous soil the equivalent length, l_e, of the embedded portion of the pile is,

$$l_e = 2\left(EI/k\right)^{1/4} \qquad [2.5.22]$$

and for piles in a soil with a linear increase in soil stiffness,

$$l_e = 2\left(EI/n_h\right)^{1/5} \qquad [2.5.23]$$

Fleming et al then compared the values of the buckling load given by equation [2.5.18] and [2.5.21] with the condition for flutter to occur during installation. They concluded that the buckling of long piles into deep layers of soft soil will be a secondary problem to that of actually installing them. However, end-bearing piles, or piles with a significant length of free standing section which are installed in soft deposits, should be assessed for possible buckling under static load.

2.5.5 Vibrational problem

Modal clusters, where consecutive modes are almost equal in value, were found to occur in the vibrational problem of a partially embedded beam in an Elastic Winkler foundation by West (1991) (figure 2.5.15). δ is the proportion of the beam embedded in the supporting medium, in this case halve the beam is embedded ($\delta = 0.5$). In this case the natural frequencies at low values of soil stiffness, λ, are approximately the same as the unembedded natural frequency. At high soil stiffness the natural frequencies are associated with mode shapes where the embedded portion of the beam behaves like a fixed end-condition. Due to the natural similarity between the vibrational and buckling problem of beams modal clusters and plateau would be expected to occur in the buckling problem also.

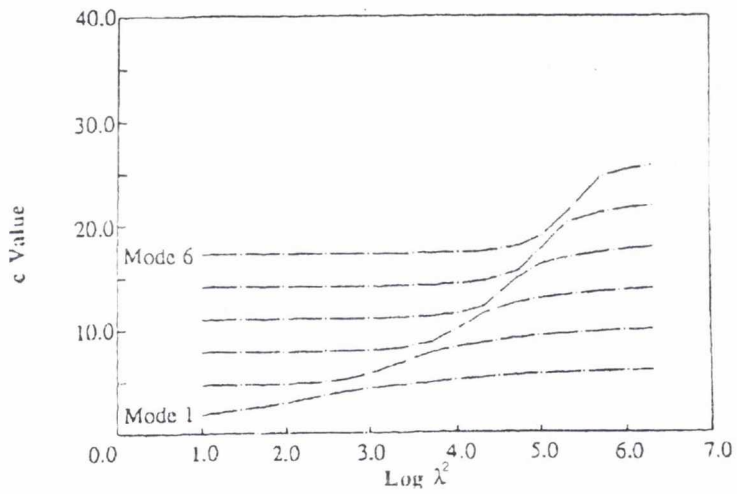

Figure 2.5.15. First six vibrational (c is the non-dimensional frequency parameter) modes for a fixed-free partially embedded ($\delta = 0.25$) beam (West, 1991).

2.5.6 Conclusion

The previous work on beams on elastic foundation has concentrated on individual problems rather than identify trends in the behavioural patterns. The work on Winkler foundations in particular has concentrated on the use of symmetric boundary conditions and constant soil stiffness as this produces exact solution in terms of trigonometric or hyperbolic functions. Other works which take

into account non-homogeneity in the soil medium are not exact solutions as they tend to be based on either assumptions to the expected mode shapes or on finite-element methods. The solutions to the problem of partially embedded structures has been produced using a simplification of the problem under consideration.

It will be possible to discuss the effect of the assumptions when the results presented in this literature review are compared to the results produced in this thesis. This will be done in chapter 6.

Finally the vibration case of partially embedded beams was briefly presented. It was found that consecutive modes can approach each other closely depending on the value of the soil stiffness parameter. Such modal clustering will also be expected in the buckling problem considered in this thesis.

2.6. Buckling of piles

2.6.1 Full scale and model tests

There have been several papers on the subject of buckling of actual piles *in situ*. A much quoted paper, Francis et al (1962) details a series of load tests on a pile in very soft soil. The pile was 1029 inches in length and had a flexural rigidity EI = 206.6 Mlb.in^2. Some of the results have already been described in the section on load transfer along the pile shaft. However, they went on to discuss the likelihood of the buckling of the pile.

Francis et al calculated the short-column compressive strength of the pile to be 85,000 lb. (the short-column strength actually measured was 79,200 lb.) and the buckling load in an appropriate homogeneous soil (k = 100 lb./in^2) , after Hetényi (1946), would be, they quote, eleven times the measured short column strength (that is 871,000 lb.). The buckling load of the pile in free air would be 1,924 lb.. The maximum sustained load was measured as 68,000 lb.. They conclude that buckling did not occurr and that this could be predicted by reference to Hetényi. The measured bending moments in the pile, when subject to a load of 45,000 lb., indicated a deflected form of five half waves (figure 2.6.1). For short-term loads they concluded that the very soft soils provided ample support against buckling. This results, calculations and conclusions will be discussed with reference to the results presented in this thesis in chapter 6.

Lee (1968) uses the results from small scale laboratory test in order to verify the work of Davisson and Robinson (1965). He concludes that the load test on 1/4 inch to 1/2 inch diameter piles in dry sand are in agreement with Davisson and Robinson. The dry sand was modelled as having a soil stiffness which was linearly increasing with depth from a zero value at the surface. Klohn and Hughes (1964) produced buckling in a full size timber pile and the buckling loads predicted by Davisson and Robinson are also close to the appropriate predicted values.

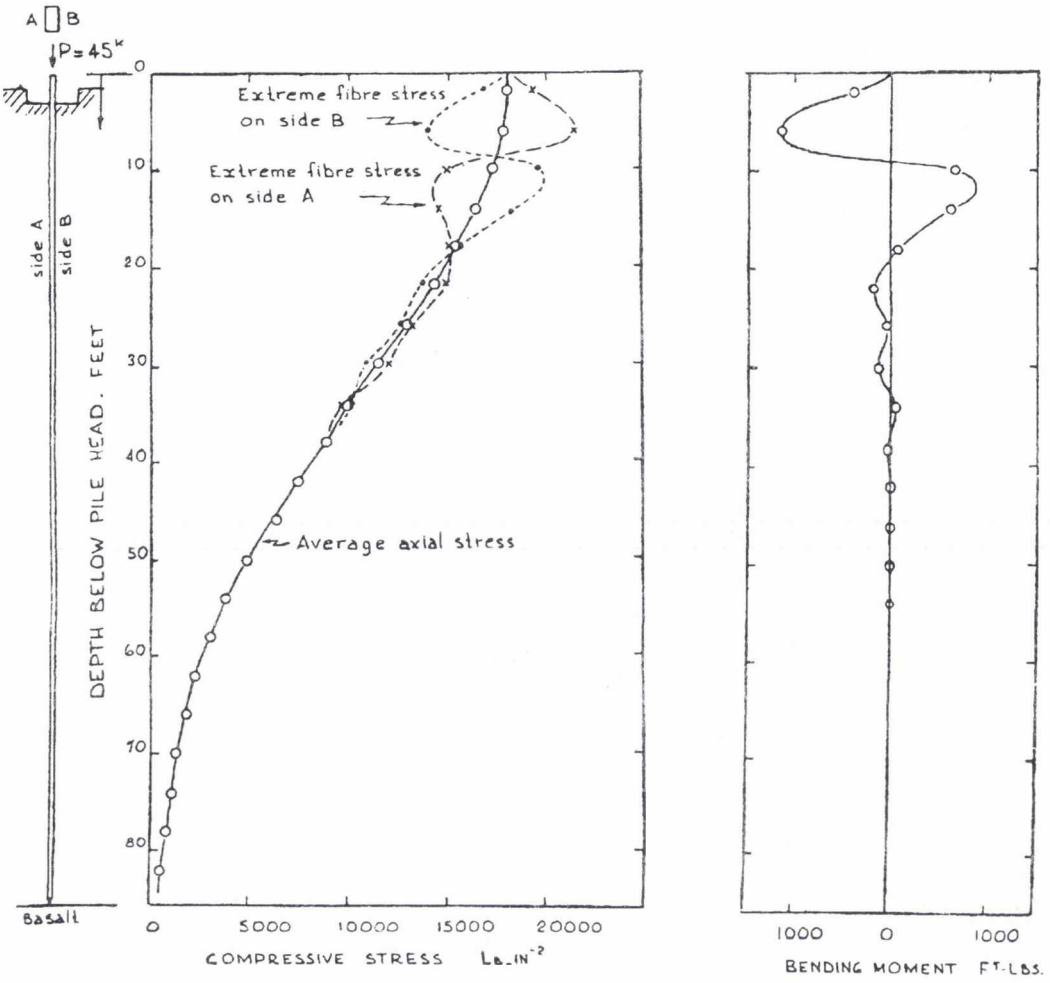

Figure 2.6.1. Stresses and bending moments in pile under an axial load of 45 kips (Francis et al, 1962).

In Guvenot (1975), the author uses results from Mendel (1936), which are identical to Hetényi (1946), in order to predict the buckling of three test piles, two of which are embedded in peat and the third in a soft clay. The results are summarised in table 2.6.1. The theoretical results are all over-estimates of the buckling load actually achieved. Guvenot suggested that a safety factor of three should be used when buckling loads are calculated using Mendel.

Test Date	Soil Type	Soil Stiffness (MPa/cm)	Theoretical Buckling Load (N)	Measured Buckling Load (N)
2-12-1974	peat	0.006	3×10^4	1.5×10^4
7-12-1974	peat	0.006	3×10^4	2×10^4
12-12-1974	soft clay	0.015	5×10^4	4×10^4

Table 2.6.1. Summary of test results (Gouvenot, 1975).

2.6.2 Conclusion

The previous section outlined some test data on the buckling of piles. The conclusions are varied. Francis et al (1962) concluded that buckling was not a problem. They suggest that the buckling load would not be approached before the pile failed in compression. Lee (1968) concluded that the existing theory suggested by Davisson and Robinson (1965) accurately predicted the buckling loads in a heterogeneous medium. Finally, Gouvenot (1975) concluded that the buckling loads they calculated were over-estimates of the actual buckling load and, hence, that a safety factor of three would have to be taken into account when determining actual buckling loads. In chapter 6 a comprehensive comparison between these results and those that will be presented later will be undertaken.

2.7. Conclusion

In this chapter two distinct approaches to the problem of partially embedded piles in soils have been highlighted. Firstly there is that of the structural engineer who makes a set of assumptions about the nature of the soil and then, using these assumptions, produces a model. The geotechnical specialist, on the other hand, tends to use test piles and the results from real piles to see if there are any generic trends to be observed. This approach does not lead to exact 'results' but tends to produce empirical expressions which can then be used with appropriate factors of safety to produce a safe design.

The various soil models have been presented for a static (and some dynamic) interaction between soil and structure. The accuracy of any model has been shown to be suspect as soon as the relationship between the model parameters and real geotechnical properties have been taken into consideration. This leads to the conclusion that the more complicated models, while perhaps exhibiting more of the generic properties of real soils, are not necessarily more accurate in solving a 'real' problem. Their use may be attractive to an engineer, but they can also lead to an unjustified complication of the problem and, hence, such models should be used after careful consideration of their applicability to the problem in hand. It can be concluded that the Winkler model is sufficient for the problem to be considered in this thesis.

This thesis will use the Winkler model to provide the equation for the soil-structure interaction of a pile. However, as mentioned before, it is necessary to be able to model such effects as the non-homogeneity of the soil. Even though the non-homogeneity can take several forms it will be limited to linear variations in both soil stiffness and shear friction on the shaft. Initially only fully embedded beams will be taken into consideration. However, the ability to model partially embedded piles will not be ignored as those piles used for the foundations of wharves and jetties are hardly ever fully embedded. The effect of partial embedment on the buckling load could be important.

The literature review has produced results from several different sources which will be compared to the results produced by the algorithm in this thesis. They come in three general groups. The first are exact solutions which have been formulated for problems which are a simplified version

of the problem under consideration. Hence, for example, when the soil stiffness tends to zero for end-bearing piles the results are identical to those predicted by Euler. The second group are for approximate models to particular problems. It will, for example, be possible to compare the model in Fleming et al (1992), for partially embedded end-bearing piles, to an exact solution. Finally, results from tests on both small and full scale embedded piles can be compared to the results outlined in this thesis.

In the vibrational case, investigated by West (1991), consecutive mode shapes clustered together at particular values of soil stiffness. This is expected in the buckling problem and methods of the prediction of such clustering will be discussed.

In conclusion, previous work on the calculation of the buckling load of a partially embedded beam has concentrated on end-bearing beams. Except for Hetényi (1946), there has been no attempt to accurately predict the buckling mode shapes. In the cases of Prakash (1987) and Davisson and Robinson (1965) the mode shapes have been assumed and then the buckling load calculated. The analysis that will be undertaken will address these shortcomings. In chapter 6 the literature review will be again considered with reference to the results presented in the next three chapters. The assumptions and conclusions of previous authors will be discussed in the light of the analysis performed in this thesis.

Chapter 3

Dimensionless Solution to the Governing Equations

3.1. Introduction

It has been shown in the previous chapter that the Winkler foundation model can be used to approximate many practical problems, given the difficulty in establishing model parameters from actual geotechnical measurements. In this chapter, a model consisting of a Euler beam resting on such a foundation, will be used to provide the solution to the problem of the buckling of a partially embedded beam.

Non-dimensional parameters will be introduced in order to present the results in a condensed format and to allow an easy parametric study of the generic trends. The problem of fully embedded beams can be expressed as a fourth order differential equation with non-constant coefficients. It will be shown that it is possible to produce an exact closed-form solution for all possible cases with varying soil stiffness, end conditions, embedment ratio and load transfer to the soil medium.

The governing equation for the embedded case leads to an infinite series solution which, it is possible to prove, converges under all circumstances and this has been solved by the use of a computer to an accuracy of twelve significant figures. The solution of this problem then requires the specification of the boundary conditions at the extremities of the pile.

In order to solve the problem of the buckling of a partially embedded beam it is necessary to solve for the non-embedded and embedded portions of the beam separately. The non-embedded solution is that of Euler buckling for an unsupported beam and the solution to the embedded portion is identical to that for a fully embedded beam. The end conditions are specified and continuity conditions are then applied at the boundary between the two regions to arrive at a solution.

3.2. Formulation of the problem

The problem to be considered in this thesis is that of a beam of overall length l and flexural rigidity EI embedded a distance of l_2 in a Winkler foundation, leaving a length l_1 of the beam unsupported by the beam. The Winkler foundation has a spring stiffness of k_1 at the boundary of the foundation and a stiffness of k_2 at the end of the beam (figure 3.2.1). It should be noted that since non-dimensional parameters are to be used in the solution to the problem that either imperial or metric units may be used as long as a consistent set of units are used throughout.

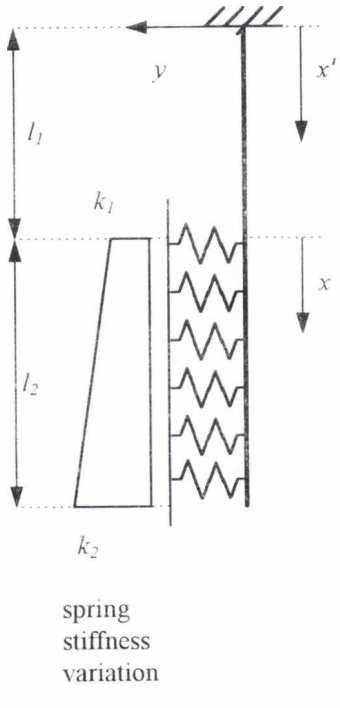

Figure 3.2.1. Axes origins of partially embedded fixed-free beam.

In order to specify the amount by which the pile is supported by friction it is necessary to define three non-dimensional parameters. The first of these, μ, defines the proportion of the buckling load which is supported at the base of the pile. In this way, piles completely supported by friction will have $\mu = 0$, and end-bearing piles with no friction will have $\mu = 1$. The other two parameters represent the variation of friction along the pile shaft. The are f_1 and f_2, and are defined at $x' = l_1$ and $x' = l_2$ respectively, such that $f_1 + f_2 = 1$. [3.2.1]

The friction varies linearly between these two values. For instance a uniform friction will be defined by a value of $f_1 = f_2 = 0.5$, and a linearly proportional friction to depth will have $f_1 = 0$ and $f_2 = 1$ (figure 3.2.2).

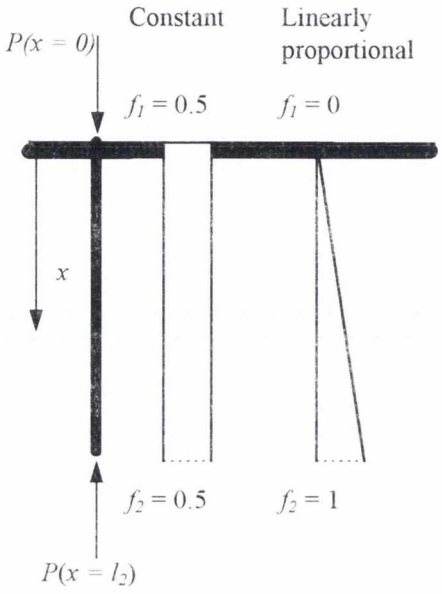

Figure 3.2.2. Variation of skin friction along the embedded beam.

For the overall solution it is now convenient to introduce the following non-dimensional parameters which will be used in the formulation of the solution and the discussion thereafter.

$$\theta = \frac{P_{crit}}{P_E} \qquad [3.2.2]$$

$$\lambda = \left(\frac{k_2 l^4}{EI}\right)^{1/2} \qquad [3.2.3]$$

$$F = \frac{k_1}{k_2} \qquad [3.2.4]$$

$$\delta = \frac{l_2}{l} \qquad [3.2.5]$$

where P_{crit} is the buckling load of the beam. P_E is the buckling load of a simply supported beam with no elastic supports along its span and is given by $P_E = \frac{\pi^2 EI}{l^2}$. θ and λ are the dimensionless buckling force and stiffness parameters as defined by Hetényi (1946) and used in subsequent material by other authors. F defines the degree of non-homogeneity in the soil stiffness and δ is the embedment ratio, which is the ratio of embedded pile length to the total length of the pile.

3.3. The governing equations for the buckling load of a pile

In order to solve the problem the beam has to be split into two regions. Firstly the unembedded region and then the embedded region, will be considered. The governing equations for both regions will be derived and the steps that were used to produce buckling loads and buckling modes will be shown.

3.3.1 The unembedded region

The solution for an unsupported Euler beam is a classical problem which has been solved by Euler, as set out in Hetényi (1946). It is included in order to clarify the approach taken in the more complicated cases of a beam supported by a Winkler foundation and a beam axially supported by a frictional force. This solution is also required for the partially embedded problem. The governing equation for the non-embedded bar subjected to a force, P, is given by (note that the second variable is x' and not x),

$$EI\frac{d^4y}{dx'^4}+P\frac{d^2y}{dx'^2}=0 \qquad [3.3.1]$$

where EI is the minimum flexural rigidity of the member and is constant along its length in the present analysis. If the variable $\zeta=\sqrt{\frac{P}{EI}}x'$ is introduced, then the solution of this differential equation can be given as:-

$$y=A_0\cos\zeta+A_1\sin\zeta+A_2\zeta+A_3 \qquad [3.3.2]$$

It is necessary to translate this equation into the co-ordinate system that will be used for the embedded bar. Now $x = x' - l_1$ and, hence, $\zeta=\sqrt{\frac{P}{EI}}(x+l_1)$ or $\zeta=\eta(x+l_1)$ where

$$\eta = \sqrt{\frac{P}{EI}} \qquad [3.3.3]$$

In order to solve the overall problem expressions for zero displacement, slope, bending moment and shear force will be required later. These expressions are required at the extremities of the beam portions, that is at $x' = 0$ or $x' = l_1$ (or $x = -l_1$ and $x = 0$ respectively). Now with respect to x these quantities are, respectively,

$$y = 0,\ \frac{dy}{dx} = 0,\ \frac{d^2y}{dx^2} = 0 \text{ and } \frac{d^3y}{dx^3} + \frac{P}{EI}\frac{dy}{dx} = 0 \qquad [3.3.4],\ldots\ldots,[3.3.7]$$

but with respect to ζ, they are

$$y = 0,\ \eta\frac{dy}{d\zeta} = 0,\ \eta^2\frac{d^2y}{d\zeta^2} = 0 \text{ and } \eta^3\frac{d^3y}{d\zeta^3} + \eta^3\frac{dy}{d\zeta} = 0 \qquad [3.3.8],\ldots\ldots,[3.3.11]$$

3.3.2 The embedded region

End bearing piles

The governing equation for the deflected shape of a bar supported laterally by a Winkler foundation and vertically at the ends only is, (Hetényi, 1946)

$$EI\frac{d^4y}{dx^4} + P\frac{d^2y}{dx^2} + k(x)y = 0 \qquad [3.3.12]$$

where EI and P are as given above. The foundation stiffness parameter, k (x), is assumed to vary linearly with x, the distance below the surface of the elastic medium so that ,

$$k(x) = k_1 + n_h x \qquad [3.3.13]$$

where k_1 and n_h are constants for the foundation. k_2 is defined as the maximum value of the stiffness parameter which exists at the bottom of the pile at $x = l_2$. The homogeneous solution ($k(x) = k_1$) is incorporated in this solution, and is found by setting $n_h = 0$.

If the variable $\xi = \left(\frac{k_1 + n_h l_2}{EI}\right)^{1/4}(x - l_2) = \alpha(x - l_2)$ is introduced [3.3.14]

then $$x = \frac{\xi}{\alpha} + l_2 \text{ and } \frac{d\xi}{dx} = \alpha \qquad [3.3.15],\ [3.3.16]$$

Further

$$\frac{d}{dx} = \frac{d\xi}{dx} \cdot \frac{d}{d\xi} = \alpha \frac{d}{d\xi} \quad [3.3.17]$$

so that

$$\frac{dy}{dx} = \alpha \frac{dy}{d\xi} \quad [3.3.18]$$

and, generally,

$$\frac{d^n y}{dx^n} = \frac{d}{dx}\left(\frac{d^{n-1} y}{dx^{n-1}}\right) = \alpha^n \frac{d^n y}{d\xi^n} \quad [3.3.19]$$

The governing equation with respect to ξ can be written as,

$$\frac{d^4 y}{d\xi^4} + \frac{P}{\alpha^2 EI}\frac{d^2 y}{d\xi^2} + \frac{k_1 + \frac{n_h \xi}{\alpha} + n_h l_2}{\alpha^4 EI} y = 0 \quad [3.3.20]$$

Now, let

$$\frac{P}{\alpha^2 EI} = \frac{P}{\sqrt{(k_2 EI)}} = \beta \quad [3.3.21]$$

also,

$$\frac{k_1 + \frac{c\xi}{\alpha} + cl_2}{\alpha^4 EI} = \frac{k_2}{\alpha^4 EI} + \frac{n_h \xi}{\alpha^5 EI} = 1 + \gamma\xi \quad [3.3.22]$$

where,

$$\gamma = \frac{n_h}{\alpha k_2} \quad [3.3.23]$$

Hence, the dimensionless governing equation is,

$$\boxed{\frac{d^4 y}{d\xi^4} + \beta \frac{d^2 y}{d\xi^2} + (1 + \gamma\xi) y = 0} \quad [3.3.24]$$

Assuming a solution of the form,

$$y = \sum_{n=0}^{\infty} a_n \xi^n \quad [3.3.25]$$

and substituting it into the dimensionless governing equation, the following are produced,

$$y = a_0 + a_1\xi + a_2\xi^2 + a_3\xi^3 + \ldots\ldots + a_n\xi^n \quad [3.3.26]$$

$$\frac{d^2 y}{d\xi^2} = 2.1a_2 + 3.2a_3\xi + 4.3a_4\xi^2 + 5.4a_5\xi^3 + \ldots\ldots (n+2)(n+1)a_{n+2}\xi^n \quad [3.3.27]$$

$$\frac{d^4y}{d\xi^4} = 4.3.2.1a_4 + 5.4.3.2a_5\xi + 6.5.4.3a_6\xi^2 + 7.6.5.4a_7\xi^3 + \ldots + (n+4)(n+3)(n+2)(n+1)a_{n+4}\xi^n \quad [3.3.28]$$

These polynomials are then introduced into the governing equation so that power terms can be calculated as in table 3.3.1 In order that the assumed polynomial is a solution of the governing equation [3.2.24] all the coefficients of a given power must be equal to zero.

term in governing equation	power of ξ				
	ξ^0	ξ^1	ξ^2	ξ^3	ξ^n
y	a_0	a_1	a_2	a_3	a_n
$\gamma\xi y$		γa_0	γa_1	γa_2	γa_{n-1}
$\beta\frac{d^2y}{d\xi^2}$	$2.1.\beta.a_2$	$3.2.\beta.a_3$	$4.3.\beta.a_3$	$5.4.\beta.a_5$	$(n+2).(n+1).\beta.a_{n+2}$
$\frac{d^4y}{d\xi^4}$	$4.3.2.1.a_4$	$5.4.3.2.a_5$	$6.5.4.3.a_6$	$7.6.5.4.a_7$	$(n+4).(n+2).(n+2).(n+1).a_{n+4}$

Table 3.3.1. Coefficients of the power terms in the governing equation for an end-bearing pile.

If the coefficients for the general power are used one can form the following equation.

$$(n+4)(n+3)(n+2)(n+1)a_{n+4} + (n+2)(n+1)\beta a_{n+2} + \gamma a_{n-1} + a_n = 0 \quad [3.3.29]$$

If the parameter, n, is adjusted such that n+4 is changed to n it is possible to produce the following recurrence relationship between the coefficients a_n,

$$a_n = -\frac{\beta a_{n-2}}{n(n-1)} - \frac{a_{n-4}}{n(n-1)(n-2)(n-3)} - \frac{\gamma a_{n-5}}{n(n-1)(n-2)(n-3)} \quad [3.3.30]$$

By introducing factorials, an alternative expression can be obtained,

$$a_n = -\frac{\beta(n-2)!a_{n-2}}{n!} - \frac{(n-4)!a_{n-4}}{n!} - \frac{\gamma(n-4)!a_{n-5}}{n!} \quad [3.3.31]$$

Since a_n is a linear function of a_0, a_1, a_2 and a_3, the general solution to the differential equation is (remembering that the subscripts 0 to 3 are used for the unembedded beam),

$$y = \sum_{i=4}^{7} A_i Y_i \qquad [3.3.32]$$

where, $$Y_{i+4} = \xi^i + \sum_{n=4}^{\infty} a_n \xi^n \qquad [3.3.33]$$

for i = 0 to 3, and for $n \leq 3$, $a_n = 1$ if n = i or $a_n = 0$ if $n \neq i$ and A_4 to A_7 represent the four constants of integration.

To obtain the buckling load of the pile and the corresponding mode shape, the boundary conditions at the ends of the member and at the soil-air interface must be specified. Expressions for displacement, slope, bending moment and shear force with respect to ξ are required. They are,

$$y = 0,\ \alpha \frac{dy}{d\xi} = 0,\ \alpha^2 \frac{d^2y}{d\xi^2} = 0 \text{ and } \alpha^3 \frac{d^3y}{d\xi^3} + \alpha^3 \beta \frac{dy}{d\xi} = 0 \quad [3.3.34],\ldots,[3.3.37]$$

Friction piles

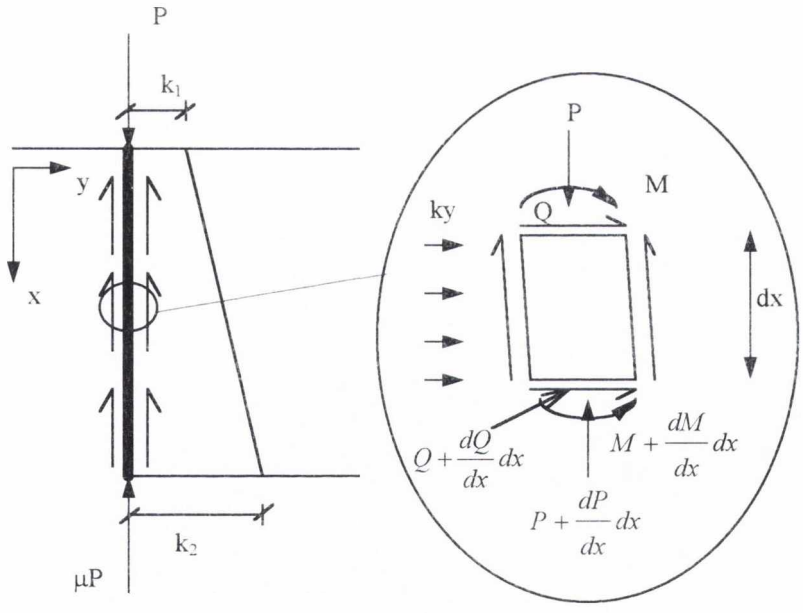

Figure 3.3.1. A fully embedded pile in a linearly varying elastic foundation supported by a frictional force.

Using an approach similar to that of Hetényi (1946) and taking the element dx of the embedded pile in figure 3.3.1 it may be seen that, for moment equilibrium,

$$\frac{dM}{dx} - P(x)\frac{dy}{dx} - Q(x) = 0 \qquad [3.3.38]$$

where P(x) is the axial compressive force which is dependent on x, the distance along the bar and Q(x) is the shear force at a point x along the pile. These variables can be written as

$$M = -EI\frac{d^2y}{dx^2},\ P(x) = P_0 - \int_{x=0}^{x} f(x)dx \text{ and } \frac{dQ}{dx} = k(x)y \qquad [3.3.39],\ [3.3.40],\ [3.3.41]$$

where EI is defined as before, $f(x)$ is the friction per unit length of pile and k is the modulus of subgrade reaction. $f(x)$ and $k(x)$ are assumed to vary linearly with x, the distance below the top of the embedded portion of the bar or pile. As stated earlier, $f(x)$ is defined by the use of f_1 and f_2 and $k(x)$ varies linearly as for end-bearing piles. $P_{friction}$ is the load supported by the shaft friction and χ is the force factor required to multiply $f(x)$ by in order to define the load (in Newtons) at any point on the shaft. They are related by,

$$\begin{aligned} P_{friction} &= \int_{x=0}^{l} f(x)dx = \int_{x=0}^{l} \chi\left(f_1 + (f_2 - f_1)\frac{x}{l}\right)dx \\ &= \chi\frac{(f_1 + f_2)\cdot l}{2} \end{aligned} \qquad [3.3.42]$$

Hence, using equations [3.2.1] and [3.3.42] the following relationship can be formed,

$$P_{friction} = (1-\mu)P_0 = \frac{\chi\, l}{2} \qquad [3.3.43]$$

Differentiating [3.3.38] with respect to x and then substituting the variables from [3.3.39] to [3.3.43], the following is produced

$$EI\frac{d^4y}{dx^4} + \left(P_0 - \int f(x)dx\right)\frac{d^2y}{dx^2} - f(x)\frac{dy}{dx} + (k_1 + n_h x)y = 0 \qquad [3.3.44]$$

If the variable $\xi = \left(\frac{k_1 + n_h l}{EI}\right)^{1/4}(x - l) = \alpha(x - l)$ is introduced, [3.3.45]

expressions for the $f(x)$ terms in equation [3.3.44] in terms of ξ are required.

Observe that,

$$\begin{aligned}\int_{x=0}^{x} f(x)dx &= \int_{x=0}^{x} \chi\left(f_1 + (f_2 - f_1)\frac{x}{l}\right)dx \\ &= \chi\left(f_1 x + (f_2 - f_1)\frac{x^2}{2l}\right) \\ &= \chi\left(f_1\left(\frac{\xi}{\alpha} + l\right) + \frac{(f_2 - f_1)}{2l}\left(\frac{\xi}{\alpha} + l\right)^2\right) \\ &= \frac{\chi}{2}\left((f_2 - f_1)\left(\frac{\xi^2}{\alpha^2 l}\right) + f_2 2\frac{\xi}{\alpha} + l\right) \\ &= \left(P_0(1-\mu)(f_2 - f_1)\left(\frac{\xi^2}{\alpha^2 l^2}\right) + 2P_0(1-\mu)f_2\frac{\xi}{\alpha l} + P_0(1-\mu)\right)\end{aligned} \quad [3.3.46]$$

Two further non-dimensional variables shall now be defined, V and W such that,

$$V = \frac{(1-\mu)(f_2 - f_1)P_0}{\alpha^4 EIl^2} = \frac{(1-\mu)(f_2 - f_1)\beta}{\lambda} \quad [3.3.47]$$

$$W = \frac{(1-\mu)f_2 P_0}{\alpha^3 EIl} = \frac{(1-\mu)f_2\beta}{\lambda^{0.5}} \quad [3.3.48]$$

Hence, equation [3.3.46] becomes

$$\int_{x=0}^{x} f(x)dx = \left(\alpha^2 EI\xi^2 V + 2\alpha^2 EI\xi W + P_0(1-\mu)\right) \quad [3.3.49]$$

Now,

$$\begin{aligned}f(x) &= \chi\left(f_1 + (f_2 - f_1)\frac{x}{l}\right) \\ &= \frac{2P_0(1-\mu)}{l}\left(f_1 + (f_2 - f_1)\left(\frac{\xi}{\alpha l} + 1\right)\right) \\ &= 2W\alpha^3 EI + 2V\alpha^3 EI\xi\end{aligned} \quad [3.3.50]$$

It is possible to substitute for $f(x)$ in terms of the dimensionless parameters into the governing equation which can now be formed, with respect to ξ, as,

$$\frac{d^4 y}{d\xi^4} + \frac{P_0 - \int f(x)dx}{\alpha^2 EI}\frac{d^2 y}{d\xi^2} - \frac{f(x)}{\alpha^3 EI}\frac{dy}{d\xi} + \frac{k_1 + \frac{n_h\xi}{\alpha} + n_h l}{\alpha^4 EI}y = 0 \quad [3.3.51]$$

as before in equation [3.3.21],

$$\frac{P_0}{\alpha^2 EI} = \beta$$

and,

$$\frac{P_0 - \int f(x)dx}{\alpha^2 EI} = \frac{P_0}{\alpha^2 EI} - V\xi^2 - 2W\xi - \frac{P_0(1-\mu)}{\alpha^2 EI} \qquad [3.3.52]$$
$$= \mu\beta - V\xi^2 - 2W\xi$$

also,

$$\frac{f(x)}{\alpha^3 EI} = 2W + 2V\xi \qquad [3.3.53]$$

Again from equation [3.3.22]

$$\frac{k_1 + \frac{n_h\xi}{\alpha} + n_h l}{\alpha^4 EI} = 1 + \gamma\xi$$

Hence, the final non-dimensional governing differential equation as,

$$\boxed{\frac{d^4y}{d\xi^4} + \left(\mu\beta - 2W\xi - V\xi^2\right)\frac{d^2y}{d\xi^2} + \left(2W + 2V\xi\right)\frac{dy}{d\xi} + \left(1 + \gamma\xi\right)y = 0} \qquad [3.3.54]$$

Assuming a solution of the above equation of the form,

$$y = \sum_{n=0}^{\infty} a_n \xi^n \qquad [3.3.55]$$

and performing the substitution as before, the following recurrence relationship between the coefficients a_n is produced,

$$a_n = -\frac{\mu\beta(n-2)!a_{n-2}}{n!} + \frac{2(n-3)W(n-3)!a_{n-3}}{n!} + \frac{(n-4)V(n-3)!a_{n-4}}{n!} \qquad [3.3.56]$$
$$-\frac{(n-4)!a_{n-4}}{n!} - \frac{\gamma(n-4)!a_{n-5}}{n!}$$

Again, if factorials are cancelled then an alternative expression for the recurrence equation is,

$$a_n = -\frac{\mu\beta a_{n-2}}{n(n-1)} + \frac{2(n-3)Wa_{n-3}}{n(n-1)(n-2)} + \frac{(n-4)Va_{n-4}}{n(n-1)(n-2)} \qquad [3.3.57]$$
$$-\frac{a_{n-4}}{n(n-1)(n-2)(n-3)} - \frac{\gamma a_{n-5}}{n(n-1)(n-2)(n-3)}$$

Since a_n is a linear function of a_0, a_1, a_2 and a_3, the general solution to the differential equation is (remembering that the subscript 0 to 3 are used for the unembedded beam),

$$y = \sum_{i=4}^{7} A_i Y_i \qquad [3.3.58]$$

where,

$$Y_i = \xi^{i-4} + \sum_{n=4}^{\infty} a_n \xi^n \qquad [3.3.59]$$

for i = 4 to 7, and for $n \leq 3$, a_n = 1 if n = i or a_n = 0 if $n \neq i$, where A_4 to A_7 represent the four constants of integration.

Expressions for displacement, slope, bending moment and shear force with respect to ξ are required. They are,

$$y = 0,\ \alpha \frac{dy}{d\xi} = 0,\quad {}^{2}\frac{d^2y}{d\xi^2} = 0,\ \alpha^3 \frac{d^3y}{d\xi^3} + \alpha^3\left(\mu\beta - V\xi^2 - 2W\xi\right)\frac{dy}{d\xi} = 0 \qquad [3.3.60],\ldots\ldots,$$

[3.3.63]

It should be noted that if μ = 1 then V and W are zero and hence the recurrence equation and other equations are all identical to the non-friction case.

3.4. Overall Solution

In order to solve the buckling problem of a partially embedded pile it is necessary to specify a set of conditions in order to solve for the constants A_0 to A_7. The specification of the two boundary conditions at the extremities of the pile and four continuity conditions at the junction of the two regions yields eight homogeneous equations,

$$[\mathbf{M}]\underline{\mathbf{A}} = \underline{0} \qquad [3.4.1]$$

In this thesis the first four rows of **M** are given by continuity at the junction, the fifth and sixth rows are given by the boundary conditions at the unembedded end and the last two rows are given by the boundary conditions at the embedded end. For example, for a fixed-free pile, the matrix **M** would be as produced in equation [3.4.2], with $\underline{\mathbf{A}}$ in equation [3.4.3].

Y_4 to Y_7 are defined in the sections above for the solution of the embedded beam in either the end-bearing or friction cases. Y_0 to Y_3 are defined by the solution for the non-embedded beam.

Equation [3.4.1] represents an eigenvalue problem and the equation $|\mathbf{M}| = 0$ gives the eigenvalues corresponding to the buckling load of the pile. A modified sign count algorithm (West, 1993) is used to find the eigenvalues which are expressed in terms of β. Hence, the values of the constants of integration A_0 to A_7 relative to each other are obtained for a particular eigenvalue and the buckling mode shape is calculated.

Initially this thesis will concentrate on fully embedded beams. There are two techniques by which the matrix **M** may be formed in this case. The first is to use the same formulation as for partially embedded beams except that the embedment ratio is set as close to unity as possible. A value of $\delta = 0.999$ does not alter the solution produced significantly. The second, and more exact, method is to redefine **M** and $\underline{\mathbf{A}}$. Only four constants A_4 to A_7 are required. The first two rows of the new matrix define the end condition at the top of the pile while the third and fourth rows define the end condition at the bottom. Hence, **M** is now only a 4x4 matrix and the solution time is significantly reduced (by approximately a factor of four). In equations [3.4.4] and [3.4.5] **M** and $\underline{\mathbf{A}}$ have been described for the case of a fixed-free beam.

$$[\boldsymbol{M}] = \begin{bmatrix} Y_0(0) & Y_1(0) & Y_2(0) & Y_3(0) & Y_4(0) & Y_5(0) & Y_6(0) & Y_7(0) \\ \eta Y_0'(0) & \eta Y_1'(0) & \eta Y_2'(0) & \eta Y_3'(0) & \alpha Y_4'(0) & \alpha Y_5'(0) & \alpha Y_6'(0) & \alpha Y_7'(0) \\ \eta^2 Y_0''(0) & \eta^2 Y_1''(0) & \eta^2 Y_2''(0) & \eta^2 Y_3''(0) & \alpha^2 Y_4''(0) & \alpha^2 Y_5''(0) & \alpha^2 Y_6''(0) & \alpha^2 Y_7''(0) \\ \eta^3 (Y_0'''+ Y_0(0)) & \eta^3 (Y_1'''+ Y_1(0)) & \eta^3 (Y_2'''+ Y_2(0)) & \eta^3 (Y_3'''+ Y_3(0)) & \alpha^3 (Y_4'''+ Y_4(0)) & \alpha^3 (Y_5'''+ Y_5(0)) & \alpha^3 (Y_6'''+ Y_6(0)) & \alpha^3 (Y_7'''+ Y_7(0)) \\ Y_0(-l_1) & Y_1(-l_1) & Y_2(-l_1) & Y_3(-l_1) & 0 & 0 & 0 & 0 \\ \eta Y_0'(-l_1) & \eta Y_1'(-l_1) & \eta Y_2'(-l_1) & \eta Y_3'(-l_1) & 0 & 0 & 0 & 0 \\ 0 & 0 & 0 & 0 & \alpha^2 Y_4''(l_2) & \alpha^2 Y_5''(l_2) & \alpha^2 Y_6''(l_2) & \alpha^2 Y_7''(l_2) \\ 0 & 0 & 0 & 0 & \alpha^3 (Y_4'''+ Y_4(l_2)) & \alpha^3 (Y_5'''+ Y_5(l_2)) & \alpha^3 (Y_6'''+ Y_6(l_2)) & \alpha^3 (Y_7'''+ Y_7(l_2)) \end{bmatrix} \quad [3.4.2]$$

$$\underline{A} = \begin{bmatrix} A_0 \\ A_1 \\ A_2 \\ A_3 \\ A_4 \\ A_5 \\ A_6 \\ A_7 \end{bmatrix} \quad [3.4.3]$$

$$[\boldsymbol{M}] = \begin{bmatrix} Y_4(0) & Y_5(0) & Y_6(0) & Y_7(0) \\ \alpha Y_4'(0) & \alpha Y_5'(0) & \alpha Y_6'(0) & \alpha Y_7'(0) \\ \alpha^2 Y_4''(l_2) & \alpha^2 Y_5''(l_2) & \alpha^2 Y_6''(l_2) & \alpha^2 Y_7''(l_2) \\ \alpha^3 \left(Y_4''' + Y_4(l_2)\right) & \alpha^3 \left(Y_5''' + Y_5(l_2)\right) & \alpha^3 \left(Y_6''' + Y_6(l_2)\right) & \alpha^3 \left(Y_7''' + Y_7(l_2)\right) \end{bmatrix} \quad [3.4.4]$$

$$\underline{\boldsymbol{A}} = \begin{bmatrix} A_4 \\ A_5 \\ A_6 \\ A_7 \end{bmatrix} \quad [3.4.5]$$

3.5. Methods of eigenvalue determination

The buckling problem has now been reduced to that of the eigenvalue and eigenvector determination of an 8x8 (partially embedded case) or a 4x4 (fully embedded case) matrix **M**. There are numerous methods which are appropriate to specific types of matrices, i.e. real, Hermitian, orthogonal, symmetric, etc., which are described in such books as Schwarz et al (1973) and Collar and Simpson (1987). However, the problem under consideration in this thesis does not lend itself to any of the powerful methods available because **M** is non-symmetric and has real coefficients which vary non-linearly with the buckling parameter, β. There are two methods by which the eigenvalues and, hence, the eigenvectors may be calculated for this problem. They are the determinant search and the method proposed by West (1991). West (1991) provides a summary of methods to solve other related eigenvalue problems such as symmetrical transcendental matrices.

3.5.1 The determinant search

The determinant search method can be applied to any type of matrix in order to calculate the eigenvalues and eigenvectors. If the eigenvalues of **f** (ω) are required, where **f** (ω) is defined by,

$$\mathbf{f}(\omega) = \begin{bmatrix} f_{11}(\omega) & f_{12}(\omega) & \cdots \\ f_{21}(\omega) & f_{22}(\omega) & \cdots \\ \cdots & \cdots & f_{nn}(\omega) \end{bmatrix} \qquad [3.5.1]$$

where ω is generally termed as a frequency parameter in the literature (however it will be identical to the non-dimensional buckling parameter, β, in this thesis) then for any particular value of ω the determinant of **f** (ω) may be calculated. If, as ω increases, | **f** (ω) | changes from being positive to negative, or vice versa, then an eigenvalue of the matrix must lie in the interval of the two values of ω. It is then possible to use an iterative method such as bisection to calculate the eigenvalue to any required accuracy. The eigenvector can then be calculated using back substitution in the original matrix.

The method of calculation of the determinant depends on the type of matrix. For small matrices it is possible to use the direct evaluation of minors method, however, for larger matrices,

with the use of computers, it is more normal to triangulate the matrix into either upper or lower form. The determinant is then equal to the trace of the triangular matrix (the product of the diagonal elements).

The initial step in ω is crucial to this method. The smaller the step size the longer it takes to find any given eigenvalue. However, if the step in ω is too large then it is possible not to detect two closely spaced eigenvalues because if the determinant is positive below the first eigenvalue of the pair, it will be negative between the two eigenvalues and positive again above the second. In the case of vibrational and buckling problems, eigenvalues are often very close, almost identical. It is essential that a more robust method is used for such problems.

3.5.2 Significant methods

West (1991) describes a rigorous method of identifying eigenvalues which, unlike the determinant search method, will cope with closely spaced eigenvalues. The method is based on a method described by Wittrick and Williams (1971) which can be described as follows.

Wittrick and Williams (1971) method

If a real symmetric dynamic stiffness matrix, **K** is assembled for a structure with an infinite number of degrees of freedom (for which **KD** = 0, **D** = some displacements), then the number of natural frequencies of vibration which exist below some chosen circular frequency ω^*, termed $J(\omega^*)$, is given by:-

$$J(\omega^*) = J_0(\omega^*) + s\{\mathbf{K}(\omega^*)\} \qquad [3.5.2]$$

where $J_0(\omega^*)$ is the number of natural frequencies which would still be exceeded by ω^* if n constraints were imposed so as to make all the displacements **D** (at the discretised nodes) equal to zero, and $s\{\mathbf{K}(\omega^*)\}$ is the sign count of the matrix $\mathbf{K}(\omega^*)$. The sign count is defined as the number of times the sign of the elements in the leading diagonal of **K** change from positive to negative. Unfortunately, because the problem under consideration will not be symmetric, this method cannot be used. It is briefly described because the West method is based upon it.

West (1991) method

The West method was designed to solve the problem of identifying modal clusters in the vibration of partially embedded beams. This meant that the matrix **f** was defined by two parameters, the stiffness of the embedded medium, λ, and the vibration frequency parameter, c. The steps of the method described in West (1991) are as follows;

1. The elements of **f**, f_{nn} (λ, c), are calculated for given values of λ, c.
2. Using elementary row operations only, **f** is transformed into upper triangular form $\mathbf{f}^{\Delta}$.
3. The sign pattern is then defined by the signs of the elements of the leading diagonal of $\mathbf{f}^{\Delta}$.
4. λ, c are varied over predefined ranges until trends in the way the sign pattern changes can be identified.

The trends can best be described by plotting the sign pattern as λ, c vary (figure 3.5.1). In order to help the discussion S(λ, c) will be defined as the sign pattern at a point λ, c. If the number of changes between S(λ, c) and S(λ, $c+dc$), where dc is the increment in c, is odd then this signifies that an eigenvalue is present at that soil stiffness between c and $c+dc$ (for example between sections A-D; D-I; J-M; K-N; B-E; E-J; etc. in figure 3.5.1). If the number of changes is even then this can signify either that there are two eigenvalues present (E-N) or that that two of the signs in the leading diagonal have changed simultaneously (E-F; F-H; J-K; etc.). These simultaneous changes in the signs of the elements of the leading diagonals lie on two types of lines; those that are invariant with λ (at c $\approx$ 7.9, M-N; J-K; etc.) and those that change with λ (B-A; D-E; I-J; B-C; E-F; H-G; L-K). West (1991) related the invariant lines with the problem of the calculation of the natural frequency of a partially embedded beam. In this case the invariant lines coincide with the natural frequencies of the unembedded portion of the beam with the embedded beam being replaced by a fixed end condition. The variable lines relate to the natural frequencies of the embedded beam, however, their relation with this problem is so complex that it does not provide any information which can be realistically used to solve the more complex problem.

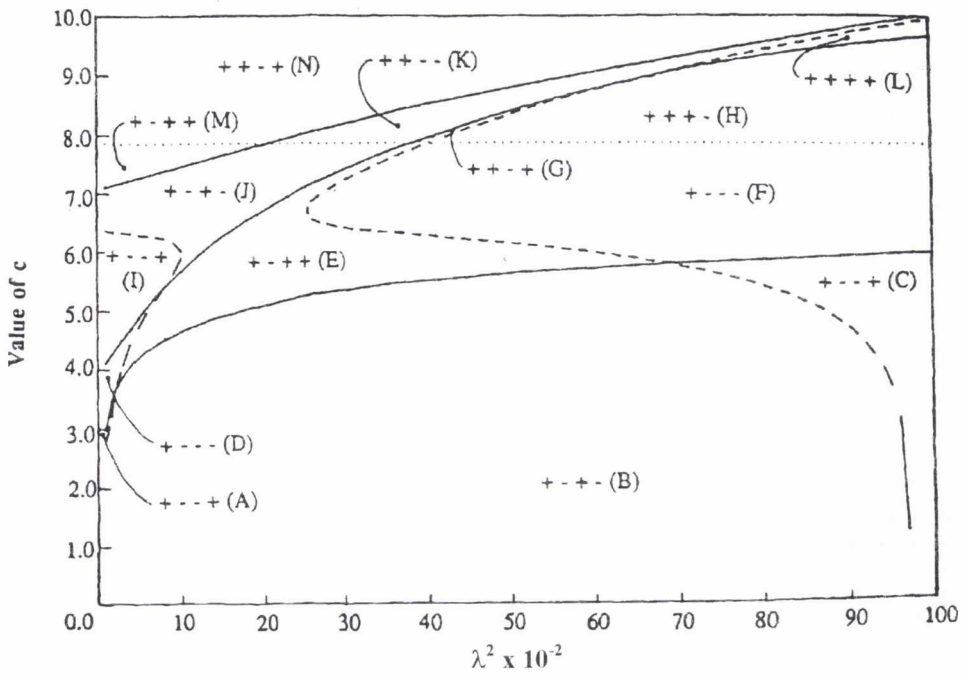

Figure 3.5.1. Sign pattern diagram for a pinned-free beam with embedment ratio, $\delta = 0.5$, generated by West (1991).

West and Pavlović (1993) produced an algorithm by which the eigenvalues may be calculated. This involved using a dynamic variable *dc* in order to investigate any interval where the sign pattern changes. Initially S(λ, *c*) is calculated using a coarse interval in *c*. If a change is discovered between S(λ, *c*) and S(λ, *c*+*dc*) than dc is divided by a suitable factor and the interval is again examined. This continues until *dc* is less than a preset tolerance. Whether the change in sign pattern indicates an eigenvalue can then be determined. The performance of this method depends on some initial decisions on the parameters. If the original coarse parameter is too large then it is possible that the sign pattern can change and then change again and revert to the original sign pattern within one increment (for example A-I; B-J; E-N). This will not be detected. If the end tolerance is set too large and eigenvalues are close together then the two eigenvalues may still not be detected (H-N at $\lambda = 0.8$) as the change can be wrongly determined as crossing a line of simultaneous change of sign. In the above diagram such an error can be easily discovered. However, the modes can approach much closer to each especially in the case of homogenous end-bearing piles. In this case great care has to be taken to determine that no modes are missed. The smaller either parameter is, the longer the program takes to run because there is an increase in the number of sign patterns that have to be determined.

However, West found that, with a suitable initial increment and end tolerance, the method should identify all eigenvalues.

3.6. Computer algorithm

A simplified flow chart for a computer program to find the solutions to equation [3.4.1] is shown in figure 3.6.1. It shows the basic format of the Pascal program that was used to solve the problem. Some of the terms have been expanded in table 3.6.1. The algorithm is based on West (1991).

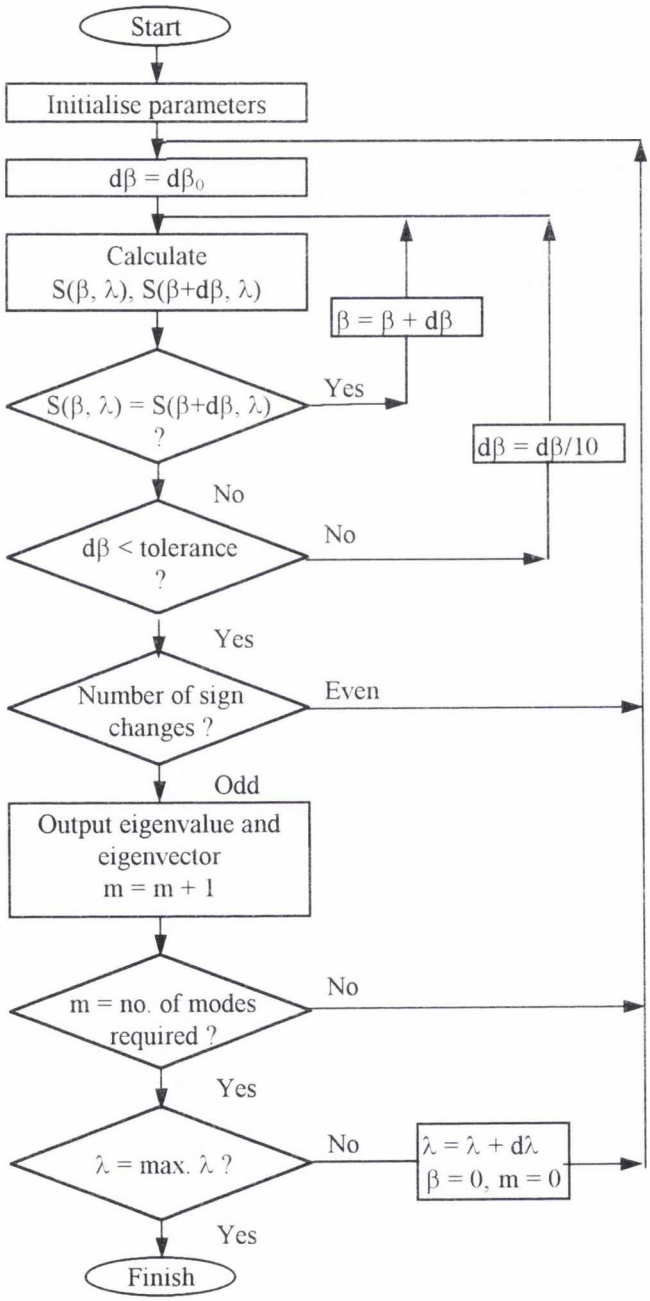

Figure 3.6.1. Flow chart for the buckling program.

$d\beta_0$ is the predefined maximum allowable increment in the buckling parameter, β. $d\lambda$ is the increment in the soil stiffness parameter, λ.

Box Description	Definition
Initialise parameters	define problem; end conditions, embedment ratio etc; set soil stiffness, λ , to starting value, set load parameter, $\beta = 0$; decide upon number of modes required, m = 0.
Calculate S(β, λ)	evaluate non-dimensional parameters, i.e. γ, V and W; evaluate terms in matrix **M**; triangulate **M**; sign pattern = signs of leading diagonal
Output eigenvalue and eigenvector	Use values of β and $\beta+d\beta$ and a method such as bisection to converge onto the eigenvalue to an increased tolerance, calculate the eigenvector by back-substitution

Table 3.6.1. Definition of terms in figure 3.6.1.

The above flow chart will find all the eigenvalues provided suitable values of $d\beta_0$ are chosen initially. Because buckling loads will be detected normally across a range of soil stiffnesses it is possible to improve the program performance by reference to the previous results. For instance, if the first buckling load has been determined for a lower soil stiffness previously, then the search for the first buckling mode can be started at the previous value rather than at zero. It is also possible to produce an algorithm to determine a dynamic $d\beta_0$ from previous results. The ability to predict lines of change in sign pattern which are invariant with λ could also be programmed.

3.7. Program validation

The solution presented in the previous sections will be compared to two other methods in order that the validity of the solution can be assessed. The first comparison is to an exact solution that is limited to fully embedded end-bearing beams with symmetric end-condition as presented by Hetényi (1946). The second is to a finite element analysis program Map which uses the algorithm presented in Lawther and Kabaila (1982). There are, of course, many other solutions that it would be possible to use, but these two will show that the solutions produced by the method described previously are accurate.

In figure 3.7.1 a beam resting on a Winkler foundation is presented. In table 3.7.1 solutions to the exact formula as presented by Hetényi (1946) and the solutions from the algorithm described in this thesis are tabulated. As can be seen they are identical.

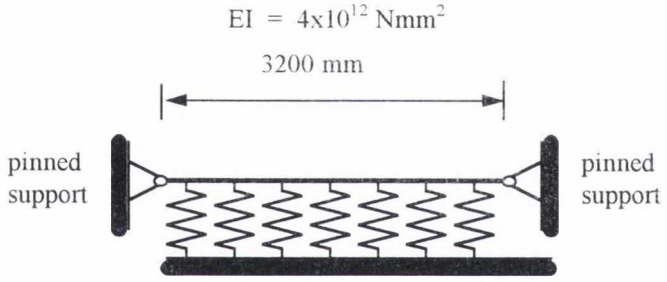

Figure 3.7.1. A pinned-pinned bar on a homogeneous foundation.

lambda	Hetényi Buckling Force	Calculated Buckling Force
5	1.256649556	1.256649556
10	2.026598225	2.026598225
50	10.41623891	10.41623891
100	20.40664695	20.40664695

Table 3.7.1. First mode non-dimensional buckling loads from Hetényi (1946) compared to the calculated buckling load from Heelis (1996).

The author has run the MAP finite element analysis program for the more complicated partially embedded, non-homogeneous and friction cases and is satisfied that the results tend to the exact solution produced by the algorithm used in this thesis. For example, the case of a partially embedded pile with length, flexural rigidity and end-conditions as the previous example, half embedded in a soil with linearly increasing soil stiffness and friction with depth (figure 3.7.2). The

load is completely supported by shaft friction. The results are as shown in table 3.7.2 for the cases of 16, 32 , 64 finite elements in the model and the solution produced by the method described earlier. It is generally excepted that models with a large number of elements are more accurate than those with a fewer number. As can be seen the error between the finite element results and the solution calculated using the proposed method reduces with an increase in the number of finite elements. The problem under discussion is the most complicated under discussion in this thesis as it is partially embedded with non-constant shaft friction and soil stiffness. Hence, it can be concluded that the proposed method is an accurate solution to the problem.

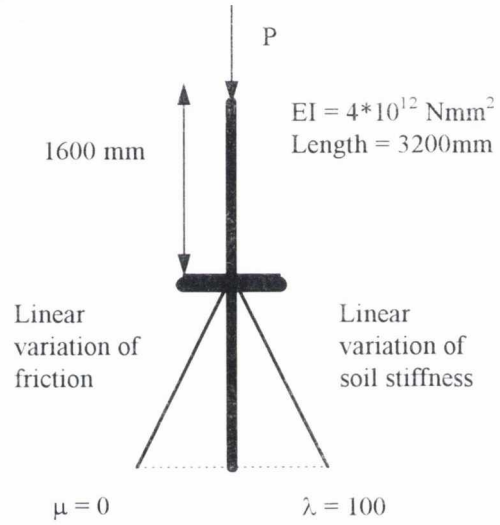

Figure 3.7.2. Model with pinned-pinned ends for finite element comparison.

number of finite elements	mode 1	error %	mode 2	error %
16	$1.52288*10^7$	9.4	$4.29184*10^7$	8.6
32	$1.40083*10^7$	0.6	$3.96787*10^7$	0.4
64	$1.39432*10^7$	0.2	$3.95658*10^7$	0.1
'Exact' Solution	$1.39217*10^7$		$3.95280*10^7$	

Table 3.7.2. Solutions for model in figure 3.7.2 with $\lambda = 100$.

Whilst trying to produce the results on the finite element package it was discovered that the method suggested by Lawther and Kabaila had a tendency, if buckling modes were close together, to converge on either the upper or lower mode in a somewhat random fashion. This meant that it was

sometimes possible for the finite element package to miss modes. It was possible to rectify this by limiting the range in which the program searched for buckling modes so that the range only spanned a single mode. Obviously this assumes a priori knowledge of the result required and highlights one of the disadvantages of finite element analysis.

There are further examples of comparing the method outlined in this chapter to other authors work in chapter 6. Although there may be differences, they can be explained once the methods used by the other author are considered.

Program performance

The plots of buckling loads in the following chapters normally consist of the first six buckling modes of a problem for a range of soil stiffness parameter $0 < \lambda < 300$. The step, $d\lambda$, is normally equal to two. Hence, for each plot 150 points are plotted along the x axis and six lines are plotted. This means a total of 900 buckling modes have been found. On the IBM compatable DX2-66 and with the program written in Turbo Pascal (Borland, 1985) this would take approximately 6 hours, or one eigenvalue found every 24 seconds. The number of terms in the polynomial series to converge to an accuracy of twelve significant figures varies according to the size of μ, β, V and W (Equation [3.3.57]) and λ . While using the algorithm the additional terms were not calculated once the series had converged. It appeared that the number of terms never exceeded 500, and for fully embedded end-bearing piles a maximum of 200 was observed.

3.8. Conclusion

In this chapter the problem of the buckling of a partially embedded pile has been solved. The problem was considered in two parts. The first part, that of the unembedded portion of the beam, had been solved previously. The problem of the embedded portion of the beam has also been split into two. The first problem is that of a beam which is supported by end-bearing only; this is the simpler of the two problems. The second model also incorporates friction as a method of supporting the load, though not necessarily without a degree of end-bearing support as well. The soil in both cases has been modelled as a Winkler foundation (either homogeneous or non-homogeneous) as was suggested from the previous chapter.

Each problem can be defined by a fourth order differential equation. In the case of the unembedded section of the beam this can be solved exactly using a combination of trigonometric and simple polynomials functions. The governing equations for the embedded portion of the beam can be solved using an infinite power series solution. The recurrence equations which define the power series have been deduced.

The computer program developed to calculate the buckling loads and mode shapes presented in later chapters is then briefly described. It used the eigenvalue search method outlined in West and Pavlović (1993). The final section in the chapter described two methods by which the results from the computer program have been validated.

Chapter 4

Fully embedded piles

4.1. Introduction

In the previous chapter the method of analysis has been outlined. However, it should be noted that the method is equally applicable to beams which are fully embedded in the medium as well as those which are only partially embedded. Homogeneous and non-homogeneous soil can also be modelled. In this case the homogeneity is defined with respect to soil stiffness. The soil stiffness can be modelled varying linearly increasing with depth or being constant. It is also possible to vary the way that the load is supported by the soil. The type of support can be in one of three categories:

1. **End-bearing piles**. These piles support the load by an end reaction at the base of the pile. It is assumed that there is no friction present from the walls of the pile. These are the simplest cases to consider.

2. **Pure friction piles**. It is assumed that friction in these piles is the only method of support and that there is no contribution from end bearing. As discussed in section 2.4, the friction on the pile shaft can vary with depth below the surface. A simple form of variation of friction has to be assumed in order for the problem to be solvable. It will be assumed that there is either constant friction or a linear variation in friction with depth and these are reasonable approximations to real soils. This is the second type of non-homogeneous behaviour that can be defined in the model used.

3. **Composite end-bearing and friction piles**. These are probably the most realistic piles where friction can vary and, at the same time, there is some proportion of the applied load which is supported by end-bearing at the bottom of the pile.

In this chapter, firstly the buckling behaviour of end-bearing piles which are fully embedded will be presented and discussed. For the case of symmetric end-conditions (that is, fixed-fixed, pinned-pinned and free-free beams) with a homogeneous soil foundation, an exact solution already exists as presented by Hetényi (1946) in a trigonometric/hyperbolic form. The solutions are presented here, however, for comparison because they are used in subsequent analysis for more complex cases as a convenient reference point. Due to the nature of the problem, these classical cases can be used to

illustrate some of the behavioural characteristics of buckling, such as modal clustering and mode shape changes, which are also present in the more complex cases but do not occur in such clearly defined ways.

The results in this thesis will be presented by the use of graphs which are plotted with the critical load factor, P_{crit}/P_E (equation 3.2.2), against the dimensionless soil parameter, λ, which varies between 0 and 300. This means that for a pile with flexural rigidity of 46.5 MNm^2 (a Larson BP2 box pile), in a stiff clay with k = 2.4 MN/m^2, that a pile of up to 35m can be modelled. This range is wide enough to cover most piles and yet is sufficiently well focused so that the detail in the buckling behaviour can also be identified. In the figures of buckling loads in this chapter will normally be plotted with the first six buckling modes as this enables the identification of generic trends in the lower buckling modes which would be less easy to distinguish if only one or two modes are plotted.

4.1.1 Modal clusters and plateaux

Modal clusters and plateau were found to occur in the vibrational problem of a partially embedded beam in an Elastic Winkler foundation by West (1991) (figure 4.1.1). Due to the natural

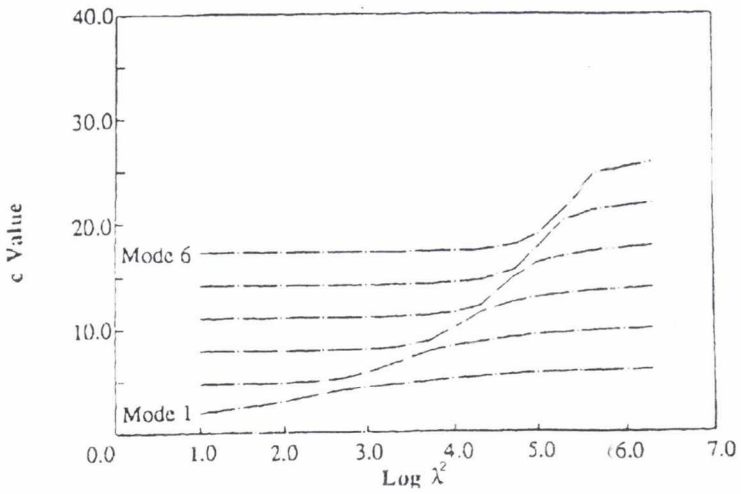

Figure 4.1.1. First six vibrational (c is the non-dimensional frequency parameter) modes for a fixed-free partially embedded (δ = 0.25) beam (West, 199).

similarity between the vibrational and buckling problem of beams modal clusters and plateau would be expected to occur in the buckling problem also. In order to introduce the terms modal clustering

and modal plateaux which will be used regularly in this thesis, the case of a fully embedded end-bearing pile in a homogeneous medium with fixed-fixed end conditions will be considered initially (see figure 2.5.3). Note that the axes are reversed in this chapter in order that the dependent variable, the buckling load is on the y axis. In figure 4.1.2 the curves are presented which represents the variation in the first two buckling modes as the soil stiffness increases. As would be expected when $\lambda = 0$, the buckling loads are identical to those that would be predicted by the classical Euler formula. They are $P_{crit}/P_E = 4$ and 8.182994 for the first and second buckling modes respectively. The buckling loads then gradually increase until the first and second mode converge on each other. The section of the curve for the second mode, where the buckling mode remains approximately the same is defined as a modal plateaux. It is characterised by the mode shape being practically identical for all values of λ across this range.

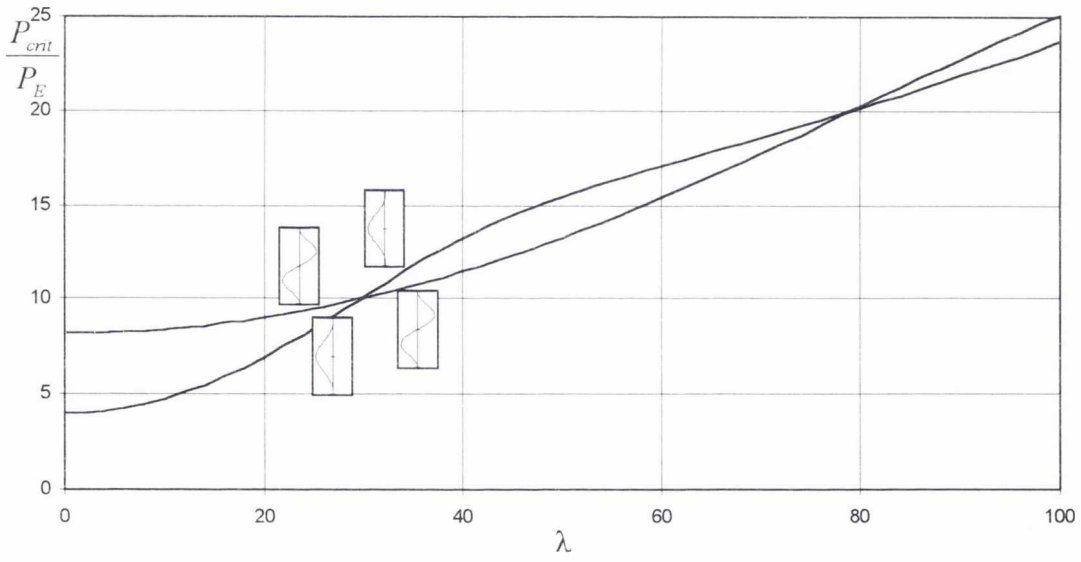

Figure 4.1.2. First two buckling modes for a fixed-fixed end-bearing beam fully embedded in a homogeneous soil.

Mode shapes can be categorised by the number of half waves (or maxima and minima) that make up their shape. A modal cluster is defined to exist where the difference between the buckling loads of consecutive modes, evaluated at the same soil stiffness, is at a minimum, for example at $\lambda = 3\pi^2$ (29.61)and $P_{crit}/P_E = 10$. The mode shapes for the first and second modes at a soil stiffness just below and just above the modal cluster appear to be swapped as shown in figure 4.2, where the mode

shapes evaluated at λ = 28 and 30 are plotted on the respective mode lines. Inspection of figure 4.1.3 shows how the mode shape for the upper mode varies as λ continues to increase.

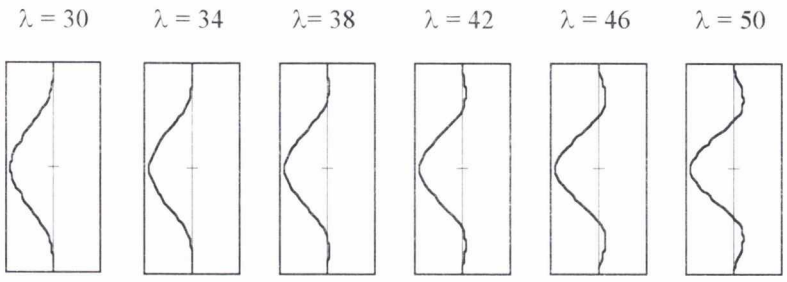

Figure 4.1.3. Mode shapes of the second mode in figure 4.1.2.

The second mode shape at λ = 30 looks similar to the first mode at λ = 28. However if the mode shape is plotted accurately enough it can be seen that there are, in fact, three half waves not one. This mode shape can more easily be distinguished at λ = 50 in figure 4.1.3. Hence, all the mode shapes for the second mode between λ = 30 and λ = 50 have three half waves. For conciseness, such a section on a buckling mode curve will be associated with a single mode shape in the text. The mode shape will have all three half waves with sufficient amplitudes in order that they can be easily distinguished. Hence, the mode shape associated with a section will tend to be more characteristic of the soil stiffness at the upper range for the section. It should be remembered that the buckling mode usually changes gradually and it is difficult to define the exact soil stiffness when the mode shape of a buckling mode changes. This will be particularly so when beams are studied which are neither end-bearing nor in a homogeneous medium.

4.2. End bearing piles

4.2.1 Homogeneous medium

It is possible to predict the incidence of modal clusters and, hence the plateaux boundaries for symmetric boundary conditions with uniform soil stiffness (that is, F = 1) using formula derived from Hetényi (1946). The change-over between consecutive symmetric and anti-symmetric mode shapes all lie on the series of parabolas defined by,

$$\frac{P_{crit}}{P_E} = n^2 + \frac{1}{\pi^4 n^2}\lambda^2 \qquad [4.2.1]$$

where n = 1, 2, 3, ... for fixed-fixed, pinned-pinned and the free-free cases. In the case of the free-free beam, however, the equation applies only to the buckling modes higher than the second (figure 4.2.1). These lines signify solutions with mode shapes which have n = 1, 2, 3, ... half waves in them as will be described when the pinned-pinned solution is discussed. It should be noted that the mode clusters between modes also lie on straight lines which have equations of the form

$$\frac{P_{crit}}{P_E} = 4m^2 + \frac{2\lambda}{\pi^2} \qquad [4.2.2]$$

where m = 1, 2, 3, ... for fixed-fixed case and m = 1/2, 1, 3/2,.... for the pinned-pinned case. The first value of m indicates the line through the modal clusters between mode 1 and mode 2, the second value indicates the line through mode 3-mode 4 clusters, etc. For the free-free case, only modes higher than the second display these characteristic lines for values of m = 1, 2, 3, ..., the first-second mode cluster lies on a line which goes through the origin and has a gradient of half that in equation 4.2.2.

The results for the three end-fixity cases have been plotted in figures 4.2.1 to 4.2.3. These figures display identical results for the first mode (the only mode considered) as plotted by Hetényi (see section 2.5.1). Superimposed on these plots are the modal cluster lines as defined by equation 4.2.1 and 4.2.2. The value of the relevant parameter n, m is displayed next to the line. In figure 4.2.2

the lines m = 1, m = 2 have not been plotted in order not to over-complicate the diagram, however, these lines do go through the modal clusters between modes 2-3 and mode 3-4 respectively.

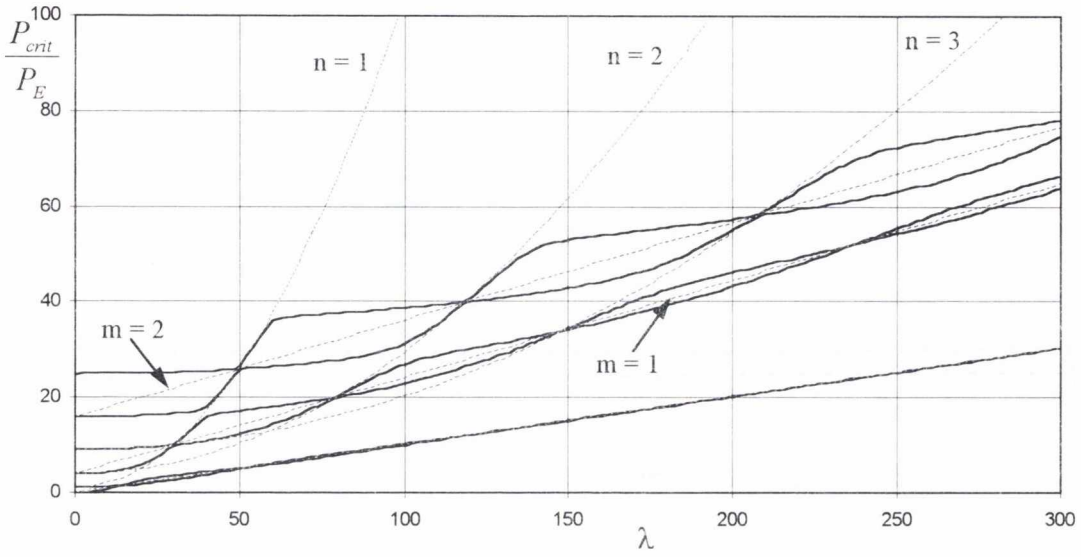

Buckling loads [———], modal cluster envelope lines [·····].

Figure 4.2.1. The first six buckling loads for a free-free end-bearing beam fully embedded in a homogeneous soil compared to the modal cluster envelope lines.

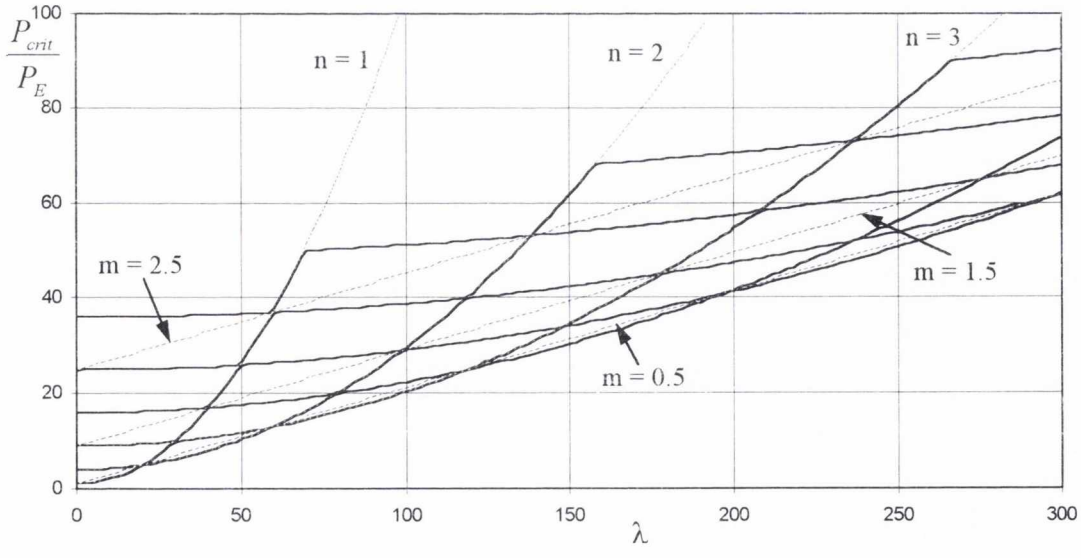

Buckling loads [———], modal cluster envelope lines [·····].

Figure 4.2.2. The first six buckling loads for a pinned-pinned end-bearing beam fully embedded in a homogeneous soil compared to the modal cluster envelope lines.

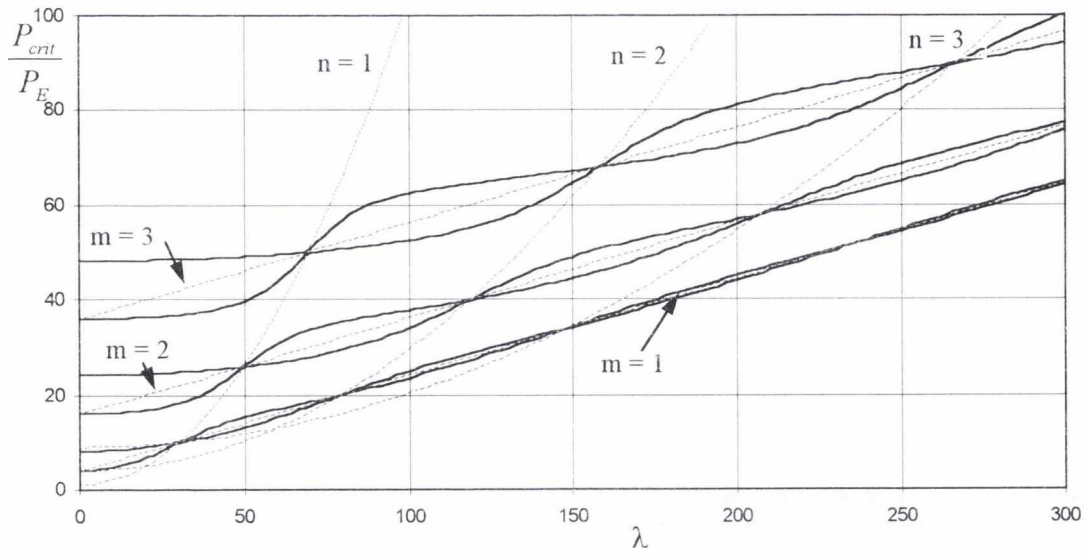

Buckling loads [——], modal cluster envelope lines [·····].

Figure 4.2.3. The first six buckling loads for a fixed-fixed end-bearing beam fully embedded in a homogeneous soil compared to the modal cluster envelope

If figures 2.5.1 to 2.5.3, which were reproduced from Hetényi (1946) are now compared to figures 4.2.1 to 4.2.3 it can be seen how by inspection of the higher modes the trends in the lowest mode can more easily be visualised. It should be remembered that, normally, the lowest buckling mode is the only one of interest.

It should be noted that in the free-free case the first two modes have significantly different mode shapes to the third and higher modes. In figure 4.2.4 the mode shapes for the plateaux in figure 4.2.1 are plotted for the first three modes. The first four columns represent the characteristic mode shapes whereas the fifth column demonstrates a transitional buckling mode as the soil stiffness increases. The first and second buckling modes obviously alternate between mode shapes which can be characterised by the fact that the deflection in the middle tends to be less than at the ends. The third (and subsequent modes) tend to have deflections which are largest towards the centre of the beam. They are similar to the mode shapes for a pinned-pinned beam. It should be remembered that the third buckling mode and above follow the lines m = 1, m= 2, etc. (figure 4.2.1). These parametric lines also coincide with the buckling modes with pinned ends. Hence, because the free-free buckling

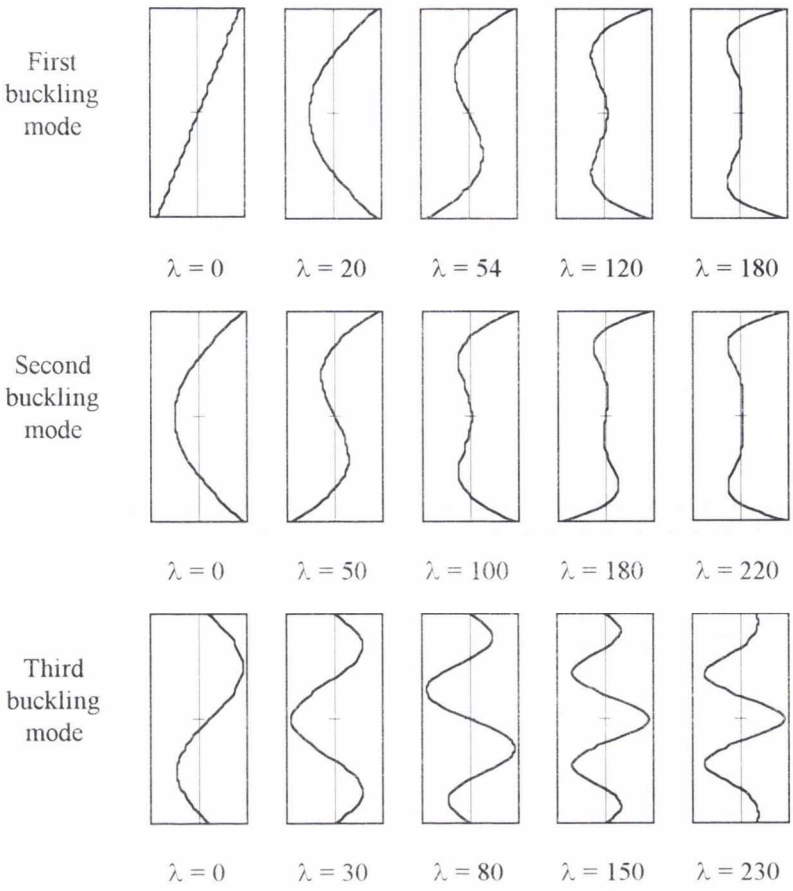

Figure 4.2.4. Mode shapes for the plateaux of the first three modes for a free-free end-bearing beam fully embedded in a homogeneous soil.

modes lie on these lines, especially just after mode clusters, the mode shapes of the upper modes in the free-free case are similar to the pinned-pinned buckling modes.

The first and second transitional buckling mode shapes have the characteristic behaviour of having smaller amplitudes in a section at the centre of the mode shape compared to the extremes. The third transitional mode is different in that the amplitude at the ends decreases.

It is interesting to note that, in the pinned-pinned case illustrated in figure 4.2.5, the mode shapes for the second mode do not proceed regularly by having an extra half sine wave in subsequent modes. Instead, between the mode shape with two and three half sine waves there is, briefly, a mode shape with only one half sine wave; similarly between three and four half sine waves there is briefly a mode shape with two sine half waves. This is because, if figure 4.2.2 is considered, it will be noticed that the buckling loads always lie on parabolic mode cluster lines. These parabolic mode cluster lines

all signify lines associated with a single mode shape with a particular number of sine waves. When m = 1 then there is one half sine wave, m = 2, two half sine waves and so on. This holds for whichever mode (1, 2, 3,..) that actually lies on the parabolic line at the time. Hence, in figure 4.2.5, as the second mode changes with increasing soil stiffness (a-b-c-d), initially (a-b) the mode shape has two half sine waves, this changes to one half sine wave (b-c) and, finally, (c-d) the mode shape has three half sine waves. The first mode shape changes from one, to two, to three half sine waves as the soil stiffness increases (as reproduced in figure 2.5.2 from Heténvi's work).

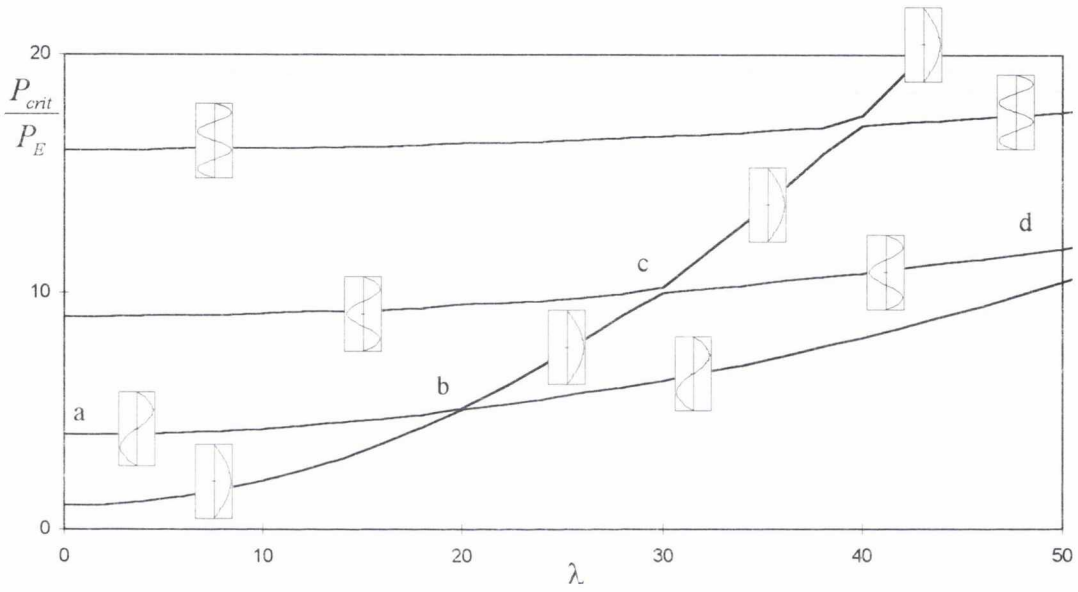

Figure 4.2.5. Exact mode shapes for a pinned-pinned end-bearing beam fully embedded in a homogeneous soil.

Figure 4.2.6 shows the variation in the first six buckling loads for a fixed-free beam (note due to the homogeneous Winkler foundation the results for a fixed-free beam are identical to a free-fixed beam). It can be seen that although the modal clusters are no longer as distinct as in the symmetric cases, they still lie on a series of parabolae and straight lines. The first mode is different from the rest and the reason for this is clear when the first two mode shapes are inspected in figure 4.2.7. The first mode gradually changes from the mode shape at $\lambda = 0$ to that at $\lambda = 300$, via the mode shape at $\lambda = 65$ as the soil stiffness increases. It can be seen that the buckled shape is due to the free nature of the embedded end and for the larger soil stiffnesses the displacement is concentrated at the embedded end. Higher modes have buckled shapes which are not concentrated next to the embedded end as can be

seen when the second mode is examined in figure 4.2.7. This is the reason why the first mode is significantly lower than the other modes in figure 4.2.6.

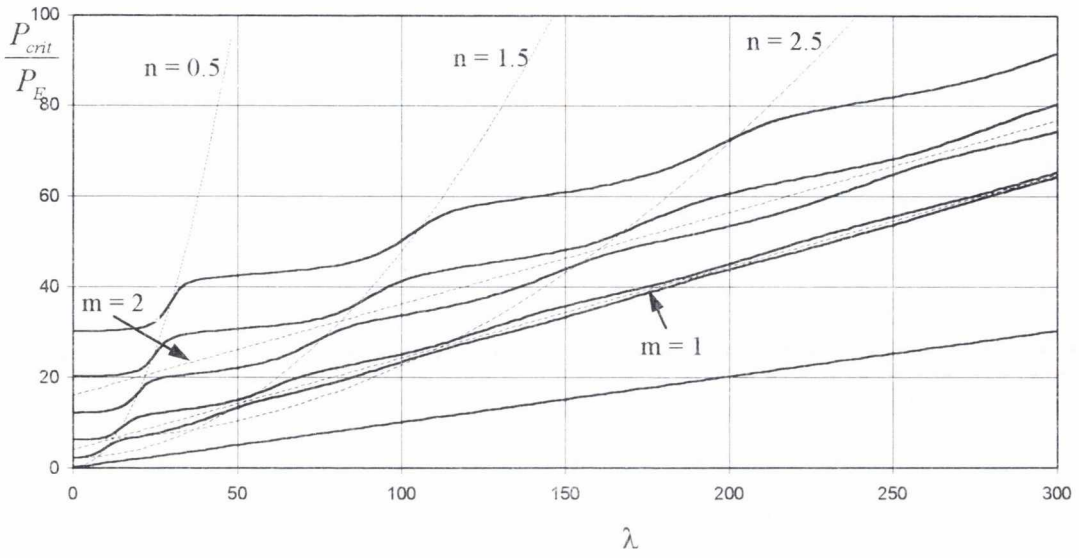

Buckling loads [——], modal cluster envelope lines [·····].

Figure 4.2.6. Buckling loads for a fixed-free end-bearing beam fully embedded in a homogeneous soil compared to modal cluster prediction lines.

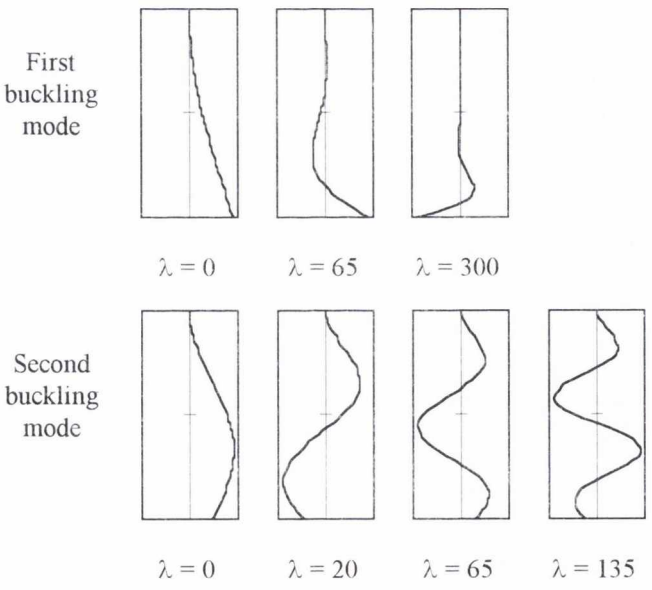

Figure 4.2.7. Mode shapes of the first two modes in figure 4.2.6.

4.2.2 Non-homogeneous medium

In figure 4.2.8 the first buckling mode with free-free end conditions is plotted for varying homogeneity of the soil foundation. As would be expected, because λ is defined as the maximum soil

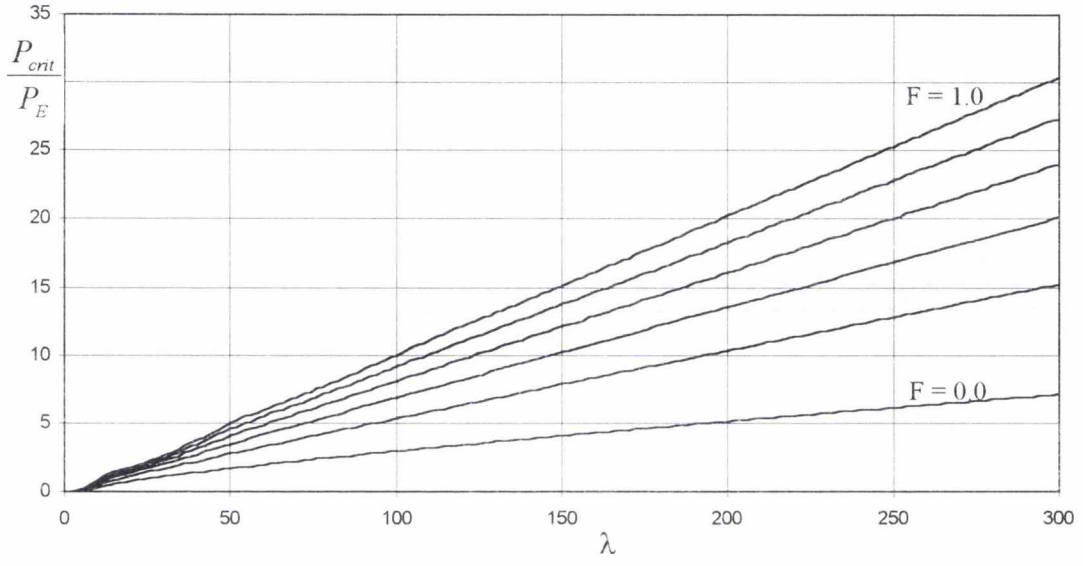

Figure 4.2.8. The first buckling mode for a free-free end-bearing beam fully embedded in a non-homogeneous soil with F = 0.0, 0.2, 0.4, 0.6, 0.8 and 1.0.

stiffness at the bottom of the pile as the variation changes from a constant (F = 1) to a triangular (F = 0) distribution, the buckling load decreases.

In figure 4.2.9 the modes are again plotted except in this case the buckling load is plotted against $\lambda_{average}$ where,

$$\lambda_{average} = \left(\frac{k_1 + k_2}{2} \frac{l^4}{EI} \right)^{1/2} = \left(\frac{1+F}{2} \right)^{1/2} \lambda \qquad [4.2.3]$$

which is the non-dimensional soil stiffness parameter when a soil with a linearly varying stiffness is modelled by a soil with a constant stiffness, the average soil stiffness being the same. Note that the term 'average soil stiffness' means that the soil stiffness, $k(x)$, is averaged and **not** the soil stiffness parameter, λ. In figure 4.2.9 there is a significant error if the classical Hetényi solution for homogeneous soils is used to approximate a linearly varying soil. As can be seen the estimated

buckling loads can be as much as 2.5 times the actual buckling load when an average soil stiffness is being used to estimate a non-homogeneous soil (F = 0).

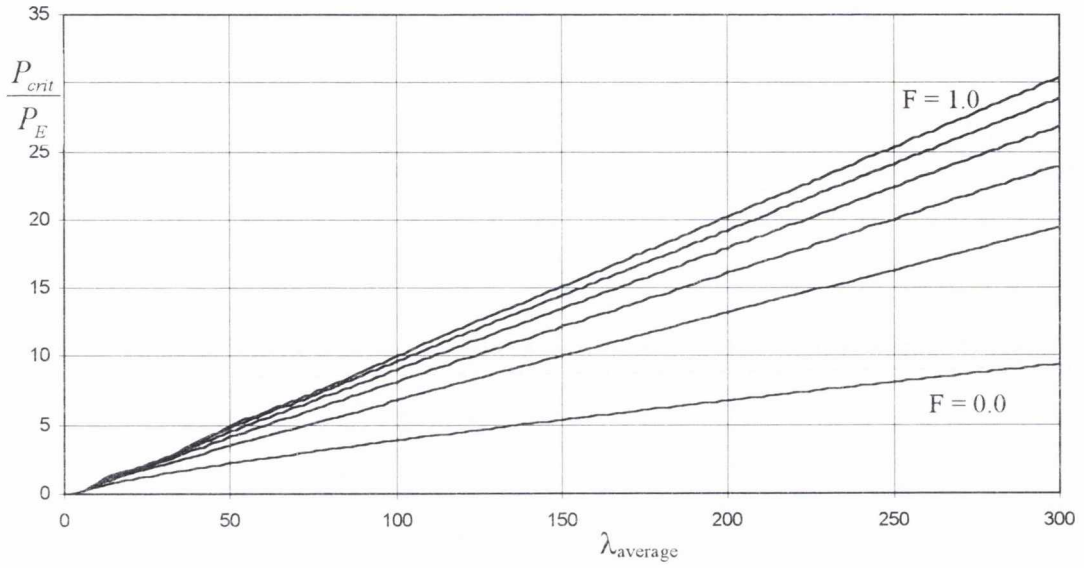

Figure 4.2.9. First buckling mode for a free-free end-bearing beam fully embedded in a non-homogeneous soil plotted against the average soil stiffness as F varies.

In figure 4.2.10 the mode shapes with a soil stiffness of $\lambda_{average}$ = 150 are plotted as F varies. As would be expected, the effect of a greater stiffness at the bottom than the top of the pile produces reduced deflections at the bottom, even for minor differences in the soil stiffness between the top and bottom (F = 0.8). The problem with using an average soil stiffness to produce results for mode shapes can be identified. The constant soil stiffness mode shape is significantly different to all other mode shapes which have negligible amplitudes in the bottom half of the pile.

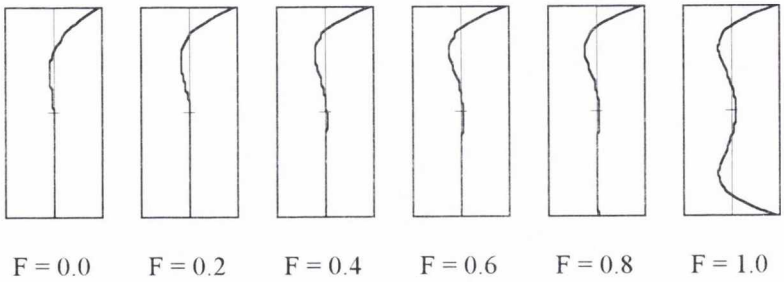

Figure 4.2.10. Mode shapes for the first mode with an average soil stiffness of $\lambda_{average}$ = 150 in figure 4.2.9.

Figure 4.2.11 shows the first six buckling modes with free-free end conditions and triangular (F = 0) and constant (F = 1) soil stiffnesses. The triangular soil has a first mode which is separated

from the second mode, whereas, the constant stiffness soil has the first and second mode much closer together. Figure 4.2.12 shows the first three mode shapes for the triangular variation in soil stiffness.

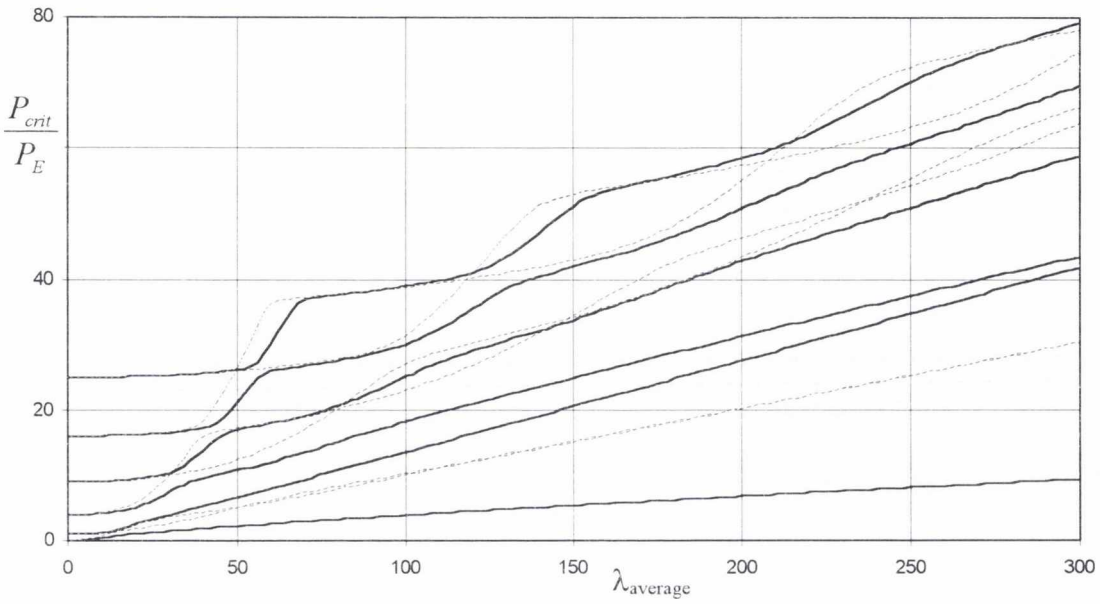

Non-Homogeneous soil (F = 0) [——], homogeneous soil (F = 1) [·····].

Figure 4.2.11. First six buckling loads for F = 0 and F = 1 for a free-free fully embedded end-bearing beam plotted using an average soil stiffness.

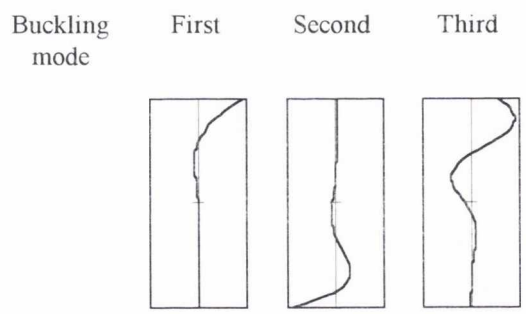

Figure 4.2.12. Mode shapes of the first three modes for F = 0, free-free with an average soil stiffness $\lambda_{average} = 150$.

It can be seen that the second mode is significantly different to the first and third because the largest displacements are actually at the bottom of the pile. This is surprising because this is where the soil is at its stiffest. Subsequent modes have the largest displacements at the top as would be expected. It can be seen that as $\lambda_{average}$ tends to 300 that the second buckling mode approaches the third mode. For

higher values of λ the mode with a maximum amplitude at the bottom becomes the third mode (then the fourth, etc).

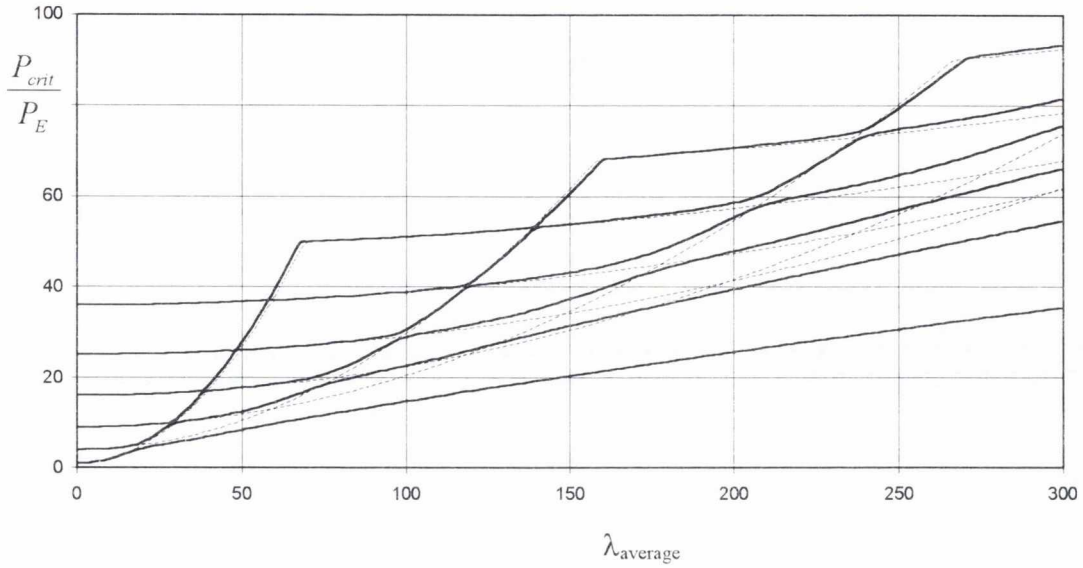

Non-homogeneous soil (F = 0) [——], homogeneous soil (F = 1) [·····].

Figure 4.2.13. First six buckling loads for F = 0 and F = 1 for a pinned-pinned fully embedded end-bearing beam plotted using an average soil stiffness.

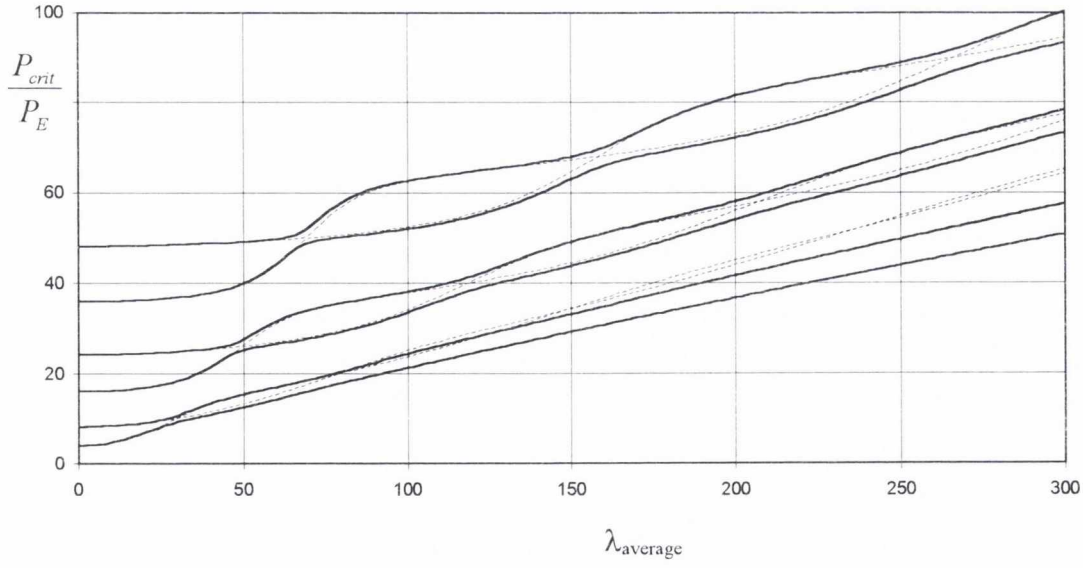

Non-homogeneous soil (F = 0) [——], homogeneous soil (F = 1) [·····].

Figure 4.2.14. First six buckling loads for F = 0 and F = 1 for a fixed-fixed beam plotted using an average soil stiffness.

Figures 4.2.13 and 4.2.14 show how the buckling loads vary for pinned-pinned and fixed-fixed end conditions and a constant and a triangular variation in soil stiffness. As in the free-free case,

the upper modes are not significantly different in the buckling load for the constant and triangular variations. The buckling load of the first mode is always significantly less for the F = 0 case compared to the F = 1 case. However, if the three cases are compared with each other, it can be seen that the type of support at the ends affects how much the first mode is weaker. If the ends are fixed then there is only a moderate difference between the triangular and constant cases (at $\lambda_{average}$ = 300 the buckling load for the F = 0 case is 79.0% of the F = 1 load). The difference increases for the pinned case (57.5%) and is greatest for the free case (30.8%). Of course, the end condition next to the less stiff soil is more significant than the end condition in the stiffer soil.

If the mode shapes for the free-free case in figure 4.2.12 are inspected then it obviously does not matter what the end condition is at an end of zero displacement. If it is zero with zero slope with a free boundary condition, then it will also be zero for all other end conditions. This means that the mode shape and corresponding buckling load will occur in the fixed case as well as the free case. However, there may be additional solutions in the free embedded end case. In figure 4.2.15 the first six buckling loads for F = 0 fully embedded fixed-fixed and fixed-free cases are plotted.

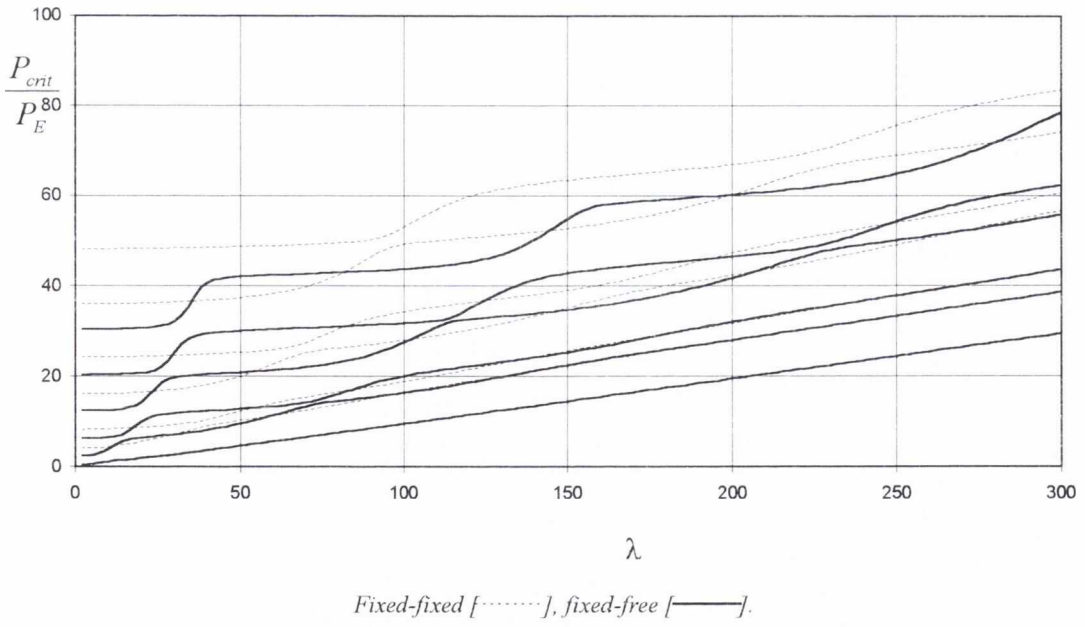

Figure 4.2.15. First six buckling modes for F = 0 fixed-fixed and fixed-free end conditions for a fully embedded end-bearing beam in a non-homogeneous soil.

It can be seen in figure 4.2.16 that the second mode in the fixed-free case tends to the first mode in the fixed-fixed case, the third mode in the fixed-free tends to the second mode in the fixed-

fixed case, etc., as soil stiffness increases. In figure 4.2.16 the six mode shapes for the two cases at λ = 300 are plotted. As would be expected the first fixed-free mode shape is unique to this case and can be categorised by displacement at the free end. The fixed embedded end would prevent this mode shape or any like it. The second fixed-free mode is obviously of the same family as the first fixed-fixed mode shape. This relationship continues for the higher modes except for the sixth fixed-free mode, where the soil stiffness is not sufficiently large to produce this result. If a higher soil stiffness was considered then the effect described above would also apply to the sixth mode.

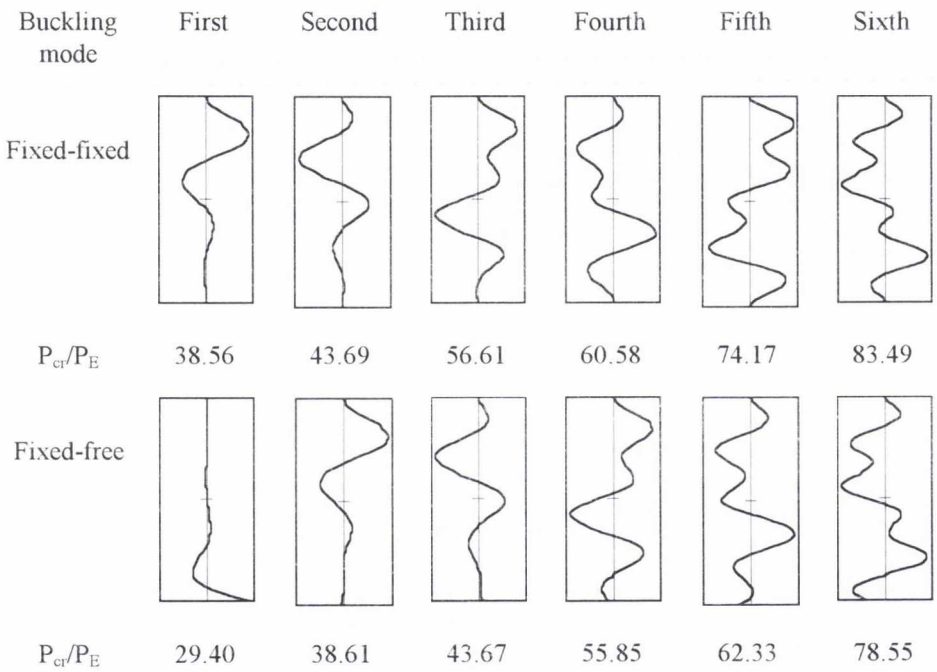

Figure 4.2.16. Mode shape plots for the first six modes for figure 4.2.15 at λ = 300.

It would be expected that if a sufficiently stiff soil was considered then it would prevent the first mode having its maximum amplitude at the bottom. If this is the case then the first and second buckling load should swap at a particular soil stiffness. This, indeed, happens at a soil stiffness of $\lambda \approx$ 1200 as can be seen in figure 4.2.17. This is also the point where the buckling loads for fixed-fixed and fixed-free converge. The fundamental mode shapes for $\lambda > 1200$ are identical as the fixed-free buckling mode shape has no amplitudes close to the free embedded end. The mode shape with a maximum amplitude at the bottom is then the second mode shape for a range of soil stiffness (figure 4.2.18).

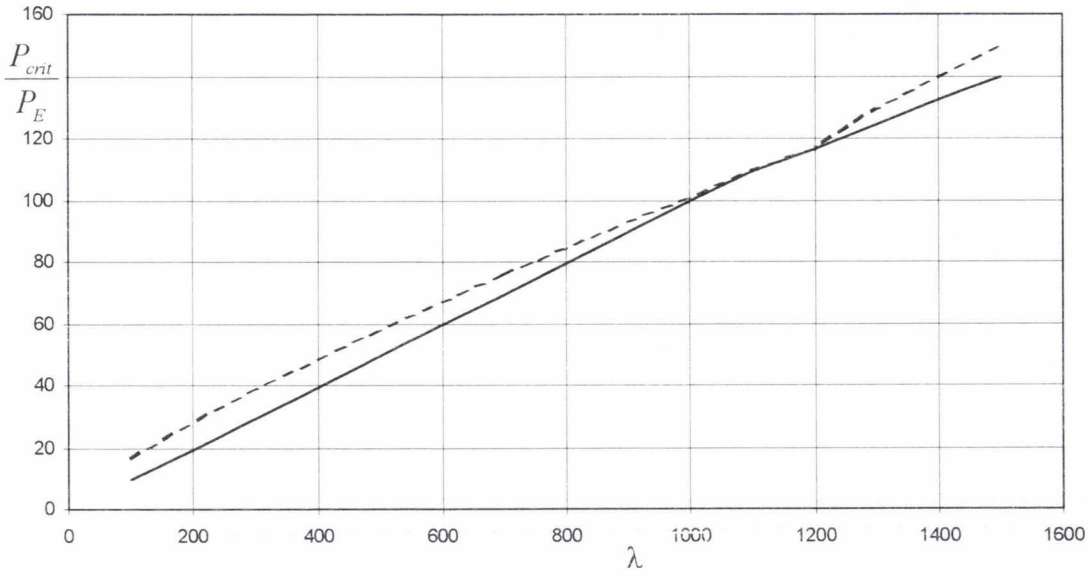

Figure 4.2.17. First two buckling loads for a fixed-free fully embedded end-bearing beam in a non-homogeneous (F= 0) soil.

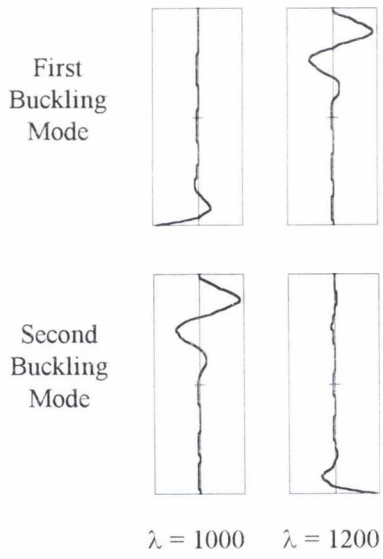

Figure 4.2.18. First two mode shapes for figure 4.2.17.

In order to prevent the mode shape with amplitude at the bottom of the pile occuring in the first buckling mode for other values of F, a minimum value of soil stiffness, $\lambda \approx 1200$, is required for a fixed-free end-bearing pile. This minimum value will increase as F increases. As mentioned previously, the range $0 < \lambda < 300$ takes into account most real piling conditions, in which case the mode shape with maximum amplitude at the bottom is likely to be the fundemental mode. This will be an important consideration when real piles are considered in Chapter 6.

4.2.3 Summary

The following figures are plots of the principal buckling load for all end conditions and for triangular and constant soil stiffnesses. Each plot represents a particular unembedded boundary condition. On each plot there are four lines representing the four possible embedded end-conditions.

Homogeneous soils (F = 1)

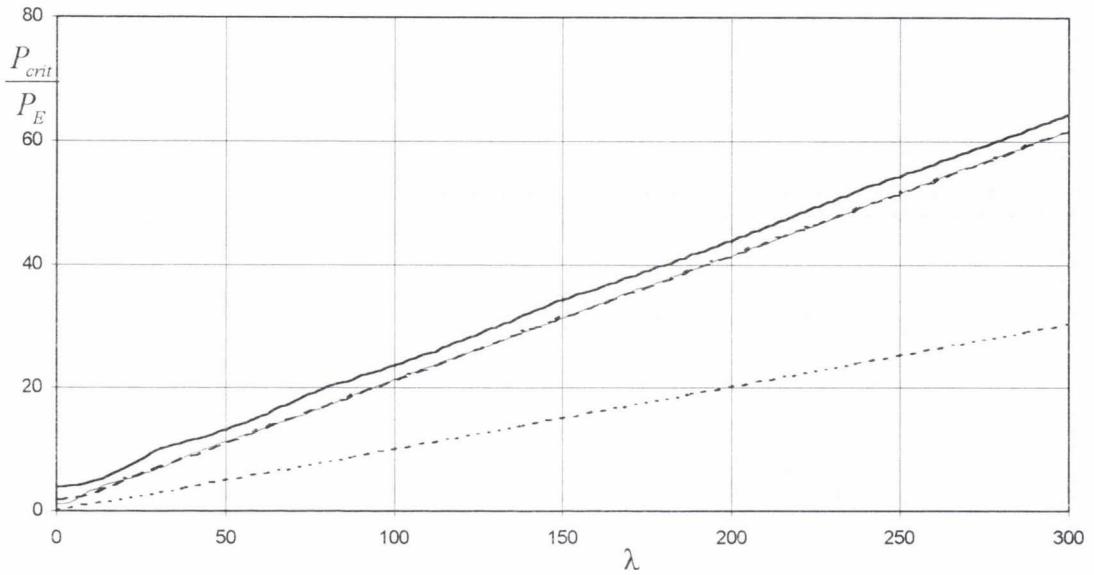

Fixed [——], pinned [– – –], no rotation/translation only [——], free [· · · ·].

Figure 4.2.19. First buckling loads for a fully embedded end-bearing beam with a fixed unembedded end in a homogeneous soil (F = 1).

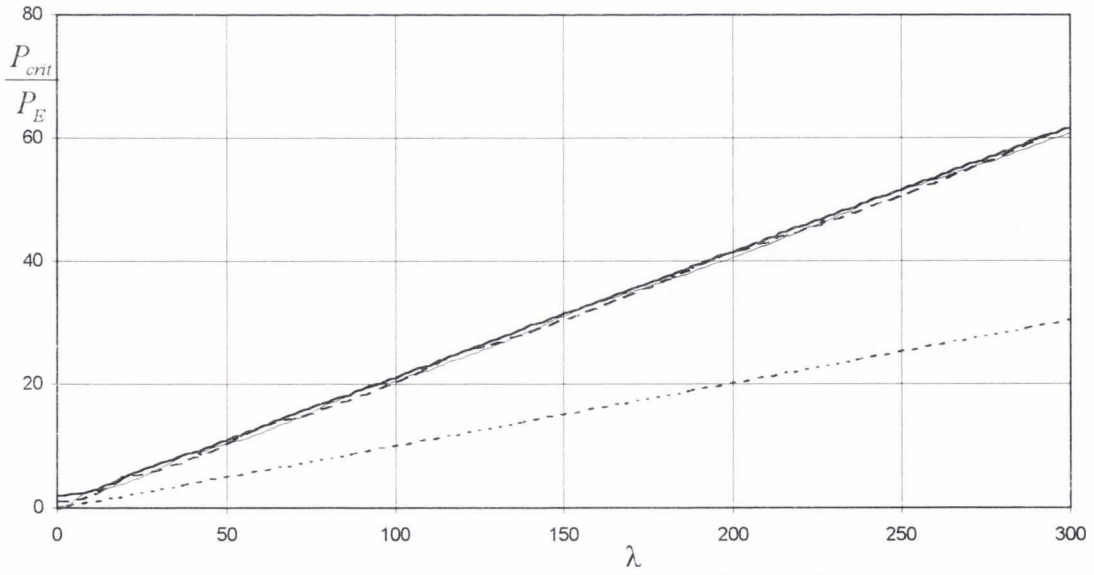

Fixed [——], pinned [– – –], no rotation/translation only [——], free [· · · ·].

Figure 4.2.20. First buckling loads for a fully embedded end-bearing beam with a pinned unembedded end in a homogeneous soil (F = 1).

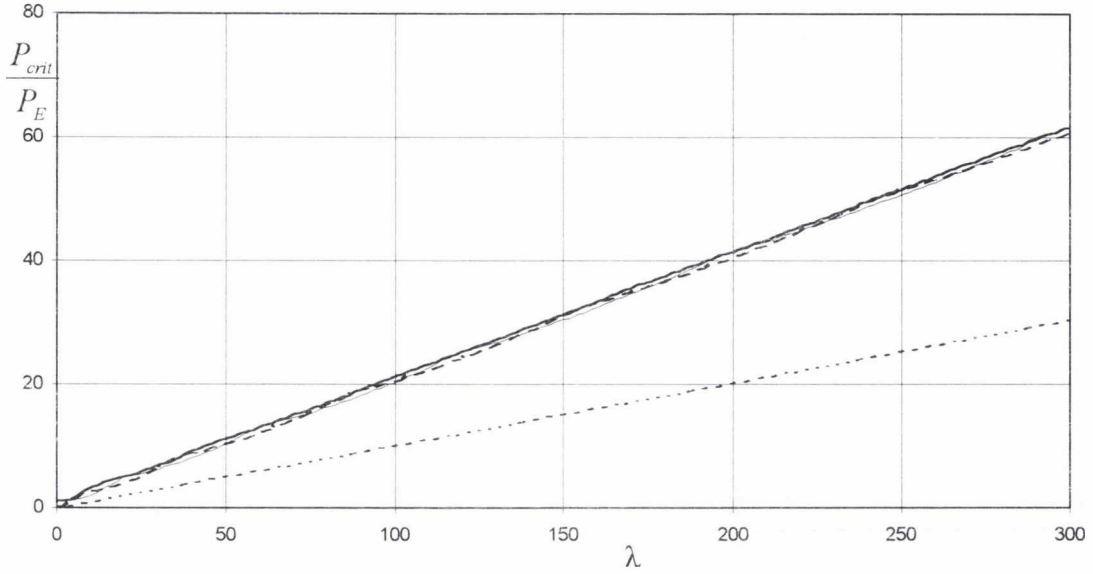

Fixed [———], pinned [– – –], no rotation/translation only [———], free [· · · ·].

Figure 4.2.21. First buckling loads for a fully embedded end-bearing beam with a no rotation unembedded end in a homogeneous soil (F = 1).

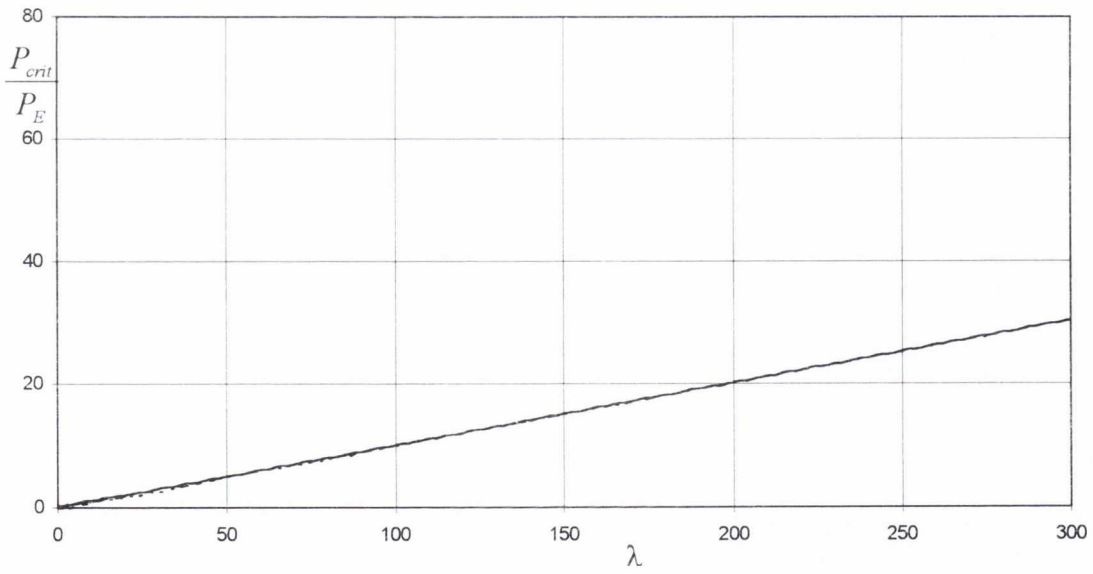

Fixed [———], pinned [– – –], no rotation/translation only [———], free [· · · ·].

Figure 4.2.22. First buckling loads for a fully embedded end-bearing beam with a free unembedded end in a homogeneous soil (F = 1).

Non-homogeneous soils (F = 0)

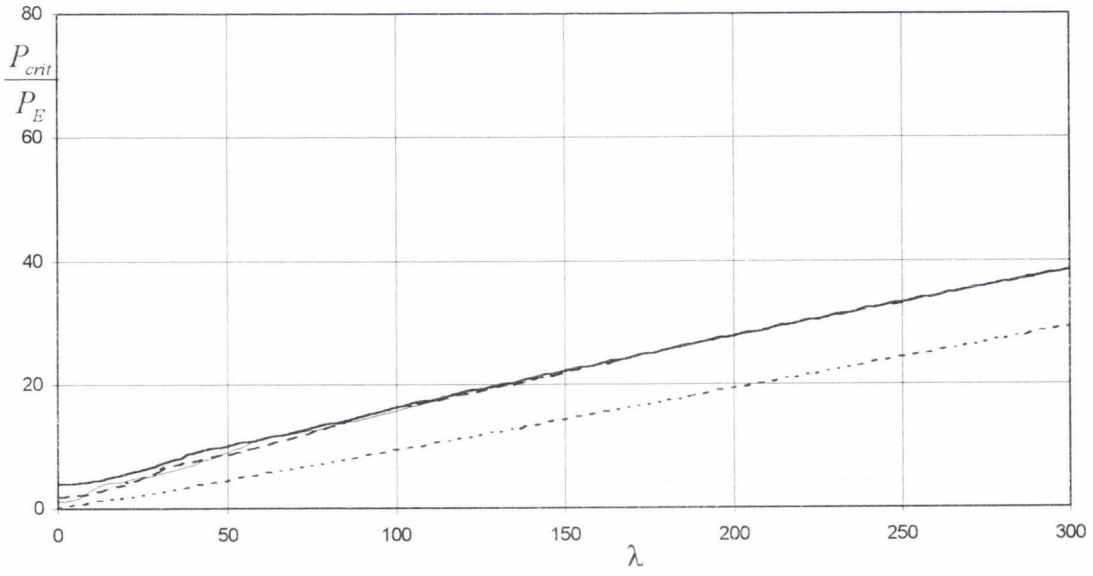

Fixed [———], pinned [– – –], no rotation/translation only [———], free [· · · ·].

Figure 4.2.23. First buckling loads for a fully embedded end-bearing beam with a fixed unembedded end in a non-homogeneous soil (F = 0).

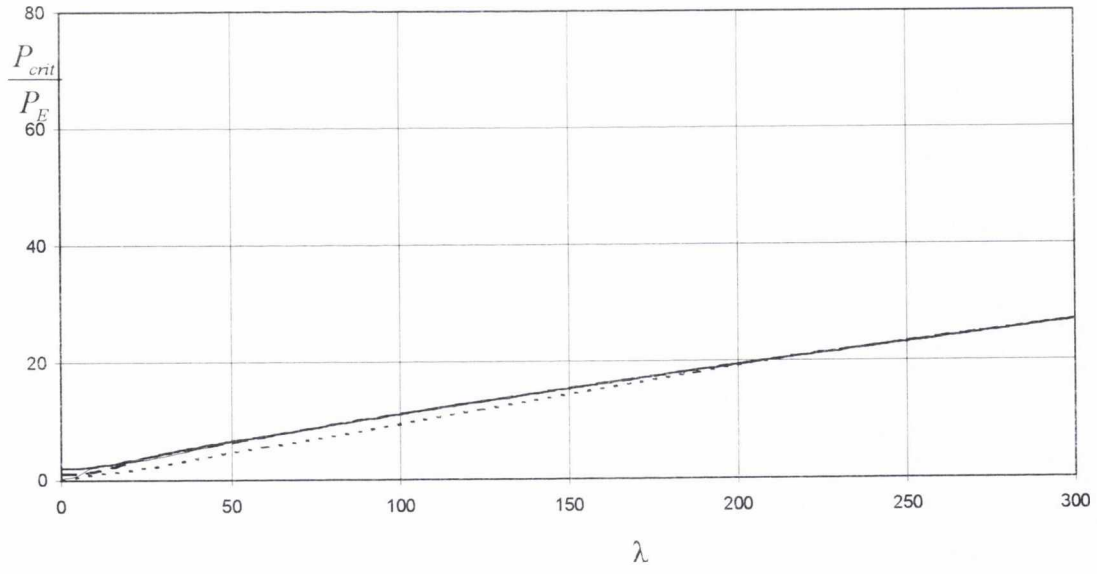

Fixed [———], pinned [– – –], no rotation/translation only [———], free [· · · ·].

Figure 4.2.24. First buckling loads for a fully embedded end-bearing beam with a pinned unembedded end in a non-homogeneous soil (F = 0).

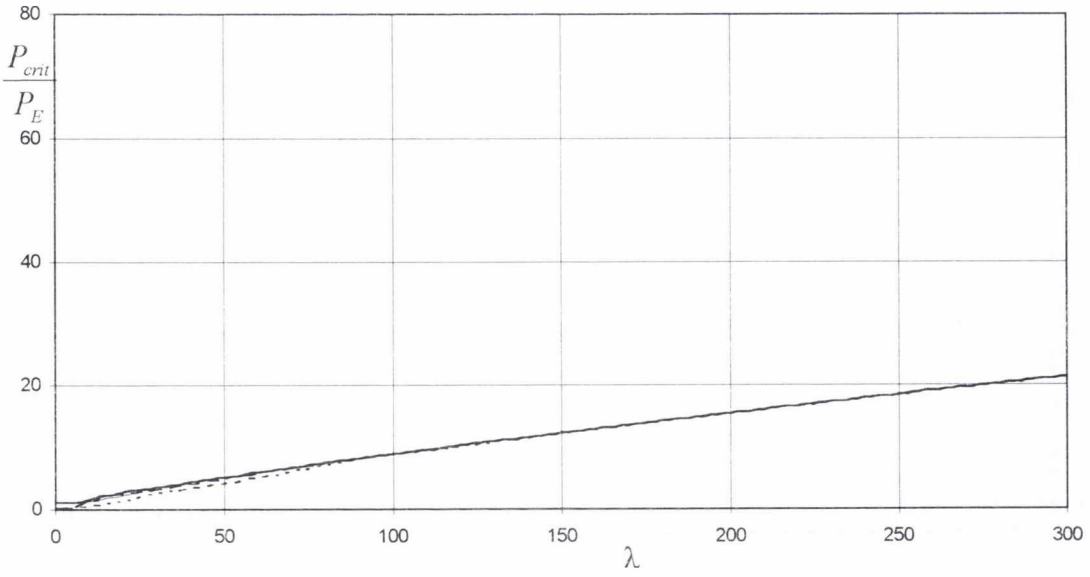

Fixed [———], pinned [– – –], no rotation/translation only [———], free [· · · ·].

Figure 4.2.25. First buckling loads for a fully embedded end-bearing beam with a no-rotation unembedded end in a non-homogeneous soil (F = 0).

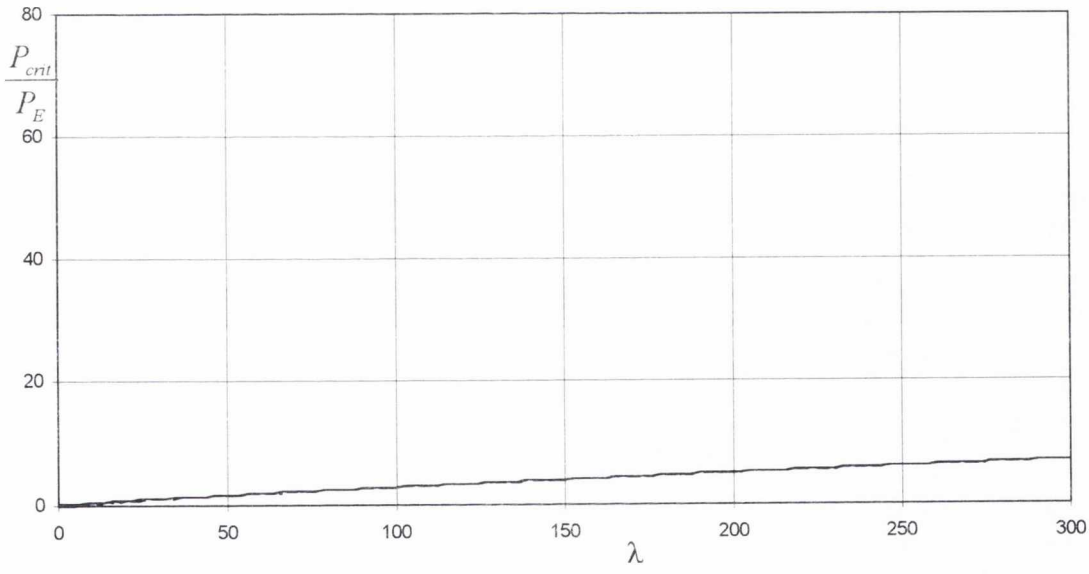

Fixed [———], pinned [– – –], no rotation/translation only [———], free [· · · ·].

Figure 4.2.26. First buckling loads for a fully embedded end-bearing beam with a free unembedded end in a non-homogeneous soil (F = 0).

In tables 4.2.1 and 4.2.2 the buckling loads for $\lambda > 50$ have been fitted to a straight line for homogeneous and non-homogeneous soils respectively. The reason the points with a soil stiffness parameter less than 50 have been ignored is that the behaviour of the buckling load line is less linear

for this range of soil stiffness and so cannot be fitted to a straight line. This can be seen in Appendix A.1 where the buckling loads for $0 < \lambda < 50$ are plotted. The lines are defined by using equation [4.2.4] (also equation [4.2.2]). The maximum error for these lines for values of $\lambda > 50$ is approximately 6 %. They may be used to approximate for buckling loads for the higher soil stiffnesses considered in the preceeding sections.

$$\frac{P_{cr}}{P_E} = m + c \cdot \frac{\lambda}{\pi^2} \qquad [4.2.4]$$

Homogeneous soil F = 1

End conditions	m	c	max % error $50 < \lambda < 300$
fixed-fixed	3.44	2.01	2.6
fixed-pinned	1.02	2.00	1.2
fixed-translation	0.99	2.00	1.3
fixed-free	0.01	1.00	0.3
pinned-fixed	1.02	2.00	1.2
pinned-pinned	0.34	2.00	4.7
pinned-translation	0.31	2.00	3.7
pinned-free	0.00	1.00	0.1
translation-fixed	0.99	2.00	1.3
translation-pinned	0.31	2.00	3.7
translation-translation	0.34	2.00	4.8
translation-free	0.00	1.00	0.1
free-fixed	0.01	1.00	0.3
free-pinned	0.00	1.00	0.1
free-translation	0.00	1.00	0.1
free-free	-0.15	1.01	2.1

Table 4.2.1. Fundamental buckling loads with $50 < \lambda < 300$ for a fully embedded end-bearing beam in a homogeneous soil ($F = 1$).

Non-homogeneous soil F = 0

End conditions	m	c	max % error $50 < \lambda < 300$
fixed-fixed	9.79	2.80	5.1
fixed-pinned	9.71	2.80	6.1
fixed-translation	9.70	2.80	5.0
fixed-free	9.54	2.81	6.3
pinned-fixed	3.22	2.34	3.4
pinned-pinned	3.21	2.34	3.7
pinned-translation	3.21	2.34	3.3
pinned-free	3.18	2.34	3.8
translation-fixed	3.73	2.34	3.3
translation-pinned	3.70	2.34	3.3
translation-translation	3.70	2.35	3.7
translation-free	3.69	2.35	3.7
free-fixed	0.48	1.03	1.1
free-pinned	0.48	1.03	1.1
free-translation	0.48	1.03	1.2
free-free	0.48	1.03	1.2

Table 4.2.2. Fundamental buckling loads with $50 < \lambda < 300$ for a fully embedded end-bearing beam in a non-homogeneous soil ($F = 0$).

4.3. Pure friction piles

4.3.1 Homogeneous medium

Of the remaining soil conditions which will be considered, the one with constant soil stiffness and constant friction along the pile is the most fundamental. The effect of constant friction on a pile is that the load transferred through the pile is triangular (figure 4.3.1). This means that the top of the pile has a greater tendency to buckle than the lower portion. The larger amplitudes of the buckling mode shapes thus tend to be concentrated at the top. This effective 'shortening' of the pile causes the buckling loads for friction piles to be greater than the corresponding end-bearing piles (in terms of end conditions and soil stiffness).

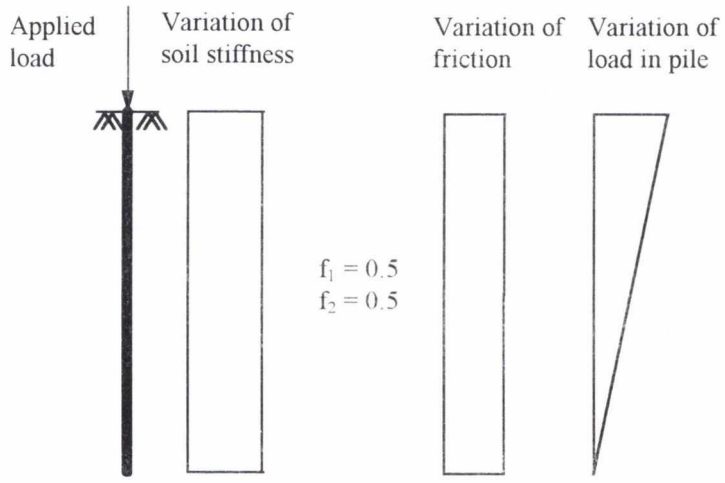

Figure 4.3.1. Constant soil stiffness and linearly varying shaft friction with depth.

In this section the results for pure-friction piles fully embedded in a homogeneous soil are presented. A comparison can be made with end-bearing piles in homogeneous soils, however, in section 4.4, on composite friction and end-bearing piles, the two extremes of end-bearing ($\mu = 1$) and pure friction ($\mu = 0$) piles are plotted on the same graphs as well as the transient solutions ($0 < \mu < 1$). It is in this section that a comparison between end-bearing and pure-friction piles will be made.

In 4.3.2 the first six buckling loads for free-free end conditions have been plotted. Modal cluster lines have also been shown (dashed). The first two modal cluster prediction lines have been plotted with values of n in equation 4.2.1 of 0.6 and 1.1 as these constants define lines which

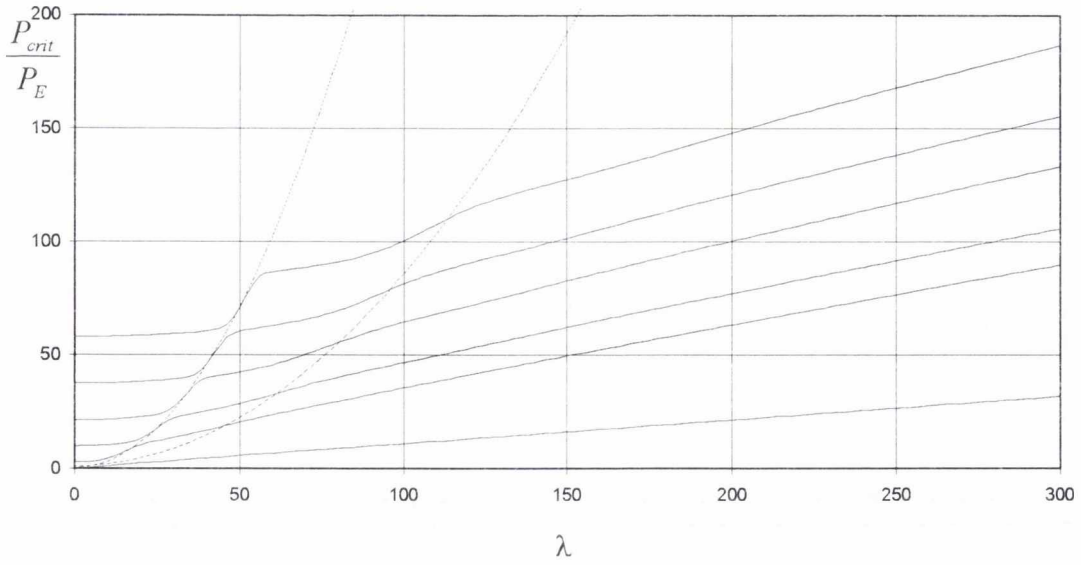

Buckling loads [———], modal cluster envelope lines [·····].

Figure 4.3.2. Buckling loads for a free-free fully embedded pure friction pile in a homogeneous soil.

indicate the location of the modal clusters. The fact that the constant defining the second line does not appear to be a multiple of the first constant and that the second mode clusters are not distinct (there only one obvious change in the slope of the lines) shows that it is of limited use to continue plotting these predictive lines.

In figure 4.3.3 the mode shapes for various soil stiffness and mode numbers for the free-free case are plotted. The first mode only has one change of mode shape in the range shown. At $\lambda = 0$ there are no half waves, but at $\lambda = 300$ there is one. In the range of λ between 100 and 200 it can be seen that the second and third modes keep the same characteristic number of half waves. The effect of increasing the soil stiffness is to concentrate the mode shape higher up the pile where the load in the pile is greatest. It should be noted that although the first mode appears to have only a single half wave the second has four. It could be argued that additional half waves are present in the first mode shape but the amplitudes of these half waves are so small that they are difficult to distinguish.

The reason the mode shapes at $\lambda = 17$ and 25 have been plotted is because at these approximate values of soil stiffness the parabola with $m = 0.6$ intersects the buckling load curves for the second and third modes respectively. The mode shapes can be categorised by the mode shape in

the upper half of the beam; the lower half of the beam is relatively straight. The top half of the beam has one and two half waves in the second and third mode respectively.

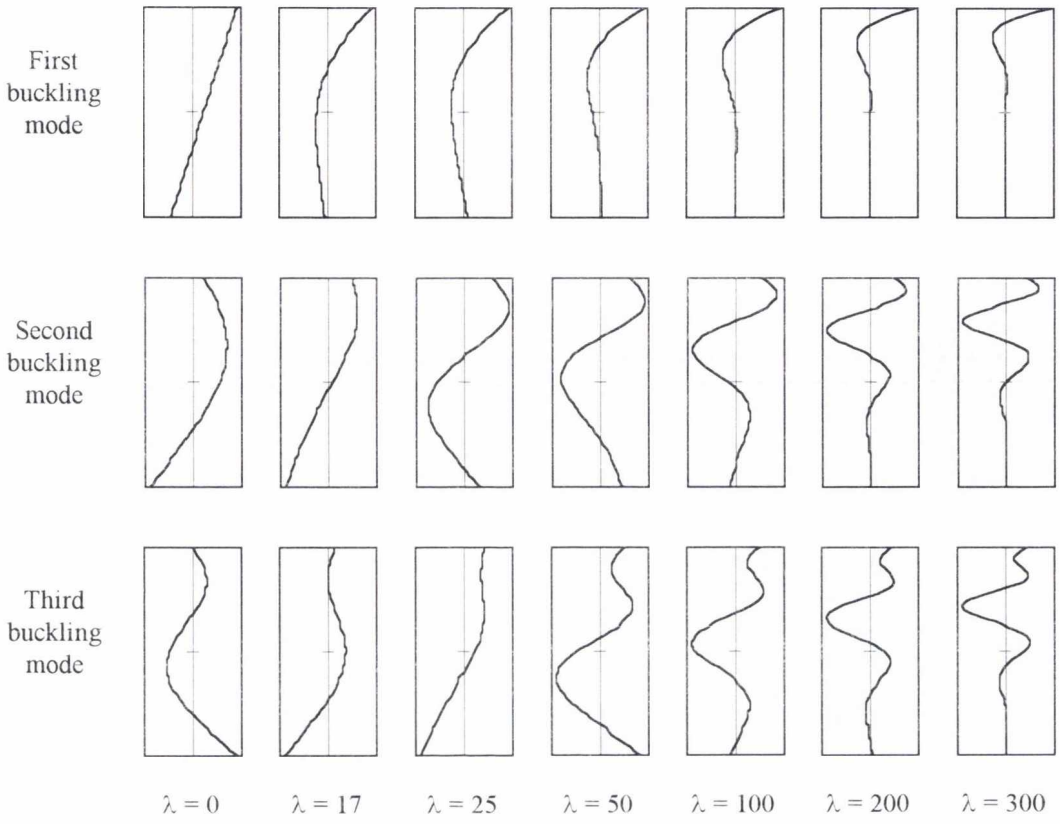

Figure 4.3.3. Mode shapes for figure 4.3.2.

In figure 4.3.4 it can be seen that the mode shapes for the pinned-pinned friction pile are regularly spaced, that is, there are no modal clusters for all but the lower soil stiffness and even here they are not distinctive. If the mode shapes at $\lambda = 300$ in figure 4.3.5 are taken as the characteristic mode shapes, an explanation of the regular spacing can be seen. The half wave with the largest amplitude progresses steadily down the pile with increasing mode number. Due to the linear nature of the load in the pile, this would indicate that the buckling load would increase at a constant rate between modes.

In figure 4.3.6 the buckling loads for the fixed-fixed end conditions are plotted. Unlike the pinned-pinned case in figure 4.3.4 it can be seen that the buckling modes are paired. The first and second mode are much closer together than the second and third, and the third and fourth mode are also closer together than the fourth and fifth. Looking at the buckling mode shapes in figure 4.3.7 the

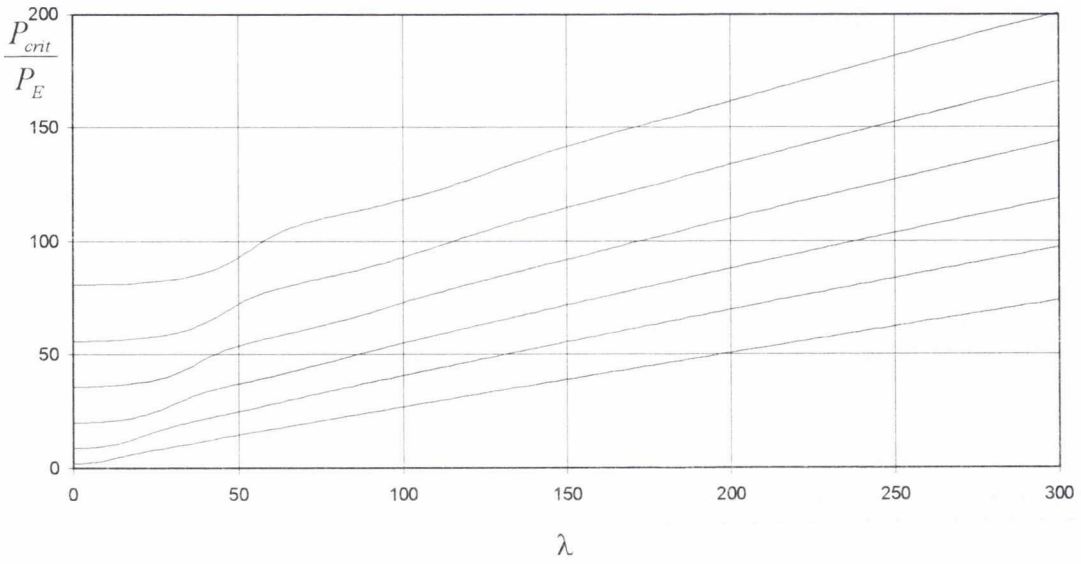

Figure 4.3.4. Buckling loads for a pinned-pinned fully embedded pure-friction pile in a homogeneous soil.

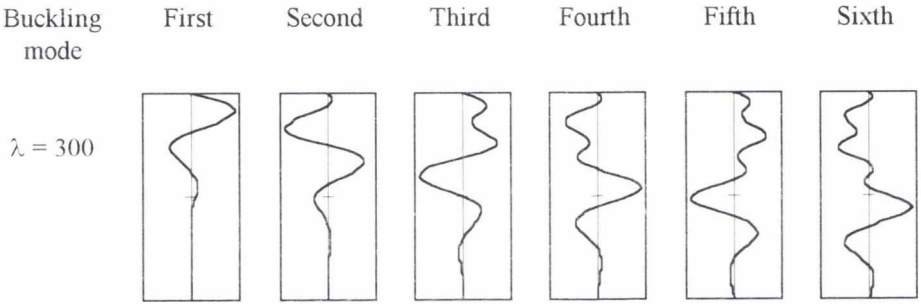

Figure 4.3.5: The first six mode shapes at λ = 300 for figure 4.3.4.

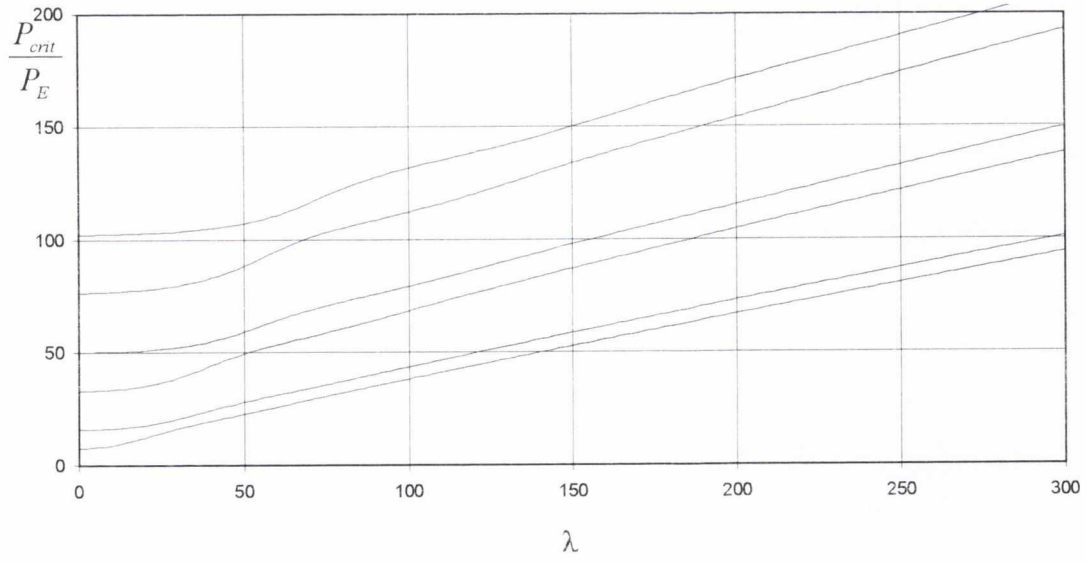

Figure 4.3.6. Buckling loads for a fixed-fixed fully embedded pure-friction beams in a homogeneous soil.

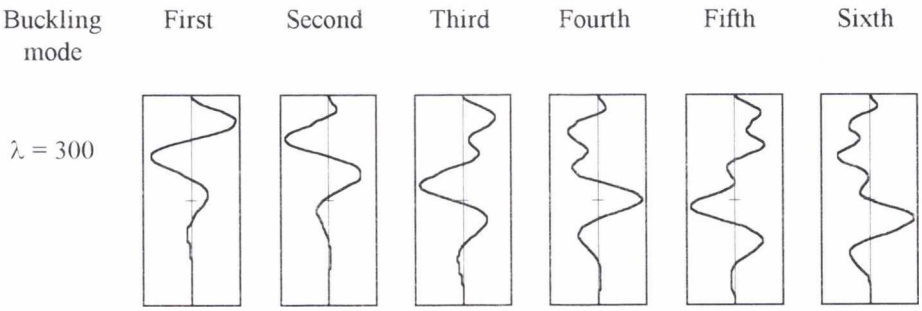

Figure 4.3.7. Mode shapes for λ = 300 for figure 4.3.6.

buckling shapes are similarly paired. The half wave with the largest amplitude in the first and second modes are at a similar distance along the beam, the difference between the mode shapes being an extra half wave near the top of the beam.

As the first buckling mode shape is heavily concentrated in the upper portion of the pile, it would be expected that the lower boundary condition would not affect the buckling mode shape and buckling load. If the embedded end is changed from fixed to free end, for a pile with a fixed unembedded boundary condition then the actual difference in the first modes at $\lambda = 300$ is less than 0.1 % (figure 4.3.8). It should be noted that if a fixed-free pile is considered, unlike the end-bearing

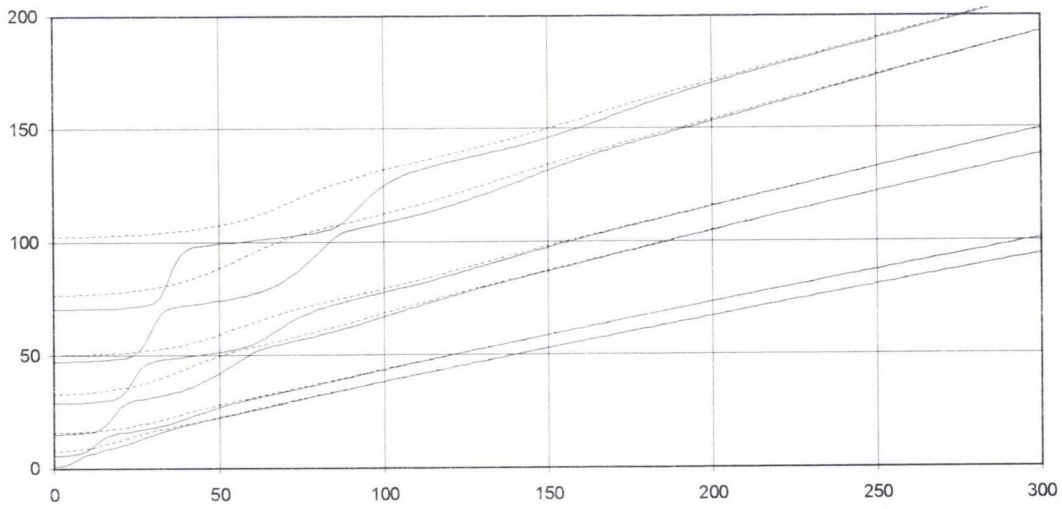

Fixed-free [——], fixed-fixed [·····].

Figure 4.3.8. Buckling loads for a fixed-fixed and fixed-free fully embedded pure-friction beams in a homogeneous soil.

case, the mode shape with maximum amplitude at the bottom of the pile is prevented from occurring for all but the lowest soil stiffness ($\lambda < 50$) due to the reduced load carried at the bottom of the pile. In 4.3.9 the mode shapes for the fixed-fixed and fixed-free cases are presented. For $\lambda > 50$ there are few differences between the mode shape for the two sets of end-conditions. Although there are amplitudes at the pile base for the free embedded end case, these do not signify a great reduction in buckling load as the load in the pile in this section is minimal.

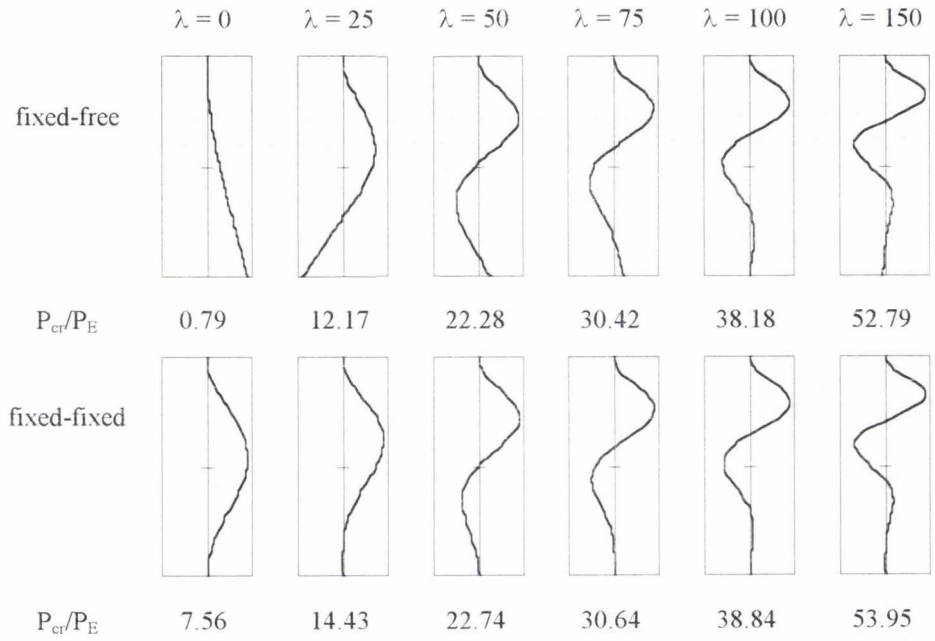

Figure 4.3.9. Mode shapes for figure 4.3.8.

4.3.2 Non-homogeneous medium

In the case of pure-friction piles, the non-homogeneity in the medium can take two forms; variations in the soil stiffness and variations in the friction along the shaft. It would be expected that the soil stiffness and friction on the pile vary in the same way with depth as they both depend on the same parameters (Poulos, 1989). However, it is also interesting to be able to observe whether the two types of variation produce different effects in the solution to the problem or if one is more significant than the other. Hence, the solutions to varying soil stiffness and constant friction, constant soil stiffness and varying friction, and varying soil stiffness and friction are considered in turn. It is possible that in particular conditions a real soil may approximate to one such model.

Varying soil stiffness and constant friction

In figure 4.3.10 the assumed variation of soil stiffness and constant friction, resulting in a linearly decreasing variation in load down the pile, has been shown. It may be noted that where the soil stiffness is largest, the load in the pile is least and the maximum amplitude in expected in the buckling mode shapes will, therefore, be concentrated away from this area.

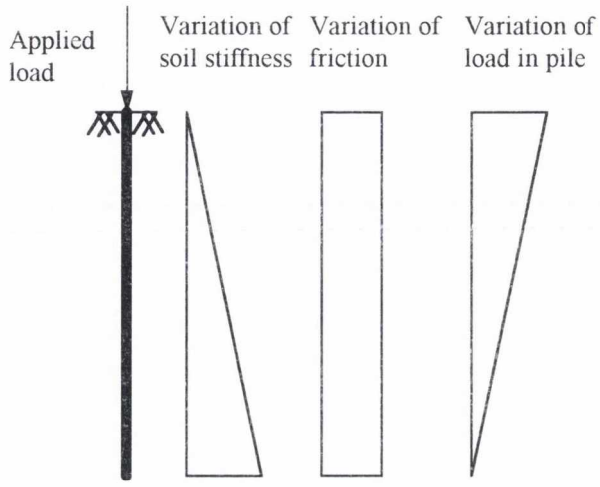

Figure 4.3.10. Linearly increasing soil stiffness and constant shaft friction with depth.

In figure 4.3.11 the results for the first six modes with constant friction and varying soil stiffness are plotted when the ends are fixed-fixed. Although it is possible to provide complete solutions (with six buckling modes) for the other boundary conditions this will not be done as only the similarities and differences between this and the following problems are of interest. The buckling loads for the fundemental mode will be presented in the summary, section 4.3.3, for the complete set of boundary conditions.

In figure 4.3.12 the buckling loads for a uniform and a triangular soil stiffness have been plotted. It can be noted for the upper modes that the triangular variation of soil stiffness produces an increase in buckling load for particular soil stiffness. In figure 4.3.13 the buckling mode shapes with $\lambda_{average} = 25$ have been plotted. The buckling load parameter for the second mode is larger for a non-homoegenous soil than for a homogeneous soil. The reason for this is that the larger amplitudes in the mode shape are in the lower half of the beam where the soil stiffness is greater in this section of the pile for F = 0 than for F = 1.

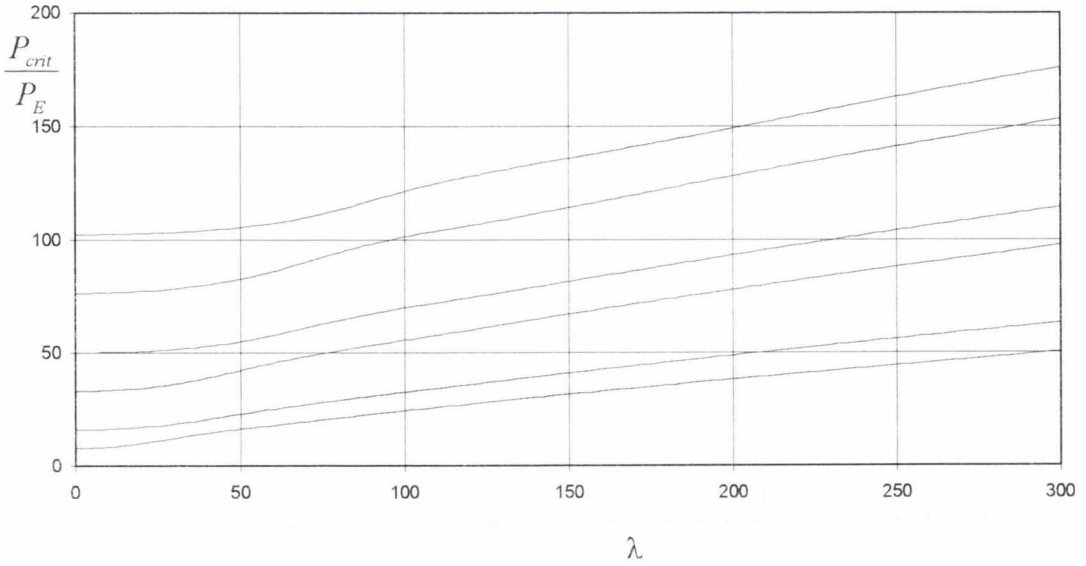

Figure 4.3.11. Buckling loads for a fixed-fixed fully embedded pure-friction beam with constant friction and triangular soil stiffness results.

It could be argued that the effect of a linear variation in soil stiffness would be to push the maximum amplitudes towards the top of the pile. This causes a shorter effective length and, hence, an increase in the buckling load. This arguement is incorrect if figure 4.3.13 is inspected for $\lambda_{average}$ = 300. The effective length of the pile is indeed shorter for a beam in a non-homoegenous soil and,

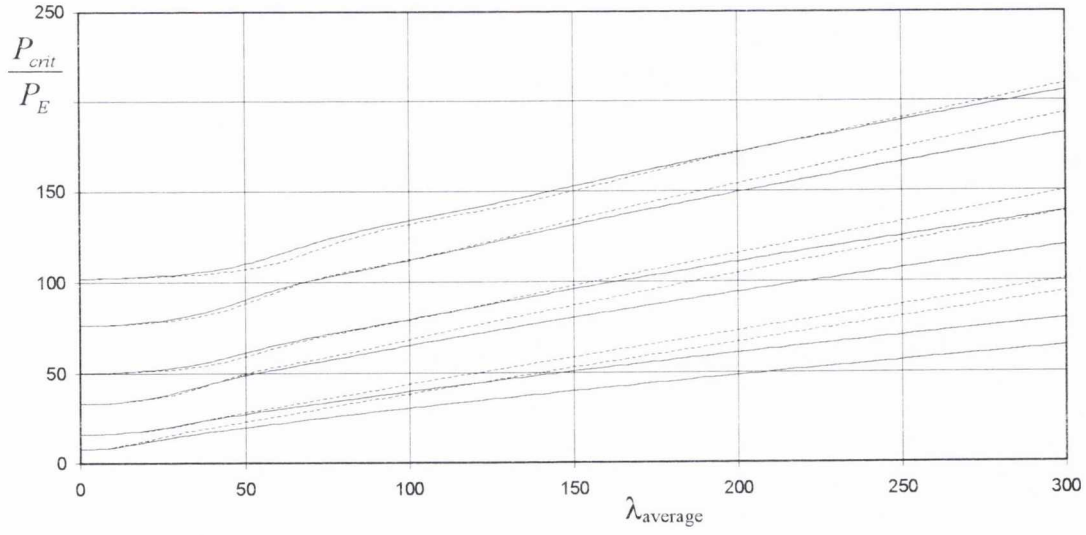

Homogeneous soil (F = 1) [———], homogeneous soil (F = 0) [·····].

Figure 4.3.12. Buckling loads for a fixed-fixed fully embedded constant pure-friction beam with either a triangular or a constant soil stiffness model with the same average soil stiffness.

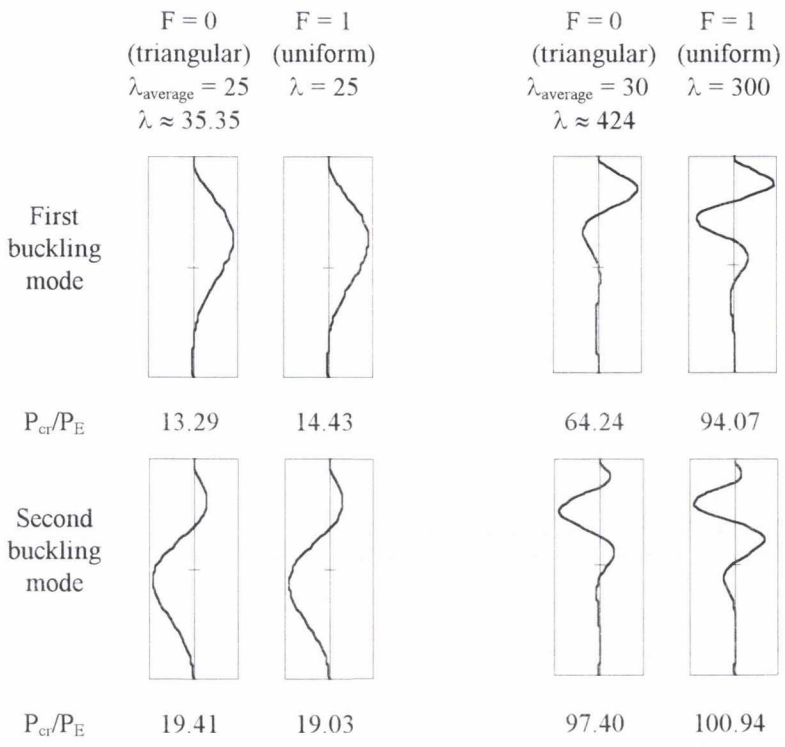

Figure 4.3.13. First two mode shapes for F = 0 and F = 1 for figure 4.3.12.

indeed, there are in fact fewer half waves in the mode shape. However, because the soil stiffness is less in the non-homogeneous case where the mode shape amplitude is large (in the top half of the pile) the shorter effective length is not accompanied by an increase in buckling load.

In figures 4.3.14 and 4.3.15 the buckling loads for pinned-pinned and free-free end conditions are plotted. The results are similar to those for fixed-fixed conditions where at high λ the non-homogeneous results are lower than for the homogeneous buckling loads. Again there are sections at low values of soil stiffness, $\lambda \approx 50$, where the non-homogeneous results for the higher modes are greater than the homogeneous buckling loads. The reason for this can most easily be explained using the free-free case as an example. The section of the higher modes where the non-homogeneous buckling load is greater than the homogeneous load corresponds to mode shapes which have a maximum amplitude at the pile toe. Because the soil stiffness is greater at this point in the non-homogeneous case a higher buckling load is produced. A similar effect for pinned and fixed end-conditions is caused by the possibility of a mode shape occuring with the half wave with the maximum amplitude appearing in the lower half of the beam.

Hence, the way the buckling load varies between the homogeneous (F = 1) and non-homogeneous (F = 0) soil stiffness cases is of a complex nature. If an average soil stiffness is used to model a non-homogeneous case it can be seen that, depending on the value of the soil stiffness, it is possible for the model to either over or under-estimate the buckling load for modes other than the fundamental buckling mode.

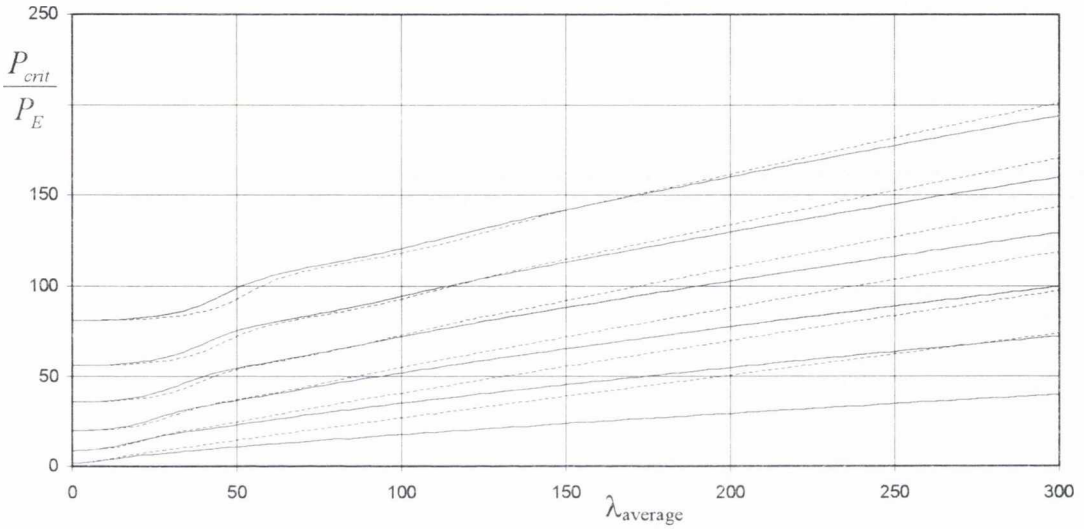

Homogeneous soil (F = 1) [——], non-homogeneous soil (F = 0) [·····].

Figure 4.3.14. Buckling loads for a pinned-pinned fully embedded constant pure-friction beam with either a triangular or a constant soil stiffness model with the same average soil stiffness.

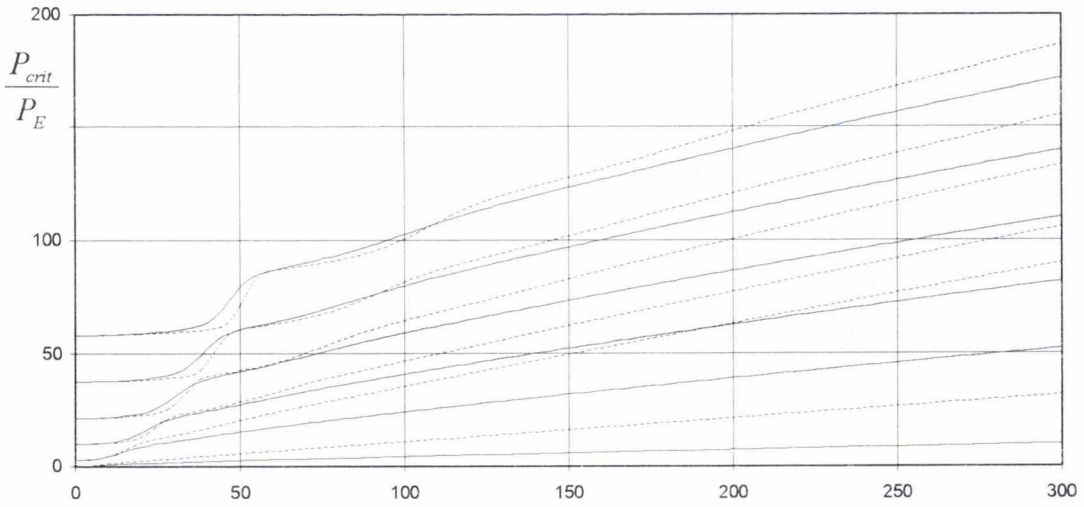

Homogeneous soil (F = 1) [——], non-homogeneous soil (F = 0) [·····].

Figure 4.3.15. Buckling loads for a free-free fully embedded constant pure-friction beam with either a triangular or a constant soil stiffness model with the same average soil stiffness.

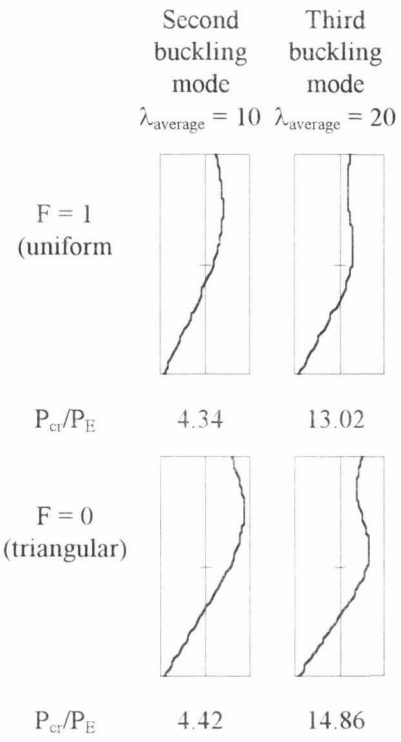

Figure 4.3.16. First two mode shapes for F = 0 and F = 1 with the same average soil stiffness for figure 4.3.15.

Constant soil stiffness and varying friction.

Figure 4.3.17 illustrates the possible variations of the shaft friction and the corresponding load distribution in the pile. Although they are all possible, it is unlikely that the friction will decrease with depth. This is because in order for this distribution to occur the shaft friction would not be approaching the maximum shaft friction that the soil can sustain. Obviously, buckling is more likely to occur as the maximum load capacity of the pile is approached. It should also be noted that this soil conditions is associated with higher buckling loads and, hence, using the other buckling loads would, in any case, provide a margin of safety.

As discussed earlier, this section is most relevant in a discussion with the immediately previous results. Figure 4.3.18 shows the results for fixed-fixed end conditions as the friction varies between lower triangular (with $f_1 = 0$), constant ($f_1 = 0.5$) and upper triangular ($f_1 = 1$).

The mode shapes which are associated with the mode shapes for the first four modes are displayed in figure 4.3.19. As would be expected, when the friction is greatest at the bottom of the pile (and, hence, the load in the pile at the top is largest) the buckling amplitude is more concentrated in the upper portion of the beam. It can be seen that the wavelength of the mode shapes are relatively

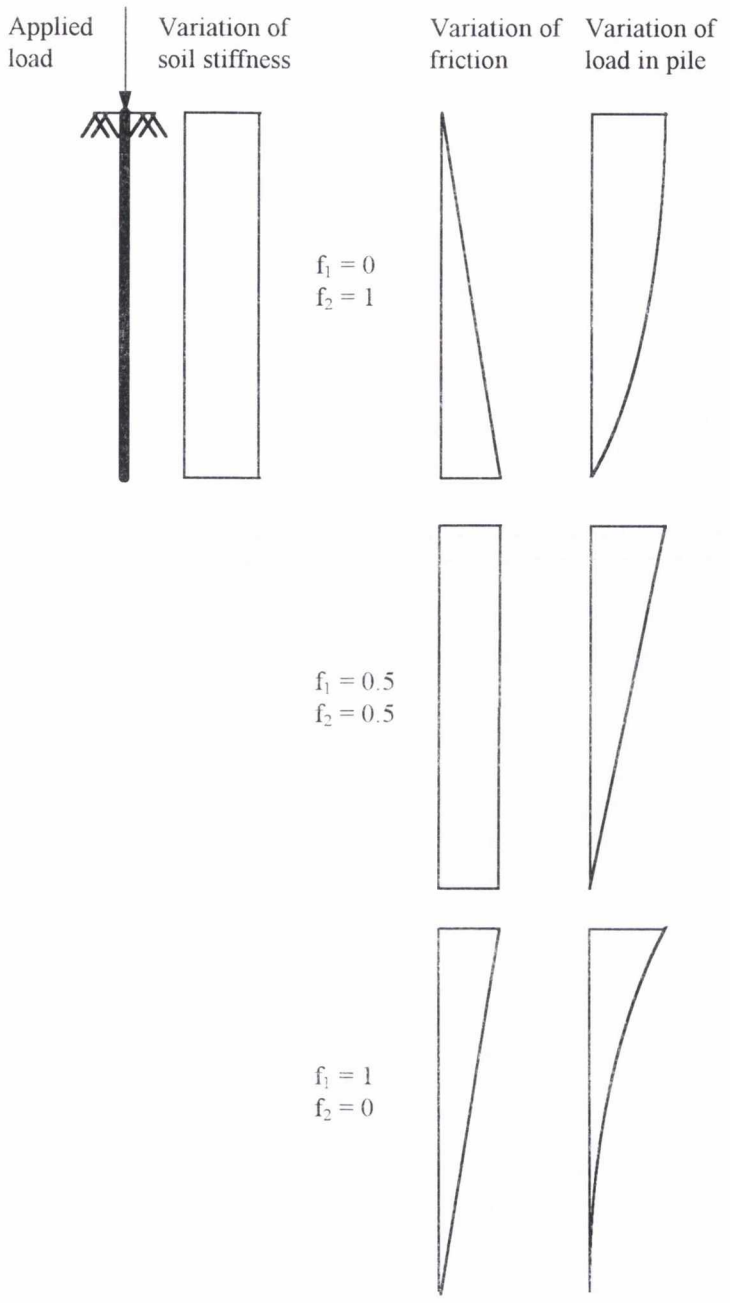

Figure 4.3.17. Constant soil stiffness and linearly varying shaft friction with depth.

consistent as f_1 varies. For $f_1 = 1$ the modes shape tend to be more concentrated in the upper portion. This effective shortening of the pile produces the increase in buckling load evident in figure 4.3.19. The reason for this upper concentration is because the load in the pile in the bottom half is much smaller than that in the top due to the concave parabolic nature of the load in the pile (figure 4.3.17).

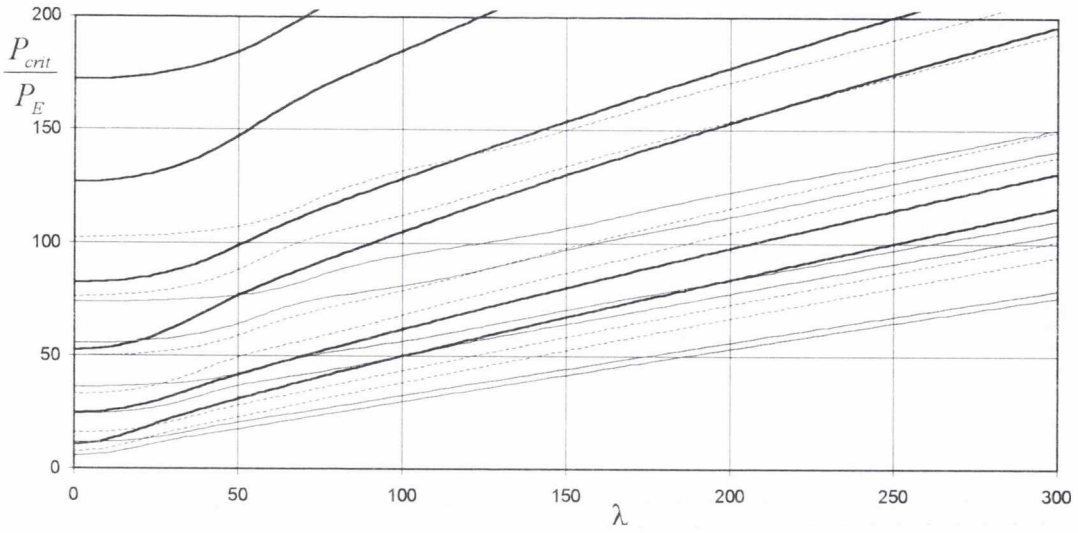

Figure 4.3.18. Fixed-fixed fully embedded pure-friction beam with constant soil stiffness and either linearly increasing or decreasing or constant shaft friction.

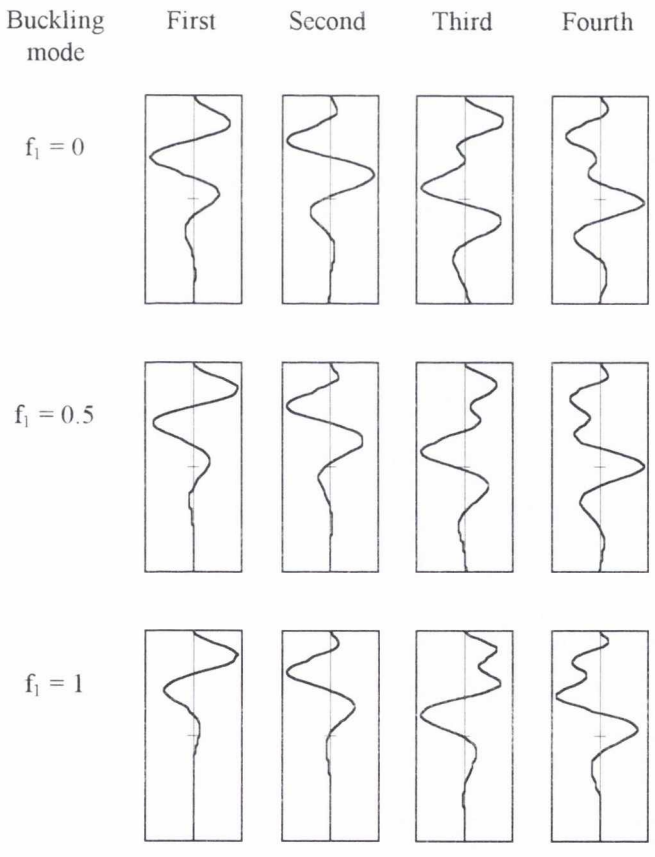

Figure 4.3.19. The first four buckling mode shape with λ = 300 for figure 4.3.18.

Discussion

In the previous two sections the effect of varying the load in the pile and the soil stiffness with depth has been investigated. If a triangular distribution of soil stiffness (F = 0) is compared to a triangular variation in friction ($f_1 = 0$) then it can be seen that the general effects on the mode shape are the same. In both cases the mode shape is concentrated in the upper portion of the pile.

In figure 4.3.20 the buckling loads for a fixed-fixed beam are plotted for three types of soil conditions. They are a homogeneous soil (constant soil stiffness and constant shaft friction) and non-homogeneous soil (constant soil stiffness and linearly increasing shaft friction with depth; linearly increasing soil stiffness with depth and constant shaft friction). Again, the soil stiffness parameter is calculated by averaging the soil stiffness along the length of the pile. The non-homogeneous soils produce a reduction in the fundamental buckling load whatever the nature of the non-homogeneity. When the non-homoegeneity is applied to the soil stiffness the 'effective' length of the beam is reduced and the wavelength of the associated mode shape is increased (figure 4.3.21). The first effect

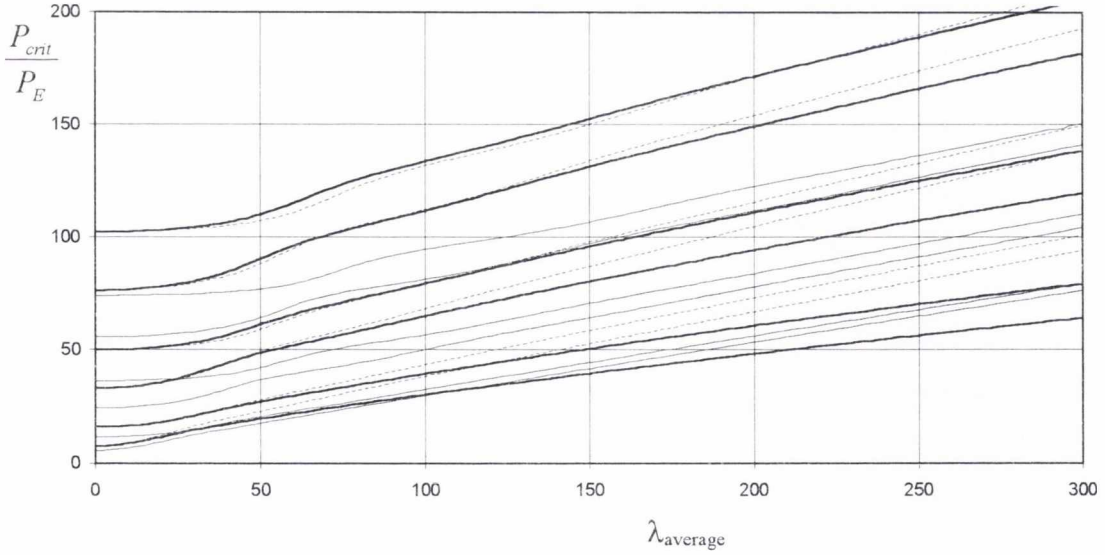

F = 1 and f_1 = 0 [———],F = 1 and f_1 = 0.5 [·····] or F = 0 and f_1 = 1 [———]

Figure 4.3.20. The first six buckling modes of a fixed-fixed fully embedded pure-friction beam with a non-homgenous soil.

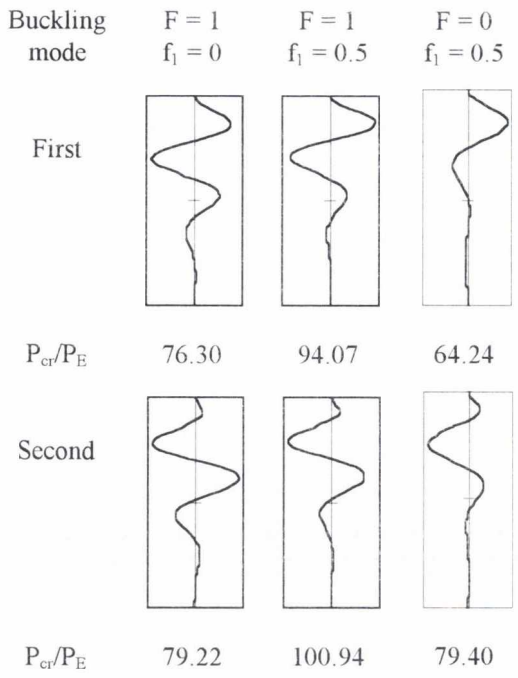

Figure 4.3.21. The first four buckling mode shape with $\lambda_{average} = 300$ for figure 4.3.20.

would intuitively produce an increase in buckling load whereas the second would tend to decrease the predicted load. Overall the two effects produce a decrease in the predicted buckling load. Hence, it can be concluded that in non-homogenous soil (soil stiffness) the 'effective' length of a pile is not as important as the location of the half wave with the maximum amplitude. If this half wave is in an area of low soil stiffness then the buckling load will be less than if it is an area of high soil stiffness. Of course, if the effective length is small then the maximum amplitude half wave will be closer to the soil surface and, hence, in an area of low soil stiffness. In the case of homogenous soils (soil stiffness) this effect can no longer occur and it appears that the 'effective' length argument does hold with respect to increasing buckling load. It can be seen that there are no hard and fast rules that apply to all soil situations and which can be used to predict the trends in mode shape and buckling loads so the rigorous exact solution outlined in this thesis should always be used.

Linear variations in both soil stiffness and friction

As described in the literature review, it would normally be expected that under conditions where the soil stiffness varies linearly (increasing) with depth, the maximum shaft friction will vary similarly (figure 4.3.22). Although in certain circumstances a combination of a linear increasing variation of one soil parameter with the other parameter constant may occur, it has never been

reported that the skin friction would increase while the soil stiffness decreases with depth and, hence, this set of conditions will not be discussed in depth in this section. The buckling loads to this 'academic' problem are presented for the fundamental mode in the Chapter summary. It should be remembered that a safe approximation to this problem is to use the results with the appropiate soil stiffness variation and a constant shaft friction. In the previous sections it has been shown the effects that defining a linear increasing soil stiffness and shaft friction with depth individually produce. In this section the problem of varying both the soil stiffness and friction with depth will be examined.

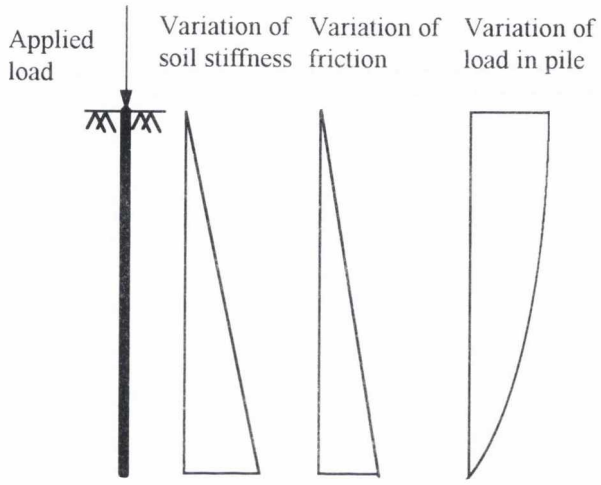

Figure 4.3.22. Linearly increasing soil stiffness and shaft friction with depth.

In each of figures 4.3.23, 4.3.25 and 4.3.27, the buckling loads have been plotted for two distinct types of soil for symmetrical boundary conditions. The first soil type is the homogeneous soil, where the soil stiffness and shaft friction are constant with depth, and the second is the non-homogeneous soil, where soil stiffness and shaft friction increase linearly with depth. In figures 4.3.24, 4.3.26 and 4.3.28 it can be seen that, in all cases, by the time the soil stiffness parameter, λ, has reached 300, the buckling modes are concentrated away from the embedded end of the beam. This is true especially in the all-important first mode at high values of soil stiffness. It can be concluded from this that the embedded end condition is not important in either defining the buckling load or buckling mode shape in soils with a high stiffness.

If the buckling loads are examined it can be seen that the strengthening effect of the homogeneity in soil conditions depends on the upper end condition. In the case of the fixed and pinned end conditions, the buckling load of the beam in the homogeneous soil is approximately two

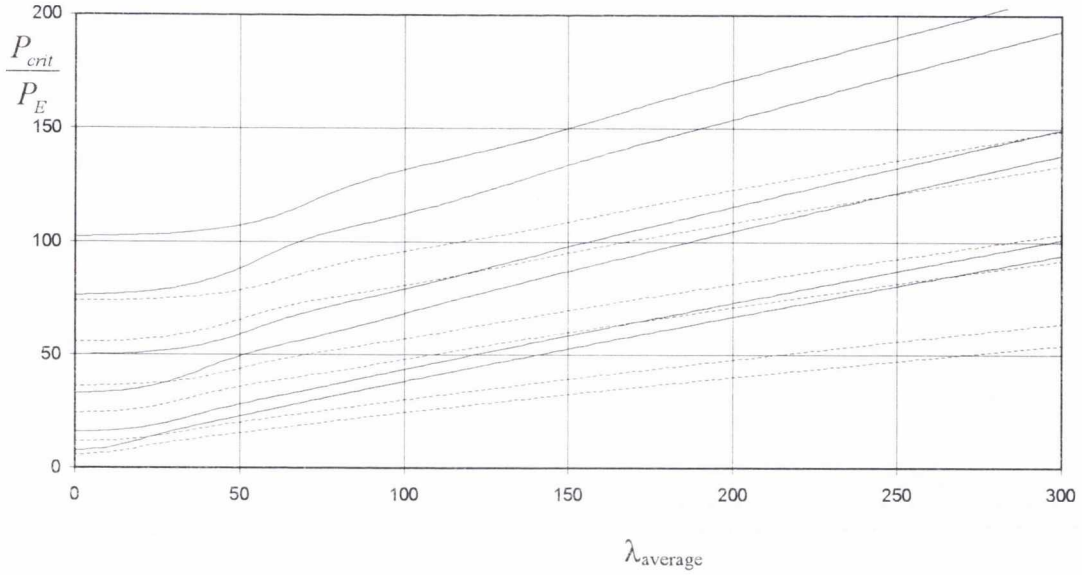

F = 1 and f_1 = 0.5 [——], F = 0 and f_1 = 0 [·····]

Figure 4.3.23. Buckling loads for constant soil stiffness and friction compared to linearly increasing soil stiffness and friction with depth for a fixed-fixed fully embedded pure-friction beam.

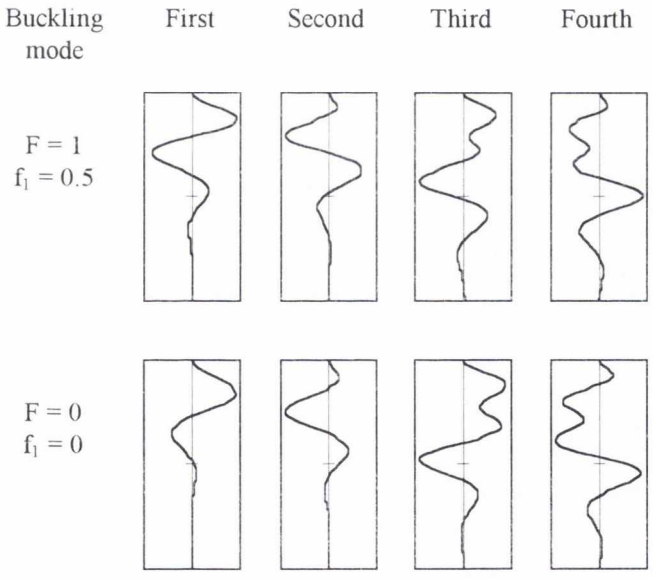

Figure 4.3.24. Buckling modes at $\lambda_{average}$ = 300 for constant stiffness and friction (top) and linearly increasing stiffness and friction with depth (bottom) for figure 4.3.23.

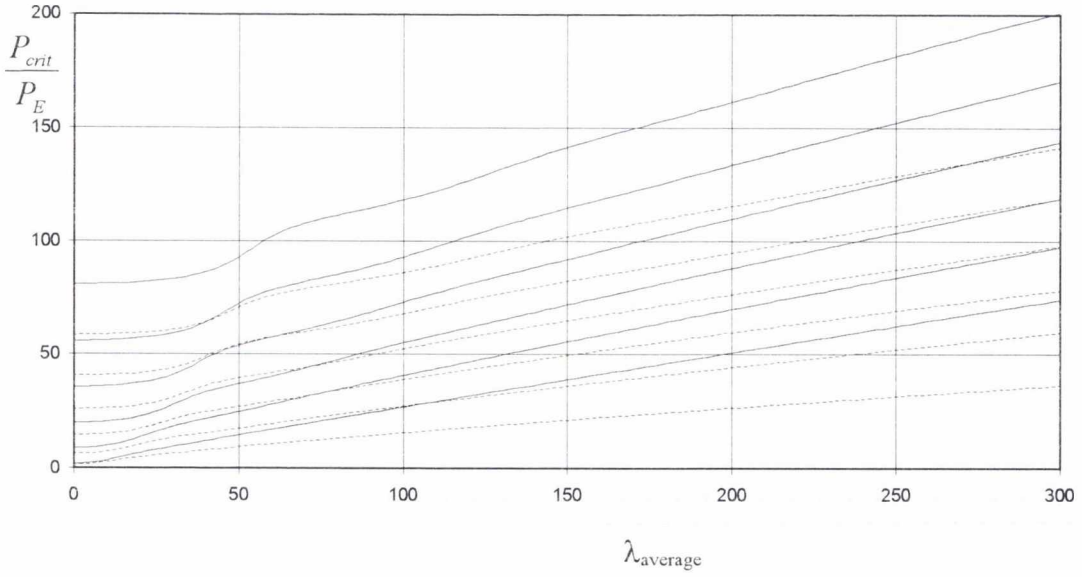

F = 1 and f_1 = 0.5 [———], F = 0 and f_1 = 0 [·····]

Figure 4.3.25. Buckling loads for constant soil stiffness and friction compared to linearly increasing soil stiffness and friction with depth for a pinned-pinned fully embedded pure-friction beam.

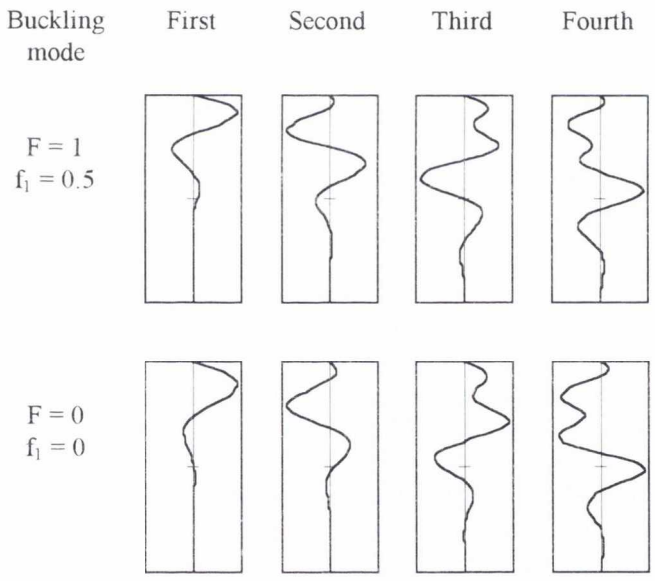

Figure 4.3.26. Buckling modes at $\lambda_{average}$ = 300 for constant stiffness and friction (top) and linearly increasing stiffness and friction with depth (bottom) for figure 4.3.25.

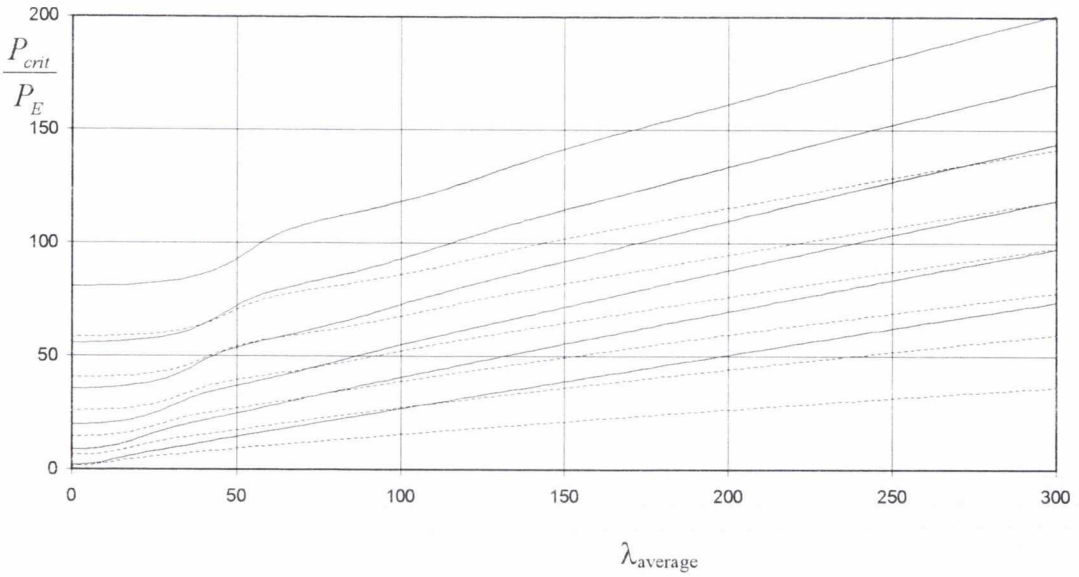

F = 1 and f_1 = 0.5 [———], F = 0 and f_1 = 0 [·····]

Figure 4.3.27. Buckling loads for constant soil stiffness and friction compared to linearly increasing soil stiffness and friction with depth for a free-free fully embedded pure-friction beam.

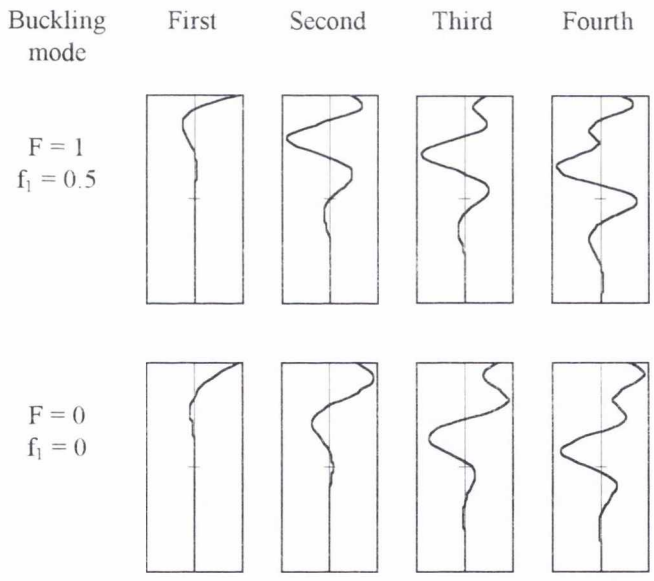

Figure 4.3.28. The first four buckling mode shapes at $\lambda_{average}$ = 300 for constant stiffness and friction (top) and linearly increasing stiffness and friction with depth (bottom) for figure 4.3.27.

and a half times the buckling load in the non-homogeneous soil when the average soil stiffness parameter is equal to 300. In the free case this is increased to a factor of about four and a half. The reason for the greater difference in the free case is that the soil conditions where the amplitude of the buckling shape is greatest (the very top) change considerably between the homogeneous and non-

homogeneous cases. For the pinned and fixed cases where the maximum amplitude is necessarily further down the pile the difference in soil conditions between the two cases is less.

If figure 4.3.29 is inspected it can be seen that the buckling loads for a fixed-free pile rapidly converges onto the other solutions for a pile with a fixed embedded end for a pure friction beam. This means that for the range $\lambda > 50$ that the buckling load and, hence, mode shapes will be identical to those for a fixed-fixed beam, because the combination of high soil stiffness and relatively low load in the beam means that the embedded end now acts like a fixed end-condition.

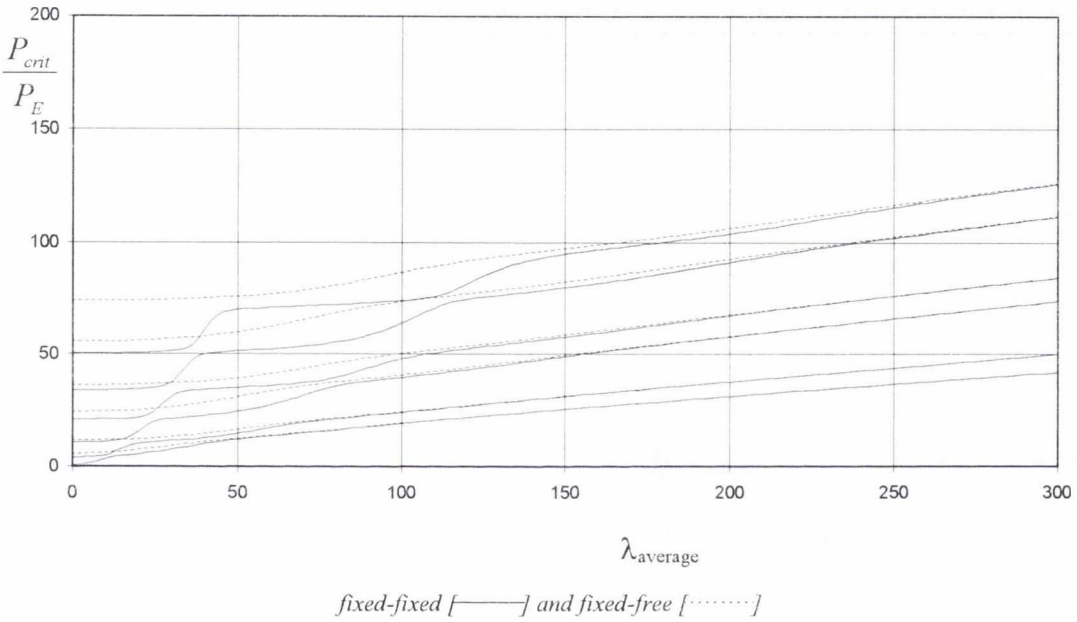

Figure 4.3.29. The first six buckling loads for a linearly increasing soil stiffness and friction with depth for a fixed-fixed and a fixed-free fully embedded pure-friction beam.

4.3.3 Summary

In figure 4.3.30 the fundamental buckling loads are ploted for a pure-friction pile in a homogeneous soil ($F = 1$, $f_1 = f_2 = 0.5$) with a fixed unembedded end-condition. As can be seen for all but the lowest soil stiffnesses ($\lambda < 50$) the buckling loads are identical. This is also the case for the other unembedded end-conditions and, hence, the embedded end-condition does not affect the buckling load. In figures 4.3.31 to 4.3.36 the fundamental buckling loads are plotted according to the unembedded boundary condition. The lines are the average of the buckling loads as the embedded end-condition is varied and cease to be plotted once the maximum errors between the average and any

one of the four embedded end-condition exceeds 5 %. The buckling loads for soil stiffness below the cut off point can be found in Appendix A.

Homogeneous soil (F = 1, $f_1 = f_2 = 0.5$)

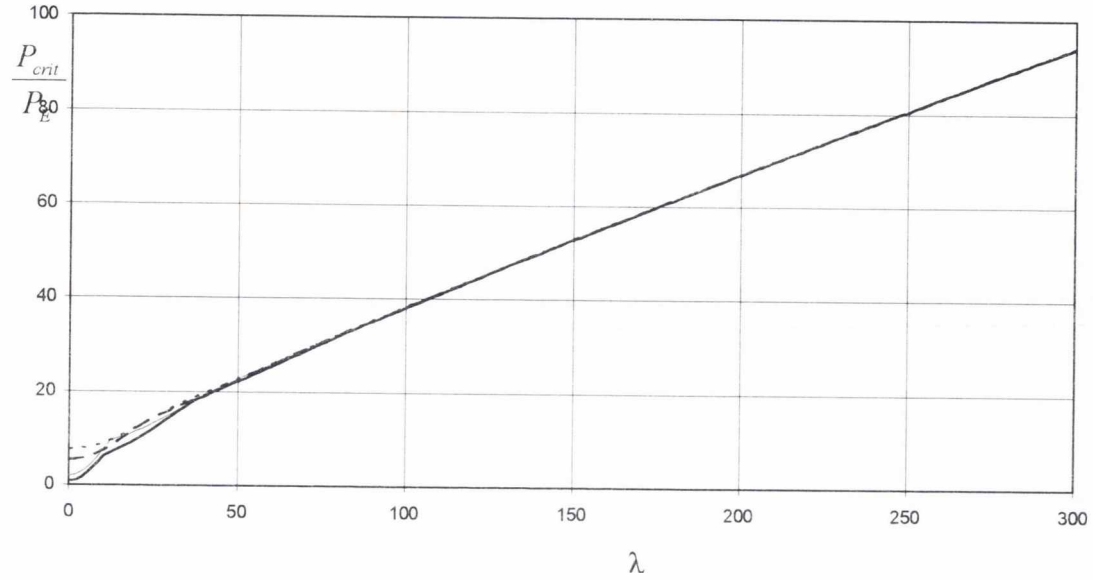

Fixed [· · · ·], pinned [– – –], no rotation/translation only [ ], free [———].

Figure 4.3.30. First buckling loads for a fully embedded pure-friction beam with a fixed unembedded end in a homogeneous soil with constant soil stiffness (F = 1) and constant shaft friction ($f_1 = f_2 = 0.5$).

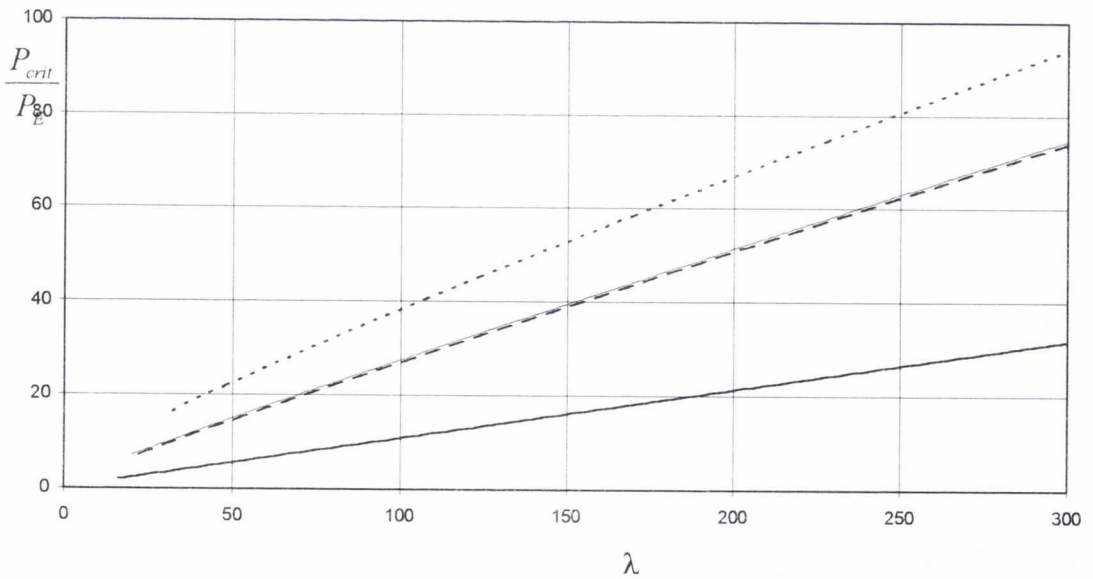

Fixed [· · · ·], pinned [– – –], no rotation/translation only [ ], free [———].

Figure 4.3.31. First buckling loads for a fully embedded pure-friction beam in a homogeneous soil with constant soil stiffness (F = 1) and constant shaft friction ($f_1 = f_2 = 0.5$).

Non-homogeneous soil (F = 0, f_1 = 0 and f_2 = 1)

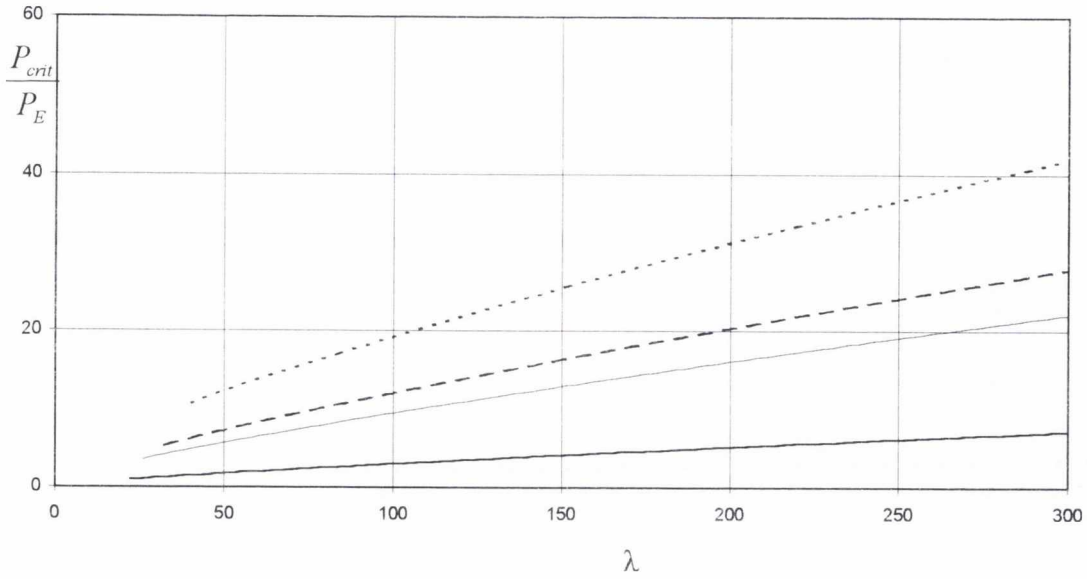

Fixed [· · · ·], pinned [– – –], no rotation/translation only [——], free [——].

Figure 4.3.32. First buckling loads for a fully embedded pure-friction beam with a no rotation unembedded end in a homogeneous soil with triangular soil stiffness (F = 0) and triangular shaft friction (f_1 = 0, f_2 = 1).

Non-homogeneous soil (F = 1, f_1 = 0 and f_2 = 1)

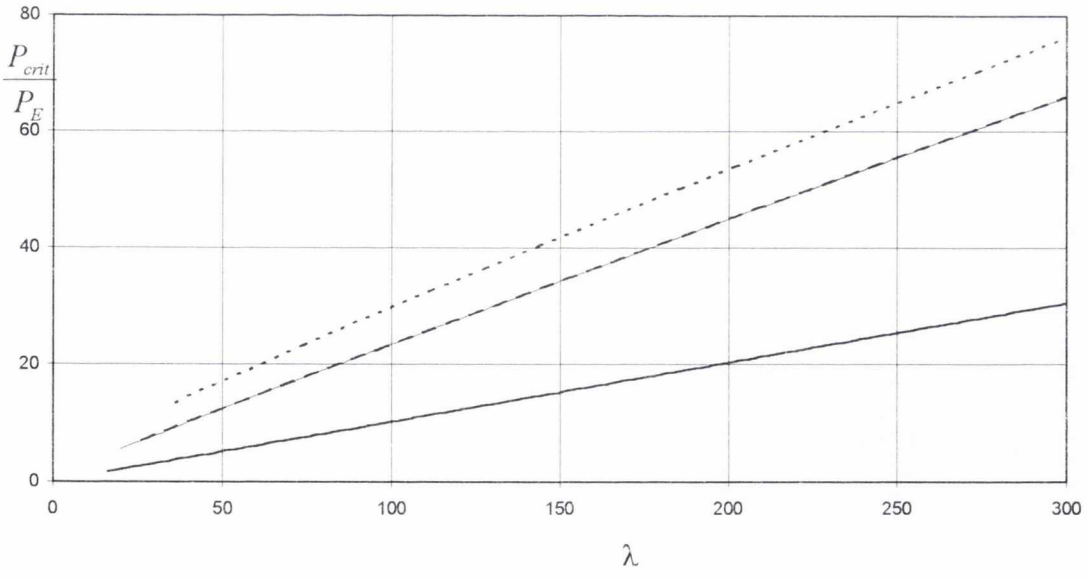

Fixed [· · · ·], pinned [– – –], no rotation/translation only [——], free [——].

Figure 4.3.33. First buckling loads for a fully embedded pure-friction beam in a non-homogeneous soil with constant soil stiffness (F = 1) and triangular shaft friction (f_1 = 0, f_2 = 1).

Non-homogeneous soil (F = 0 and $f_1 = f_2 = 0.5$)

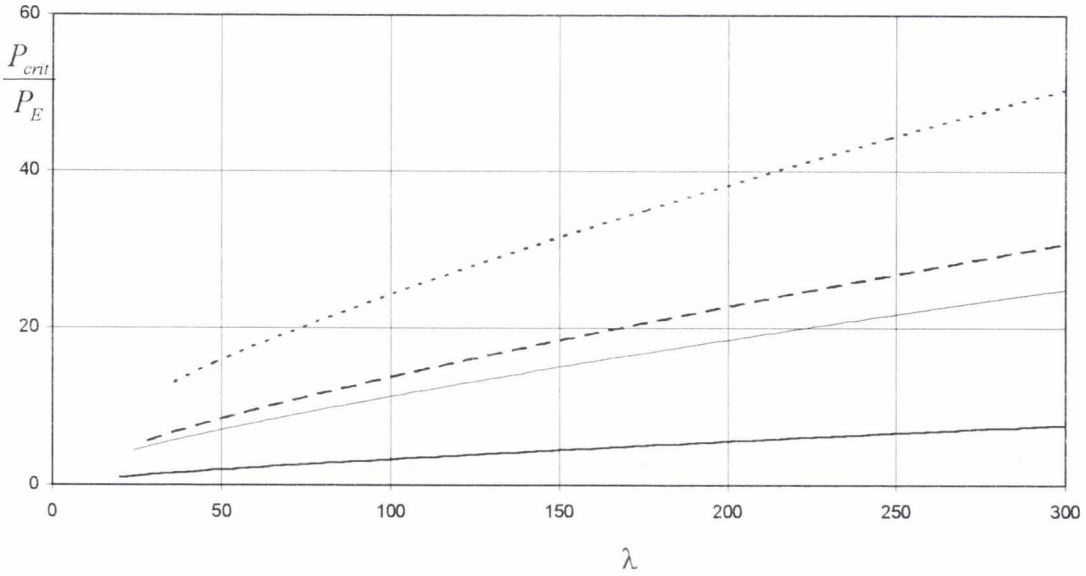

Fixed [· · · ·], pinned [— — —], no rotation/translation only [ ], free [———].

Figure 4.3.34. First buckling loads for a fully embedded pure-friction beam in a non-homogeneous soil with triangular soil stiffness (F = 0) and constant shaft friction ($f_1 = f_2 = 0.5$).

Non-homogeneous soil (F = 1, $f_1 = 1$ and $f_2 = 0$)

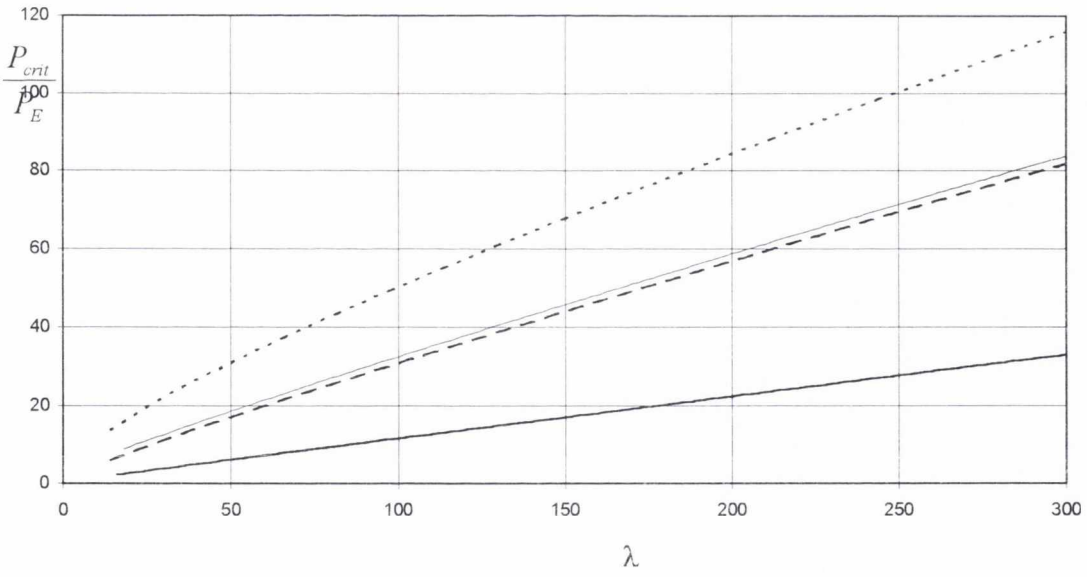

Fixed [· · · ·], pinned [— — —], no rotation/translation only [ ], free [———].

Figure 4.3.35. First buckling loads for a fully embedded pure-friction beam in a non-homogeneous soil with constant soil stiffness (F = 1) and triangular shaft friction ($f_1 = 1, f_2 = 0$).

Tables 4.3.1 to 4.3.5 give straight line approximations to the curves in the previous figures according to equation 4.2.5. In order to calculate the parameters *m* and *c* only buckling loads for soil stiffness, $\lambda > 50$, have been used. The results for $\lambda < 50$ are presented in Appendix A.2. These straight lines can be used to extrapolate for soil stiffnesses $\lambda > 300$. The maximum error is approximately 10% and this indicates that the lines plotted above are not strictly straight and, hence, extrapolation should not be extended excessively.

$$\frac{P_{cr}}{P_E} = m + c \cdot \frac{\lambda}{\pi^2} \qquad [4.2.5]$$

Homogeneous soil F = 1, $f_1 = f_2 = 0.5$

Unembedded end condition	m	c	max % error $50 < \lambda < 300$
fixed	9.68	2.80	7.0
pinned	3.21	2.34	4.0
translation	3.71	2.34	4.0
free	0.48	1.03	1.0

Table 4.3.1. First buckling loads for a fully embedded pure-friction beam in a homogeneous soil with constant soil stiffness (F = 1) and constant shaft friction ($f_1 = f_2 = 0.5$).

Non-homogeneous soil F = 0, $f_1 = 0$ and $f_2 = 1$

Unembedded end condition	m	c	max % error $50 < \lambda < 300$
fixed	7.37	1.16	8.0
pinned	3.83	0.80	9.0
translation	2.95	0.64	9.0
free	0.85	0.21	10.0

Table 4.3.2. First buckling loads for a fully embedded pure-friction beam in a non-homogeneous soil with triangular soil stiffness (F = 0) and triangular shaft friction ($f_1 = 0, f_2 = 1$).

Non-homogeneous soil F = 1, f_1 = 0 and f_2 = 1

Unembedded end condition	m	c	max % error $50 < \lambda < 300$
fixed	6.10	2.32	7.0
pinned	1.98	2.11	3.0
translation	1.99	2.11	3.0
free	0.12	1.00	0.0

Table 4.3.3. First buckling loads for a fully embedded pure-friction beam in a non-homogeneous soil with constant soil stiffness (F = 1) and triangular shaft friction (f_1 = 0, f_2 = 1).

Non-homogeneous soil F = 0, f_1 = f_2 = 0.5

Unembedded end condition	m	c	max % error $50 < \lambda < 300$
fixed	10.54	1.34	9.0
pinned	4.83	0.87	10.0
translation	4.16	0.70	10.0
free	1.04	0.22	10.0

Table 4.3.4. First buckling loads for a fully embedded pure-friction beam in a non-homogeneous soil with triangular soil stiffness (F = 0) and constant shaft friction (f_1 = f_2 = 0.5).

Non-homogeneous soil F = 1, f_1 = 1 and f_2 = 0

Unembedded end condition	m	c	max % error $50 < \lambda < 300$
fixed	16.37	3.32	7.0
pinned	4.94	2.54	5.0
translation	6.46	2.56	5.0
free	0.90	1.06	2.0

Table 4.3.5. First buckling loads for a fully embedded pure-friction beam in a non-homogeneous soil with constant soil stiffness (F = 1) and triangular shaft friction (f_1 = 0, f_2 = 1).

4.4. Composite end-bearing and friction piles

In sections 4.2 and 4.3 the buckling of pure end-bearing and pure-friction piles respectively were investigated. Having considered these extreme cases, it is natural then to discuss next fully embedded beams which are partially supported by end-bearing and partially by friction. This is the case in most real piles as the pressure bulb under the foot of the pile is able to take vertical loads and friction simultaneously exists along the shaft walls. In the literature review of chapter 2, geotechnical studies on real piles showed that the proportion of the load carried at the base of the pile tends to vary from approximately 20 - 80 % of the applied load at the head of the pile. This would correspond to values of μ = 0.2 to 0.8 (as in equation [3.3.27]). The variation in buckling load, and the corresponding mode shape, as the proportion of the applied load which is carried by the end force at the foot varies will be investigated.

In order to present a more focussed discussion, the solution for the two more common soil conditions will be presented although the 'exact' solution for all cases has been deduced in section 3.3. These are the homogeneous soil, with constant soil stiffness and shaft friction, and the non-homogeneous, with linearly increasing soil stiffness and friction with depth. Not only are these two soil types the most common, but also they represent the two extreme conditions and so it is justifiable to concentrate on these. From the comments on the variations of buckling load and mode shapes between pure-friction (μ = 0) and end-bearing (μ = 1) the behaviour of the other soils considered can be interpolated from the results in the previous two sections.

4.4.1 Homogeneous medium

The first buckling load of piles with fixed-fixed end conditions is plotted in figure 4.4.1 as λ and μ vary. The variation with μ is approximately linear with the buckling load increasing as μ decreases as shown in figure 4.4.2. In figure 4.4.3 the mode shapes for the first buckling modes are plotted. It should be noted that the buckling loads for the two extremes μ = 0 and μ = 1 have been plotted in the previous two sections, figure 4.2.3 and 4.3.6 respectively. There are two distinct trends;

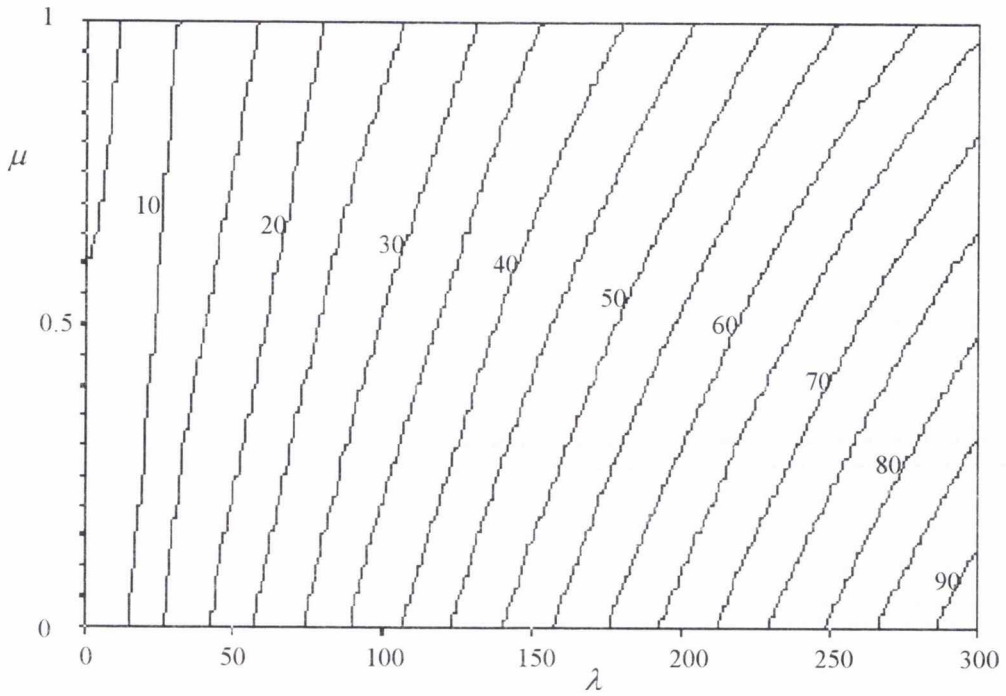

Figure 4.4.1. Buckling load (P_{cr}/P_E) contours for the first mode in a homogeneous soil for a fixed-fixed fully embedded pile.

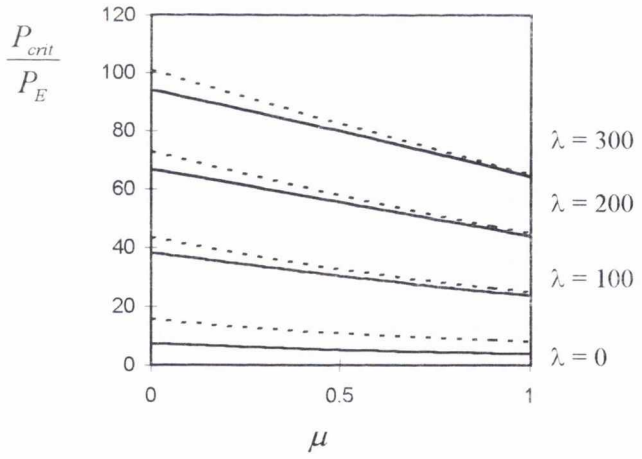

First buckling mode [——], second buckling mode [- - - -].

Figure 4.4.2. Buckling load for the first and second modes for λ = 0, 100, 200 and 300 in figure 4.4.1.

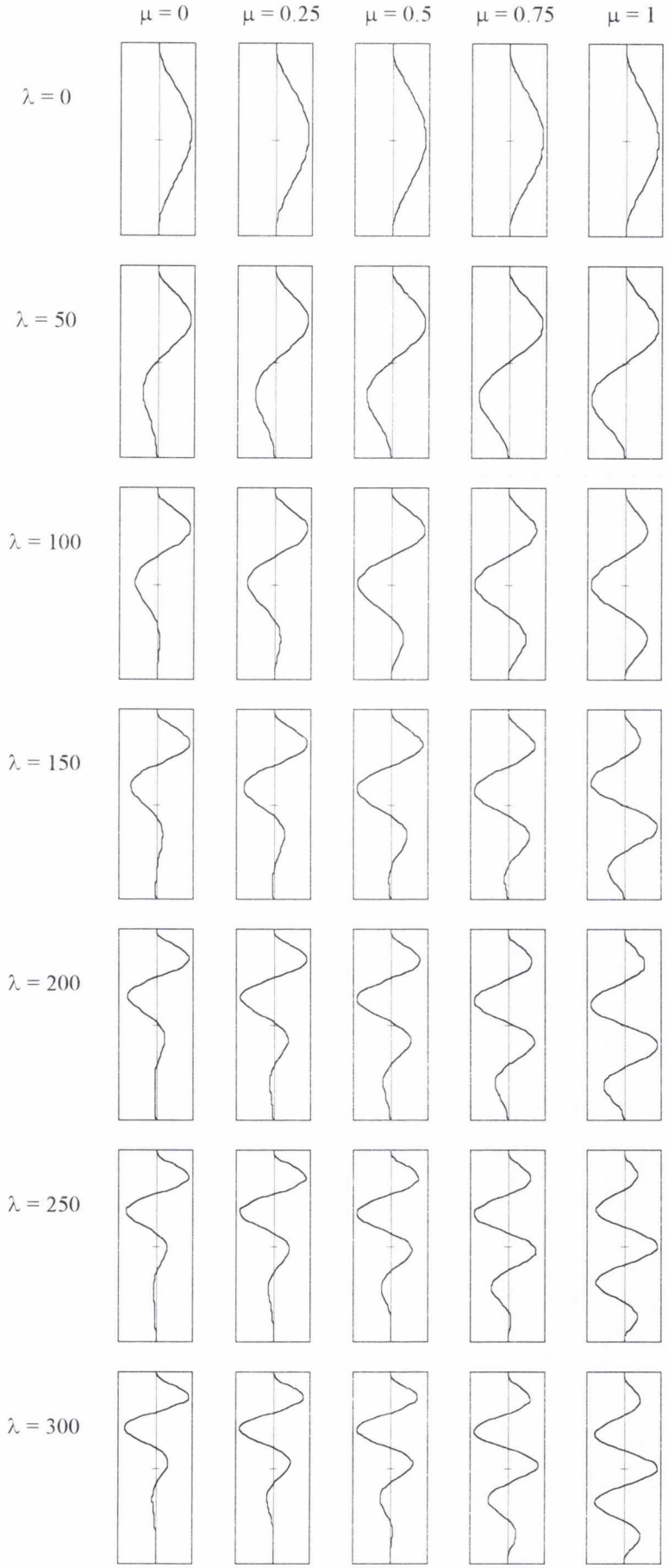

Figure 4.4.3. Buckling mode shapes for the first mode for figure 4.4.1.

1. As the proportion of friction carrying the load increases (μ decreases) the mode shapes tend to have large displacements only in the upper two thirds of the beam for moderate to high soil stiffness.

2. The wavelength of the waves making up the mode shape tends to remain constant for a constant value of soil stiffness.

It could be argued that the number of half waves present for a given value of λ remains the same as μ varies, the sole difference being that, for low values of μ, the amplitudes of the half waves in the bottom third of the pile are so small that they cannot be distinguished when plotted. The loads for the second buckling mode are plotted in figure 4.4.4. It should be noted how the contours show a linear variation with μ and indeed with λ for all but the lowest values of soil stiffness. Figure 4.4.2 shows that there does not appear to be any significant modal clustering as μ varies. The first two modes tend to approach each other linearly as μ tends to unity. This effect can also be seen in the mode shapes of the second mode (figure 4.4.5) which are plotted in order to compare with the results of the second mode in the free-free case later.

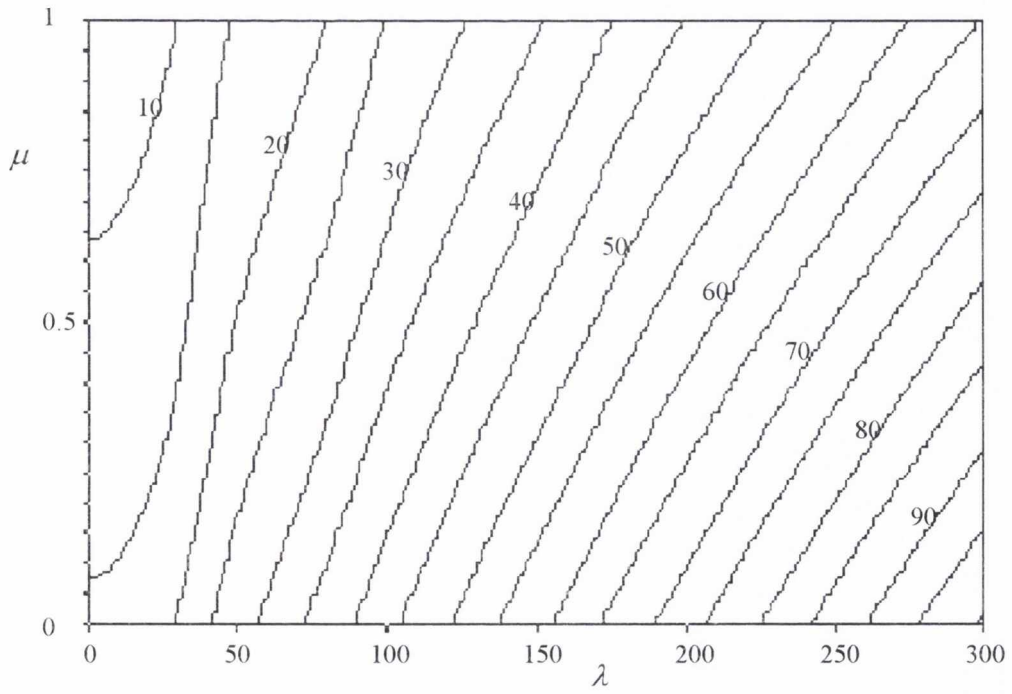

Figure 4.4.4. Buckling load (P_{cr}/P_E) contours for the second mode in a homogeneous soil for a fixed-fixed fully embedded beam.

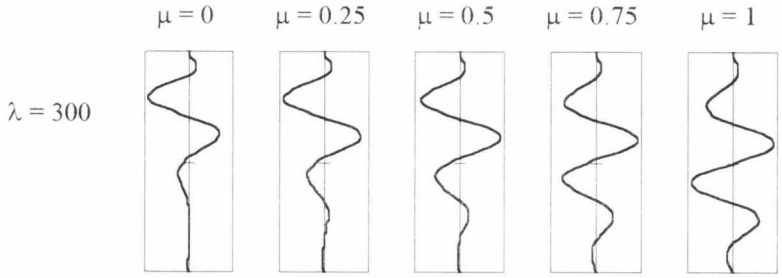

Figure 4.4.5. Buckling mode shapes for the second mode for figure 4.4.4.

Figure 4.4.6 shows a similar plot of the buckling loads for a homogeneous soil with pinned-pinned end conditions for the first mode. The first mode indicates that, again, the variation with respect to μ is broadly linear (figure 4.4.7). The mode shapes in figure 4.4.8 show that the first buckling mode is unlikely to extend below the half way point of the pile for moderate soil stiffness if there is any significant proportion of the load being supported by shaft friction. It can be seen that all the mode shapes tend to fall into two groups, namely the mode shapes when μ = 1, which are either symmetric or anti-symmetric, and the rest. The other mode shapes have amplitudes tending to zero at the bottom of the pile.

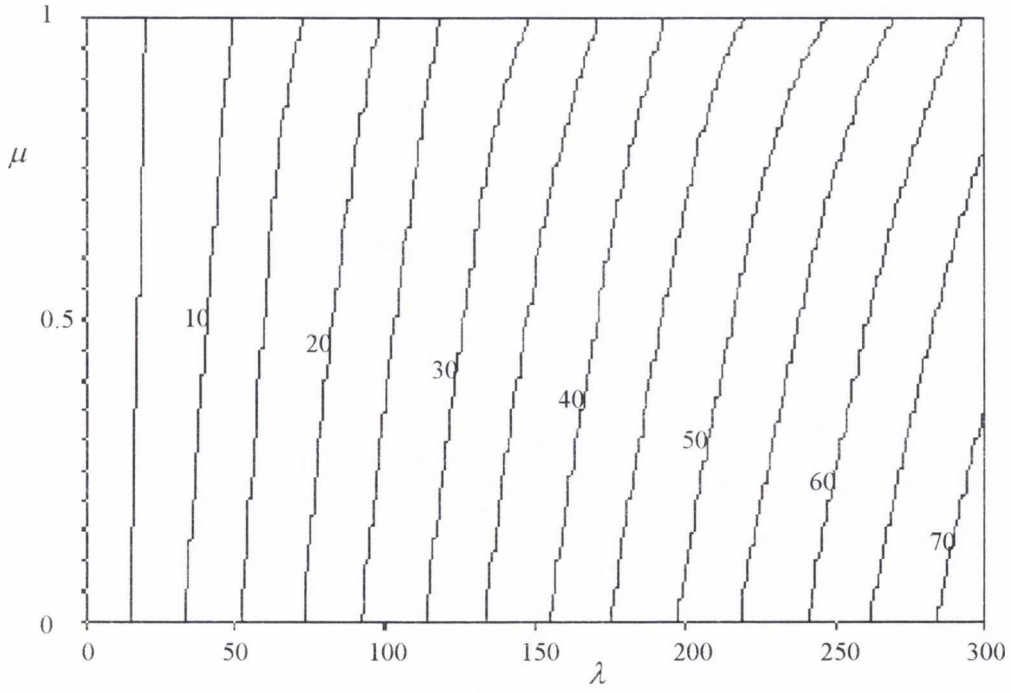

Figure 4.4.6. Buckling load (P_{cr}/P_E) contours for the first mode in a homgoenous soil for a pinned-pinned embedded beam.

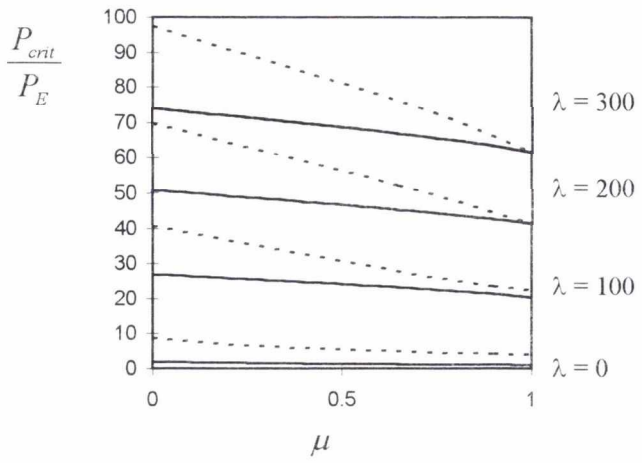

First buckling mode [——], second buckling mode [- - - -].

Figure 4.4.7. Buckling loads for the first and second modes with λ = 0, 100, 200 and 300 for figure 4.4.6.

In figure 4.4.9 the buckling loads for the second modes are plotted with pinned-pinned end conditions. The behaviour at high λ and low μ is linear, however as μ approaches unity (end-bearing) the pattern appears to be more complicated. This is due to the piecewise parabolic nature of the solution which was discussed in Hetényi and section 4.2 for the solution of pinned-pinned end-bearing piles.

In figures 4.4.10 and 4.4.11 the buckling loads of the first mode with free-free ends are plotted. The buckling load is linear with respect to soil stiffness, λ. However, there is only a very slight variation with μ, even at high soil stiffness, and this is reflected in the mode shapes in figure 4.4.12. All the mode shapes are practically identical for all soil stiffness greater than zero or end bearing μ less than 1. The mode shapes for μ = 1 are similar to other values of μ for a given value of soil stiffness, except the upper mode shape is mirrored below the half-way point on the beam. This is not surprising as pure end-bearing piles (μ = 1) are necessarily either symmetric or anti-symmetric (section 4.2), but when friction is present the load at the pile head does not significantly change yet, at the pile toe, it is reduced significantly. Hence, the conditions, in terms of lateral support and load in the pile, are similar at the top of the pile whether friction is present or not, but change significantly near the bottom of the pile. This means that the only effect of the addition of friction to the system considered is to prevent the mode shape forming in the lower half of the pile.

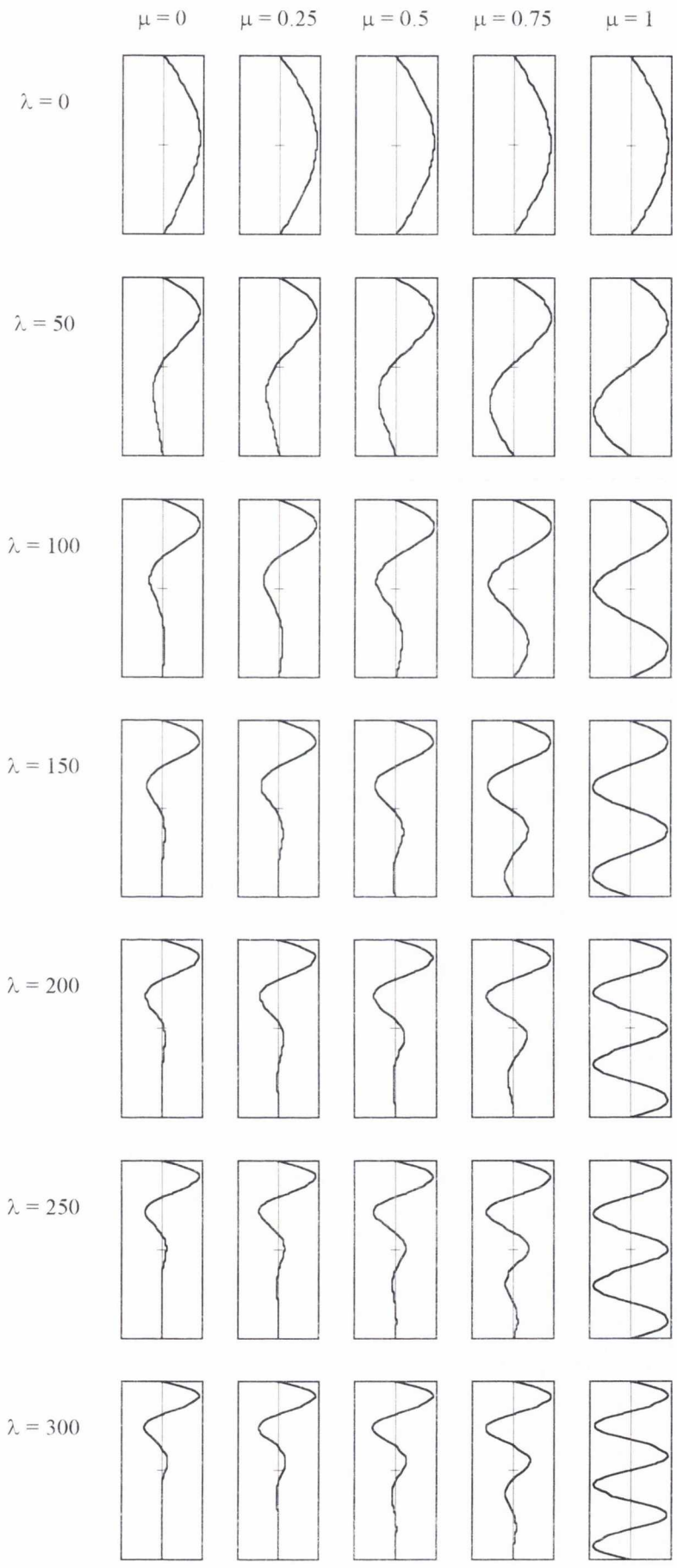

Figure 4.4.8. Buckling mode shapes for figure 4.4.7.

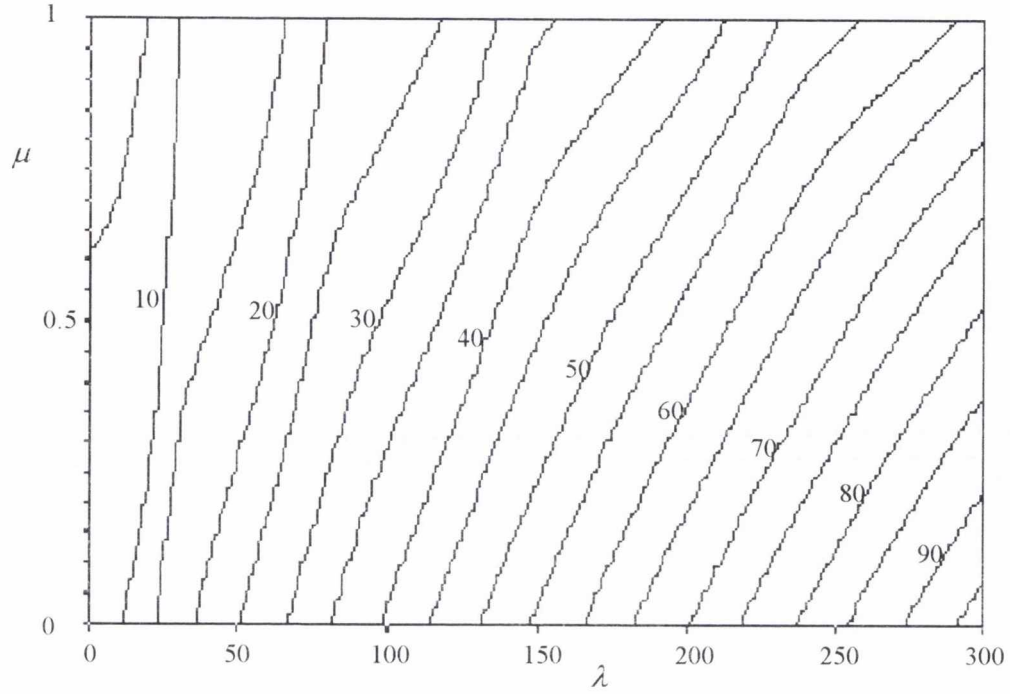

Figure 4.4.9. Buckling load (P_{cr}/P_E) contours for the second mode in a homogeneous soil for a pinned-pinned fully embedded beam.

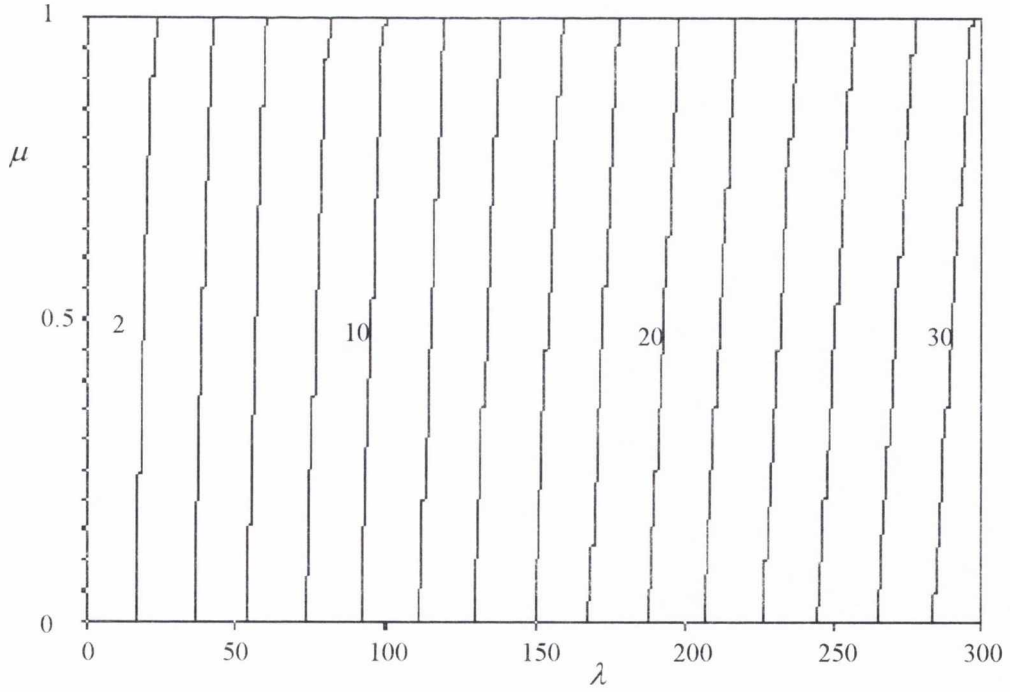

Figure 4.4.10. Buckling load (P_{cr}/P_E) contours for the first mode in a homogeneous soil for a free-free fully embedded beam.

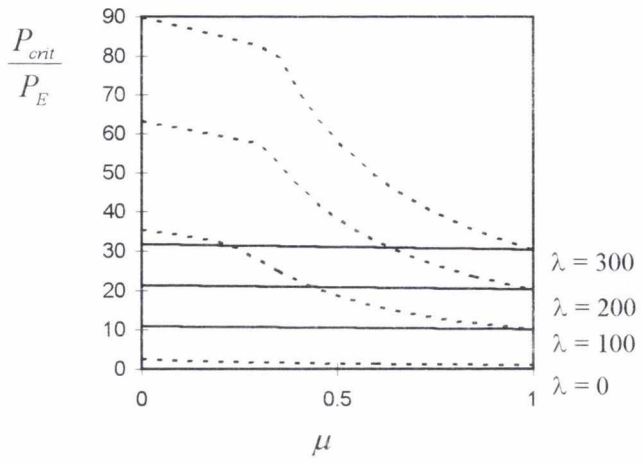

First buckling mode [——], second buckling mode [- - - -].

Figure 4.4.11. Buckling loads for the first and second modes for λ = 0, 100, 200 and 300 for figure 4.4.10.

In figure 4.4.13 the buckling loads for the second mode are plotted. There are two distinct trends present in the region of medium to high soil stiffness. Between μ = 0 and 0.35 the buckling loads gradually decreases for constant λ, yet above μ = 0.35 there is a rapid reduction in buckling load, in an approximately parabolic way, as can be seen in figure 4.4.13. In figure 4.4.14 the mode shapes at λ = 300 for the second mode are plotted. The mode shape for the lower values of μ is concentrated in the upper portion of the beam and, surprisingly, has two extra half waves when compared to the first mode under similar conditions. Above μ = 0.35, the mode shape is approximately a mirror image of the first mode about the beam's midpoint. This is surprising as the mode shape is largest in an area of reduced load in the pile.

The parabolic curve identified above can be seen to extend above the second mode and depending on the value of μ it forms sections of the second and above modes (mode 2, for $0.4 < \mu < 1$; mode 3, $0.35 < \mu < 0.4$; mode 4, $0.25 < \mu < 0.15$; etc). This line has a characteristic mode shape with a maximum amplitude at the bottom of the pile where the soil stiffness is largest and the load in the pile is least (examples of such a mode shape can be identified in figure 4.4.15).

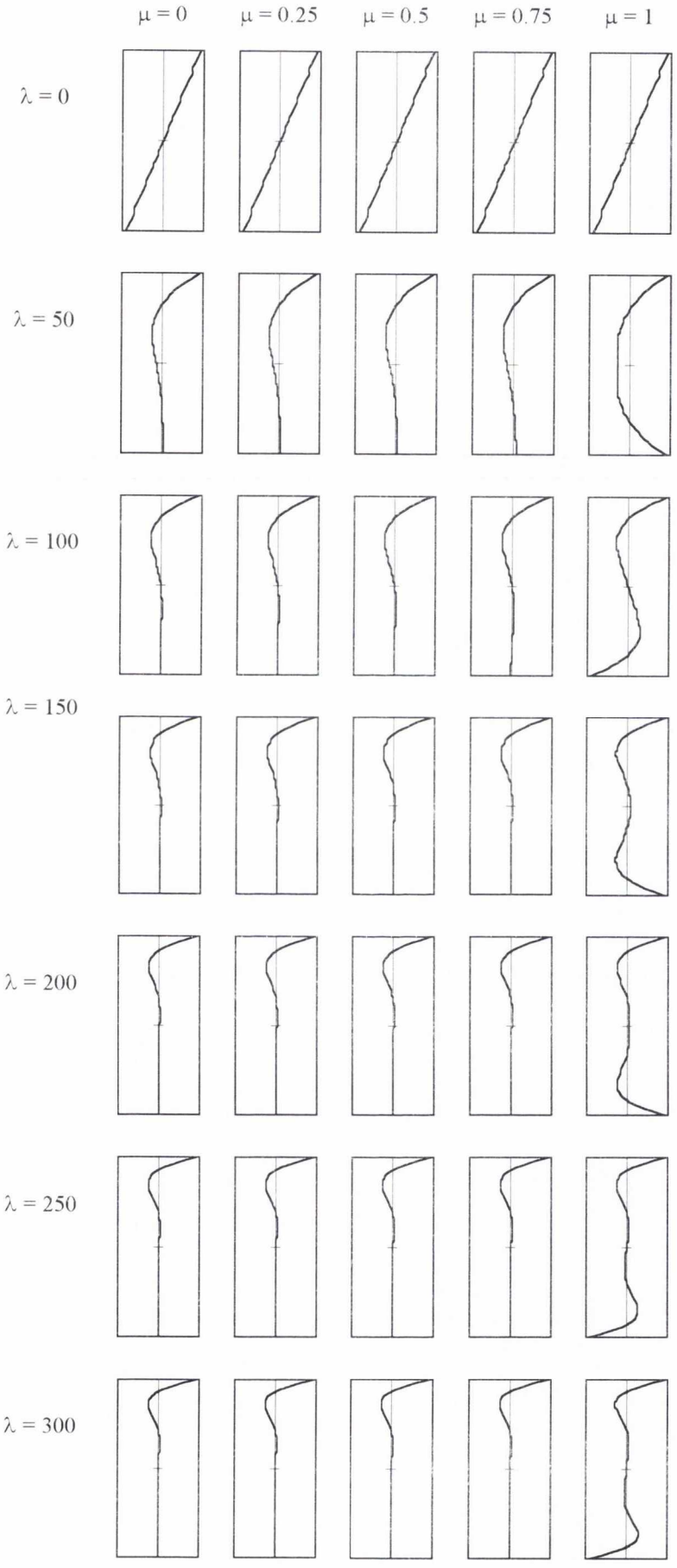

Figure 4.4.12. Buckling mode shapes for figure 4.4.10.

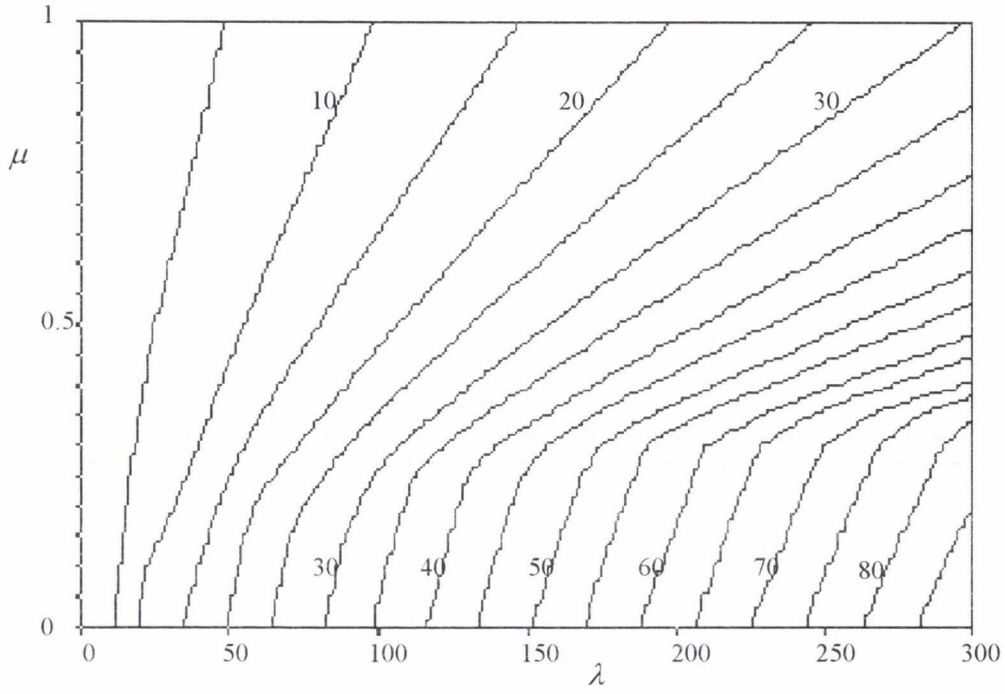

Figure 4.4.13. Buckling load (P_{cr}/P_E) contours for the second mode in a homogeneous soil for a free-free fully embedded beam.

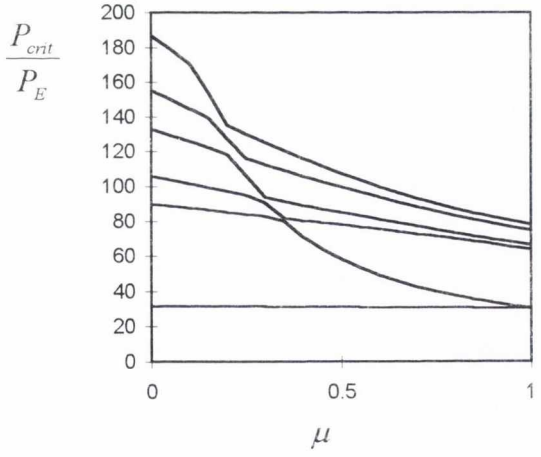

Figure 4.4.14. Buckling load for the first six modes for $\lambda = 300$ for figures 4.4.10 and 4.4.13.

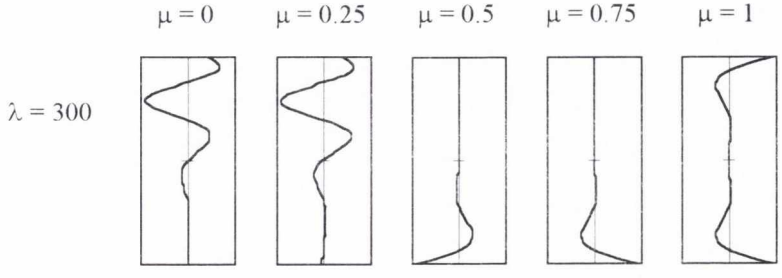

Figure 4.4.15. Buckling mode shapes for the second mode for figure 4.4.14.

In figures 4.4.16 and 4.4.17 the buckling loads for the first mode with fixed-free end conditions are plotted. It should be remembered from previously that the end-bearing case ($\mu = 1$) has a mode shape with maximum amplitude at the bottom for values of $\lambda < 1200$, yet the pure-friction case ($\mu = 0$) only has such a mode shape for a very limited range of low soil stiffness. It can be seen in figure 4.4.18 that these two types of buckling mode shape can be associated with different areas of the graph. The mode shape with maximum amplitude at the pile bottom is associated with a paraboloic variation in μ which occurs at approximately $\mu > 0.3$, whereas the other mode shape is associated with a linear variation with respect to μ for lower values of μ. In figure 4.4.18, at $\lambda = 300$, it can be seen that this mode shape does not just have a single half wave. This is not surprising as it is identical in form to the first mode at a similar soil stiffness with fixed-fixed end-conditions (figure 4.4.3). If figure 4.4.17 is inspected then it can be seen that the straight line associated with this mode shape is an extension of the line for the second buckling load for high values of μ.

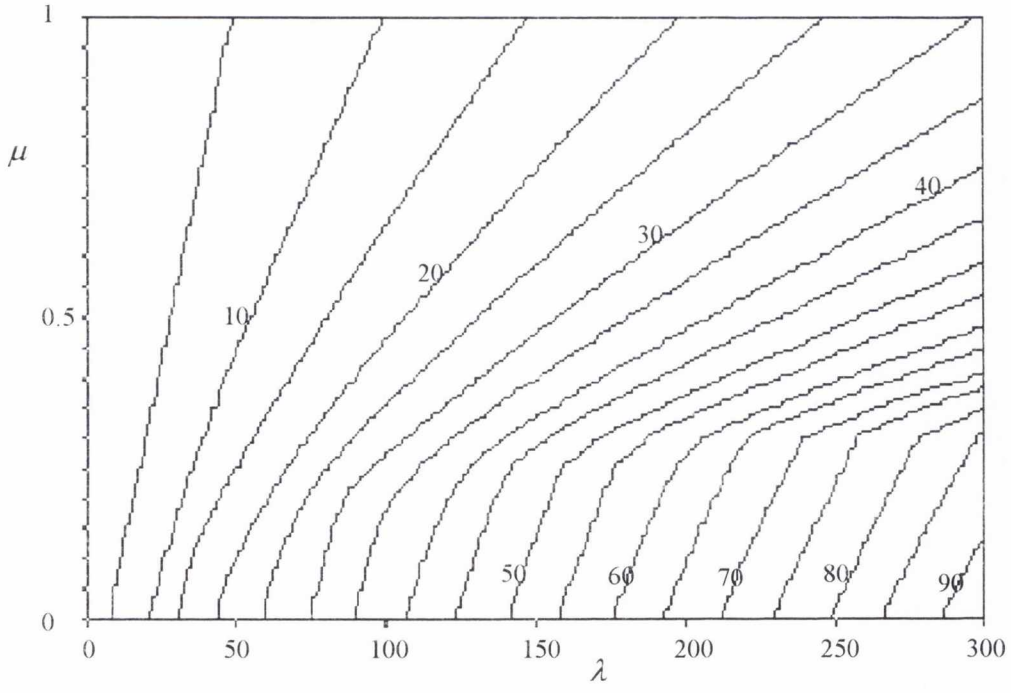

Figure 4.4.16. Buckling load (P_{cr}/P_E) contours for the first mode in a homogeneous soil for a fixed-free fully embedded beam.

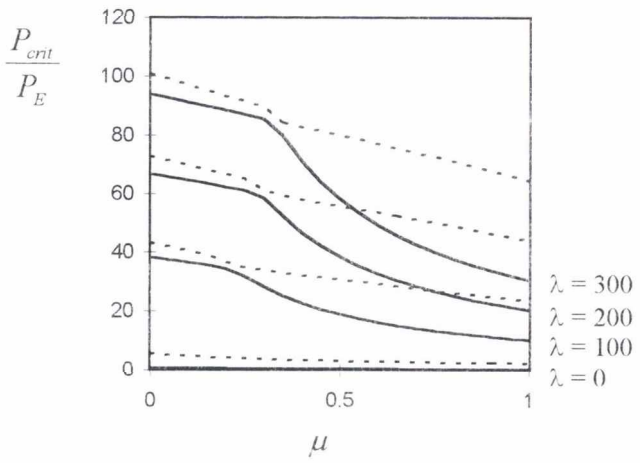

First buckling mode [——], second buckling mode [- - - -].

Figure 4.4.17. Buckling load for the first mode for λ = 0, 100, 200 and 300 for figure 4.4.16.

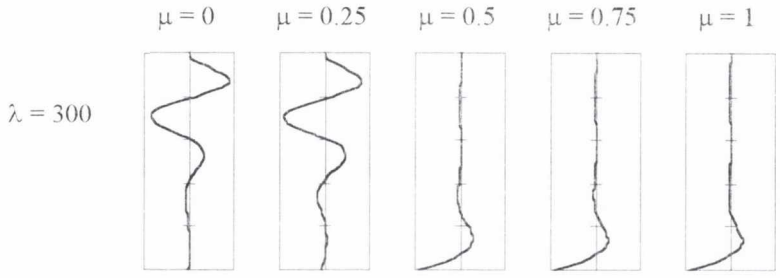

Figure 4.4.18. Buckling mode shapes for the first mode for figure 4.4.17.

4.4.2 Non-homogeneous medium

The buckling loads of the first mode with fixed-fixed end-conditions are plotted with linearly increasing soil stiffness (F = 0) and friction (f_1 = 0) with depth in figure 4.4.19. It can be seen that the variation between buckling loads as μ varies is much less distinct than for the homogeneous equivalent. If the mode shapes for the first mode are inspected in figure 4.4.21 then it can be seen that there are also no significant variations in mode shape as μ varies. There is a linear variation as soil stiffness increases. This is because where the soil stiffness is least at the top of the pile the force in the pile, whatever the value of μ, is always at a maximum, yet even if the value of μ changes between 0 and 1, the load in the beam at this point does not change significantly if the same load is applied. This is shown in figure 4.4.20. Hence, when the variation in soil stiffness is taken into account, the area of least resistance to lateral load is always the area with the maximum load in the beam and, thus, the buckling load is not particularly sensitive to μ (figure 4.4.22).

Like the homogeneous case the second mode, in figure 4.4.22, is also linear with respect to μ. However, in this case, the first and second mode do not approach each other closely as μ tends to unity. Hence, close modal clusters tend not to occur and so a the detailed contour plots of the second mode will not be reproduced. The similarity in mode shape for the second mode as μ varies for a constant soil stiffness can be identified in figure 4.4.23. Because of the non-homogeniety in the soil stiffness the second mode shape is restricted to just one form and is not affected by varying μ.

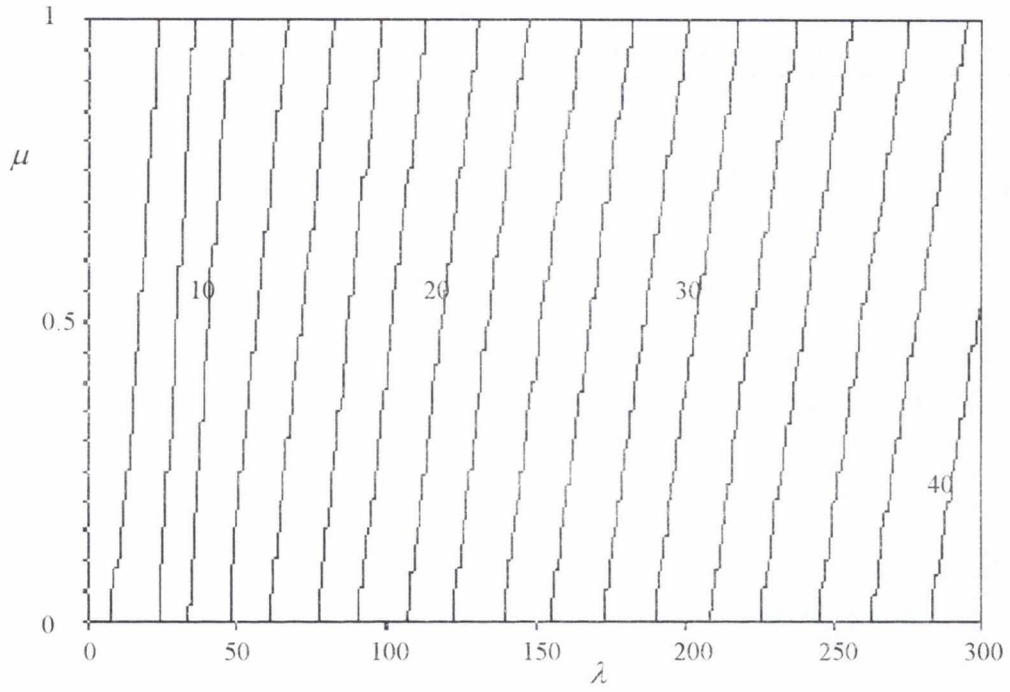

Figure 4.4.19. Buckling load (P_{cr}/P_E) contours for the first mode in a non-homogeneous soil for a fixed-fixed fully embedded beam.

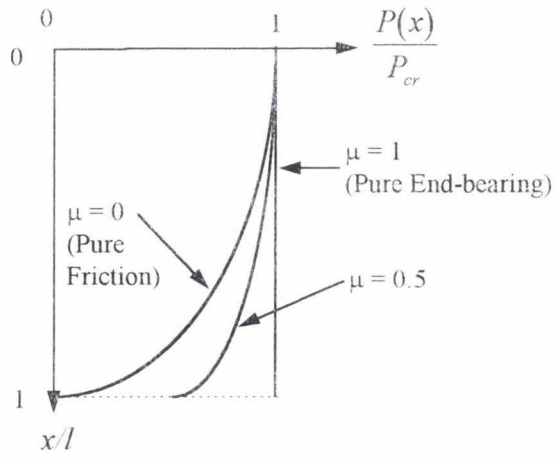

Figure 4.4.20. Variation of buckling load for a beam as μ varies for linear increasing shaft friction.

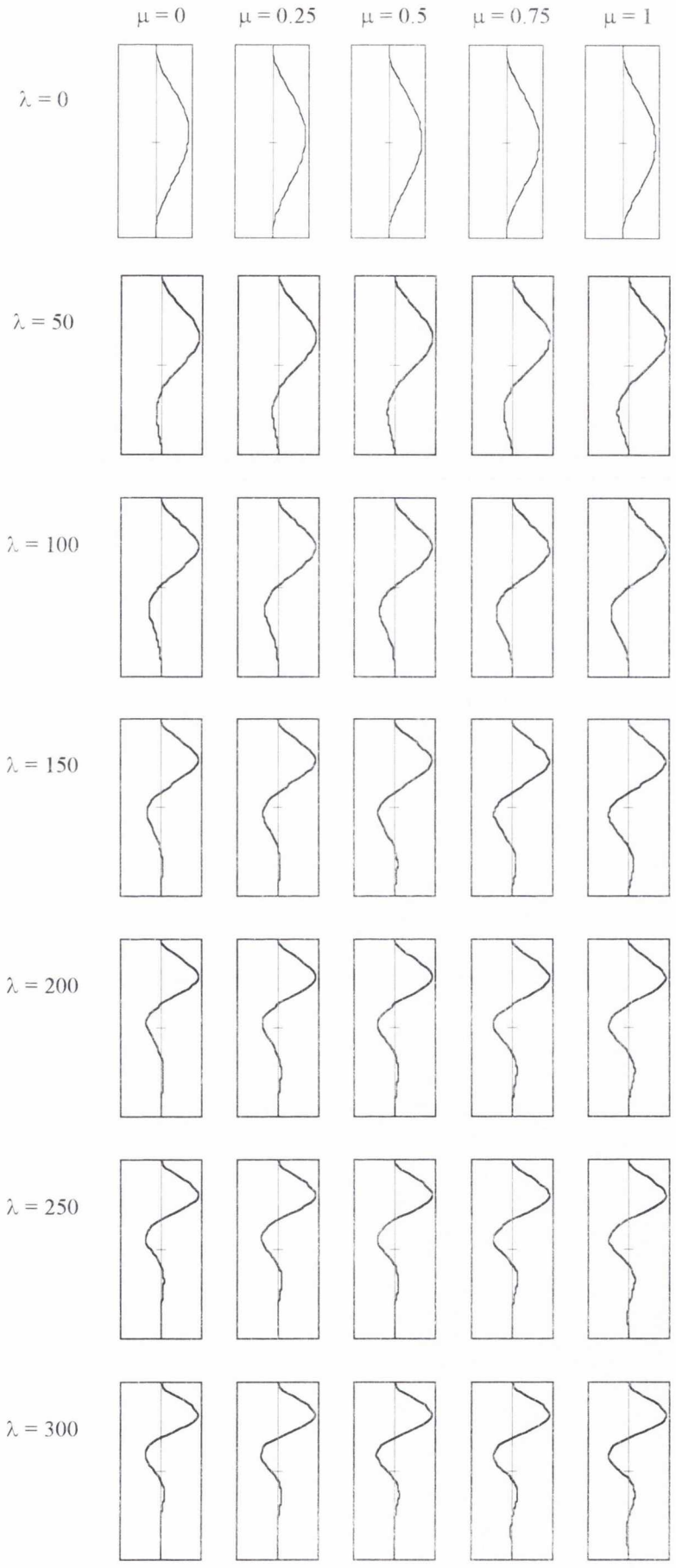

Figure 4.4.21. Buckling mode shapes for the first mode in a non-homogeneous soil for figure 4.4.19.

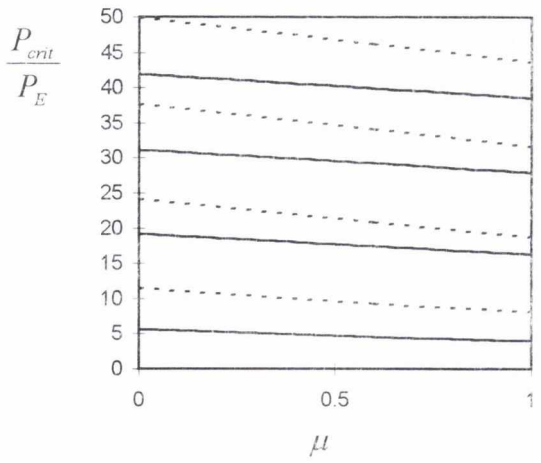

First buckling mode [——], second buckling mode [- - - -].

Figure 4.4.22. Buckling load for the first mode for λ = 0, 100, 200 and 300 for figure 4.4.19.

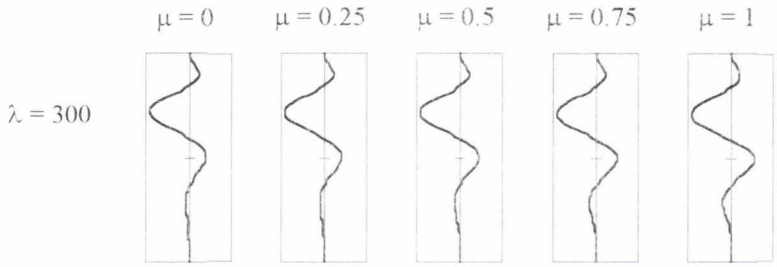

Figure 4.4.23. Buckling mode shapes for the second mode in a non-homogeneous soil for figure 4.4.22.

In figure 4.4.24 the first buckling mode for pinned-pinned end conditions are plotted. The arguments dealing with the sensitivity of the buckling load to μ apply to the pinned-pinned case as in the fixed-fixed case and, hence, only the first buckling load (figure 4.4.24) is plotted. As in the fixed-fixed case the mode shapes do not vary with μ and even the variation with soil stiffness, λ, is very limited. This is the case for both the first mode (figure 4.4.25) and the second mode (figure 4.4.26). In figure 4.4.24 it can be seen that the first and second modes are widely separated and, hence, an in-depth review of the second mode is not applicable.

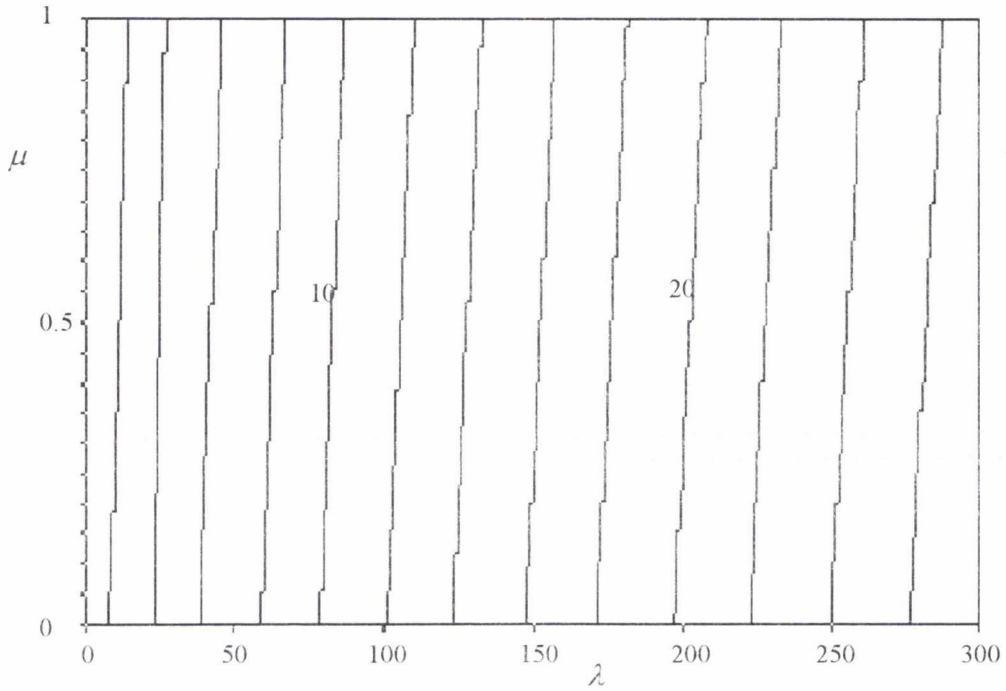

Figure 4.4.24. Buckling load (P_{cr}/P_E) contours for the first mode in a non-homogeneous soil for a pinned-pinned fully embedded beam.

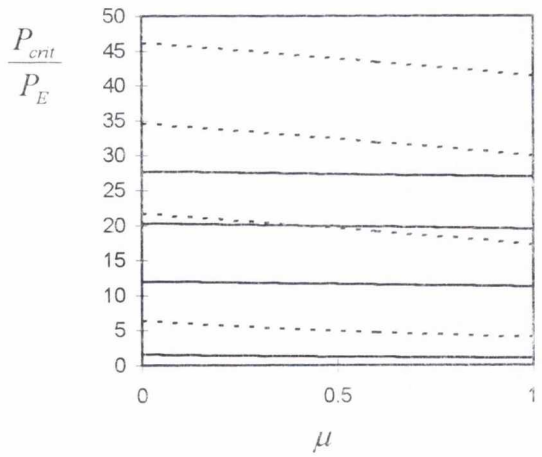

First buckling mode [———], second buckling mode [- - - -].

Figure 4.4.25. Buckling load for the first mode for λ = 0, 100, 200 and 300 for figure 4.4.24.

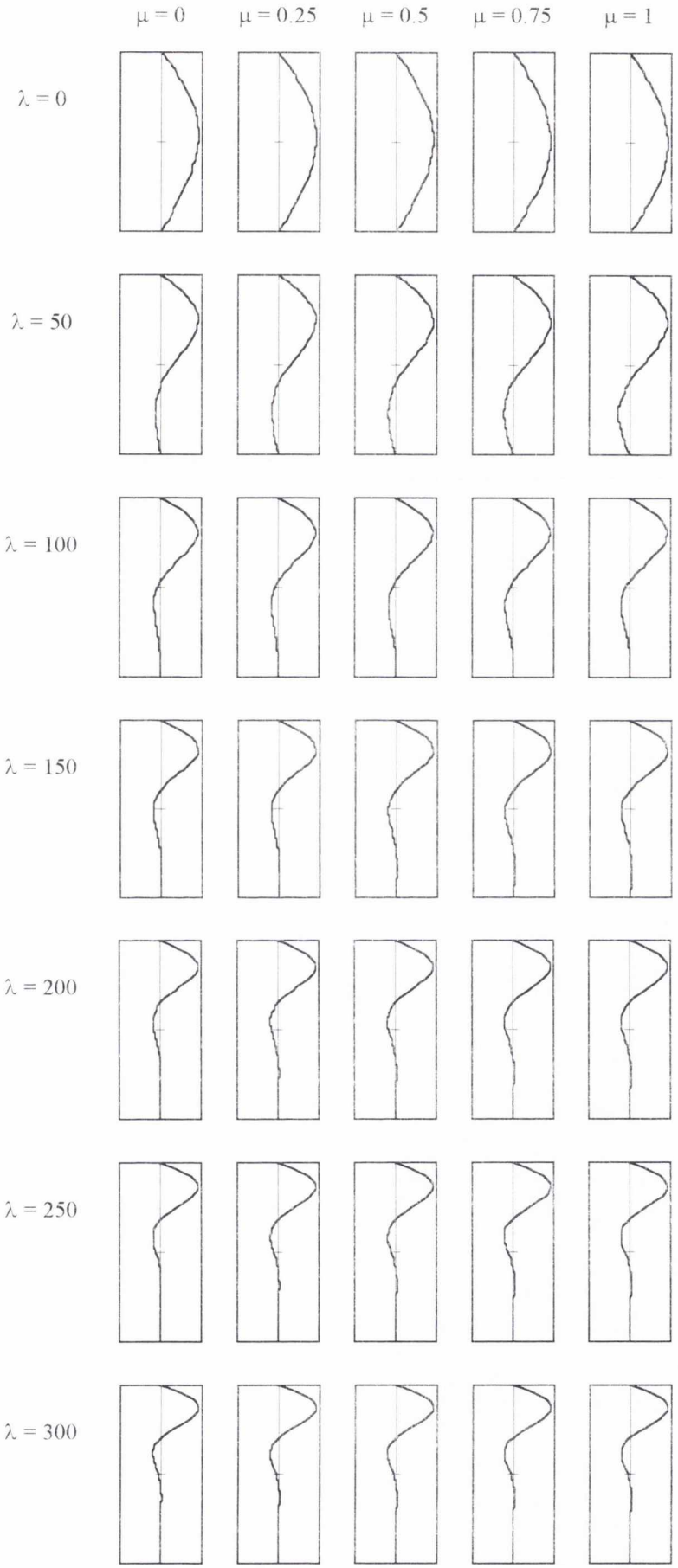

Figure 4.4.26. Buckling mode shapes for the first mode in a non-homogeneous soil for figure 4.4.24.

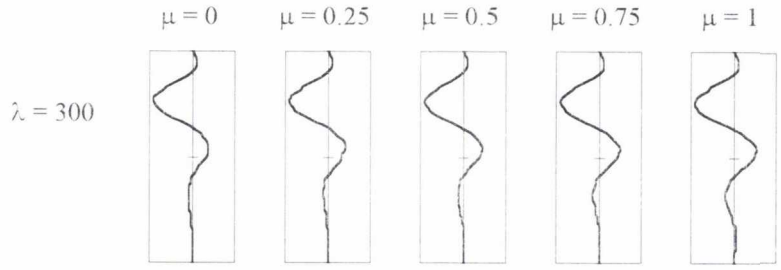

Figure 4.4.27. Buckling mode shapes for the second mode in a non-homogeneous soil for figure 4.4.25.

The buckling loads for the free-free case are presented in figure 4.4.28. It should be remembered that the second mode in the homogeneous case was significantly different from the first mode, having mode shapes which had its maximum displacement at the bottom of the pile. The fundemental mode shapes of the non-homogeneous case in figure 4.4.29 is predictable with the maximum displacement being at the top of the pile. The buckling loads of the second mode are plotted in figure 4.4.30 from which it may be seen that, as in the homogeneous case, there is a plateau at high soil stiffness and low μ. If the first six modes are inspected for λ = 300 in figure 4.4.31 then it can be seen that, again, there is a curve which intersects the second and higher modes. This is characterised

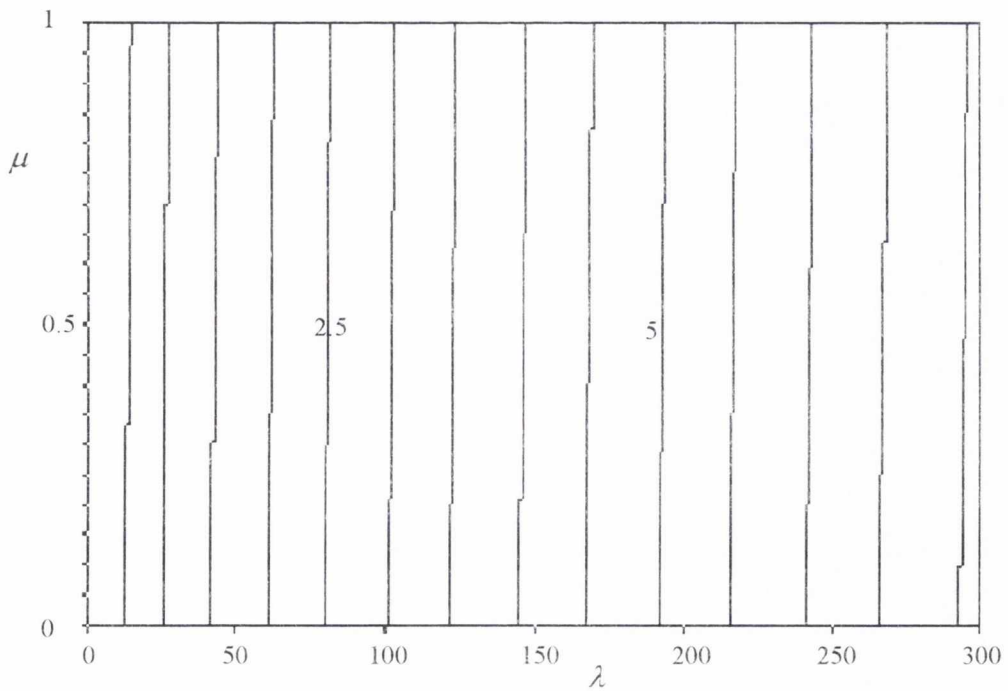

Figure 4.4.28. Buckling load (P_{cr}/P_E) contours for the first mode in a non-homogeneous soil for a free-free fully embedded beam.

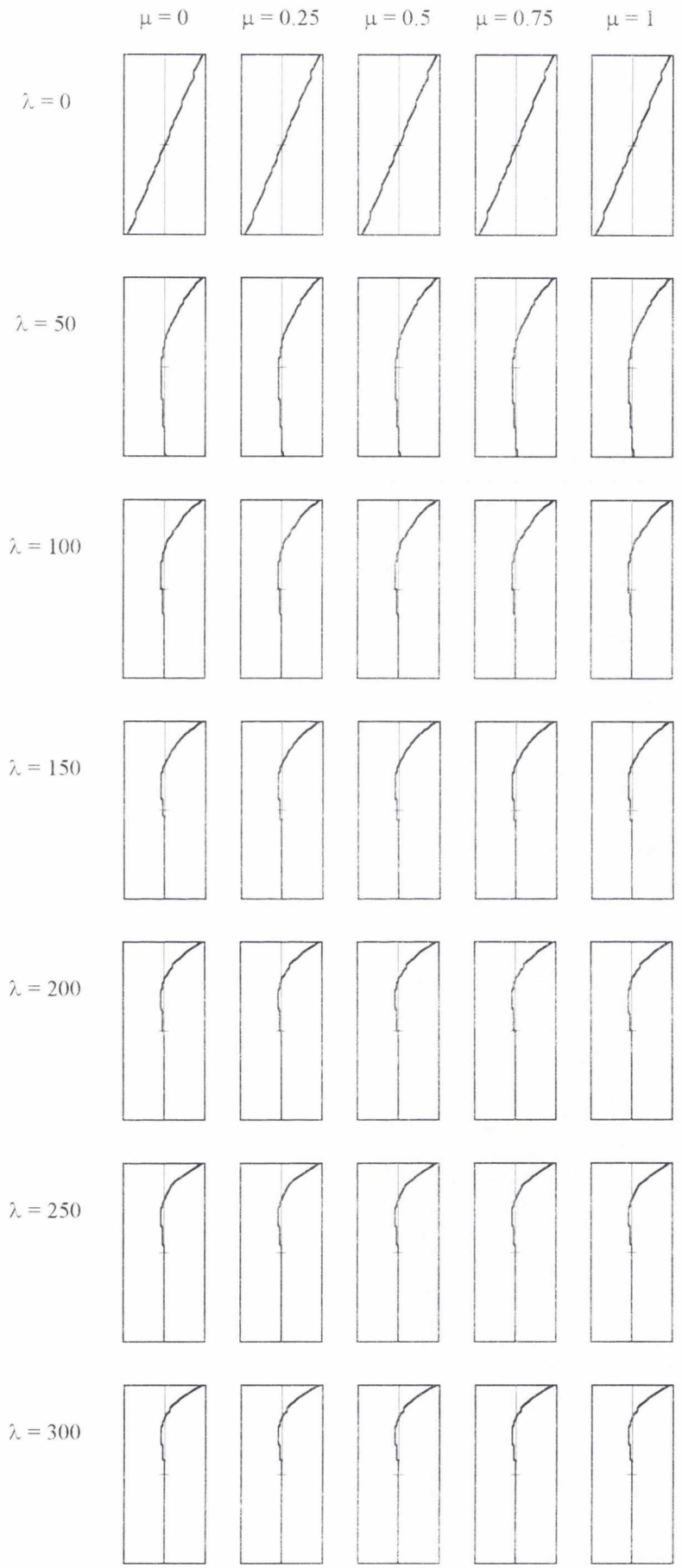

Figure 4.4.29. Buckling mode shapes for the first mode in a non-homogeneous soil for figure 4.4.28.

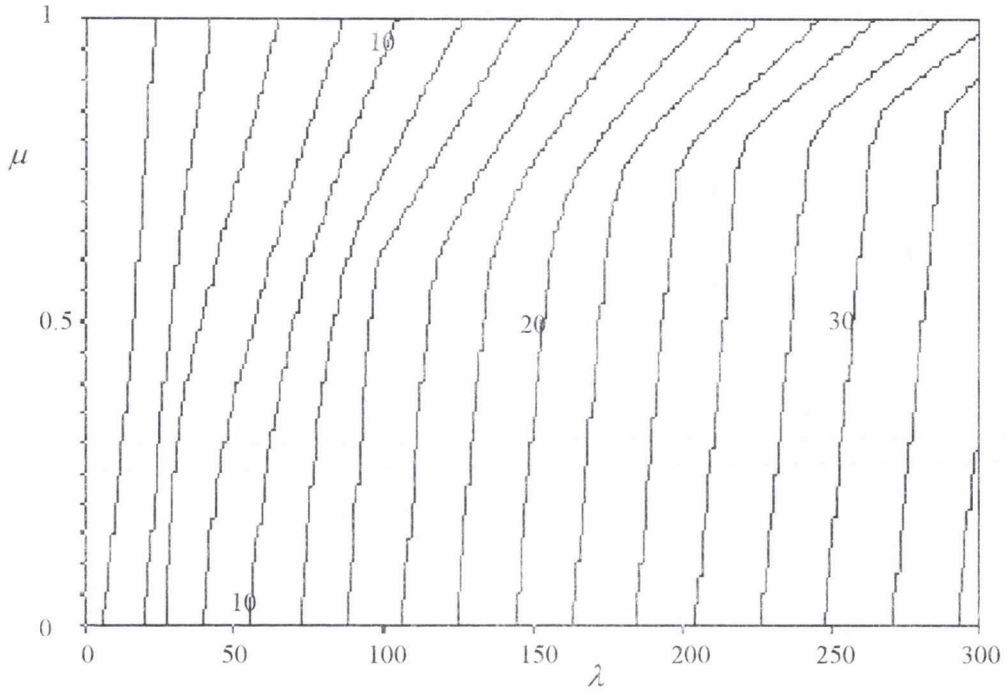

Figure 4.4.30. Buckling load (P_{cr}/P_E) contours for the second mode in a non-homogeneous soil for a free-free fully embedded beam

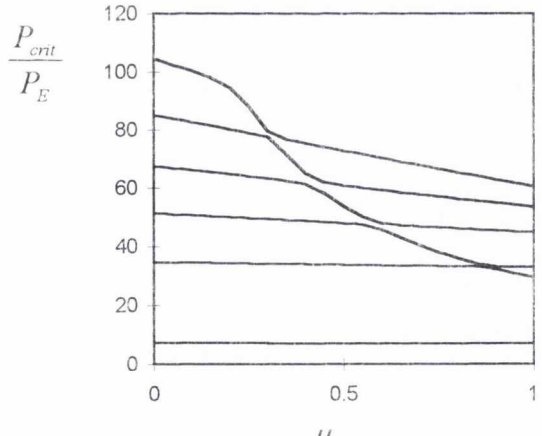

Figure 4.4.31. Buckling loads for the first six modes for λ = 300 in a non-homogeneous soil for a free-free fully embedded beam.

by a mode shape which has the maximum amplitude at the bottom of the pile as can be seen in figure 4.4.32. The bottom of the pile has relatively higher soil stiffness and lower load in the pile than the top and thus the buckling load is greater than in the homogeneous case for a similar mode shape. Hence, the first and second mode are more distinct than the homogeneous case as μ tends to unity and the mode shape for the second mode has a maximum amplitude at the pile base.

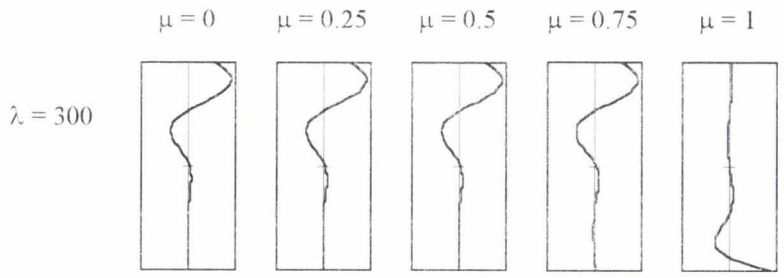

Figure 4.4.32. Buckling mode shapes for the second mode in a non-homogeneous soil for figure 4.4.31.

In figures 4.4.33 and 4.4.34 the buckling loads for a fixed-free beam in a non-homogeneous soil are plotted. Like the homogenous case, the graph can be divided into two sections. The first can be related to mode shapes with a maximum amplitude at the bottom, next to the free end, and the second related to mode shapes with maximum amplitudes present in the upper section of the beam which is supported by the weaker lateral support. An example of such mode shapes have been plotted in figure 4.4.35.

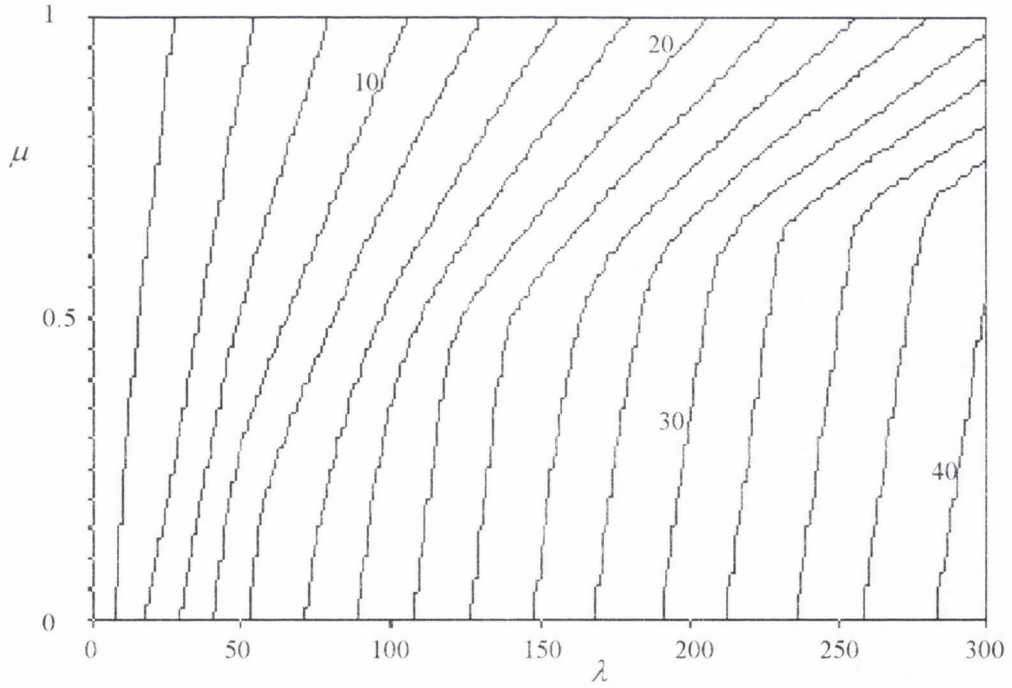

Figure 4.4.33. Buckling load (P_{cr}/P_E) contours for the first mode in a non-homogeneous soil for a fixed-free fully embedded beam.

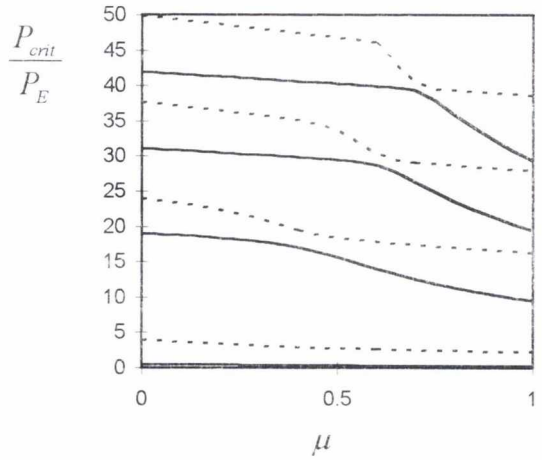

First buckling mode [——], second buckling mode [- - - -].

Figure 4.4.34. Buckling load for the first mode for λ = 0, 100, 200 and 300 for figure 4.4.33.

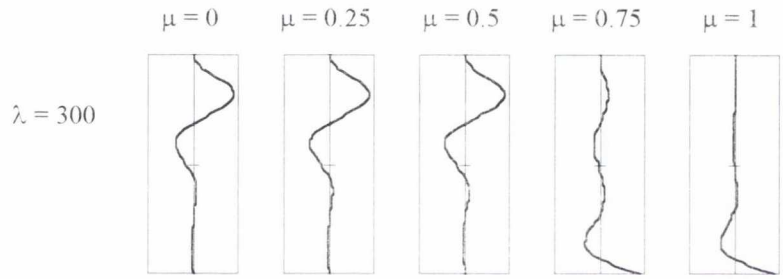

Figure 4.4.35. Buckling mode shapes for the first mode in a non-homogeneous soil for figure 4.4.33.

Other non-homogeneous soils

In this section a method by which the buckling loads for other non-homogeneous soils will be briefly outlined. In figures 4.4.36 and 4.4.37 the buckling loads for the symmetric end conditions are plotted for a soil stiffness λ = 300. The variation with μ is approximately linear and so interpolation can be used between the pure-friction and end-bearing results presented in section 4.2 and 4.3.

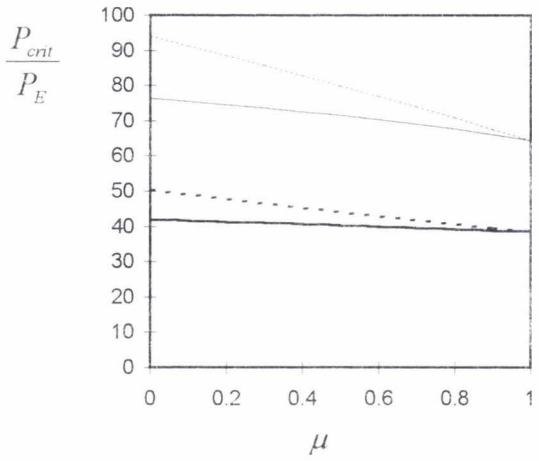

F = 0 and f_1 = 0 [———], F = 0 and f_1 = 0.5[- - - -], F = 1 and f_1 = 0 [———], F = 1 and f_1 = 0.5[·····].

Figure 4.4.36. Buckling load for a fixed-fixed beam in a non-homogeneous soil at λ = 300.

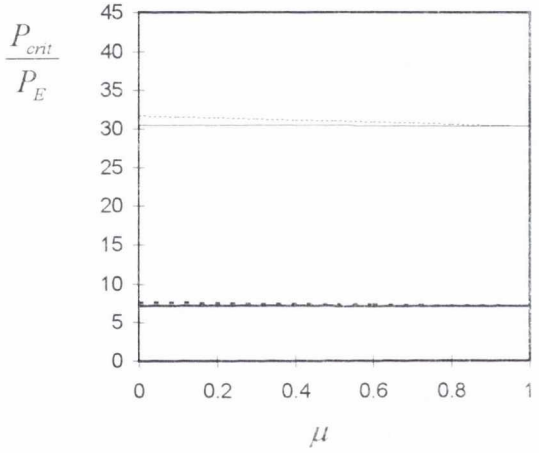

F = 0 and f_1 = 0 [———], F = 0 and f_1 = 0.5[- - - -], F = 1 and f_1 = 0 [———], F = 1 and f_1 = 0.5[·····].

Figure 4.4.37. Buckling load for a free-free beam in a non-homogeneous soil at λ = 300.

In order to provide the approximation of the buckling loads of non-symmetric end conditions, for example a fixed-free beam in a non-homogeneous soil with F = 1 and f_1 = 0, two results are required. The first is the symmetric result for the uembedded end condition in the appropriate soil condition, in the example fixed-fixed with F = 1 and f_1 = 0. As mentioned before this can be approximated by a linear variation between the results for an end-bearing pile with F = 1 and a pure-friction pile with F = 1 and f_1 = 0 which have been previously presented in the summaries of 4.2 and 4.3. The second solution required is the results with a fixed unembedded end and the appropiate unembedded end-condition, in this case a free end, with an homogenous soil (F = 1 and f_1 = 0.5). The

buckling load can then be approximated by using the lower of the two solutions. The above example at $\lambda = 300$ is shown in figure 4.4.38. The bold line is the exact solution to the problem of a fixed-free beam in a non-homogeneous soil ($F = 0$, $f_1 = 0.5$). It can be seen that the errors involved in taking the lower of the other two lines are minimal ($\approx 5\%$) especially when the accuracy of the geotechnical data that has to be used is taken into consideration.

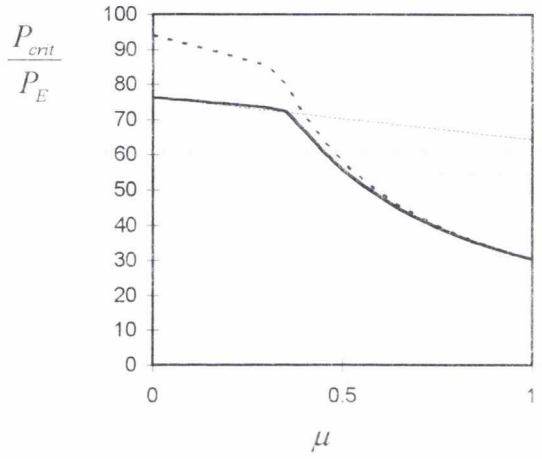

Fixed-free $F = 0$ and $f_1 = 0.5$ [——], fixed free $F = 1$ and $f_1 = 0.5$[- - -], fixed-fixed $F = 0$ and $f_1 = 0.5$ [·····].

Figure 4.4.38. Buckling load approximation for a fixed-free beam in a non-homogeneous soil at $\lambda = 300$.

4.4.3 Summary

The buckling loads for all variations of end conditions for homogeneous soils ($F = 1$, $f_1 = 0.5$) and non-homogeneous soils are plotted in Appendix A.1 with a range of soil stiffness $0 < \lambda < 300$. As has been mentioned above in order to approximate other non-homogeneous soil conditions the only results required are those with a fixed embedded end-condition. These are presented in Appendix A.3. Combining the results from these two Appendices it is possible to approximate results to a high accuracy ($\approx 5\%$) for all combination of variations in soil stiffness and shaft friction previously considered.

4.5. Conclusions

In this chapter the results produced by the proposed algorithm for fully embedded beams have been discussed. The topic has been split into several distinct sections. The first section comprises those beams which are supported entirely by an end-bearing force at the bottom of the pile. The soil medium can be defined either as homogeneous (constant soil stiffness with depth) or non-homogeneous (where the soil increases linearly with depth). These classifications of soil stiffness can also be applied to the problem where the pile is supported to some degree by a frictional force along the shaft of the pile.

The solution to symmetric end conditions of an end-bearing beam in a homogeneous medium have been presented previously by Hetényi (1946). The solution provided by the algorithm presented has been shown to be identical to that by Hetényi. Hetényi noted a pattern in the buckling loads with symmetric end-conditions where the mode shape of the lowest mode 'switched' between a symmetric and anti-symmetric mode shape as soil stiffness increased. It was shown that these patterns can be extended to modes other than the fundamental in order to predict modal clustering between successive modes. These modal clusters indicate the location of the changes in mode shapes for all modes. When the end-conditions are pinned-pinned, these patterns also exactly predict the buckling loads and mode shapes, which comprise of an integer number of half sine waves, of all buckling modes. With other symmetric end conditions the mode shapes between successive modal clusters have been shown to be of a complex form. The buckling loads and mode shapes of a beam with free-free end conditions can be divided into two. The first and second modes produce significantly lower buckling loads (approximately half of the third mode) than the higher modes. The higher modes have mode shapes which are similar to those produced with pinned-pinned end conditions, whereas the first two modes have shapes whose amplitudes are at a maximum at the extremes of the beam. The solution in chapter 3 has also extended Hetényi's work to non-symmetric end conditions and it was shown that modal clustering no longer occurs to such an extent.

The buckling loads of beams in a homogeneous soil and a non-homogeneous soil, with a linearly varying soil stiffness, were then compared. As would be expected, the symmetric/anti-symmetric mode shapes found in the homogeneous case no longer occur even when the end conditions

are symmetric. This is also associated with a reduction in the predicted buckling load although the mode shapes no longer extend to such a great depth and the 'effective' length is reduced. A technique to predict modal clusters using an average soil stiffness has been investigated. Although the technique can be used to predict the modal clusters in higher modes it cannot do so for the more important lower modes. The buckling loads predicted using an average soil stiffness are also significantly different (by a factor of two or more in some cases) from the exact solution. In Chapter 6 it will be shown that it has been common practice for other authors to attempt to predict buckling loads of real piles in non-homogeneous soils by using an average value of soil stiffness with depth. The results presented in this thesis have shown that this is flawed.

The results for an non-symmetric end-condition case were presented next. Despite there being a large soil stiffness at the base of the pile compared to the top, it was shown that the buckling load of a fixed-free beam is significantly lower than a fixed-fixed or fixed-pinned beam for soil stiffness up to $\lambda = 1100$. This is mirrored to a lesser degree for a pinned-free or a pinned-pinned beam compared to a pinned-fixed beam up a soil stiffness $\lambda = 200$. This is of some significance because of the difficulty in predicting the support conditions at the base of the pile. In previous work it has been assumed that the pile foot will act like a pinned constraint because large displacements at the pile foot obviously do not occur in practice. This would appear to be an assumption which will need to be considered when the buckling loads of real piles are considered in Chapter 6.

The solutions to piles supported entirely by shaft friction in an homogeneous soil, with constant soil stiffness and shaft friction with depth, were presented next. Although the use of modal cluster prediction lines from the end-bearing solution are no longer applicable, modal clustering has been shown to occur, especially when there is a free end-condition present. The clustering of modes in pairs for free-free end conditions was indicated. However, for the pinned-pinned solution there appears to be little modal clustering for all but the lowest values of λ, the soil stiffness parameter. The predicted buckling loads for the pure-friction case are significantly higher than those for the end-bearing case. The more complicated results for a free embedded end condition, where the second mode is close to the fundamental load, no longer occur except for very small values of λ. This is

because the load carried in the lower portion of the pile is significantly reduced and, hence, the mode shape does not extend to a depth that is affected by the lower end-condition.

A brief discussion on the relative effects of the two forms of non-homogeneity in the soil, those of lateral soil stiffness and shear friction applied to the pile shaft, was presented next. When either parameter is defined as linearly increasing with depth then there is a large reduction in the buckling load. In the case of changing the soil stiffness this is accompanied by an increase in mode shape wavelength. However, if the shaft friction is changed there is an increase in the depth to which the mode shape extends. This 'effective lengthening' of the pile produces the decrease in buckling load.

In the last section to this chapter the effect of varying the proportion of the load carried by shaft friction and end-bearing was discussed. The solution is bounded by the previous results, as $\mu = 1$ indicates the load is completely supported by end-bearing and $\mu = 0$ implies that the load is carried by pure shaft friction only. In the case of the first modes it has been shown that the variation between the two extremes is approximately linear for most end-conditions and soil stiffnesses. This is particularly the case with symmetric end-conditions. In homogeneous soils it was observed that the wavelength of buckling modes remained approximately constant as μ varied for a constant soil stiffness, λ. However, because the depth to which the mode shape extended reduced as μ decreased the 'effective' length of the piles decreased and, hence, the buckling load increased. These results can also be applied to the second modes of the fixed-fixed and pinned-pinned results. However, in the case of a free-free pile the second mode no longer behaves as simply as in other symmetric cases. This is because in the other symmetric case the second mode consists of the second mode of the Heténi problem except that the amplitudes at the bottom of the pile have been reduced. This is due to the reduction of the load in the pile in this section. If the embedded boundary condition is free then a distinctly different mode shape is possible where the maximum amplitude is concentrated close to the bottom of the pile. However, this can only occur when the load in the pile at the pile toe is not significantly less than the applied load, that is, μ is not nearly zero. It should be remembered that in the end-bearing case that the first two modes are much closer to one another, for all λ, compared to the other symmetric end-conditions. In the case of a fixed-free pile this mode shape actually becomes the fundamental mode for a large

range of λ and μ. It should be noted that the fixed-free case is the extreme non-symmetric case because the unembedded boundary has the greatest degree of fixity, whereas the embedded end has the least. Similar mode shapes can also occur in the case of pinned-free homogeneous piles but over a much smaller range of λ and μ.

In the case of non-homogeneous ($F = 0$ and $f_l = 0$) foundations the effect of μ is much reduced. Not only do the buckling modes appear to remain similar as μ varies, but also the buckling load does not increase significantly. The second mode is also more much separated from the first mode for all the different possible end-conditions in the non-homogeneous case compared to the previous homogeneous case. This is not surprising when the previous results for pure end-bearing and pure friction piles are considered.

Finally the results for other non-homogeneous soils are investigated. For symmetric end-conditions it is found that the variation with μ is approximately linear and, hence, interpolation of results from the pure-friction and the end-bearing cases can be used with small error ($< 5\%$). In the case of non-symmetric end-conditions it has been shown that a similar approximation can be made by using the above approximation and an appropriate solution of the homogenous case with a fixed unembedded end condition. In this case the need to produce more contour plots of each solution is not necessary.

This completes the parametric study of the fully embedded problem of pile supported by an elastic Winkler foundation. It has been found that the variation of buckling load with soil stiffness and method of vertical support is of a complex nature. This is especially the case when the embedded end-condition is free to rotate and translate.

Chapter 5

Partially embedded piles

5.1. Introduction

In the case of piles used for wharves, jetties and deep sea structures such as oil platforms, there is a likelihood that the pile will not be fully embedded in the supporting medium. These piles, generally referred to as partially embedded piles, are the subject of the current chapter. It should be remembered that in chapter 3 the theoretical work for partially embedded piles has already been set out. The solution is now in the form of an eigenvalue problem of an 8x8 matrix where four of the rows define the end-conditions at either end of the pile and the other four are used to define continuity of displacement, slope, shear force and bending moment at the interface of the two regions. Again, the buckling load will be affected by the homogeneity or non-homogeneity of the supporting medium, as well as the method by which the load is supported in the medium, that is, either by end-bearing or frictional loads.

5.2. Partially embedded end-bearing piles

As was the case for the fully embedded pile, the simplest problem is that when the load is carried completely by an end-bearing force at the bottom of the pile. The trends which can be distinguished in the following figures are twofold. Firstly, at low soil stiffness, the beam's mode shapes change with increasing soil stiffness in a similar manner to the fully embedded solution. The mode shapes have the same number of half waves, but the amplitudes of the half waves are larger towards the head of the pile. Secondly, when the pile is embedded in a sufficiently stiff soil, the embedded portion of the beam has its deflection substnonally inhibited. In the extreme case of an infinite soil stiffness, the soil would behave like a fixed support at the interface between the two regions. Between these two extremes the solutions tend to have mode shapes which have amplitudes in the unembedded and upper portion of the embedded section of the beam. These amplitudes tend to zero at a depth below the pile head and below which the amplitude remains zero. At such a point the deflection and slope are zero and, hence, could be modelled by a fixed end condition at such a point. However, the location of the 'apparent fixity' is very difficult to predict and is highly case specific. The upper portion of the beam, in both cases, behaves like a typical unsupported Euler beam. In terms of buckling loads, the effect of the very stiff soil giving rise to an approximation to a fixed support at the soil-air interface is that the buckling loads tend to those predicted by simple Euler theory for a beam with a reduced length. In figure 5.2.1 mode shapes are plotted for a beam with fixed-fixed boundary conditions which is half embedded (an embeddment ratio, $\delta = 0.5$) in a homogeneous soil with fixed-fixed end conditions. For an infinite soil stiffness the apparent length of the beam is halved. Due to the inverse-squared relationship of the Euler buckling load to length this means that the buckling load will be four times as large as that with $\lambda = 0$. The buckling load in terms of the non-dimensional load parameter, P_{cr}/P_E is 4 at $\lambda = 0$ and 16 at $\lambda = \infty$. If the mode shape at $\lambda = 100$ is inspected, it can be seen that mode shapes between the two extremes are of a more complex nature, in this case with two half waves.

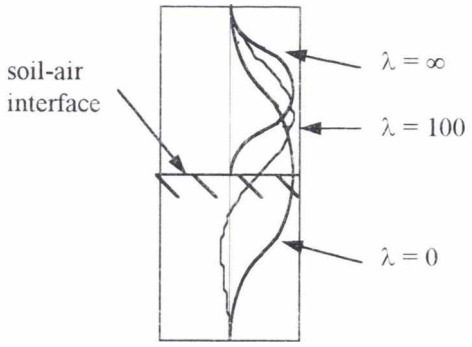

Figure 5.2.1. Buckling mode shapes for a fixed-fixed partially embedded end-bearing beam with $\delta = 0.5$ and soil stiffness $\lambda = 0$, $\lambda = 100$ and $\lambda = \infty$

5.2.1 Homogeneous soil.

In figure 5.2.2 the buckling loads for the first six modes with fixed-fixed end conditions are plotted for an embedment ratio, $\delta = 0.5$. It can be seen that the first mode initially increases at an increasing rate and then slowly approaches a load parameter of 16 which is the value of the Euler buckling mode if the soil acts as a fixed end condition. Similarly the second mode can be seen to be approaching the buckling load with $\lambda = \infty$. However, it should be noted that the convergence onto these solutions is very limited and a very stiff soil ($\lambda > 300$) is required for the soil to behave at all like a fixed end condition.

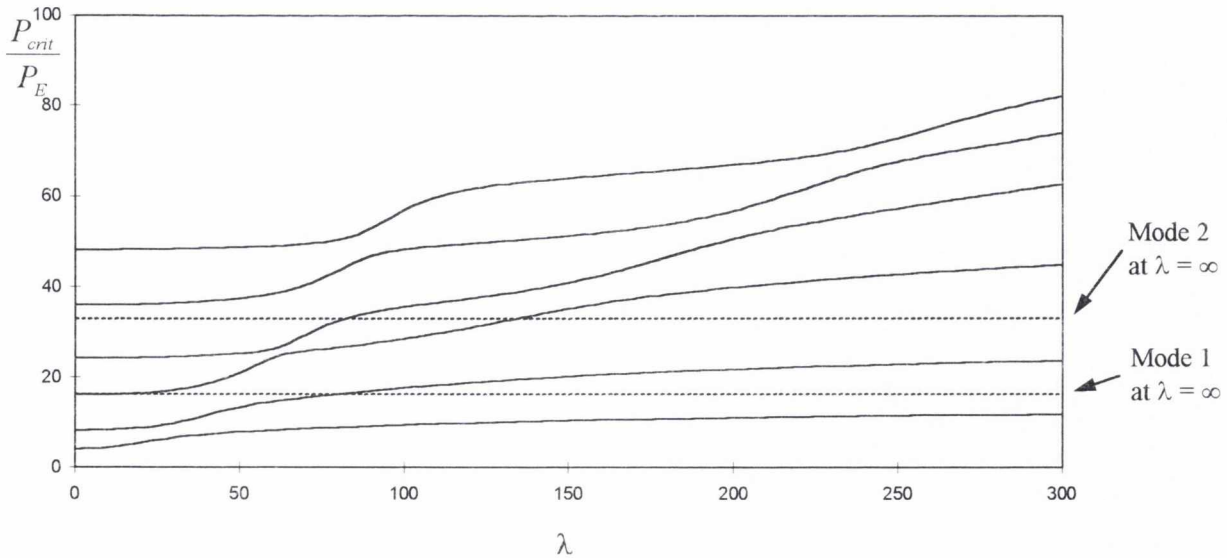

Figure 5.2.2. First six buckling loads of a fixed-fixed partially embedded end-bearing beam with $\delta = 0.5$ in a homogeneous soil.

In figure 5.2.3 the buckling load for the first mode is plotted for varying degrees of embedment, δ = 0.25, 0.5, 0.75 and 1. The buckling loads for δ = 0.25 and δ = 0.5 when the soil stiffness, λ approaches ∞ have also been superimposed on figure 5.2.3. The fundamental buckling load for δ = 0.25 has approached to within 20 % of its final buckling load in the given range of soil stiffnesses. Due to the buckling loads for the shorter unembedded sections being larger, a higher soil stiffness is required for them to approach to such a degree (for δ = 0.5 and δ = 0.75 the fundamental loads only approach to within 30% and 50% respectively of the final load at a soil stiffness, λ = 300). As previously mentioned in section 4.2 the buckling loads for δ = 1 increase approximately linearly for all values of λ.

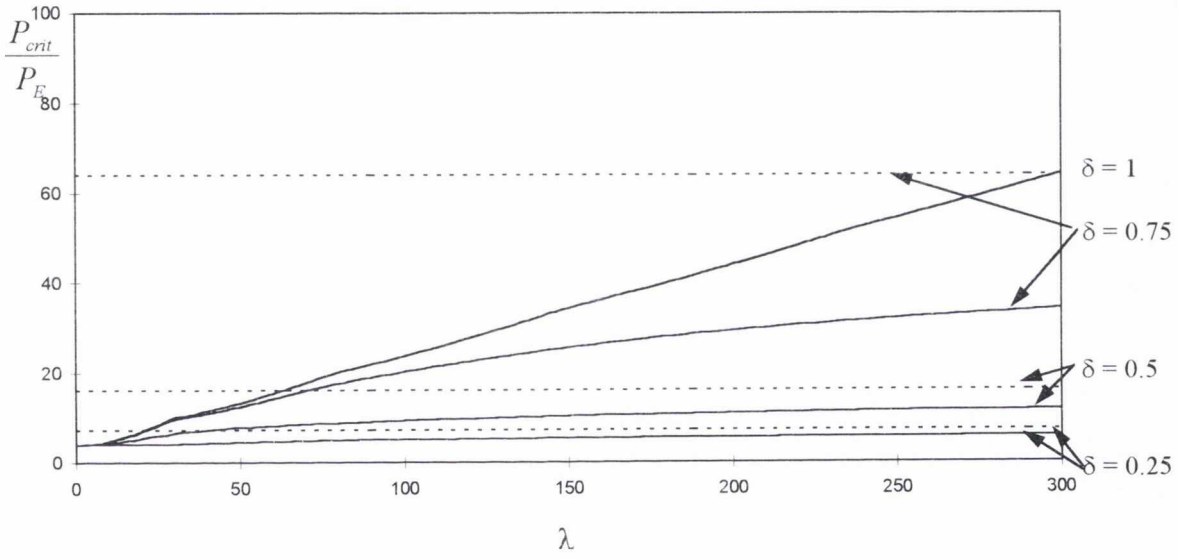

Buckling loads [——], buckling loads with $\lambda = \infty$ [·····]

Figure 5.2.3. First buckling load for δ = 0.25, 0.5, 0.75 and 1 for a end-bearing pile with fixed-fixed end conditions in a homogeneous soil.

In figure 5.2.4 the buckling loads for the first mode in a homogeneous soil with fixed-fixed end conditions have been plotted on a two dimensional contour plot as δ and λ vary. At high soil stiffnesses and for $\delta < 0.875$ the buckling loads approximately lie on a parabolic curve as δ varies as can be seen in figure 5.2.5. The buckling mode shapes in figure 5.2.6 indicate that this curve represents the family of mode shapes which have minimal amplitude in the embedded portion of the beam. These mode shapes tend to the mode shape for $\lambda = \infty$ for the relevant value of δ as would be expected. The mode shapes corresponding to the plateau in buckling load at high values of δ appear

have a similar mode shape as that as $\delta = 1$ (for instance at $\lambda = 300$ all mode shapes for $\delta \geq 0.9$ and at $\lambda = 50$ for $\delta \geq 0.75$). This mode shape indicates that the soil is not sufficiently stiff to produce an "apparent fixity" in the soil and, hence, the mode shape extends to the pile bottom. A reason for this can be explained if the embedded and the unembedded portions are considered separately. For the mode shape to extend throughout the pile length it is necessary for the buckling loads of the unembedded portion of the beam to be approximately greater than or equal to the buckling load of the embedded portion. This means at higher soil stiffnesses the unembedded length must be shorter than for low soil stiffnesses, therefore, the plateau at which these mode shape occurs extends for a smaller range of δ at high soil stiffness. At low soil stiffness the plateau associated with such a mode shape can extend for a maximum range of $0.5 < \delta \leq 1$.

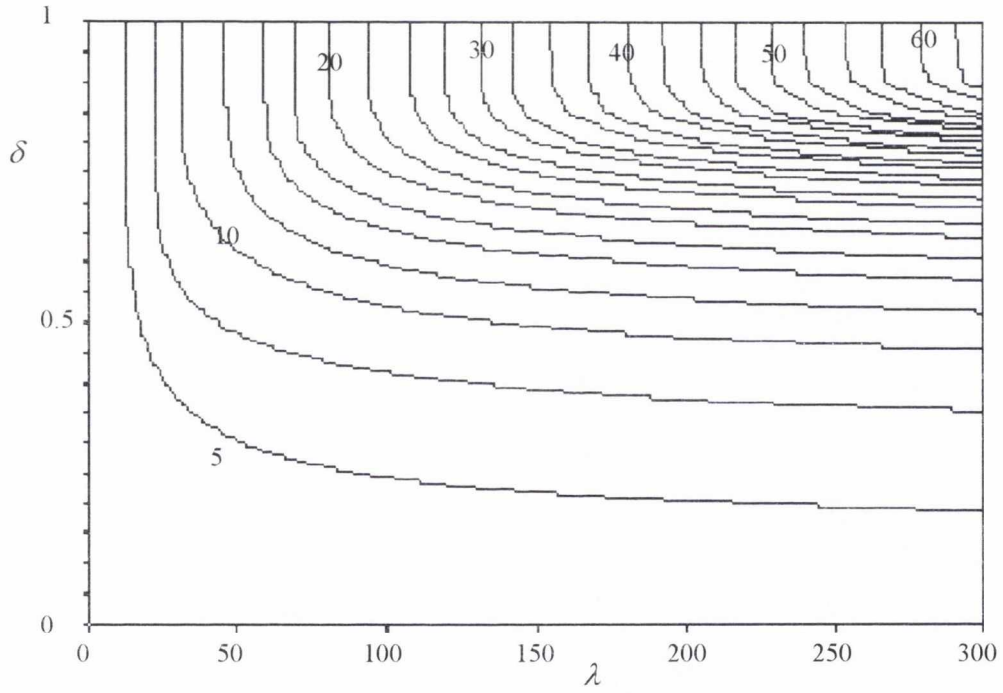

Figure 5.2.4. Buckling load (P_{cr}/P_E) contours for the first mode in a homogeneous soil with fixed-fixed end conditions of a partially embedded end-bearing pile.

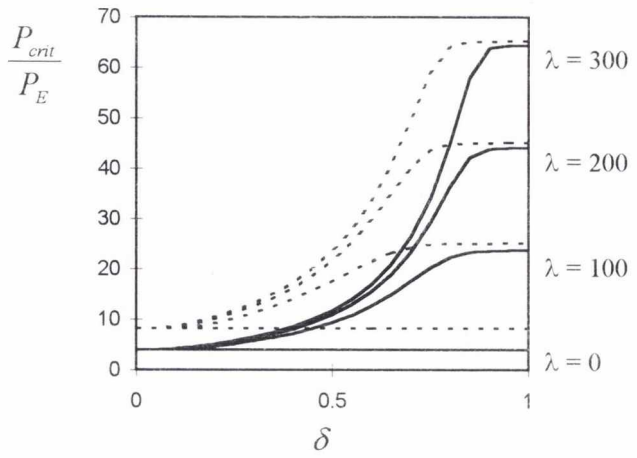

First buckling mode [——], second buckling loads [·····]

Figure 5.2.5. Buckling loads for λ = 0, 100, 200 and 300 for figure 5.2.4.

Since the buckling loads in the parabolic portions of the curves correspond to mode shapes which do not extend into the embedded portion of the pile, it might be assumed that the effect of the lower end-condition is no longer relevant and, hence, changing it would not affect either the mode shape or the buckling load. This does not actually happen. The most extreme case of defining the unembedded end as a free condition will be taken as an example (figure 5.2.7). As would be expected at low values of δ the embedded length is not sufficient to produce an "apparent fixity" and, hence, the buckling load is lower with a mode shape with maximum amplitude at the pile bottom. At high embedment ratios the maximum buckling load is equal to the fully embedded load of a fixed-free pile. This is significantly lower than that for the fixed-fixed pile and, hence, the plateau at high δ is enlarged. With moderate values of δ the buckling loads are indeed identical in the fixed-fixed and fixed-free cases.

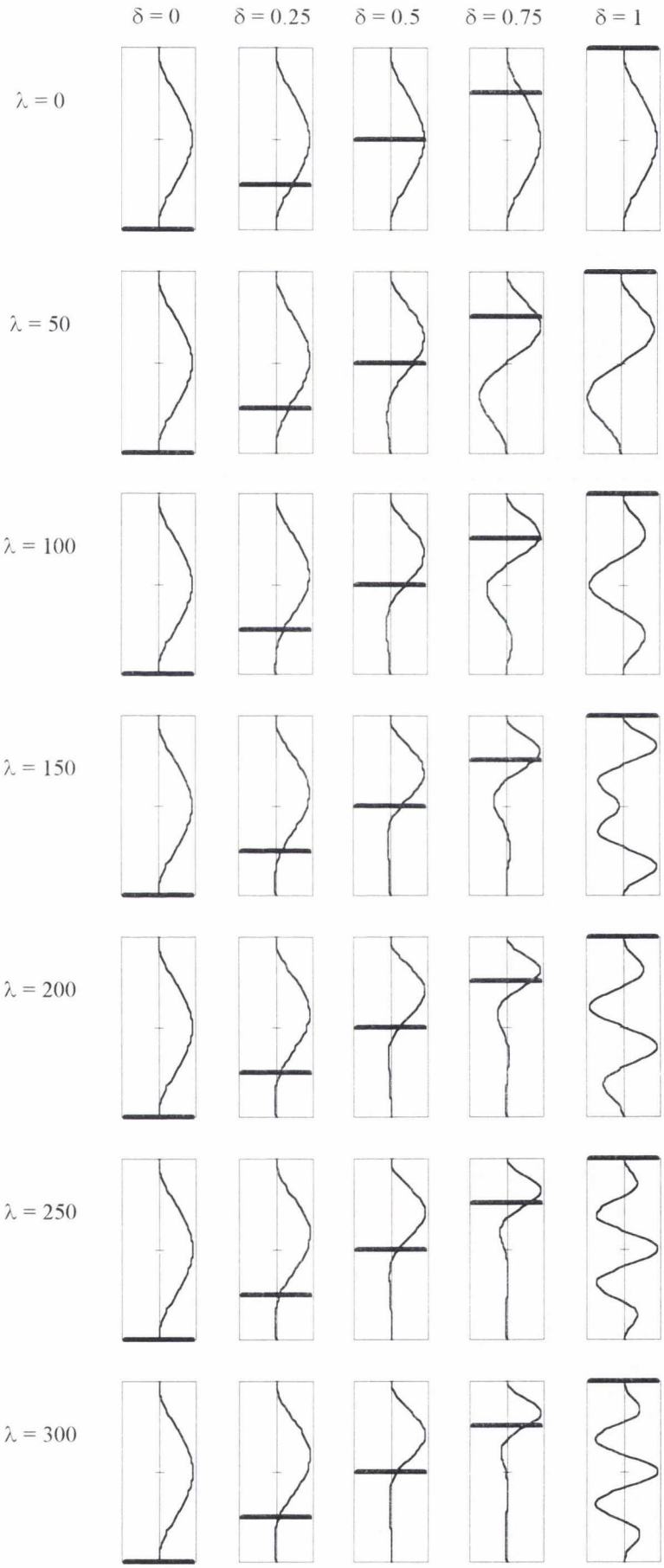

Figure 5.2.6. Buckling mode shapes for the first mode for figure 5.2.4.

A method of producing a concise summary of results could now be suggested where for each unembedded end-condition the buckling loads are plotted for the case when the embedded end-condition is fixed, in this case a partially embedded fixed-fixed pile. For example, the buckling load of a fixed-free pile which has an embedment ratio, $\delta = 0.65$, is required. If the buckling load of a partially embedded ($\delta = 0.65$) fixed-fixed pile ($P_{cr}/P_E = 20.92$) is compared to the buckling load of a fully embedded fixed-free pile ($P_{cr}/P_E = 30.40$), then the lower of these two values will accurately predict the buckling load for a partially embedded ($\delta = 0.65$) fixed-free pile. If the process is repeated for an embedment ratio of $\delta = 0.80$ then the values calculated are 44.96 and 30.40 and the actual buckling load is $P_{cr}/P_E = 30.40$.

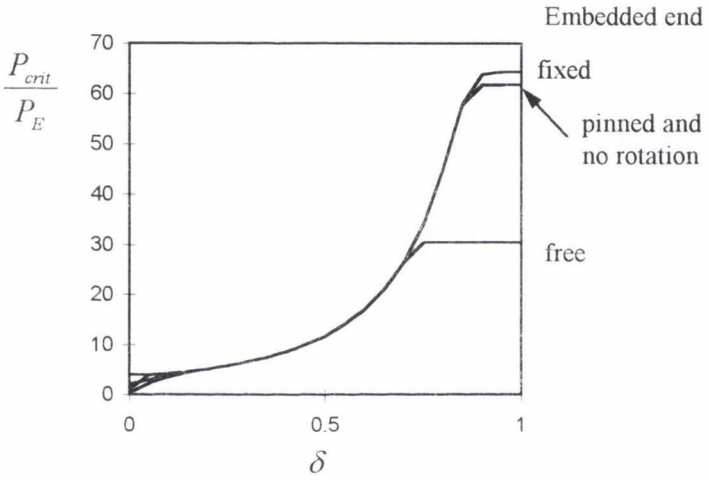

Figure 5.2.7. Buckling loads for the first mode for $\lambda = 300$ in a homogeneous soil with a fixed unembedded end conditions of a partially embedded pile.

Figure 5.2.8 shows the buckling load for the second mode with a homogeneous soil and fixed-fixed end-conditions for a end-bearing pile. It is really of academic interest to investigate how the second mode behaves as can be seen in figure 5.2.5 the only time modal clusters occur is for high value of the embedment ratio, δ. This clustering shown is due to the closeness of the first two modes in the fully embedded case which has been previously investigated in section 4.1. The plateau for high δ is again present and extends to lower values of δ than for the first mode. Figure 5.2.5 shows that below this plateau the buckling loads vary approximately parabolically with δ as before. Figure 5.2.9, which plots the second mode shape for $\lambda = 300$ as δ varies, shows that the mode shapes for the plateau

are significantly different from the other mode shapes for lower δ. The plateau has mode shapes which extend to the bottom of the pile.

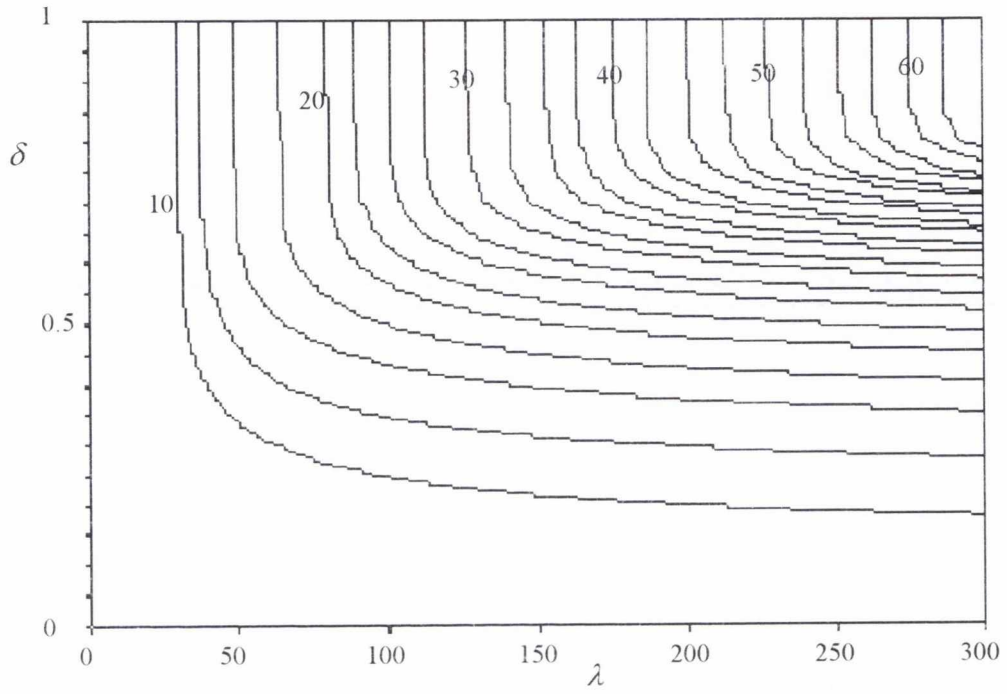

Figure 5.2.8. Buckling load (P_{cr}/P_E) contours for the second mode in a homogeneous soil with fixed-fixed end conditions of a partially embedded end-bearing pile.

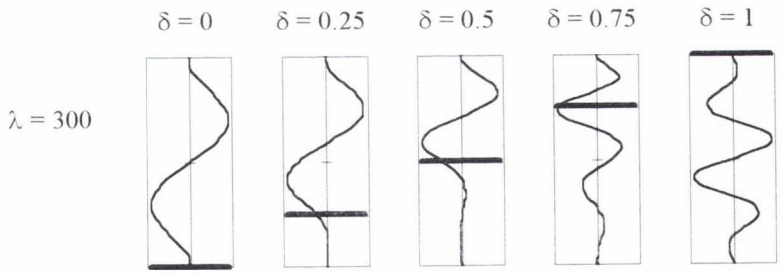

Figure 5.2.9. Buckling mode shape for the second mode for figure 5.2.7.

Figure 5.2.10 plots the first six modes at a soil stiffness λ = 300. It is interesting to note how there are modal clusters between the first and second modes at high values of δ, but not for moderate values. The modal clusters for fully embedded beams (δ = 1) and the way they tend to be formed in pairs, have already been described in section 4.2. The sections of the higher modes which are constant with respect to δ also signify mode shapes which extend to the lower portion of the pile.

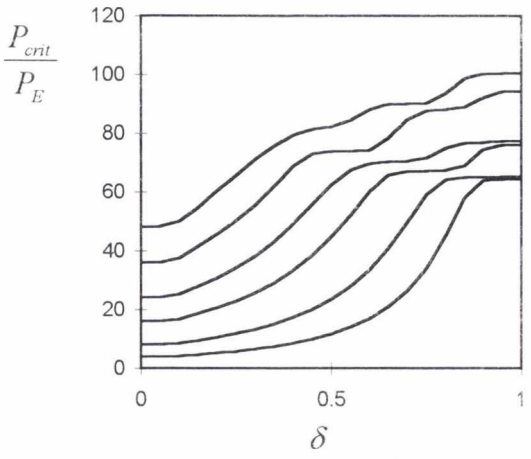

Figure 5.2.10. First six buckling load for λ = 300 in a homogeneous soil with fixed-fixed end conditions of a partially embedded end-bearing pile.

Figure 5.2.11 shows the first mode with pinned-pinned end conditions as δ and λ vary. If figure 5.2.12 is compared to figure 5.2.5, for the fixed-fixed case, it can be seen that the upper plateau is smaller for all values of λ. This is because when the unembedded boundary condition is pinned the buckling mode can be formed easier at the top of the pile. The buckling mode is, thus, less likely to extend into the embedded portion of the pile. This can be seen in figure 5.2.13 where an apparent fixity is formed in the supporting medium for all but the lowest soil stiffnesses and the highest values of embedment ratio. Figure 5.2.12 also indicates that, like the fixed-fixed case, modal clustering occurs only as δ approaches unity.

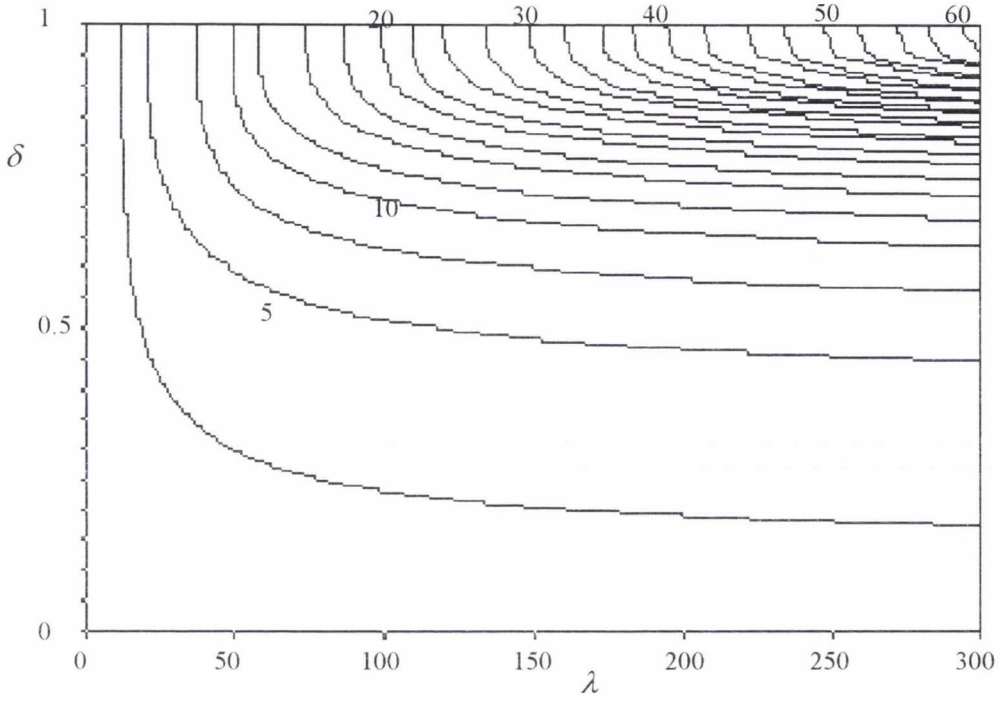

Figure 5.2.11. Buckling load (P_{cr}/P_E) contours for the first mode in a homogeneous soil with pinned-pinned end conditions of a partially embedded end-bearing pile.

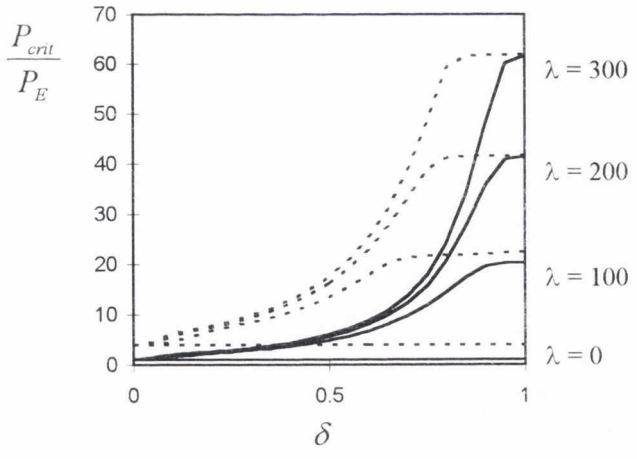

First buckling mode [——], second buckling loads [·····]

Figure 5.2.12. Buckling loads for λ = 0, 100, 200 and 300 for figure 5.2.11.

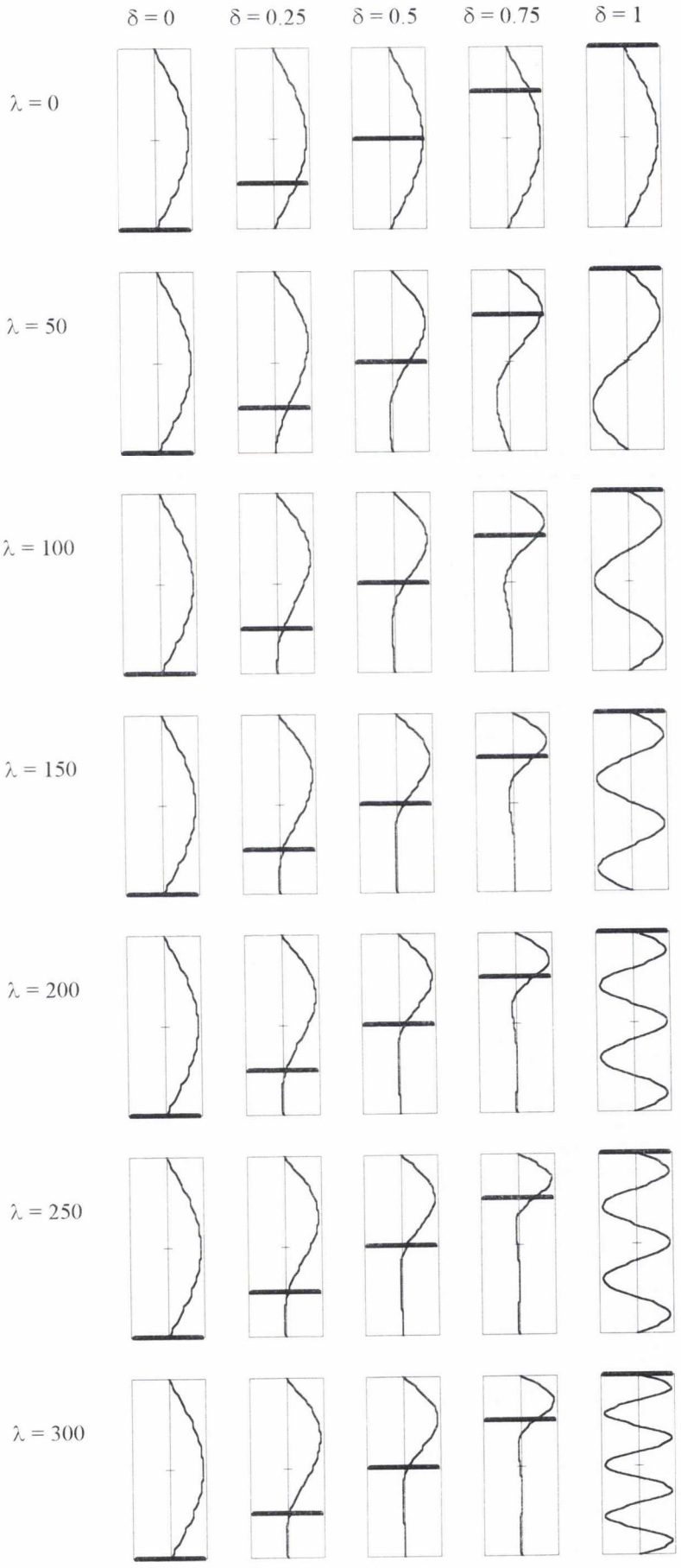

Figure 5.2.13. Buckling mode shape for the first mode for figure 5.2.11.

In figure 5.2.14 the buckling loads for the second mode are plotted. As would be expected, the upper plateau is larger than the first mode plateau but smaller than the second plateau in the fixed-fixed case. The previous comments on the extent of the mode shape into the embedded portion of the beam are still valid. The reason why the contours are not regularly spaced in the upper plateau can be related back to the fully embedded case where it should be remembered the mode clusters for the pinned-pinned case followed the modal prediction lines exactly. Hence, for the second mode, but not so obviously for the first, there are discontinuities in the slope of the buckling load as λ increases where the mode cluster parabolas meet (section 4.2). It is interesting to note that for the second mode that the wavelength of the half waves decreases as δ increases except for the final mode shape where there is a significant reduction (figure 5.2.14).

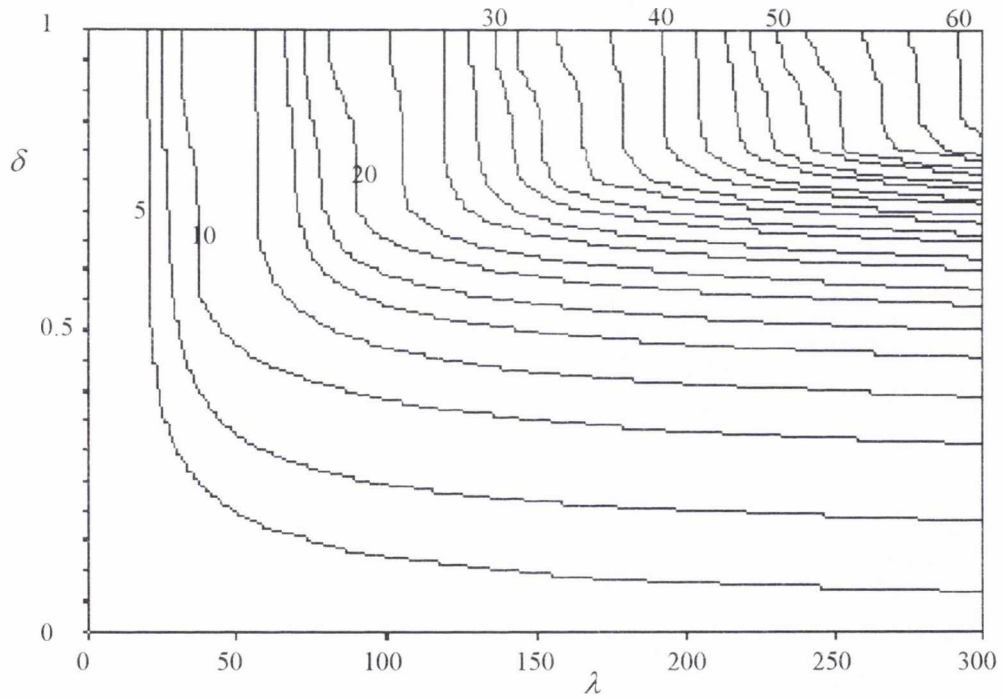

Figure 5.2.14. Buckling load (P_{cr}/P_E) contours for the second mode in a homogeneous soil with pinned-pinned end conditions of a partially embedded end-bearing pile.

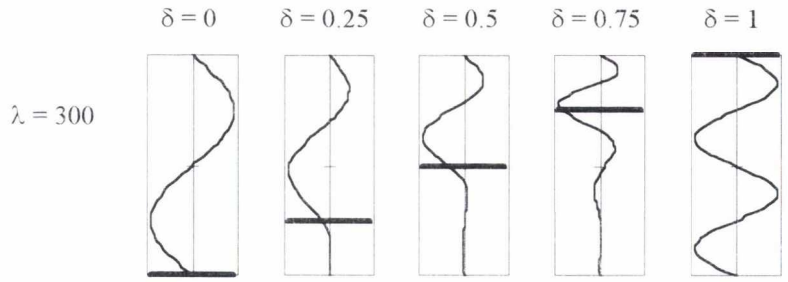

Figure 5.2.15. Buckling mode shape for the second mode for figure 5.2.14.

In figures 5.2.16 and 5.2.17 the buckling loads for the first mode of the free-free end-bearing case are plotted. Due to the relative flexability of the unembedded end condition compared to the other possible end conditions, the first buckling mode has the maximum amplitude at the unembedded end (figure 5.2.18). In every case, except the fully embedded case, a small soil stiffness is sufficient for the embedded portion of the pile to approximate to a fixed boundary condition near the soil surface. Although the mode shapes look similar to the mode shapes that would be expected at $\lambda = \infty$ the buckling loads are significantly lower compared to the respective free-fixed Euler case. For instance, at $\lambda = 300$, with $\delta = 0.25$, 0.5 and 0.75 the buckling loads are 81, 74 and 57% of the respective Euler loads.

As can be seen in figure 5.2.17 the first buckling load in this case is significantly increased when the beam is fully embedded compared to any other degree of embedment. This corresponds to symmetric or anti-symmetric buckling modes only being present when the beam is fully embedded. It should be noted that the displacement at the foot of the pile would correspond to a discontinuity in the embedding medium. However, if the fixed-fixed case is remembered the parabolic lines indicate that the buckling load are not affected by the lower boundary condition. In this case because the discontinuity at the bottom of the pile is already prevented by the soil stiffness then the buckling load is not significantly increased when the embedded boundary condition is altered (figure 5.2.18).

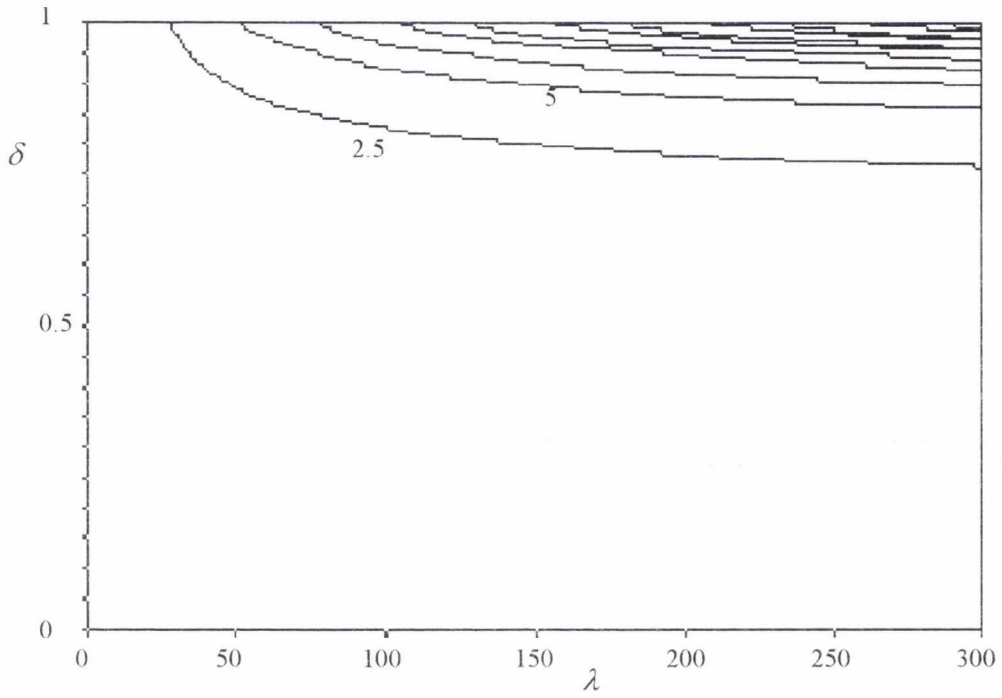

Figure 5.2.16. Buckling load (P_{cr}/P_E) contours for the first mode in a homogeneous soil with free-free end conditions of a partially embedded end-bearing pile.

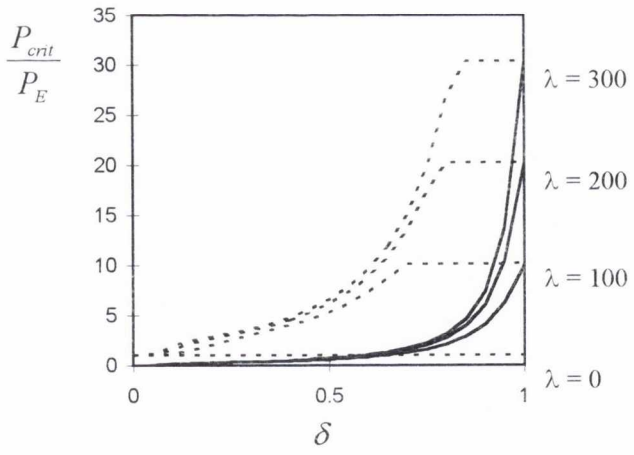

First buckling mode [——], second buckling loads [·····]

Figure 5.2.17. Buckling loads for the first mode for λ = 0, 100, 200 and 300 for figure 5.2.16.

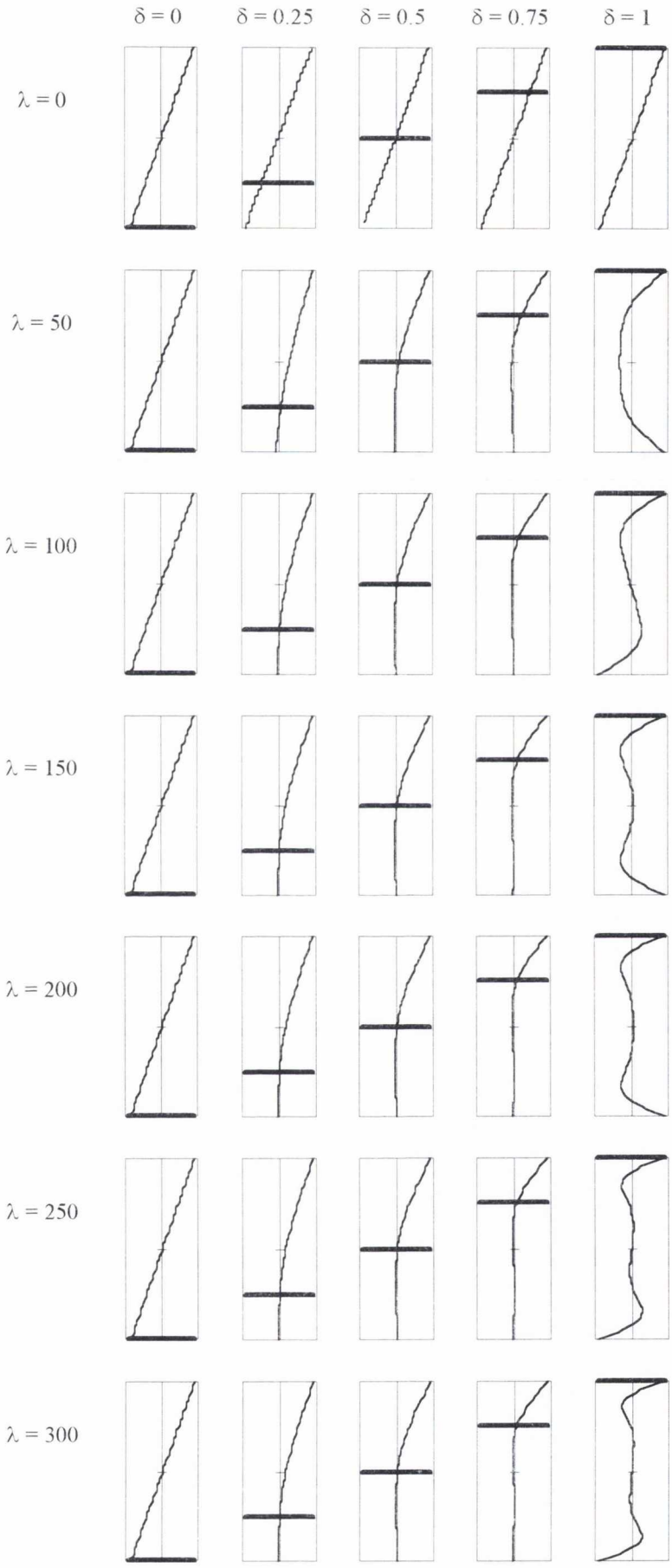

Figure 5.2.18. Buckling mode shapes for the first mode for figure 5.2.16.

In figure 5.2.19 the buckling loads for the second mode are plotted in the free-free end-bearing case. The transition between buckling modes with large amplitudes in the embedded portion of the beam can again be seen in the second mode with $\delta \approx 0.75$ as illustrated in figure 5.2.20. The transition occurs at a lower soil stiffness than with the pinned-pinned end-conditions. The buckling mode with $\lambda = 100$ and $\delta = 0.75$ can be seen to lie on the plateau in figure 5.2.17. However, it can be seen that $\lambda = 300$ and $\delta = 0.75$ is not on the plateau and so has a different mode shape.

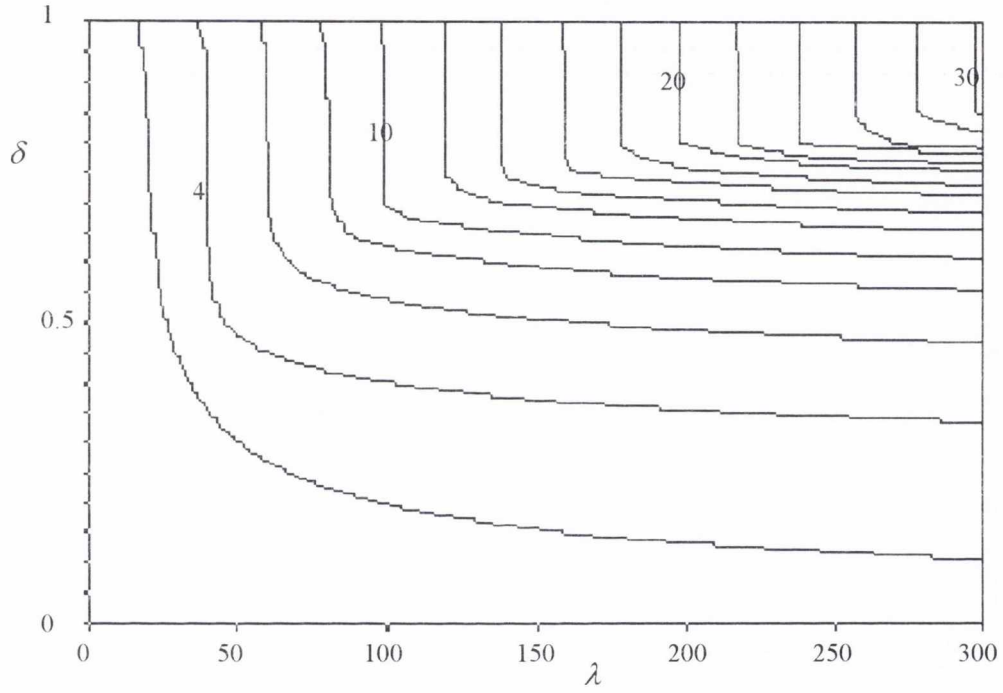

Figure 5.2.19. Buckling load (P_{cr}/P_E) contours for the second mode in a homogeneous soil with free-free end conditions of a partially embedded end-bearing pile.

In figure 5.2.20 the first six buckling loads are plotted for a soil stiffness of $\lambda = 300$ for the free-free case. The noticeable plateau at $P_{cr}/P_E \approx 30$ can be related to the mode shape with the maximum amplitude at the bottom of the pile such as in figure 5.2.21. The plateau at $P_{cr}/P_E \approx 66$ has more complicated mode shapes as would be expected for the higher modes.

The buckling modes for $P_{cr}/P_E \approx 30$ all have the same mode shape. It would, therefore, be expected that, as the embedment ratio decreases, the buckling load would also decrease. However, this is not the case because the amplitudes are always in the embedded section of the pile. Once the interface approaches the upper extent of this mode shape the buckling load should decrease. This, however does not occur, instead the mode shape ceases to form ($\delta < 0.4$).

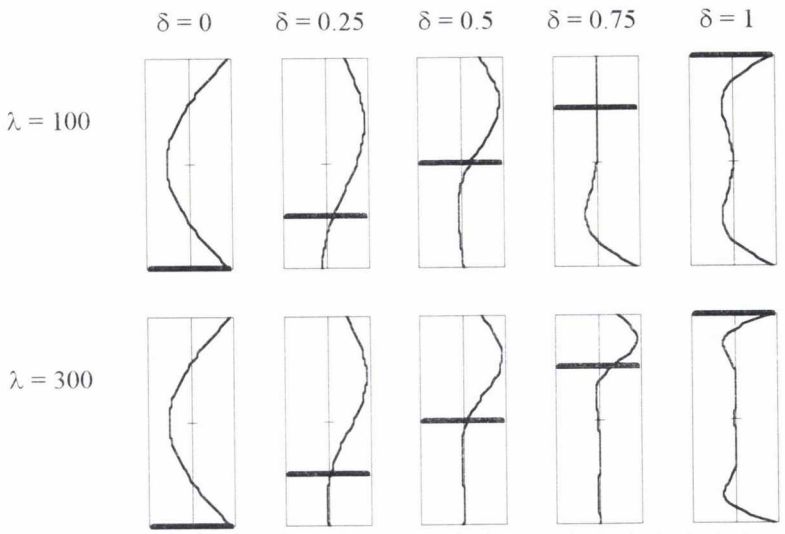

Figure 5.2.20. Buckling mode shape for the second mode for figure 5.2.19.

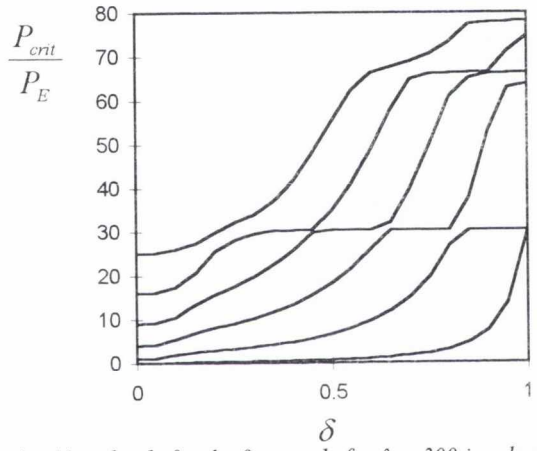

Figure 5.2.21. First six buckling loads for the first mode for λ = 300 in a homogeneous soil with free-free end conditions of a partially embedded end-bearing pile.

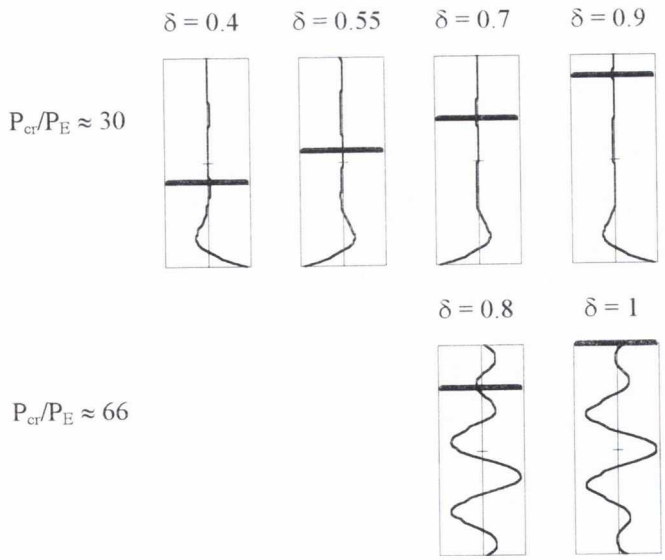

Figure 5.2.22. Buckling mode shapes for the second mode with free-free end conditions of a partially embedded end-bearing pile in a homogeneous soil.

5.2.2 Non-homogeneous soil.

The next case to consider is that of non-homogeneous end-bearing piles. As in the fully embedded case, it is useful to consider a linear increase of soil stiffness (F = 0) with depth as it is the most extreme case of non-homogeneity in the supporting medium. If the buckling loads for the first mode with fixed-fixed end conditions are inspected in figures 5.2.23 and 5.2.24 then it can be seen that there is no longer a plateau at high values of δ. This is mirrored in figure 5.2.25, where the mode shapes which extend to the bottom of the pile are no longer present, even at $\delta = 1$. This is hardly surprising as the non-homogeneity of the soil would hinder such modes being formed while encouraging mode shapes with amplitudes in or near the unembedded portion of the pile. Also, due to the lack of soil stiffness at the top of the embedded portion of the pile the buckling loads do not approach those calculated if the soil stiffness $\lambda = \infty$. At a soil stiffness of $\lambda = 300$, the buckling loads with $\delta = 0.25$ is 72% of its maximum, with $\delta = 0.5$, 57% and with $\delta = 0.75$ the buckling load is only 31% of that expected with $\lambda = \infty$. It should be noted how in figure 5.2.25 the number of half waves increase with δ as well as the wavelength of the half waves decreasing.

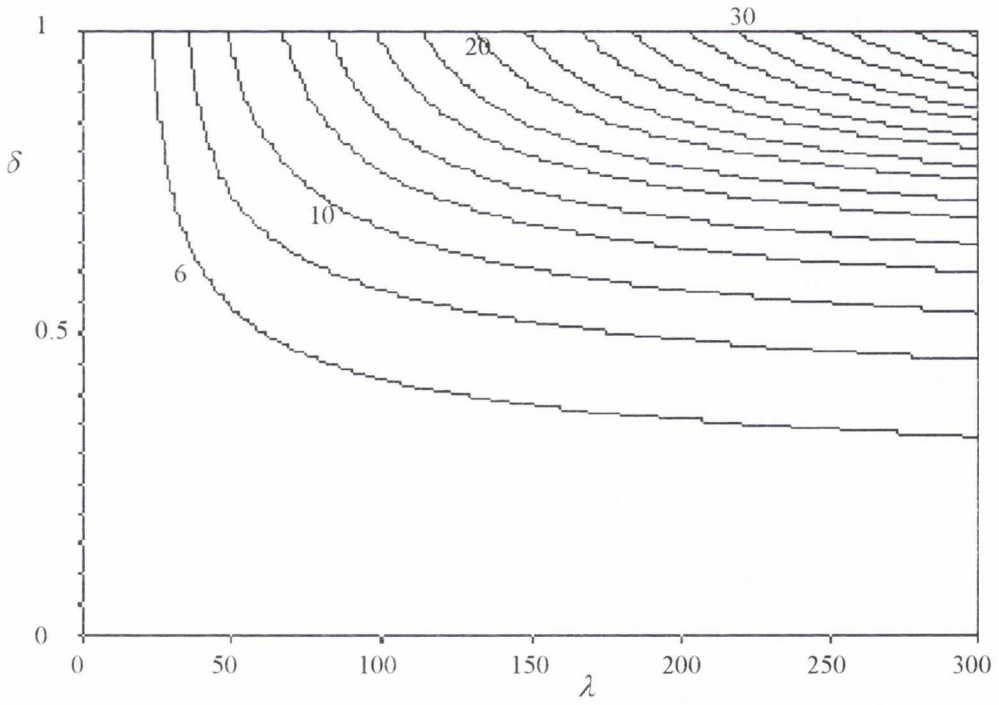

Figure 5.2.23. Buckling load (P_{cr}/P_E) contours for the first mode in a non-homogeneous soil with fixed-fixed end conditions of a partially embedded end-bearing pile.

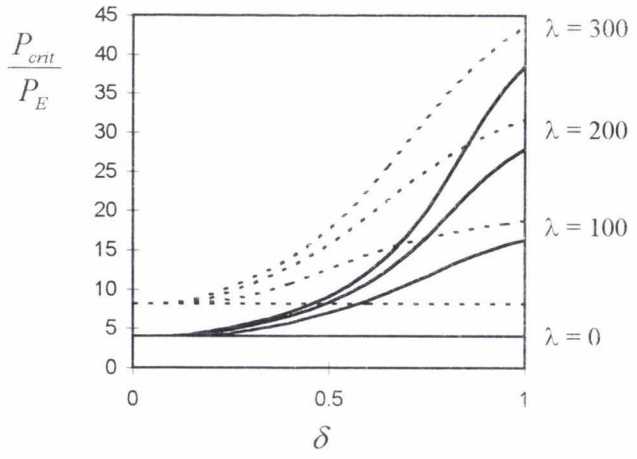

First buckling mode [——], second buckling loads [·····]

Figure 5.2.24. Buckling for λ = 0, 100, 200 and 300 for figure 5.2.23.

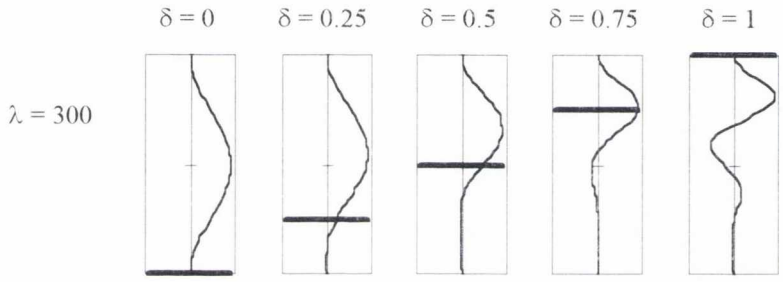

Figure 5.2.25. Buckling mode shapes for the first mode for figure 5.2.23.

If the mode shapes for the second mode in figure 5.2.26 are compared to those for the first mode in figure 5.2.25 then it can be seen that the only difference for a particular value of δ is that the number of half waves increases by one. Due to this being consistent for all values of δ it can be seen in figure 5.2.24 that there are hardly any modal clusters as δ varies. In figure 5.2.27 this also holds for the higher modes, and although not shown, again the mode shapes have a regular increase of halfwaves.

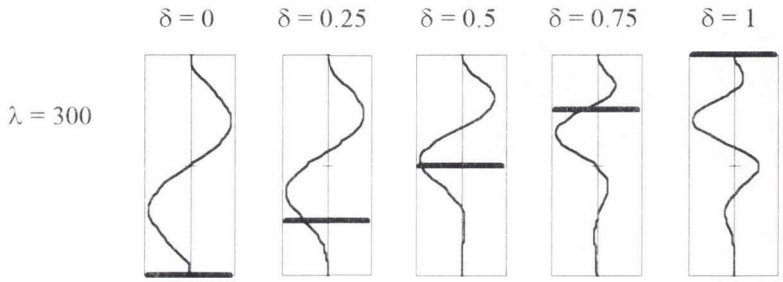

Figure 5.2.26. Buckling mode shapes for the second mode for figure 5.2.24.

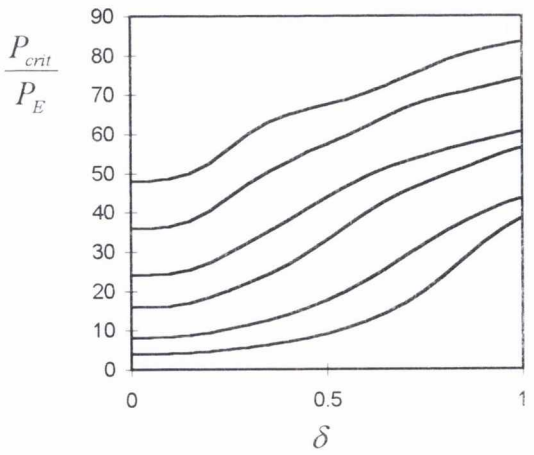

Figure 5.2.27. First six buckling loads for λ = 300 in a non-homogeneous soil with fixed-fixed end conditions for a partially embedded end-bearing pile.

Figure 5.2.28 and 5.2.29 are included for completeness. They show the variation of the buckling load with δ and λ for a partially embedded end-bearing pile in a non-homogeneous soil with pinned-pinned ends. The comments above for fixed piles apply. Although not shown, the second buckling load behaves in a similar fashion to the second buckling load for fixed-fixed end-conditions.

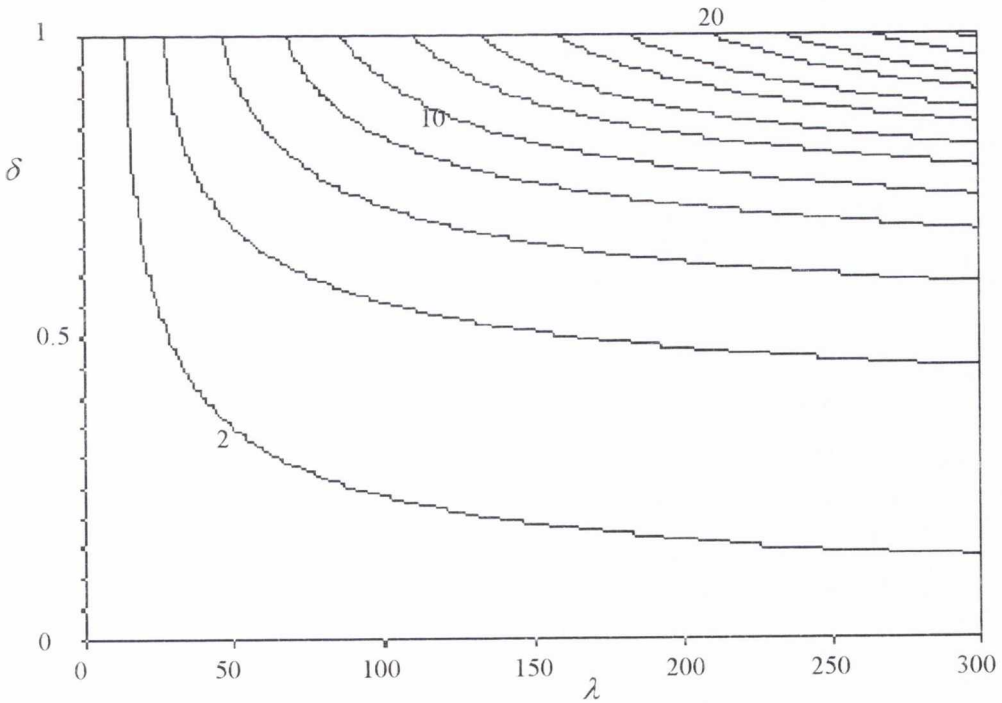

Figure 5.2.28. Buckling load (P_{cr}/P_E) contours for the first mode in a non-homogeneous soil with pinned-pinned end conditions for a partially embedded pile.

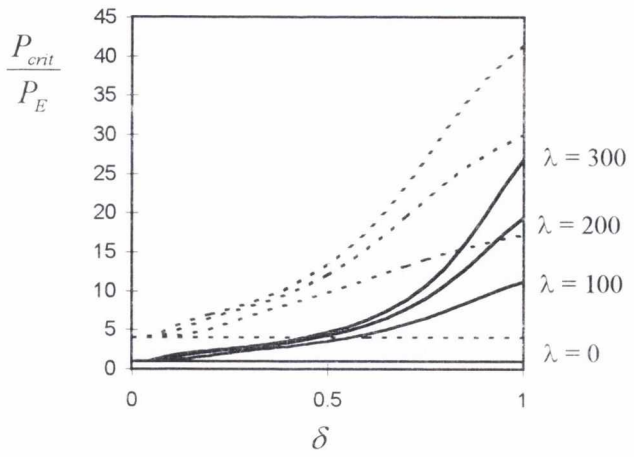

First buckling mode [——], second buckling loads [·····]

Figure 5.2.29. Buckling loads for λ = 0, 100, 200 and 300 for figure 5.2.28.

Similarly, figure 5.2.30 and 5.2.31 show the load for the first buckling mode with free-free end-conditions. The first mode behaves in a similar way as if supported by a homogeneous way except that the buckling loads are reduced. This is because the main effect of the soil stiffness is to prevent any mode shape amplitude at the pile toe and at this point the soil stiffness in the homogeneous and

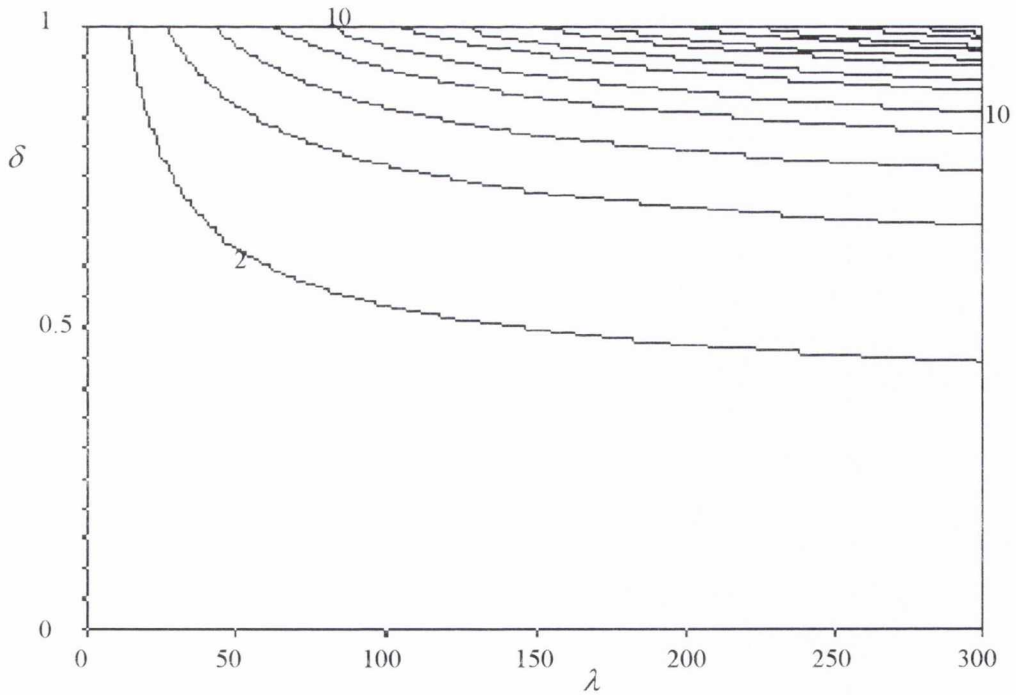

Figure 5.2.30. Buckling load (P_{cr}/P_E) contours for the first mode in a non-homogeneous soil with free-free end conditions of a partially embedded pile.

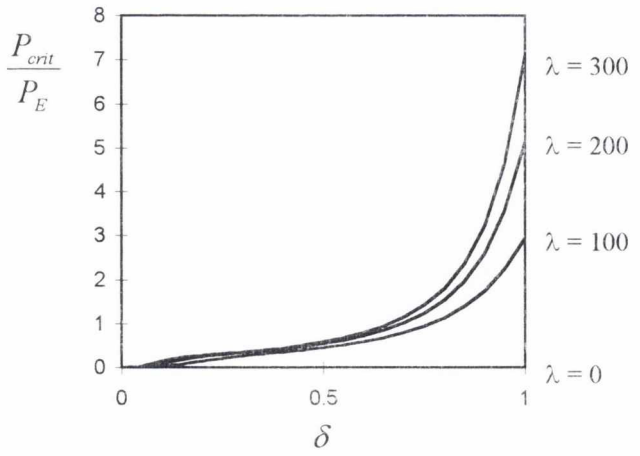

Figure 5.2.31. Buckling loads for the first mode for λ = 0, 100, 200 and 300 for figure 5.2.30.

non-homogenous cases are identical. The mode shapes for the first mode extend further down the pile than if a homogeneous soil was present, figure 5.2.32, because at this point the non-homogeneous soil has a smaller soil stiffness. Due to this apparent lengthening of the pile the buckling load is reduced.

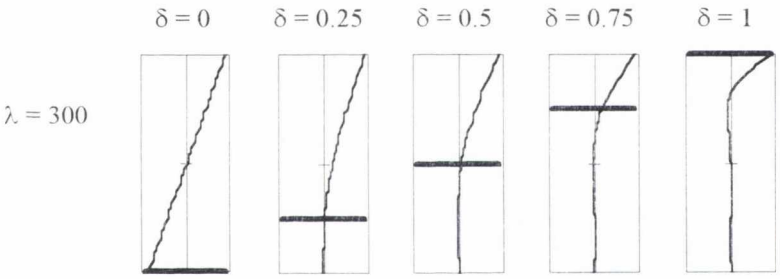

Figure 5.2.32. Buckling mode shapes for the first mode for figure 5.2.30.

If the second buckling load with free-free ends is inspected in figure 5.2.33 and 5.34 then it can be seen that the large plateau in the homogeneous case has practically disappeared. Above $\lambda \approx$ 425 the plateau is so small that δ = 0.99 no longer has a mode shape with the maximum amplitude in the lower portion of the pile. However, despite the non-homogeneity in the soil the buckling mode at δ = 1 and λ = 300 can still be seen to have its maximum amplitude at the bottom of the pile. This was discussed in section 4.3 on fully embedded piles and the mode shape occurs for a wide range of soil stiffnesses λ < 1200. It should be noted that the type of mode shape will be present for any point on the plateau and, also, it represents a unrealistic discontinuity in the soil at the bottom of the pile as discussed in section 4.2.

In figure 5.2.36 the first six buckling modes at $\lambda = 300$ are plotted. There is a plateau at $P_{cr}\backslash P_E \approx 28$ and the corresponding mode shapes are plotted in figure 5.2.37. Apart from the mode shape at low δ, the mode shapes can be categorised as having their maximum amplitude at the pile foot. This was also seen in the homogeneous case, figure 5.2.18. Although this pattern has been noted

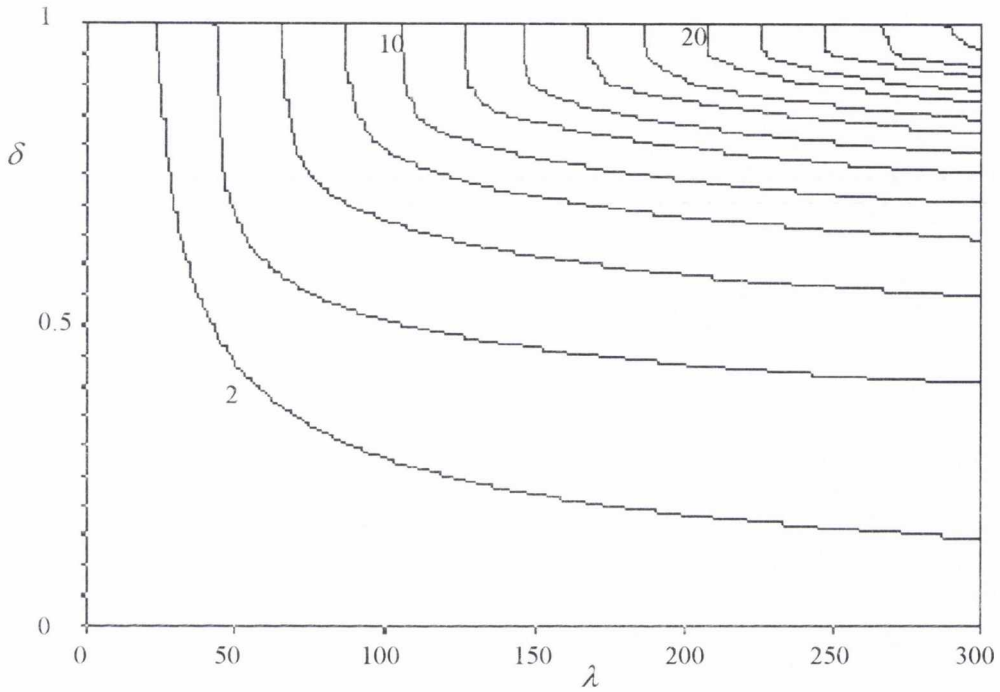

Figure 5.2.33. Buckling load (P_{cr}/P_E) contours for the second mode in a non-homogeneous soil with free-free end conditions of a partially embedded pile.

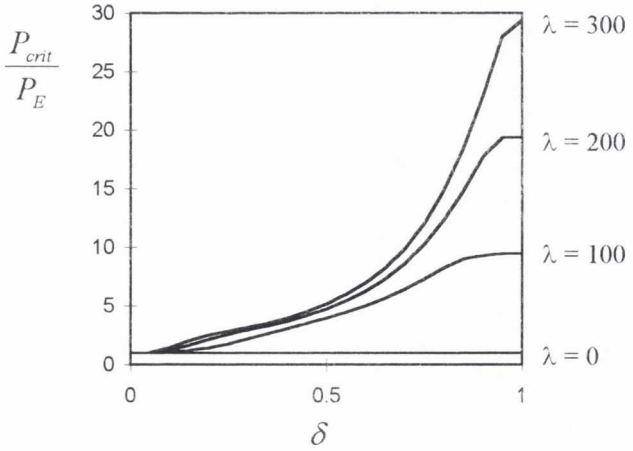

Figure 5.2.34. Buckling loads for the first mode for $\lambda = 0$, 100, 200 and 300 for figure 5.2.33.

it is of much more limited concern because, unlike the homogeneous case, the buckling load associated with this mode is at least a factor of 4 above the first mode at any value of δ. In the homogeneous case the plateau corresponded to a buckling load $P_{cr}\backslash P_E \approx 30$, the addition of the non-homogeneity in the soil has reduced this to $P_{cr}\backslash P_E \approx 28$ in the non-homogenous case although the mode shape remains the same.

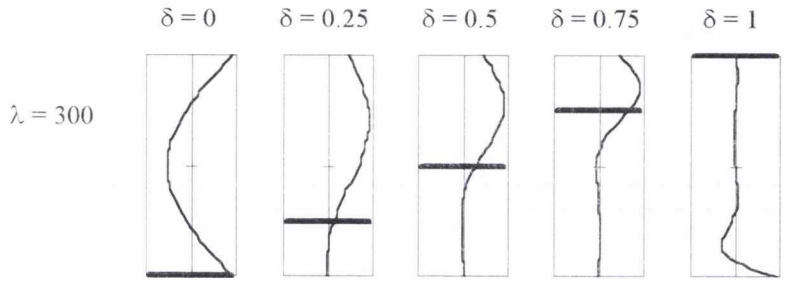

Figure 5.2.35. Buckling mode shapes for the second mode for figure 5.2.33.

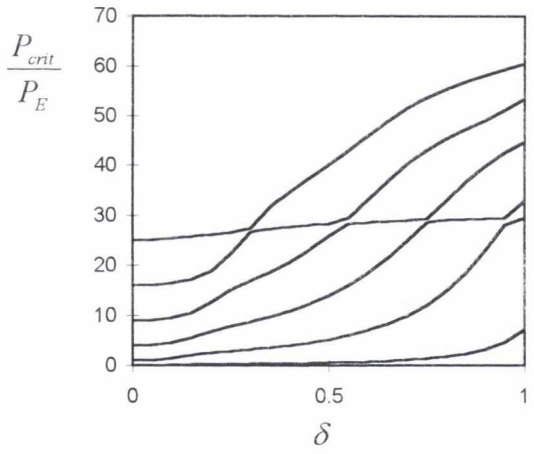

Figure 5.2.36. First six buckling loads for λ = 300 in a non-homogeneous soil with free-free end conditions of a partially embedded end-bearing pile.

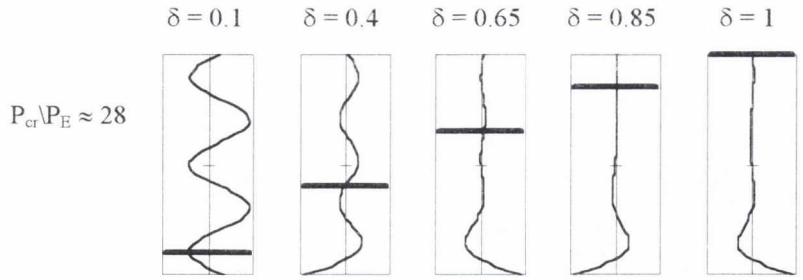

Figure 5.2.37. Buckling mode shapes with $P_{cr}/P_E \approx 28$ in a homogeneous soil with free-free end conditions of a partially embedded end-bearing pile.

In figure 5.2.38 the first buckling load for $\lambda = 300$ is plotted with a fixed unembedded end condition and either a fixed or a free embedded boundary condition. There is little difference between the two buckling loads apart from at very low and very high embedment ratios. If the fully embedded summary is looked at in section 4.2.3 for non-homogeneous end-bearing piles, it can be seen that the fixed-pinned and fixed-no rotation have identical loads to the fixed-fixed case. The buckling loads for other values of δ and λ will thus be identical to the fixed-fixed case except for very low λ and very high δ.

If the summary in section 4.2.3. is further inspected it can be seen that the previous case, namely changing a fixed embedded end condition to a free one with a fixed unembedded end, is the only one where there is a significant difference in buckling loads. It is, thus, possible to use the symmetric solutions presented previously to accurately predict the buckling loads for non-symmetric end-conditions for all but the lowest values of δ. In general, as long as $\delta > 20\%$ there is no significant difference in the solutions as the embedded boundary condition varies, provided that the relevant fully embedded buckling load is not exceeded. This is due to an "effective fixity" occurring within the soil medium.

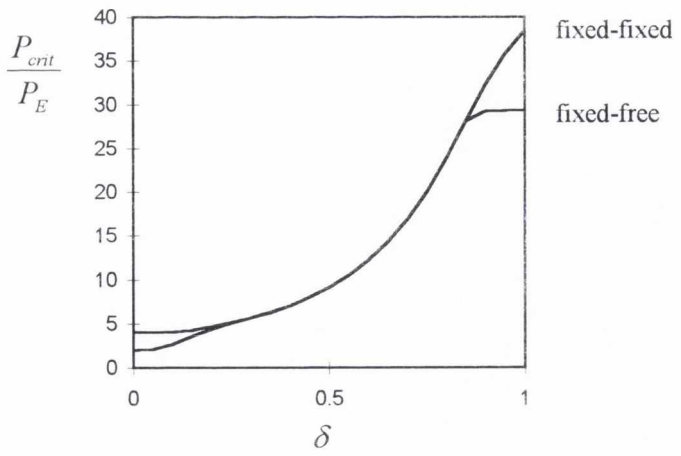

Figure 5.2.38. First buckling loads for a fixed-free and a fixed-fixed end conditions with $\lambda = 300$ in a non-homogeneous soil end conditions of a partially embedded end-bearing pile.

5.3. Partially embedded friction piles.

In order to emphasis the differences between end-bearing and friction piles the extreme case when there is no end-bearing at the bottom of the pile will be used. Only two sets of soil conditions will be considered, namely homogeneous and non-homogeneous. As before, the homogeneity, or lack of it, will define both the shaft friction as well as the soil stiffness.

5.3.1 Homogeneous soil (Constant shaft friction and soil stiffness).

The first buckling loads and mode shapes for friction pile in homogeneous soils are plotted on the following pages for symmetric end-conditions (figure 5.3.1 to 5.3.2). In the case of the fixed-fixed and pinned-pinned beams there is a plateau for $\delta \approx 1$, though it is not as well defined as in the end-bearing case. This plateau is associated with mode shapes that extend into the embedded medium. When the mode shapes are inspected in figure 5.3.3 for the fixed-fixed cased it can be seen that the "apparent" length decreases as δ increases for $0 < \delta < 0.75$, but actually increases between from the mode shape with $\delta = 0.75$ to the shape at $\delta = 1$. Yet, despite this increase in "apparent" length, the buckling load still increases for the whole range of δ. A similar effect can be identified in the pinned-pinned case, whereas it is not as obvious for free-free end conditions.

The similarity in mode shapes between the end-bearing and pure friction homogeneous is very obvious when the relevant cases are compared (figure 5.2.7 and 5.3.1, figure 5.2.13 and 5.3.3 and figure 5.2.18 and 5.3.5). The only difference being when $\delta = 1$, but this is not surprising as it is the fully embedded case and has been discussed in section 4.4. The buckling load variation is also similar for both end-bearing and pure friction cases, with an increase in the pure friction case as would be expected. The main difference is that unlike the end-bearing case which tend to have a plateau at high values of δ the pure-friction case appears to continue increasing as δ approaches unity. However, because this variation is only present for $\delta > 0.85$ in the end-bearing case (figure 5.2.4) it can be seen that the effect of changing the method by which the load is supported axially has a very limited effect.

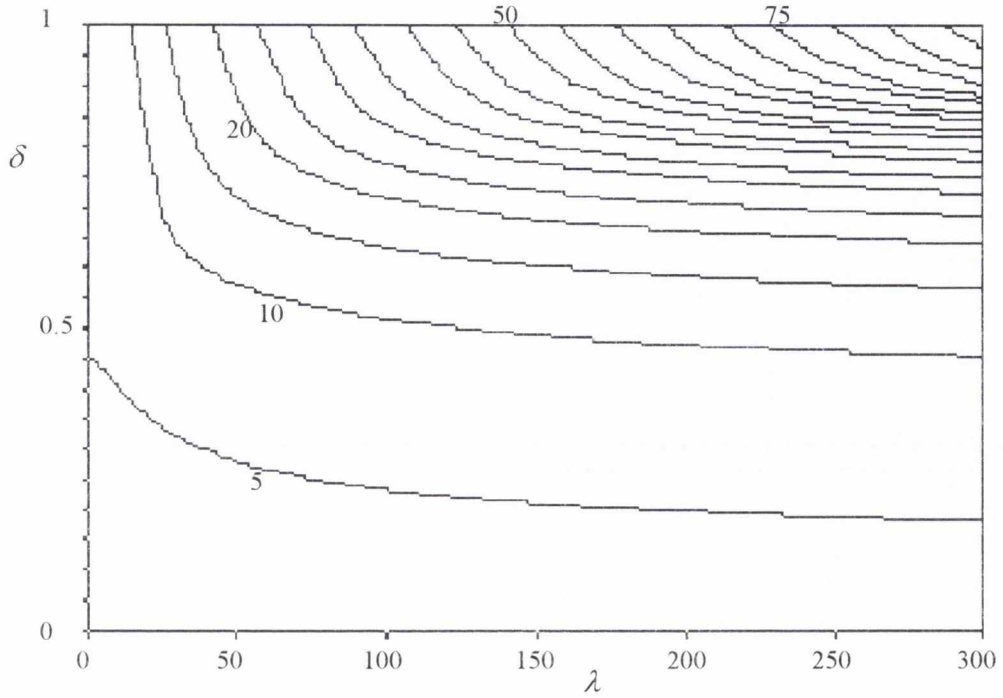

Figure 5.3.1. Buckling load (P_{cr}/P_E) contours for the first mode in a homogeneous soil with fixed-fixed end conditions of a partially embedded pure-friction pile.

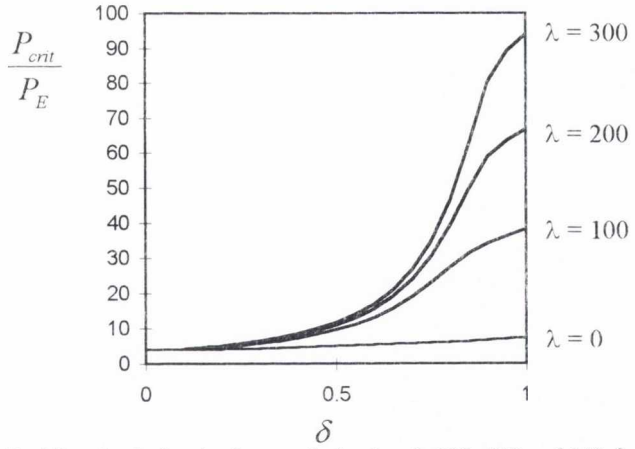

Figure 5.3.2. Buckling loads for the first mode for λ = 0, 100, 200 and 300 for figure 5.3.1.

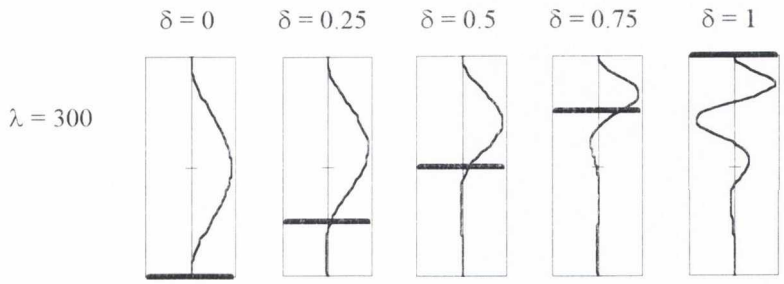

Figure 5.3.3. Buckling mode shapes for the first mode for figure 5.3.1.

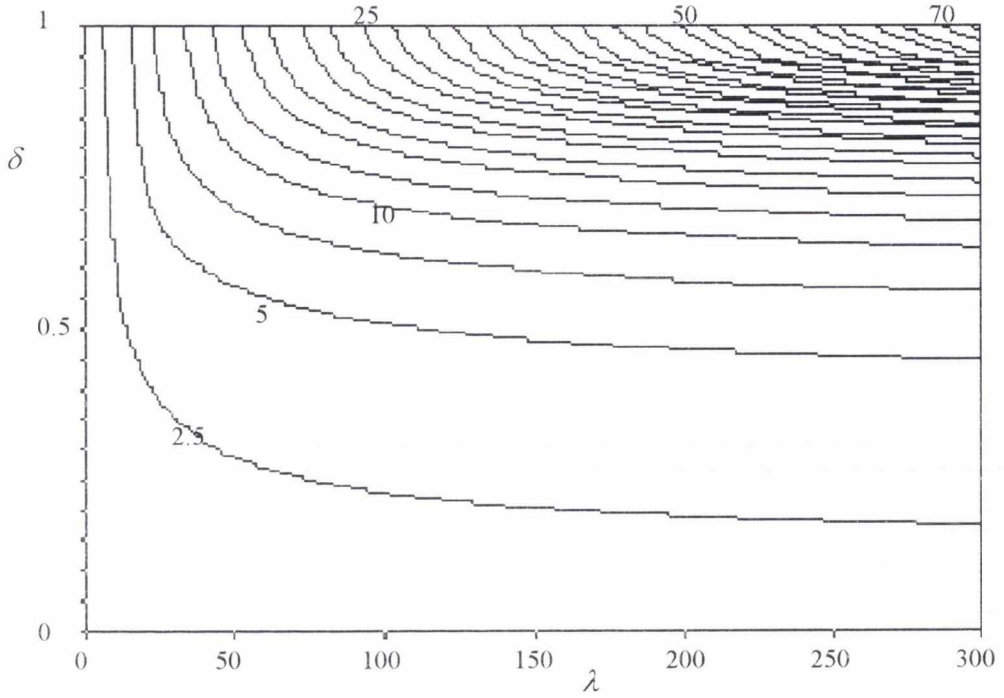

Figure 5.3.4. Buckling load (P_{cr}/P_E) contours for the first mode in a homogeneous soil with pinned-pinned end conditions of a partially embedded pure-friction pile.

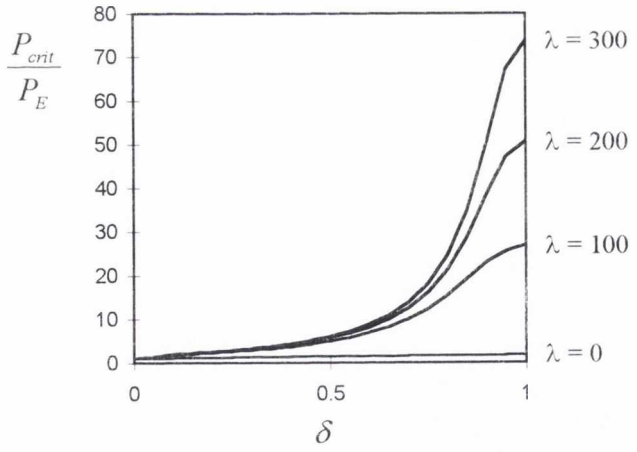

Figure 5.3.5. Buckling loads for the first mode for λ = 0, 100, 200 and 300 for figure 5.3.4.

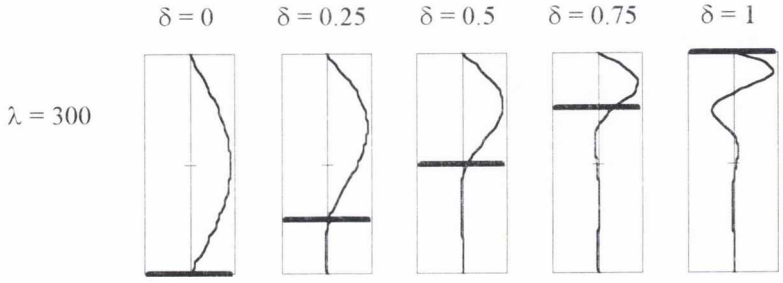

Figure 5.3.6. Buckling mode shapes for the first mode for figure 5.3.4.

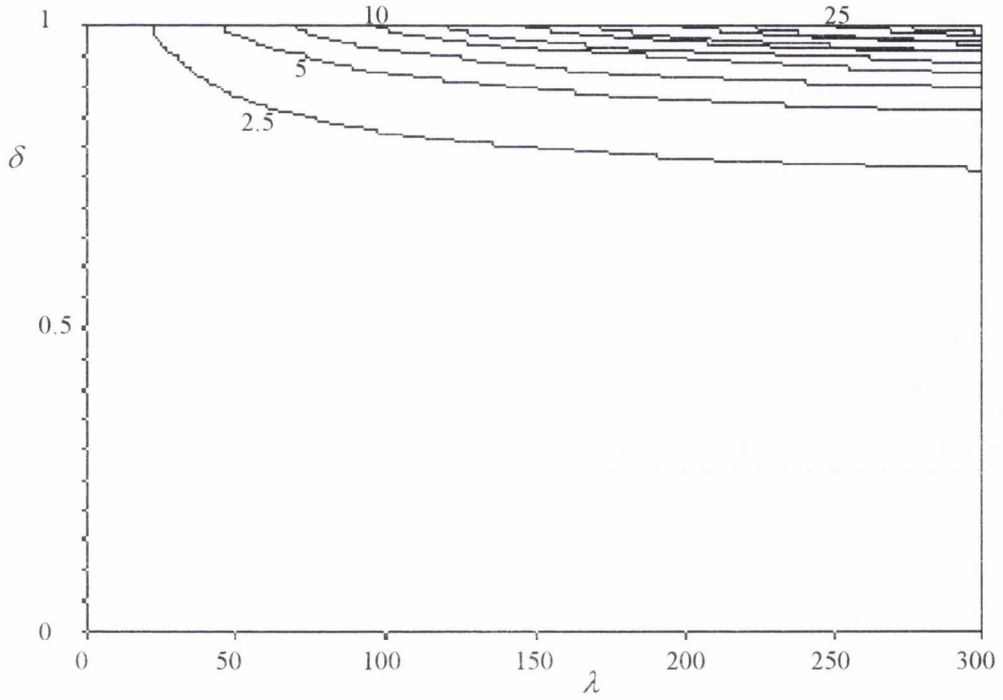

Figure 5.3.7. Buckling load (P_{cr}/P_E) contours for the first mode in a homogeneous soil with free-free end conditions of a partially embedded pure-friction pile.

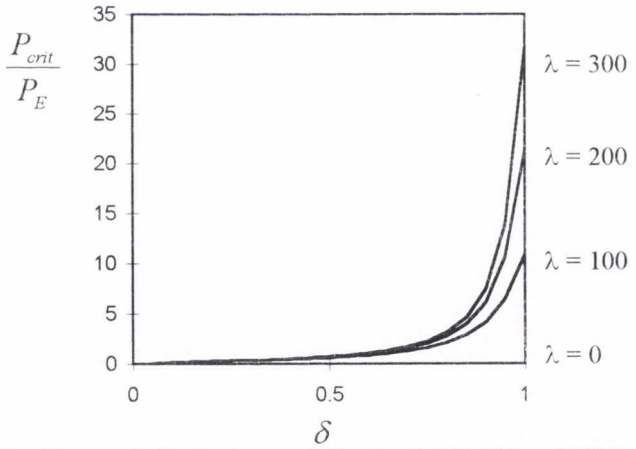

Figure 5.3.8. Buckling loads for the first mode for λ = 0, 100, 200 and 300 for figure 5.3.7.

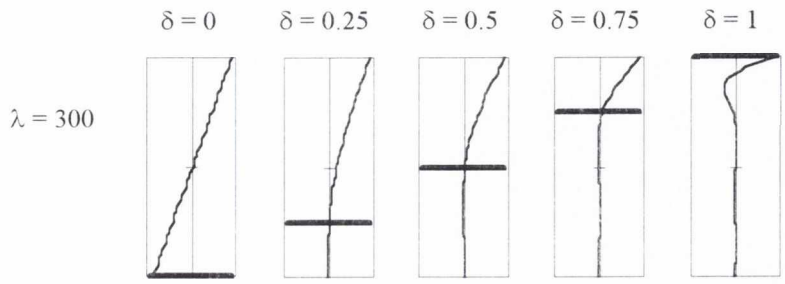

Figure 5.3.9. Buckling mode shapes for the first mode for figure 5.3.7.

As for homogeneous end-bearing piles it can be assumed that. apart from very low values of δ, the effect of changing the embedded boundary condition is negligible. If the summary in section 4.3.2 is studied, it can be seen that the unembedded boundary condition does not in this case effect the fully embedded solution and, hence, the solutions for $\delta = 1$ are applicable whatever the unembedded boundary condition. If the fully embedded solution is not affected by the embedded end condition then also the other solutions where there is an "apparent fixity" formed can also be applied to all boundary conditions. This will be true for all solutions except where either the soil stiffness is very weak or there is not sufficient embedded depth to form a "fixity". This, in itself, should not be surprising when the limited depth the buckling mode shapes, that have been presented previously in this section, have extended down the pile is taken into consideration.

5.3.2 Non-homogeneous soils (Linearly increasing shaft friction and soil stiffness).

The buckling loads and typical mode shapes for a non-homogeneous pure-friction pile are plotted in the figures 5.10 to 5.18. The buckling loads can be seen to vary in a similar way as the non-homogeneous end-bearing case. Due to the effect of the redistribution of load by the friction the buckling loads are slightly larger than those for the end-bearing case. However, if the mode shapes are compared to the respective end-bearing case it can be seen that they are almost identical. It can be concluded that, except for the fully embedded homogenous case, the significant factors in determining mode shapes are twofold. Firstly and unsurprisingly, the embedment ratio is the over-riding factor and secondly, the form that the variation of the soil stiffness takes. The effect of changing the soil stiffness from homogenous to non-homogenous is to increase the "apparent length" of the mode shape. This is associated with an expected decrease in the buckling load. It appears that the introduction of shaft friction has little effect on the mode shape produced but does increase the buckling load.

As in the end-bearing non-homogeneous case the effect of changing the end-condition at the bottom of the pile is minimal, apart from the cases when either the soil stiffness, λ, or the embedment ratio, δ approach zero.

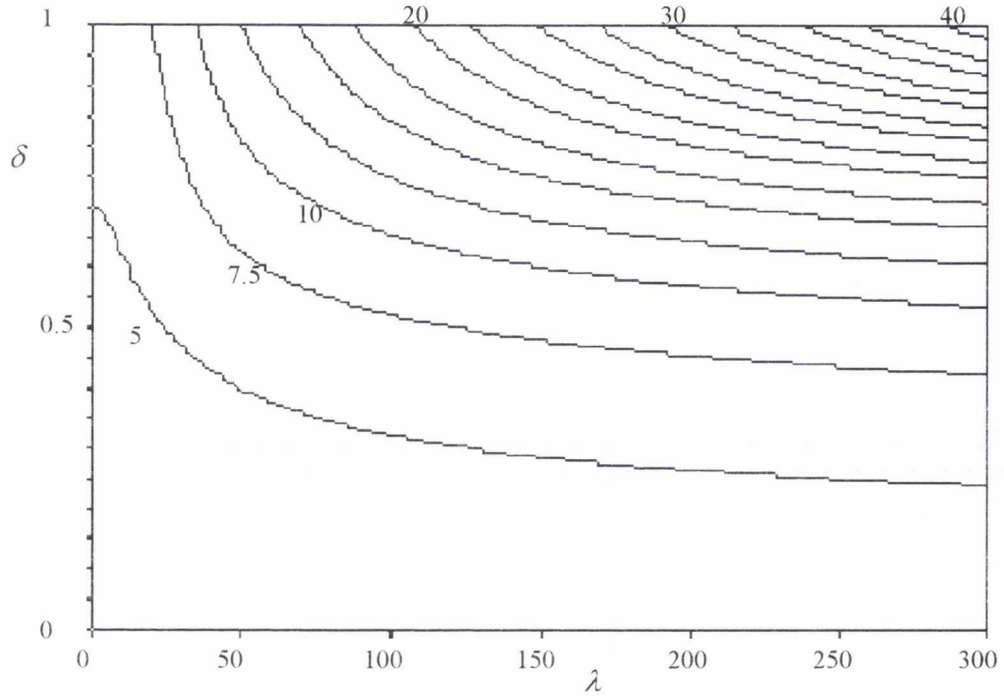

Figure 5.3.10. Buckling load (P_{cr}/P_E) contours for the first mode in a non-homogeneous soil with fixed-fixed end conditions of a partially embedded pure-friction pile.

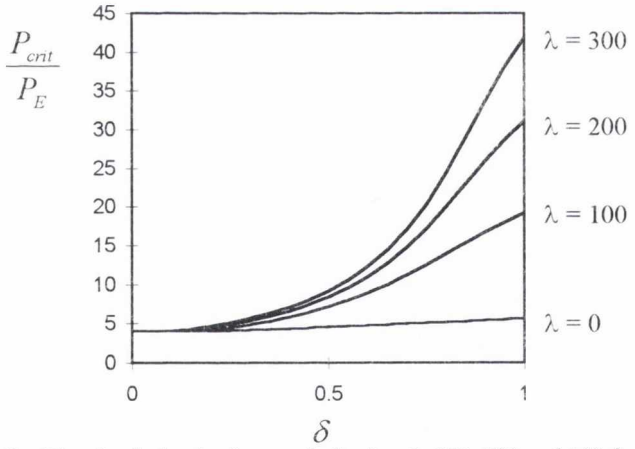

Figure 5.3.11. Buckling loads for the first mode for λ = 0, 100, 200 and 300 for figure 5.3.10.

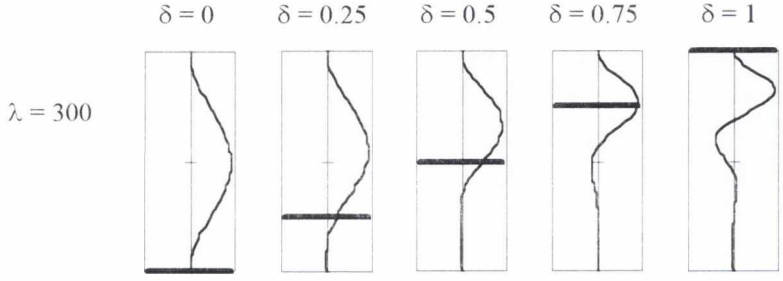

Figure 5.3.12. Buckling mode shapes for the first mode for figure 5.3.10.

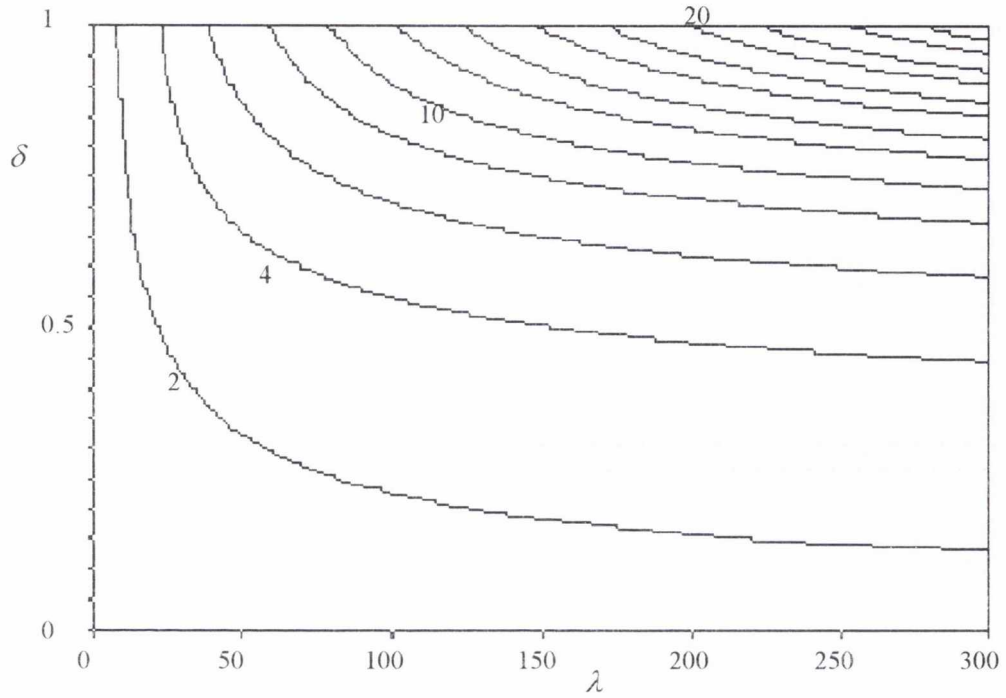

Figure 5.3.13. Buckling load (P_{cr}/P_E) contours for the first mode in a non-homogeneous soil with pinned-pinned end conditions of a partially embedded pure-friction pile.

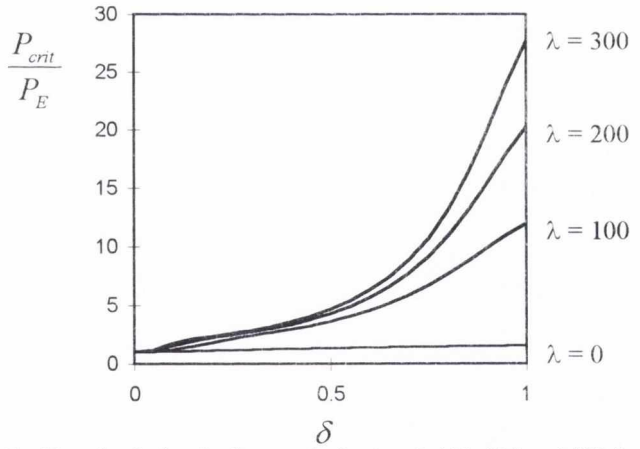

Figure 5.3.14. Buckling loads for the first mode for λ = 0, 100, 200 and 300 for figure 5.3.13.

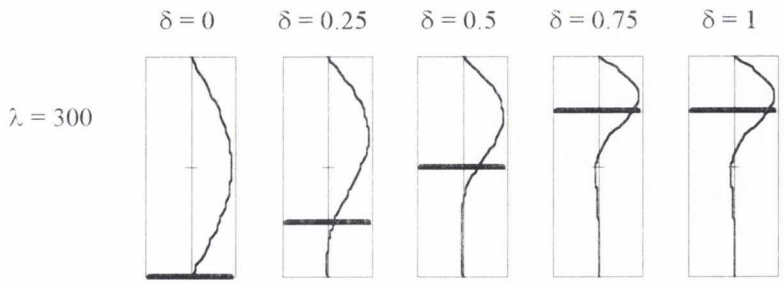

Figure 5.3.15. Buckling mode shapes for the first mode for figure 5.3.13.

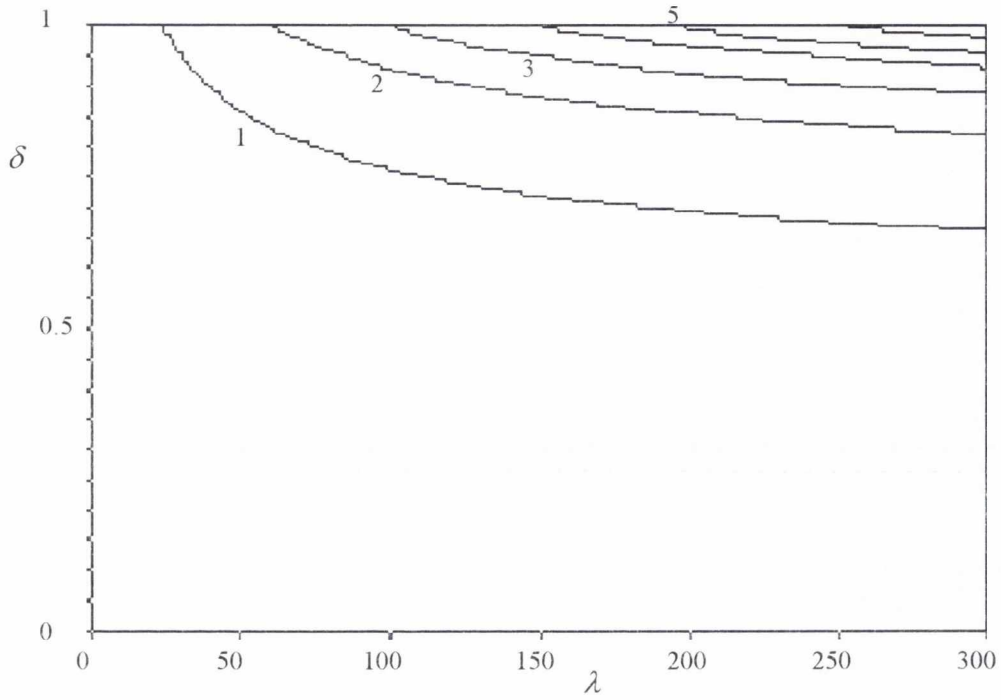

Figure 5.3.16. Buckling load (P_{cr}/P_E) contours for the first mode in a non-homogeneous soil with free-free end conditions of a partially embedded pure-friction pile.

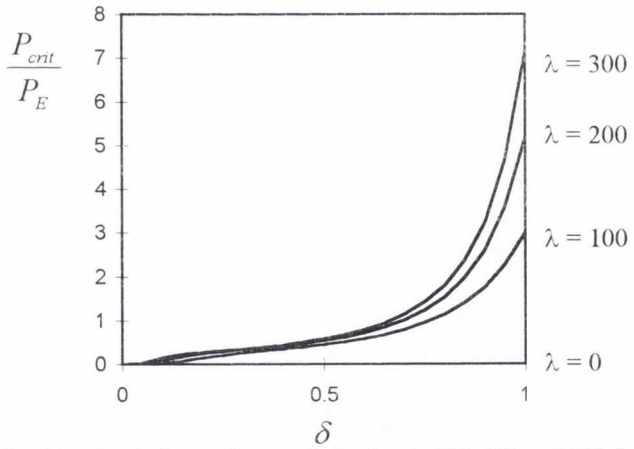

Figure 5.3.17. Buckling loads for the first mode for λ = 0, 100, 200 and 300 for figure 5.3.16.

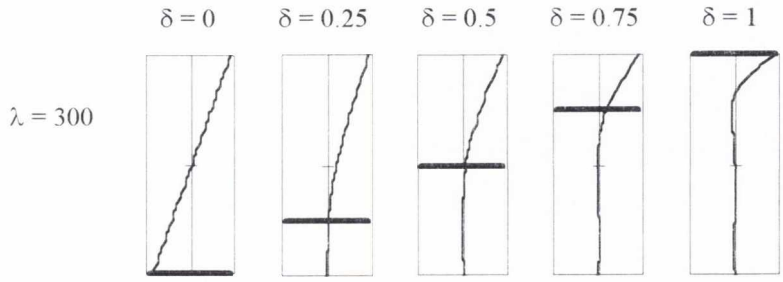

Figure 5.3.18. Buckling mode shapes for the first mode for figure 5.3.16.

5.4. Conclusions

In this chapter the buckling loads and mode shapes have been presented for partially embedded beams. The solution to end-bearing piles were initially considered and it was shown that, for homogeneous soil conditions, the buckling loads could be approximated by using two sets of results. The first is the partially embedded case where the embedded boundary condition was changed to a fixed condition and the second result is that of the fully embedded problem with the relevant end boundary conditions. This solution is accurate for all but the smallest embedment ratios, $\delta < 10\%$. The reason that this method is of interest is that not only does it predict approximate buckling loads, but also that the mode shapes predicted are approximately correct as well. However, this is only of limited interest as a similar technique cannot be applied to the other sets of soil conditions. The plateaux that are found for high embedment ratios, $\delta > 0.85$, are associated with buckling mode shapes which extend past the soil-air interface almost to the bottom of the pile. These mode shapes are associated with a buckling load almost equal to that of the fully embedded case. They do not occur if the unembedded boundary condition is defined as being free. It would be expected that, for high soil stiffness, the buckling load would approach that of the buckling load of the unembedded portion of the pile with a fixed end-condition at the soil surface. This does not happen to a significant degree in the range of λ considered here except at very low embeddment ratios, $\delta < 0.25$.

For a non-homogeneous soil supporting an end-bearing pile the plateau found in the homogeneous case for high δ no longer exist in the solutions of the first buckling mode, except for the case of fixed-free end conditions. This is predictable when the fully embedded solution presented in the previous chapter is considered and coincides with a mode shape with a maximum amplitude at the pile toe. This would produce a discontinuity in the supporting medium. In comparison to the homogeneous case the mode shapes in the symmetric case always tend to the unembedded or upper section of the pile where the soil stiffness is least.

A mode shape with a maximum amplitude at the toe is also produced in the free-free case if modes higher than the fundamental are considered. This mode shape has a buckling load which is approximately constant as the embedment ratio varies, although the mode the mode shapes represent

changes. For example, at $\lambda = 300$ and $\delta = 1$ it is the second mode and at $\lambda = 300$ and $\delta = 0.1$ it is the sixth. This mode shape, however, is of only very limited academic interest, because not only is it approximately four times the fundamental mode for any value of δ but also it produces a discontinuity in the supporting medium at the pile base. A similar buckling mode was found in the homogenous case, which was of more interest because it has a buckling load which approaches the first mode as δ tends to unity.

The second section concentrates on the buckling of piles which are completely supported by shaft friction. The results in both the homogeneous and non-homogeneous soils considered are very similar to those for the respective end-bearing piles. The mode shapes, apart for fully embedded homogeneous soils, are almost identical. The buckling load patterns are also very similar except for a slight increase in the actual buckling loads found. Also the plateaux corresponding to the fully embedded buckling loads of the homogeneous soil do not occur in the pure friction case, however, this would be expected since they correspond to symmetric/anti-symmetric mode shapes which are only found in the homogeneous end-bearing fully embedded cases.

With respect to other pure friction cases it can be seen that the soil stiffness variation is the most important in defining how mode shape that the partially embedded pile will take at a particular soil stiffness. The effect of altering how the shaft friction varies with depth is very limited for instance if a fixed-fixed beam is taken as an example then at $\delta = 0.8$ and $\lambda = 300$ the buckling load in a homogenous soil with end-bearing is $P_{cr}/P_E = 44.96$ and with a friction pile $P_{cr}/P_E = 46.58$, a difference of less than 5%. Obviously, if the parameter μ is again included then the buckling load will lie somewhere between the end-bearing and pure-friction cases with the appropriate variation in soil stiffness with depth.

Chapter 6

Comparison with other works

6.1. Introduction

This chapter will use the results from the previous two chapters and compare them with the published work as discussed in parts of Chapter 2, the literature review. Some of the solutions presented in the literature review can be used as bounding solutions in order to verify the accuracy of the method used in this thesis. For instance, it would be expected that as the soil stiffness tends to zero that the solution would tend to the Euler buckling load. This is indeed the case, however other more rigorous tests can also be applied. There are a subset of solutions to the end-bearing problem which produce results which are identical to those presented in this thesis. However, the authors have not used non-dimensional parameters and it is important to ensure that such results coincide with the ones presented in Chapters 4 and 5. Some authors have presented approximate solutions to the particular problems, such as partially embedded end-bearing beams, and it is informative to compare these with the 'exact' solution produced in Chapter 2. The final section compares load tests on real structures with the buckling loads predicted by the suggested algorithm and the problems in relating the theoretical solution with experimental results are discussed.

6.2. Exact solutions

6.2.1 Euler solutions

The Euler solution to the buckling of end-bearing beams, unsupported laterally along their length is well known and is presented in many texts, for instance Timoshenko and Gere (1961). The classic results are summarised in Howatson, Lund and Todd (1972) for four cases, they are fixed-free, pinned-pinned, fixed-pinned and fixed-fixed, table 6.2.1. The method in this thesis can be used to approximate these solutions as λ tends to zero (if $\lambda = 0$ is put into the developed equations then it is found that one of the non-dimensional parameters goes to infinity). In table 6.2.1, the buckling loads for the four cases are calculated for very low values of the soil stiffness parameter, λ, for an end-bearing homogeneous foundation solution. As the soil stiffness is reduced the buckling load rapidly converges onto the exact Euler solution from above as would be expected. It should be noted that this is not a rigorous check on the algorithm presented earlier

	fixed-free	pinned-pinned	fixed-pinned	fixed-fixed
P_{cr}	$\frac{\pi^2 EI}{4l^2}$	$\frac{\pi^2 EI}{l^2}$	$\frac{\pi^2 EI}{0.49l^2}$	$\frac{4\pi^2 EI}{l^2}$
θ_{exact}	0.25	1	2.04574852	4
θ, $\lambda = 10$	1.21549078	2.02659822	2.86806138	4.76276444
θ, $\lambda = 1$	0.26849337	1.01026598	2.05411092	4.00769879
θ, $\lambda = 0.1$	0.25018622	1.00010266	2.04583215	4.00007699
θ, $\lambda = 0.01$	0.25000186	1.00000103	2.04574935	4.00000077
θ, $\lambda = 0.001$	0.25000002	1.00000001	2.04574852	4.00000001

Table 6.2.1. Euler critical buckling loads.

6.2.2 Hetényi solutions

In Hetényi (1946), the buckling solutions for end-bearing beams supported on a homogeneous Winkler foundation were presented. The end-conditions are required to be symmetric in order to use hyperbolic or trignometric functions to solve the problem. It was shown in chapter 4 that

the solution in this thesis is identical to the solution in Hetényi with the added ability to model non-symmetric problems.

6.2.3 Davisson solutions

These solutions were sumarised by Prakash and Sharma (1989). Davisson presented solutions for fully embedded end-bearing piles which had pinned or free embedded conditions. He suggested that the upper boundary condition could be free, pinned or able to translate and not rotate. The latter boundary condition could represent a pile in a pile group it was suggested. The soil conditions modelled are either constant soil stiffness or soil stiffness increasing linearly with depth from a zero value at the surface.

The results from Davisson were presented in Chapter 2. The non-dimensional parameters used are U_{cr} and Z_{max} for the constant soil stiffness equations 2.5.4-2.5.7. These are defined in terms of a third parameter R as follows,

$$U_{cr} = \frac{P_{cr} R^2}{EI}, \quad Z_{\max} = \frac{L}{R} \qquad [6.2.1], [6.2.2]$$

where,

$$R = \sqrt[4]{\frac{E_p I_p}{k}}, \qquad [6.2.3]$$

EI is the flexural rigidity of the pile and k is the soil stiffness.

The non-dimensional parameters used in this thesis are,

$$\vartheta = \frac{P_{cr}}{P_E} = \frac{P_{cr} l^2}{\pi^2 EI} \text{ and } \lambda = \left(\frac{kl^4}{EI}\right)^{1/2} \qquad [6.2.4], [6.2.5]$$

Hence,

$$U_{cr} = \frac{P_{cr}}{(EIk)^{1/2}} = \pi^2 \frac{P_{cr} l^2}{\pi^2 EI}\left(\frac{EI}{kl^4}\right)^{1/2} = \frac{\pi^2 \vartheta}{\lambda} \qquad [6.2.6]$$

and

$$Z = \left(\frac{kl^4}{EI}\right)^{1/4} = \lambda^{1/2} \qquad [6.2.7]$$

Davisson presents the solutions for the triangular variation in soil stiffness with the following non-dimensional parameters.

$$V_{cr} = \frac{P_{cr}T^2}{EI}, \quad Z_{\max} = \frac{L}{R} \qquad [6.2.8], [6.2.9]$$

where,

$$T = \sqrt[5]{\frac{E_p I_p}{n_h}} \qquad [6.2.10]$$

and n is defined by the equation $k(x) = n_h x$ where x is the distance below ground level and k is, again, the soil stiffness. Remembering that λ is defined at the maximum depth, l, the definition of n can be changed to $n_h = k/l$. Hence,

$$V_{cr} = \frac{P_{cr}\left(EIl/k\right)^{2/5}}{EI} = \frac{P_{cr}l^{2/5}}{(EI)^{3/5}k^{2/5}} = \pi^2 \frac{P_{cr}l^2}{\pi^2 EI}\left(\frac{EI}{kl^4}\right)^{2/5} = \frac{\pi^2 \vartheta}{\lambda^{4/5}} \qquad [6.2.11]$$

and

$$Z_{\max} = \frac{l}{\left(EIl/k\right)^{1/5}} = \frac{k^{1/5}l^{4/5}}{(EI)^{1/5}} = \lambda^{2/5} \qquad [6.2.12]$$

Figures 6.2.1 and 6.2.2 were created using data from the method outlined in this thesis. They are for the most part identical to the results produced in Davisson (1963) and section 2.5.1, the only difference being that the original results of Davisson in figure 2.5.4 and 2.5.5 do not appear to have been plotted completely.

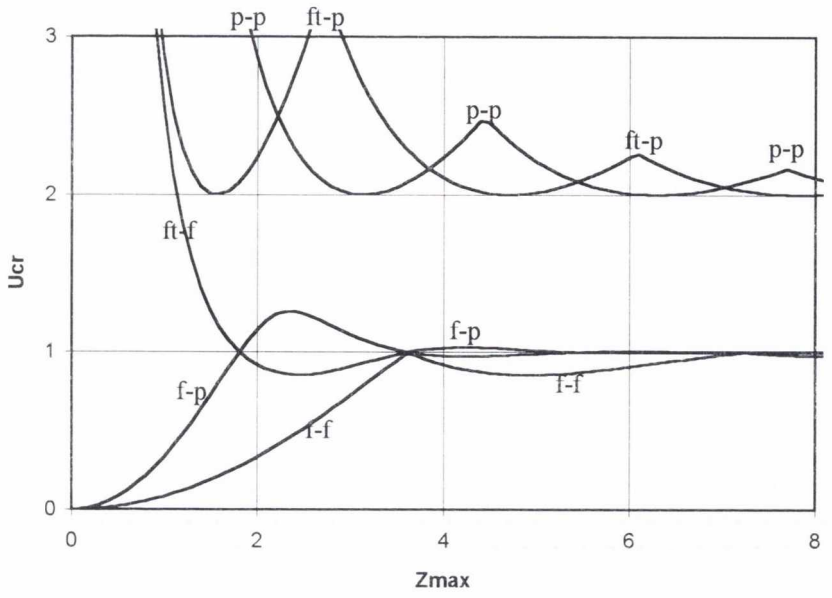

Figure 6.2.1. Buckling loads for a homogeneous soil.

f = free p = pinned ft = fixed, translating

Note : Upper end condition listed first

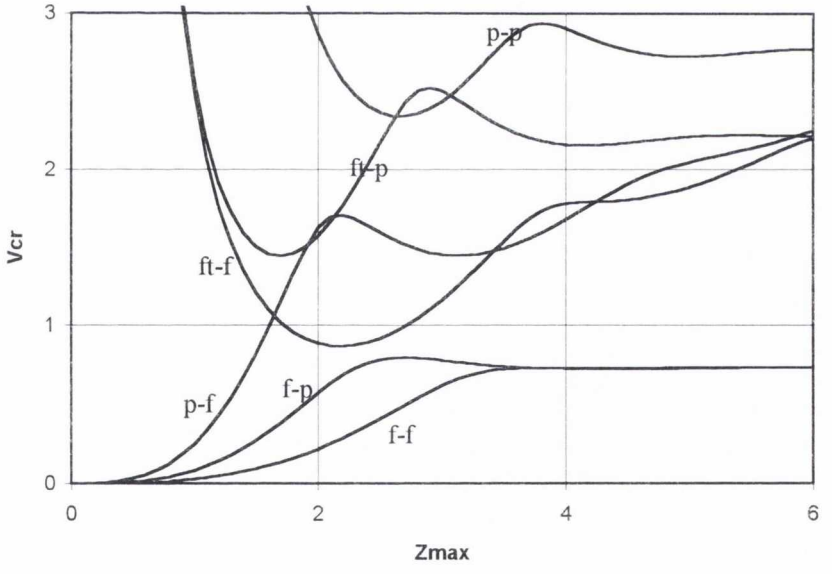

Figure 6.2.2. Buckling loads for a non-homogeneous soil.

6.3. Approximate solutions

The solutions in this section are approximate and have been suggested by the various authors in order to produce practical guidelines. Both authors have modelled a partially embedded end-bearing pile by defining a fixed end-condition at an arbitrary position in the soil medium. The location of this end-condition is defined by different methods.

6.3.1 Davisson and Robinson solution.

The solution discussed by Davisson and Robinson (1965) was developed with the following non-dimensional parameters as presented in section 2.5.5.

$$S_R = \frac{L'_S}{R} \text{ and } J_R = \frac{L_U}{R} \qquad [6.3.1], [6.3.2]$$

where R is defined by Davisson in equation 6.2.3, L'_s is found from figure 6.3.1 and L_U is the unembedded length of the beam.

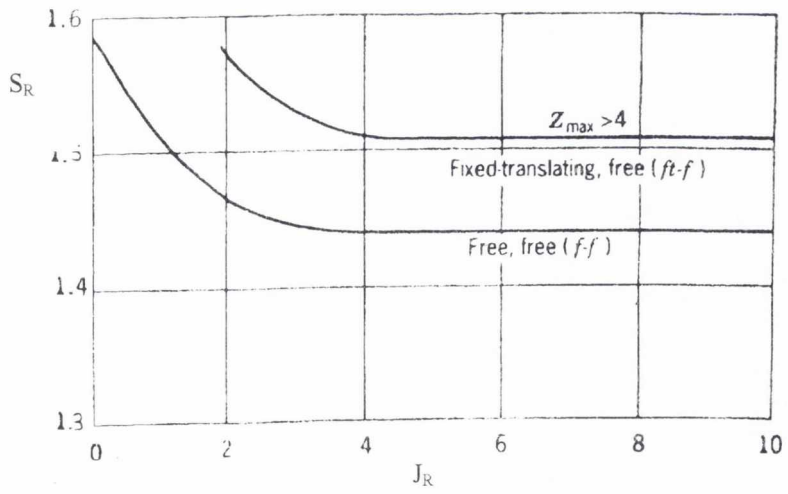

Figure 6.3.1. Dimensionless depth of fixity for buckling k = constant (Davisson and Robinson, 1965).

The critical buckling load is then defined by,

$$P_{cr} = \frac{\pi^2 EI}{4\left(S_R + J_R\right)^2 R^2} \qquad [6.3.3]$$

where, in this case, the factor, 4, implies that the unembedded end is free. The factor is calculated using the Euler formula with the embedded end-condition being replaced by a fixed end. Hence, the factor for fixed, pinned and translate-no rotation are, 0.25, approximately 0.49 and 1 respectively. However, using the free unembedded boundary condition parameter, for example,

$$\vartheta = \frac{P_{cr} l^2}{\pi^2 EI} = \frac{l^2}{4\left(S_R + J_R\right)^2 R^2} \qquad [6.3.4]$$

now

$$\frac{l}{R} = \sqrt[4]{\frac{kl^4}{EI}} = \sqrt{\lambda} \qquad [6.3.5]$$

hence

$$\vartheta = \frac{\lambda}{4\left(S_R + J_R\right)^2} \qquad [6.3.6]$$

so

$$\left(S_R + J_R\right)^2 = \frac{\lambda}{4\vartheta} \qquad [6.3.7]$$

and

$$S_R = \sqrt{\left(\frac{\lambda}{4\vartheta}\right)} - J_R \qquad [6.3.8]$$

where

$$J_R = \frac{(1-\delta)l}{R} = (1-\delta)\lambda^{0.5} \qquad [6.3.9]$$

Equation 6.3.9 in conjunction with equation 6.3.8 now means that it is possible to convert the non-dimensional parameters used previously into those used by Davisson and Robinson. In figures 6.3.2 to 6.3.4 S_R and J_R have been plotted using the algorithm presented in this thesis with results using embedment ratios of 0.125, 0.25, 0.375, ..., 0.875. It should be noted that fully embedded results cannot be plotted on these diagrams due to the definition of J_R. Non-embedded results also cannot be plotted on the graphs. Hence, the two boundary conditions for minimum and maximum buckling load cannot be used to bound the results plotted. The solution suggested by Davisson and Robinson in figure 6.3.2 is a lower bound solution for the free-free case. However this does not appear to be so when the unembedded boundary condition is allowed to translate (figure 6.3.3). In figure 6.3.4, when the buckling loads are plotted for a pinned-pinned pile another effect of the definition of the dimensionless parameters can be seen. The buckling load lines do not converge onto each other

from above or below, rather the lines oscillate above and below. This means that trends in buckling loads as J_R (the soil stiffness parameter) varies are obscured. In Sharma and Prakash (1989) it was suggested that, for practical cases a value of $S_R = 1.33$ should be used. However, this is an unconservative recommendation as the smaller the value of S_R the larger the value of the calculated buckling load. The important calculation is to determine the minimum load the pile can support before buckling!

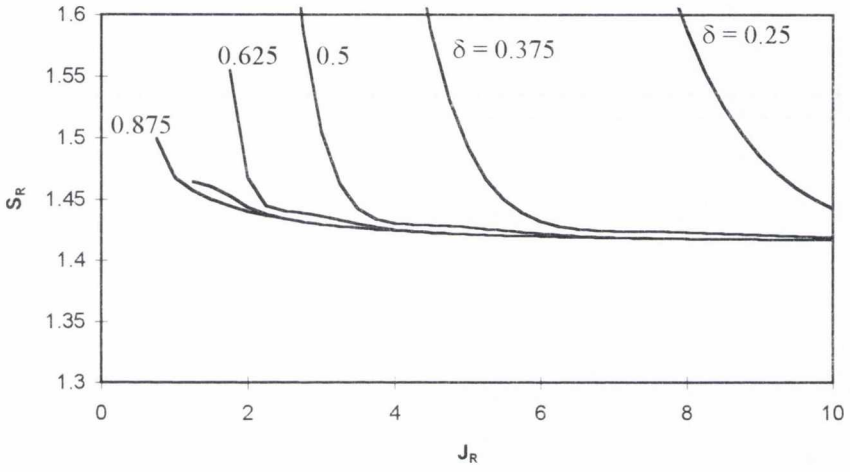

Figure 6.3.2. Buckling load and soil stiffness parameters for a free-free pile.

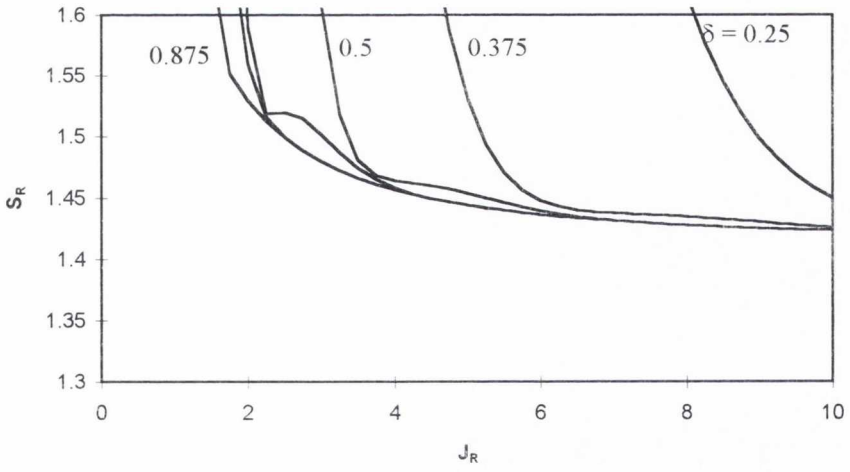

Figure 6.3.3. Buckling load and soil stiffness parameters for a fixed-translating(no rotation) pile.

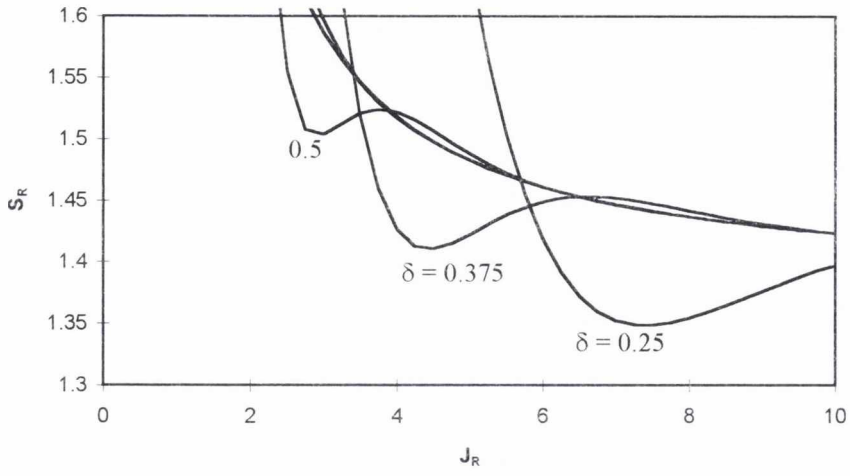

Figure 6.3.4. Buckling load and soil stiffness parameters for a pinned-pinned pile.

6.3.2 Prakash results

Prakash (1987) obtained solutions for buckling loads in closed-form by energy methods for fully embedded vertical piles for pinned-pinned and fixed-fixed end conditions as presented in section 2.5.1. The soil stiffness can vary linearly with depth. Buckling loads and buckling mode shapes were solved with EI = 477 tm^2. K_o, the soil stiffness at the top of the pile, could vary up to 2000 t/m^2 and n_h, the increase in soil stiffness per unit depth, up to 2000 t/m^3. Results from Pakash (1987) were presented in figures 2.5.6 and 2.5.7. The graph presented in figures 6.3.5 and 6.3.6 are similar to the results presented by Prakash for low values of n_h. However, because Prakash assumed a buckling mode shape and then calculated the force required to produce that buckling mode, the method is highly dependent on the assumed mode shape. It appears that Prakash assumed symmetric/anti-symmetric mode shapes. As presented in chapter 4, these mode shapes do not actually occur when a rigorous analytical solution is produced, except for the homogenous solution, $n_h = 0$. Hence, for lengths over 5 m and $n_h > 0$ the method used by Prakash significantly over-estimates the predicted buckling load from the exact solution. The trends in mode shape patterns cannot be identified as exact mode shapes are not produced by this method. Prakash also does not use non-dimensional parameters which means that the problem must be solved for each particular set of initial conditions.

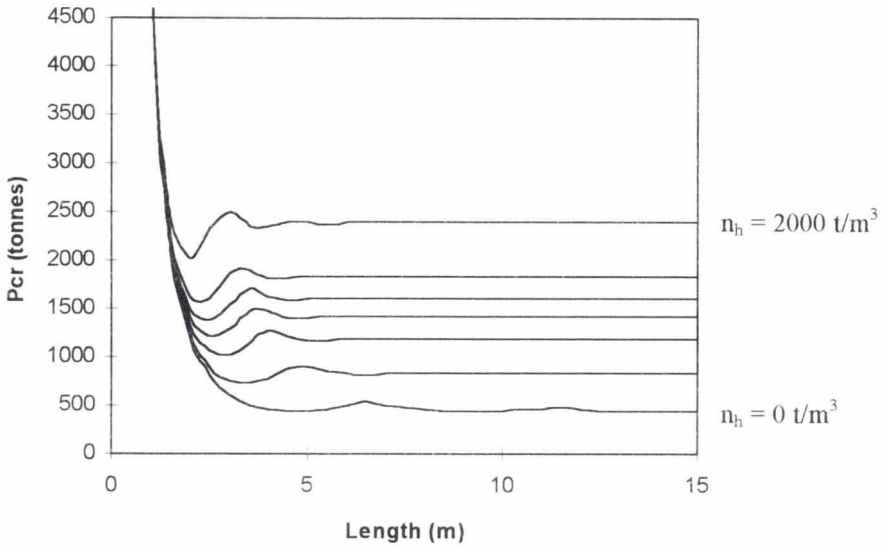

Figure 6.3.5. Exact critical buckling load for a pinned-pinned pile when k_0 = 100 t/m^2 n_h = 0, 100, 300, 500, 700, 1000, 2000 t/m^3.

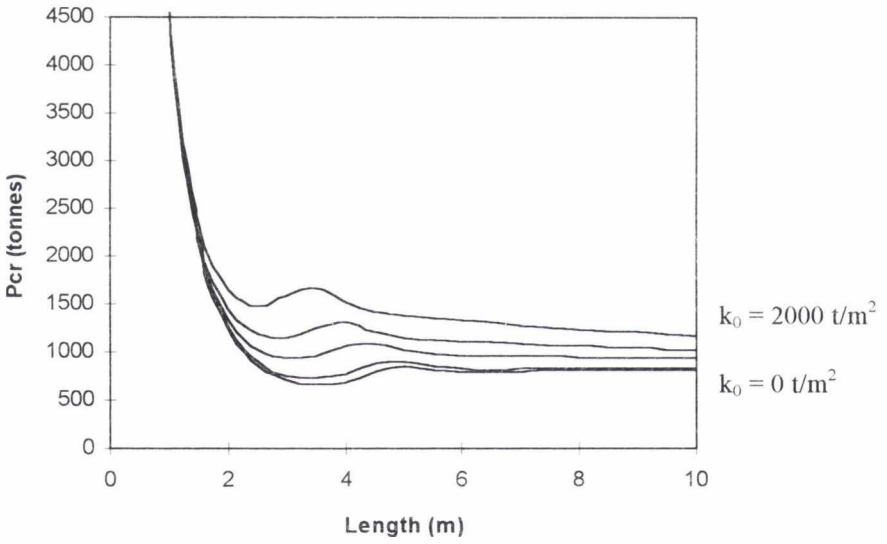

Figure 6.3.6. Exact critical buckling load for a pinned-pinned pile when n_h = 100 t/m^3. k_0 = 0, 100, 500, 1000, 2000 t/m^3.

6.3.3 Fleming solutions

The solution to the problem of a partially embedded beam has been solved using an approximate method by Fleming et al (1992) as summarised in section 2.5.5. It is similar to the Davisson and Robinson solution above and can be defined by the equations,

$$P_{cr} = \frac{\pi^2 EI}{4\left(l_f + l_e\right)^2} \qquad [6.3.10]$$

where $$l_e = {}^{l_c}/_{2} \approx 2\left({}^{EI}/_{k}\right)^{0.25} \quad or \quad 2\left({}^{EI}/_{n}\right)^{0.2} \qquad [6.3.11], [6.3.12]$$

l_c is the critical length, which is defined by Matlock and Reese (1960), as the length beyond which the pile behaves as if it was infinitely long. l_f is the unembedded length and l_e is the effective length of the embedded portion of the pile. The method is consistent with Davisson and Robinson with S_R or S_T defined as being equal to two. Figures 6.3.7 to 6.3.8 indicate that this method can underestimate the buckling load by a significant amount in most practical circumstances. However, it should be remembered that there is no mathematical limit to S_R when exact calculations are performed and the use of the predefined factor is not accurate at low soil stiffness and small values of the embedment ratio.

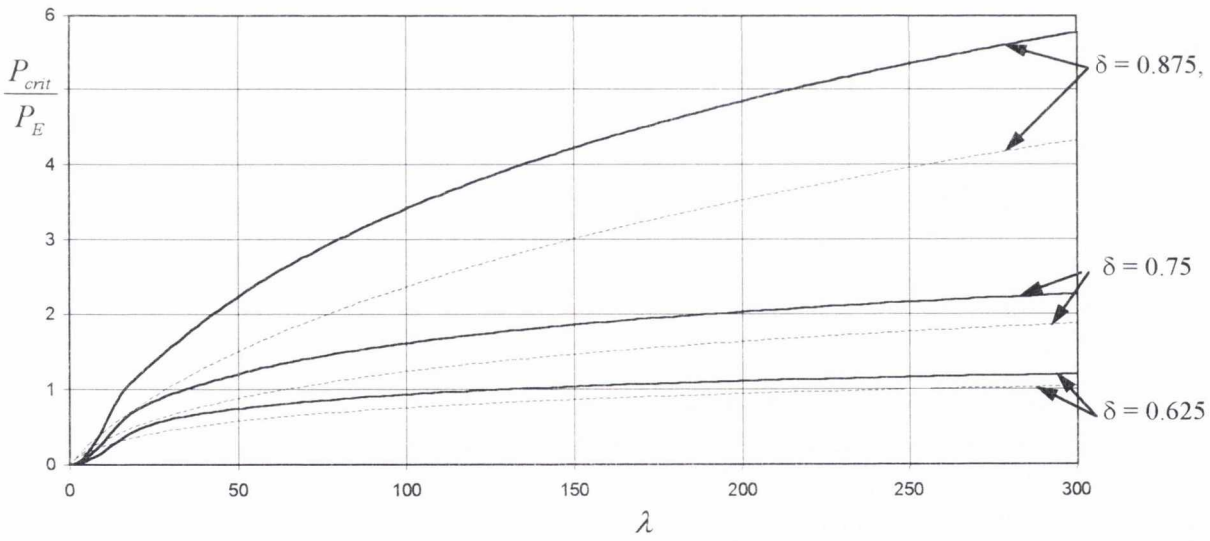

Exact solution [——], Fleming et al solution [·····]

Figure 6.3.7. Buckling loads exact and approximated for a free-free pile in a homogeneous soil.

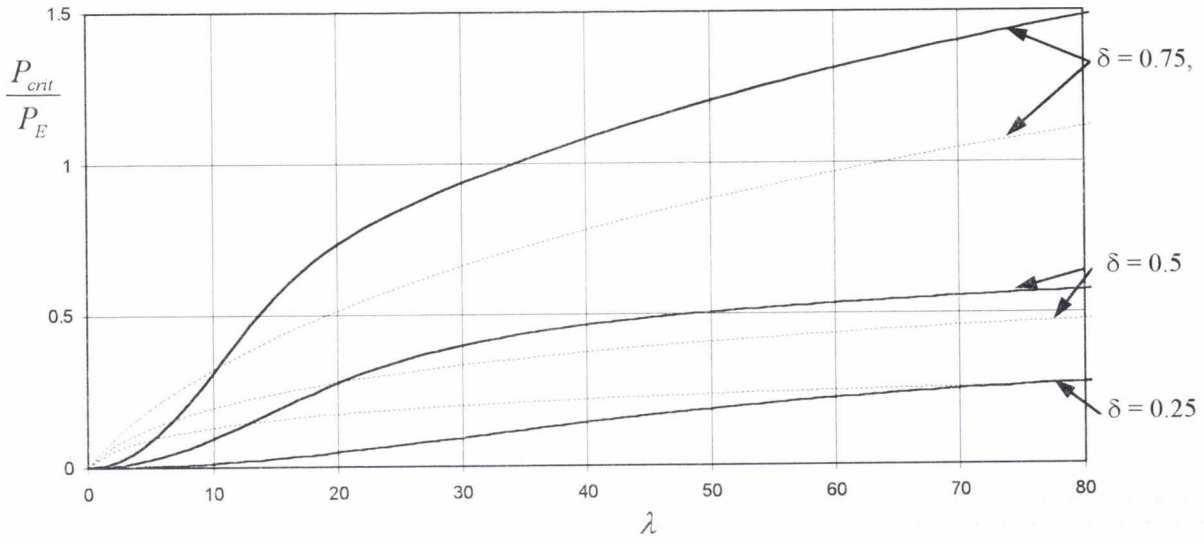

Exact solution [———], Fleming et al solution [·····]

Figure 6.3.8. Buckling loads exact and approximated for a free-free pile in a homogeneous soil.

6.4. Buckling loads of actual piles in the field.

6.4.1 Francis, et al (1962)

A load test was carried out on a long experimental hollow steel pile by Francis et al (1962). The pile had a length of 85.75 feet and a flexural stiffness of 206.6 lbs.inch^2. It was initially pulled down through the soft soil by a 5-ton winch to a depth of 55 feet. The final stage of driving was by a 1,700 lb drop hammer with a fall of 18 inches until it was considered that it was resting on an underlying basalt layer. The authors calculated that the squash load was $85x10^3$ lb. assuming a yield stress of 15.25 tons/inch^2. The squash load of a small length of the pile was observed to be $79.2x10^3$ lb. The maximum load sustained by the pile was $68x10^3$ lb.. As can be seen in figure 2.4.6, when the load transfer curves were being reviewed, the load in the pile reduced approximately linearly with depth, indicating a constant shaft friction, and had practically no end-bearing load. The load was applied using a pinned connection at the pile head. The soil stiffness was estimated, by Francis et al, to be constant and equal to 100 lb/inch^2.

Francis et al used the results from Hetényi for an end-bearing pile (recall that because non-dimensional parameters are used, consistent imperial units can be used throughout the calculations if required) with a homogeneous soil of 100 lb/inch^2 to calculate a buckling load of $300x10^3$ lb.. When a constant shaft friction was defined as supporting the load the buckling load calculated was $330x10^3$ lb..

However, if the penetrometer test results plotted by Francis et al are examined, the actual variation in soil stiffness is, in fact, linearly increasing with depth to a maximum of approximately 150 lb./in^2 at a depth of 88 ft, as can be seen in figure 6.4.1. The buckling loads for an end-bearing and a pure-friction beam, with constant shaft friction, are $125x10^3$ lb. and $136x10^3$ lb. respectively with a proportionally increasing soil stiffness. These values are still double the maximum load that was applied to the pile.

It should be noted that the bending moments plotted in figure 6.4.2 indicate bending in the upper portion of the beam. This bending is in a number of half waves and although Francis et al

conclude that the pile is not buckling, the reason behind this bending has to be considered in some depth. A possible answer is that the bending moments are caused due to initial deflections in the pile, that is, that the pile is not absolutely straight. In that case even moderate loads would cause bending and the buckling load would be reduced from the theoretical minimum. It is interesting to note the similarity between the actual bending moments and those predicted if the friction model with a linearly increasing soil stiffness is used as seen in figure 6.4.2.

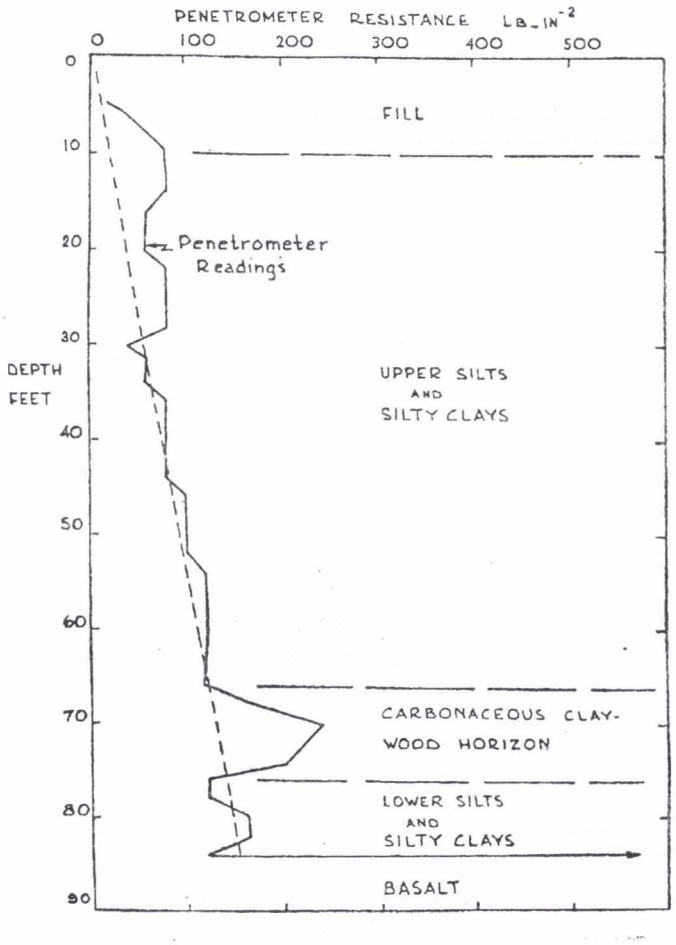

Figure 6.4.1. Soil strata at test-pile site (Francis et al, 1962).

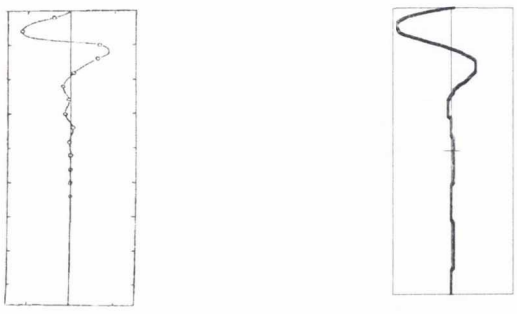

(a) *(b)*

Figure 6.4.2. (a) Measured and (b) predicted bending moment distribution for the pile.

In conclusion, the pile failed by bending. This bending was probably caused by the buckling load being approached for the initially non-straight beam. Unfortunately, there is not enough data to attempt to adjust the predicted buckling load for irregularities in the pile. This study indicates that the problem of pile buckling is more than just of academic interest.

6.4.2 Lee (1968)

Lee (1968) presented laboratory tests which were used to validate the results presented by Davisson and Robinson. As has already been shown, these results are approximately the same as those that are produced by using the algorithm outlined in this thesis. Several beams were tested in medium loose and dense sand for which values of $n_h = k/l$ were 9.3 lb/inch^3 and 60 lb/inch^3 respectively. The buckling load for a hollow aluminium tube of length 64 inches and stiffness EI=2950 lb.inch^2 embedded 33 inches into the medium loose sand (n = 9.3 lb/inch^3) was 50 lb. The buckling load for a steel rod length 62 $^1/_4$ inches and stiffness EI=23,400 lb.inch^2 embedded 33 inches into the dense sand (n_h = 60 lb/inch^3) was 280 lb. The unembedded end-condition was a pinned restraint and the only restraint for either lateral translation or rotation at the embedded end was provided by the soil. Unfortunately there was no information on either how the load in the pile or shaft friction varied with depth and so the way the buckling load varies according to the way in which the load in the pile varies will be discussed. Results using the method described in Chapter 3 are presented in table 6.4.1. Four theoretical models were used. The first is a model using the Euler buckling load for a pinned-fixed end-bearing beam with the fixed end-condition defined at the bottom of the pile. The second model is similar, except with the fixed end-condition defined at the soil-air interface. The third model has the load supported only in end-bearing at the bottom of the pile with soil stiffness varying with depth. The final model is a friction model with friction varying linearly with depth increasing from zero at the surface. This model was used as it assumes that the shaft friction varies in an identical manner to the soil stiffness as would normally be the case.

Pile	Actual Buckling Load (lb.)	Model 1 Buckling load (lb.)	Model 2 Buckling load (lb.)	Model 3 Buckling load (lb.)	Model 4 Buckling Load (lb.)
Aluminium Tube	50	14.54	61.97	49.02	49.03
Steel Rod	280	121.92	433.85	328.24	328.70

Table 6.4.1. Theoretical compared to Lee's experimental buckling loads.

As would be expected, the first two models under and over estimate the buckling load significantly. This is due to the buckling occurring in the unsupported section of the beam. The buckling loads for the aluminium tube are approximately with in 2% of each other. However, the calculated and test results for the steel rod are approximately 20% apart. If Lee's paper is examined the result for this particular buckling load also has the largest error from Davisson and Robinson, which suggests this reading may be affected by experimental errors.

The conclusion of this comparison between Lee's test and the exact theoretical solution, outlined in Chapter 2, is that the theoretical method is able to predict the buckling loads of the scale model Lee within experimental error.

6.4.3 Gouvenot (1975)

As described in chapter 2, Gouvenot (1975) instrumented and load tested three piles, two in peat and the third in soft clay. The concrete piles were 60mm in diameter with a central core of 20mm diameter steel reinforcement, giving a flexural stiffness, EI, of 8.0×10^9 N.mm^2. They were 4000mm in length. He produced experimental buckling loads for the three piles. These are compared to the theoretical buckling loads calculated by the author in table 6.4.2. The three theoretical loads are calculated on the following bases:-

(a) The buckling load of an end-bearing pile in a homogeneous soil with pinned-pinned end conditions as was used by Gouvenot and solved by Hetényi (1946).

(b) The buckling load of an end-bearing pile in a homogeneous soil with pinned-free end conditions.

(c) The buckling of a pinned-free pile which has three quarters of the load transferred to the foot, the rest being taken by a constant frictional force along the pile shaft in a homogeneous soil.

Soil Type	Soil stiffness N/mm^2	Experimental buckling load in kN	Theoretical buckling load (a) in kN	Theoretical buckling load (b) in kN	Theoretical buckling load (c) in kN
Peat	0.036	15	34	17	21
Peat	0.036	20	34	17	21
Soft Clay	0.090	40	56	27	35

Table 6.4.2. Theoretical compared to Gouvenot's experimental buckling loads.

The theoretical buckling load (a) can be seen to be a considerable over-estimate of the actual buckling load. Load (b) with a free embedded end condition is an under-estimate of the actual load. However, due to the change in load between (a) and (b) it can be concluded that the definition of the embedded end condition was a significant factor in the calculation of the buckling load, especially for the pile in soft clay. It should be noted that the mode shape predicted (figure 6.4.3) had a maximum amplitude at the base of the pile. The buckling load values for a pinned-free beam supported fully by shaft friction would be 51 kN and 76 kN for piles in peat and clay, respectively which are excessive. However, when the load transfer curves in Gouvenot are taken into account, approximately 25% of the applied load can be seen to be taken by an approximately constant shaft friction leading to results (c). These are of the same order as the measured buckling loads.

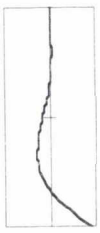

Figure 6.4.3. Predicted mode shape for a pinned-free end-bearing pile in soft clay.

The diagram in Gouvenot (figure 6.4.4) shows that there is a significant increase in the load in the pile in the bottom quarter of the pile embedded in clay. This is extraordinary as it indicates that there is some form of negative-skin friction. Normally it would be expected that negative-skin friction loads would occur at the top of the pile. This may indicate some problem in the instrumentation of the pile. This could affect the correlation between the theoretical and experimental buckling load by making the approximation of the amount of load supported by shaft friction inaccurate. If half the load

is assumed to be supported by a constant shaft friction the buckling load predicted by this author's method increases to 48.1 kN. Obviously, the experimental buckling load could be related to a degree of skin friction between 0.5 and 0.25. However, without reliable experimental data this is not a worthwhile exercise.

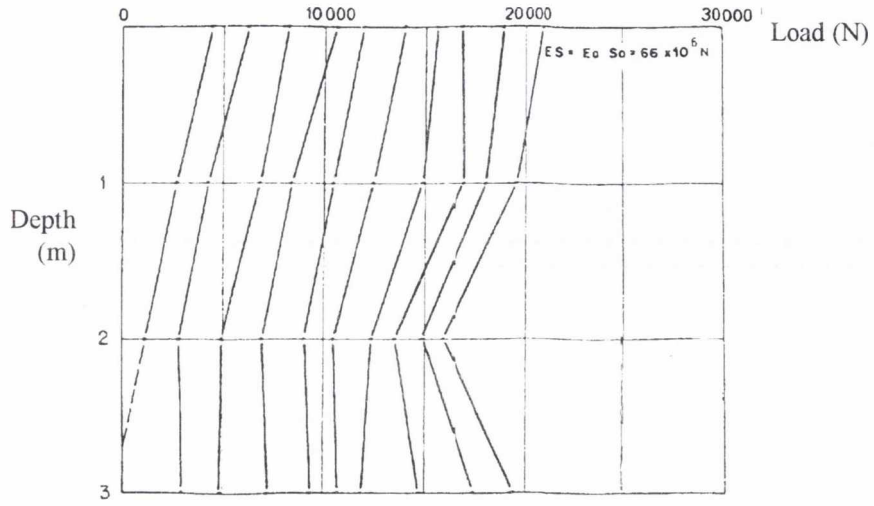

Figure 6.4.4. Load transfer curve for a pile in soft clay (Gouvenot, 1975).

To conclude the use of the method outlined by Hetényi predicted results that were greatly in excess of the experimental loads. If a design was based on such calculations this would be an unsafe method and hence, Gouvenot suggested a safety factor of 3 should be used. This was due to the requirement of using symmetrical end-conditions. Once a free end-condition is defined at the base of the pile, the method produces a safe method of design. However, the buckling mode shape is unrealistic, because there is a discontinuity in the soil medium immediately below the pile. An explanation for this could be that once the buckling load has been exceeded, buckling starts, and then a more complex form of failure occurs. This means that the buckling calculations outlined in this thesis is applicable, but the use of mode shapes indicating a discontinuity in the soil at the pile base should be applied with caution. More accurate predictions of the actual buckling load can be achieved, but rely on a knowledge of the variation of the shaft friction, which may not always be available, or reliable. In this particular case it would be appropriate to use either method (b) with no factor of safety or method (c) with a suitable factor of safety.

6.5. Alternative use of solution.

In Timoshenko and Gere (1961) the problem is presented of the buckling collapse of a unsupported beam column under its self-weight as in figure 6.5.1.

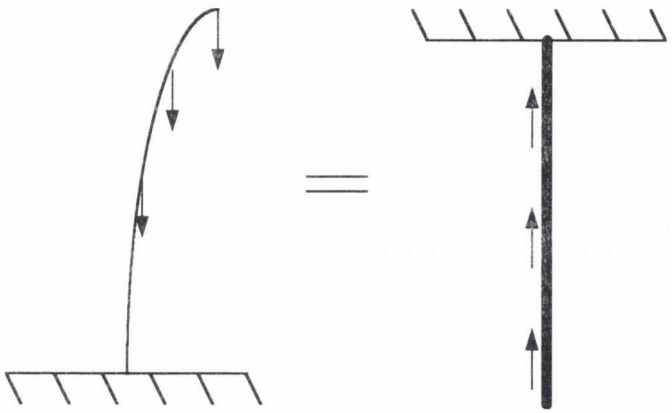

Figure 6.5.1. Beam buckling under self-weight and equivalent pile model.

The self weight of the beam can be modelled by the friction on the pile. This means that, with the current algorithm, two different configurations can be modelled. A constant shaft friction would be identical to a constant beam weight per unit length. Secondly, a linearly decreasing shaft friction with depth, for example, is the same as a beam whose weight per unit length decreases linearly with height above the ground. The soil stiffness in the above problem is zero.

Results are presented in Tomoshenko and Gere for the two cases outlined in figure 6.5.2 where the weight per unit length, q, and the critical buckling load are defined by,

$$q(x) = q_2\left(\frac{x}{l}\right)^p \qquad [6.5.1]$$

$$P_{cr} = \frac{mEI}{l^2} \qquad [6.5.2]$$

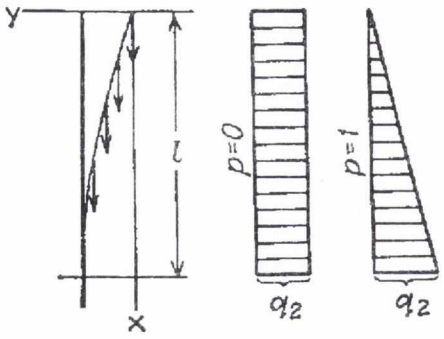

Figure 6.5.2. Beam buckling under self-weight.

The parameter m is quoted in Timoshenko and Gere as being equal to 7.84 when p = 0, and 16.1 when p = 1. When the algorithm described in Chapter 3 is used, the values determined are 7.8437 and 16.1137 respectively to 4 decimal places. This agrees with Timoshenko and Gere.

6.6. Conclusions

In this chapter the results of the author's work have been compared to results from other sources. The sources can be broadly separated into three groups. The first group are exact solutions to particular conditions considered in the main part of the thesis. The second are results from laboratory test and actual piles. The last grouping is that of different formulations of the problem which require the same analytical solution.

It can be seen in section 6.2, that the results obtained using the technique described in this thesis tend to the Euler solutions when the soil stiffness is reduced to zero. The results are identical to those formed by Hetényi for symmetrical end-conditions for fully embedded beams in homogeneous media. The work done by Davisson also agrees on the buckling loads determined in this thesis.

The work by Prakash provides an over-estimate of the buckling load when mode shapes that are not trigonometrical functions are predicted by this author's method. This is because the mode shape form was incorrectly assumed by Prakash in order to calculate the buckling load of end-bearing beams in non-homogeneous soils. The exact solutions and trends in mode shapes have been discussed previously in section 4.2.2. The results presented by Davisson and Robinson are broadly in line with the results presented in the earlier chapters. However, their choice of non-dimensional parameters lead to confusing graphs, where trends in buckling loads as the embedment ratio changes are very difficult to identify. The definition of the non-dimensional load parameter actually depends on the unembedded end condition. It appears that the predicted buckling loads can either be under or over-estimates of the exact method suggesting the work by Davisson and Robinson cannot be used to safely design piles against the possibility of collapse by buckling. Sharma and Prakash actually suggest using a non-dimensional buckling load parameter that over-estimates the buckling load! Fleming et al, who use a similar approach to Davisson and Robinson, discuss a simple method for the estimation of buckling loads of partially embedded piles. This method's predictions are again unsafe to use, especially at low embedment ratios or soil stiffnesses. The buckling loads predicted for high embedment ratios and soil stiffnesses are very conservative. In general, all the methods discussed have been found to lead to unsafe estimates for critical buckling loads in some circumstances.

The previous works in determining buckling loads have not considered the effect of the supporting medium on the mode shape produced. For instance, Davisson and Robinson assume that the depth the mode shape extends to reduces as the embedment ratio increases. It was shown, in Chapter 5, that this is not the case, as fully embedded piles can have mode shapes which extend further than those piles who are embedded for three quarters of their length. Modal clustering has not be considered previously and it has been shown that, for particular soil conditions, the second mode closely approaches the first.

The ability of the exact method outlined in Chapter 3 to predict the buckling loads of actual embedded structures has been discussed. The test reported by Francis et al indicates that the bending moment patterns predicted by the exact method occur in reality, although in this case the original authors state that buckling does not occur, evidence to the contrary can be seen. If buckling did occur then it shows that, with the information available, the use of a factor of safety of approximately two may be required to take into account the initial shape of the pile. Unfortunately there is not sufficient data in the published paper to determine what the exact behaviour of the pile was. The exact method has been used in the case of the results by Lee and Gouvenot to predict the buckling loads of real structures within experimental error, thus indicating the advantage of the exact method over previous approximate ones.

The use of these results for other applications is briefly outlined in the last section of this chapter. The results arise from the solution of a differential equation and so can be applied to any other problem which has the same governing equation. With moderate changes it would also be possible to create the analytically exact solution for other second order differential equations.

Chapter 7

Conclusions and further work

7.1. Conclusions

The problem of the buckling of the Bernoulli-Euler beams fully or partially embedded in an elastic Winkler foundation has been examined in depth in this thesis. Although, buckling is not generally thought of as one of the main criteria in the design of piles it has been shown that with certain soil conditions it is a possible failure mechanism. Previous research has provided only part solutions to the overall solution. An exact solution to the problem of the stability of fully and partially end-bearing and friction piles has been derived and the properties of such a solution have been investigated. This chapter will briefly restate the main simplifying assumptions used to determine the model used, the method used to produce the exact solution, the trends and characteristic behaviour of the said solution and, finally, the comparison between the theoretical solution and results taken from other authors' works, both theoretical and experimental.

7.1.1 The theoretical model

In Chapter 2 various soil models have been presented for the interaction between soil and structure. It was shown that the use of complicated models, with more than one soil parameter, are suspect when the ability to relate the model parameters to 'in situ' geotechnical properties is considered. In such circumstances, the one parameter elastic Winkler foundation is the appropriate model to utilise. Although it is attractive for the sake of simplicity to model a soil as a Winkler foundation with a constant stiffness with respect to depth it has been shown that it is, for certain soil conditions, especially sands, more realistic to allow a variation in the soil stiffness parameter. It would be expected that soil stiffness increases proportionally with such effects as the over-burden pressure and, hence, a model is proposed that allows for a linear variation of soil stiffness with depth. In later chapters the effect of this variation on the predicted buckling load and mode shape has been shown to be considerable.

It has long been accepted that the load applied to a pile is not always transferred in its entirety to the base of the pile. Frictional effects along the pile shaft can carry as much as 80% of the applied load. Such a load transfer would significantly affect the load that is required to produce buckling. It, therefore, cannot be ignored and the pile model has been defined in such a way that any

proportion of the applied load can be transferred to the surrounding soil through shaft friction. The shaft friction tends to vary with depth according to the same parameters as soil stiffness and the model allows this to be the case.

7.1.2 The solution to the buckling equations

In the following chapter, Chapter 3, the problem of the buckling of a fully or partially embedded pile has been solved. The problem was considered in two parts. The first part, that of the unembedded portion of the beam, has been solved previously by Euler. The behaviour of the embedded beam can be defined by a fourth order differential equation, with non-constant parameters for both end-bearing and friction beams. These governing equations for the embedded portion of the beam can be solved using an infinite power series solution. The recurrence equations which define the power series have been deduced. The problem can then be reduced to the determination of the eigenvalues and vectors for a 4x4 or 8x8 matrix for the fully and partially embedded problems respectively.

The computer algorithm used to calculate the results used an eigenvalue search method outlined in West (1993). Validation tests have been performed using a Finite-Element problem to compare with the computed results and a good correlation exists.

7.1.3 Fully embedded piles

Initially the results for an end-bearing pile fully embedded in a soil with constant soil stiffness with respect to depth below the ground surface are presented. This problem has been solved previously by Hetényi (1946) for symmetric end-conditions in a trigonometric/hyperbolic function form and it is shown that the results from the suggested algorithm are identical. For certain soil stiffnesses it is shown that modal clustering occurs when consecutive buckling modes have almost identical buckling loads. Along with this modal clustering there are unexpected changes in mode shape as soil stiffness increases. These phenomenon has previously been shown to appear in the vibrational problem of partially embedded beams. Hetényi's work may be expanded to predict these modal clusters for buckling in the homogeneous soil conditions for end-bearing piles with symmetric end-conditions. However, if the model under investigation has either non-symmetric end-conditions or

has a soil stiffness varying linearly with depth, it is no longer possible to predict the occurrence of modal clusters. In these cases the modes tend not to be clustered to such an extent as the symmetric end-condition with a homogenous soil case.

A popular method of using an average soil stiffness to model non-homogeneous soil conditions is found to be unsatisfactory. Not only can it significantly under-estimate buckling loads but it also predicts mode shapes which are clearly incorrect. Trends in the actual mode shapes have been discussed. The "effective length" of the mode shape in a non-homogeneous soil decreases and it would be expected that this would be associated with an increase in the buckling load. This increase does not occur because the large amplitudes of the mode shape occur in less stiff soils than for the homogeneous case, that is, in the upper half of the pile.

It has been generally predicted that the embedded end condition in the case of a non-homogeneous soil should not significantly affect the buckling load of a pile. However, if a free embedded end condition is defined, this can have the effect of significantly lowering the predicted buckling loads for end-bearing piles compared to a pinned or a fixed embedded end condition when the unembedded end condition is fixed (and to a lesser extent when it is pinned). Since the determination of the exact conditions at the pile base with respect to shear forces is of crucial importance this effect indicates that the use of the summary charts of buckling loads must be used with caution for an end-bearing beam. Although the mode shape for the free embedded end has its maximum amplitude at the bottom and, hence, indicates a discontinuity in the lateral support medium it may be incorrect to assume that the buckling load should not be used. The mode shape for a pinned or a fixed embedded end condition requires zero amplitude at the pile toe and, hence, the significantly lower buckling mode for the free embedded end indicates that any movement at the pile toe will reduce the buckling load. In the case of pile design it would be normal and safe to use a conservative estimate of the buckling load and, hence, assumptions of the ability of the pile toe to resist lateral movement (or indeed rotation) should not be used. Hence, the buckling load with a free embedded end should normally be used for design purposes.

The solutions to piles supported entirely by shaft friction in an homogeneous soil, with constant soil stiffness and shaft friction with depth, are presented next and although the use of modal

cluster prediction lines from the end-bearing solution are no longer applicable, modal clustering has been shown to occur, especially when there is a free end condition present. The predicted buckling loads are, as expected, higher than for the end-bearing case. This is due to an effective shortening of the pile length due to the reduction of the load in the pile in the lower portion of the pile.

Pure-friction piles in non-homogeneous soils were examined next. The non-homogeneity can take two forms; firstly as a variation of soil stiffness with depth, as before, and secondly as a variation in the shaft friction with depth. As in the case of end-bearing piles a linearly varying soil stiffness with depth decreases the buckling load compared to a constant soil stiffness. A linearly increasing shaft friction with depth also decreases the buckling load compared to a constant shaft friction because the load in the pile does not reduce as quickly with depth. In the case of changing the soil stiffness it appears that the wavelength of the halfwaves in the mode shape are increased. However, if the shaft friction is varied there is an increase in the "apparent length" of mode shape of the pile. This is associated with the reduction in the buckling load.

The last topic for discussion of fully embedded piles is that of the variation in buckling loads and mode shapes as the proportion of the load carried by the end-bearing is varied. The solution is bounded by the previous results, as $\mu = 1$ indicates the load is completely supported by end-bearing and $\mu = 0$ that the load is carried by pure shaft friction only. In the case of the fundamental mode it has been shown that the variation between the two extremes is normally approximately linear. However, in the case of a free end condition being present at the lower end of the beam it was shown that a buckling load associated with a mode shape with a maximum amplitude at the bottom varies approximately parabolically with decreasing μ. This mode is more significant in the homogeneous case than the non-homogeneous, as it will approach the first mode more closely for high μ in the former case. The mode shape is also significant in the case of fixed-free or pinned-free where it is the fundamental mode for piles which approach end-bearing conditions for a wide range of soil stiffnesses.

It was finally shown that buckling loads for partly homogeneous soils, ones where either the soil stiffness or shaft friction are non-homogeneous, but not both, can be estimated by the use of

interpolation of the end-bearing and pure-friction results. This completes the investigation of fully embedded pile.

7.1.4 Partially embedded piles

Results are presented for the effect of the variation in the proportion of the pile actually embedded in the supporting medium. The problem is again split into those of end-bearing and pure friction support of the applied load, and homogeneous and non-homogeneous soil conditions.

The solution to end-bearing piles were initially considered and the results for symmetric end-conditions in homogeneous soil plotted. It was shown that, surprisingly, as the embedment ratio increases the embedded boundary condition can produce a limit on the buckling loads predicted. It was shown that for homogeneous soil conditions that the buckling loads with non-symmetric end-conditions could be approximated by using the lower of the solutions to the case where the bottom boundary condition was fixed and the solution to the fully embedded problem with the actual end boundary conditions. This method is only of limited interest as a similar technique is not applicable to the other sets of soil conditions. For certain end-conditions and moderate to high soil stiffnesses, the buckling loads at high embedment ratios tend to remain constant and, so, on contour plots they appear as plateaux. These plateaux are associated with buckling mode shapes which extend past the soil-air interface almost to the bottom of the pile. The plateaux described in the homogeneous case for high embedment ratios are no longer found in the non-homogeneous partially embedded end-bearing case. However, in both homogeneous and non-homogenous soils when the embedded end condition is free a mode shape with a maximum amplitude at the pile toe once more occurs when the unembedded end condition is not also free. This mode shape can only occur as the fundamental mode when more than half the pile is unembedded. For other embedment ratios it was shown to occur, at the same buckling load, but for modes higher than the fundamental.

In the case of pure-friction beams it has been concluded that, apart from low soil stiffness and low embedment ratios, the solutions can be used without consideration of the embedded boundary condition. In the case of a homogeneous soil, where the shaft friction and soil stiffness are constant with depth, the buckling load and mode shapes are very similar to those for the end-bearing case

except for embeddment ratios approaching unity. This is when the end-bearing homogeneous buckling loads form the plateau with buckling loads approximately the same as the fully embedded case.

In the case of a non-homogenous soil it was found that the results, in terms of buckling load and mode shape, of the end-bearing and pure friction support cases are also very similar. As would be expected the frictional support produces slightly higher buckling loads. This means that for conciseness only the end-bearing results need to be initially looked at, as these also will provide an under-estimate for the buckling loads of the frictional results.

7.1.5 Comparison with other published results

Previous work that derived exact solutions for part of the problem considered in this thesis has been compared to the algorithm suggested in Chapter 3. The results have been found to be identical. The buckling loads that have been put forward by some other authors have been found either to be difficult to use or in some cases actually predict theoretical buckling loads which are excessive. This would lead to the possibility of unsafe design and pile failure. The previous work tends not to consider modes higher than the first and, hence, have not found the evidence of modal clustering. Although this is not as important as in the vibrational problem, mode clustering could be dangerous if a design strategy was considered that tried to inhibit the lower mode, or modes, in order to increase the stability of a pile design. The effect of the soil stiffness on the predicted mode shape has only been considered in the homogeneous end-bearing problem, (in Hetényi). It was shown, in Chapter 5, that this is not consistent with some methods of buckling load determination where the extent of the buckling mode shape down the pile is used to determine the buckling load.

A limited comparison of the predicted buckling load and mode shapes is undertaken with real piles, either scale models or full-size. Although limited by the data that can be determined from several published works, the proposed method is found to predict the actually buckling loads within experimental error. It is also found to be a more consistent method than those proposed by other authors where a safety factor is used on the simple solution found in Hetényi.

7.2. Further work

The algorithm, outlined in Chapter 3, takes the form of the determination of the eigenvalues and vectors of a transient non-symmetric matrix. This can be expanded to the solution of almost any differential equation and, hence, the ability to perform similar work is almost boundless. All that is required is to determine a problem which can be defined by a suitable differential equation. for example the stability of a flag pole (with constant flexural rigidity) under its own weight.

In the civil engineering field, however, the present work can be expanded in a number of ways. Concentrating on the buckling of piles it would be relatively straightforward to adjust the algorithm to allow for the variation of either soil-stiffness or the shaft friction to be defined by any differentiable function, although initially polynomial expressions would be sensible. Although this is possible, it should be remembered that the determination of soil stiffness coefficients 'in situ' is so difficult that such a refinement would probably not supply any significant new information. It should also be able to provide the Winkler model with a spring stiffness which can vary according to the amount of deflection, i.e. a non-linear response. Again, the requirement would be for the defining function to be differentiable. On the other hand it is equally plausible to produce a layered model, where for instance, the soil stiffness is modelled as linearly increasing to a certain depth and then constant further down. It is possible to a similar layered model with respect to the way the shaft friction is defined on particular beam sections. It could be interesting to investigate if shaft friction affects the buckling load of partially embedded piles which have an applied lateral load at the pile head. It should be remembered that the solution provides terms for shear force and bending moment at any point along the beam so it could be possible to define applied shear forces and moments at the pile head and investigate the stability of the fully or partially embedded model. On a similar basis the shear force at the pile toe could be varied in order to investigate the elimination of the mode shapes which produces a discontinuity in the soil medium at the pile toe. These problems require that zero vector in the matrix equation [3.4.1] in chapter 3 is replaced with a non-zero vector.

Other additional work that would be appropriate is more experimental in nature. It may be in the form of model tests in order to validate the underling theory and assumptions. Other work might

be full scale tests in order to correlate the predicted and actual buckling strengths of piles. It would also be possible to produce a in-situ test of the strength of soil based on the ability to buckle thin piles, however, because the installation process tends to disturb the soil medium such a test might be unreliable.

Bibliography

A.I.S.I. (1975), 'Steel pile load test data', *American Iron and Steel Construction*, 400 N. Michigan Ave., Chicago, IL, 60611.

Atkinson J.K. (1973). *'The deformation of undisturbed London clay'*, Ph.D. Thesis, University of London.

API (1984), API recommended practice for planning, designing and constructing fixed offshore platforms, 15/e, *American Petroleum Institute*, API RP2A, 115 pp.

Baldi G. et al (1981), 'Cone resistance in dry NC and OC sands', *Proc. Session: Cone Penetration Testing and Experience, ASCE*, 145-177.

Beaufait, F.W. and Hoadley, P.W. (1980), 'Analysis of elastic beams on non-linear foundations', *Comp. Struct.*, 12, 669-676.

Borland Int. Inc. (1985), *'Turbo Pascal: Reference Manual'*, Ver. 6.0, California.

Bond A.J. (1989), *'Behaviour of displacement piles in overconsolidated clays'*, Ph.D. Thesis, Univ. of London (Imperial College).

Boussinesq J., (1883), *'Application des potentials a l'etude de l'equilibre et due mouvement des solides elastique'*, Gautier-Villars, Paris.

Bowles J.E. (1988), *'Foundation Analysis and Design'*, McGraw-Hill, Inc., Singapore.

Briaud J.L. and Tucker L.M. (1988), *'Measured and predicted axial response of 98 piles'*, J. Geotech. Eng. ASCE, 114 (9), 984-1001.

Burland J.B. (1973), 'Shaft friction piles in clay - A simple fundamental approach', *Ground Engng.*, Vol. 6, No. 3, 30-42.

Burland J.B., Broms B.B., and De Mello, V.F.B. (1977), 'Behaviour of foundations and structures', *Proc. 9th Int. Conf. Soil Mech. Found. Engng.*, Tokyo, Vol. 2, 495-546.

Casagrande A. (1948), 'Classification and Identification of soils', *Trans. ASCE*, Vol. 113, 901-991.

Collar A.R. and Simpson A. (1987), *'Matrices and Engineering Dynamics'*, Ellis-Horwood, Chicester.

Coyle H.M. and Reese L.C. (1966), 'Load transfer of axially loaded piles in clay', *J. Soil Mech. Found. Div., ASCE*, Vol. 92 SM 2, March, 1-26.

D'Appolonia E. and Romualdi J.P. (1963), 'Load Transfer in end bearing steel H-piles', *J. Soil Mech. Found. Engng., ASCE*, Vol. 89, SM 2, 1-26.

D'Appolonia E. (1968), 'Load transfer-Pile clusters', *Proc. lecture series on found. Engng.* Northwestern Univ., 93-152.

Davisson M.T. (1963), 'Estimating buckling loads for piles', *Proceedings, 2nd Pan American Conference on Soil Mechanics and Found. Engng*, Brazil, Vol. 2, 351-369.

Davisson M.T. and Gill H.L. (1963), 'Laterally loaded piles ina layered soil', *Proceedings of ASCE, ASCE*, SM 3.

Davisson M.T. and Robinson K.E. (1965), 'Bending and buckling of partially embedded piles', *Proceedings of the 6th Int. Conf. on Soil Mech. and Found. Engng.*, Vol. 2, 243-246.

Eisenberger M. and Clastornik J. (1987), 'Vibrations and buckling of beams on variable Winkler elastic foundation', *J. Sound Vib.*, 115(2), 233-241.

Eisenberger M. and Clastornik J. (1987), Beams on variable two-parameer elastic foundation', *J. Engng. Mech., ASCE*, 113, 10, 1454-1467.

Essenger F. (1962), 'Shear deformation in beams on elastic foundations', *J. Appl. Mech.*, ASME, 29(2), 313-317.

Filonenko-Borodich M.M. (1940), *'Some approximate theories of the elastic foundation'*, Uchenyie Zapiski Moskovskogo Gosudarstvennogo Universiteta Mekhanuca, 46, 1040, 3-18.

Fleming W.G.K., Weltman A.J., Randolph M.F. and Elson W.K. (1992), *'Piling Engineering'*, Blackie Academic and Professional, Glasgow and London.

Francis A.J., Savory N.R., Stevens L.K. and Trollope D.H. (1962), 'The behaviour of slender point-bearing piles in soft clay', *Proceedings Univ. Hong Kong Golden Jubilee Congress*, 25-50.

Garassino A., Jamilolkoowshi M. and Pasqueline E. (1976), 'Soil modulus for laterally loaded piles in sands and NC clays', *Proc. 6th European Conf. Soil Mech. Found. Engng.*, Vienna, Vol. 2, 429-434.

Gibson R.E. (1973), 'The analytical method in soil mechanics', *Geotechnique*, 24, 115-140.

Guvenot D. (1975), 'Essais de chargement et de flambement de pieux aiguilles', *Annales de l'Institut Technique du Batiment et des Travaux Publics*, 334, 25-39.

Hetényi M. (1946), *'Beams on elastic foundations'*, The Univ. of Michigan Press, Ann Arbor, Michigan.

Hetényi M. (1966), 'Beams and plates on elastic foundations and related problems', *Appl. Mech. Review*, 19, 2, 95-102.

Horvath J.S. (1983), 'New subgrade model applied to mat foundations', *J. Geotech. Engng., ASCE*, 10, 12, 1567-1587.

Howatson A.M., Lund P.G. and Todd J.D. (1972), *'Engineering tables and data'*, Chapman and Hall, London and New York.

Janbu N. (1976), 'Static bearing capacity of friction piles', *Proc. 6th European Conf. on Soil Mech. Found. Engng.*, Vol. 1.2, 479-488.

Kerr A.D. (1961), 'Viscoelastic Winkler foundation with shear interactions', *Proc. ASCE*, 87, EM 3, 13-20.

Kerr A.D. (1964), 'Elastic and viscoelastic foundation models', *J. Appl. Mech., ASME*, 41, 4, 491-498.

Kerr A.D. (1985), 'On the determination of foundation soil parameters', *J. Geotech. Engng. Div., ASCE*, 111, 1334-1340.

Klohn E.J. and Hughes G.T. (1964), 'Buckling of long unsupported timber piles', *J. Soil Mech. Found. Div., ASCE*, 90, SM 6, 107-123.

Kneifati M.C. (1985), 'Analysis of plates on a Kerr foundation', *J. Engng. Mech., ASCE*, 111(11), 1325-1342.

Lawther R. and Kabaila A.P. (1982), 'Modification of the power method for determination of eigenvalues', *Proc. 4th Int. Conf. on Finite Elements in Aust.*, Univ of Melbourne.

Lee K.L. (1968), 'Buckling of partially embedded piles in sand', *J. Soil Mech. and Found. Div., ASCE*, 94, SM 1, 255-270.

Mansur C.I. and Kaufman R.I. (1956), 'Pile tests, low-sill structure Old River La.', *J. Soil Mech. Found. Div., ASCE*, 82, SM 4, Paper 1079.

McClelland B. and Focht J.A. (1956), 'Soil modulus for laterally loaded plates', *Trans. ASCE*, 123, Paper No. 2954, 1049-1086.

Mendel J. (1936), 'Flambage au sein d'un milieu élastique', *Annales des Ponts et Chaussées*, No. 9, 295-335.

Meyerhof G.G. (1956), 'Penetration tests and bearing capacity of cohesionless soils', *J. Soil Mech. Found. Div., ASCE*, 82, SM 1, 1-19.

Meyerhof G.G (1976), 'Bearing capacity and settlement of pile foundations', *J. Geotech. Engng. Div., ASCE*, 102 GT 3, 195-228.

Mohan D., Jain G.S. and Kumar V. (1963), 'Load bearing capacity of piles', *Geotechnique*, 13, 1, 76-86.

Nordlund R.L. (1965), 'Bearing capacity of piles in cohesionless soils', *J. Soil Mech. Found. Div., ASCE*, 89, SM 3, 1-36.

Pasternak P.L. (1954), 'On a new method of analysis of an elastic foundation by means of two foundation constants', *Gorsudurstvennue Izdateestvo Literature po Stroitelstvui Arkhitekture*, Moscow.

Pavlović M.P. and Tsikkos S. (1982), 'Beams on quasi-Winkler foundation', *Engng. Struct.*, 4, 113-118.

Poulos H.G. (1989), 'Pile behaviour - theory and application', *Geotechnique*, 98, 3, 365-415.

Poulos H.G. and Mattes N.S. (1969), 'The behaviour of axially loaded end-bearing piles', *Geotechnique*, 19, No.2, 285-300.

Prakash S. (1987), 'Buckling loads of fully embedded piles', *Int. J. Computer Geotech.*, 4, 61-83.

Prakash S. and Sharma H.D. (1989), *'Pile foundation in engineering practice'*, John Wiley & Sons.

Reddy A.S. and Valsangkar A.J. (1970), 'Buckling of fully and partially embedded piles', *J. Soil Mech. Found. Div., ASCE*, 96, SM6, 1951-1965.

Reese L.C., Cox W.R. and Koop F.D. (1974), 'Analysis of laterally loaded piles in sand', *Proc. 6th Offshore Tech. Conf.*, Houston, Texas, Paper No. 2080, 473-483.

Reissner E. (1936), 'A note on deflections of plates on a visco elastic foundation', *J. Appl. Mech., ASME*, 25, 144-145.

Schwarz H.R., Rutishauser H., and Stiefek E. (1973), *'Numerical analysis of symmetric matrices'*, Prentice -Hall Series, New Jersey.

Selvadurai A.P.S. (1979), *Elastic analysis of soil foundation Interaction*, Elsevier, Amsterdam.

Sutherland H.B. (1974), 'Granular materials', *'BGS Conf. on Settlement of structures'*, Pentech Press, Cambridge.

Terzaghi K. (1955), 'Evaluation of coefficients of subgrade reaction', *Geotechnique*, 5, 297-326.

Terzaghi K. and Peck R.B. (1948), 'Stress in concrete pavements computed by theoretical analysis', *Publ. Rds.*, 7, 25.

Thorburn S. and Macvicar R. (1971), 'Pile load test to failure in the Clyde alluvium', *Proc. Conf. on Behaviour of Piles, ICE*, 1-8.

Timoshenko S.P. and Gere J.M. (1961), *'Theory of elastic stability'*, McGraw Hill Ltd., Tokyo.

Tomlinson M.J. (1971), 'Some effects of pile driving on skin friction', *Proc. Conf. on Behaviour of Piles, ICE*, 107-114.

Tomlinson M.J. (1987), *'Pile design and construction practice'*,Viewpoint, London.

Tomlinson M.J. (1995), *'Foundation design and construction* ', Longman Ltd., Singapore.

Vesic A.B. (1963), 'Beams on elastic subgrade and Winkler hypothesis', *Proc. 5th Intnl. Conf. Soil Mech. Found. Engng.*, Paris, Vol. 1, 845-850.

Vesic A.S. (1975), *'Principles of pile foundation design'*, Soil Mech. Series No. 38, School of Engng., Duke University, 48.

Vesic A.S. (1977), *'Design of pile foundations'*, NCHRP Synthesis of Practice No. 42, Transportation Research Board, Washington D.C., 68.

Vijayvergiya V.N. and Focht J.A. (1972), 'A new way to predict capacity of piles in clay', *OTC Paper 1718, 4th Offshore Technology Conf.*, Houston, TX.

Vlaslov V.L. and Leontiev N.H. (1956), *'Beams, plates and shells on elastic foundations'*, Fizmatgiz, Moscow.

West R.P. (1991), *'Modal clustering in th vibration of beams partially embedded in a Winkler foundation'*, Ph.D. Thesis, University of Dublin, Trinity College, Ireland.

West R.P. and Pavlović M.N. (1993), *'A fast iterative algorithm for eigenvalue determination'*, Developments in Computaional Engng. Mech., edited B.H.V. Topping, Civil-Comp Press, 229-236.

Whitaker T. and Cooke R.W. (1966), 'An investigation of the shaft and base resistances of large bored piles in London clay', *Proc. Conf. Large Bored Piles, ICE*, London, 7-49.

Winkler E. (1867), *'Theory of elasticity and strength'*, Verlag H. Dominikus, Prague.

Wittrick W.H. and Williams F.W. (1973), 'A general algorithm for computing natural frequencies of elastic structures', *Quart. J. Mech. and Applied Math.*, 24, 263.

Yankelevsky D.Z. and Eisenberger M. (1986), 'Analysis of a beam column on an elastic foundation', *Comp. and Struct.*, Vol. 23, 3, 351-356.

Yoshida I. and Yoshinaka R. (1972), 'A method to estimate modulus of horizontal subgrade reaction for a pile', *Soil and Found.*, Tokyo, Japan, 12, 3, 1-17.

Appendix A

Buckling loads of fully embedded beams

This appendix can be looked upon as providing the data by which the buckling load of all fully embedded piles whatever the end-conditions or soil conditions can either be found or closely approximated by methods outlined in the body of the thesis.

In section A.1 the contour plots are for fully embedded piles with a soil stiffness parameter $0 < \lambda < 300$. They are plotted for two soil conditions; homogeneous with constant soil stiffness ($F = 1$) and shaft friction ($f_1 = f_2 = 0.5$) and non-homogeneous with triangular soil stiffness ($F = 0$) and triangular shaft friction ($f_1 = 0$, $f_2 = 1$). All possible combinations of end-conditions are considered because the soil conditions above are the most often encountered.

In section A.2 the buckling loads for $0 < \lambda < 50$ are plotted for all end-conditions and all soil conditions. They have been plotted because at low soil stiffness the behaviour of piles is more complicated than at higher soil stiffness $\lambda > 50$, and the use of the approximate methods outlined for higher soil stiffnesses can be prone to error.

The approximate methods for the less common soil conditions and higher soil stiffnesses require the use of buckling loads with a fixed-embedded end. These are plotted for the remaining soil conditions in section A.3.

Appendix A.1

Homogeneous soils (F = 1, $f_1 = f_2 = 0.5$)

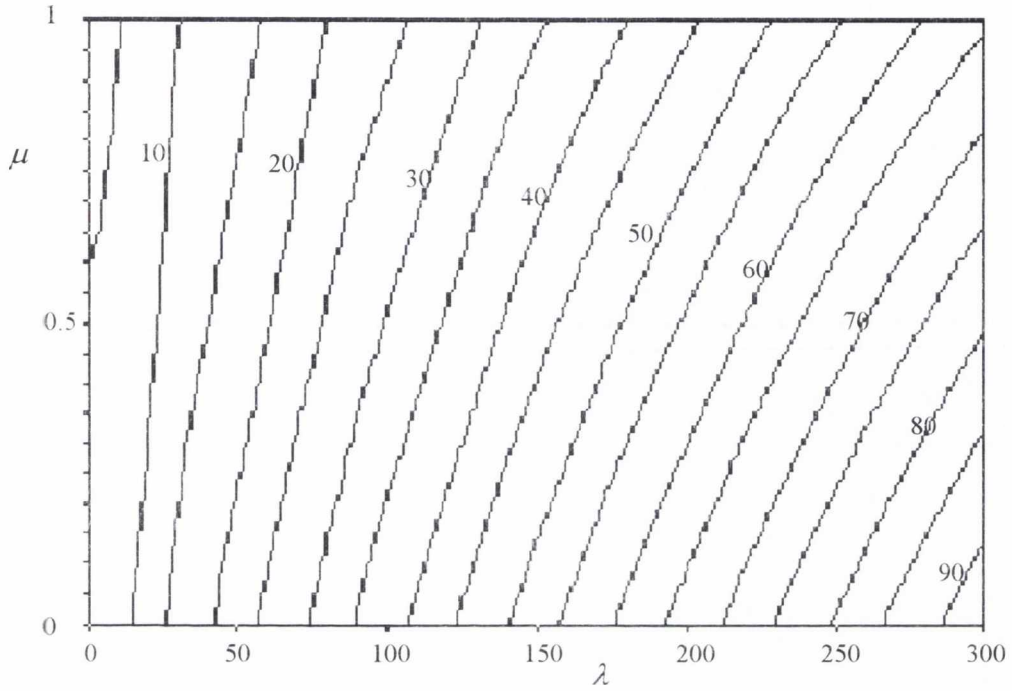

Figure A.1.1. Buckling load (P_{cr}/P_E) contours for the first mode in a homogeneous soil with constant soil stiffness (F = 1) and constant shaft friction ($f_1 = f_2 = 0.5$) for a fixed-fixed fully embedded beam.

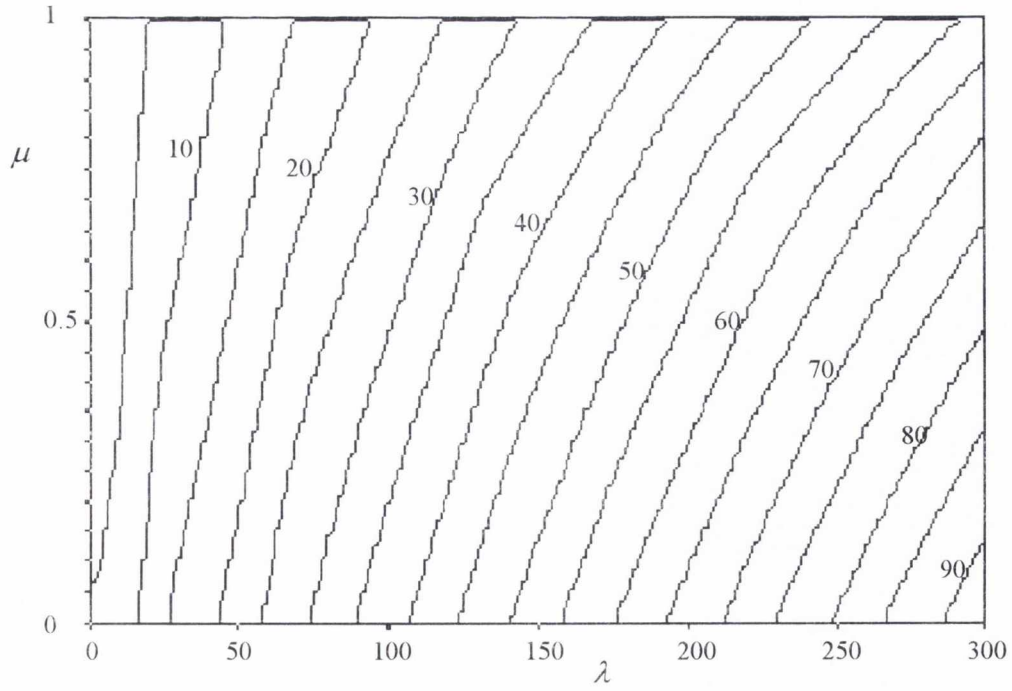

Figure A.1.2. Buckling load (P_{cr}/P_E) contours for the first mode in a homogeneous soil with constant soil stiffness (F = 1) and constant shaft friction ($f_1 = f_2 = 0.5$) for a fixed-pinned fully embedded beam.

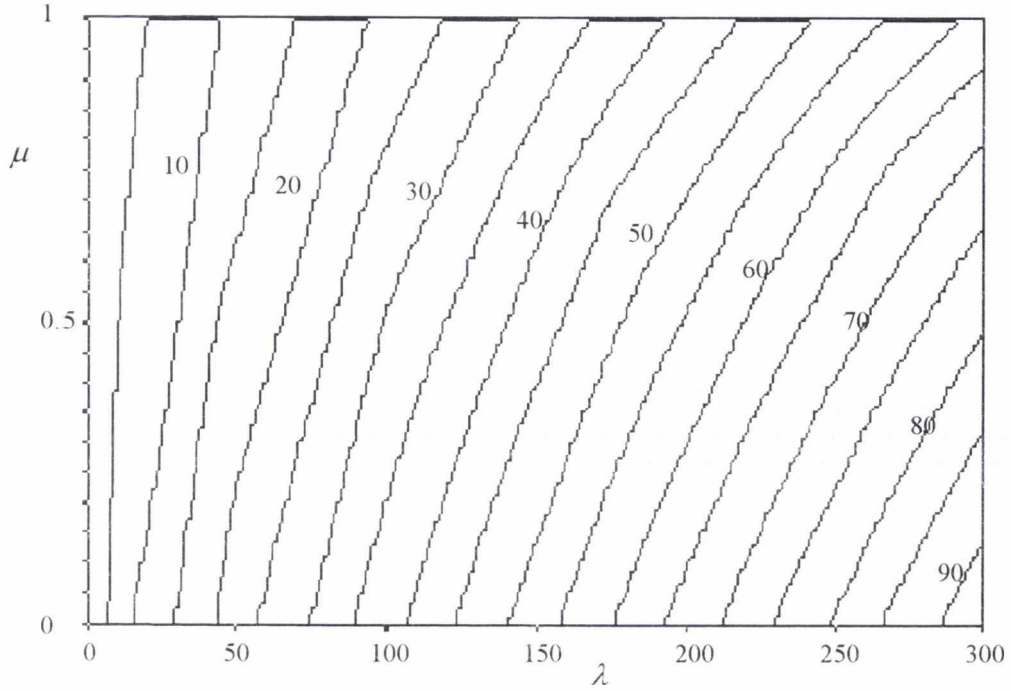

Figure A.1.3. Buckling load (P_{cr}/P_E) contours for the first mode in a homogeneous soil with constant soil stiffness ($F = 1$) and constant shaft friction ($f_1 = f_2 = 0.5$) for a fixed-no rotation fully embedded beam.

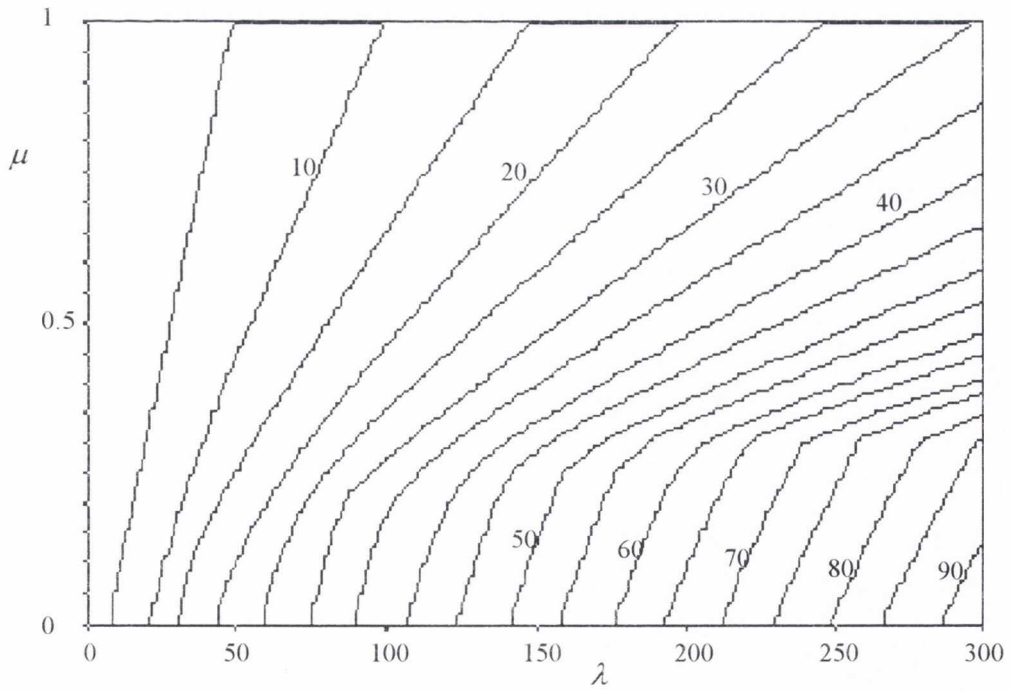

Figure A.1.4. Buckling load (P_{cr}/P_E) contours for the first mode in a homogeneous soil with constant soil stiffness ($F = 1$) and constant shaft friction ($f_1 = f_2 = 0.5$) for a fixed-free fully embedded beam.

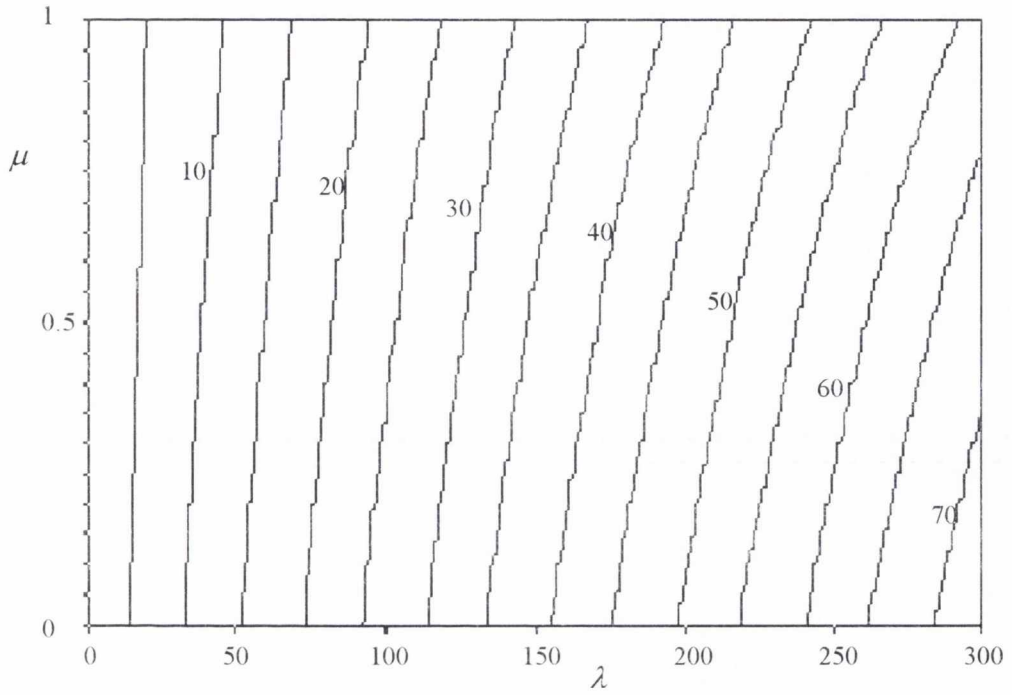

Figure A.1.5. Buckling load (P_{cr}/P_E) contours for the first mode in a homogeneous soil with constant soil stiffness ($F = 1$) and constant shaft friction ($f_1 = f_2 = 0.5$) for a pinned-fixed fully embedded beam.

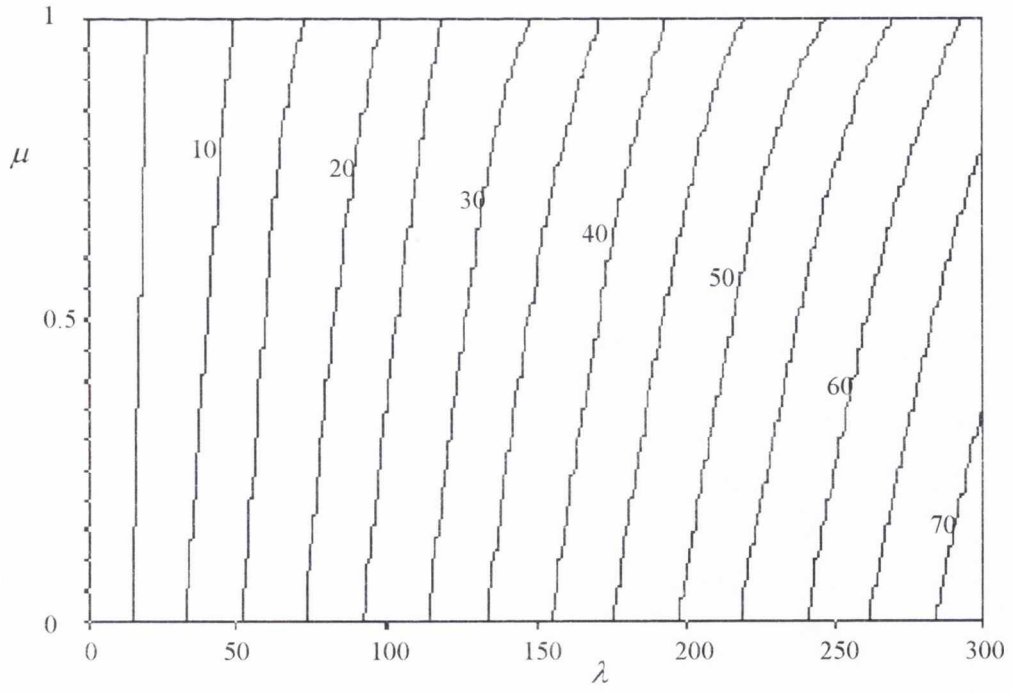

Figure A.1.6. Buckling load (P_{cr}/P_E) contours for the first mode in a homogeneous soil with constant soil stiffness ($F = 1$) and constant shaft friction ($f_1 = f_2 = 0.5$) for a pinned-pinned fully embedded beam.

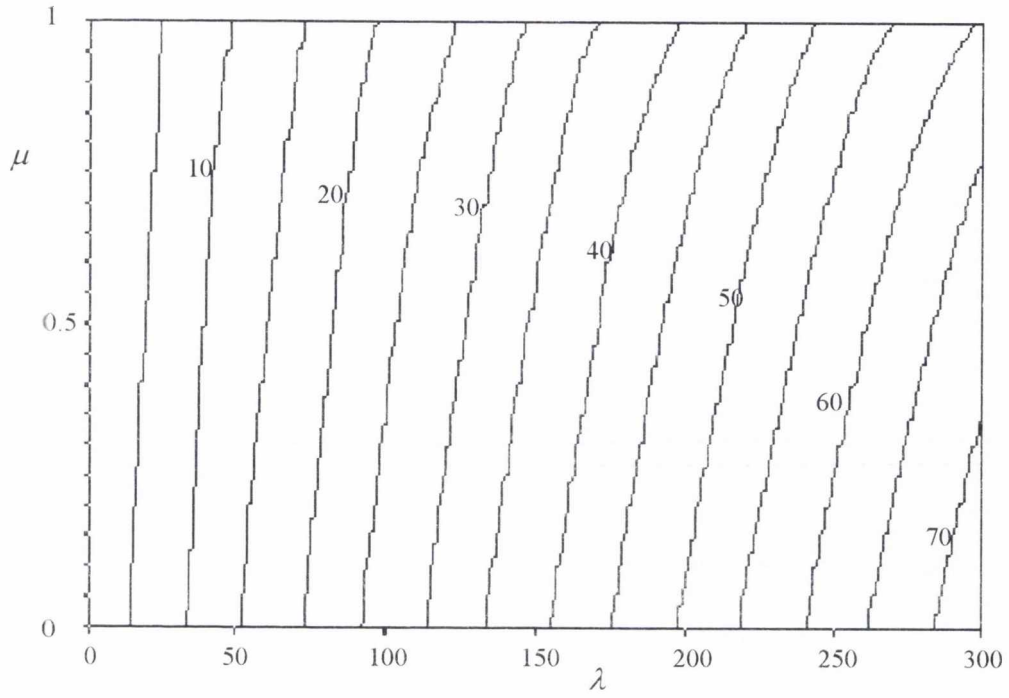

Figure A.1.7. Buckling load (P_{cr}/P_E) contours for the first mode in a homogeneous soil with constant soil stiffness ($F = 1$) and constant shaft friction ($f_1 = f_2 = 0.5$) for a pinned-no rotation fully embedded beam.

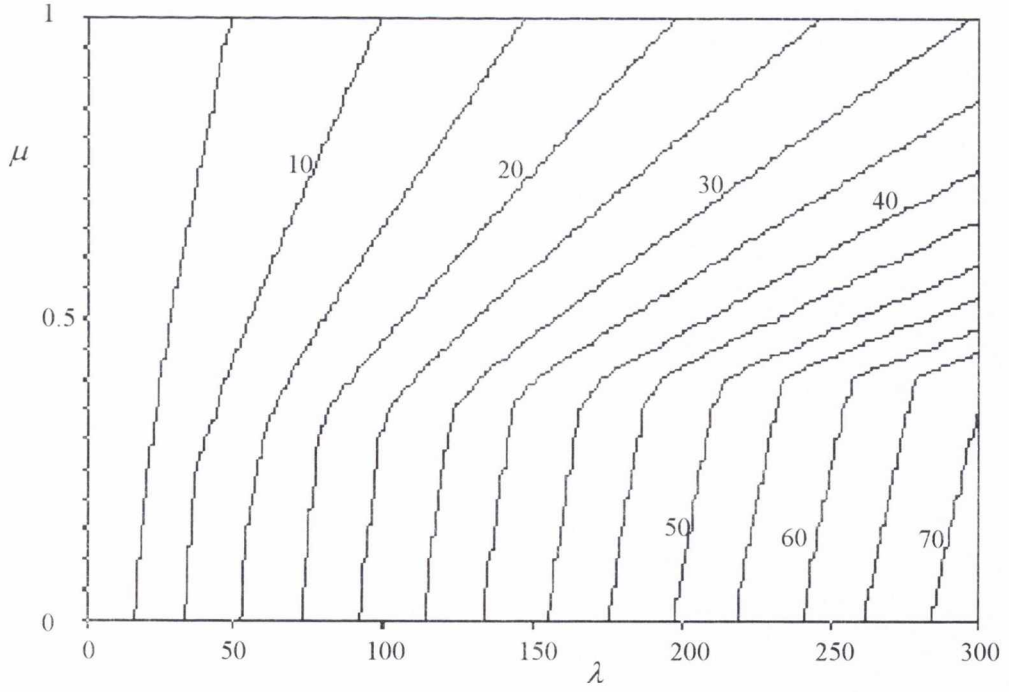

Figure A.1.8. Buckling load (P_{cr}/P_E) contours for the first mode in a homogeneous soil with constant soil stiffness ($F = 1$) and constant shaft friction ($f_1 = f_2 = 0.5$) for a pinned-free fully embedded beam.

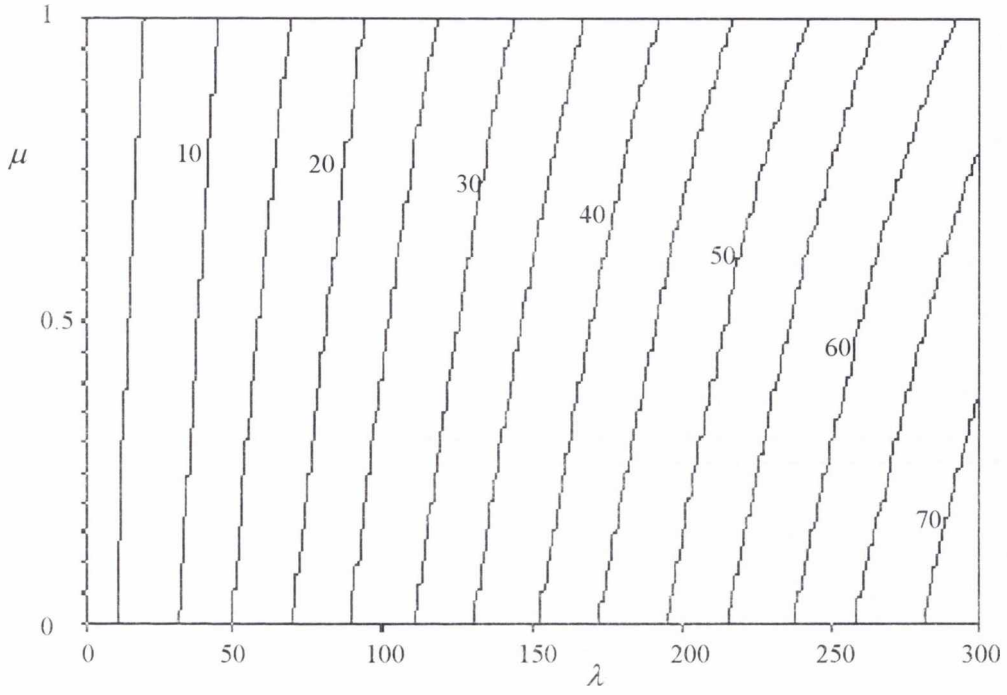

Figure A.1.9. Buckling load (P_{cr}/P_E) contours for the first mode in a homogeneous soil with constant soil stiffness ($F = 1$) and constant shaft friction ($f_1 = f_2 = 0.5$) for a no rotation-fixed fully embedded beam.

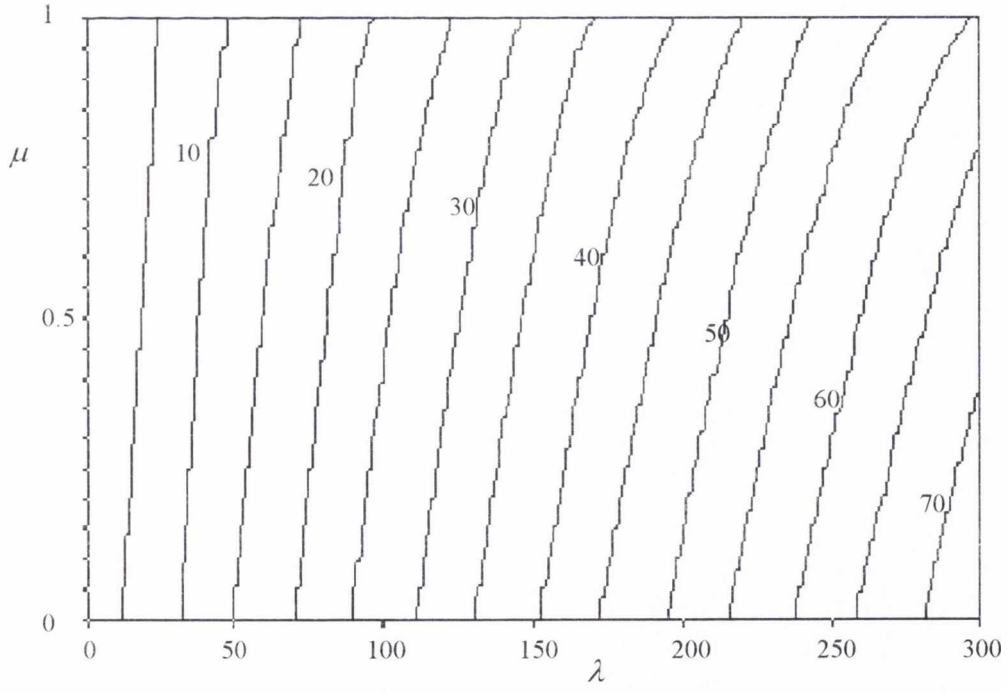

Figure A.1.10. Buckling load (P_{cr}/P_E) contours for the first mode in a homogeneous soil with constant soil stiffness ($F = 1$) and constant shaft friction ($f_1 = f_2 = 0.5$) for a no rotation-pinned fully embedded beam.

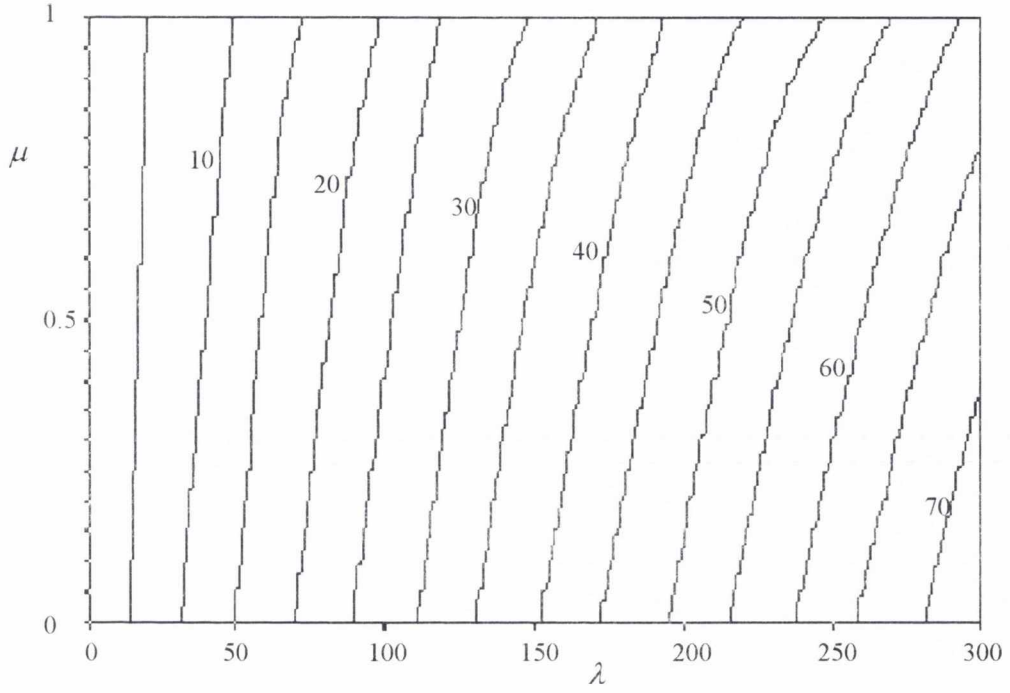

Figure A.1.11. Buckling load (P_{cr}/P_E) contours for the first mode in a homogeneous soil with constant soil stiffness ($F = 1$) and constant shaft friction ($f_1 = f_2 = 0.5$) for a no rotation-no rotation fully embedded beam.

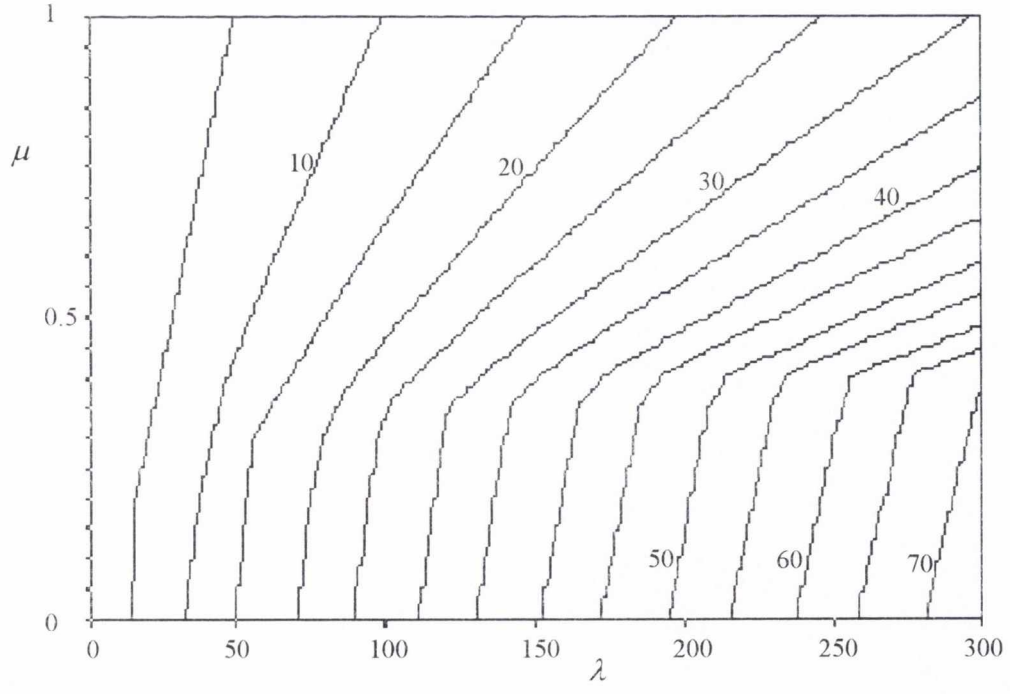

Figure A.1.12. Buckling load (P_{cr}/P_E) contours for the first mode in a homogeneous soil with constant soil stiffness ($F = 1$) and constant shaft friction ($f_1 = f_2 = 0.5$) for a no rotation-free fully embedded beam.

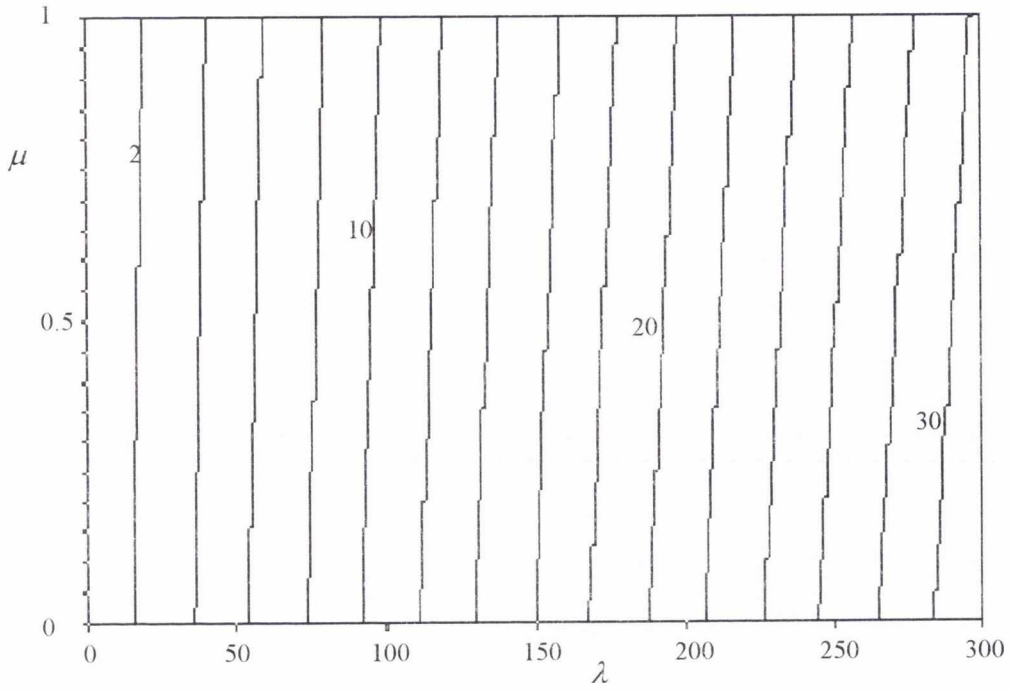

Figure A.1.13. Buckling load (P_{cr}/P_E) contours for the first mode in a homogeneous soil with constant soil stiffness ($F = 1$) and constant shaft friction ($f_1 = f_2 = 0.5$) for a free-fixed fully embedded beam.

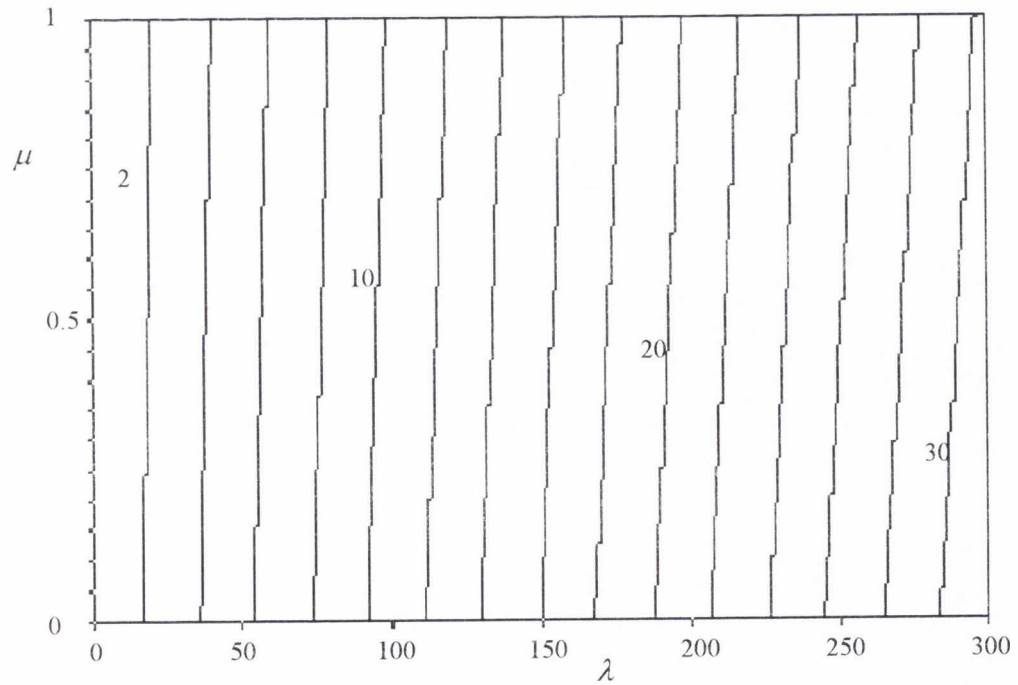

Figure A.1.14. Buckling load (P_{cr}/P_E) contours for the first mode in a homogeneous soil with constant soil stiffness ($F = 1$) and constant shaft friction ($f_1 = f_2 = 0.5$) for a free-pinned fully embedded beam.

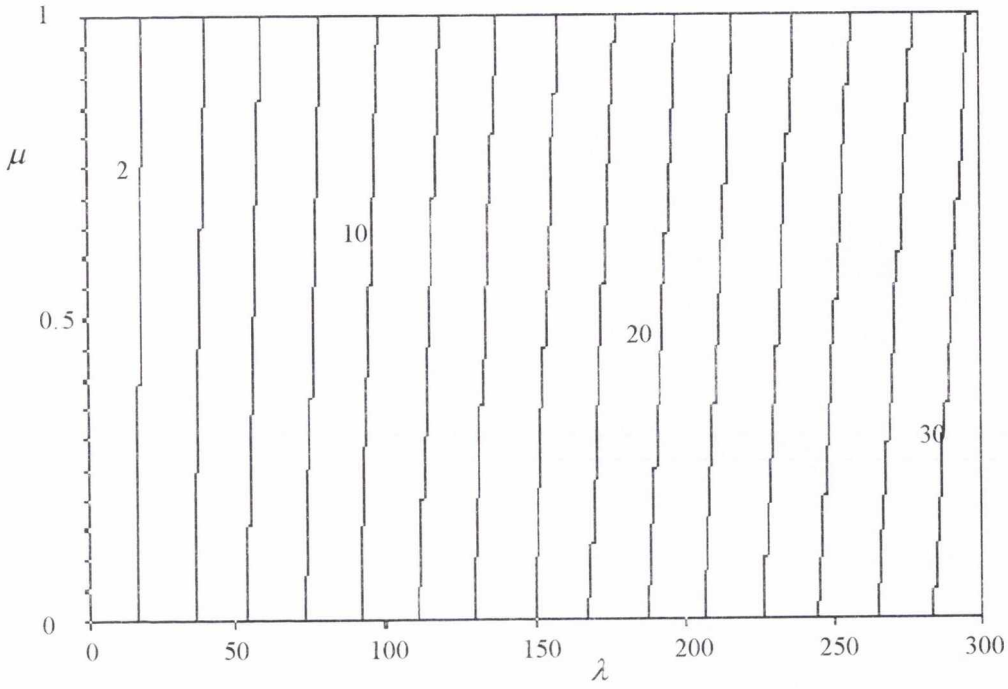

Figure A.1.15. Buckling load (P_{cr}/P_E) contours for the first mode in a homogeneous soil with constant soil stiffness ($F = 1$) and constant shaft friction ($f_1 = f_2 = 0.5$) for a free-no rotation fully embedded beam.

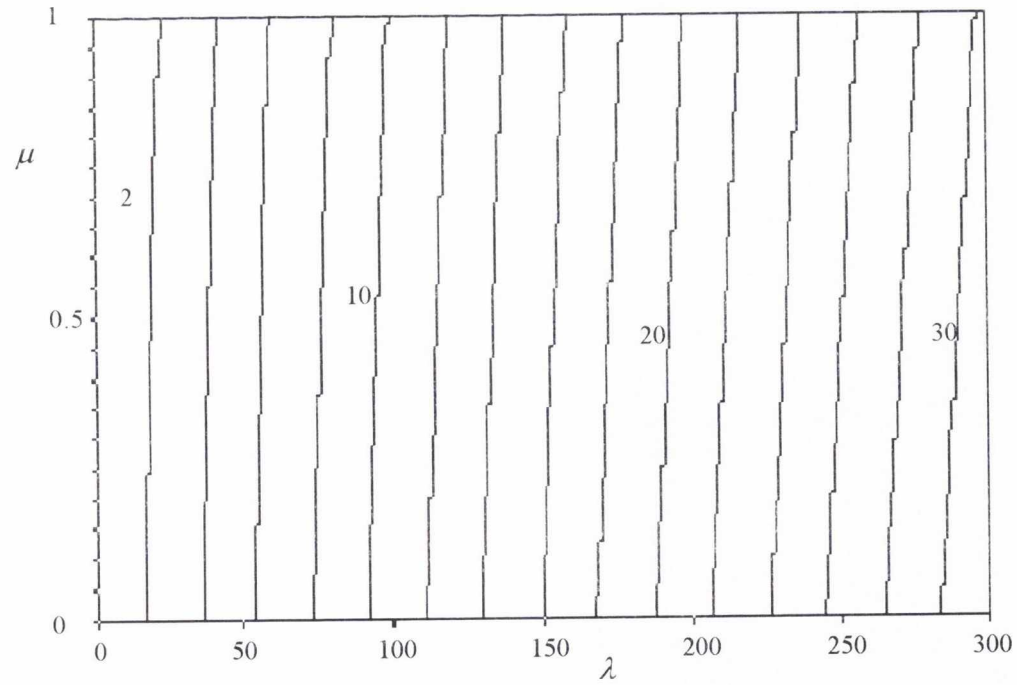

Figure A.1.16. Buckling load (P_{cr}/P_E) contours for the first mode in a homogeneous soil with constant soil stiffness ($F = 1$) and constant shaft friction ($f_1 = f_2 = 0.5$) for a free-free fully embedded beam.

Non-homogeneous soils (F = 0, f_1 = 0 and f_2 = 1)

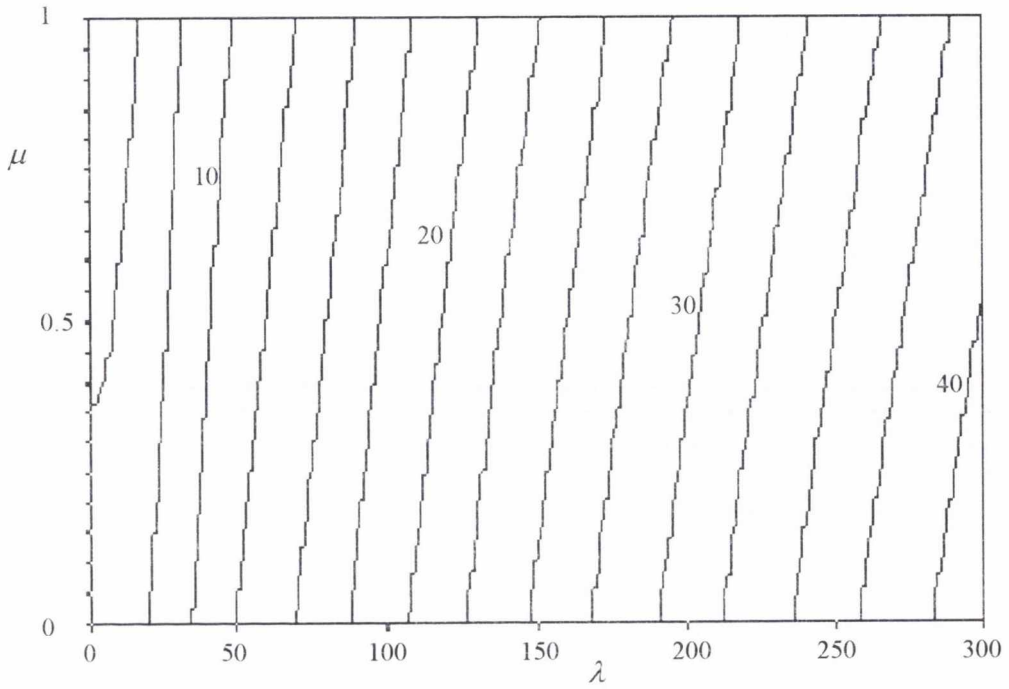

Figure A.1.17. Buckling load (P_{cr}/P_E) contours for the first mode in a non-homogeneous soil with triangular soil stiffness (F = 0) and triangular shaft friction (f_1 = 0, f_2 = 1) for a fixed-fixed fully embedded beam.

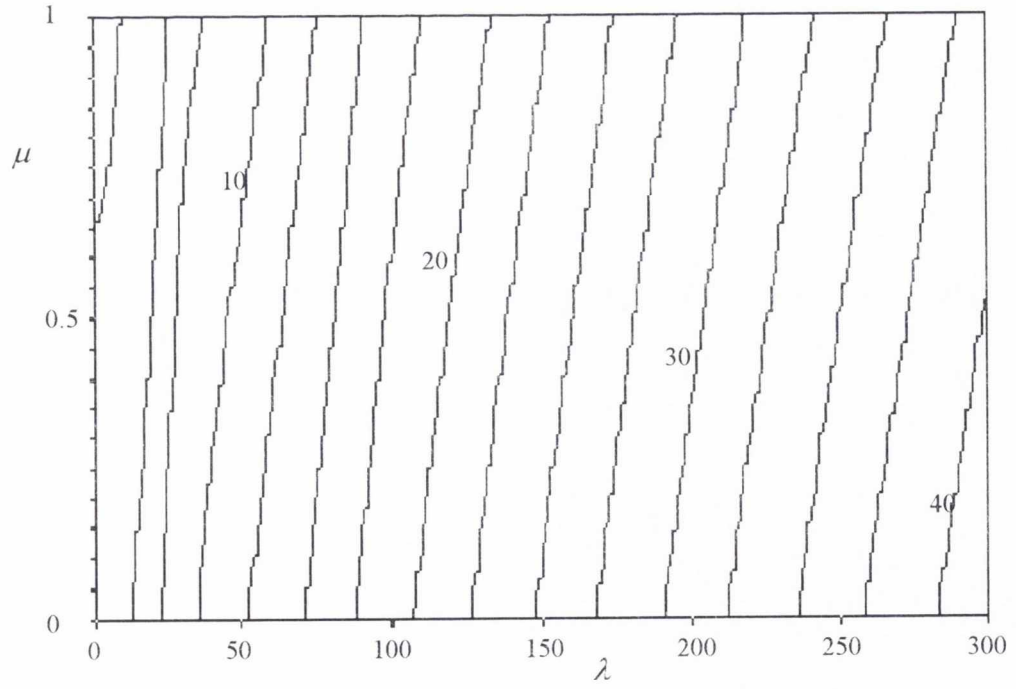

Figure A.1.18. Buckling load (P_{cr}/P_E) contours for the first mode in a non-homogeneous soil with triangular soil stiffness (F = 0) and triangular shaft friction (f_1 = 0, f_2 = 1) for a fixed-pinned fully embedded beam.

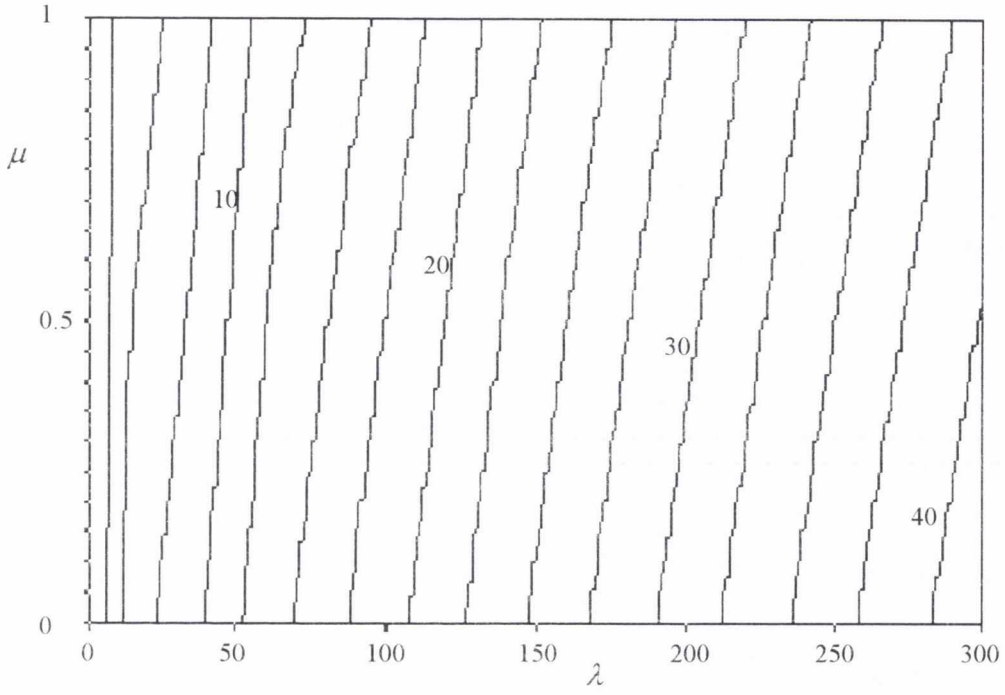

Figure A.1.19. Buckling load (P_{cr}/P_E) contours for the first mode in a non-homogeneous soil with triangular soil stiffness ($F = 0$) and triangular shaft friction ($f_1 = 0$, $f_2 = 1$) for a fixed-no rotation fully embedded beam.

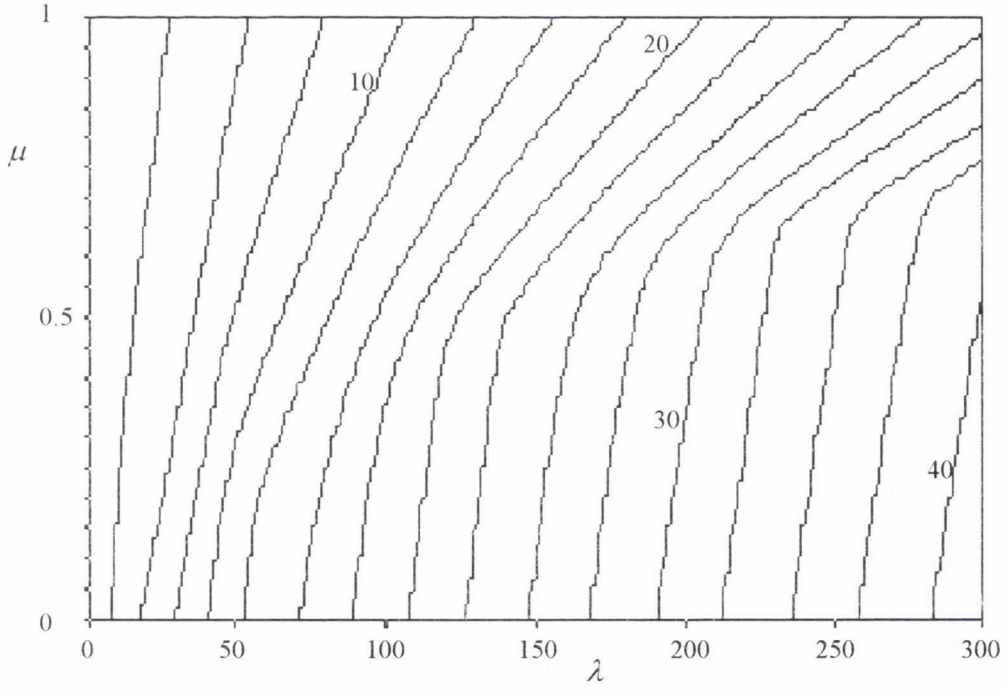

Figure A.1.20. Buckling load (P_{cr}/P_E) contours for the first mode in a non-homogeneous soil with triangular soil stiffness ($F = 0$) and triangular shaft friction ($f_1 = 0$, $f_2 = 1$) for a fixed-free fully embedded beam.

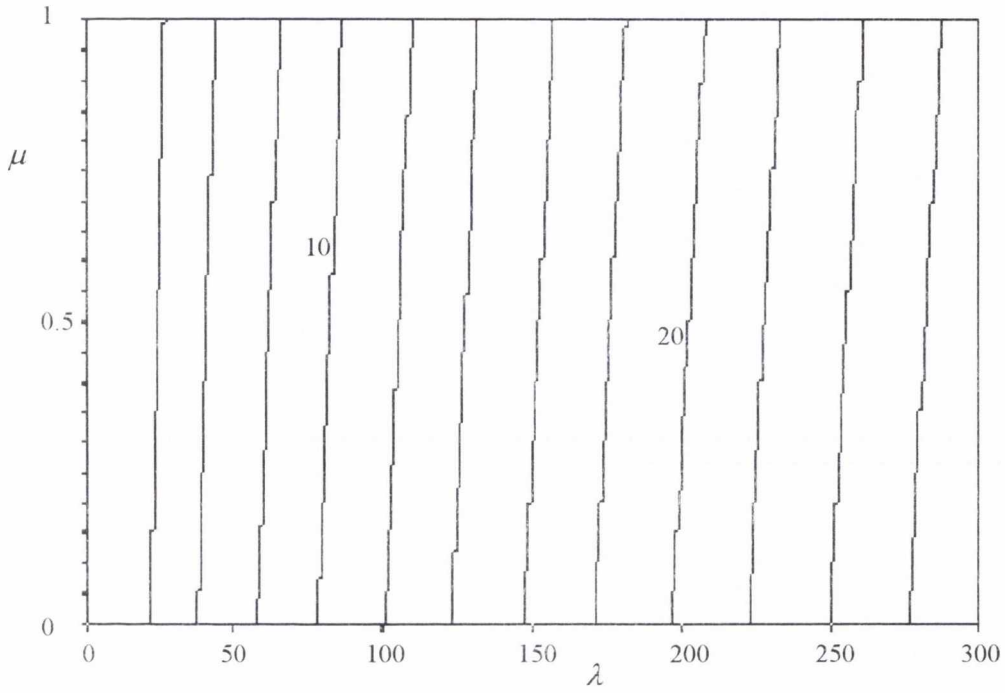

Figure A.1.21. Buckling load (P_{cr}/P_E) contours for the first mode in a non-homogeneous soil with triangular soil stiffness ($F = 0$) and triangular shaft friction ($f_1 = 0$, $f_2 = 1$) for a pinned-fixed fully embedded beam.

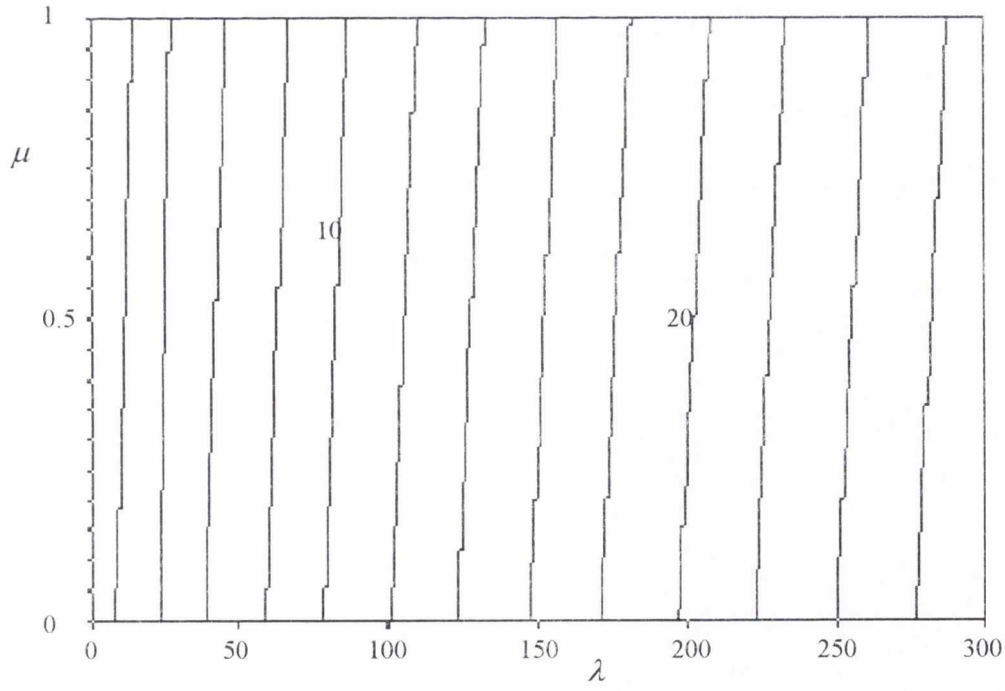

Figure A.1.22. Buckling load (P_{cr}/P_E) contours for the first mode in a non-homogeneous soil with triangular soil stiffness ($F = 0$) and triangular shaft friction ($f_1 = 0$, $f_2 = 1$) for a pinned-pinned fully embedded beam.

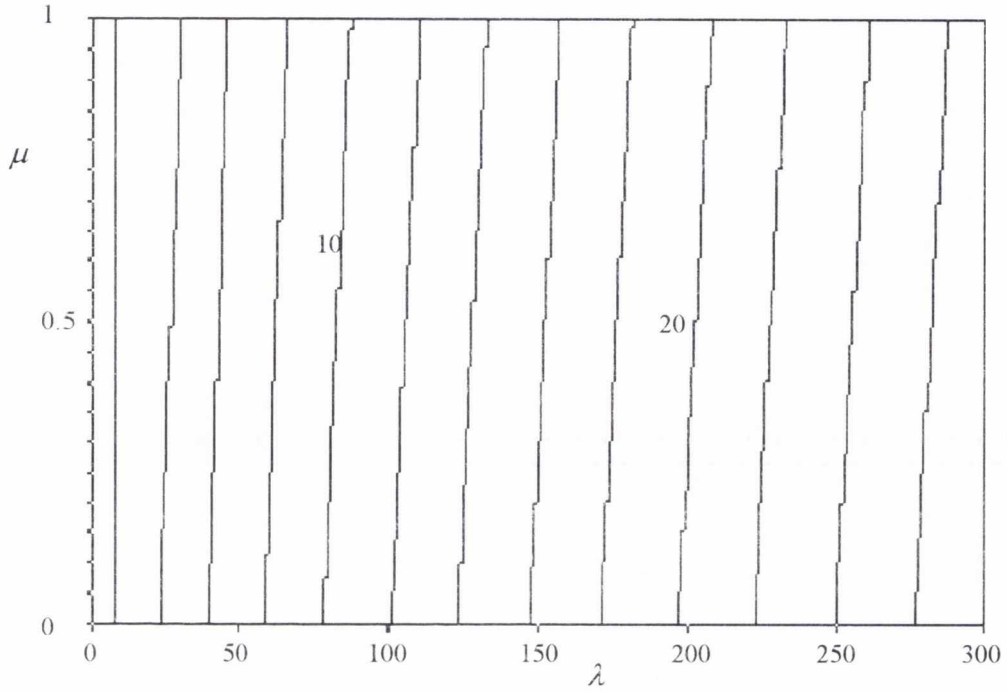

Figure A.1.23. Buckling load (P_{cr}/P_E) contours for the first mode in a non-homogeneous soil with triangular soil stiffness ($F = 0$) and triangular shaft friction ($f_1 = 0, f_2 = 1$) for a pinned-no rotation fully embedded beam.

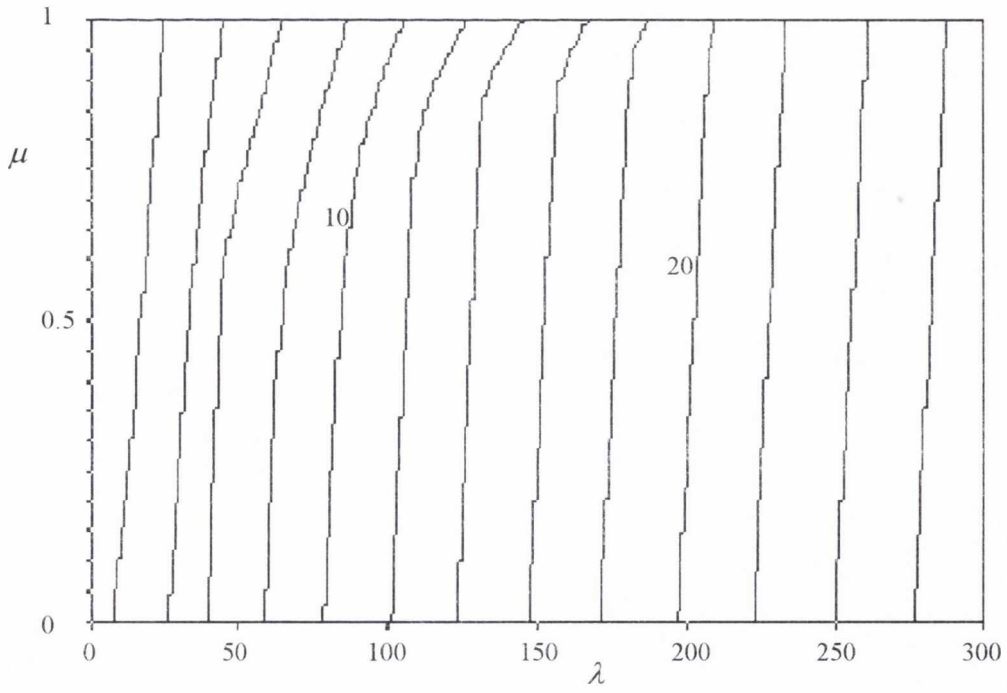

Figure A.1.24. Buckling load (P_{cr}/P_E) contours for the first mode in a non-homogeneous soil with triangular soil stiffness ($F = 0$) and triangular shaft friction ($f_1 = 0, f_2 = 1$) for a pinned-free fully embedded beam.

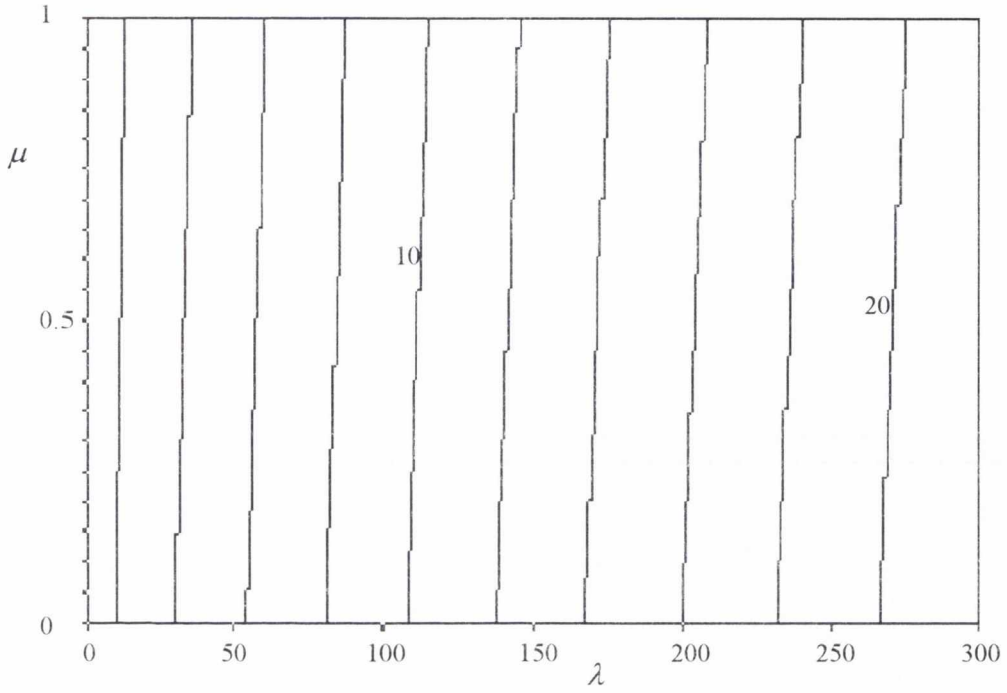

Figure A.1.25. Buckling load (P_{cr}/P_E) contours for the first mode in a non-homogeneous soil with triangular soil stiffness ($F = 0$) and triangular shaft friction ($f_1 = 0, f_2 = 1$) for a no rotation-fixed fully embedded beam.

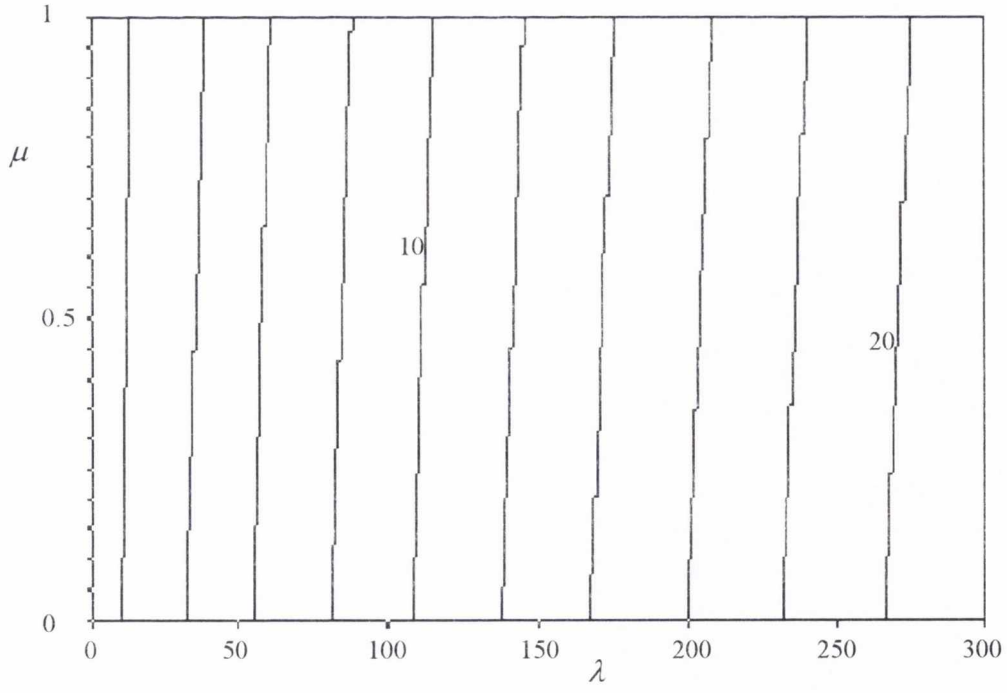

Figure A.1.26. Buckling load (P_{cr}/P_E) contours for the first mode in a non-homogeneous soil with triangular soil stiffness ($F = 0$) and triangular shaft friction ($f_1 = 0, f_2 = 1$) for a no rotation-pinned fully embedded beam.

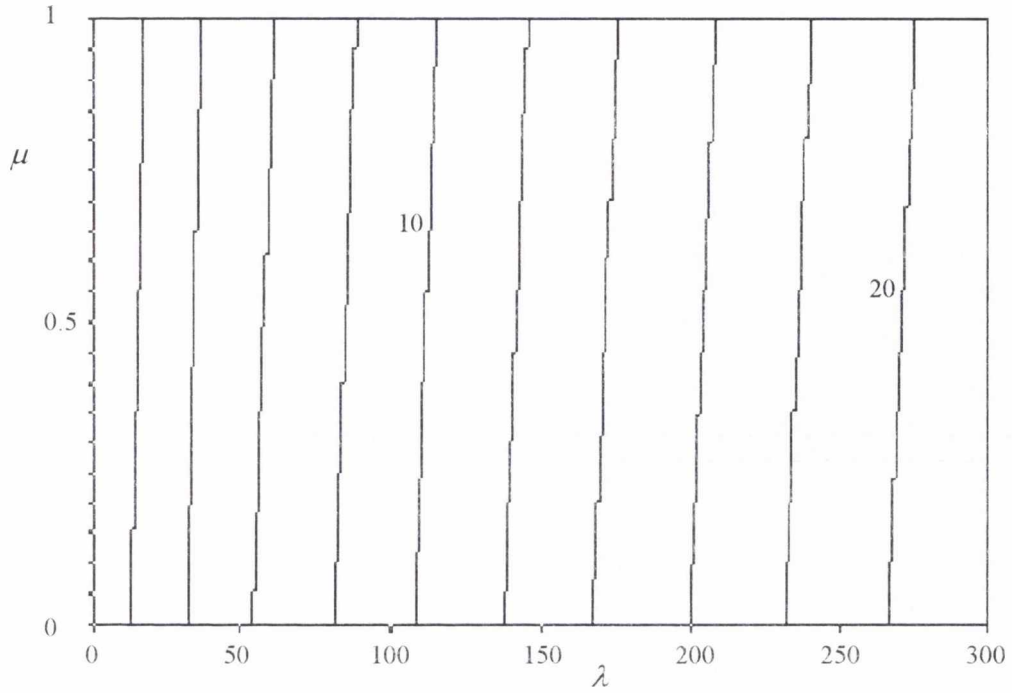

Figure A.1.27. Buckling load (P_{cr}/P_E) contours for the first mode in a non-homogeneous soil with triangular soil stiffness ($F = 0$) and triangular shaft friction ($f_1 = 0, f_2 = 1$) for a no rotation-no rotation fully embedded beam.

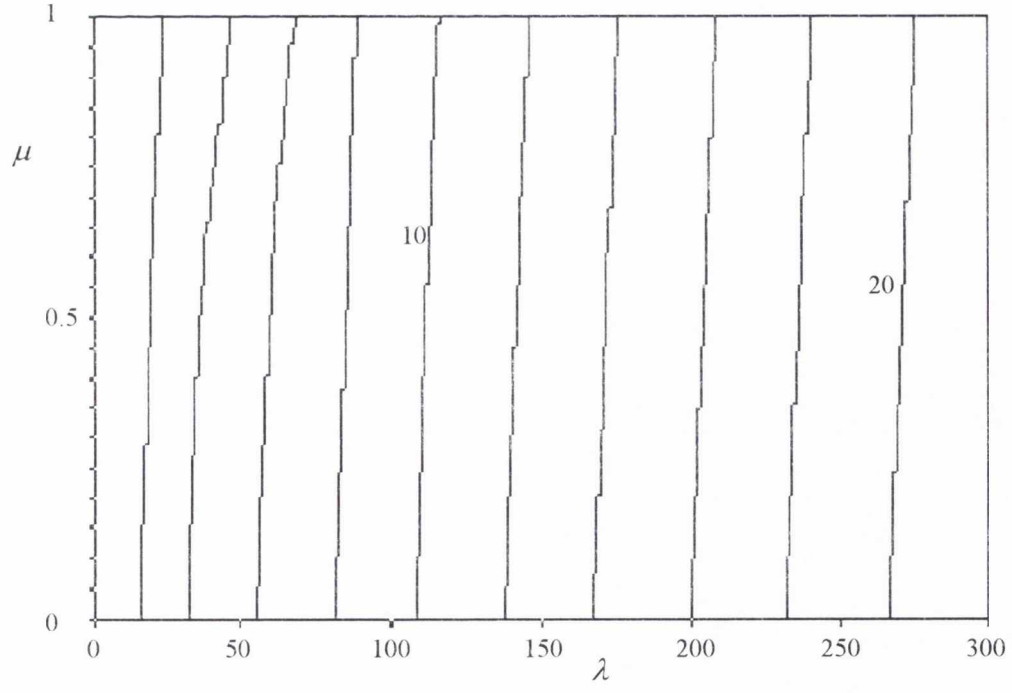

Figure A.1.28. Buckling load (P_{cr}/P_E) contours for the first mode in a non-homogeneous soil with triangular soil stiffness ($F = 0$) and triangular shaft friction ($f_1 = 0, f_2 = 1$) for a no rotation-free fully embedded beam.

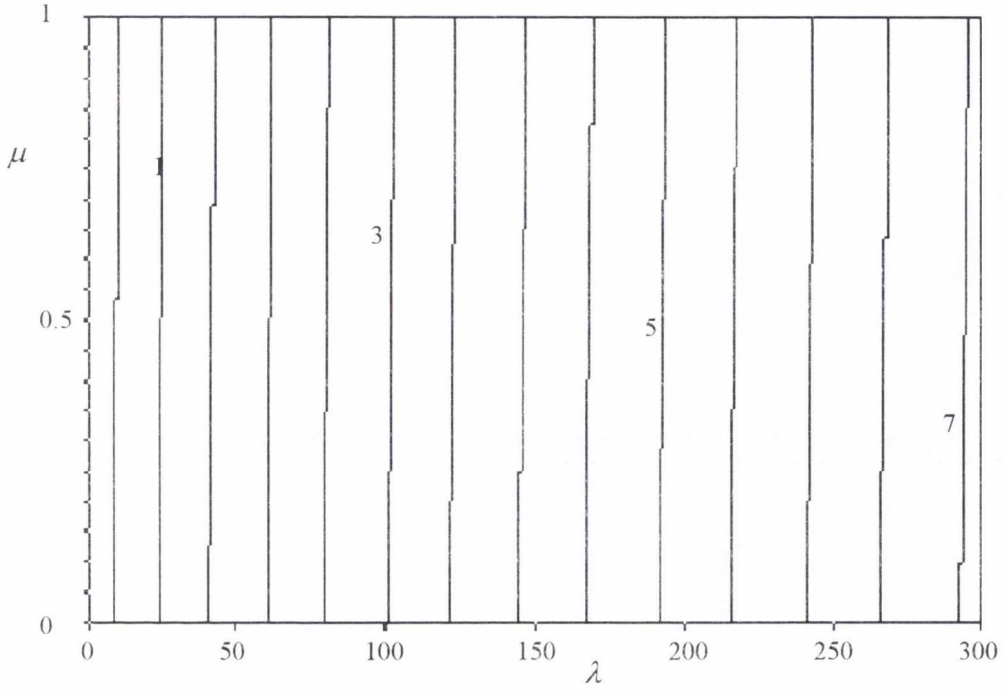

Figure A.1.29. Buckling load (P_{cr}/P_E) contours for the first mode in a non-homogeneous soil with triangular soil stiffness ($F = 0$) and triangular shaft friction ($f_1 = 0, f_2 = 1$) for a free-fixed fully embedded beam.

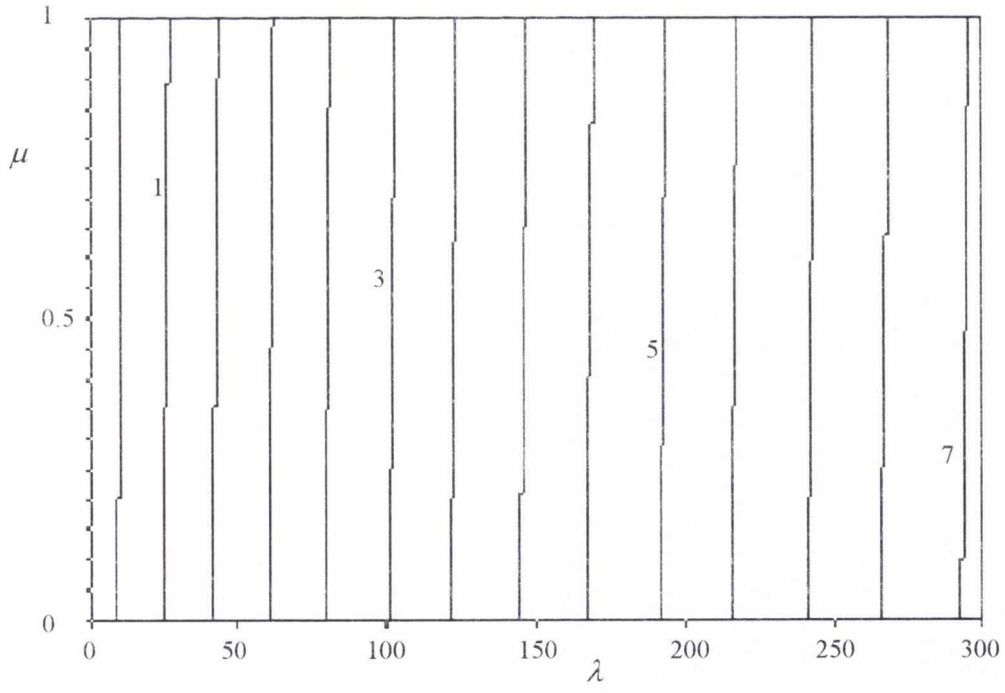

Figure A.1.30. Buckling load (P_{cr}/P_E) contours for the first mode in a non-homogeneous soil with triangular soil stiffness ($F = 0$) and triangular shaft friction ($f_1 = 0, f_2 = 1$) for a free-pinned fully embedded beam.

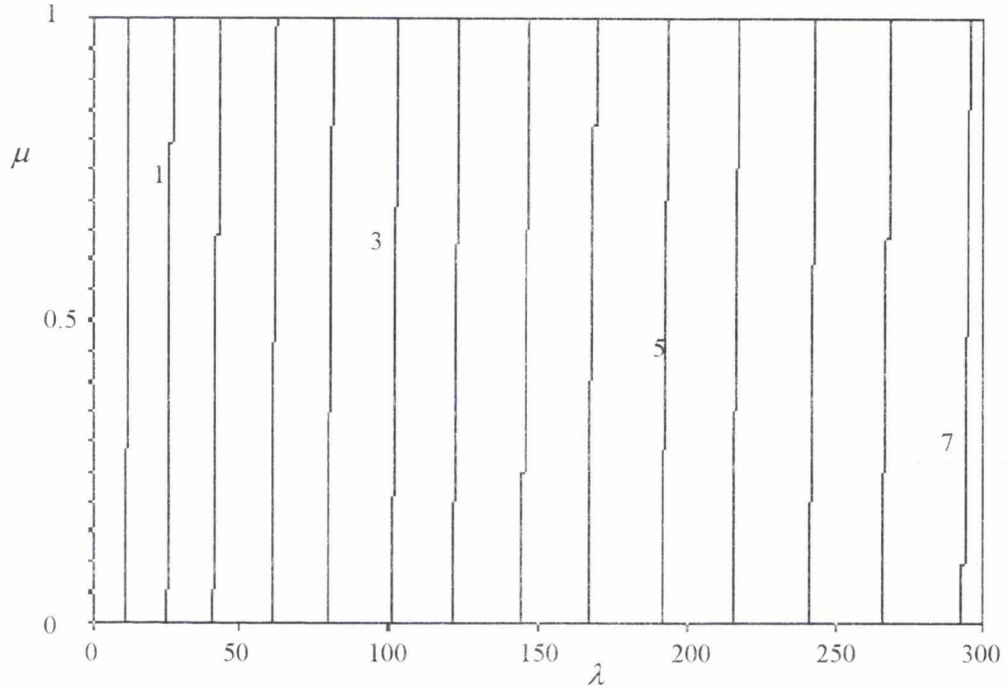

Figure A.1.31. Buckling load (P_{cr}/P_E) contours for the first mode in a non-homogeneous soil with triangular soil stiffness ($F = 0$) and triangular shaft friction ($f_1 = 0, f_2 = 1$) for a free-no rotation fully embedded beam.

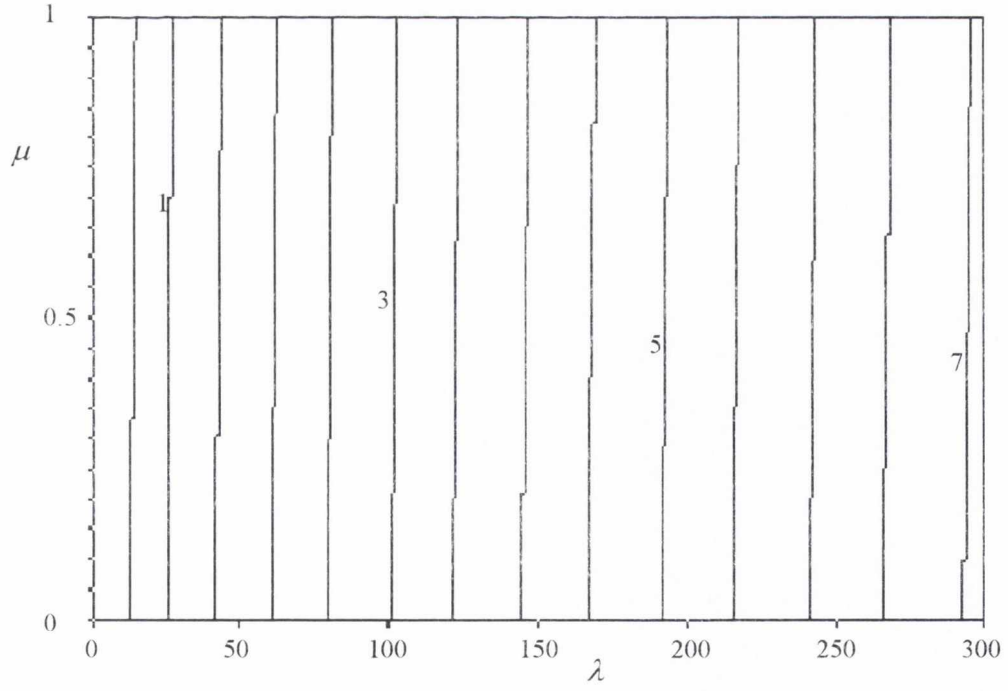

Figure A.1.32. Buckling load (P_{cr}/P_E) contours for the first mode in a non-homogeneous soil with triangular soil stiffness ($F = 0$) and triangular shaft friction ($f_1 = 0, f_2 = 1$) for a free-free fully embedded beam.

Appendix A.2

Homogeneous soils ($F = 1, f_1 = f_2 = 0.5$)

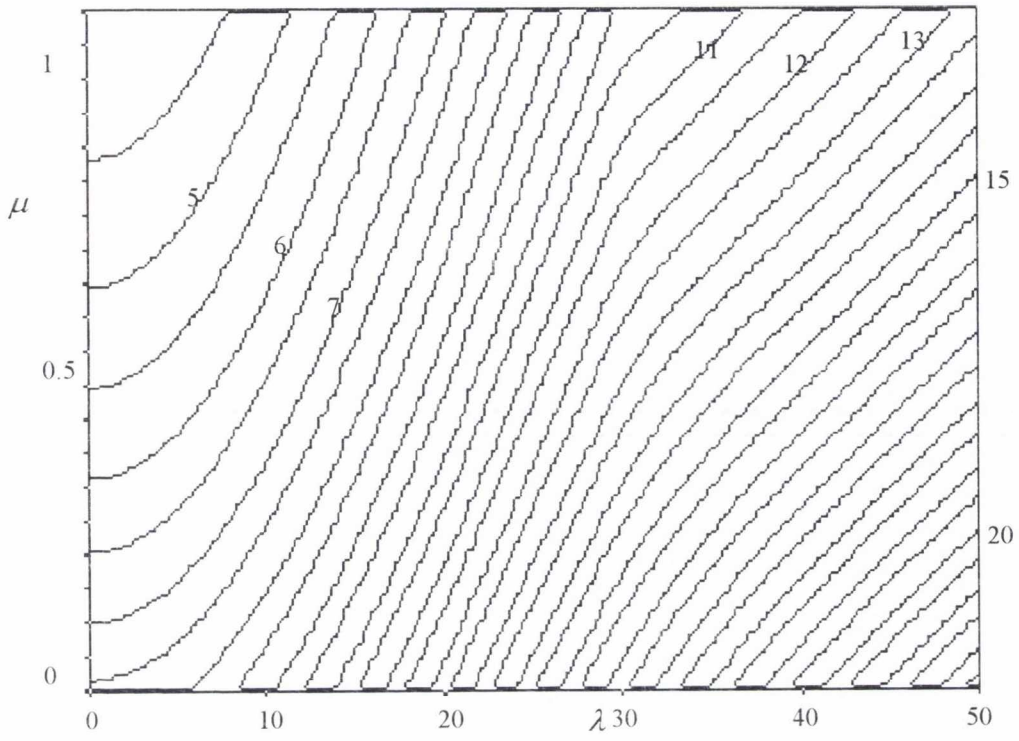

Figure A.2.1. Buckling load (P_{cr}/P_E) contours for the first mode in a homogeneous soil with constant soil stiffness ($F = 1$) and constant shaft friction ($f_1 = f_2 = 0.5$) for a fixed-fixed fully embedded beam.

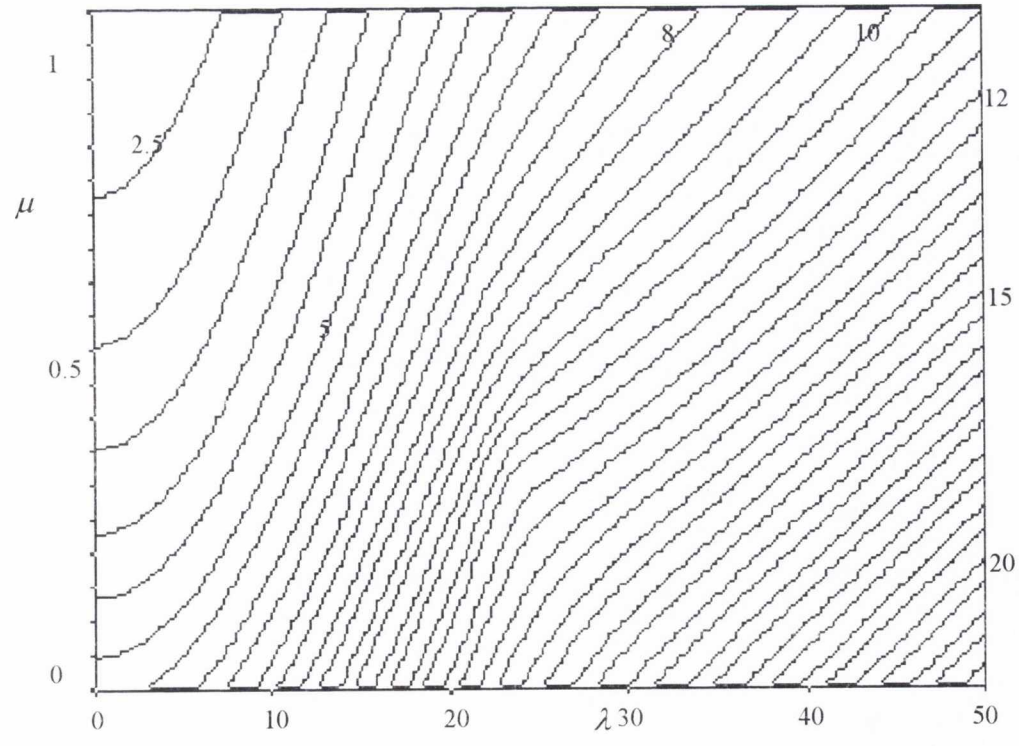

Figure A.2.2. Buckling load (P_{cr}/P_E) contours for the first mode in a homogeneous soil with constant soil stiffness ($F = 1$) and constant shaft friction ($f_1 = f_2 = 0.5$) for a fixed-pinned fully embedded beam.

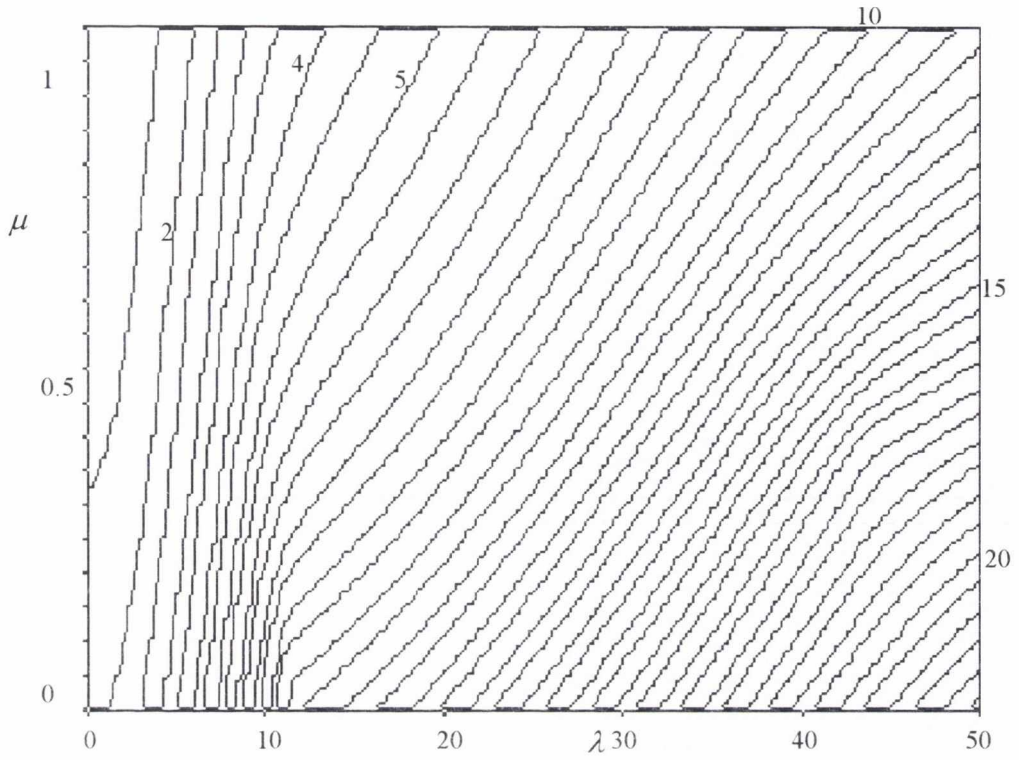

Figure A.2.3. Buckling load (P_{cr}/P_E) contours for the first mode in a homogeneous soil with constant soil stiffness ($F = 1$) and constant shaft friction ($f_1 = f_2 = 0.5$) for a fixed-no rotation fully embedded beam.

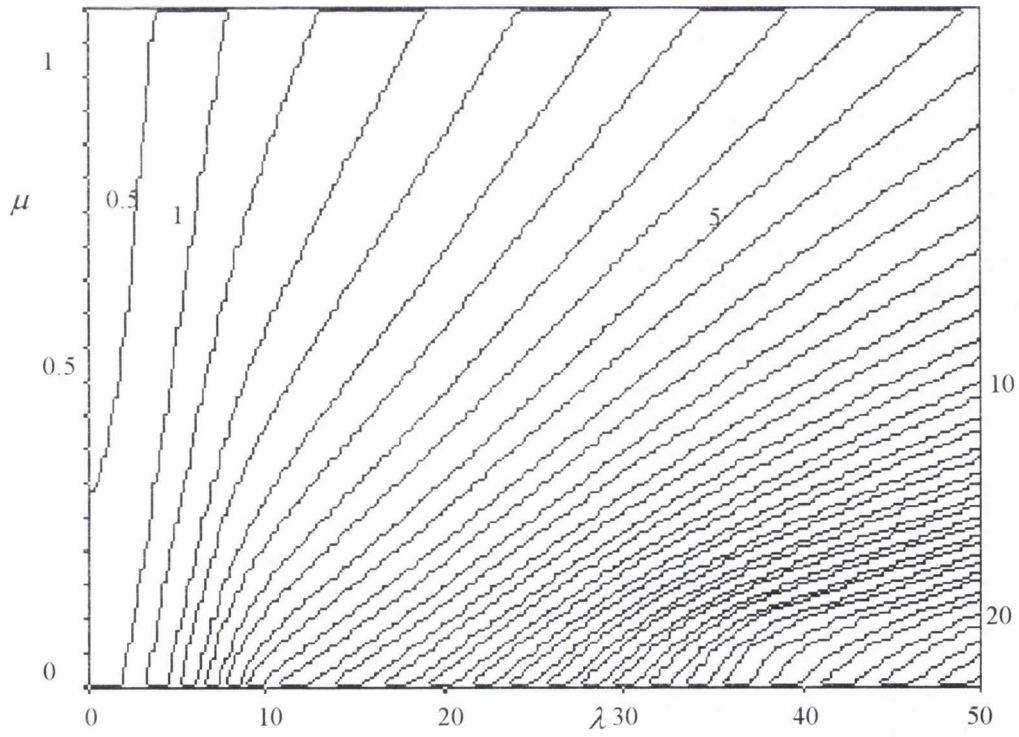

Figure A.2.4. Buckling load (P_{cr}/P_E) contours for the first mode in a homogeneous soil with constant soil stiffness ($F = 1$) and constant shaft friction ($f_1 = f_2 = 0.5$) for a fixed-free fully embedded beam.

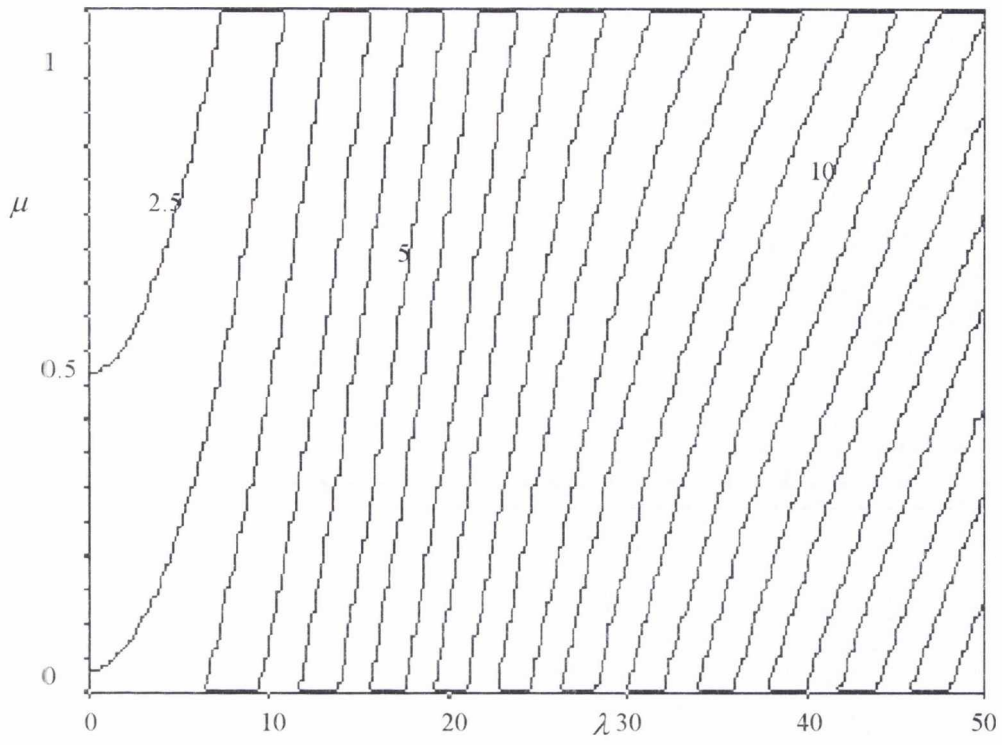

Figure A.2.5. Buckling load (P_{cr}/P_E) contours for the first mode in a homogeneous soil with constant soil stiffness ($F = 1$) and constant shaft friction ($f_1 = f_2 = 0.5$) for a pinned-fixed fully embedded beam.

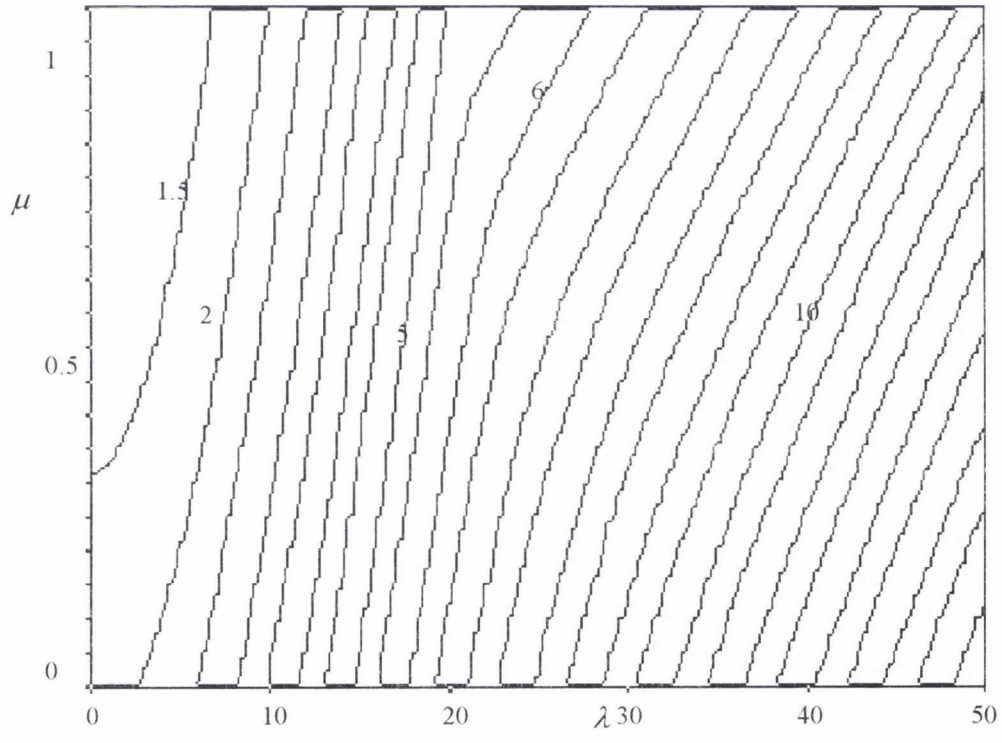

Figure A.2.6. Buckling load (P_{cr}/P_E) contours for the first mode in a homogeneous soil with constant soil stiffness ($F = 1$) and constant shaft friction ($f_1 = f_2 = 0.5$) for a pinned-pinned fully embedded beam.

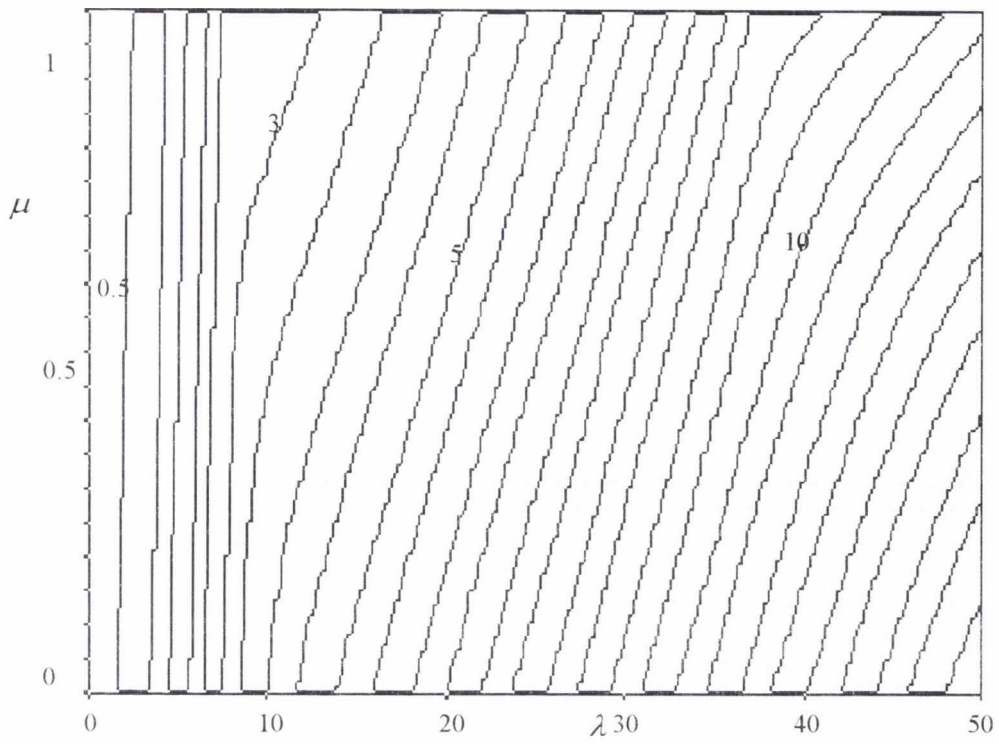

Figure A.2.7. Buckling load (P_{cr}/P_E) contours for the first mode in a homogeneous soil with constant soil stiffness ($F = 1$) and constant shaft friction ($f_1 = f_2 = 0.5$) for a pinned-no rotation fully embedded beam.

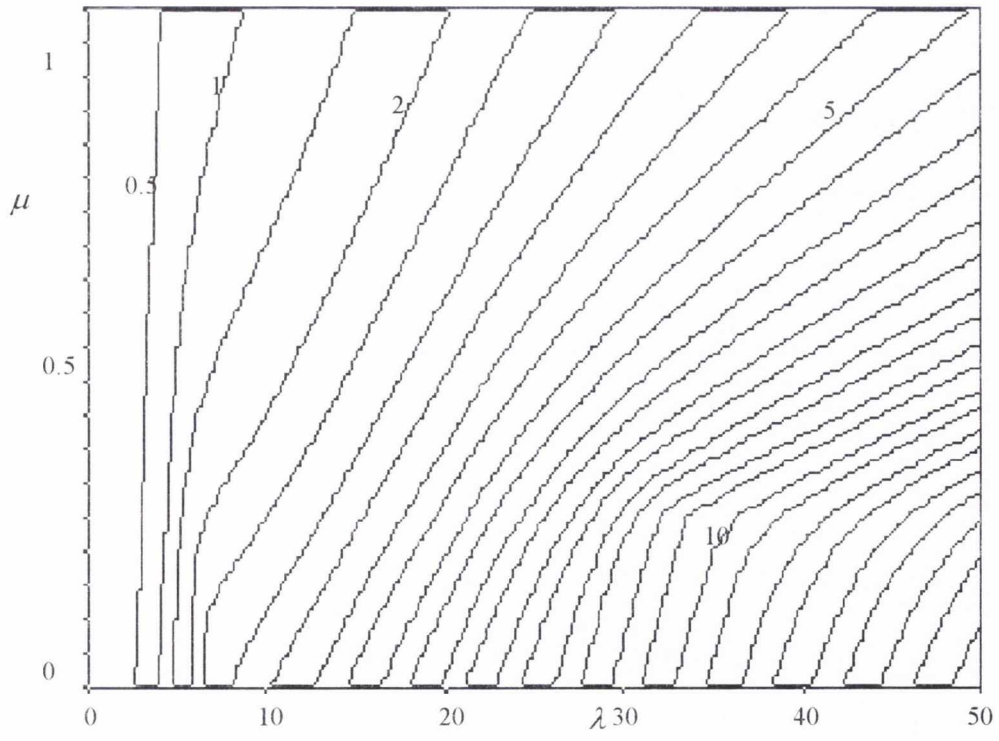

Figure A.2.8. Buckling load (P_{cr}/P_E) contours for the first mode in a homogeneous soil with constant soil stiffness ($F = 1$) and constant shaft friction ($f_1 = f_2 = 0.5$) for a pinned-free fully embedded beam.

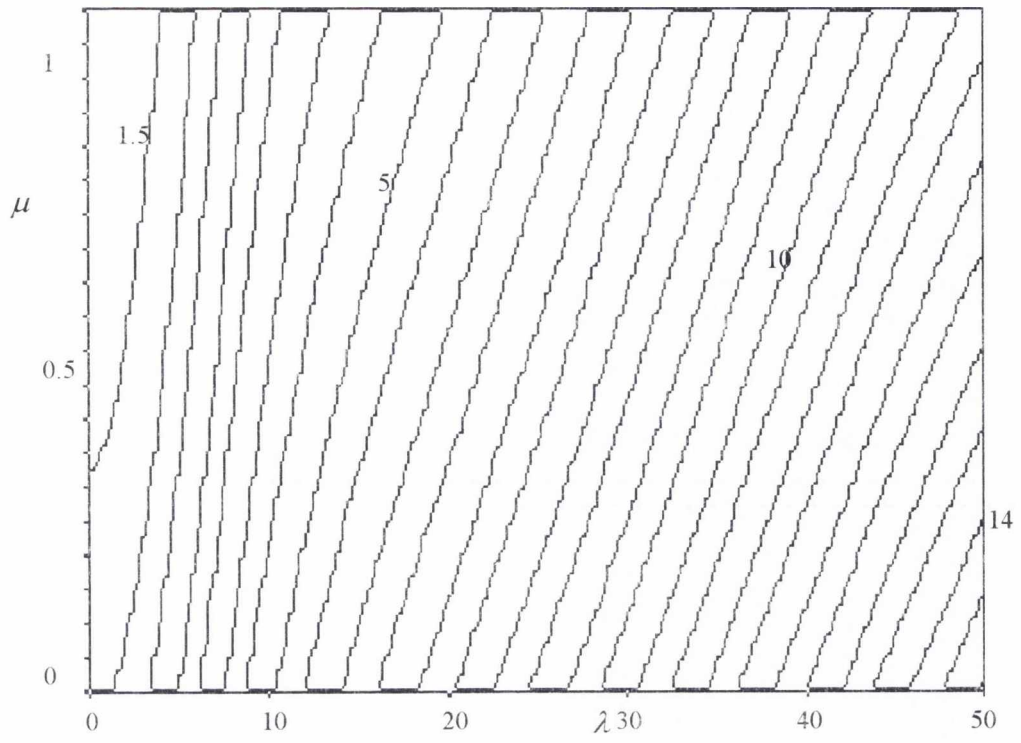

Figure A.2.9. Buckling load (P_{cr}/P_E) contours for the first mode in a homogeneous soil with constant soil stiffness ($F = 1$) and constant shaft friction ($f_1 = f_2 = 0.5$) for a no rotation-fixed fully embedded beam.

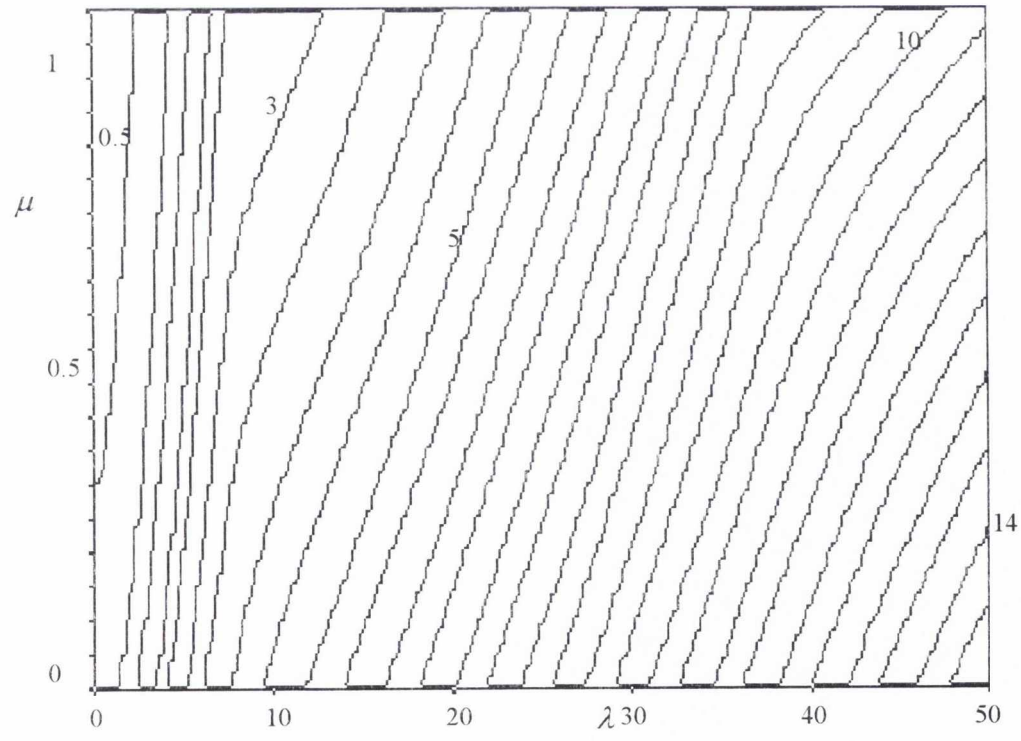

Figure A.2.10. Buckling load (P_{cr}/P_E) contours for the first mode in a homogeneous soil with constant soil stiffness ($F = 1$) and constant shaft friction ($f_1 = f_2 = 0.5$) for a no rotation-pinned fully embedded beam.

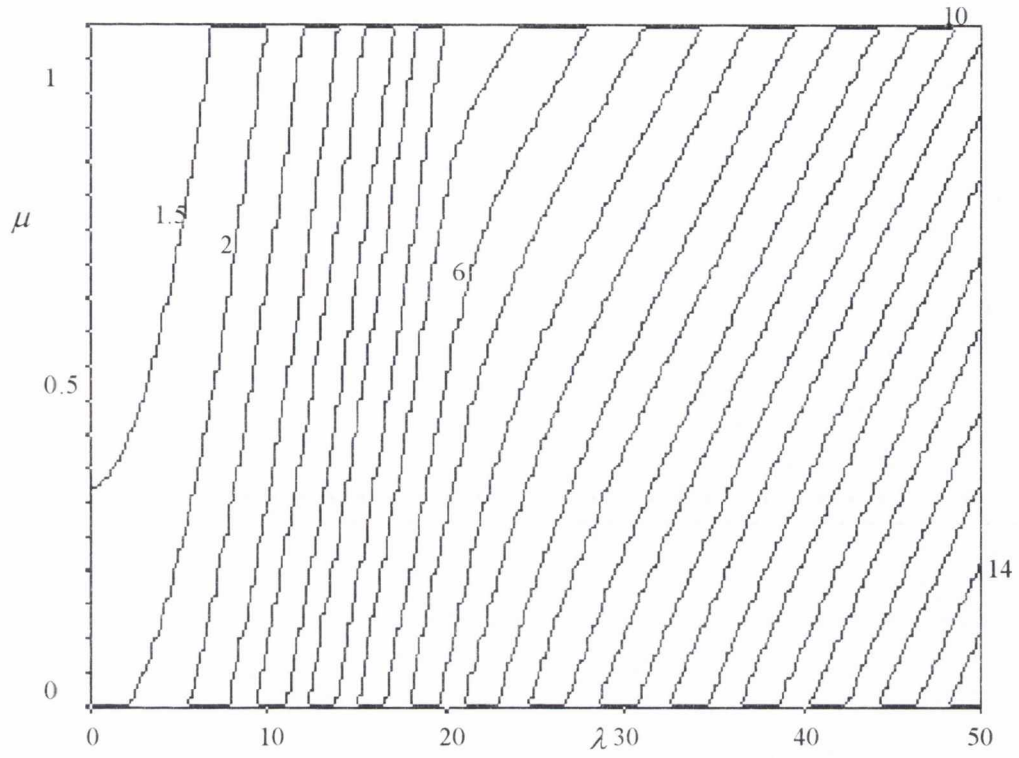

Figure A.2.11. Buckling load (P_{cr}/P_E) contours for the first mode in a homogeneous soil with constant soil stiffness ($F = 1$) and constant shaft friction ($f_1 = f_2 = 0.5$) for a no rotation-no rotation fully embedded beam.

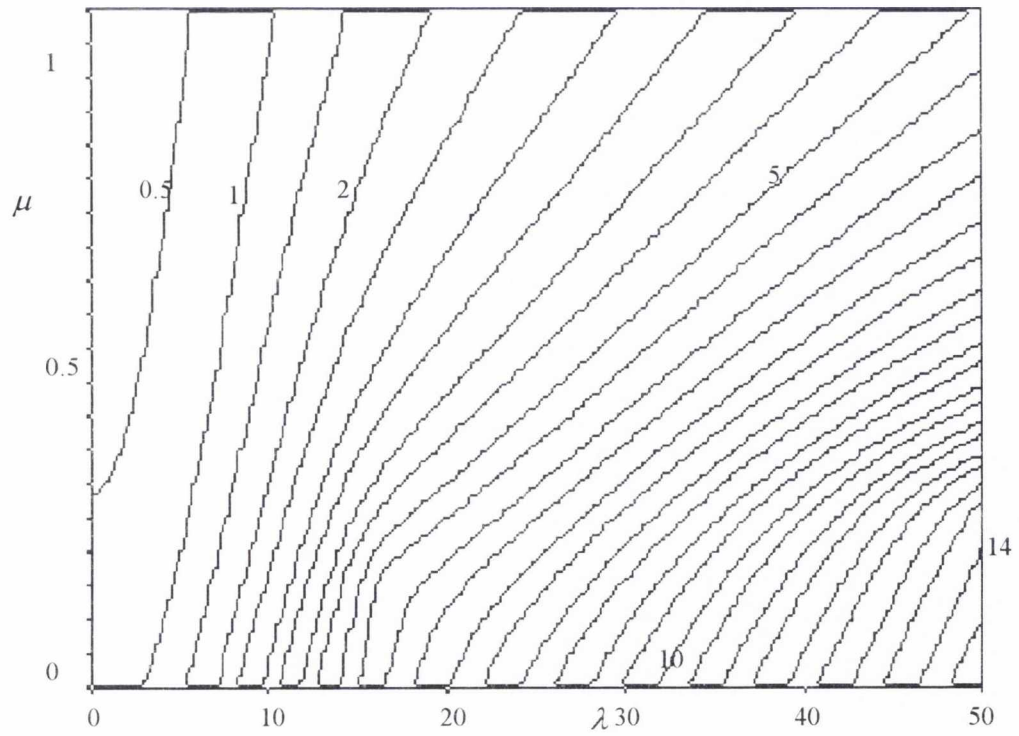

Figure A.2.12. Buckling load (P_{cr}/P_E) contours for the first mode in a homogeneous soil with constant soil stiffness ($F = 1$) and constant shaft friction ($f_1 = f_2 = 0.5$) for a no rotation-free fully embedded beam.

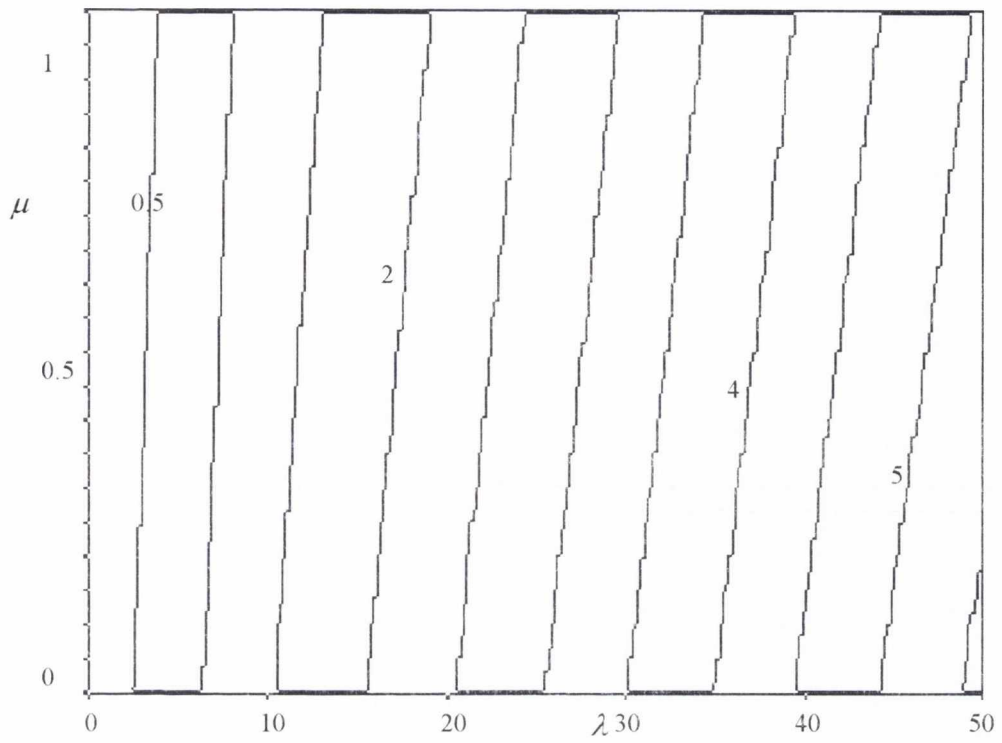

Figure A.2.13. Buckling load (P_{cr}/P_E) contours for the first mode in a homogeneous soil with constant soil stiffness ($F = 1$) and constant shaft friction ($f_1 = f_2 = 0.5$) for a free-fixed fully embedded beam.

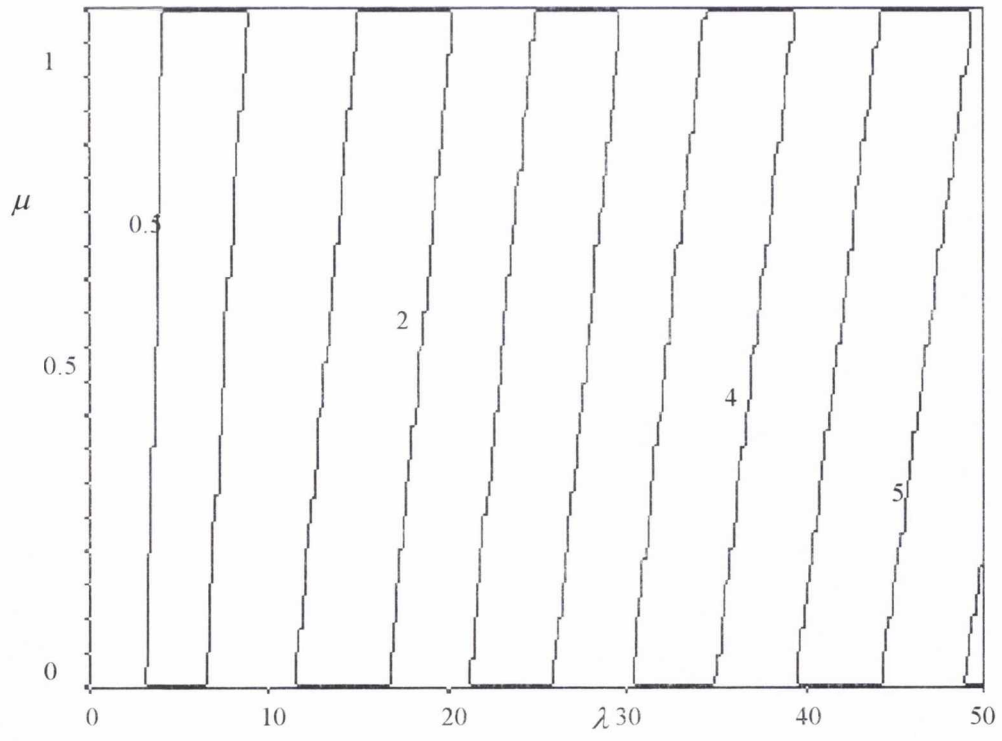

Figure A.2.14. Buckling load (P_{cr}/P_E) contours for the first mode in a homogeneous soil with constant soil stiffness ($F = 1$) and constant shaft friction ($f_1 = f_2 = 0.5$) for a free-pinned fully embedded beam.

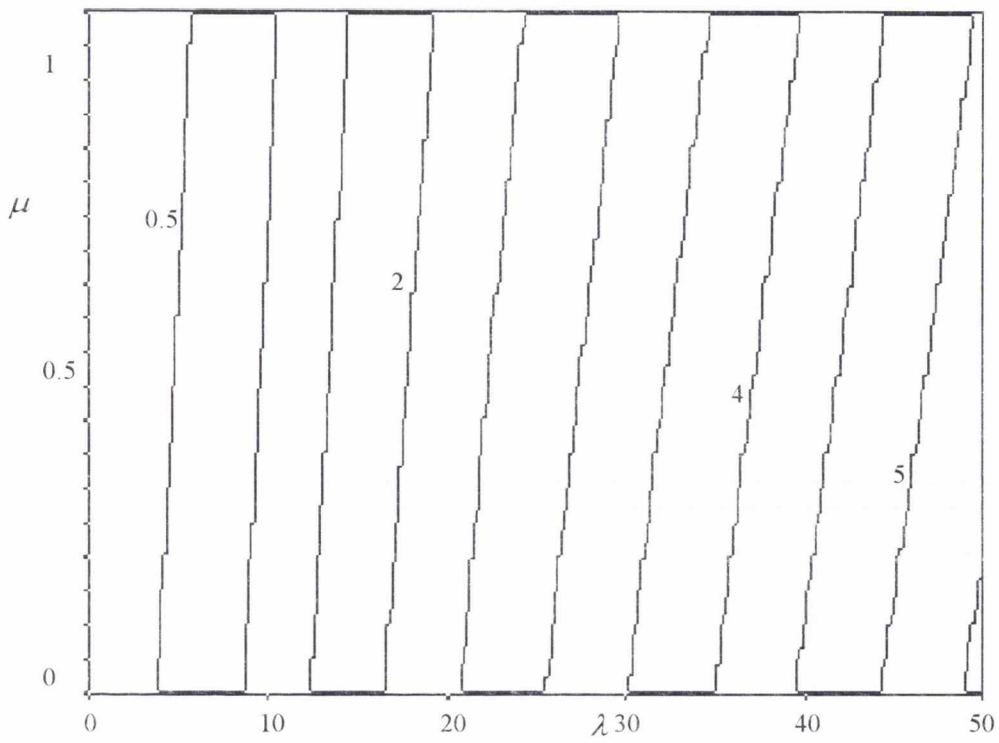

Figure A.2.15. Buckling load (P_{cr}/P_E) contours for the first mode in a homogeneous soil with constant soil stiffness ($F = 1$) and constant shaft friction ($f_1 = f_2 = 0.5$) for a free-no rotation fully embedded beam.

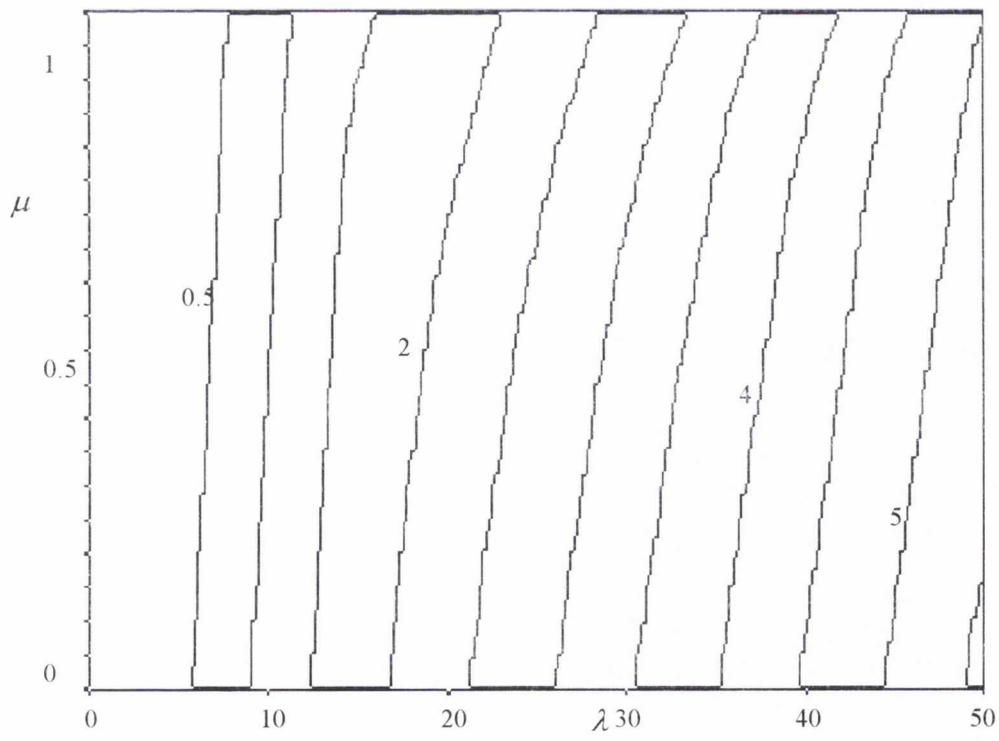

Figure A.2.16. Buckling load (P_{cr}/P_E) contours for the first mode in a homogeneous soil with constant soil stiffness ($F = 1$) and constant shaft friction ($f_1 = f_2 = 0.5$) for a free-free fully embedded beam.

Non-homogeneous soils (F = 0, f_1 = 0 and f_2 = 1)

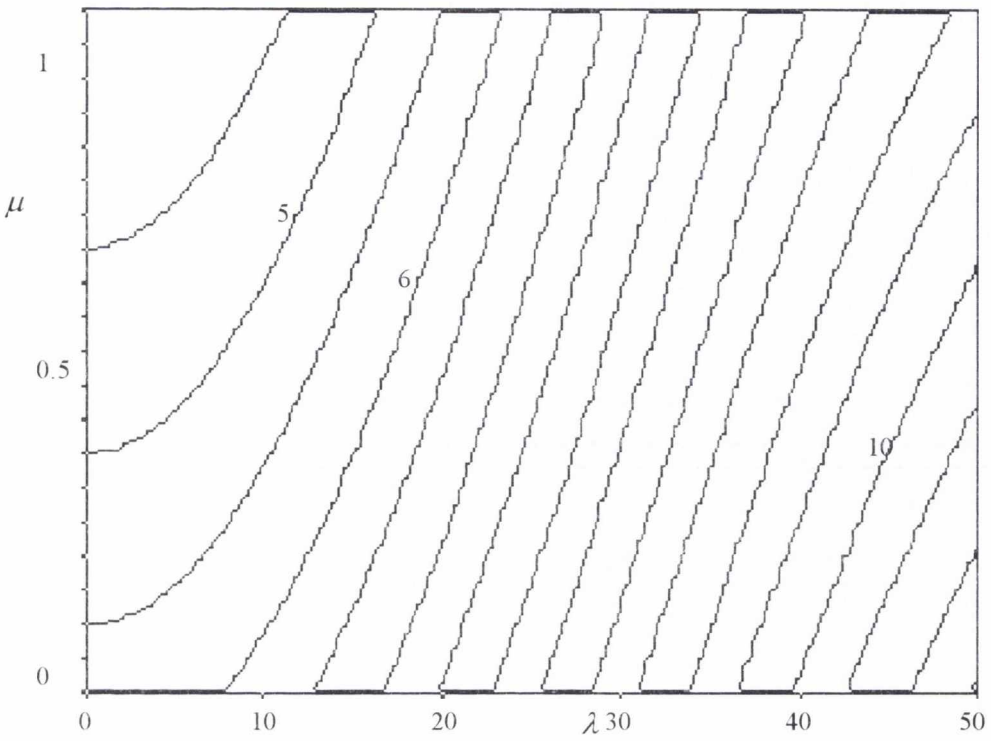

Figure A.2.17. Buckling load (P_{cr}/P_E) contours for the first mode in a non-homogeneous soil with triangular soil stiffness (F = 0) and triangular shaft friction (f_1 = 0, f_2 = 1) for a fixed-fixed fully embedded beam.

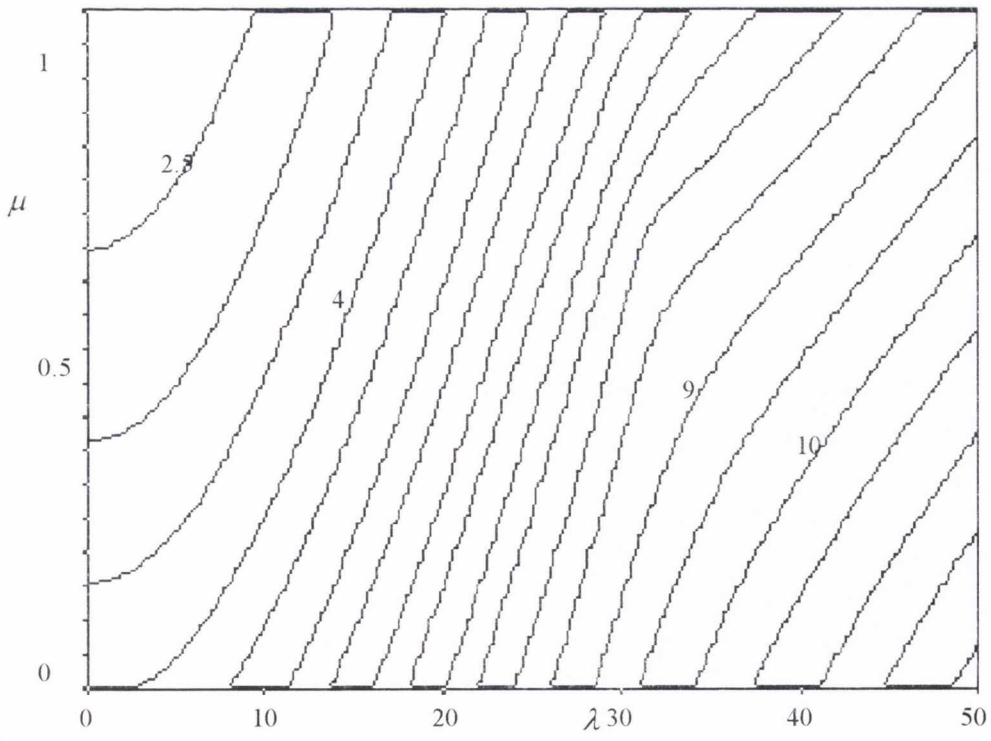

Figure A.2.18. Buckling load (P_{cr}/P_E) contours for the first mode in a non-homogeneous soil with triangular soil stiffness (F = 0) and triangular shaft friction (f_1 = 0, f_2 = 1) for a fixed-pinned fully embedded beam.

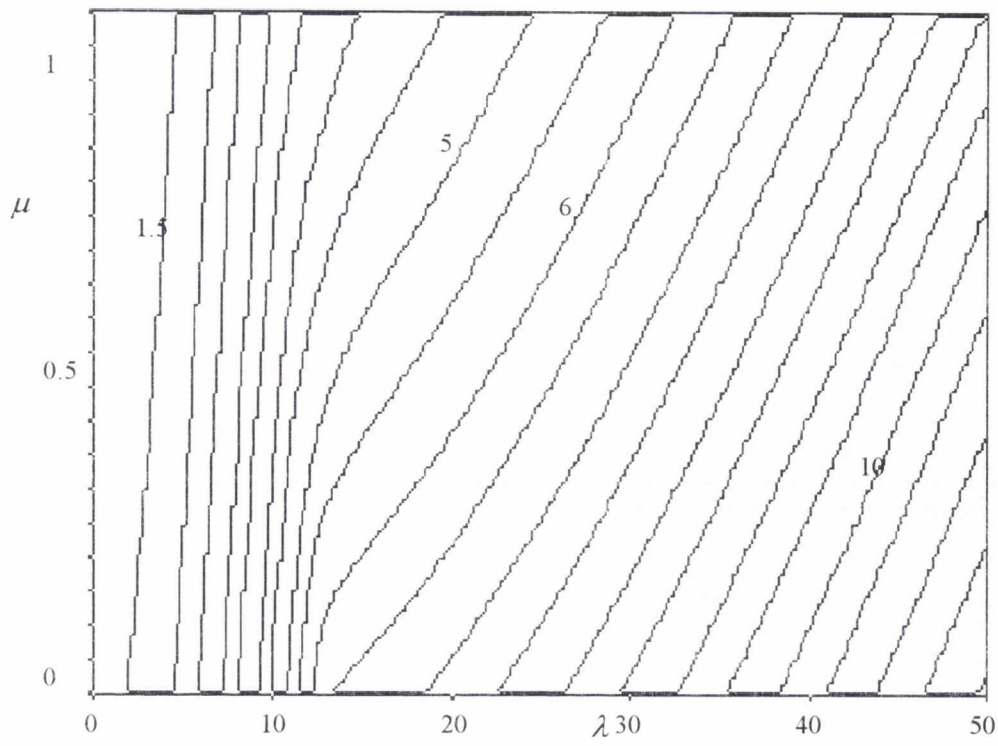

Figure A.2.19. Buckling load (P_{cr}/P_E) contours for the first mode in a non-homogeneous soil with triangular soil stiffness ($F = 0$) and triangular shaft friction ($f_1 = 0$, $f_2 = 1$) for a fixed-no rotation fully embedded beam.

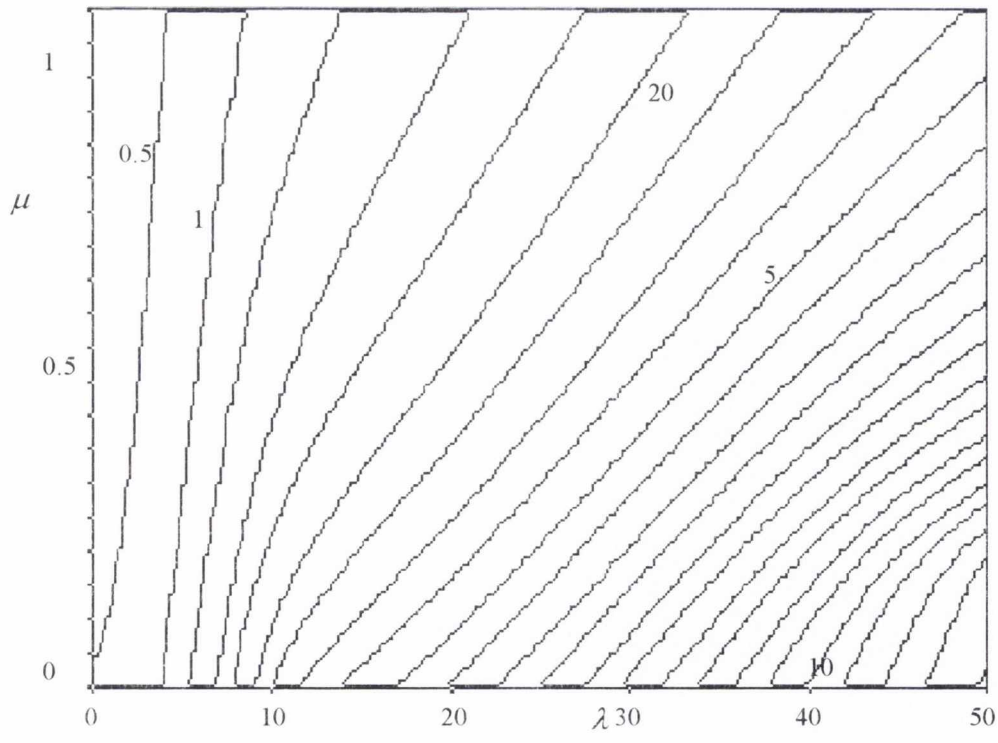

Figure A.2.20. Buckling load (P_{cr}/P_E) contours for the first mode in a non-homogeneous soil with triangular soil stiffness ($F = 0$) and triangular shaft friction ($f_1 = 0$, $f_2 = 1$) for a fixed-free fully embedded beam.

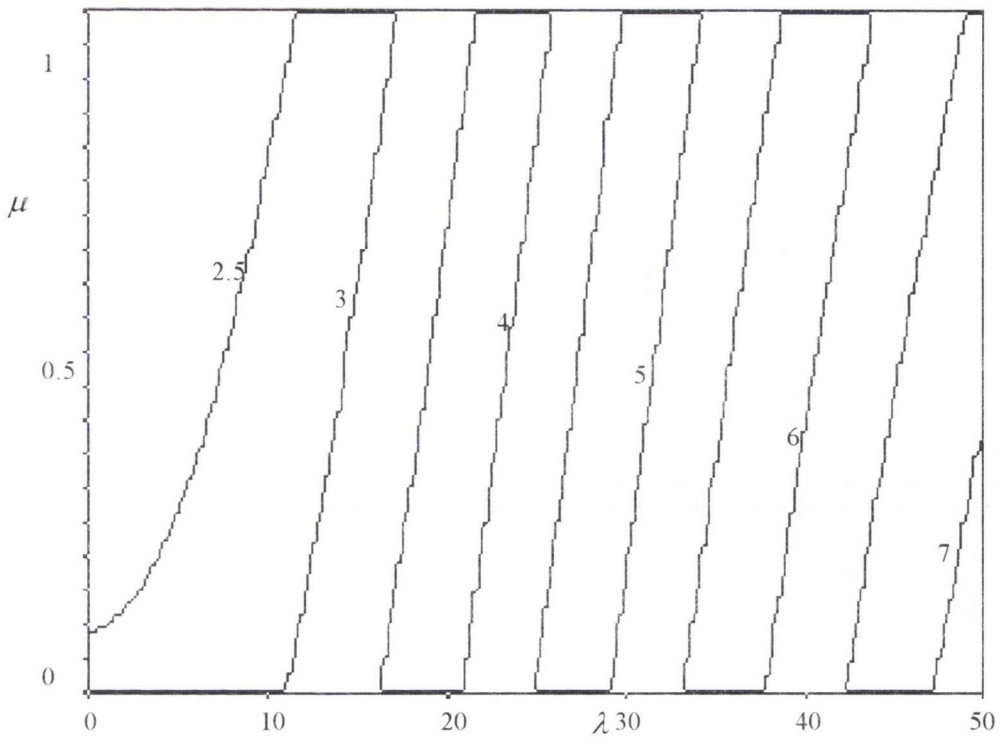

Figure A.2.21. Buckling load (P_{cr}/P_E) contours for the first mode in a non-homogeneous soil with triangular soil stiffness ($F = 0$) and triangular shaft friction ($f_1 = 0$, $f_2 = 1$) for a pinned-fixed fully embedded beam.

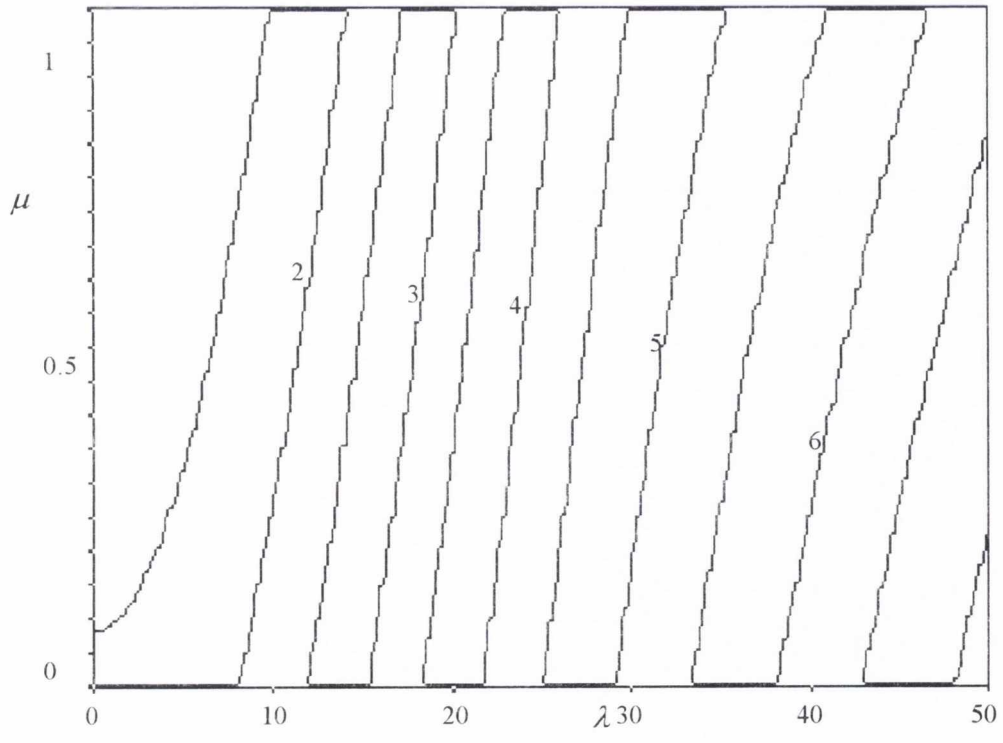

Figure A.2.22. Buckling load (P_{cr}/P_E) contours for the first mode in a non-homogeneous soil with triangular soil stiffness ($F = 0$) and triangular shaft friction ($f_1 = 0$, $f_2 = 1$) for a pinned-pinned fully embedded beam.

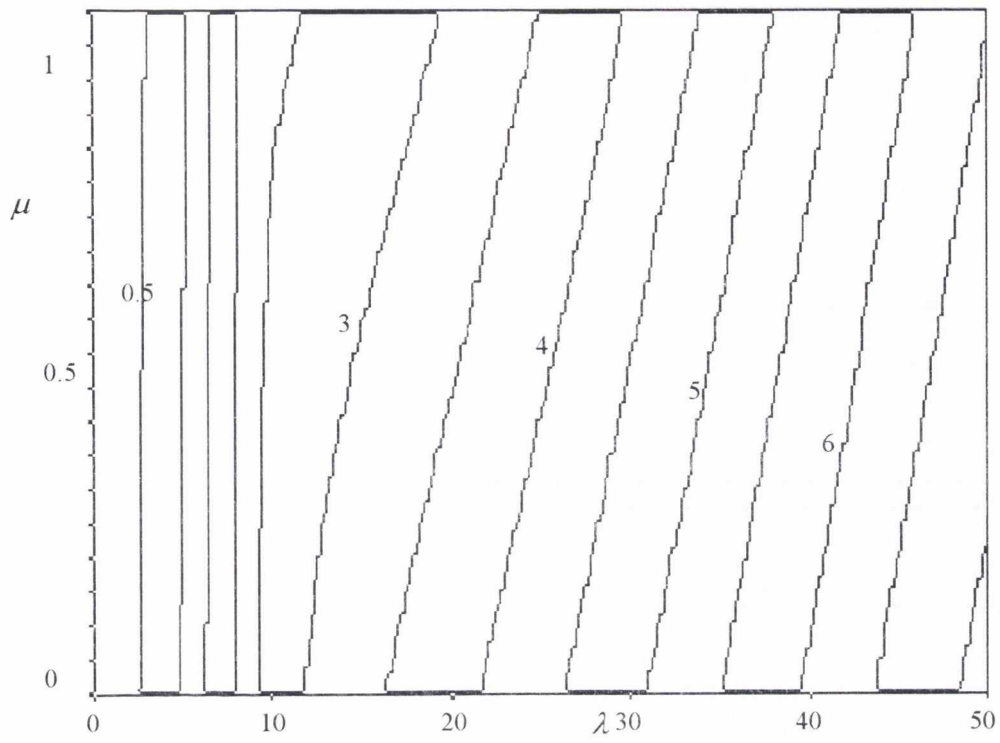

Figure A.2.23. Buckling load (P_{cr}/P_E) contours for the first mode in a non-homogeneous soil with triangular soil stiffness ($F = 0$) and triangular shaft friction ($f_1 = 0, f_2 = 1$) for a pinned-no rotation fully embedded beam.

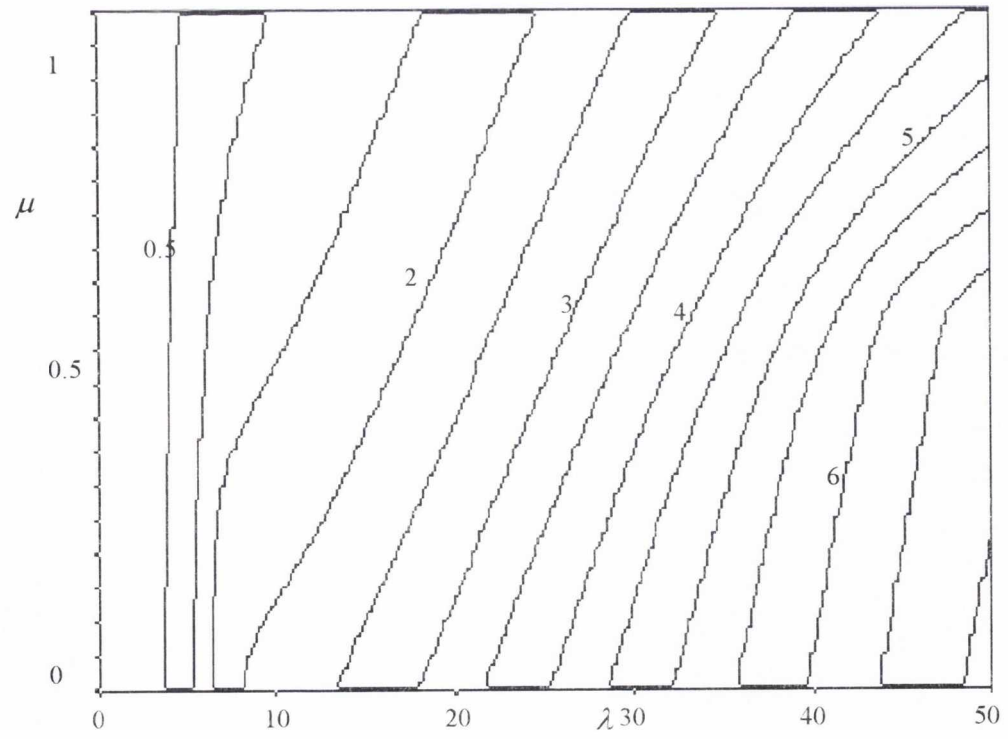

Figure A.2.24. Buckling load (P_{cr}/P_E) contours for the first mode in a non-homogeneous soil with triangular soil stiffness ($F = 0$) and triangular shaft friction ($f_1 = 0, f_2 = 1$) for a pinned-free fully embedded beam.

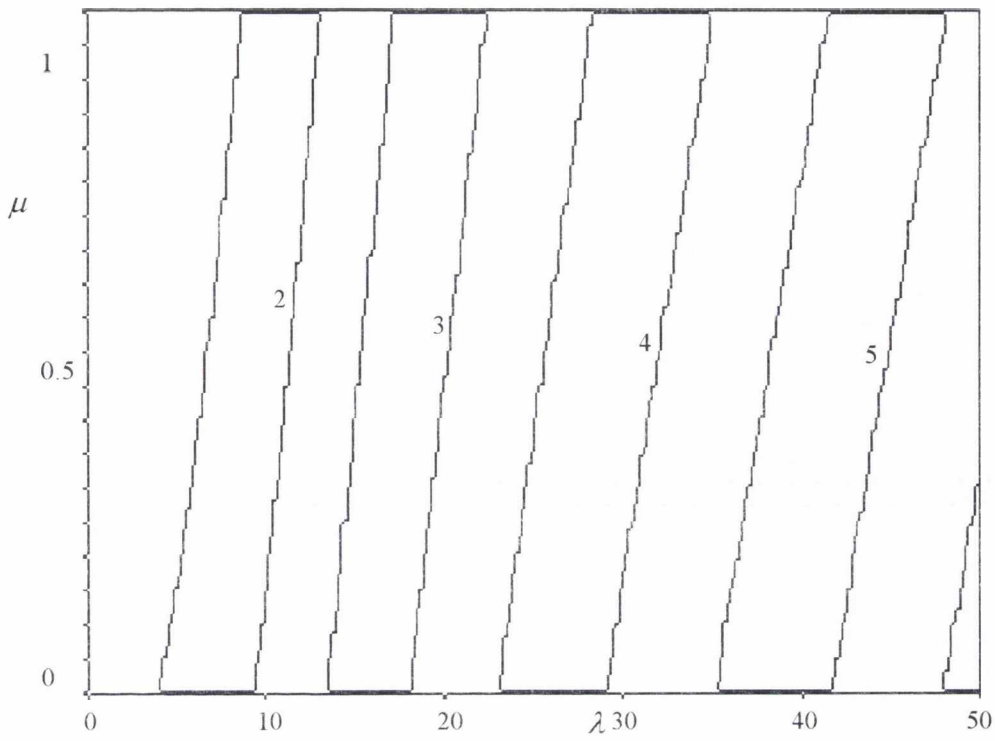

Figure A.2.25. Buckling load (P_{cr}/P_E) contours for the first mode in a non-homogeneous soil with triangular soil stiffness ($F = 0$) and triangular shaft friction ($f_1 = 0, f_2 = 1$) for a no rotation-fixed fully embedded beam.

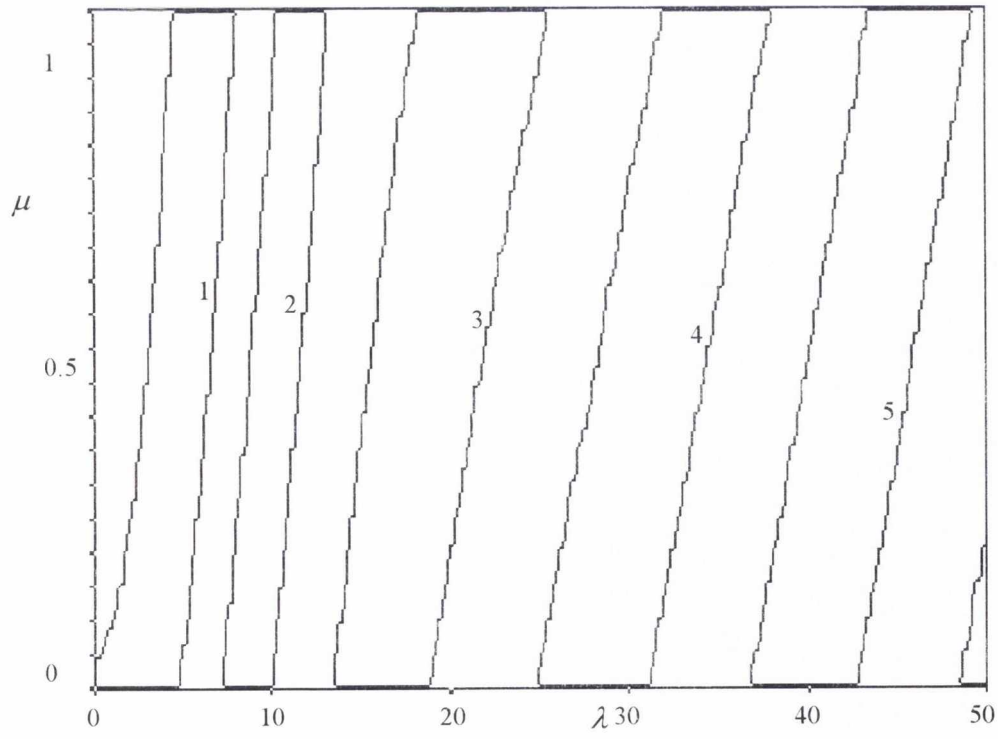

Figure A.2.26. Buckling load (P_{cr}/P_E) contours for the first mode in a non-homogeneous soil with triangular soil stiffness ($F = 0$) and triangular shaft friction ($f_1 = 0, f_2 = 1$) for a no rotation-pinned fully embedded beam.

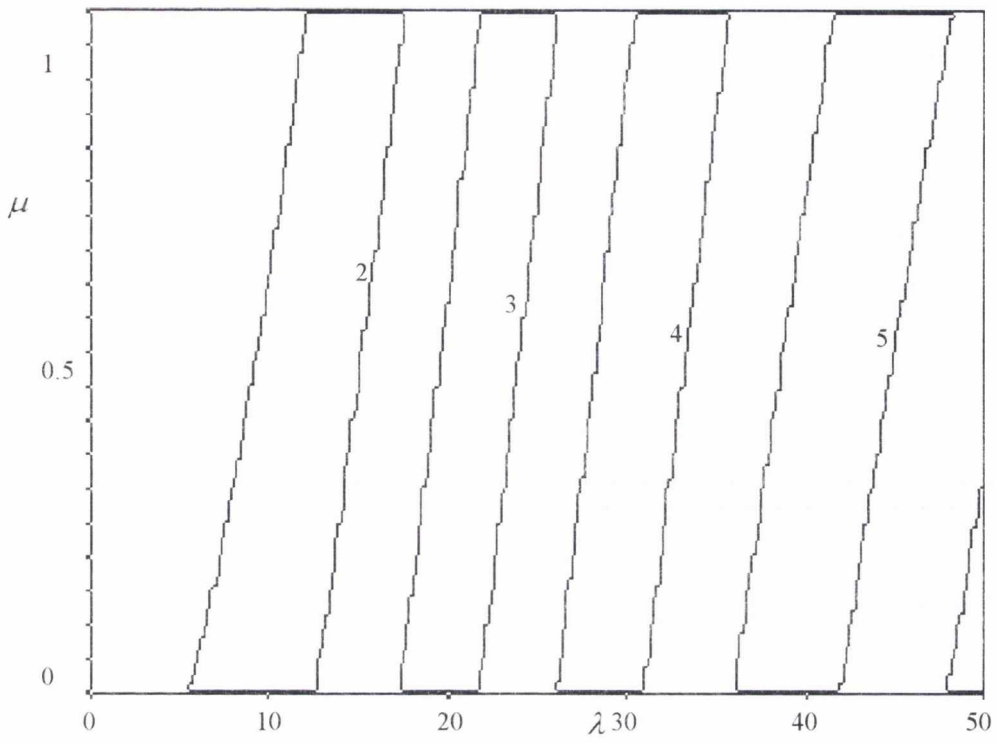

Figure A.2.27. Buckling load (P_{cr}/P_E) contours for the first mode in a non-homogeneous soil with triangular soil stiffness ($F = 0$) and triangular shaft friction ($f_1 = 0$, $f_2 = 1$) for a no rotation-no rotation fully embedded beam.

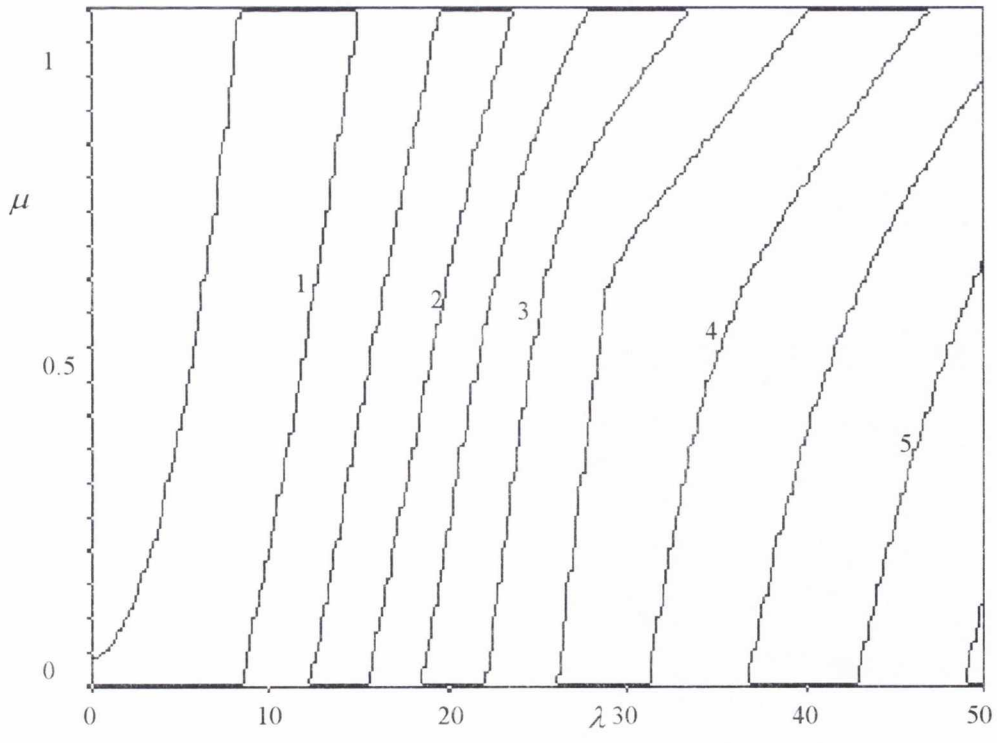

Figure A.2.28. Buckling load (P_{cr}/P_E) contours for the first mode in a non-homogeneous soil with triangular soil stiffness ($F = 0$) and triangular shaft friction ($f_1 = 0$, $f_2 = 1$) for a no rotation-free fully embedded beam.

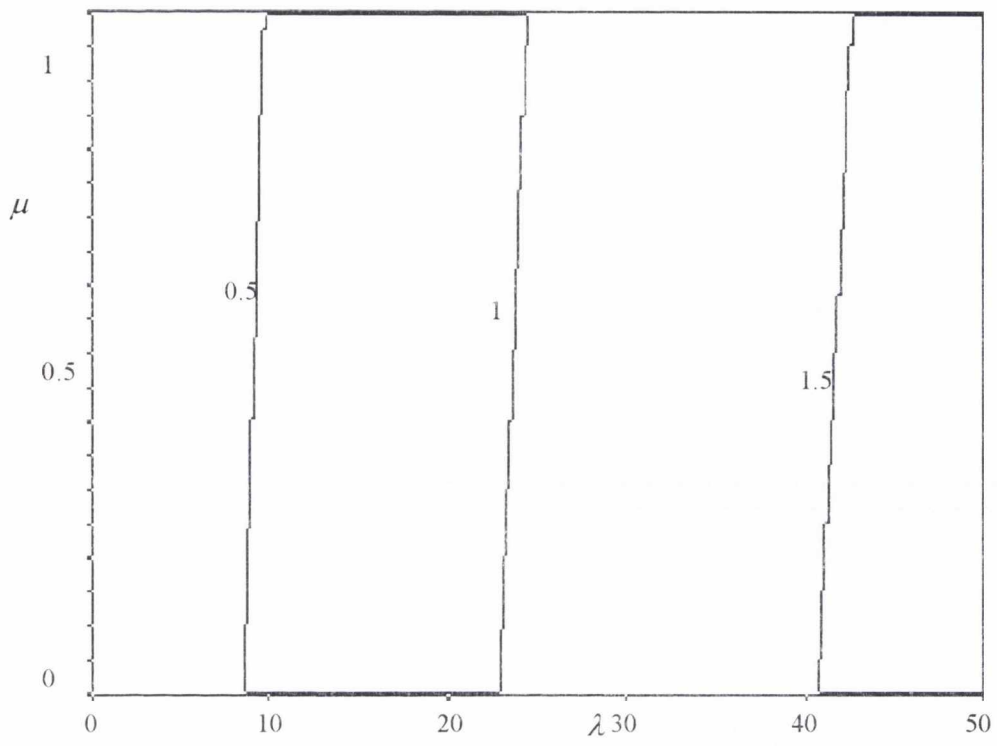

Figure A.2.29. Buckling load (P_{cr}/P_E) contours for the first mode in a non-homogeneous soil with triangular soil stiffness ($F = 0$) and triangular shaft friction ($f_1 = 0$, $f_2 = 1$) for a free-fixed fully embedded beam.

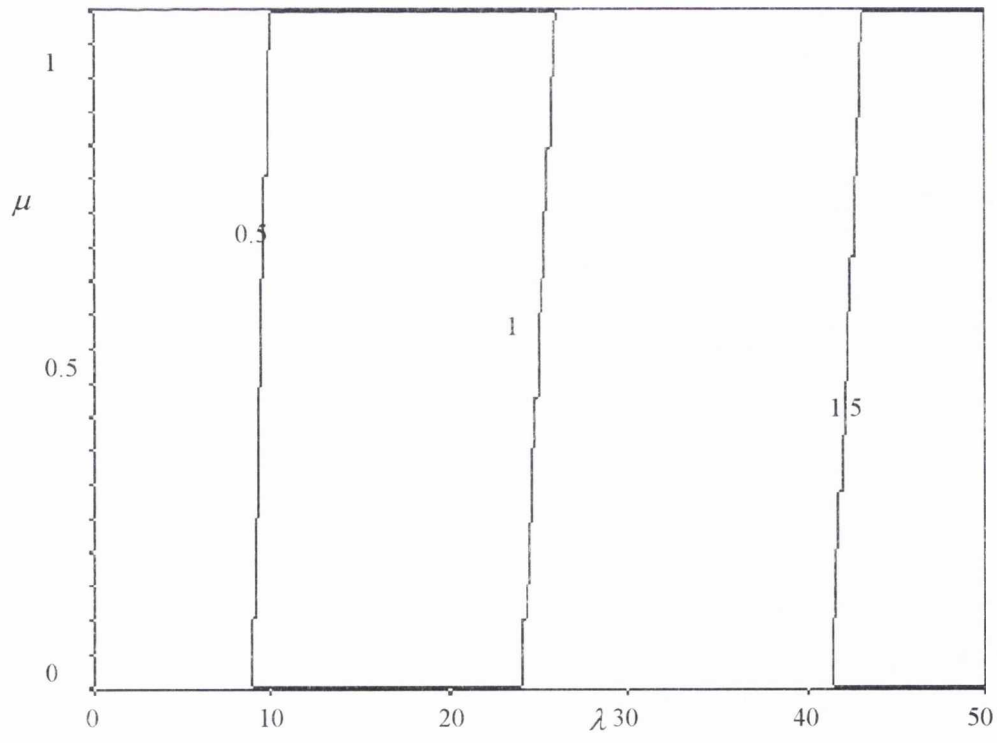

Figure A.2.30. Buckling load (P_{cr}/P_E) contours for the first mode in a non-homogeneous soil with triangular soil stiffness ($F = 0$) and triangular shaft friction ($f_1 = 0$, $f_2 = 1$) for a free-pinned fully embedded beam.

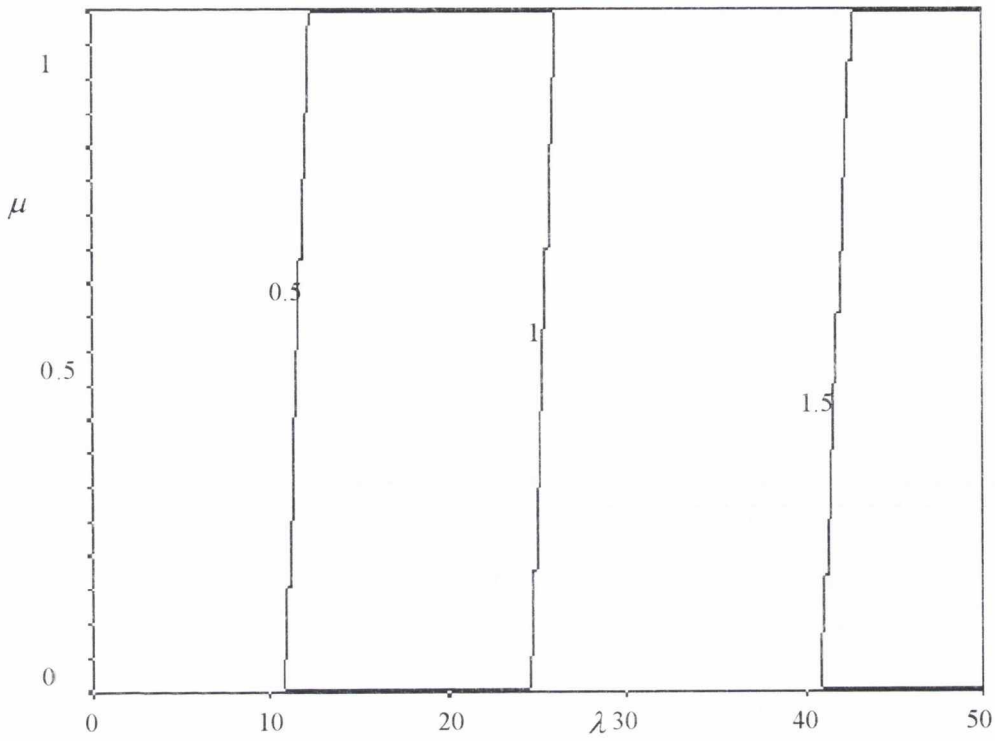

Figure A.2.31. Buckling load (P_{cr}/P_E) contours for the first mode in a non-homogeneous soil with triangular soil stiffness ($F = 0$) and triangular shaft friction ($f_1 = 0, f_2 = 1$) for a free-no rotation fully embedded beam.

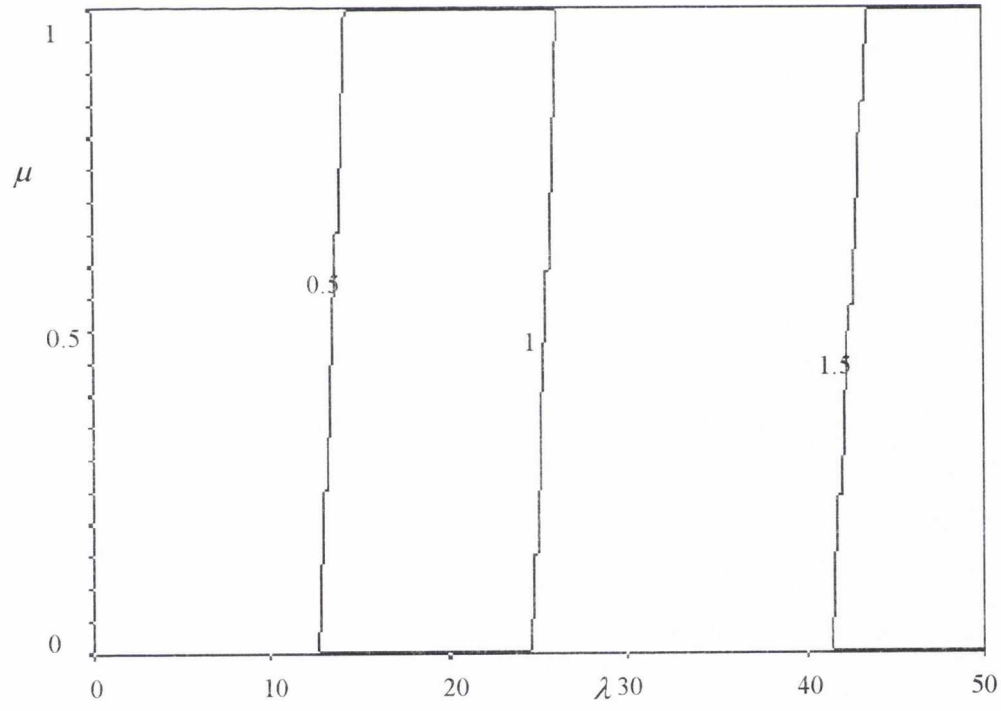

Figure A.2.32. Buckling load (P_{cr}/P_E) contours for the first mode in a non-homogeneous soil with triangular soil stiffness ($F = 0$) and triangular shaft friction ($f_1 = 0, f_2 = 1$) for a free-free fully embedded beam.

Non-homogeneous soils ($F = 0$, $f_1 = f_2 = 0.5$)

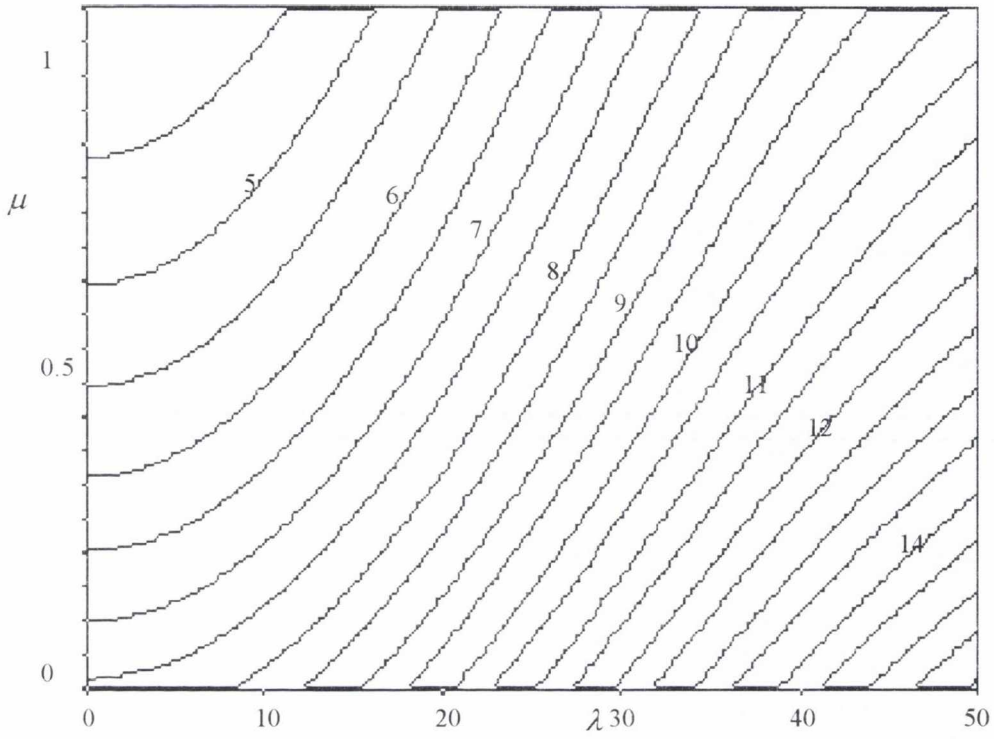

Figure A.2.33. Buckling load (P_{cr}/P_E) contours for the first mode in a non-homogeneous soil with triangular soil stiffness ($F = 0$) and constant shaft friction ($f_1 = f_2 = 0.5$) for a fixed-fixed fully embedded beam.

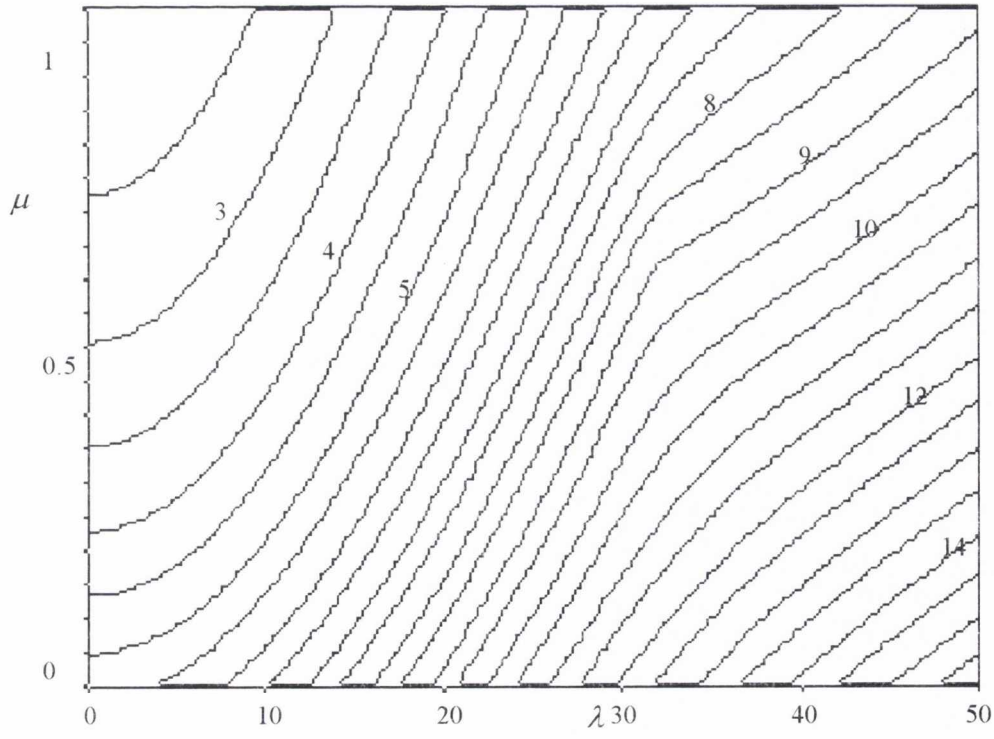

Figure A.2.34. Buckling load (P_{cr}/P_E) contours for the first mode in a non-homogeneous soil with triangular soil stiffness ($F = 0$) and constant shaft friction ($f_1 = f_2 = 0.5$) for a fixed-pinned fully embedded beam.

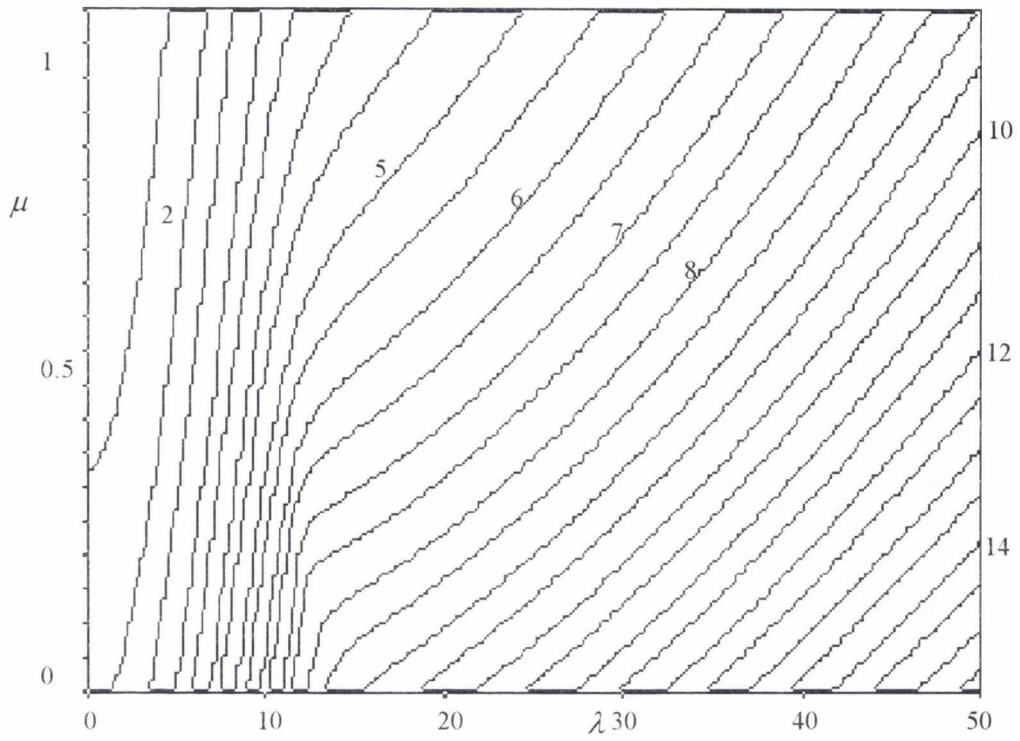

Figure A.2.35. Buckling load (P_{cr}/P_E) contours for the first mode in a non-homogeneous soil with triangular soil stiffness ($F = 0$) and constant shaft friction ($f_1 = f_2 = 0.5$) for a fixed-no rotation fully embedded beam.

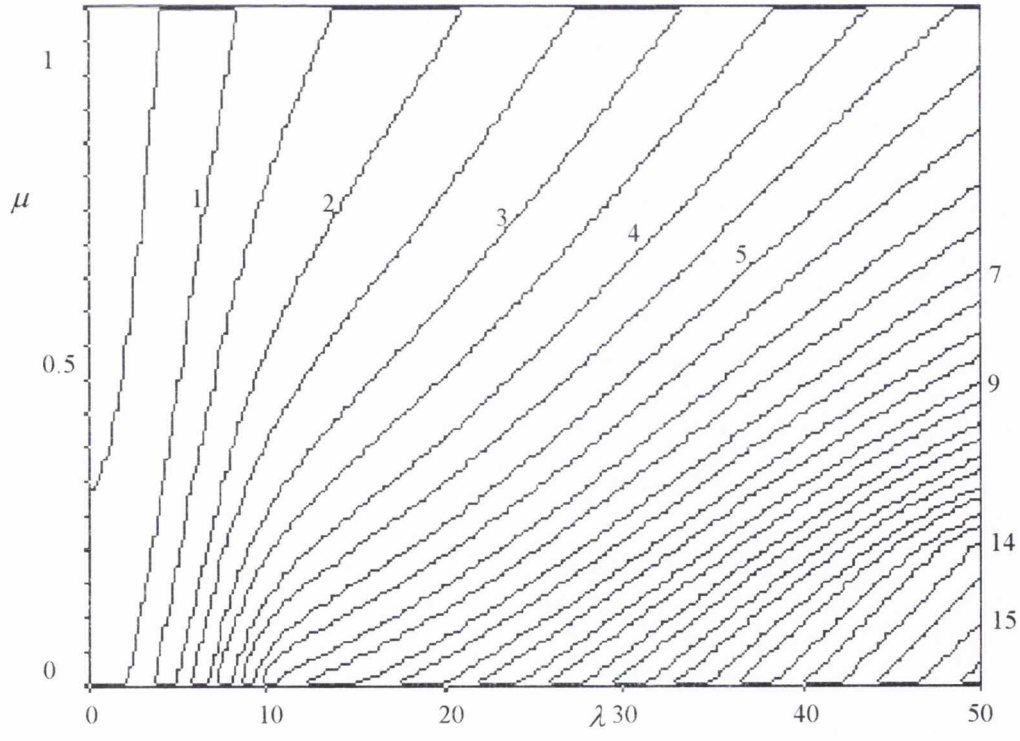

Figure A.2.36. Buckling load (P_{cr}/P_E) contours for the first mode in a non-homogeneous soil with triangular soil stiffness ($F = 0$) and constant shaft friction ($f_1 = f_2 = 0.5$) for a fixed-free fully embedded beam.

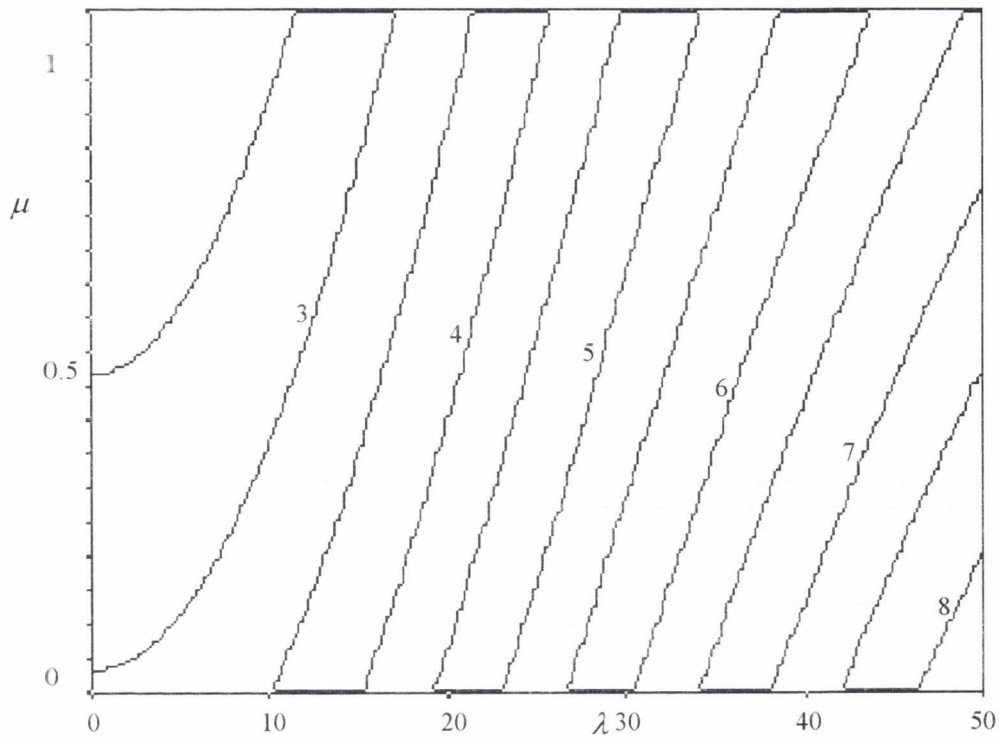

Figure A.2.37. Buckling load (P_{cr}/P_E) contours for the first mode in a non-homogeneous soil with triangular soil stiffness ($F = 0$) and constant shaft friction ($f_1 = f_2 = 0.5$) for a pinned-fixed fully embedded beam.

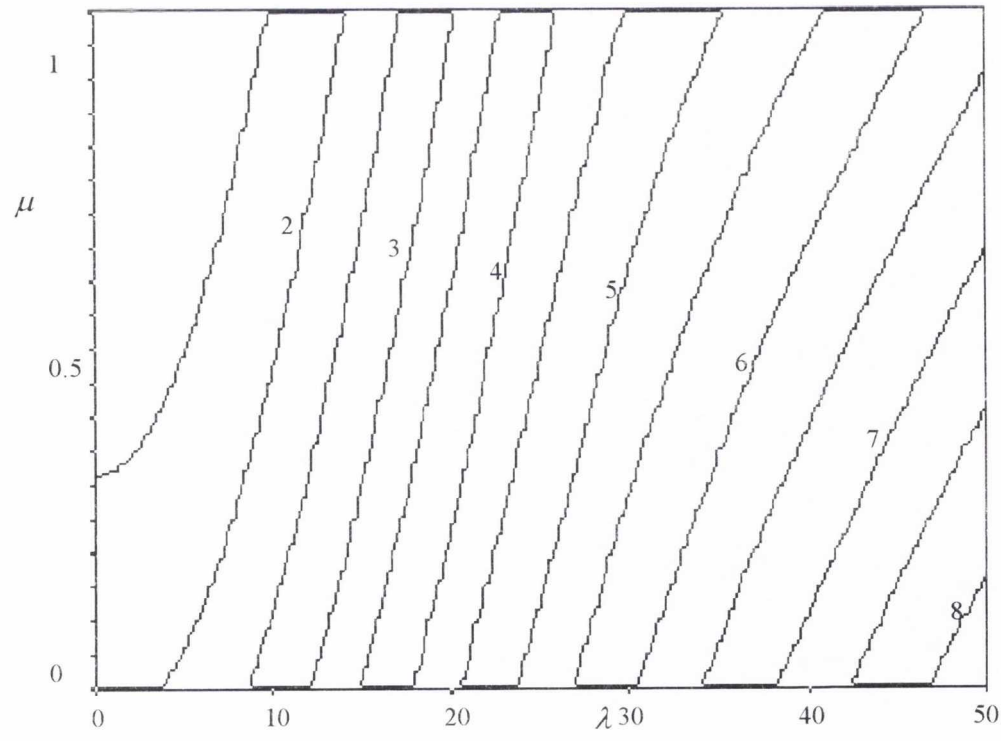

Figure A.2.38. Buckling load (P_{cr}/P_E) contours for the first mode in a non-homogeneous soil with triangular soil stiffness ($F = 0$) and constant shaft friction ($f_1 = f_2 = 0.5$) for a pinned-pinned fully embedded beam.

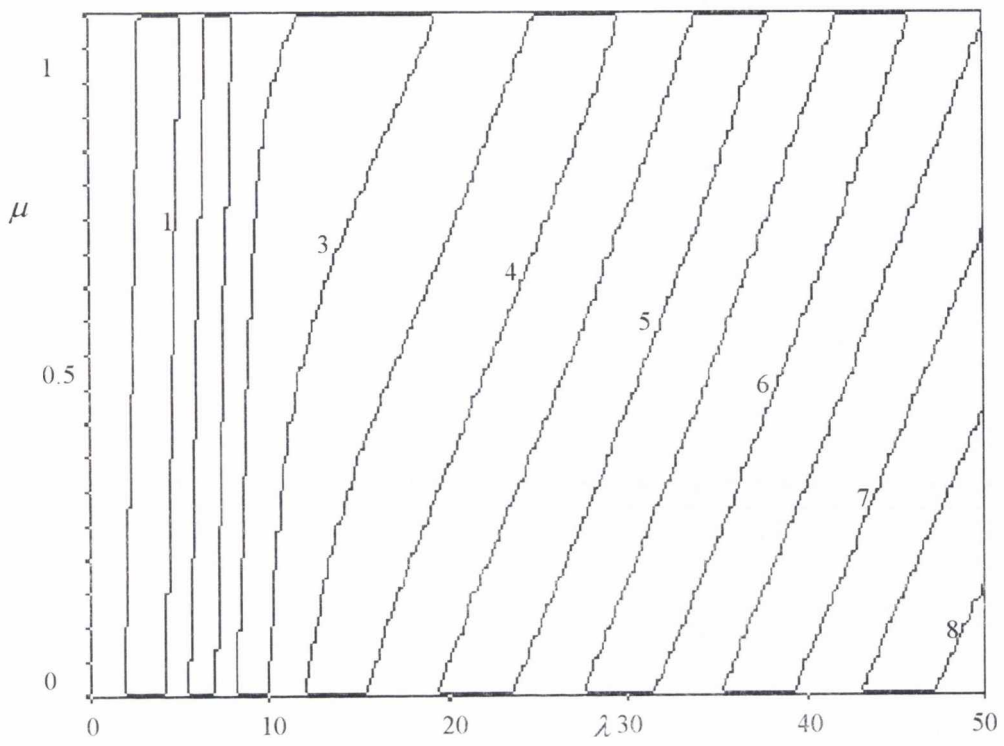

Figure A.2.39. Buckling load (P_{cr}/P_E) contours for the first mode in a non-homogeneous soil with triangular soil stiffness ($F = 0$) and constant shaft friction ($f_1 = f_2 = 0.5$) for a pinned-no rotation fully embedded beam.

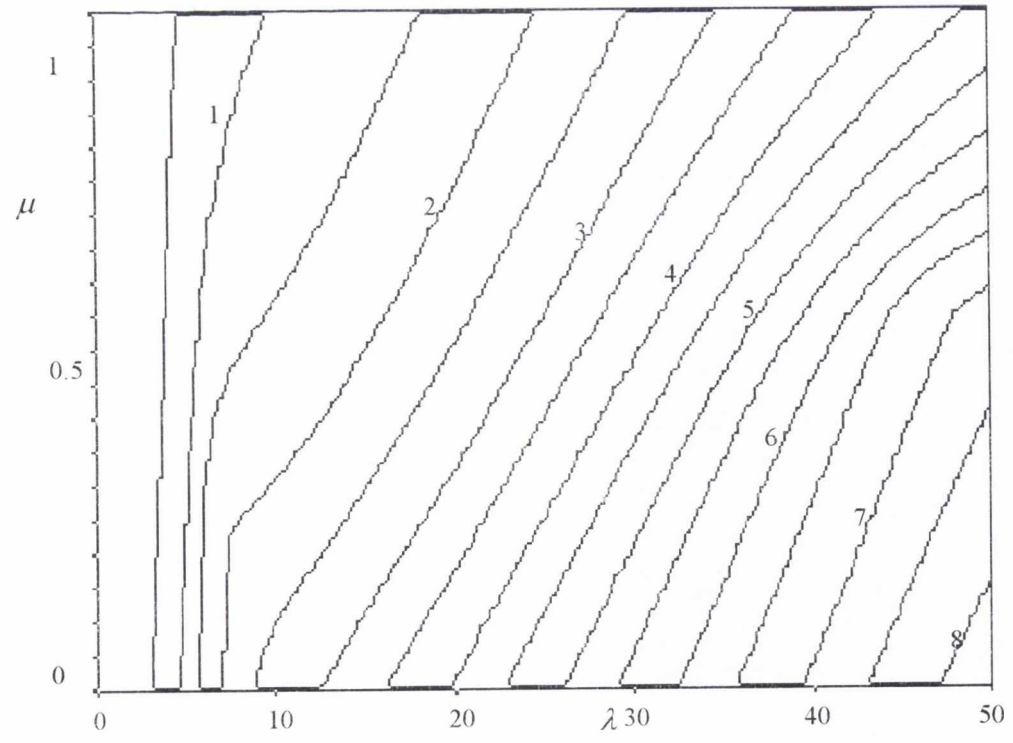

Figure A.2.40. Buckling load (P_{cr}/P_E) contours for the first mode in a non-homogeneous soil with triangular soil stiffness ($F = 0$) and constant shaft friction ($f_1 = f_2 = 0.5$) for a pinned-free fully embedded beam.

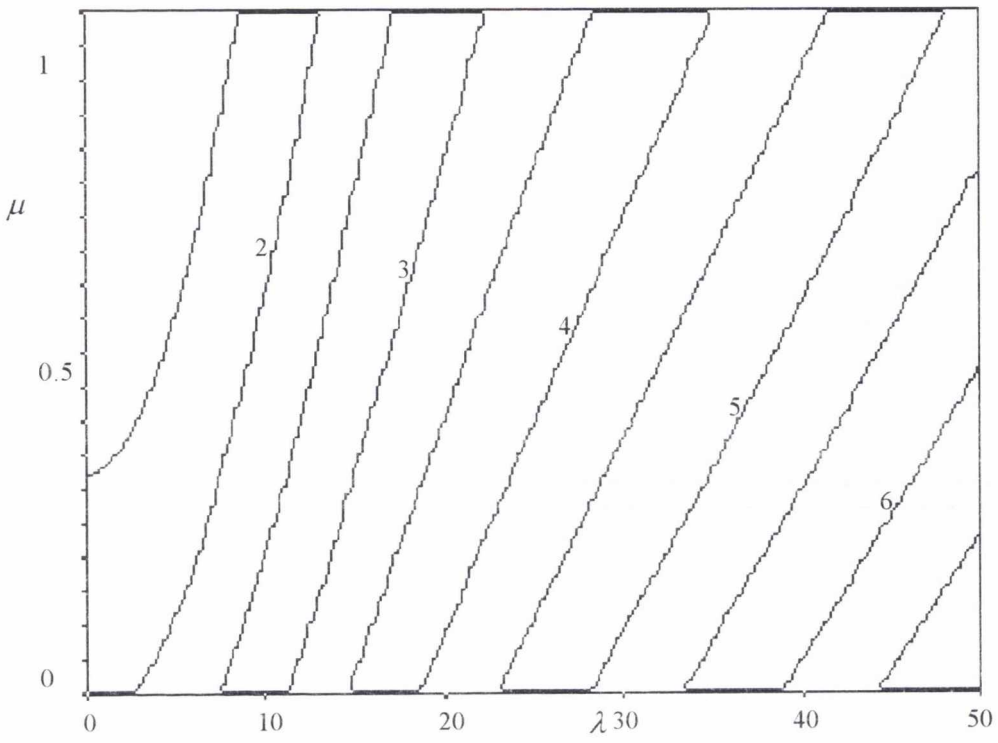

Figure A.2.41. Buckling load (P_{cr}/P_E) contours for the first mode in a non-homogeneous soil with triangular soil stiffness ($F = 0$) and constant shaft friction ($f_1 = f_2 = 0.5$) for a no rotation-fixed fully embedded beam.

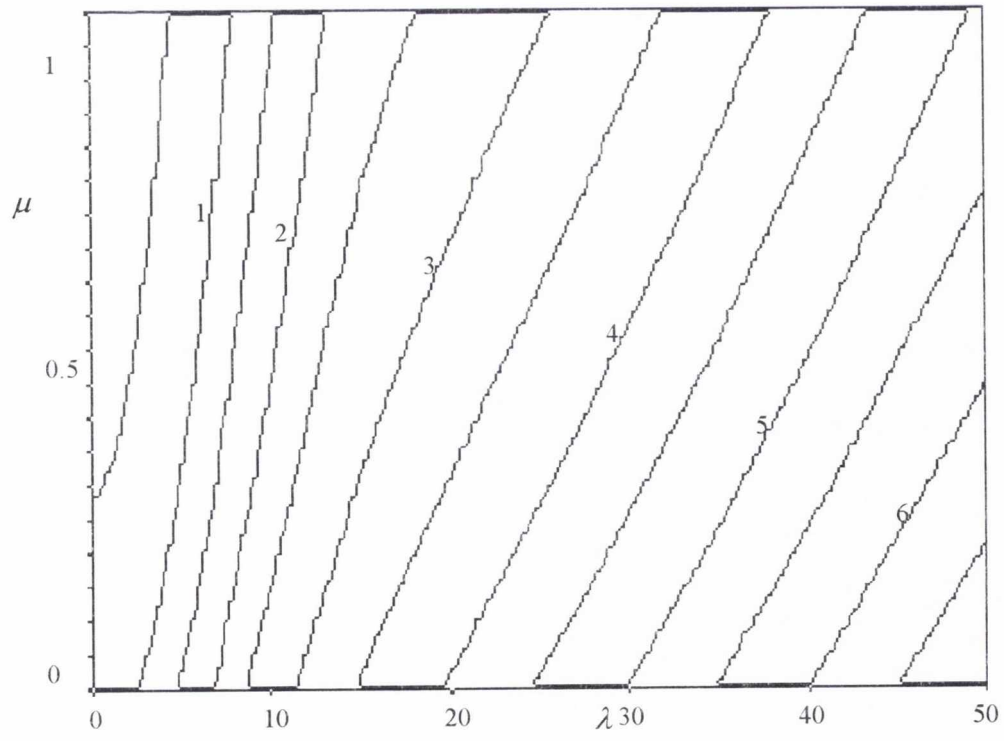

Figure A.2.42. Buckling load (P_{cr}/P_E) contours for the first mode in a non-homogeneous soil with triangular soil stiffness ($F = 0$) and constant shaft friction ($f_1 = f_2 = 0.5$) for a no rotation-pinned fully embedded beam.

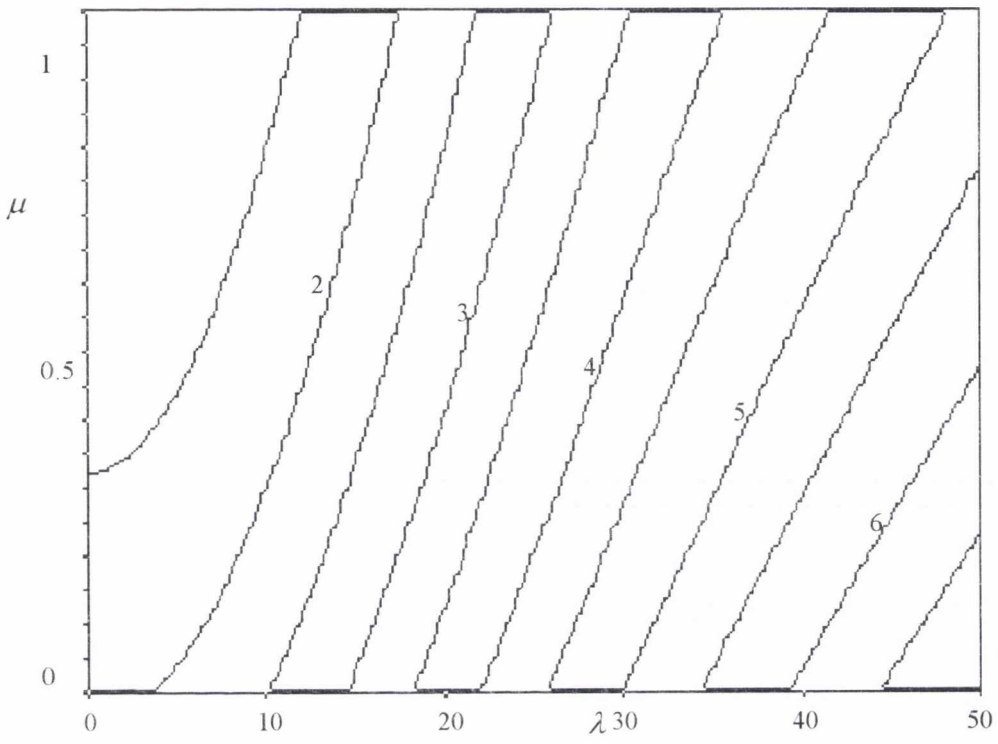

Figure A.2.43. Buckling load (P_{cr}/P_E) contours for the first mode in a non-homogeneous soil with triangular soil stiffness ($F = 0$) and constant shaft friction ($f_1 = f_2 = 0.5$) for a no rotation-no rotation fully embedded beam.

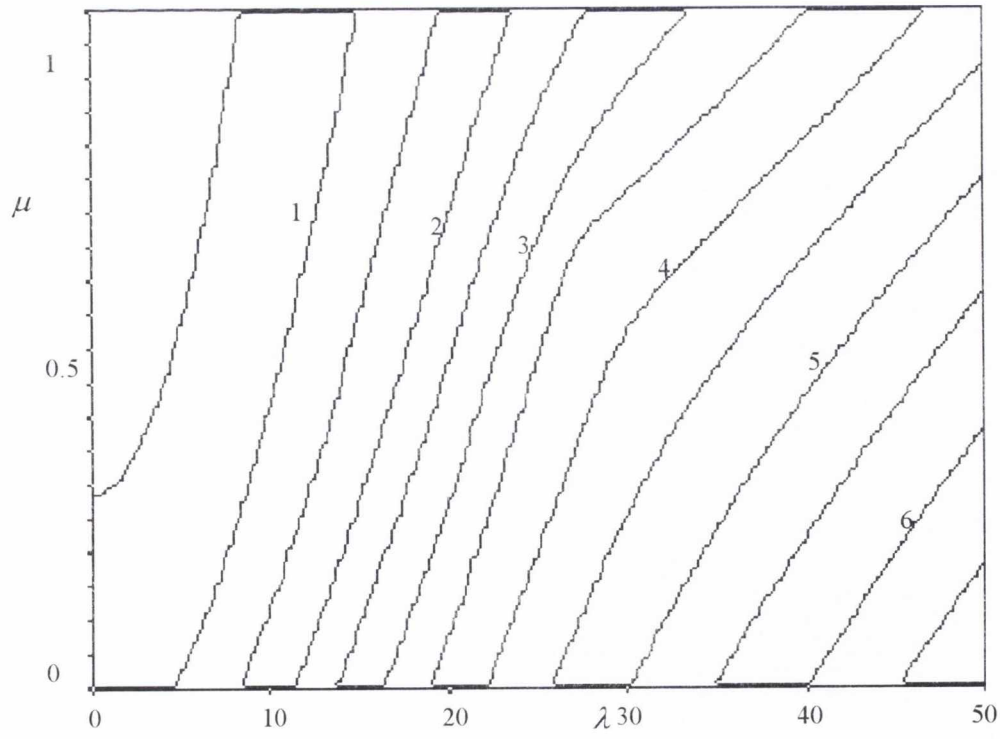

Figure A.2.44. Buckling load (P_{cr}/P_E) contours for the first mode in a non-homogeneous soil with triangular soil stiffness ($F = 0$) and constant shaft friction ($f_1 = f_2 = 0.5$) for a no rotation-free fully embedded beam.

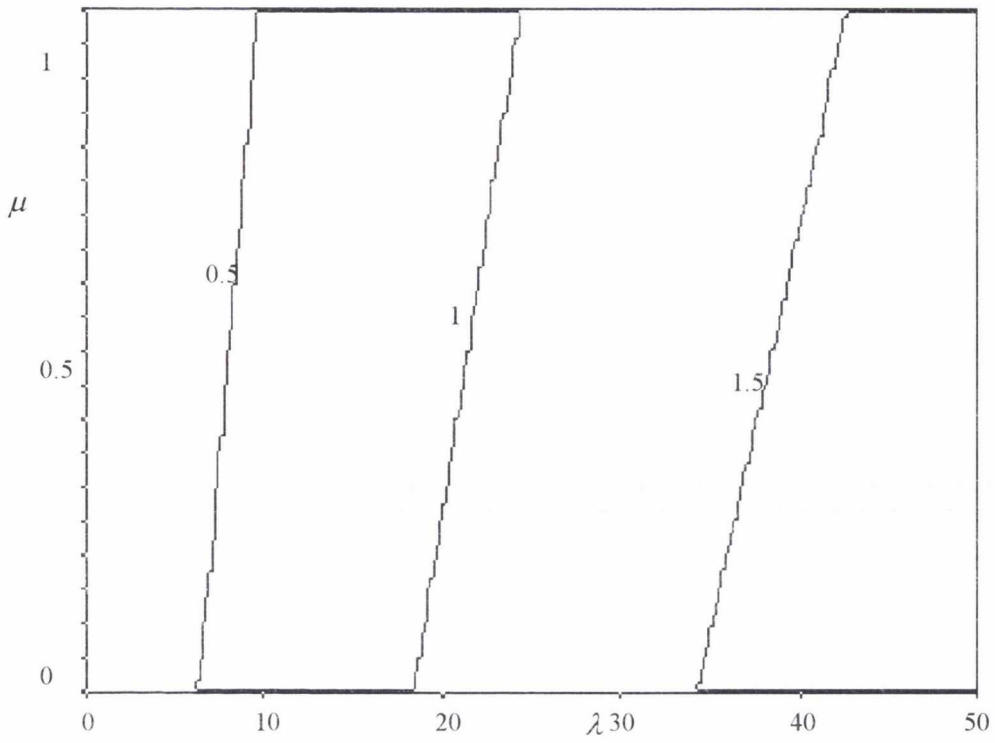

Figure A.2.45. Buckling load (P_{cr}/P_E) contours for the first mode in a non-homogeneous soil with triangular soil stiffness ($F = 0$) and constant shaft friction ($f_1 = f_2 = 0.5$) for a free-fixed fully embedded beam.

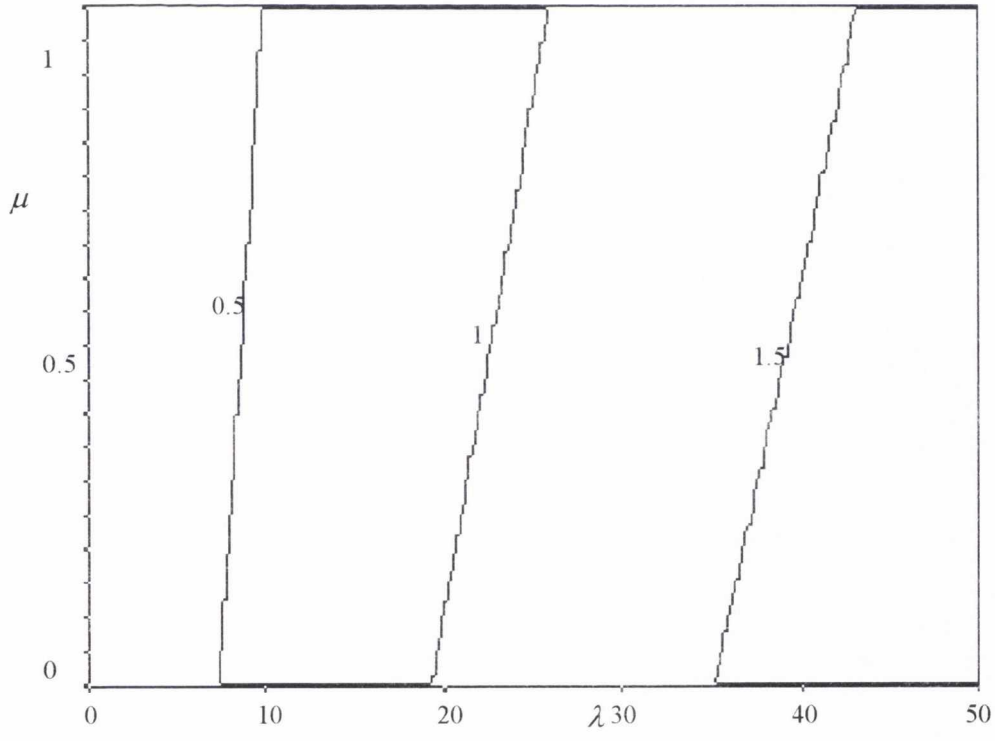

Figure A.2.46. Buckling load (P_{cr}/P_E) contours for the first mode in a non-homogeneous soil with triangular soil stiffness ($F = 0$) and constant shaft friction ($f_1 = f_2 = 0.5$) for a free-pinned fully embedded beam.

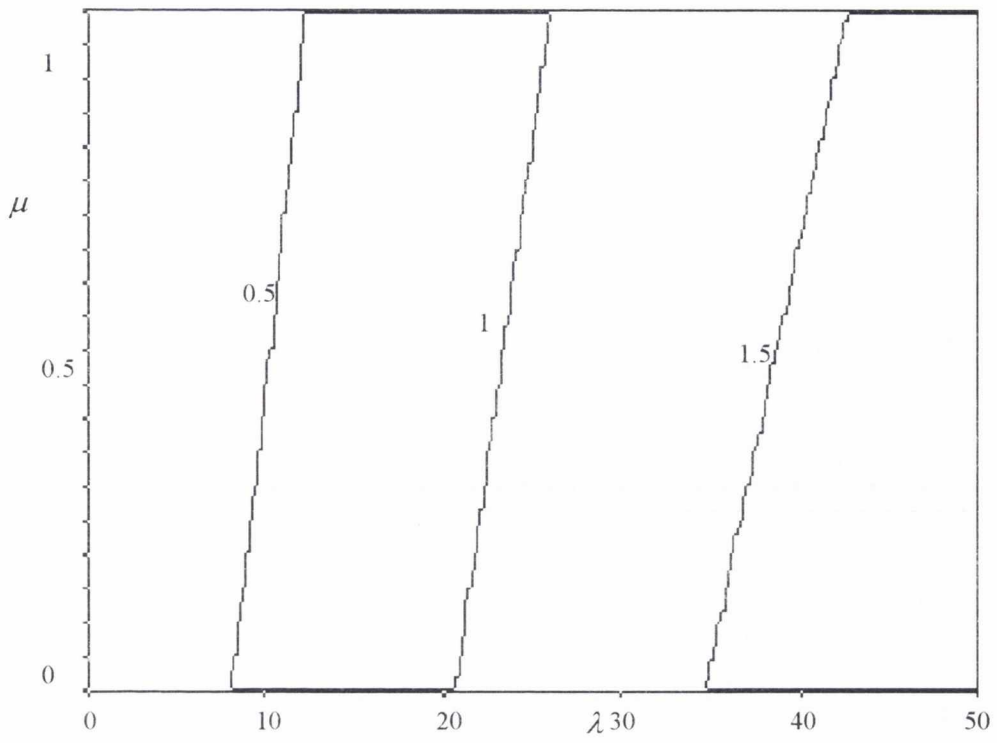

Figure A.2.47. Buckling load (P_{cr}/P_E) contours for the first mode in a non-homogeneous soil with triangular soil stiffness ($F = 0$) and constant shaft friction ($f_1 = f_2 = 0.5$) for a free-no rotation fully embedded beam.

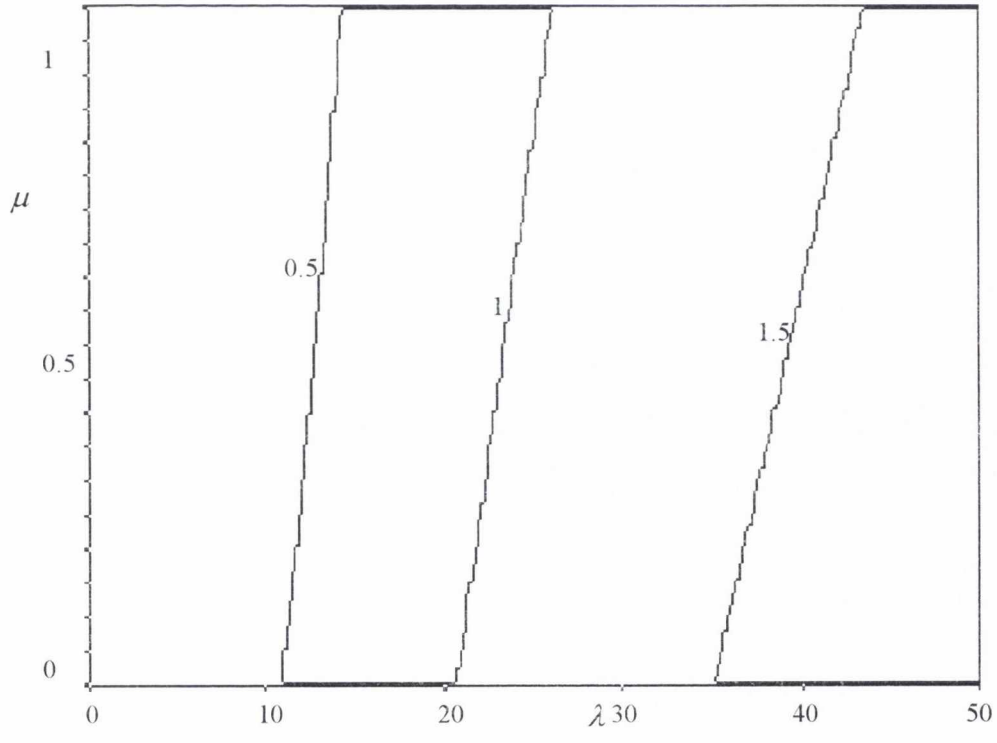

Figure A.2.48. Buckling load (P_{cr}/P_E) contours for the first mode in a non-homogeneous soil with triangular soil stiffness ($F = 0$) and constant shaft friction ($f_1 = f_2 = 0.5$) for a free-free fully embedded beam.

Non-homogeneous soils (F = 1, f_1 = 0 and f_2 = 1)

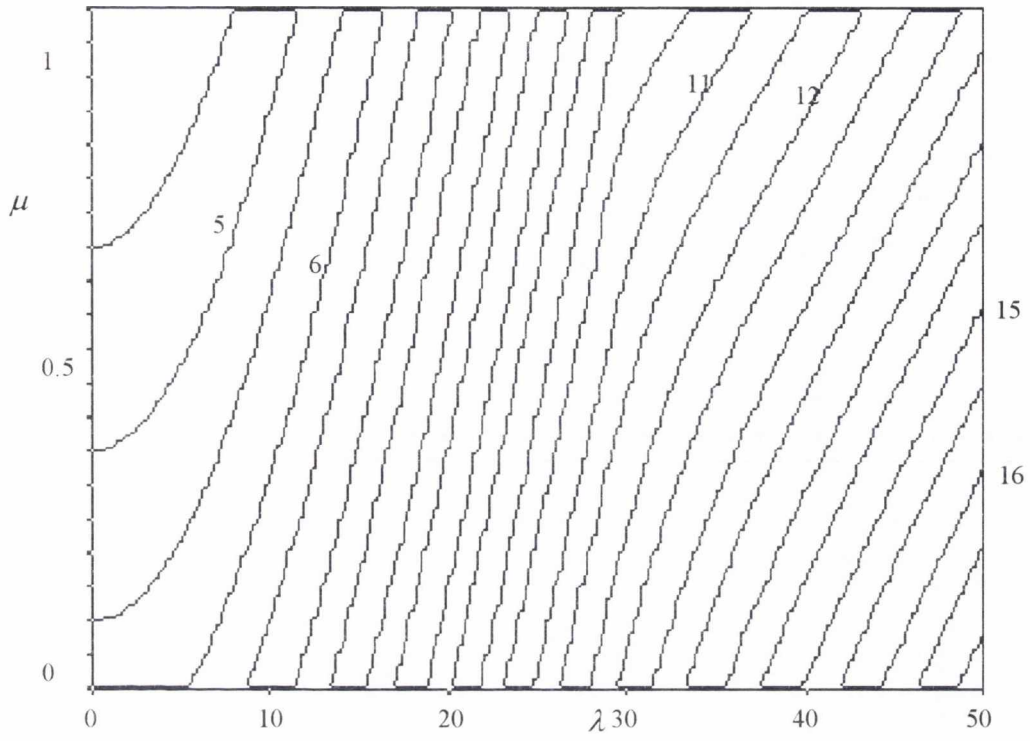

Figure A.2.49. Buckling load (P_{cr}/P_E) contours for the first mode in a non-homogeneous soil with constant soil stiffness (F = 1) and triangular shaft friction (f_1 = 0, f_2 = 1) for a fixed-fixed fully embedded beam.

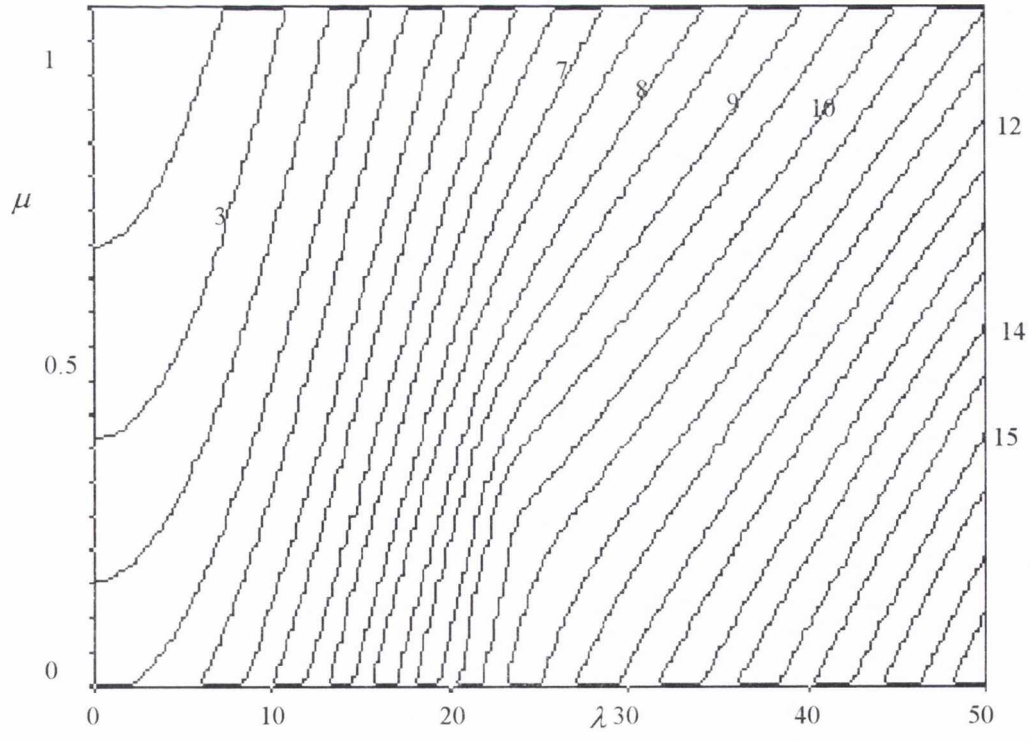

Figure A.2.50. Buckling load (P_{cr}/P_E) contours for the first mode in a non-homogeneous soil with constant soil stiffness (F = 1) and triangular shaft friction (f_1 = 0, f_2 = 1) for a fixed-pinned fully embedded beam.

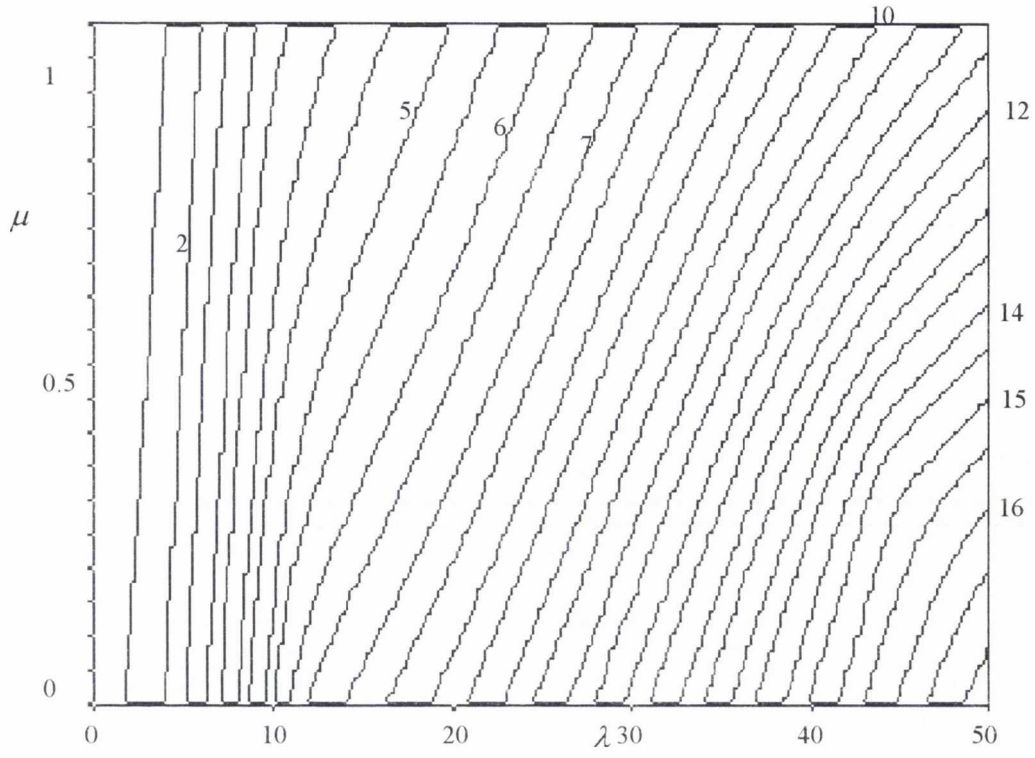

Figure A.2.51. Buckling load (P_{cr}/P_E) contours for the first mode in a non-homogeneous soil with constant soil stiffness ($F = 1$) and triangular shaft friction ($f_1 = 0, f_2 = 1$) for a fixed-no rotation fully embedded beam.

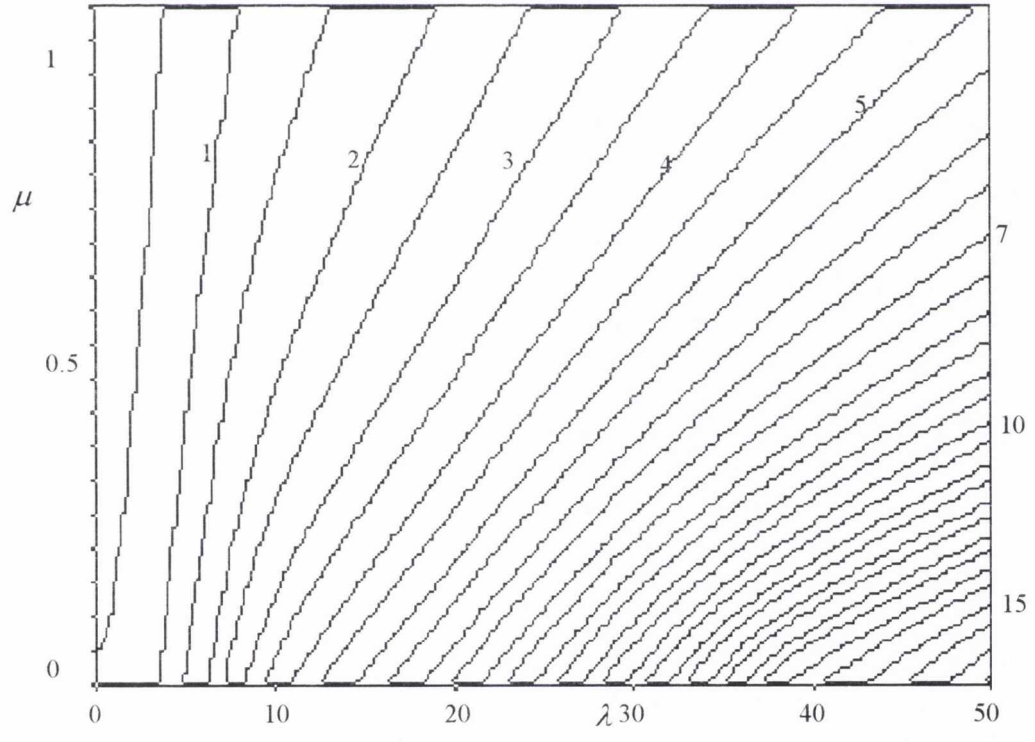

Figure A.2.52. Buckling load (P_{cr}/P_E) contours for the first mode in a non-homogeneous soil with constant soil stiffness ($F = 1$) and triangular shaft friction ($f_1 = 0, f_2 = 1$) for a fixed-free fully embedded beam.

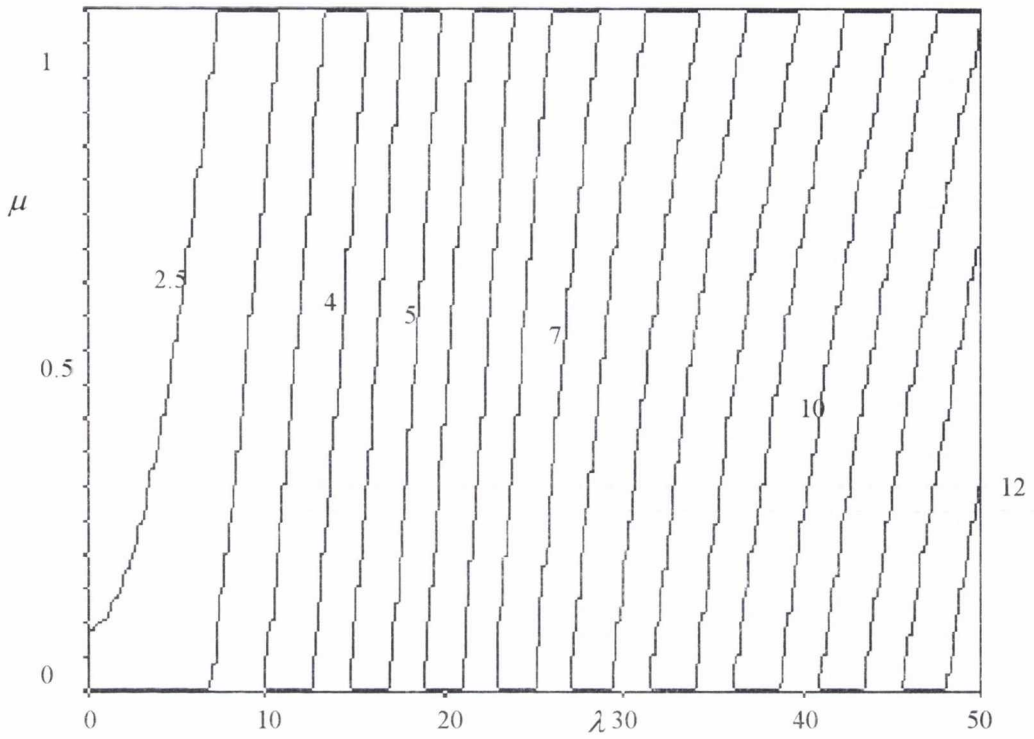

Figure A.2.53. Buckling load (P_{cr}/P_E) contours for the first mode in a non-homogeneous soil with constant soil stiffness ($F = 1$) and triangular shaft friction ($f_1 = 0$, $f_2 = 1$) for a pinned-fixed fully embedded beam.

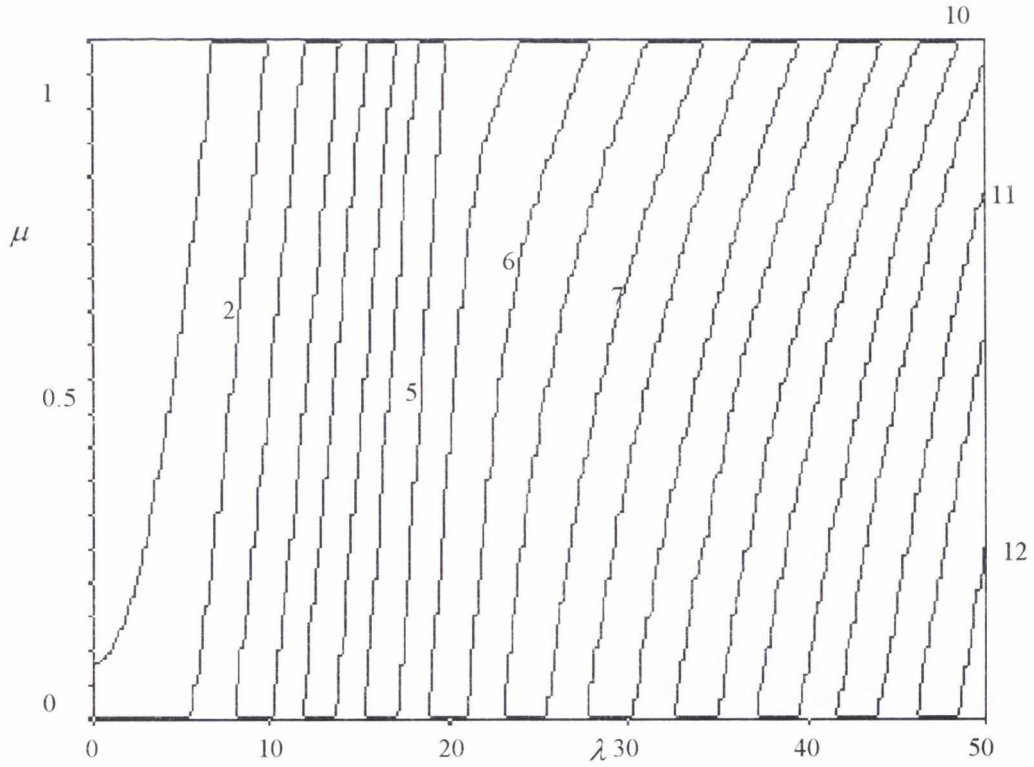

Figure A.2.54. Buckling load (P_{cr}/P_E) contours for the first mode in a non-homogeneous soil with constant soil stiffness ($F = 1$) and triangular shaft friction ($f_1 = 0$, $f_2 = 1$) for a pinned-pinned fully embedded beam.

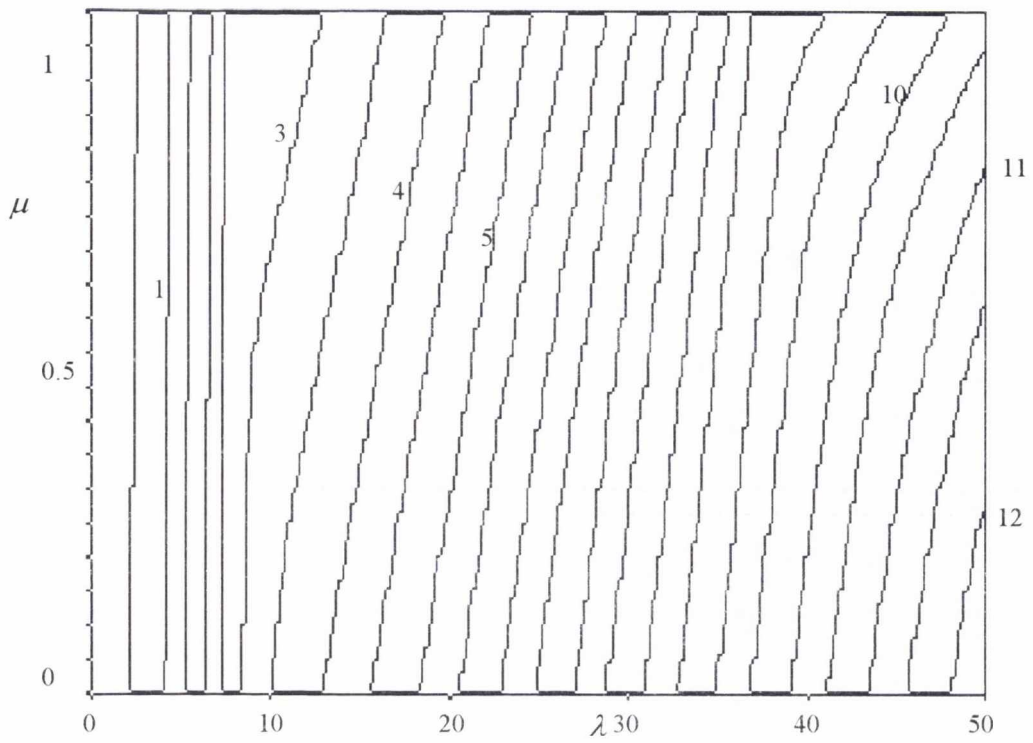

Figure A.2.55. Buckling load (P_{cr}/P_E) contours for the first mode in a non-homogeneous soil with constant soil stiffness ($F = 1$) and triangular shaft friction ($f_1 = 0, f_2 = 1$) for a pinned-no rotation fully embedded beam.

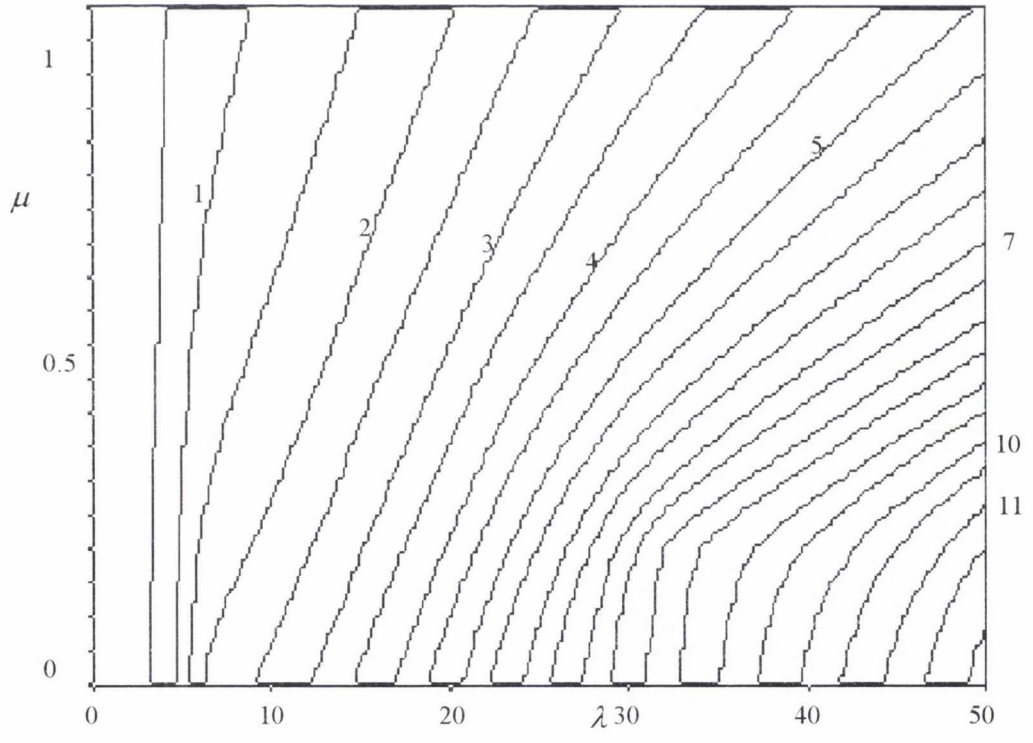

Figure A.2.56. Buckling load (P_{cr}/P_E) contours for the first mode in a non-homogeneous soil with constant soil stiffness ($F = 1$) and triangular shaft friction ($f_1 = 0, f_2 = 1$) for a pinned-free fully embedded beam.

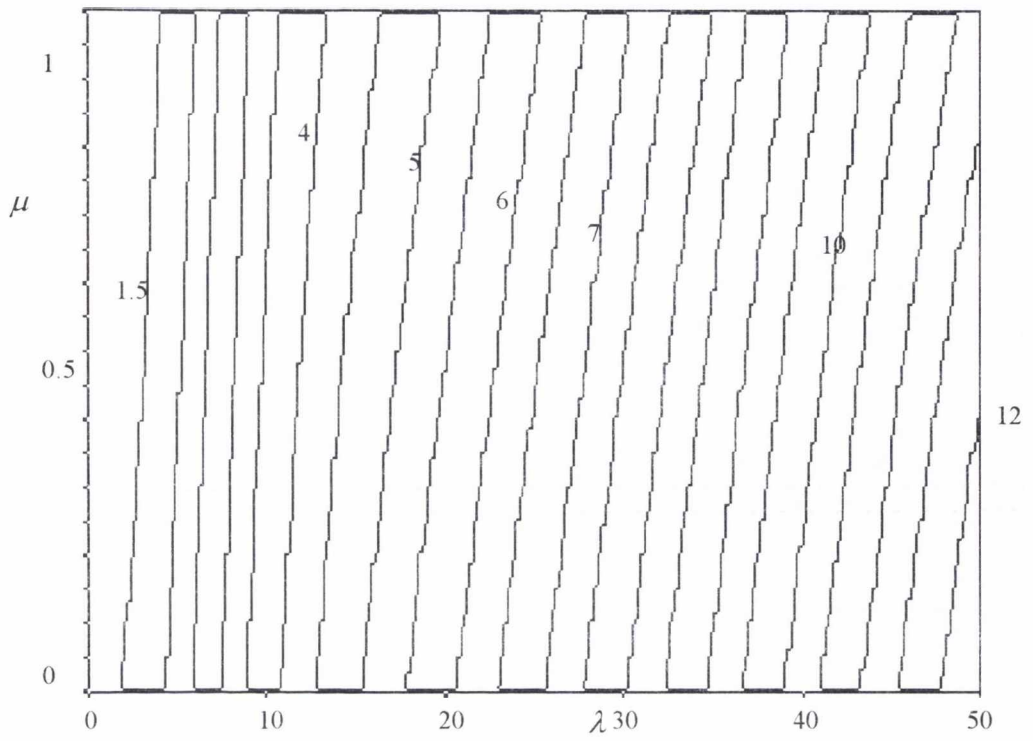

Figure A.2.57. Buckling load (P_{cr}/P_E) contours for the first mode in a non-homogeneous soil with constant soil stiffness ($F = 1$) and triangular shaft friction ($f_1 = 0, f_2 = 1$) for a no rotation-fixed fully embedded beam.

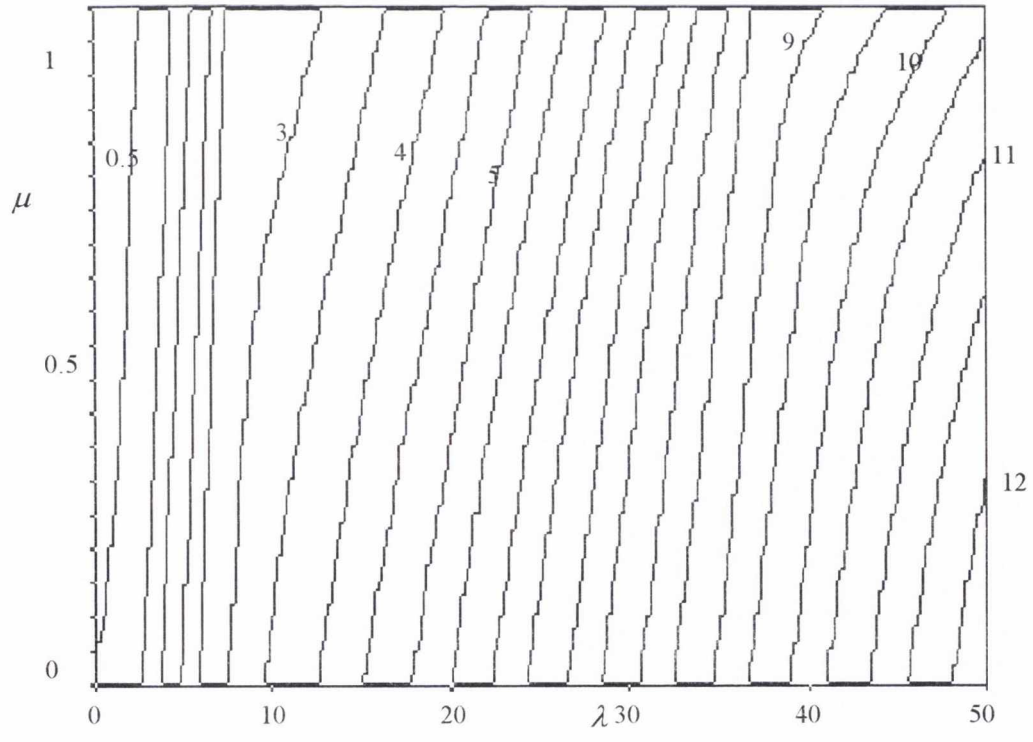

Figure A.2.58. Buckling load (P_{cr}/P_E) contours for the first mode in a non-homogeneous soil with constant soil stiffness ($F = 1$) and triangular shaft friction ($f_1 = 0, f_2 = 1$) for a no rotation-pinned fully embedded beam.

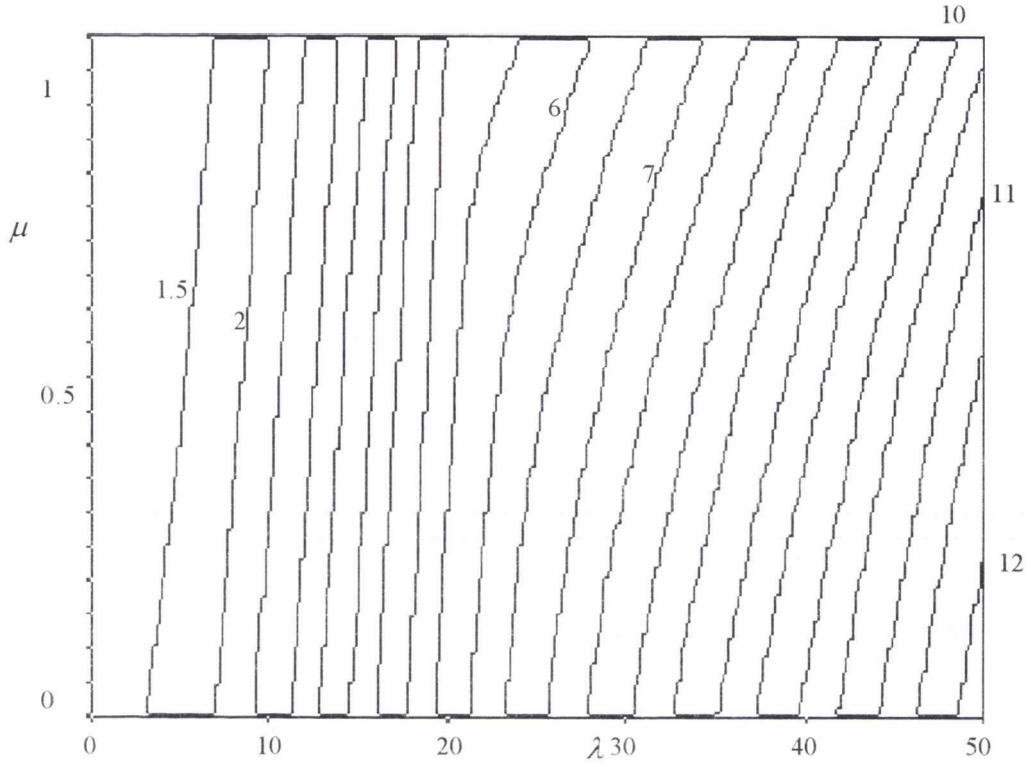

Figure A.2.59. Buckling load (P_{cr}/P_E) contours for the first mode in a non-homogeneous soil with constant soil stiffness ($F = 1$) and triangular shaft friction ($f_1 = 0$, $f_2 = 1$) for a no rotation-no rotation fully embedded beam.

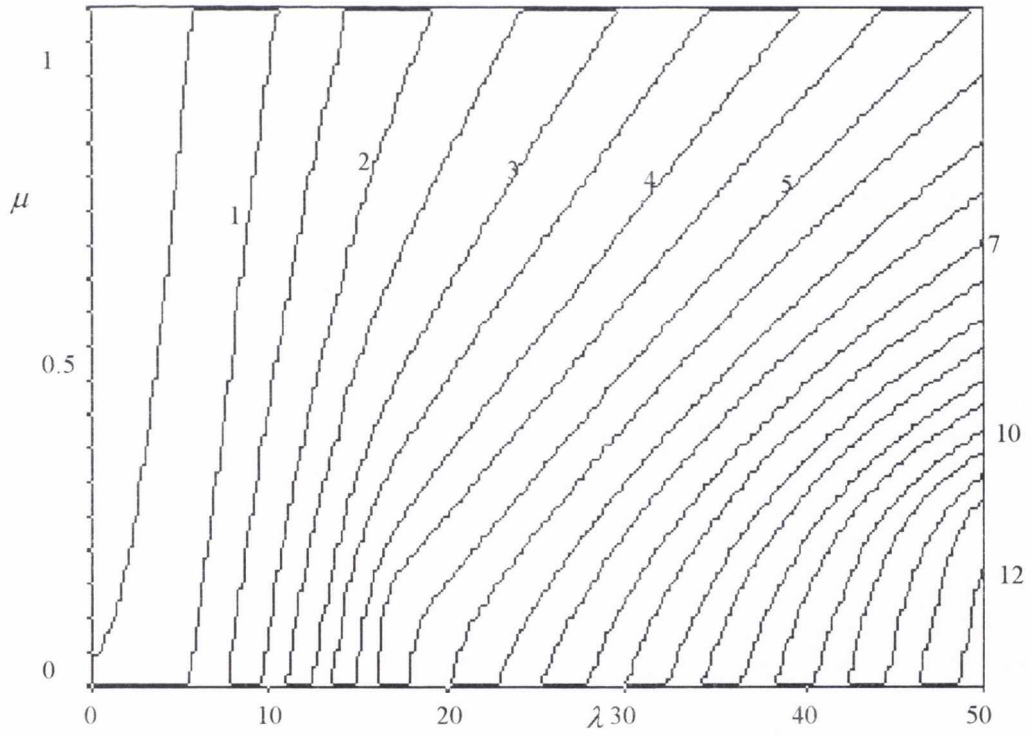

Figure A.2.60. Buckling load (P_{cr}/P_E) contours for the first mode in a non-homogeneous soil with constant soil stiffness ($F = 1$) and triangular shaft friction ($f_1 = 0$, $f_2 = 1$) for a no rotation-free fully embedded beam.

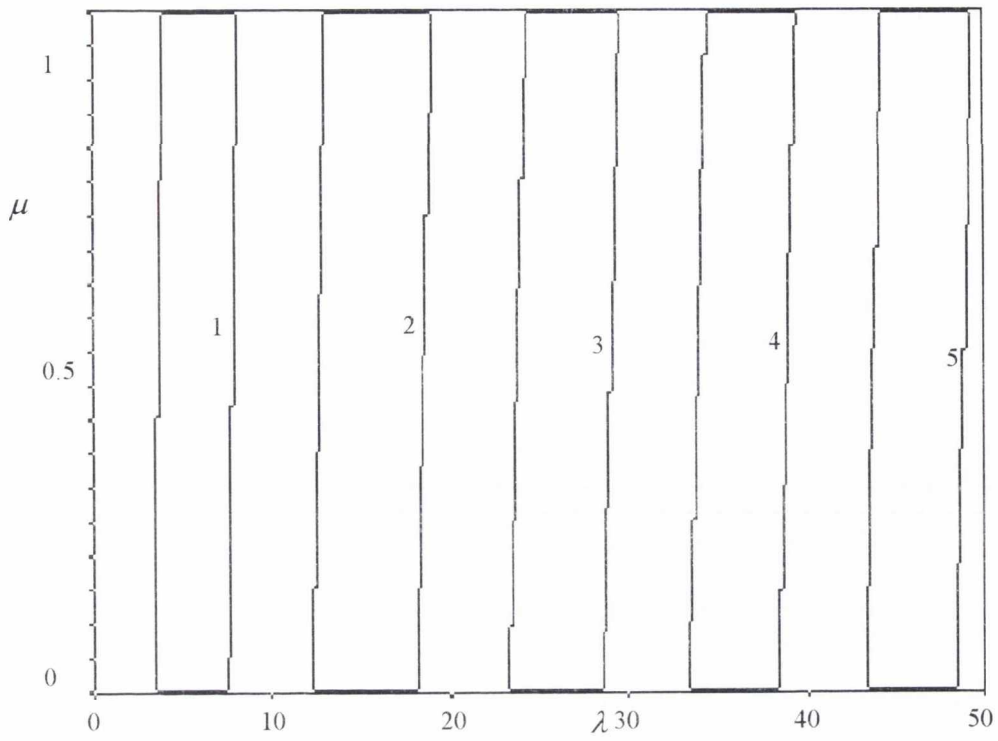

Figure A.2.61. Buckling load (P_{cr}/P_E) contours for the first mode in a non-homogeneous soil with constant soil stiffness ($F = 1$) and triangular shaft friction ($f_1 = 0$, $f_2 = 1$) for a free-fixed fully embedded beam.

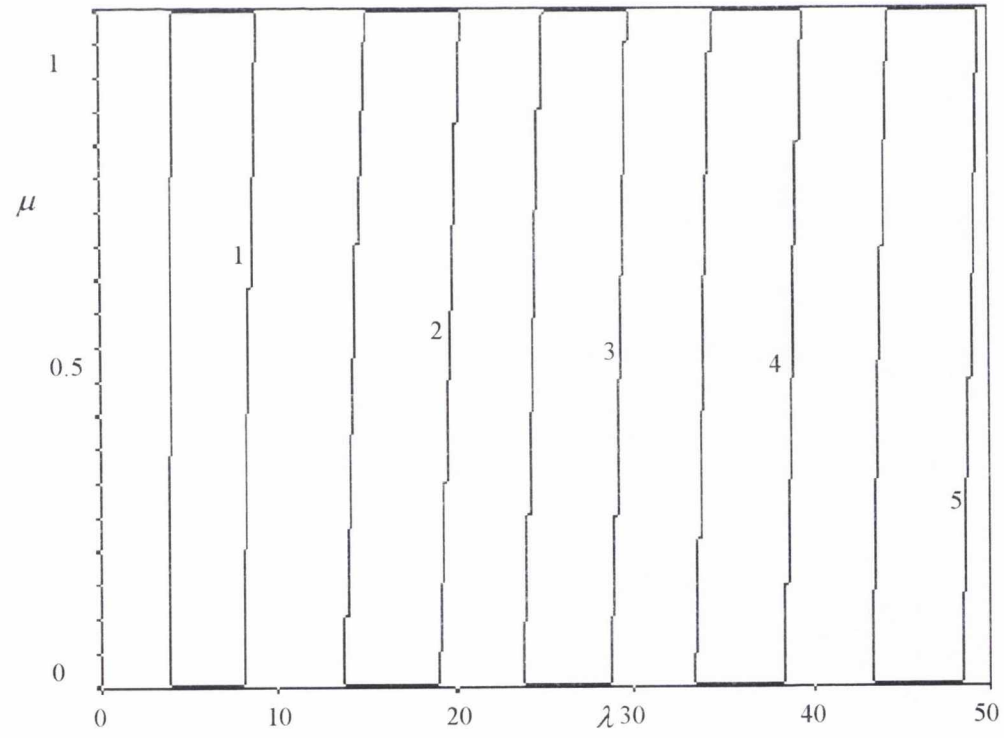

Figure A.2.62. Buckling load (P_{cr}/P_E) contours for the first mode in a non-homogeneous soil with constant soil stiffness ($F = 1$) and triangular shaft friction ($f_1 = 0$, $f_2 = 1$) for a free-pinned fully embedded beam.

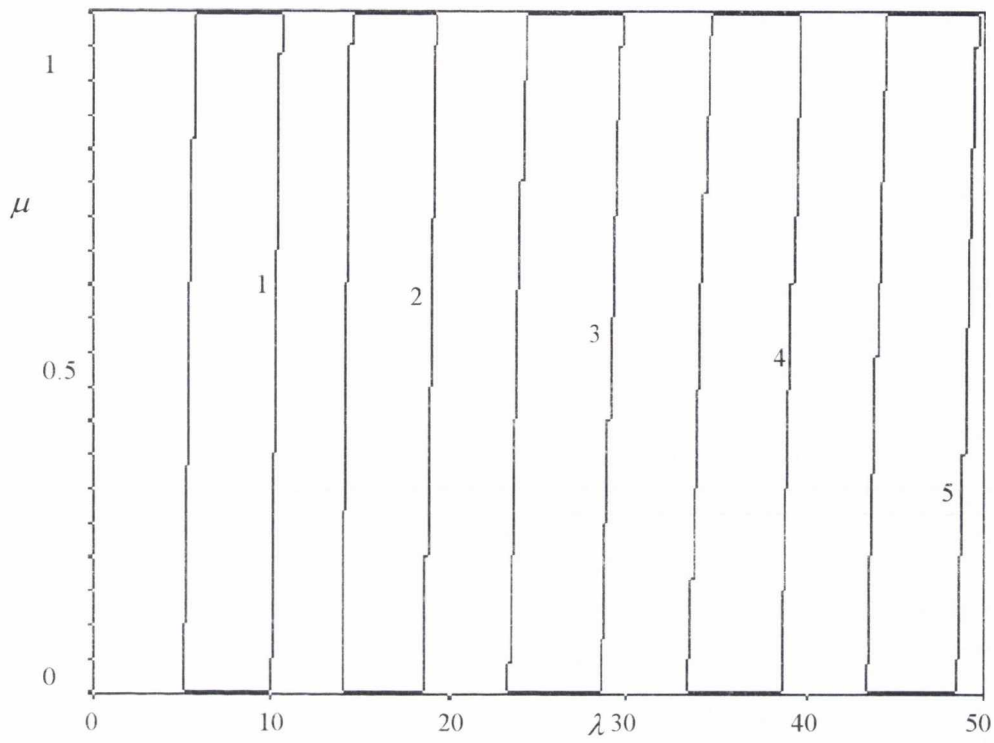

Figure A.2.63. Buckling load (P_{cr}/P_E) contours for the first mode in a non-homogeneous soil with constant soil stiffness ($F = 1$) and triangular shaft friction ($f_1 = 0$, $f_2 = 1$) for a free-no rotation fully embedded beam.

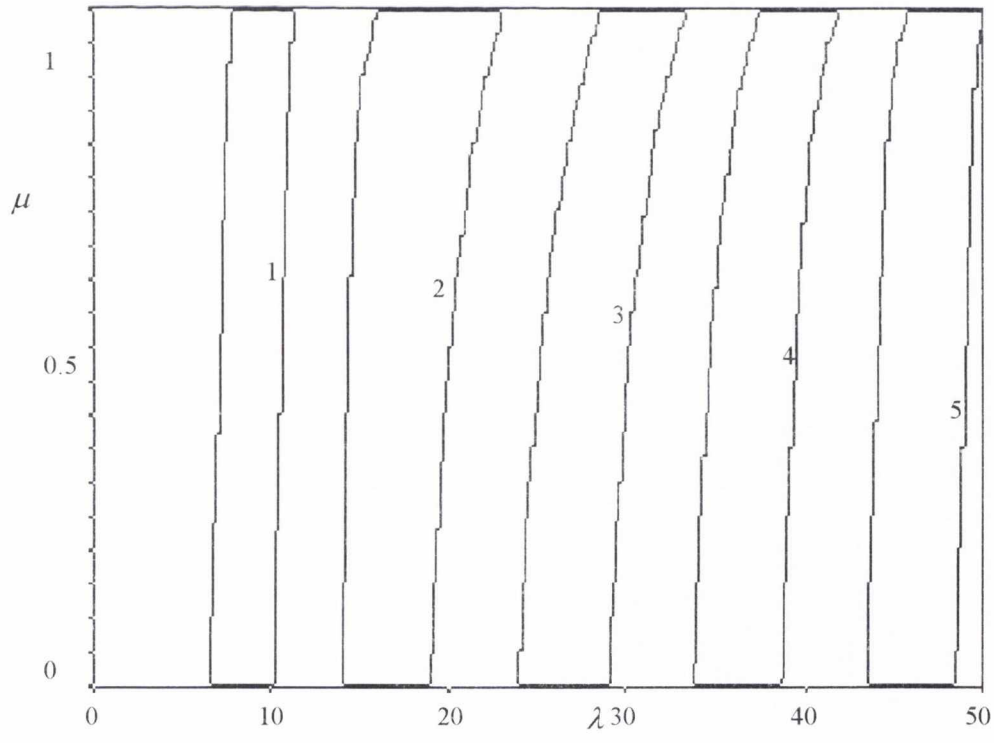

Figure A.2.64. Buckling load (P_{cr}/P_E) contours for the first mode in a non-homogeneous soil with constant soil stiffness ($F = 1$) and triangular shaft friction ($f_1 = 0$, $f_2 = 1$) for a free-free fully embedded beam.

Non-homogeneous soils (F = 1, f_1 = 0 and f_2 = 1)

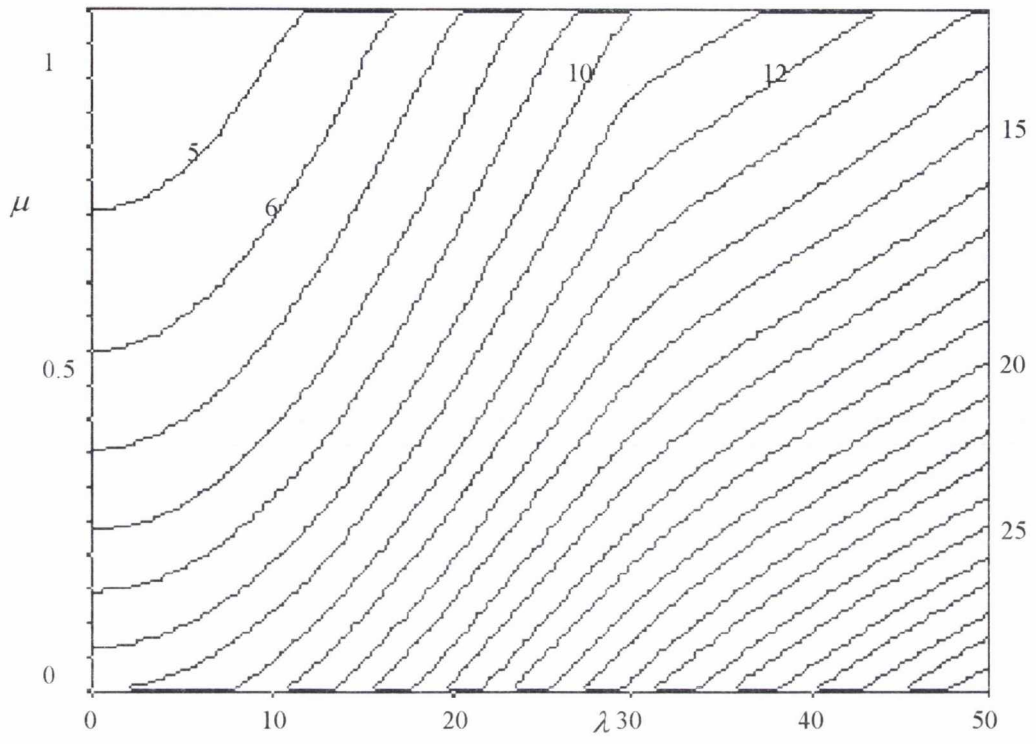

Figure A.2.65. Buckling load (P_{cr}/P_E) contours for the first mode in a non-homogeneous soil with constant soil stiffness (F = 1) and triangular shaft friction (f_1 = 0, f_2 = 1) for a fixed-fixed fully embedded beam.

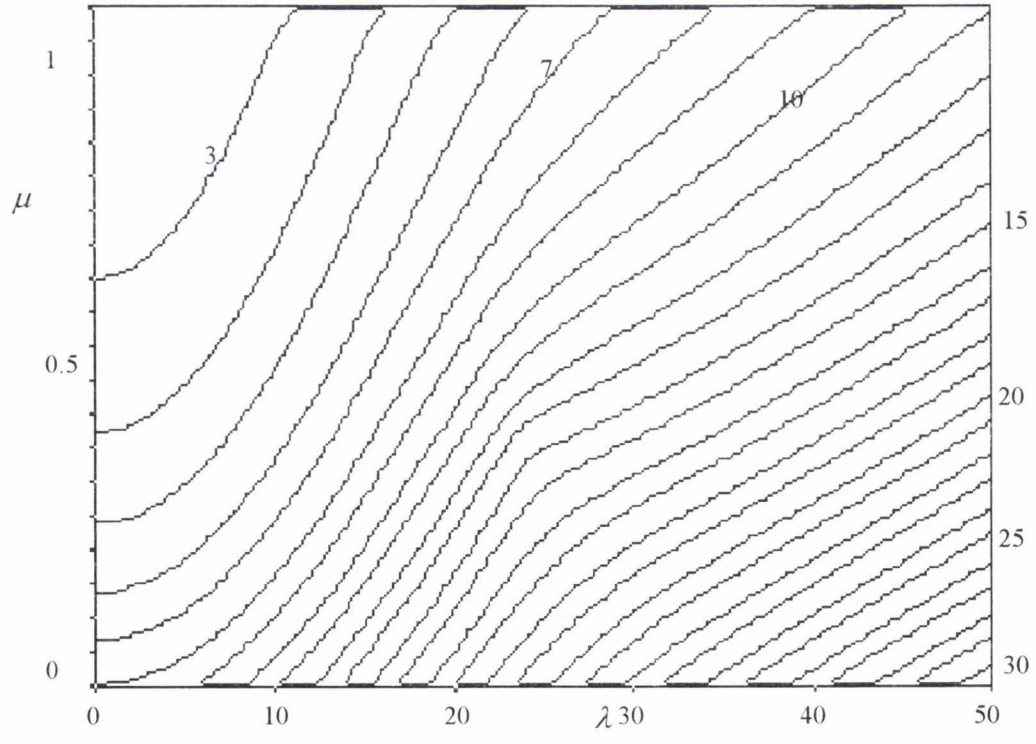

Figure A.2.66. Buckling load (P_{cr}/P_E) contours for the first mode in a non-homogeneous soil with constant soil stiffness (F = 1) and triangular shaft friction (f_1 = 0, f_2 = 1) for a fixed-pinned fully embedded beam.

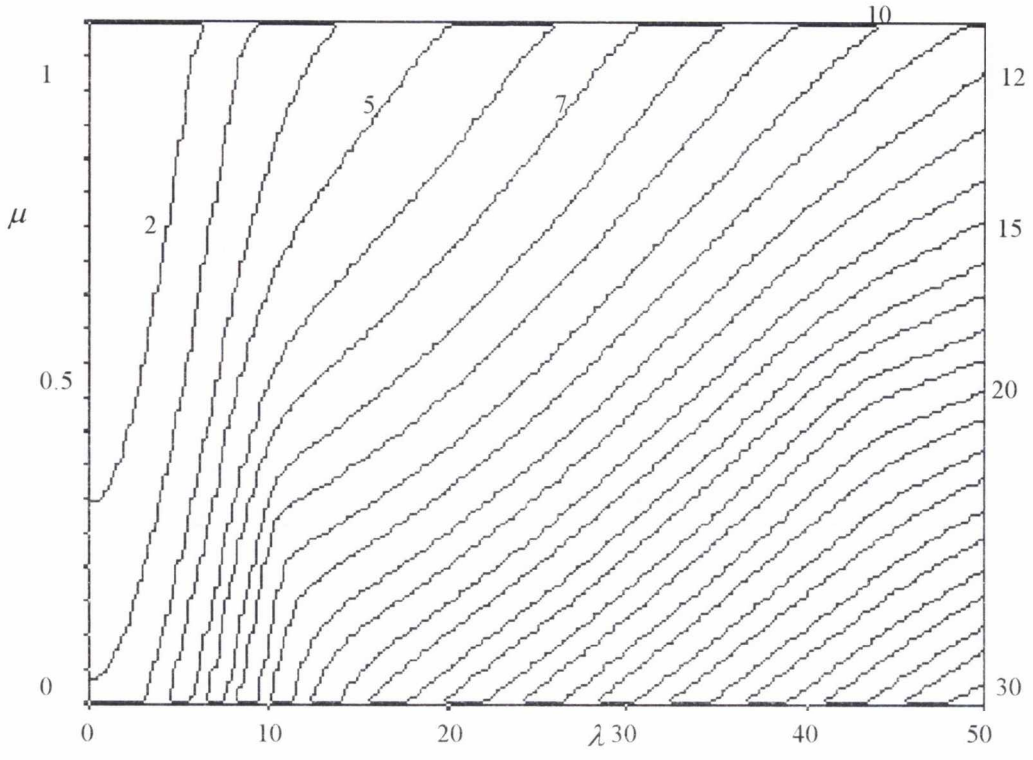

Figure A.2.67. Buckling load (P_{cr}/P_E) contours for the first mode in a non-homogeneous soil with constant soil stiffness ($F = 1$) and triangular shaft friction ($f_1 = 0$, $f_2 = 1$) for a fixed-no rotation fully embedded beam.

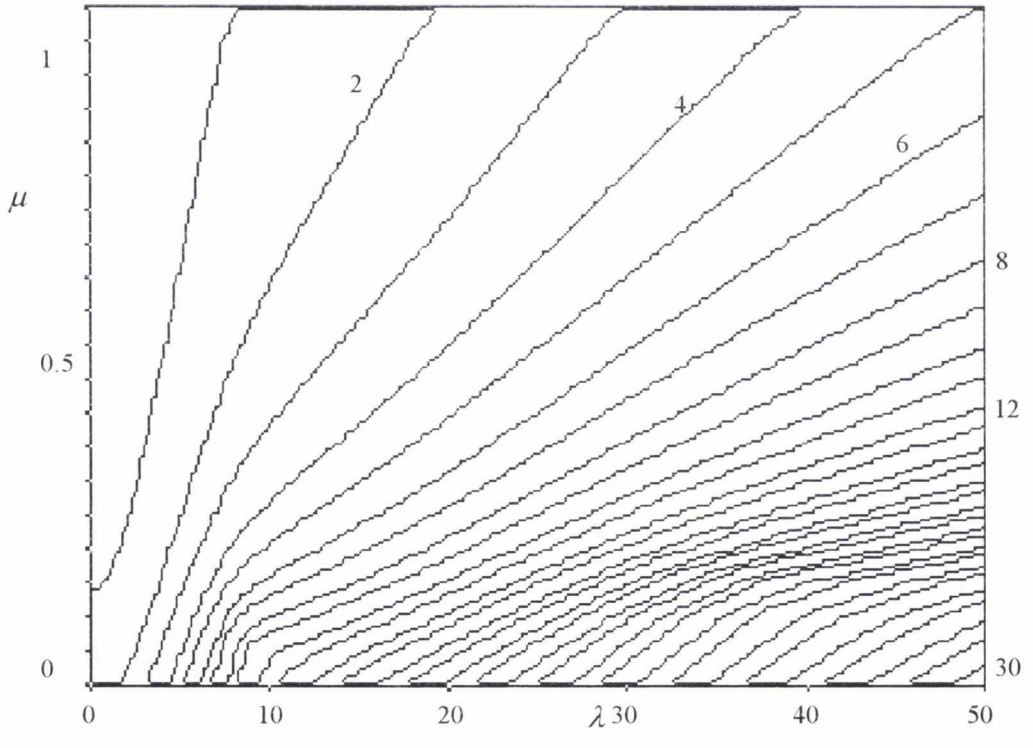

Figure A.2.68. Buckling load (P_{cr}/P_E) contours for the first mode in a non-homogeneous soil with constant soil stiffness ($F = 1$) and triangular shaft friction ($f_1 = 0$, $f_2 = 1$) for a fixed-free fully embedded beam.

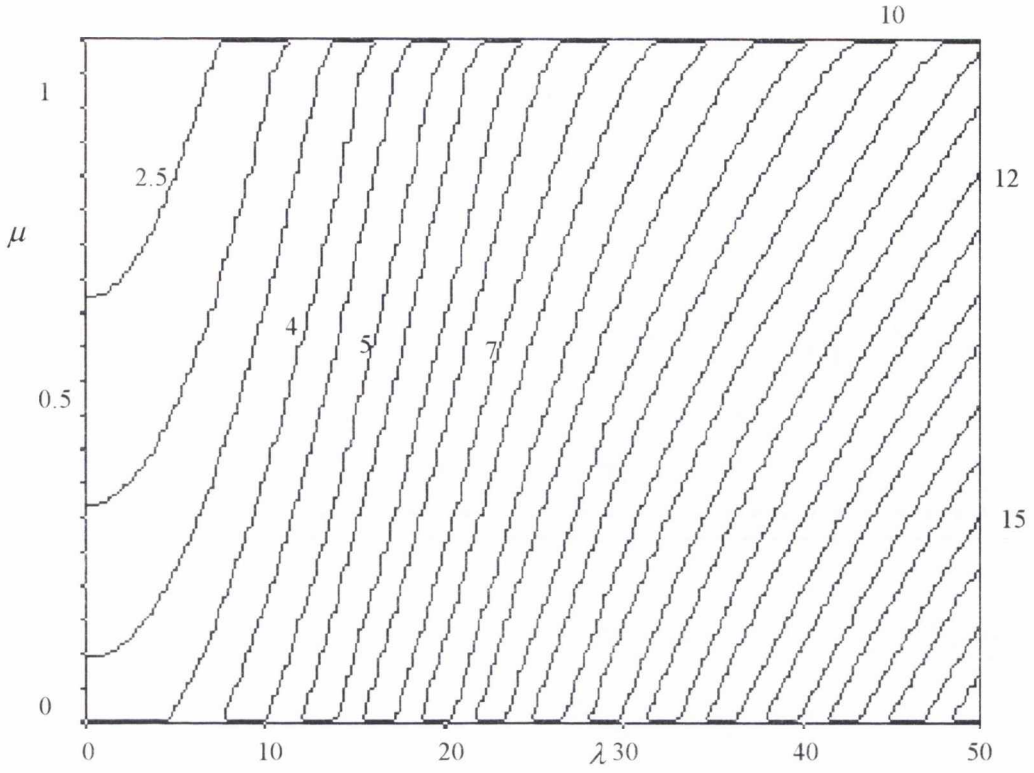

Figure A.2.69. Buckling load (P_{cr}/P_E) contours for the first mode in a non-homogeneous soil with constant soil stiffness ($F = 1$) and triangular shaft friction ($f_1 = 0$, $f_2 = 1$) for a pinned-fixed fully embedded beam.

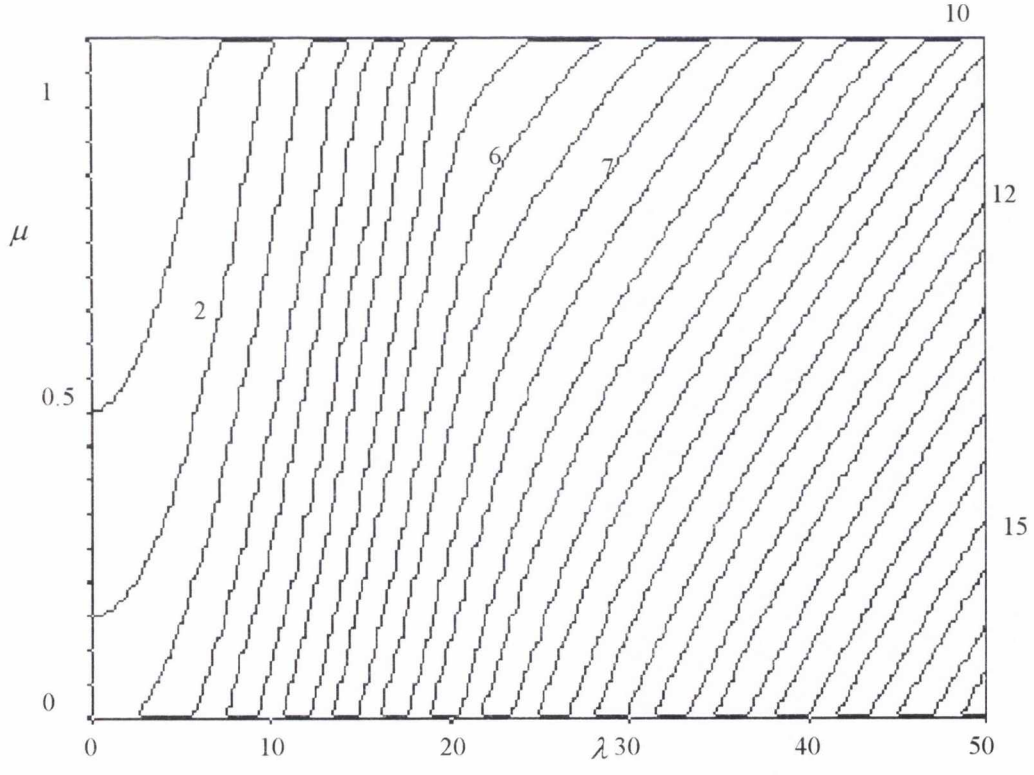

Figure A.2.70. Buckling load (P_{cr}/P_E) contours for the first mode in a non-homogeneous soil with constant soil stiffness ($F = 1$) and triangular shaft friction ($f_1 = 0$, $f_2 = 1$) for a pinned-pinned fully embedded beam.

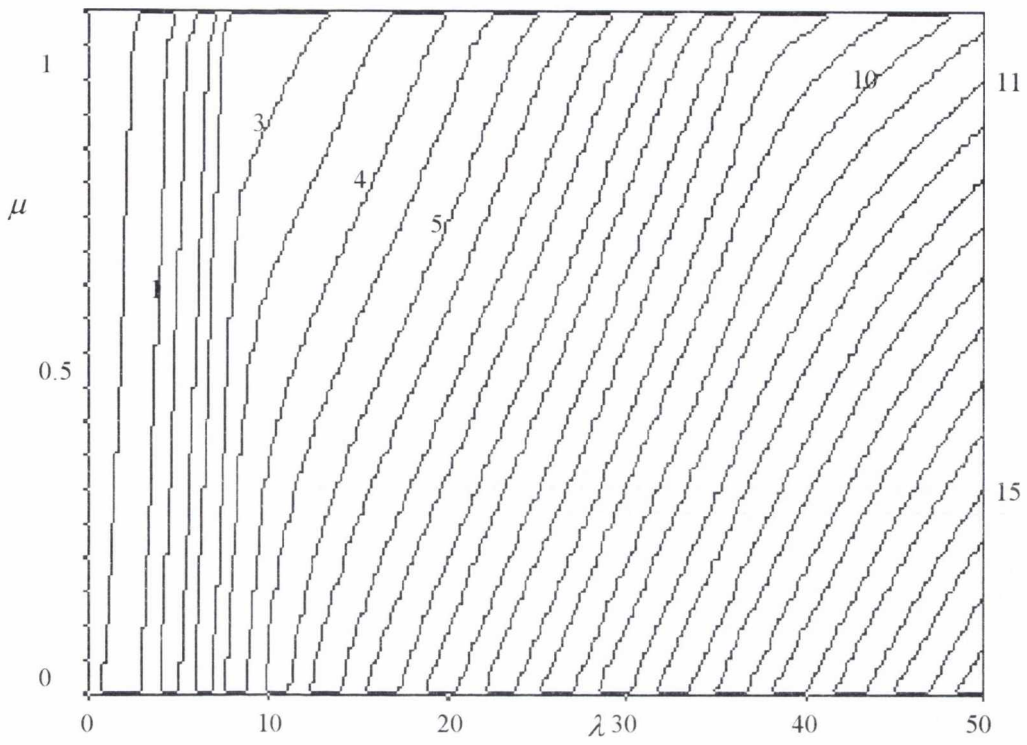

Figure A.2.71. Buckling load (P_{cr}/P_E) contours for the first mode in a non-homogeneous soil with constant soil stiffness ($F = 1$) and triangular shaft friction ($f_1 = 0, f_2 = 1$) for a pinned-no rotation fully embedded beam.

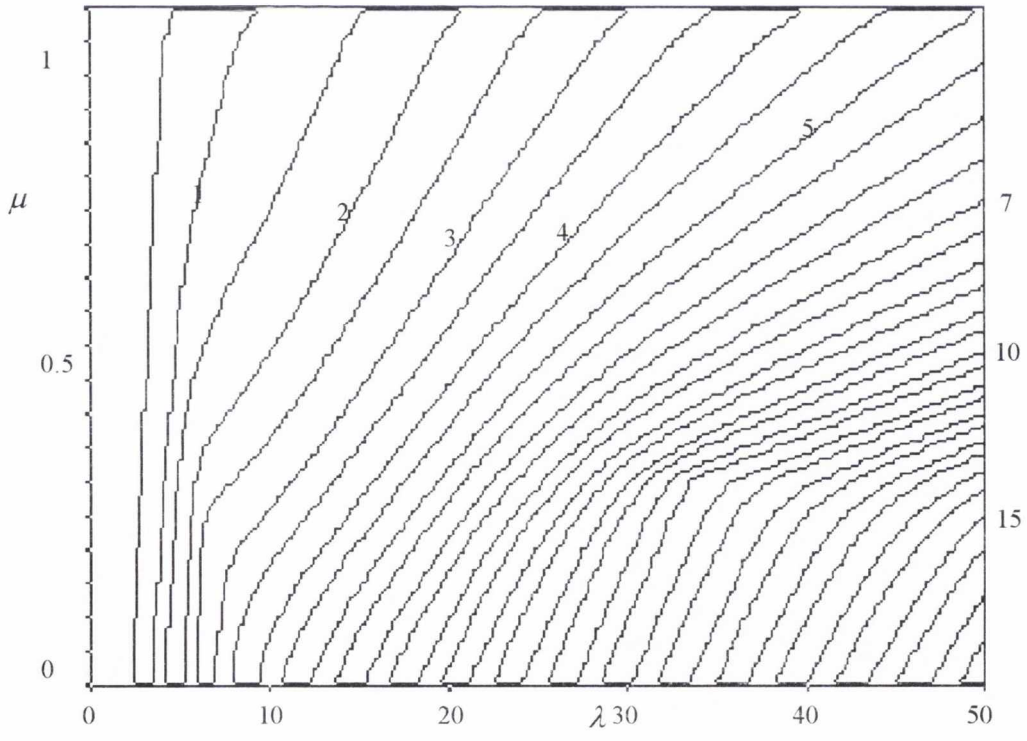

Figure A.2.72. Buckling load (P_{cr}/P_E) contours for the first mode in a non-homogeneous soil with constant soil stiffness ($F = 1$) and triangular shaft friction ($f_1 = 0, f_2 = 1$) for a pinned-free fully embedded beam.

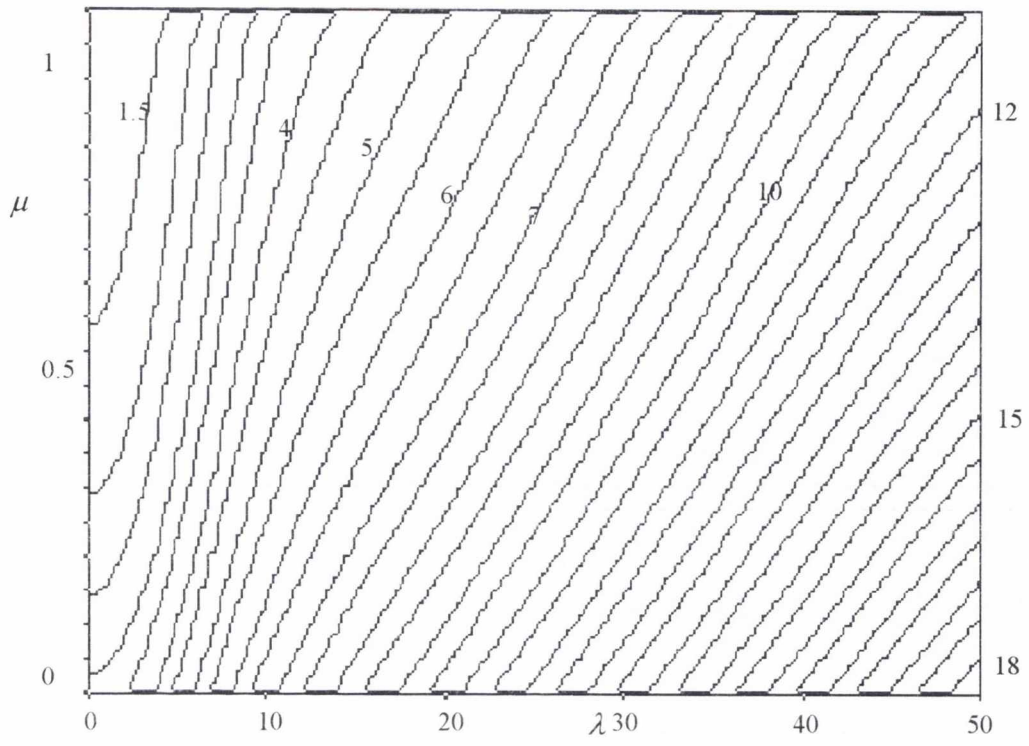

Figure A.2.73. Buckling load (P_{cr}/P_E) contours for the first mode in a non-homogeneous soil with constant soil stiffness ($F = 1$) and triangular shaft friction ($f_1 = 0, f_2 = 1$) for a no rotation-fixed fully embedded beam.

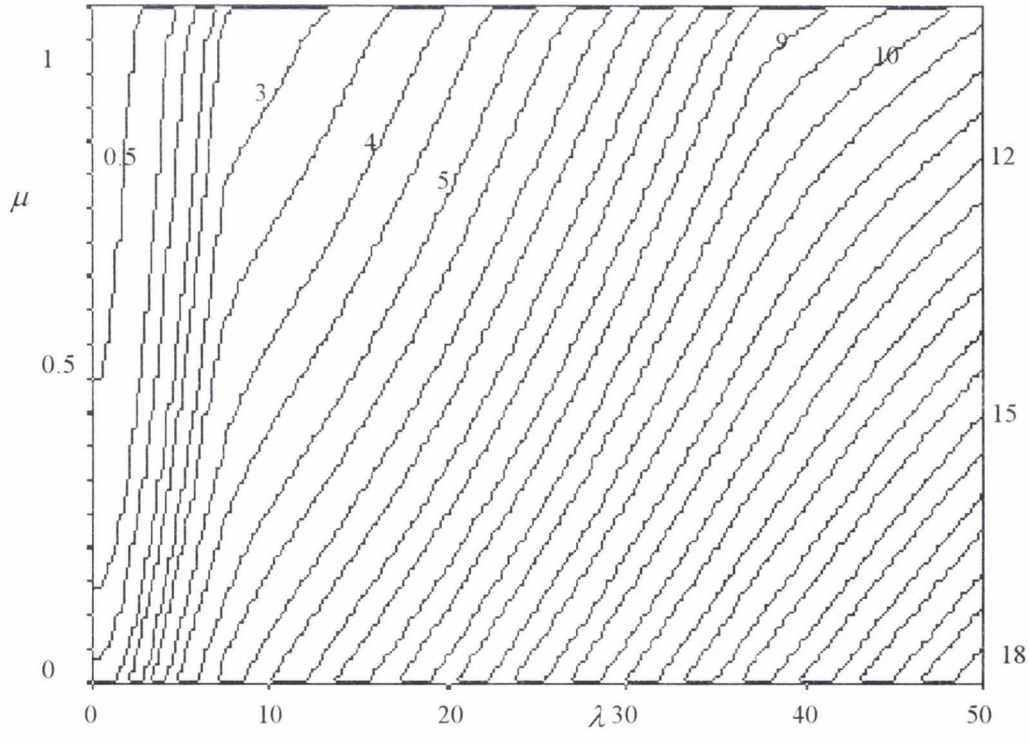

Figure A.2.74. Buckling load (P_{cr}/P_E) contours for the first mode in a non-homogeneous soil with constant soil stiffness ($F = 1$) and triangular shaft friction ($f_1 = 0, f_2 = 1$) for a no rotation-pinned fully embedded beam.

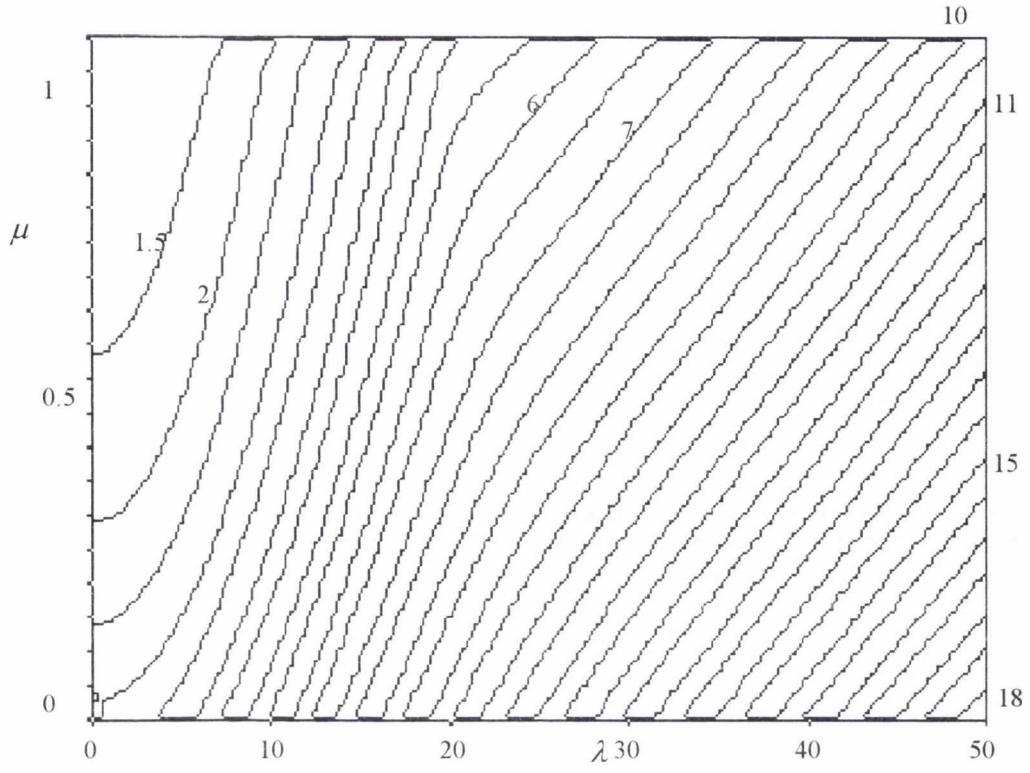

Figure A.2.75. Buckling load (P_{cr}/P_E) contours for the first mode in a non-homogeneous soil with constant soil stiffness ($F = 1$) and triangular shaft friction ($f_1 = 0$, $f_2 = 1$) for a no rotation-no rotation fully embedded beam.

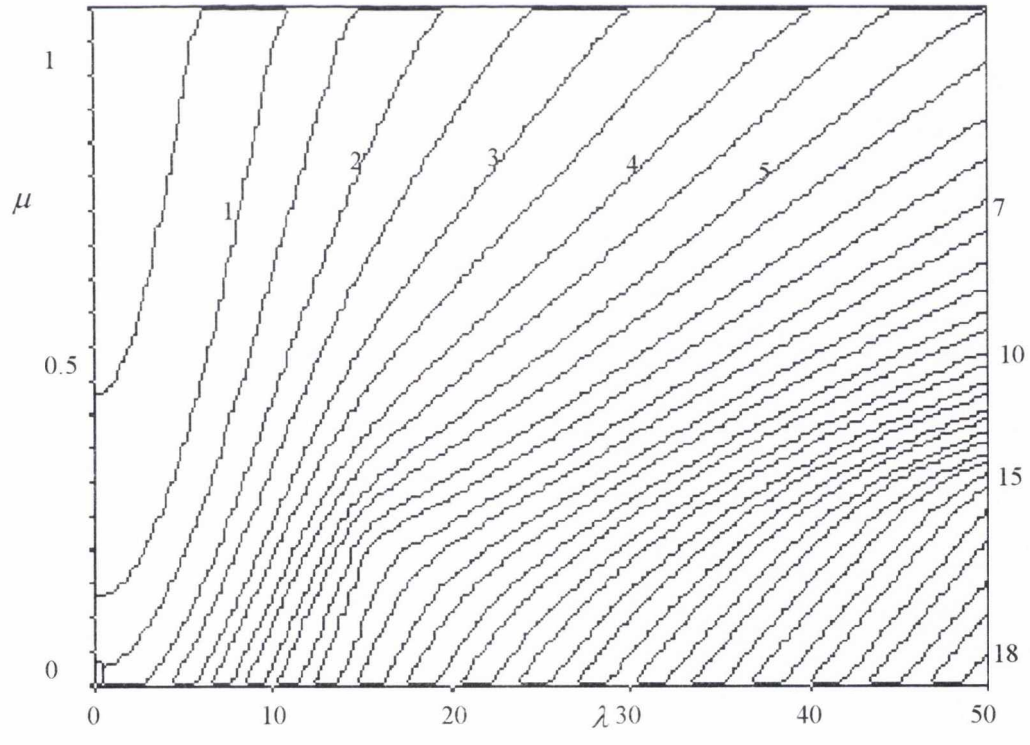

Figure A.2.76. Buckling load (P_{cr}/P_E) contours for the first mode in a non-homogeneous soil with constant soil stiffness ($F = 1$) and triangular shaft friction ($f_1 = 0$, $f_2 = 1$) for a no rotation-free fully embedded beam.

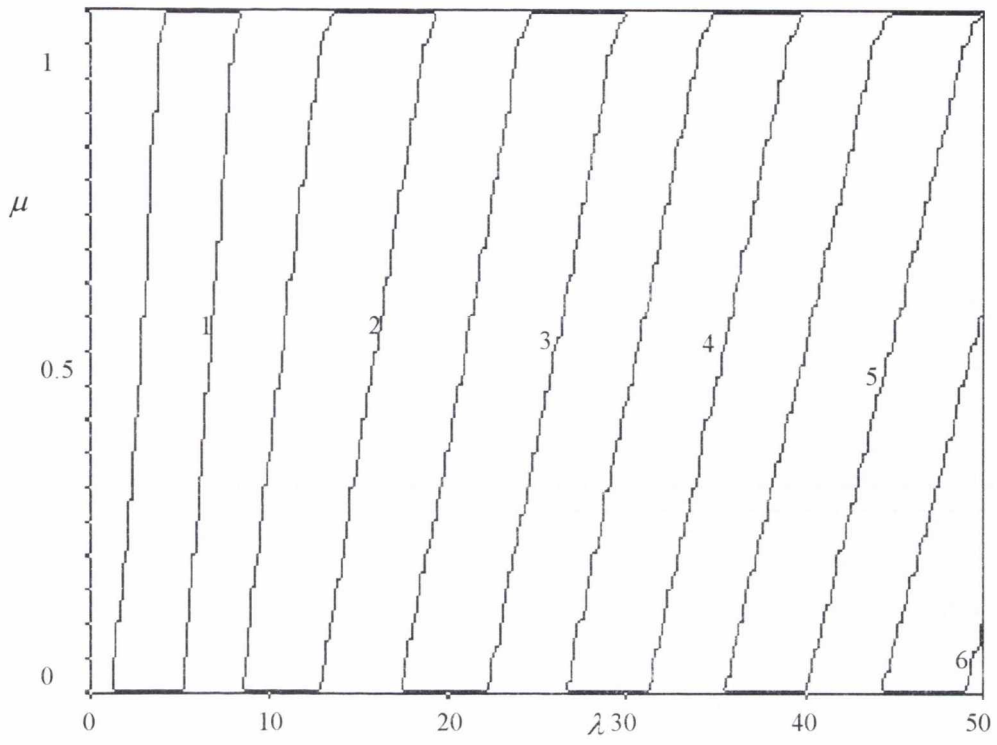

Figure A.2.77. Buckling load (P_{cr}/P_E) contours for the first mode in a non-homogeneous soil with constant soil stiffness ($F = 1$) and triangular shaft friction ($f_1 = 0$, $f_2 = 1$) for a free-fixed fully embedded beam.

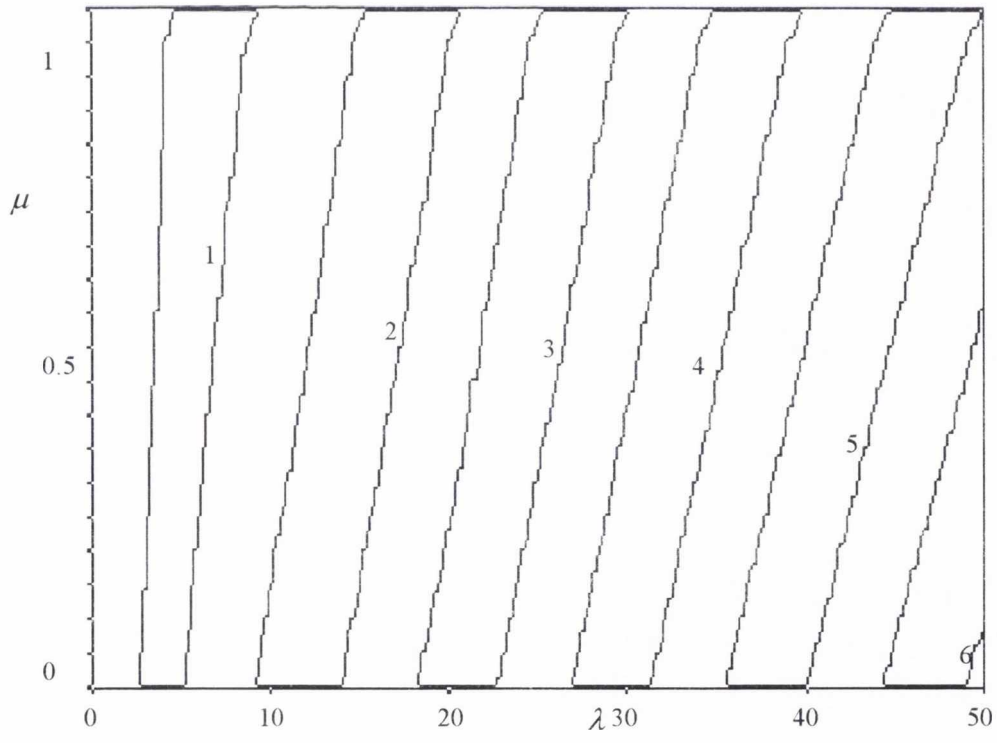

Figure A.2.78. Buckling load (P_{cr}/P_E) contours for the first mode in a non-homogeneous soil with constant soil stiffness ($F = 1$) and triangular shaft friction ($f_1 = 0$, $f_2 = 1$) for a free-pinned fully embedded beam.

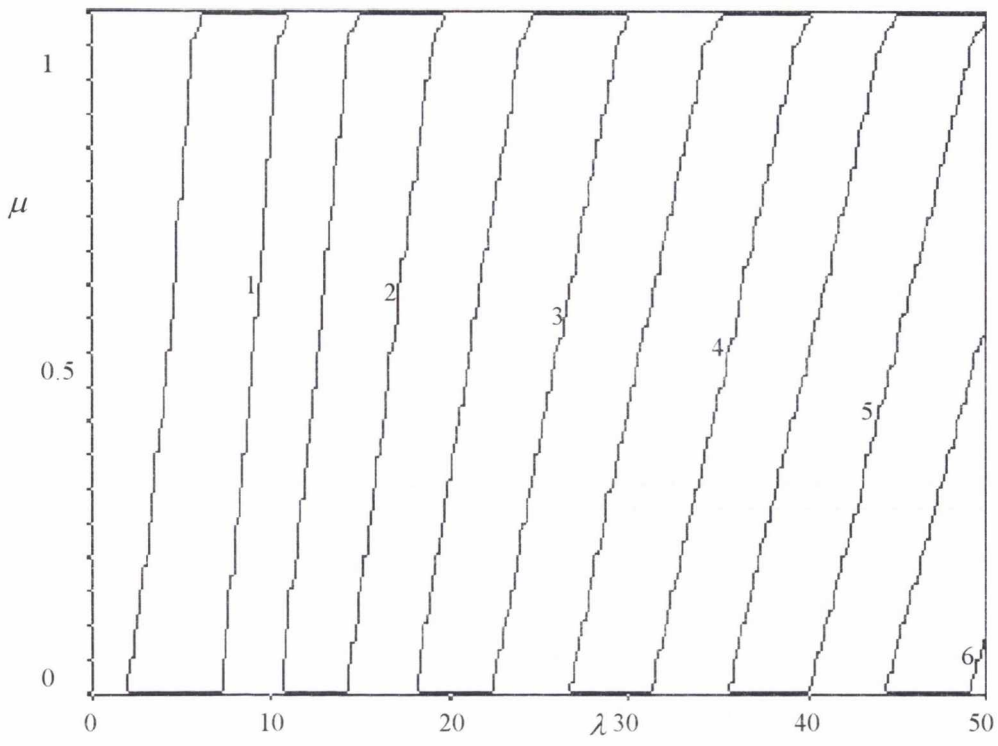

Figure A.2.79. Buckling load (P_{cr}/P_E) contours for the first mode in a non-homogeneous soil with constant soil stiffness ($F = 1$) and triangular shaft friction ($f_1 = 0, f_2 = 1$) for a free-no rotation fully embedded beam.

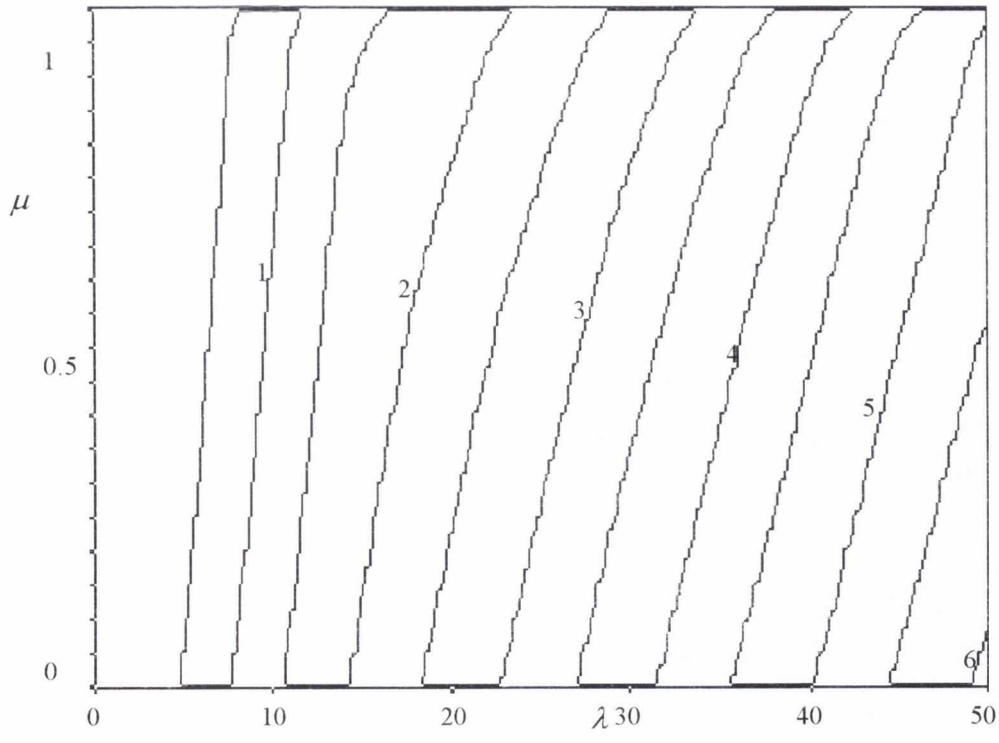

Figure A.2.80. Buckling load (P_{cr}/P_E) contours for the first mode in a non-homogeneous soil with constant soil stiffness ($F = 1$) and triangular shaft friction ($f_1 = 0, f_2 = 1$) for a free-free fully embedded beam.

Appendix A.3.

Non-homogeneous soils (F = 1, f_1 = 0, f_2 = 1)

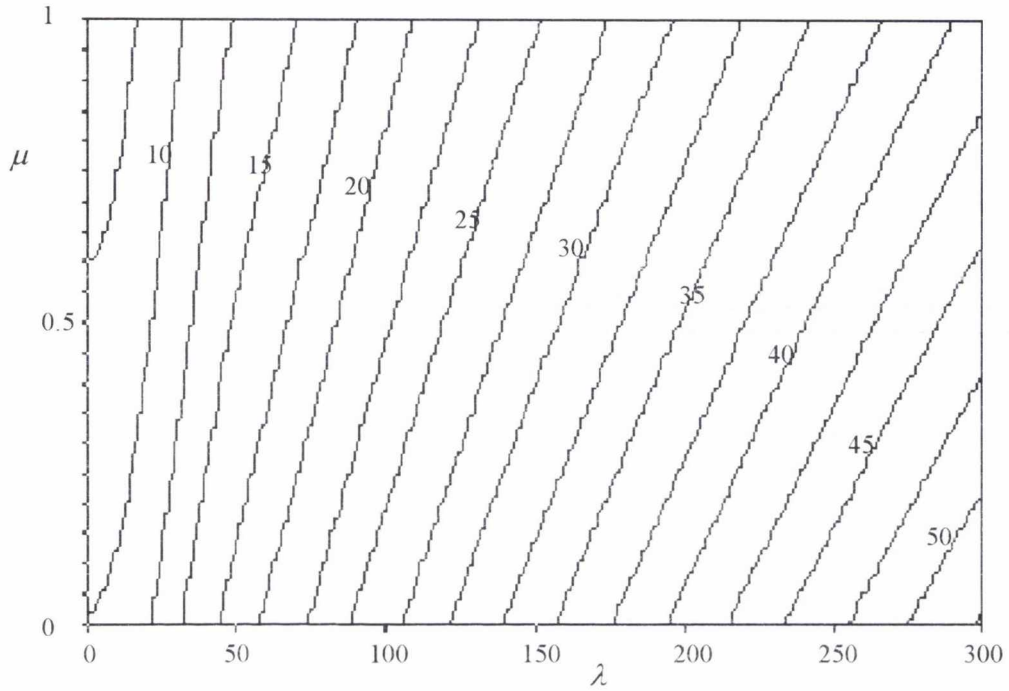

Figure A.3.1. Buckling load (P_{cr}/P_E) contours for the first mode in a homogeneous soil with constant soil stiffness (F = 1) and triangular shaft friction (f_1 = 0, f_2 = 1) for a fixed-fixed fully embedded beam.

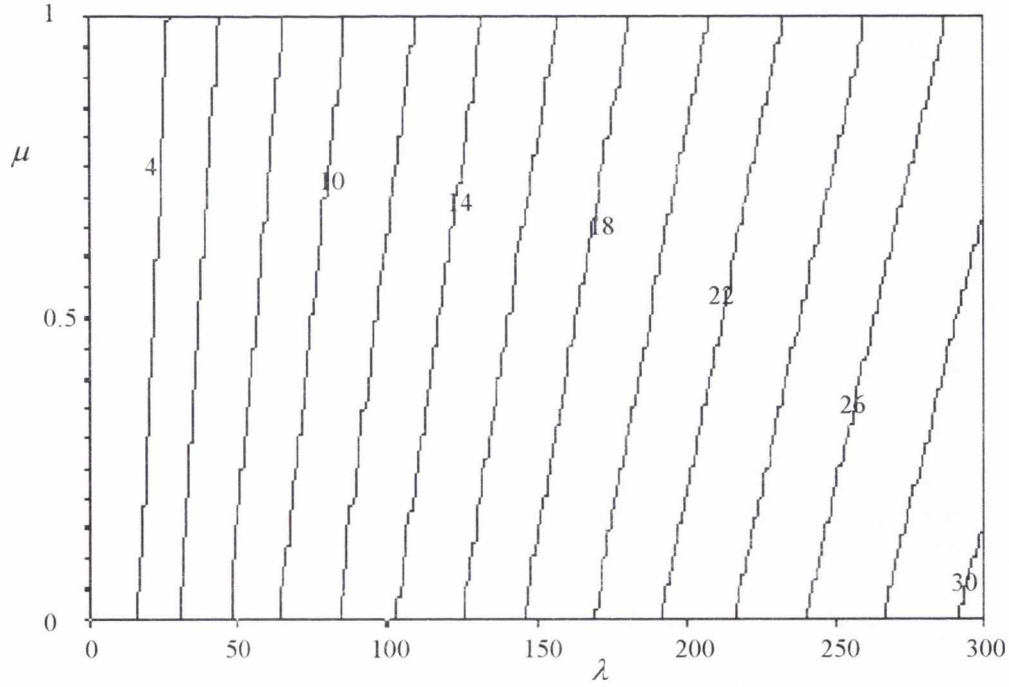

Figure A.3.2. Buckling load (P_{cr}/P_E) contours for the first mode in a homogeneous soil with constant soil stiffness (F = 1) and triangular shaft friction (f_1 = 0, f_2 = 1) for a pinned-fixed fully embedded beam.

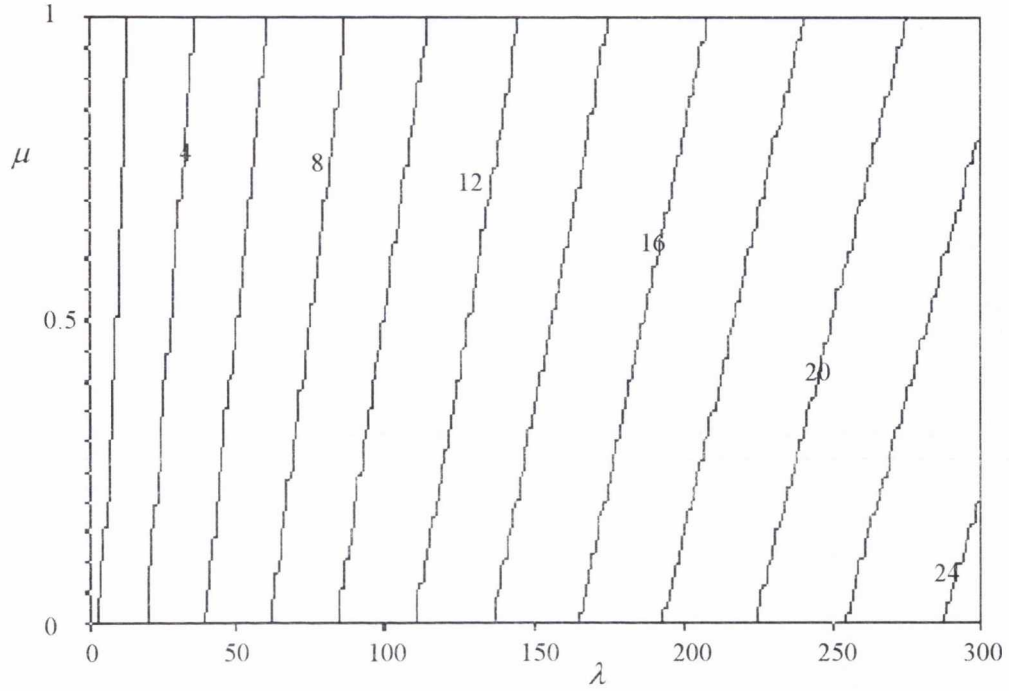

Figure A.3.3. Buckling load (P_{cr}/P_E) contours for the first mode in a homogeneous soil with constant soil stiffness ($F = 1$) and triangular shaft friction ($f_1 = 0, f_2 = 1$) for a no rotation-fixed fully embedded beam.

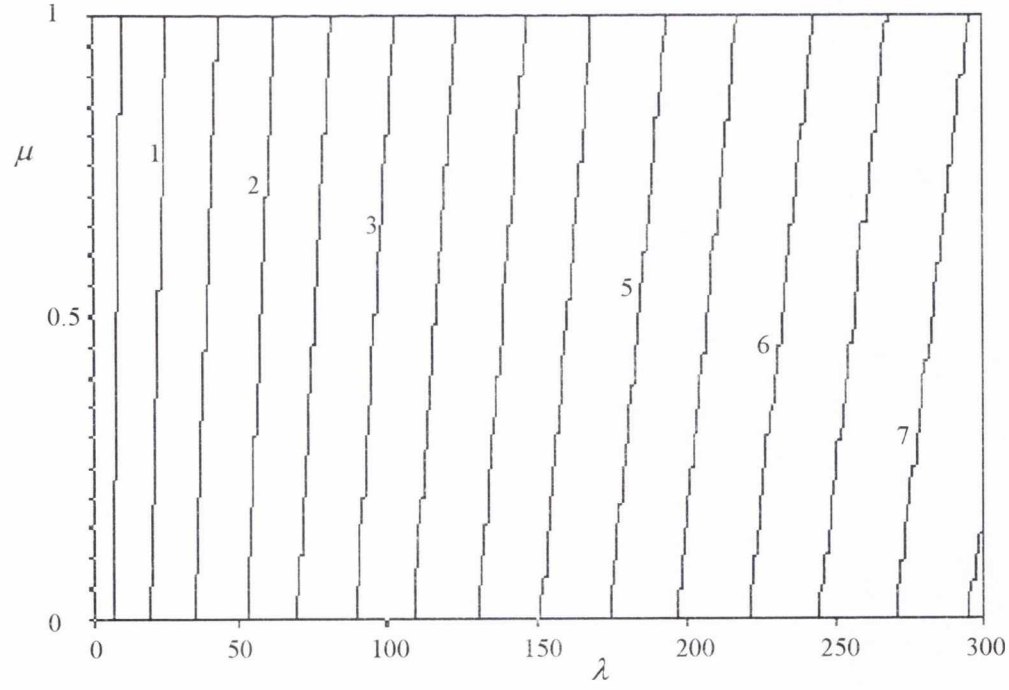

Figure A.3.4. Buckling load (P_{cr}/P_E) contours for the first mode in a homogeneous soil with constant soil stiffness ($F = 1$) and triangular shaft friction ($f_1 = 0, f_2 = 1$) for a free-fixed fully embedded beam.

Non-homogeneous soils (F = 0, $f_1 = f_2 = 0.5$)

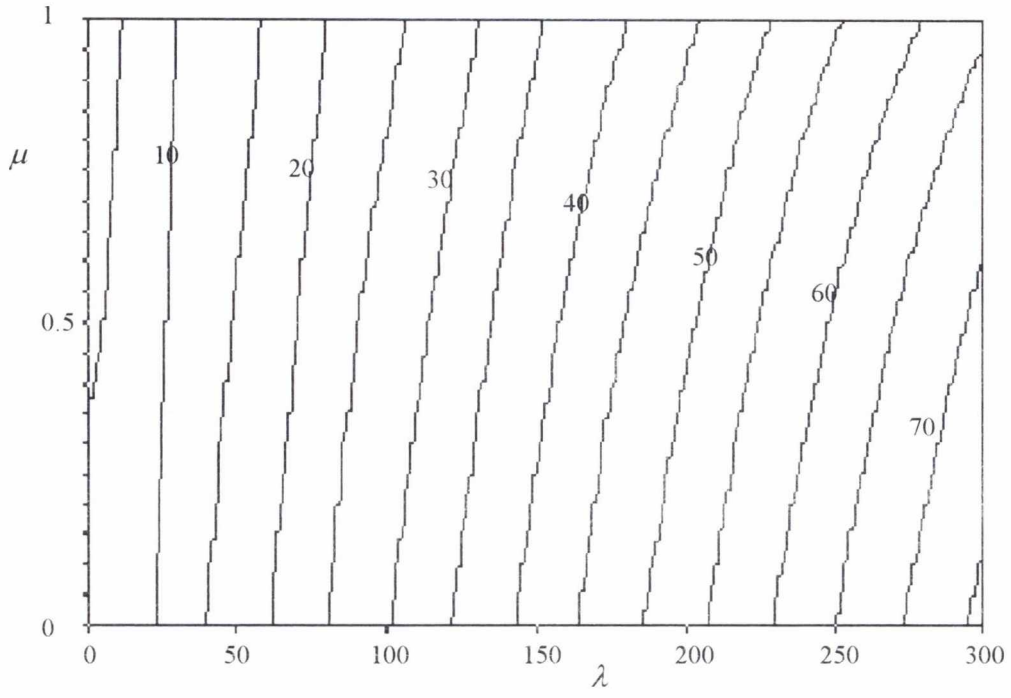

Figure A.3.5. Buckling load (P_{cr}/P_E) contours for the first mode in a homogeneous soil with triangular soil stiffness (F = 0) and constant shaft friction ($f_1 = f_2 = 0.5$) for a fixed-fixed fully embedded beam.

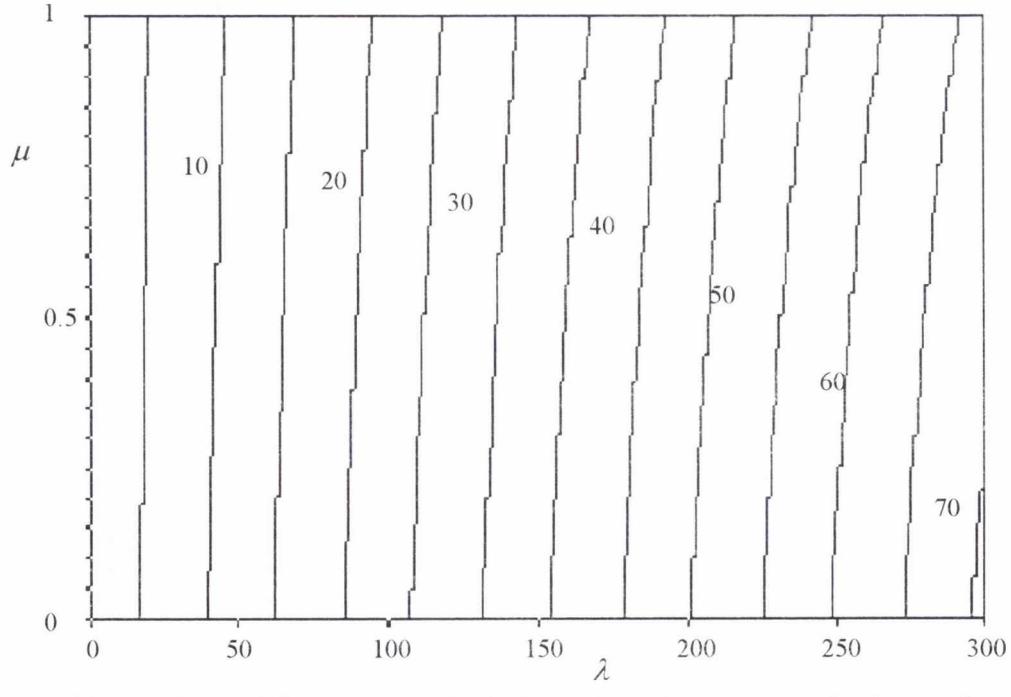

Figure A.3.6. Buckling load (P_{cr}/P_E) contours for the first mode in a homogeneous soil with triangular soil stiffness (F = 0) and constant shaft friction ($f_1 = f_2 = 0.5$) for a pinned-fixed fully embedded beam.

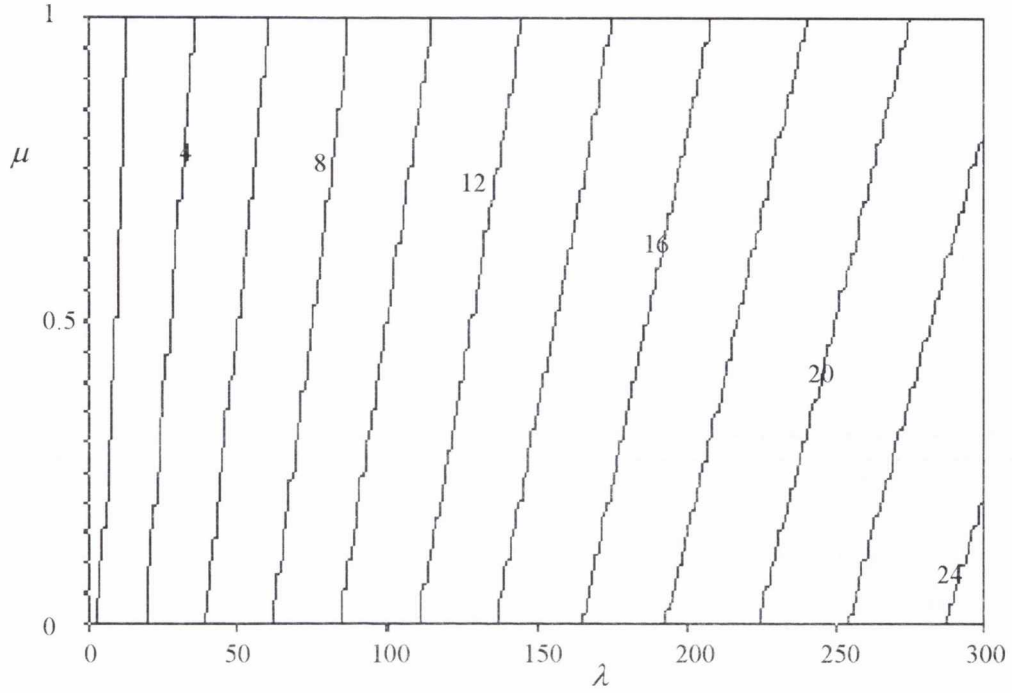

Figure A.3.7. Buckling load (P_{cr}/P_E) contours for the first mode in a homogeneous soil with triangular soil stiffness ($F = 0$) and constant shaft friction ($f_1 = f_2 = 0.5$) for a no rotation-fixed fully embedded beam.

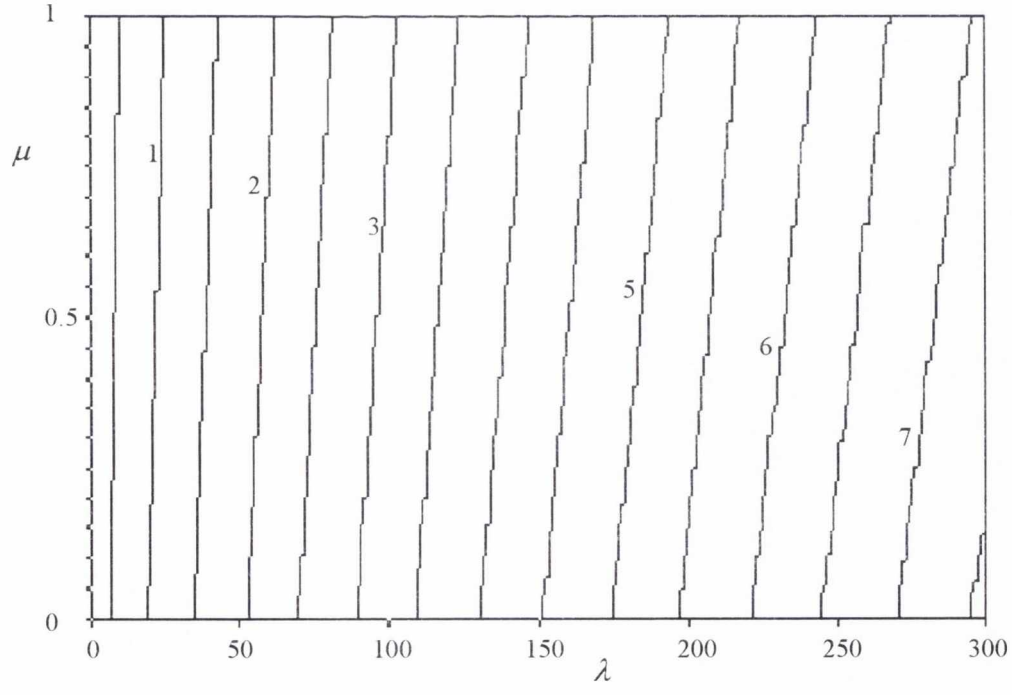

Figure A.3.8. Buckling load (P_{cr}/P_E) contours for the first mode in a homogeneous soil with triangular soil stiffness ($F = 0$) and constant shaft friction ($f_1 = f_2 = 0.5$) for a free-fixed fully embedded beam.

Non-homogeneous soils (F = 1, f_1 = 1, f_2 = 0)

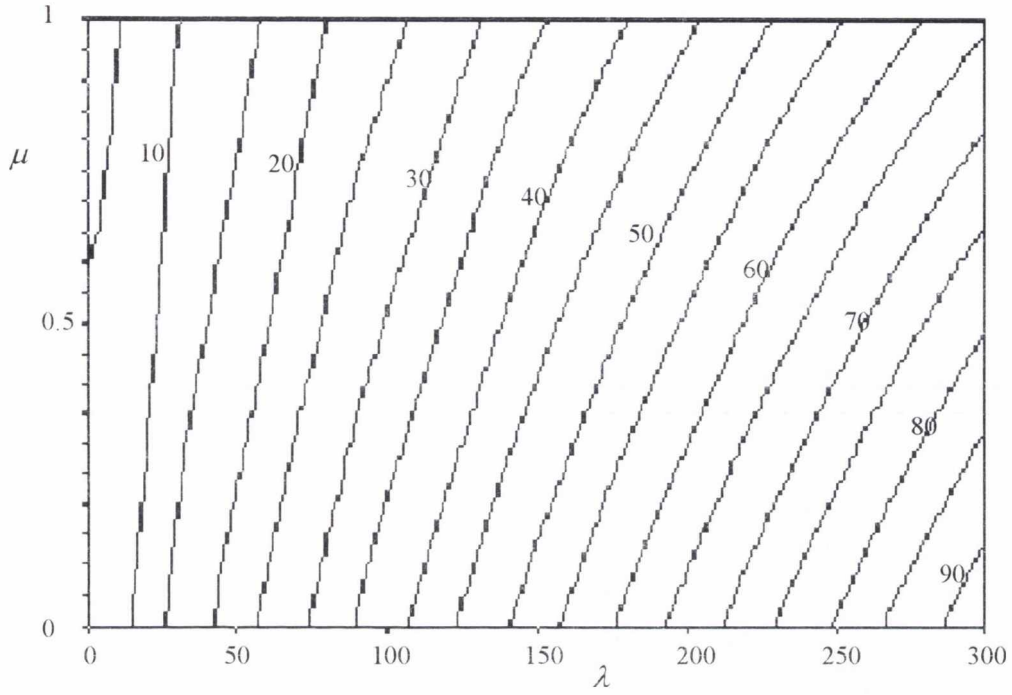

Figure A.3.9. Buckling load (P_{cr}/P_E) contours for the first mode in a homogeneous soil with constant soil stiffness (F = 1) and triangular shaft friction (f_1 = 1, f_2 = 0) for a fixed-fixed fully embedded beam.

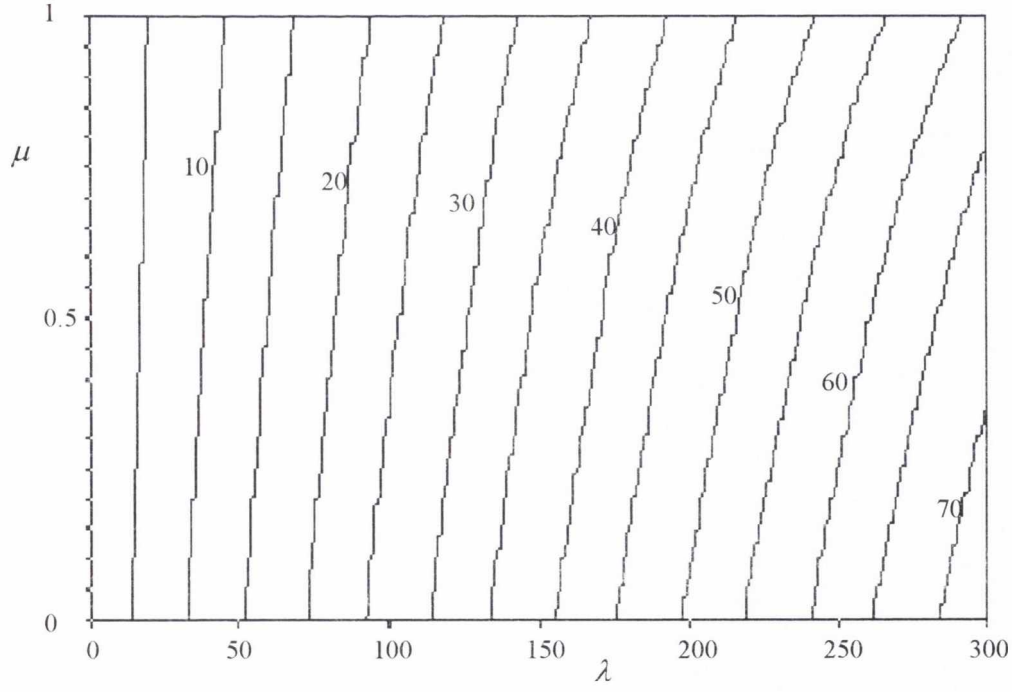

Figure A.3.10. Buckling load (P_{cr}/P_E) contours for the first mode in a homogeneous soil with constant soil stiffness (F = 1) and triangular shaft friction (f_1 = 1, f_2 = 0) for a pinned-fixed fully embedded beam.

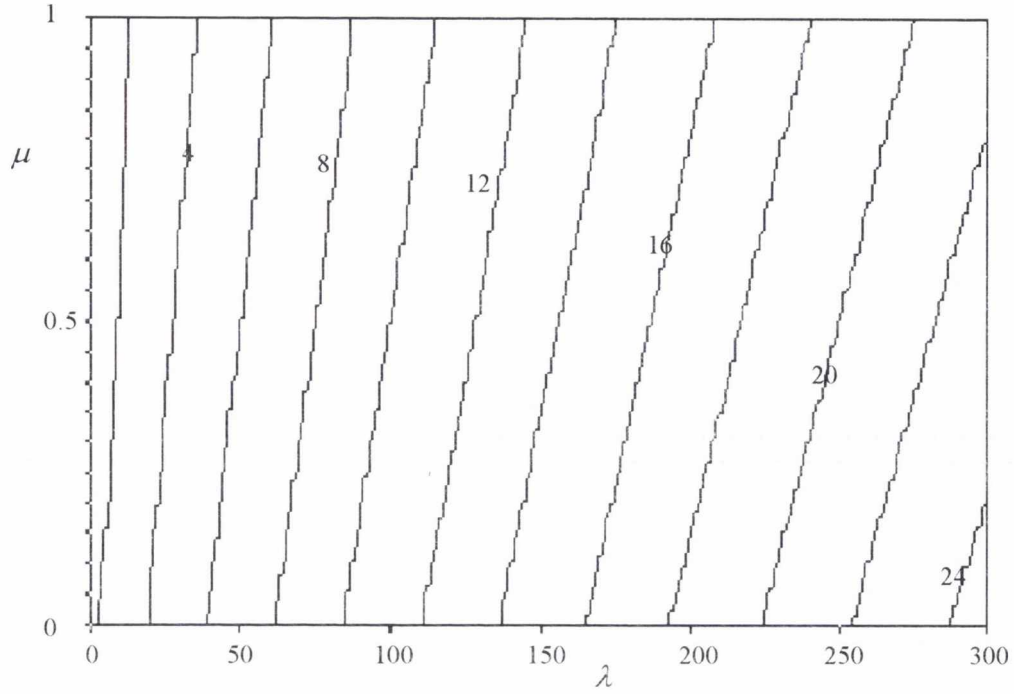

Figure A.3.11. Buckling load (P_{cr}/P_E) contours for the first mode in a homogeneous soil with constant soil stiffness ($F = 1$) and triangular shaft friction ($f_1 = 1, f_2 = 0$) for a no rotation-fixed fully embedded beam.

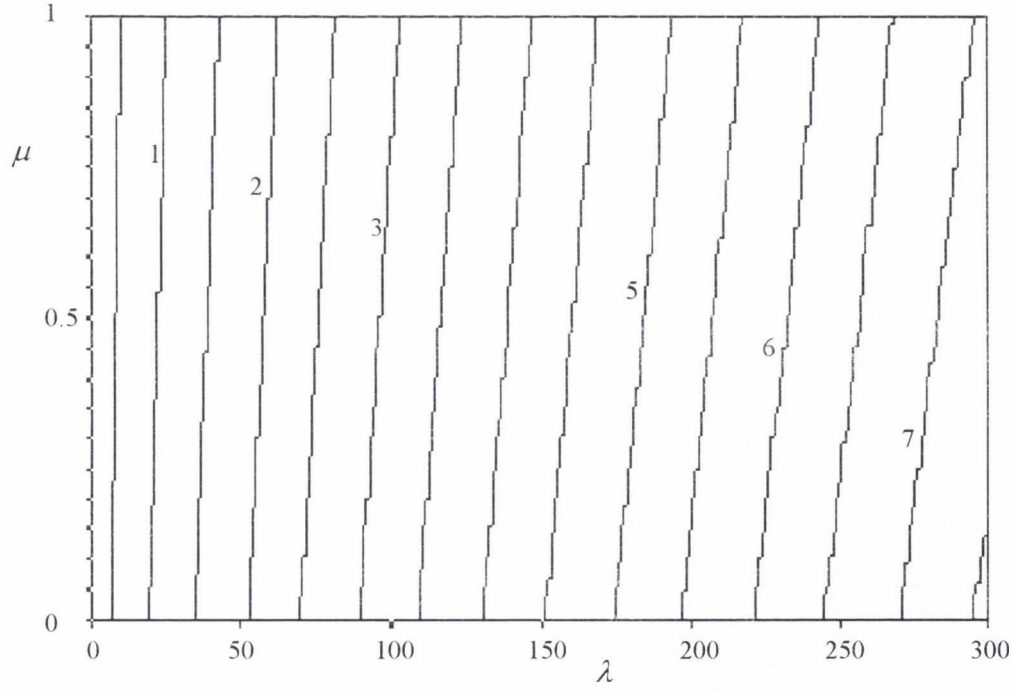

Figure A.3.12. Buckling load (P_{cr}/P_E) contours for the first mode in a homogeneous soil with constant soil stiffness ($F = 1$) and triangular shaft friction ($f_1 = 1, f_2 = 0$) for a free-fixed fully embedded beam.